

**Kristalline pyrazolhaltige Netzwerkstrukturen:
Von flexiblen Metall-organischen
Gerüstverbindungen zu Polymorphen**

Inaugural-Dissertation

zur Erlangung des Doktorgrades
der Mathematisch-Naturwissenschaftlichen Fakultät
der Heinrich-Heine-Universität Düsseldorf

vorgelegt von

Simon Philipp Millan
aus Ulm-Söflingen

Düsseldorf, Januar 2020

aus dem Institut für Anorganische Chemie und Strukturchemie I
der Heinrich-Heine-Universität Düsseldorf

Gedruckt mit der Genehmigung der
Mathematisch-Naturwissenschaftlichen Fakultät der
Heinrich-Heine-Universität Düsseldorf

Berichterstatter:

1. Prof. Dr. Christoph Janiak

2. Prof. Dr. Christian Ganter

Tag der mündlichen Prüfung:

Eidesstattliche Erklärung

Ich versichere an Eides statt, dass die vorliegende Dissertation von mir selbstständig, ohne unzulässige fremde Hilfe unter der Beachtung der „Grundsätze zur Sicherungsguter wissenschaftlicher Praxis“ an der Heinrich-Heine Universität Düsseldorf erstellt worden ist. Die aus fremden Quellen direkt oder indirekt übernommenen Gedankensowie Ergebnisse sind als solche kenntlich gemacht. Die Arbeit wurde bisher weder im Inland noch im Ausland in gleicher oder ähnlicher Form einer anderen Prüfungsbehörde vorgelegt. Es wurden keine früheren erfolglosen Promotionsversuche unternommen.

.....

Ort, Datum

.....

Unterschrift

Danksagung

Mein besonderer Dank gilt meinem Doktorvater Herrn Prof. Dr. Christoph Janiak, für die Möglichkeit der Promotion in seinem Arbeitskreis. Ich bedanke für die gewährten wissenschaftlichen Freiräume als Grundlage der Selbstentfaltung und seinen fachlichen Rat während meiner Zeit in seinem Arbeitskreis.

Herrn Prof. Dr. Christian Ganter danke ich recht herzlich für die freundliche Übernahme des Koreferates und seine stete Ansprechbarkeit.

Ich bin dem ganzen Arbeitskreis für die gute Zusammenarbeit und freundliche Arbeitsatmosphäre verpflichtet. Für die organisatorische Hilfe in vielen Fragen des Institutsalltags danke ich Birgit Tommes, Annette Ricken, Marcell Demandt, Jutta Bourgeois, Dietmar Frunzke und Claudia Schäfer.

Herrn Dr. Ishtvan Boldog danke ich besonders für seine großen Hilfsbereitschaft und seine Unterstützung in den letzten Zügen dieser Arbeit.

Jamal Nasir und Prof. Dr. Jörn Schmedt auf der Günne danke ich für die Festkörper-NMR Messungen und PD Dr. Oliver Weingart für die theoretischen Rechnungen zum Polymorph-Kapitel.

Maria Beuer, Dr. Peter Tommes und Ralf Bügel danke ich für die Anfertigung der NMR- und Massenspektren. Christina Scheelen danke ich herzlich für die DSC-Messungen.

Den von mir betreuten Bachelorstudenten Erik Milles und Guy Sado, sowie den Masterstudenten Philipp Brandt und Saskia Menzel danke ich für ihre arbeitsame Einstellung während der Anfertigung ihrer Abschlussarbeiten und den Beiträgen zu dieser Arbeit.

Während der Anfertigung einer Doktorarbeit verbringt man nicht nur Zeit im Labor zusammen. Hierbei bin ich einer Vielzahl an Personen aus dem Arbeitskreis für die schöne Zeit innerhalb und außerhalb der Universität und die Ablenkung vom „Promotionsstress“ dankbar: Anna Goldman, Alexander Nuhnen, Moritz Steinert, Dr. Emrah Hastürk, Dr. Serkan Gökpınar, Ülkü Gökcem-Demir, Dr. Sebastian Glomb, Dr. Dennis Dietrich, Dr. Gamall Makhloufi, Dr. Christian Heering, Dr. Biju Francis, Anna Kautz, Secil Öztürk, Philipp Brandt, Carsten Schlüsener, Stefanie Bügel, Bastian Moll, Alexa Schmitz, Tim-Oliver Knedel, Christian Jansen, Simon-Patrick Höfert, Yang-Yang Sun, Dr. Jun Liang, Dr. Karsten Klauke, Dr. Tobie Matemb Ma Ntep und Alexander Spieß.

Meiner Freundin Bea bin ich zu tiefst dankbar für ihre stetige Gelassenheit und Zuversicht und das Sie stets an meiner Seite war, wenn ich Sie gebraucht habe. Darüberhinaus habe

ich die unzähligen fachlichen Gespräche auf Augenhöhe sehr zu schätzen gewusst, welche an allen Ecken und Enden in diese Arbeit eingeflossen sind.

Zu guter Letzt danke ich meiner Familie insbesondere meinen Eltern für ihre stetige Unterstützung und den bedingungslosen Rückhalt während meiner gesamten Ausbildung. Ohne diese Grundlage wäre diese Arbeit nicht möglich gewesen und den Anteil an dieser Arbeit ist auch nicht in Worte zu fassen.

Düsseldorf im Januar 2020

Für meine Eltern

Der beste Weg, eine gute Idee zu haben, ist, viele Ideen zu haben.

Linus Pauling (1901 - 1994)

Kurzzusammenfassung

Pyrazole sind aufgrund ihrer vielfältigen Koordinationschemie und supramolekularer Wechselwirkungen prädestiniert ausgedehnte Netzwerkstrukturen im Festkörper auszubilden. Im Rahmen der vorliegenden Arbeit wurden sowohl bifunktionelle pyrazolhaltige Liganden zur Synthese Metall-organischer Gerüstverbindungen als auch Festkörperstrukturen eines Bispyrazols und einige Koordinationsverbindungen untersucht.

Es wurden die beiden neuen MOFs **rtl-[M(Hlsa-az-dmpz)]** ($M = Zn, Cu$) mit dem bifunktionellen Liganden 5-(4-(3,5-Dimethyl-1H-pyrazolyl)azo)isophthalat synthetisiert, welche die Hypothese verifizieren, dass auch mit Dicarboxylat-Pyrazol-Liganden, MOFs auf Basis des sogenannten „supramolecular-building-layer“-Ansatzes synthetisiert werden können. **rtl-Cu** vollzieht bei der Aktivierung einen reversiblen Phasenwechsel in eine nichtporöse Phase. **rtl-Cu-act.** zeigt ein S-förmiges Adsorptionsprofil vom Typ F-IV gepaart mit hohen Sättigungsaufnahmen von $360 \text{ cm}^3 \text{ g}^{-1}$ für N_2 bei 77 K, $310 \text{ cm}^3 \text{ g}^{-1}$ für CO_2 bei 195 K, $317 \text{ cm}^3 \text{ g}^{-1}$ für Ar bei 87 K und $270 \text{ cm}^3 \text{ g}^{-1}$ für CH_4 bei 112 K. Diese Werte liegen unter den höchsten der berichteten für flexible MOF-Materialien mit diesem Isothermen-Typ, welche aufgrund ihrer hohen potentiellen Arbeitskapazitäten für Gasspeicher- und Liefersysteme diskutiert werden.

Weiterhin wurden mit **H₂azbpz-I** und **H₂azbpz-II** zwei Polymorphe des 4,4'-Azobis(3,5-dimethyl-1H-pyrazols) isoliert, welche sich durch den Einbau zweier unterschiedlicher symmetrischer Konformere unterscheiden. Die beiden Polymorphe bilden strukturell ähnliche zweidimensionale **hcb**-Schichten, diese zeigen jedoch in **H₂azbpz-I** eine AA- und in **H₂azbpz-II** eine AB-Stapelfolge. Beide Polymorphe wurden ausführlich charakterisiert und ihre Phasentransformationen ineinander untersucht. Die Festkörperlandschaft von **H₂azbpz** wird vom Hemihydrat komplettiert, welches ein **dia**-Netzwerk mit einem pseudotetraedrischen H_2O -Molekül als Knotenpunkt bildet. $\text{H}_2\text{azbpz}\cdot0.5\text{H}_2\text{O}$ kann dementsprechend als supramolekulares Analogon des kubischen Eispolymer **I_c** angesehen werden.

Darüber hinaus beinhalten die Metall-Komplexe $[\text{Cu}(\text{NO}_3)_2(\text{H}_2\text{O})_2(\text{H}_2\text{azbpz})_2]\cdot2\text{H}_2\text{O}$ und $[\text{Ni}(\text{H}_2\text{O})_4(\text{H}_2\text{azbpz})_2](\text{NO}_3)_2\cdot2\text{H}_2\text{O}$ **H₂azbpz** als mono-dentaten Liganden und für die Erklärung der ausgebildeten supramolekularen Architekturen wurde insbesondere das Zusammenspiel aus Wasserstoffbrückenbindungsringen, Azo-Pyrazol π -Wechselwirkungen und der eingebauten molekularen Form diskutiert. Das Koordinationspolymer $[\text{Zn}(\text{Hazbpz})\text{NO}_3]\cdot$ mit Hazbpz⁻ als Pyrazol-Pyrazolat-Liganden zeigt in seiner Ethanolsorption ebenfalls ein interessantes S-förmiges Profil mit einer maximalen Aufnahmekapazität von 276 mg g⁻¹.

Abstract

Pyrazoles are predestined to construct extended network structures in the solid state on account of their coordination modes as well as their supramolecular interactions. In this work bifunctional pyrazole-containing ligands are used to synthesize metal-organic frameworks and the solid state structures of a bispyrazole and some of its coordination compounds were investigated.

The two new MOFs **rtl**-[M(H₁sa-az-dmpz)] (M = Zn, Cu) with the bifunctional ligand 5-(4-(3,5-dimethyl-1*H*-pyrazolyl)azo)isophthalat were obtained, verifying the hypothesis that such dicarboxylate-pyrazole ligands can be employed to construct MOFs under the “supramolecular-building-layer”-approach. **rtl**-Cu displays a reversible phase-change into a non-porous phase upon activation. Consequently, activated **rtl**-Cu shows S-shaped Type F-IV adsorption profiles together with high saturation uptakes of 360 cm³ g⁻¹ for N₂ at 77 K, 310 cm³ g⁻¹ for CO₂ at 195 K, 317 cm³ g⁻¹ for Ar at 87 K and 270 cm³ g⁻¹ for CH₄ at 112 K. These values belong to the highest reported for flexible MOF materials with such adsorption profiles, which are, *inter alia*, discussed in gas storage and –delivery systems due to their high working capacities.

As for bispyrazoles, the two polymorphs H₂azbpz-**I** and H₂azbpz-**II** of 4,4'-azobis(3,5-dimethyl-1*H*-pyrazol), who incorporate different symmetrical planar conformers, have been synthesized. Both polymorphs assemble via NH···N catemers into comparable two dimensional **hcb**-sheets. Nevertheless, the difference on the molecular level, leads to a staggered AA-packing of the sheets in polymorph -**I** and an eclipsed AB-packing in -**II**. Both polymorphs were thoroughly characterized and their phase transformations were investigated. The solid state landscape of H₂azbpz is complemented by its hemihydrate, whose **dia**-topology is induced by a pseudo-tetrahedral water molecule. Therefore, H₂azbpz·0.5H₂O can be interpreted as a supramolecular analogue of the cubic ice polymorph I_c.

The isolated metal-complexes [Cu(NO₃)₂(H₂O)₂(H₂azbpz)₂]·2H₂O und [Ni(H₂O)₄(H₂azbpz)₂](NO₃)₂·2H₂O contain H₂azbpz as a mono-dentate ligand. Their supramolecular architectures were analyzed regarding the interplay of hydrogen-bonded rings, azo-pyrazole π interactions and the integrated molecular form in particular. The coordination polymer [Zn(Hazbpz)NO₃], containing H₂azbpz⁻ as a pyrazole-pyrazolate ligand, also shows an S-shaped ethanol sorption profile with a maximum uptake of 276 mg g⁻¹.

Inhaltsverzeichnis

Kurzzusammenfassung	I
Abstract	II
Abkürzungsverzeichnis	V
1. Einleitung	1
1.1 Metall-organische Gerüstverbindungen	1
1.2 Überblick zum Crystal Engineering anhand von strukturellen Analogismen und Synergismen von Carbonsäuren und Pyrazolen	22
2. Motivation	32
3. Kumulativer Teil	33
3.1 rtl-M-MOFs (M = Cu, Zn) with a T-shaped bifunctional pyrazole-isophthalate ligand showing flexibility and S-shaped Type F-IV sorption isotherms with high saturation uptakes for M = Cu	36
3.2 Solid-state landscape of 4,4'-azobis(3,5-dimethyl-1H-pyrazole) with the isolation of conformer-dependent polymorphs	88
3.3 Metal-4,4'-azobis(3,5-dimethyl-1H-pyrazole) complexes with 7- and 9-membered hydrogen-bonded rings originating from the pyrrolic N-H function	156
3.4 A 2D Zinc coordination polymer built from the mono-deprotonated 4,4'-azobis(3,5-dimethyl-1H-pyrazole) ligand	198
3.5 Incorporating the thiazolo[5,4-d]thiazole unit into a coordination polymer with interdigitated structure	219
4. Weitere Ergebnisse	236
4.1 Synthese und Struktur von [Zn(lsa-az-tmpz)]	236
4.2 Synthese von 5-(3,5-dimethyl-1H-pyrazol-4-yl)isophthalsäure (H ₃ lsa-dmpz)	241
4.3 Synthese und Struktur von [Cu(Me ₂ lsa-acac)]·H ₂ O	243
5. Zusammenfassung	247
6. Experimentalteil	255
6.1 Verwendete Geräte	255
6.2 Weitere Synthesen	257
6.2.1 Synthese des 5-(3-(2,4-Pentandionyl)isophthalsäuredimethylesters	257

6.2.2	Synthese des	
	5-(4-(3,5-Dimethyl-1H-pyrazolyl))isophthalsäuredimethylesters.....	259
6.2.3	Synthese der 5-(4-(3,5-Dimethyl-1H-pyrazolyl))isophthalsäure	260
6.2.4	Synthese des	
	5-(4-(1,3,5-Trimethyl-1H-pyrazolyl)azo)isophthalsäuredimethylesters	261
6.2.5	Synthese der 5-(4-(1,3,5-Trimethyl-1H-pyrazolyl)azo)isophthalsäure	262
	Literaturverzeichnis	263
	Publikationsliste.....	278
	Spektrenanhang	280

Abkürzungsverzeichnis

BET	Brunauer-Emmett-Teller
CCDC	Cambridge crystallographic data center
CIDs	Coordination-polymers with interdigitated structures
COF(s)	Covalent organic framework(s)
DMF	<i>N,N</i> -Dimethylformamid
ELM	Elastic layered materials
HKUST	Hong Kong University of Science and Technology
MIL	Materiaux de l'Institute Lavoisier
MOF(s)	Metal-organic framework(s)
MOP(s)	Metal-organic polyhedral
PCM	Phase change materials
RCSR	Reticular Chemistry Structure Resource
SBB	Supramolecular building block
SBL	Supramolecular building layer
SBU(s)	Secondary building unit(s)
TBU(s)	Tertiary building unit(s)
ZIF(s)	Zeolitic-imidazolate framework(s)

Liganden

adi	Adiponitril
Bpy	4,4'-Bipyridin
Me ₄ bpzb ²⁻	1,4-bis(3,5-dimethylpyrazolat)benzol
H ₂ Me ₄ bpz	4,4'-bis(3,5-dimethyl-1 <i>H</i> -pyrazol)
Hdmpz	3,5-Dimethylpyrazol

dmpzca ²⁻	4-(3,5-Dimethylpyrazolat)carboxylat
Dmtdc ²⁻	3,4-Dimethylthieno[2,3-b]thiophene-2,5-dicarboxylat
Dpe	1,2-Di(4-pyridyl)ethylen
H ₂ Me ₄ mbpz	4,4'-Methylenebis(3,5-dimethyl-1 <i>H</i> -pyrazol)
5-NO ₂ -Ip	5-Nitroisophthalat
bdp ²⁻	1,4-Phenylendipyrazolat
pzca ²⁻	Pyrazolat-4-carboxylat
l _{sa} -pz ³⁻	5-(1 <i>H</i> -pyrazol-4-yl)-isophthalat
bdc ²⁻	Terephthalat
Me ₄ bpz ²⁻	3,3',5,5'-Tetramethyl-4,4'-bipyrazolat
btc ³⁻	Trimesat
pz ⁻	Pyrazolat

Topologien

ant	Anatasund
anh	hexagonaler Anatas
apo	α -Bleioxid
brk	Brookit
dia	Diamant
flu	Fluorit
hcb	Honeycomb
hxl	hexagonal lattice
lon	Lonsdaleit
kgm	Kagomé
kgd	Kagomé dual
nbo	Niob(II)oxid),

pcu	primitive cubic net
pts	Platin(II)-sulfid
pyr	Pyrit
rtl	Rutil
sql	square lattice
tbo	twisted boracite

1. Einleitung

1.1 Metall-organische Gerüstverbindungen

Metall-organische Gerüstverbindungen (engl. metal-organic frameworks, MOFs), welche durch die Kombination von Metallionen und organischen Liganden gekennzeichnet sind, stellen laut einer Empfehlung der IUPAC potentiell poröse zwei- und dreidimensionale Koordinationsnetzwerke dar.¹⁻² Dieser Definition innewohnend ist eine hierarchische Begriffsabgrenzung ausgehend von den Begriffen Koordinationspolymer über Koordinationsnetzwerk (siehe Abbildung 1).

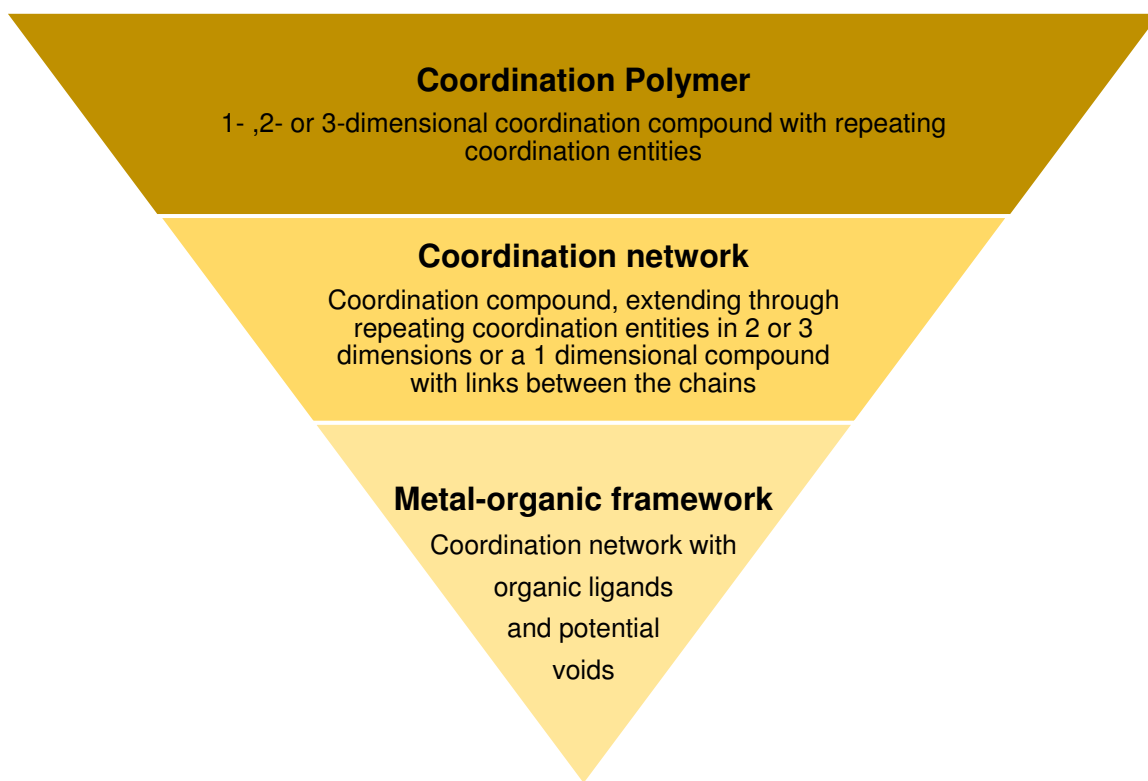


Abbildung 1. Überblick über die hierarchische Abgrenzung der Begriffe Koordinationspolymer, Koordinationsnetzwerk, und Metall-organische Gerüstverbindung (eigene Darstellung).

Die Niederschlagung des Begriffs der Porosität in der IUPAC-Definition für Metall-organische Gerüstverbindungen manifestiert die davor schon vorhandene enge Verknüpfung beider Begriffe, welche die durch Ionen und Moleküle gefüllten offenen Strukturen dieser Materialien seit jeher ausgelöst haben. Interessanterweise haben schon frühe Arbeiten an molekularen Werner-Komplexen der Zusammensetzung $[M(4\text{-methylpyridine})_4(\text{SCN})_2]$ (mit

$M = Co^{2+}, Ni^{2+}$ und Mn^{2+}) die generelle Möglichkeit der Porosität von Koordinationsverbindungen hinsichtlich von Gasen gezeigt.³

Grundlegend für den Bereich der Koordinationspolymere (engl. coordination polymers), als „Koordinationsverbindung[en] aus sich wiederholenden Einheiten, die sich in ein, zwei oder drei Dimensionen erstreck[en]“,¹ sind die Arbeiten von Hoskins und Robson, welche erstmals auf Basis rationaler topologischer Designprinzipien diamantartige, dreidimensionale, kationische Netzwerke durch die Kombination tetraedrischer Baueinheiten in Form von Metallionen und organischen Liganden synthetisierten.⁴⁻⁵ Wobei a posteriori Metall-Cyanid-Netzwerke mit bekannten Vertretern wie den Hofmann-Clathraten⁶⁻⁸ und dem Berliner Blau^{9,11} als auch das von Saito et al.¹² synthetisierte $[Cu(ADI)_2NO_3]$ (ADI = Adiponitril) als frühe Vertreter angesehen werden können (siehe Abbildung 2).

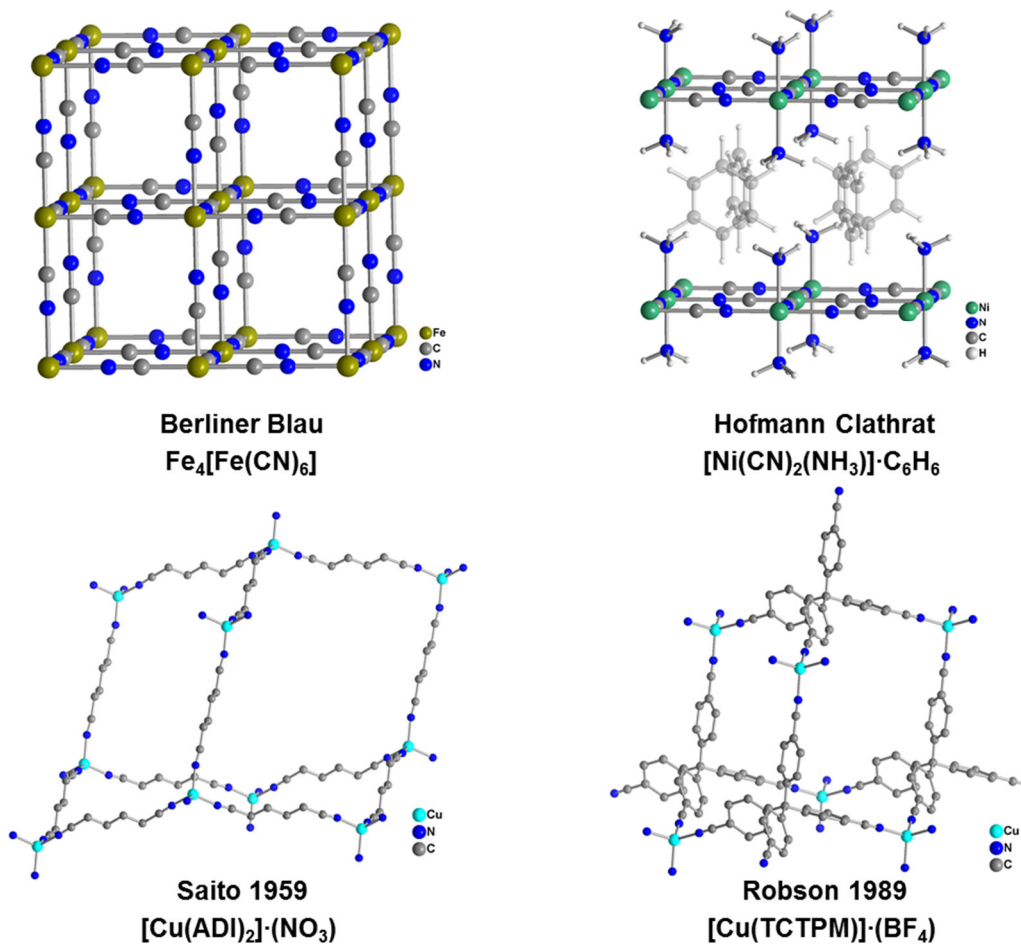


Abbildung 2. Metall-Cyanid Gerüstverbindungen in Form von Berliner Blau⁹ und des Hofmann Clathraten^{6, 13} $[Ni(CN)_2(NH_3)] \cdot C_6H_6$ als frühe Vertreter poröser Koordinationspolymere; $[Cu(ADI)_2] \cdot (NO_3)$ (ADINCU, ADI = Adiponitril) von Saito et al.¹² und $[Cu(TCTPM)] \cdot (BF_4)$ (JARMEU10, TCTPM = 4,4',4'',4'''-Tetracyanotetraphenylmethan) von Robson et al.⁴⁻⁵ als Vertreter kationischer Koordinationspolymere mit Diamant-Topologie.

Dies wurde von Yaghi unter dem Begriff der „retikulären Chemie“ (lat. reticulum = netzartig) zur Synthese ausgedehnter Netzwerkstrukturen in Form einer modularartigen Chemie tiefgehend konzeptualisiert.¹⁴⁻¹⁵ Unter retikulärer Chemie versteht man das Prinzip diskrete Baueinheiten (z.B. Metallcluster, organische Moleküle) durch gerichtete und (relativ) starke Bindungen zur Synthese von (kristallinen) Netzwerkstrukturen zu nutzen.^{14, 16} Die bekannteste Materialklasse, welche diesem Konzept entspringt, sind die eingangs bereits erwähnten Metall-organischen Gerüstverbindungen. Weitere Materialklassen die dem Konzept der retikulären Chemie entstammen, stellen die kovalent-organische Gerüstverbindungen (engl. covalent organic frameworks, COFs)¹⁷ sowie die zeolithischen-imidazolat Gerüstverbindungen (engl. zeolitic-imidazolate frameworks, ZIFs)¹⁸ dar. Auch wenn nicht in der Definition der IUPAC enthalten, so ist der Begriff der Metall-organischen Gerüstverbindungen in der Literatur eng mit dem Konzept der Nutzung von Metallhaltigen-polynuklearen Clustern als sekundäre Baueinheiten (engl. secondary building units, SBUs) und deren Verknüpfung durch organische Liganden in kristalline, ausgedehnte und poröse Netzwerkstrukturen im Sinne des Konzepts der retikulären Chemie verbunden. Der Begriff SBU stammt hierbei ursprünglich aus der Beschreibung der Strukturen von Zeolithen, in welchen die MO_4 -Tetraeder als primäre Baueinheiten größere periodische strukturelle Einheiten als SBUs bilden.¹⁹ Klassischerweise dienen hierbei Metall-Carboxylat Cluster als SBUs und Polycarboxylate, wie z.B. das Terephthalat oder Trimesat, als organische Liganden. Dies kann an den prototypischen Vertretern MOF-5,²⁰ HKUST-1²¹ und MIL-101 (Cr)²² als Meilensteine des SBU-Ansatzes verdeutlicht werden (siehe Abbildung 3).

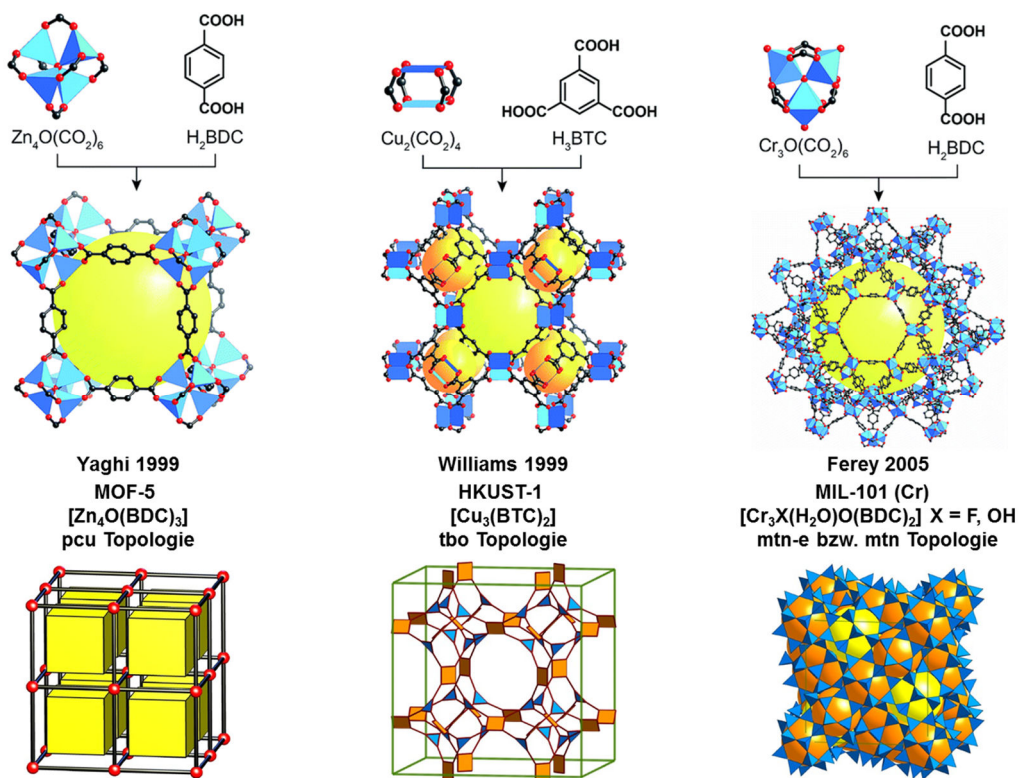


Abbildung 3. MOF-5,²⁰ HKUST-1²¹ und MIL-101 (Cr)²² als prototypische MOFs synthetisiert auf Basis des SBU-Ansatzes mit Carboxylat-basierten sekundären Baueinheiten und ihre zugrundeliegenden Topologien (© 2017 mit Erlaubnis von The Royal Society of Chemistry aus Yaghi et al.¹⁶; Bilder der Topologien entnommen aus der RCSR-Datenbank²³ unter <http://rcsr.anu.edu.au/>).

Das von Yaghi et al. synthetisierte MOF-5 [Zn₄O(BDC)₃] (BDC²⁻ = Terephthalat) basiert auf der [Zn₄O(CO₂)₆]-SBU des basischen Zinkacetats.²⁴ Während das von Williams et al. synthetisierte HKUST-1 [Cu₃(BTC)₂] (BTC³⁻ = Trimesat) das dimere [Cu₂(CO₂)₄]-Paddle-Wheel-Cluster des Kupferacetats²⁵ und das MIL-101 (Cr) [Cr₃X(H₂O)O(BDC)₂] von Ferey et al. das trimere [Cr₃O(CO₂)₆] des basischen Chromacetats als SBUs enthalten.²⁶ Diesen prototypischen MOFs konnte das in den Poren enthaltene Lösungsmittel entfernt werden und die entgasten Materialien zeigten hohe permanente Porositäten in Form von Typ-I Isothermen in Tieftemperaturgassorptionsexperimenten aufgrund ihrer hohen inneren Oberflächen.²⁷

Bei der Ansicht dieser periodischen Netzwerkstrukturen stellt sich wie generell für kristalline Festkörperstrukturen die Frage, wie diese zu ihrem besseren Verständnis beschrieben werden können. Allgemein enthält eine Kristallstruktur nicht nur Informationen hinsichtlich ihrer chemischen Zusammensetzung und Verknüpfung, sondern auch bezüglich der räumlichen Anordnung und der Symmetrie der Struktur im Ganzen. Hierbei hat sich zum Verständnis von anorganischen Kristallstrukturen der Metalle als auch von ionischen

Verbindungen die Beschreibung als Kugelpackungen, in welcher eine potentielle zweite Atomsorte die Lücken besetzt, als erfolgreich erwiesen.²⁸

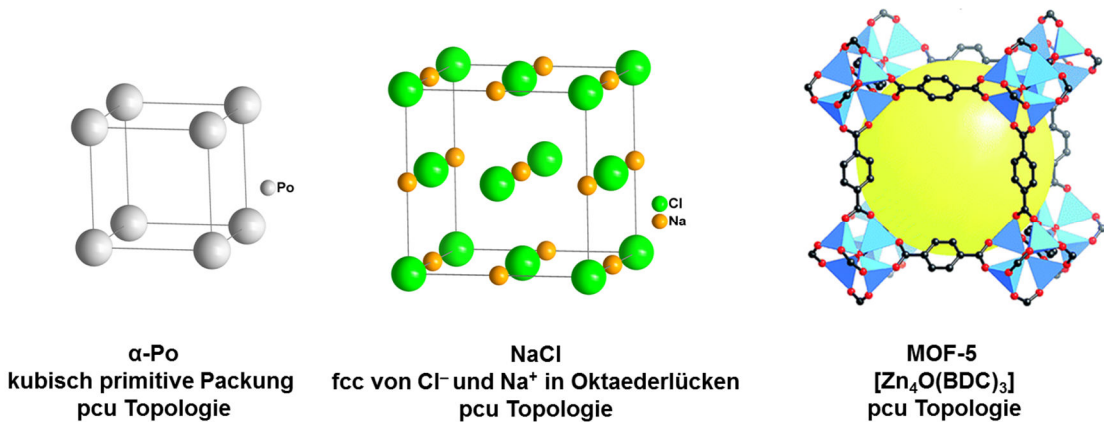


Abbildung 4. Gegenüberstellung der unterschiedlichen Strukturbeschreibungen von Kugelpackungen und Topologien an den Beispielen α -Po, NaCl und MOF-5. (in Anlehnung an Yaghi et al²⁹).

Wobei dieses Konzept zur Beschreibung ausgedehnter Netzwerkstrukturen weniger hilfreich ist und hier die Beschreibung durch die zugrundeliegenden Topologien Anwendung gefunden hat.³⁰⁻³⁴ Die vielleicht bekannteste Verbindung mit einer Netzwerkstruktur ist der Diamant mit der tetraedrischen Verknüpfung der enthaltenen Kohlenstoffatome (siehe Abbildung 5). Sein weniger bekanntes hexagonales Allotrop das Lonsdaleit formt ebenfalls ein aus tetraedrisch verknüpften Kohlenstoffatomen bestehendes dreidimensionales Netz, in welcher die strukturgebenden sechsgliedrigen Kohlenstoffringe nicht alle in einer Sesselkonformation vorliegen, sondern auch in der Bootskonformation. Im Unterschied zu den Konformeren des Cyclohexans können beide Verbindungen jedoch nicht ohne Bindungsbruch ineinander überführt werden. In diesem Sinne kann die Topologie eines Netzwerks als eine Erweiterung des Konzepts der Stereochemie für molekulare Verbindungen wie z.B. E/Z-, cis/trans-Isomeren und Diastereomeren angesehen werden und ihre Anwendung sollte in gleicher Weise erfolgen.³⁴ Neben dem Verständnis von Fetskörperstrukturen kann die Topologieanalyse auch dazu dienen neue Materialien mit der Literatur zu vergleichen, neue Materialien effizient und verständlich zu kommunizieren, „Designstrategien“ für neue Materialien zu entwerfen und auch Hilfe zum Lösen von Kristallstrukturen mittels Röntgenpulverdiffraktometrie leisten.³³

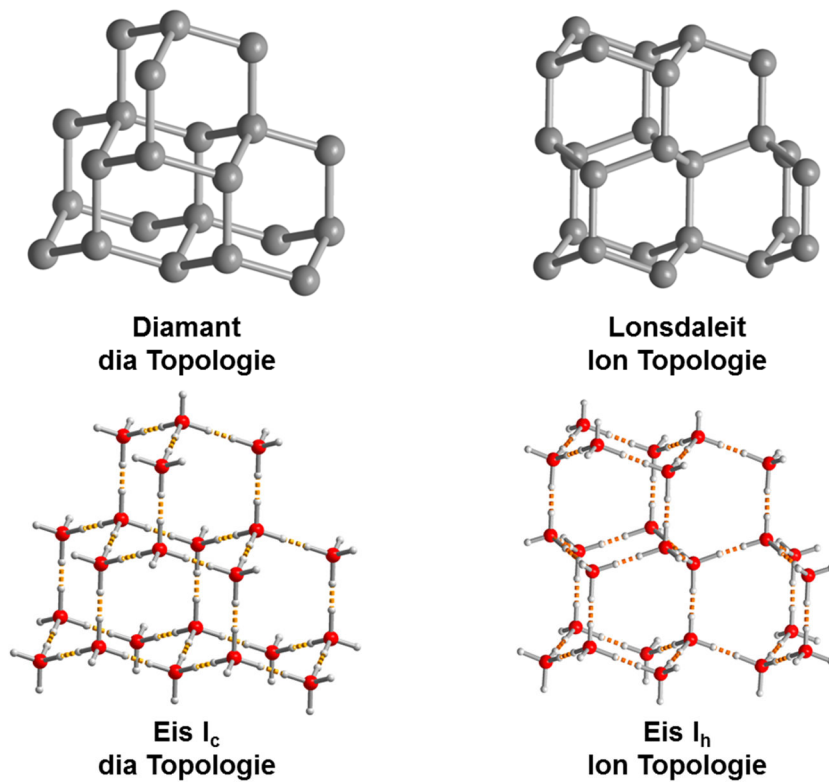


Abbildung 5. Oben: Gegenüberstellung der Netzwerkstrukturen von Diamant und Lonsdaleit als Allotrope des Kohlenstoffs mit tetraedrischen Kohlenstoffatomen als Knotenpunkte und der nach ihnen benannten Topologien. Unten: Netzwerkstrukturen des kubischen Polymorphs Eis I_c und des hexagonalen Polymorphs Eis I_h auf, welche analoge dia und ion Topologien mit tetraedrischen Wassermolekülen mit ungeordneten Wasserstoffatomen als Knotenpunkte ausbilden.

Grundlegenden Arbeiten zur topologischen Analyse von anorganischen Festkörperstrukturen lieferten hierbei Wells³⁵⁻³⁷, Smith³⁸ und O’Keefe.³⁹⁻⁴⁰ Dies verdeutlicht die Allgegenwärtigkeit und lange Tradition der Sichtweise von Festkörpermaterialien als Netzwerkverbindungen. Das Konzept der Topologie beruht darauf, die Struktur dahingehend zu vereinfachen, dass nur die Verbindungen der Komponenten berücksichtigt werden, nicht jedoch ihre chemische Natur. Hierzu werden die Netzwerke als eine Gruppe von Knoten, welche über Linker miteinander verknüpft sind, beschrieben. Ein Knoten mit k Verknüpfungen wird üblicherweise als $k\text{-c}$ (für „ k -coordinated“) bezeichnet. Netze mit „ k_1, k_2, \dots “ Knoten werden dementsprechend als $(k_1, k_2, \dots)\text{-c}$ gefolgt des Dreibuchstabencodes der RCSR-Datenbank (Reticular Chemistry Structure Resource) benannt.²³ Wobei viele Topologien ihren Namen von Mineralien oder natürlich vorkommenden Verbindungen haben (z.B. **rtl** Rutil, **pyr** Pyrit, **flu** Fluorit). Neuen Topologien wird ein eigener Dreibuchstabencode zugeteilt. Diamant formt dementsprechend das nach ihm benannte 4-c **dia** Netz und Lonsdaleit analog das 4-c **ion** Netz (Abbildung 5). Die Nützlichkeit der Beschreibung von Netzwerken mittels Topologien um strukturelle Ähnlichkeiten zwischen Verbindungen herzustellen kann an den beiden Eispolymorphen I_c

und I_h kurz verdeutlich werden. Das von König⁴¹ beschriebene metastabile kubische Eispolymorph I_c mit einem tetraedrischen Wassermolekül mit ungeordneten Wasserstoffatomen als Knotenpunkt bildet ein 4-c **dia** Netz. Wohingegen das gebildete Netzwerk des hexagonalen Eis I_h die **Ion** Topologie darstellt (Abbildung 5). An dieser Stelle soll nur kurz angemerkt dass 522 dreidimensionale Kohlenstoffallotrope mit 494 unterschiedlichen Topologien diskutiert werden.⁴² Dies zeigt das die Topologie-Analyse zur Beschreibung als auch zum Verständnis der Allotrope von Elementen als auch von Polymorphen von chemischen Verbindungen nicht nur nützlich sondern auch notwendig ist.

Für MOFs sind die Struktureinheiten zur Beschreibung ihrer Topologie typischerweise die anorganischen SBUs und die organischen Linker. Wobei in besonderen Fällen auch größere strukturelle Einheiten als Baueinheiten herangezogen werden können (siehe Beschreibung von MIL-101 (Cr) mit der **mtn** Topologie). Um zu bestimmen, welche Baueinheiten Kanten und welche Knoten sind, muss man Ausdehnungspunkte (engl. „points of extensions“) für jeden von ihnen definieren. Die Ausdehnungspunkte stellen hierbei die Anzahl an Verknüpfungen, die eine Baueinheit zu anderen macht, dar.

Für Metall-Carboxylat Cluster als SBUs sind dies üblicherweise die Kohlenstoffatome der Carboxylatfunktion. Baueinheiten, welche zwei Verbindungen haben stellen simple Kanten und alle Baueinheiten mit drei oder mehr Verbindungen stellen Knoten des Netzwerks dar. Die $[Zn_4O(CO_2)_6]$ -SBU in MOF-5 ist folglich ein oktaedrischer 6-c Knoten mit dem Terephthalat als Linker, was folglich die 6-c **pcu** (primitive cubic net) Topologie ergibt. Hier wird die Analogie der Struktur von MOF-5 zu denen von alpha-Polonium und Natriumchlorid deutlich. In beiden haben die Atome eine oktaedrische Umgebung. Wenn man diese miteinander verknüpft ergibt sich für beide auch die **pcu** Topologie als alternative Beschreibungsmöglichkeit (Abbildung 4). Für HKUST-1 ist nicht nur das $[Cu_2(CO_2)_6]$ -Paddle-Wheel-Cluster als SBU ein quadratischer 4-c Knoten, sondern auch das Trimesat ein trigonaler 3-c Knoten. Dies ergibt die 3,4-c **tbo** (twisted boracite) als die zugrundeliegende Topologie. Das bereits erwähnte MIL-101 (Cr) kann hierbei im Sinne des SBU-Ansatzes durch die Verknüpfung der trigonal prismatischen $[Cr_3O(CO_2)_6]$ -SBUs als 6-c Knoten mit dem Terephthalat als Linker mit der 6,6,6,6-c **mtn-e** Topologie beschrieben werden (siehe Abbildung 3).

Wobei MIL-101 (Cr) üblicherweise als 4,4,4-c **mtn** Netz beschrieben wird. Dies kann als Beispiel für den supramolekularen Baueinheiten-Ansatz (engl. supramolecular building block, SBB) zur (De-)Konstruktion von MOFs dienen.⁴³⁻⁴⁵ Der SBB-Ansatz beruht darauf, dass Metall-organische Polyeder⁴⁶ (engl. metal-organic polyhedra, MOPs) als supramolekulare Baueinheiten im Sinne tertiärer Baueinheiten (engl. tertiary building units, TBUs) zur

Beschreibung herangezogen werden. Hierin werden sekundäre Baueinheiten in der Form eines übergeordneten Clusters, welche die geometrischen Informationen mit den Ausdehnungspunkten zum Aufbau des Netzwerks enthalten, zusammengefasst.

In MIL-101 (Cr) werden vier der 6-c trigonal prismatischen $[\text{Cr}_3\text{O}(\text{CO}_2)_6]$ -SBUs zu einer tetraedrischen 4-c supramolekularen tertiären Baueinheit in der jede trimere SBU auf einer Ecke sitzt zusammengefasst. Die Eckenverknüpfung dieser Supertetraeder liefert die Beschreibung von MIL-101 mit einer 4,4,4-c **mtn** Topologie (siehe Abbildung 6). Dies zeigt, dass die Verknüpfung von Tetraedern neben den bereits gezeigten **dia** und **ion** Topologien auch zeolitische Topologien (hier am Beispiel von **mtn** gezeigt) liefern kann.⁴⁷

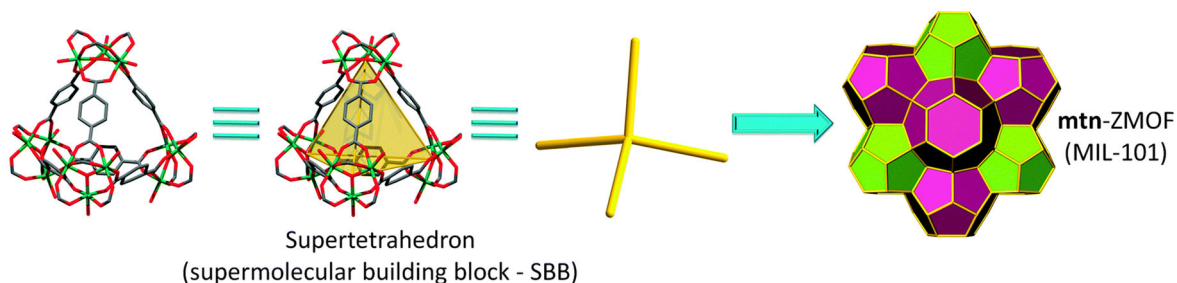


Abbildung 6. Beschreibung von MIL-101 (Cr) als 4,4,4-c mtn Topologie mit einem Supertetraeder im Sinne einer supramolekularen Baueinheit als Knotenpunkt (© 2015 mit Erlaubnis von The Royal Society of Chemistry aus Eddaoudi et al.⁴⁷)

Analog zur Sichtweise von MOPs als tertiäre Baueinheiten im SBB-Ansatz, wurde von Eddaoudi et al. mit dem „supramolecular building layer“-Ansatz (SBL) auch ein Konzept entwickelt in dem zweidimensionale Netze als Baueinheiten für MOFs angesehen werden.⁴⁴,⁴⁸ Der SBL-Ansatz basiert darauf, dass eine Vielzahl an dreidimensionalen MOF-Strukturen durch die Verbrückung („pillaring“) zweidimensionaler Schichten interpretiert werden können. Als Schichten werden hierfür die fünf kantentransitiven periodischen zweidimensionalen Netze **sql** („square lattice“), **kgm** („Kagomé“), **hcb** („Honeycomb“), **kgd** („Kagomé dual“) und **hxI** („hexagonal lattice“) als Möglichkeiten angenommen (siehe Abbildung 7).

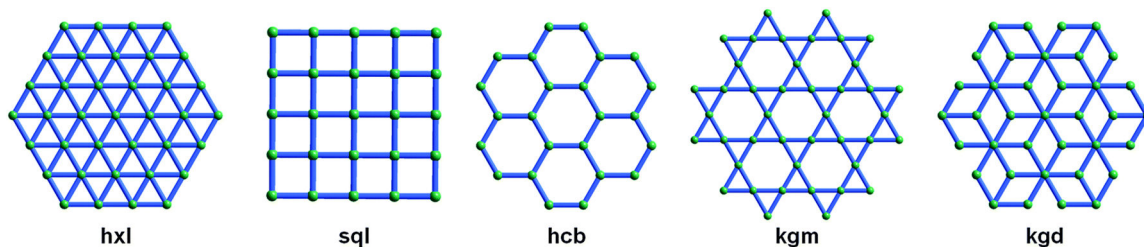


Abbildung 7. Schematische Darstellung der fünf kantentransitiven zweidimensionalen Netze hxl, sql, hcb, kgm, kgd (© 2014 mit Erlaubnis von The Royal Society of Chemistry aus Eddaoudi et al.⁴⁴).

Das bereits in der Struktur von HKUST-1 vorgestellte binukleare Paddle-Wheel-Cluster $[M_2(RCOO)_4(A)_2]$ (mit M = Metallion, A = apikaler Ligand) gehört zu den am häufigsten anzutreffenden SBUs in MOFs, unter anderem da dieses mit einer Vielzahl an Metallionen zugängig ist (z.B. $M^{2+} = \text{Zn}, \text{Cu}, \text{Ni}, \text{Co}, \text{Mn}, \text{Cr}, \text{Cd}, \text{Rh}, \text{Ru}, \text{Mo}$). Typischerweise verbrücken Dicarboxylateinheiten, wie z.B. Terephthalat und Isophthalat, diese Cluster in axialer Position. Da dann folglich vier unterschiedliche Dicarboxylatliganden an das Cluster koordinieren ergibt sich, dass es als ein quadratisch planarer 4-c Knoten fungiert (Abbildung 8).⁴⁸

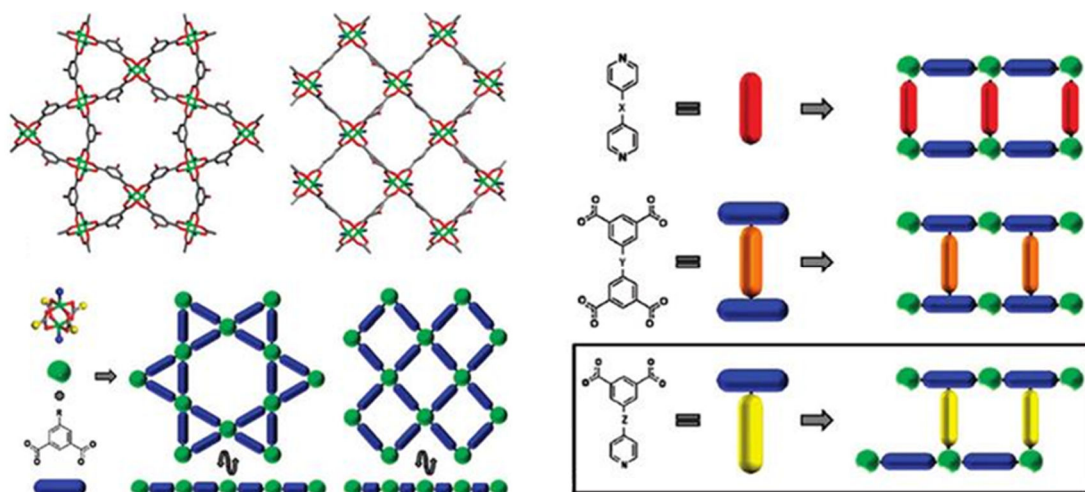


Abbildung 8. Verknüpfungsstrategien im „supramolecular-building-layer“-Ansatz: „axial-to-axial“ im Sinne einer „mixed-ligand“-Strategie (rot, linear), „ligand-to-ligand“ (blau-orange-blau, I-förmig), „ligand-to-layer“ (blau-gelb, T-förmig) (© 2011 mit Erlaubnis von The Royal Society of Chemistry aus Eddaoudi et al.⁴⁸).

Von den oben erwähnten kantentransitiven Netzen sind **sql** und **kgm** Vertreter mit 4-c Knoten, welche folglich von Paddle-Wheel-Clustern gebildet werden können. Das Paddle-Wheel-Cluster besitzt in seinen apikalen Positionen zwei weitere Koordinationsstellen,

welche typischerweise durch Lösungsmittelmoleküle (z.B. Dimethylformamid, H₂O, Pyridin) besetzt sind. Werden die so gebildeten Netze anstatt durch Lösungsmittel durch die in Abbildung 8 gezeigten neutralen ditopen Liganden (z.B. 4,4'-Bipyridin) verbrückt, ergibt sich die „axial-to-axial“-Verknüpfungsstrategie, in welcher jedes Paddle-Wheel-Cluster dann als oktaedrischer 6-c Knoten vorliegt.

Neben der oben bereits erwähnten 6-c **pcu** Topologie bei der Verknüpfung von **sql** Schichten, liefert die Verknüpfung von **kgm** Schichten die 6-c **kag** Topologie.⁴⁴ Die Verbrückung der zweidimensionalen Netze durch die direkte Verknüpfung der Dicarboxylateinheiten in Form der Verwendung von Diisophthalat-Liganden wird als „ligand-to-ligand“-Verknüpfungsstrategie bezeichnet. Da hier neben dem Paddle-Wheel-Cluster auch der Ligand ein 4-c quadratischer oder tetraedrischer Knoten ist, ergeben sich dreidimensionale MOFs mit einer Reihe von 4,4-c Topologien wie z.B. **nbo** (Niob(II)-oxid), **pts** (Platin(II)-sulfid).

Die dritte Verknüpfungsstrategie verbindet die beiden vorhergenannten, indem beide Funktionalitäten in einem T-förmigen Liganden mit der richtigen Stöchiometrie der Funktionalitäten zusammengefasst werden (siehe Abbildung 9 für einige beispielgebende Liganden).⁴⁸ Hierbei bildet der Dicarboxylatteil des Liganden, z.B. eine Isophthalateinheit, erneut die zweidimensionalen Schichten (**sql** bzw. **kgm**) und die zweite funktionelle Gruppe in Form eines heterozyklischen N-Donor-Liganden verknüpft benachbarte Schichten. Daraus ergibt sich der Name „ligand-to-axial“ für diese Verbrückungsstrategie. Da jeder T-förmige Ligand an drei unterschiedliche „paddle-wheel-Cluster“ koordiniert, ist jeder ein trigonaler 3-c Knotenpunkt. Analog zum „axial-to-axial-pillaring“ ist jedes paddle-wheel ein oktaedrischer 6-c Knoten. Daraus ergeben sich dreidimensionale MOFs mit (3,6)-c Topologien. Insgesamt sind mit **pyr** (Pyrit), **apo** (α -Bleioxid), **rtl** (Rutil), **brk** (Brookit), **ant** (Anatas) und **anh** (hexagonaler Anatas) sechs (3,6)-c Topologien auf der Basis von **sql**-Netzen und eine Topologie auf Basis eines **kgm**-Netzes (**eea**) theoretisch mit dem SBL-Ansatz zugänglich.⁴⁴

⁴⁸

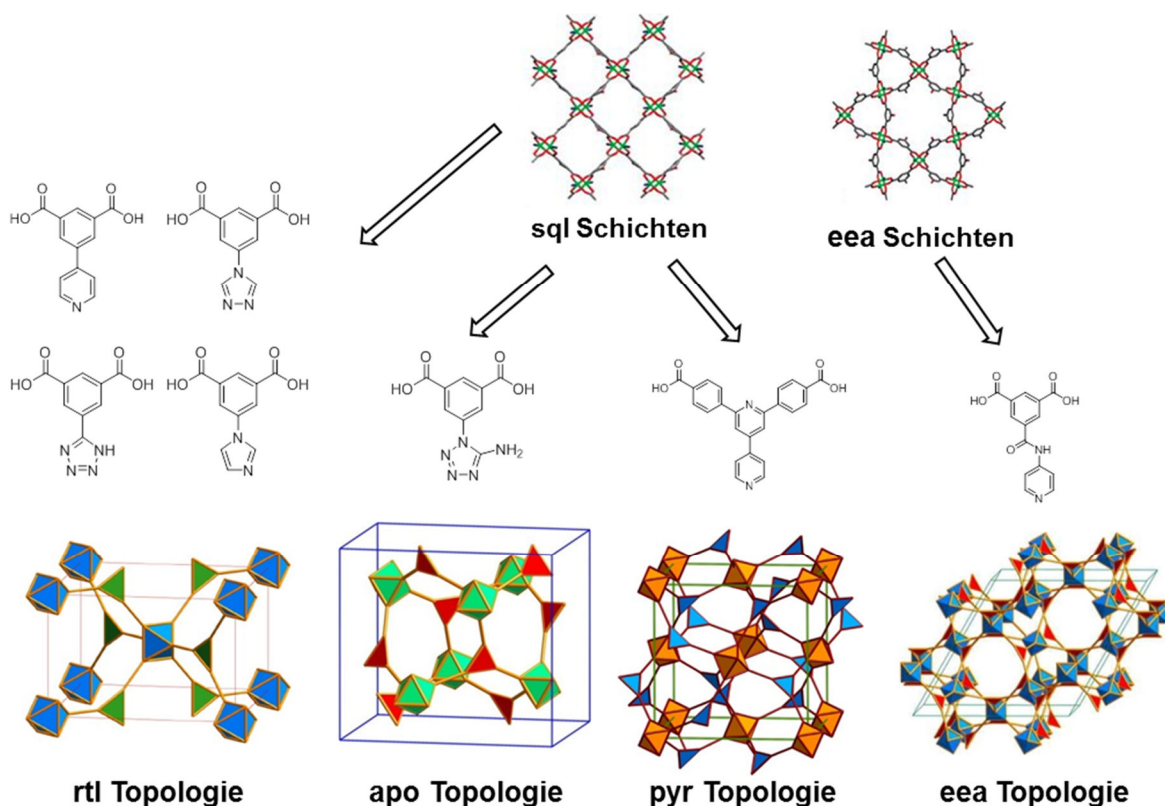


Abbildung 9. Beispiele für Topologien und bifunktionelle T-förmige Liganden, welche mittels der „axial-to-ligand“-Verknüpfungsstrategie synthetisiert wurden (Topologien sind in ihren erweiterten-Versionen (engl. augmented versions) dargestellt; Bilder der Topologien entnommen aus der RCSR-Datenbank²³ unter <http://rcsr.anu.edu.au/>).

In der Literatur sind bereits einige dieser T-förmigen Liganden bekannt und wurden in der Synthese von MOFs eingesetzt. Neben Pyridin als zweite Funktionalität haben hierbei schon Tetrazol-, Triazol- und Imidazol-haltige bifunktionelle Liganden Anwendung gefunden (Abbildung 9).⁴⁸⁻⁵¹ So haben 3,6-c MOFs auf Basis des SBL-Ansatzes durch die Funktionalisierung ihrer Kanalstruktur insbesondere hervorragende Eigenschaften in ihren Sorptionseigenschaften gezeigt. Das **eea**-Cu-MOF mit der 5-Isonicotinamidisophthalsäure (siehe Abbildung 9) zeigte z.B. sehr gute Eigenschaften für die Abtrennung von Propan und Ethan von Methan.⁵² Wobei das **apo**-Cu-MOF mit dem 5-(5-Amino-1H-tetrazolyl)isophthalsäureliganden durch die unterstützende Aminofunktionalität selektiv Acetylen aus Acetylen/Ethen-Gemischen unter industriell relevanten Bedingungen abtrennt.⁵³ Einen interessanten Fall von kristallografisch identifizierbarer Fehlordnung konnte im **rtl**-Cu-MOF mit der 5-(1H-Imidazolyl)isophthalsäure aufgedeckt und den Einfluss der Fehlordnung des Poresystems auf die Sorptionseigenschaften untersucht werden.⁵¹

Es gilt zu erwähnen, wie oben bereits angeführt, dass die Topologieanalyse von Festkörperstrukturen auch als Basis für ein späteres „Design“ von neuartigen Festkörperstrukturen angesehen wird. Als Kritik an diesen Ansätzen des „Designs“ von Festkörperverbindungen sind besonders die Einlassungen von Ferey und Jansen anzuführen.⁵⁴⁻⁵⁶ Ein häufig vorgebrachtes Argument für das „Design“ von MOFs ist, dass ihrer Synthese häufig eine gezielte Auswahl an Edukten auf Basis z.B. der bereits vorgestellten Konzepte innerhalb der retikulären Chemie vorangeht. Zusätzlich existieren für viele retikuläre Serien etablierter Syntheseprotokolle, sodass die Synthesen häufig als planbar beschrieben werden können. Wobei zu Recht auf den hohen Anteil an Serendipität von vielen Autoren im Ausgang der Synthesen hingewiesen wird.⁵⁷ Dies kann durch die vielen Beispiele, in welchen nur kleinste Veränderungen der Reaktionsparameter zu unterschiedlichen Produkten führten, unterstrichen werden. Ein Beispiel ist z.B. die Isolierung supramolekularer Isomere, in welchen gleiche Baueinheiten unterschiedliche Netzwerkstrukturen, welche konsequenterweise durch unterschiedliche Topologien beschrieben werden können, ausbilden.⁵⁸ Somit kann konstatiert werden, dass „Design“ maximal meinen kann, dass der synthetische Chemiker mit einer Idee auf Basis einer Vielzahl der hervorragenden Konzepte ins Labor geht, um ein MOF einer bestehenden MOF-Plattform zu synthetisieren. Nicht jedoch die Hybris mit Gewissheit den Ausgang der Synthesen und somit alle kinetischen und thermodynamischen Einflussfaktoren auf den Kristallisationsprozess a priori zu kennen.

Gerade auch wegen dieser Konzeptualisierung zur modulartigen Synthese von porösen Festkörperstrukturen, sind Metall-organische Gerüstverbindungen und der damit verbundenen Vielzahl an möglichen Funktionalisierungen in der Literatur mit einer Reihe an Eigenschaften und entsprechenden potentiellen Anwendungen assoziiert.¹⁶ Einen Überblick liefert Abbildung 10. Grundsätzlich sind viele der bereits erwähnten MOF-Plattformen multifunktional und wurden hinsichtlich vieler der erwähnten Anwendungen untersucht.⁵⁹

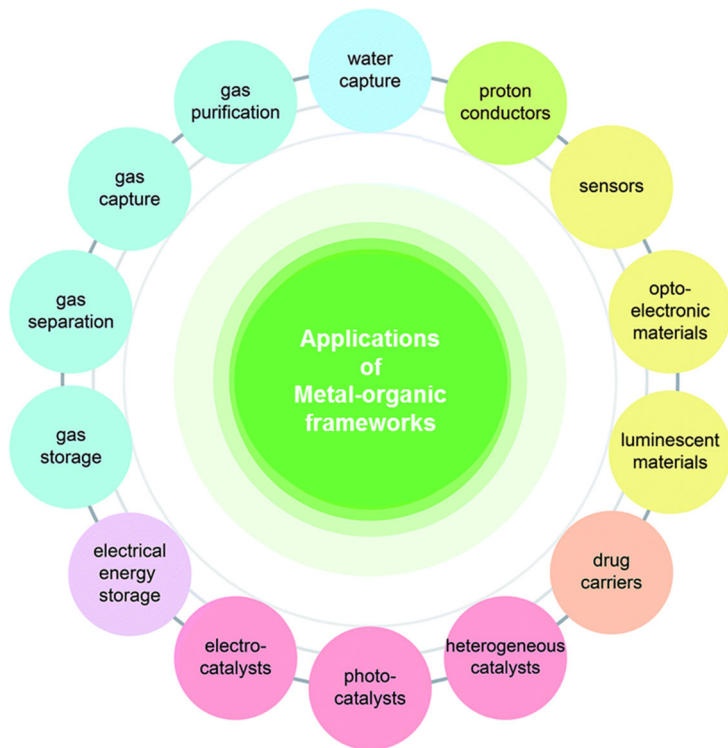


Abbildung 10. Übersicht über eine Vielzahl der Anwendungen in denen Metall-organische Gerüstverbindungen diskutiert werden (© 2017 mit Erlaubnis von The Royal Society of Chemistry in Anlehnung Yaghi et al.¹⁶)

Wie bereits aus dem SBL-Ansatz ersichtlich, können N-Heterozyklen-basierte Liganden zur Synthese von MOFs verwendet werden. Neben den oben bereits erwähnten N-Heterozyklen Pyridin, Imidazol, Triazol und Tetrazol wurden selbstverständlich auch MOFs auf Basis von Pyrazolen synthetisiert.⁶⁰ Azole haben den Vorteil häufig gerichtete und äußert inerte koordinative Bindungen zu Metallkationen einzugehen. Die sp^2 -hybrisierten N-Donoratome in den Azolen sind in ihrer Koordinationschemie identisch zu denen in Pyridinen. Azole können sowohl in neutraler Form als auch in anionischer Form als Azolate in MOFs eingebaut werden. Die Deprotonierung erhöht hierbei die Haptizität der Azolate im Vergleich zu den Pyridinen. Pyrazole haben benachbart zu einer Lewis-sauren pyrrolischen N-H-Gruppe einen Lewis-basischen pyridinische N-Donor. Pyrazolat-basierte MOFs sind bereits aufgrund ihrer hohen chemischen und thermischen Stabilität intensiv untersucht worden. Ein umfassender Überblick zu Pyrazolat-basierten (porösen) Koordinationspolymeren ist bei Galli et al. zu finden.⁶¹ Für die gängigsten Koordinationsmodi des Pyrazolats, kann hierbei Analogie zu Koordinationsmodi des Carboxylats gezogen werden (siehe Abbildung 11).

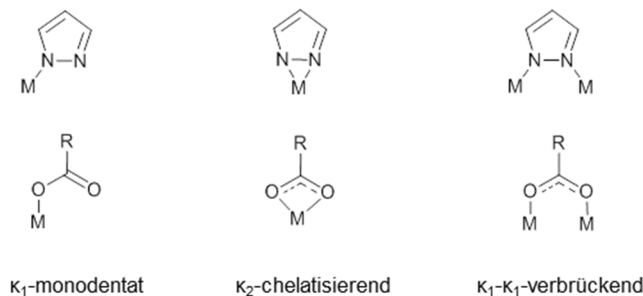


Abbildung 11. Analogie zwischen den gängigen Koordinationsmodi des Pyrazolats und Carboxylats.

Insbesondere der $\kappa_1\text{-}\kappa_1$ verbrückende Koordinationsmodus des Pyrazolats ist analog zu dem in klassischen Carboxylat-SBUs vorzufindende, häufig als syn-syn-verbrückender Koordinationsmodus beschriebene, Koordinationsmodus von Carboxylaten in MOFs. Erstmals wurde dieser Synergismus von Chen et al. in der Synthese des hydrophoben $[\text{Zn}_4\text{O}(\text{bdc})(\text{Me}_4\text{bpz})_2]$ -MOF-5-Analogons (bdc^{2-} = Terephthalat, $\text{Me}_4\text{bpz}^{2-}$ = 3,3',5,5'-Tetramethyl-4,4'-bipyrazolat) mit $[\text{Zn}_4\text{O}(-\text{pz})_4(-\text{COO})_2]$ -SBUs im Vergleich zur reinen Zink-Carboxylat $[\text{Zn}_4\text{O}(-\text{COO})_6]$ -SBUs wie in MOF-5 genutzt (siehe Abbildung 12). Die Topologie kann hierbei wie für MOF-5 als **pcu** beschrieben werden, wobei sich die gesamte Symmetrie von kubisch auf tetragonal verringert.⁶²

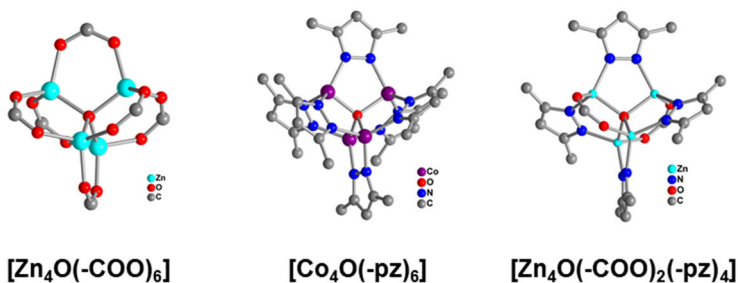


Abbildung 12. Darstellung der Analogie zwischen der $[\text{Zn}_4\text{O}(-\text{COO})_6]$ -SBU aus MOF-5 mit der $[\text{Co}_4\text{O}(-\text{pz})_6]$ -SBU in MFU-1 und der gemischten $[\text{Zn}_4\text{O}(-\text{pz})_4(-\text{COO})_2]$ -SBU.

Volkmer et al. rationalisierte den Analogismus tiefergehend anhand der Identifizierung strukturell ähnlicher Metall-Acetat und Metall-Pyrazolat-Cluster als SBUs. Dies führte u.a. zur Synthese des stabilen MOF-5-Analogons MFU-1 $[\text{Co}_4\text{O}(\text{Me}_4\text{bpzb})_3]$ ($\text{Me}_4\text{bpzb}^{2-}$ = 1,4-bis(3,5-dimethylpyrazolat)benzol) mit einer $[\text{Co}_4\text{O}(-\text{pz})_6]$ -SBU mit interessanten Eigenschaften als redoxaktiver heterogener Katalysator (Abbildung 12).⁶³ Daraus abgeleitet folgte die Verwendung bifunktioneller heteroditoper Carboxylat-Pyrazolat-Liganden häufig um stabilere Analoga der rein Carboxylat-basierten MOFs zu synthetisieren. Die Verwendung der bifunktionellen Liganden stellte häufig einen Kompromiss zwischen der guten

Kristallisierbarkeit Carboxylat-basierter MOFs und der erhöhten Stabilität aber schlechteren Kristallisierbarkeit Pyrazolat-basierter MOFs dar. Janiak et al. synthetisierten das MOF-5 Analoga $[\text{Co}_4(\mu_4\text{-O})(\text{dmpz-ba})_3]$, welches im Gegensatz zum gemischt-Liganden MOF $[\text{Zn}_4\text{O}(\text{bdc})(\text{Me}_4\text{bpz})_2]$ aus statistisch verteilten $[\text{Co}_4(\mu_4\text{-O})(\text{pz})_x(\text{COO})_{6-x}]$ -SBUs (mit $D_f = (1, 2, 3, 4, 5, 6)$) besteht. Das mit dem gleichen Liganden synthetisierte hydrophobe MAF-X8 $[\text{Zn}(\text{dmpz-ba})]$, welches das Analogon zum MFU-2 $[\text{Co}(\text{Me}_4\text{bpzb})]$ darstellt, zeigte in einer Festphasenmikroextraktion eine sehr gute Selektivität und eine niedere Detektionsgrenze für Benzolderivate.⁶⁴⁻⁶⁵

Diese Beispiele zeigen, dass Pyrazolat und Carboxylat gemeinsame Cluster ausbilden können, in denen beide aufgrund der Ähnlichkeit ihrer $\kappa_1\text{-}\kappa_1$ verbrückenden Koordinationsmodi gegeneinander substituiert werden können. Neben der Möglichkeit sich gegenseitig zu substituieren, können generell noch zwei weitere Möglichkeiten für Carboxylat-Pyrazolat-Systeme abgeleitet werden. Die eine ist, dass sich getrennte Metall-Carboxylat und Metall-Pyrazolat SBUs ausbilden und die andere besteht darin, dass zwar ein gemeinsames Cluster gebildet wird, hierin beide Funktionalitäten aber unterschiedliche Koordinationsmodi aufweisen.

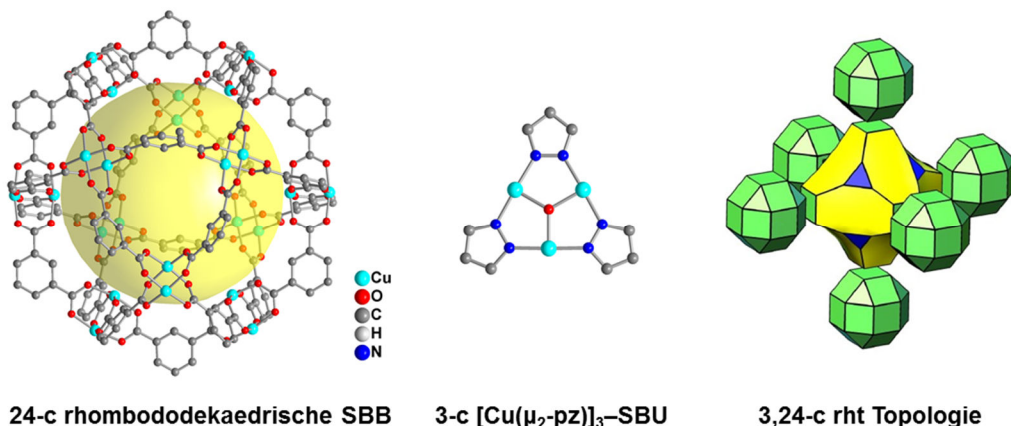


Abbildung 13. Darstellung der rht-Topologie auf Basis einer rhombododekaedrischen SBB und eines trigonalen 3-c Knotens am Beispiel des rht-MOF-pyr synthetisiert von Gao et al. als Beispiel für die Nutzung von bifunktioneller Carboxylat-Pyrazolat-Liganden mit getrennten Clustern (Refcode UGOCAW)⁶⁶⁻⁶⁷ (Bild der Topologie entnommen aus der RCSR-Datenbank²³ unter <http://rcsr.anu.edu.au/>).

Als Beispiel für den ersten Fall kann das rht-MOF-pyr $[\text{Cu}_6(\text{Isa-pz})_3]$ ($\text{Isa-pz}^{3-} = 5\text{-}(1\text{H-pyrazol-4-yl})\text{isophthalat}$) dienen, welches aus getrennten Cu-Paddle-Wheel-Clustern und der trigonalen $[\text{Cu}(\mu_2\text{-pz})]_3$ -SBU aufgebaut ist (Abbildung 13).⁶⁶⁻⁶⁷ Sie konnten eine erhöhte Stabilität und CO_2 -Selektivität im Vergleich zu den mit Triazolen und Tetrazolen synthetisierten rht-MOFs beobachten. rht-MOFs entspringen ebenfalls dem SBB-Ansatz, da ihre Topologie durch die Verknüpfung rhombocuboktaedrischer MOPs gebildet von den

Isophthalsäureeinheiten als 24-c Knoten und einem trigonalen 3-c Knoten (hier trigonales Kupferpyrazolatcluster) erklärt werden kann. Da die 3,24-c **rht**-Topologie nicht interpenetrierbar ist, sind **rht**-MOFs in der Literatur für ihre hohe Porosität bekannt. So gehört u.a. NU-110 mit einem Hexacarboxylatliganden mit der höchsten erhaltenen inneren BET-Oberfläche (nach Brunauer-Emmet-Teller) dieser Klasse an.⁶⁸ An den **rht**-MOF-pyr MOFs kann verdeutlicht werden, dass bifunktionelle T-förmige Carboxylat-Azolat-Liganden Zugang zu MOF-Topologien mit attraktiven Eigenschaften liefern können, die ansonsten nur über große und schwierig zu synthetisierende organische Liganden zugänglich sind. Natürlich liegt die Schwierigkeit darin, geeignete Synthesebedingungen zu finden, in denen beide Cluster entstehen.

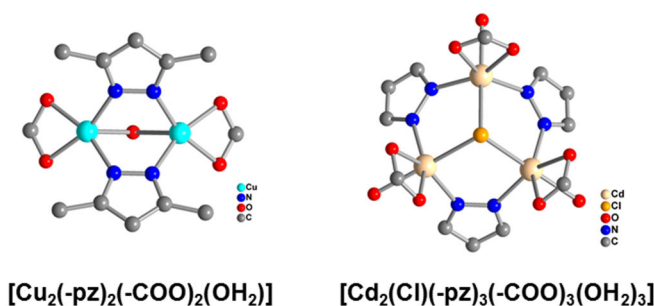


Abbildung 14. Die 4-c tetraedrische $[\text{Cu}(\text{-pz})_2(\text{-COO})_2(\text{OH}_2)]$ -SBU (aus Refcode ZECKID)⁶⁹ und 6-c oktaedrische $[\text{Cd}_2(\text{Cl})(\text{-pz})_3(\text{-COO})_3(\text{OH}_2)_3]$ -SBU (aus Refcode RUWFOQ)⁷⁰ als Beispiele für SBUs in denen die Pyrazolatfunktionen einen $\kappa_1\text{-}\kappa_1$ -verbrückenden- und die Carboxylatfunktionen einen κ_2 -chelatisierenden Koordinationsmodus aufweisen.

$[\text{Cu}_2(\text{dmpzca})_2(\text{OH}_2)]$ (dmpzca^{2-} = 4-(3,5-Dimethylpyrazolat)carboxylat) mit der **dia**-Topologie ist ein Beispiel in dem beide Funktionalitäten eine gemeinsame 4-c tetraedrische SBU ausbilden, in welcher die Pyrazolatfunktionen einen $\kappa_1\text{-}\kappa_1$ -verbrückenden- und die Carboxylatfunktionen einen κ_2 -chelatisierenden Koordinationsmodus aufweisen (siehe Abbildung 14).⁶⁹ Darüber hinaus zeigt es nach der Entfernung des μ_2 -koordinierten Wassermoleküls interessante Sorptionseigenschaften aufgrund der Kombination von struktureller Flexibilität mit koordinativer Ungesättigtheit. Gleiches gilt bezüglich des Koordinationsmodus beider Funktionalitäten in $[\text{Cd}_3\text{Cl}(\text{pzca})_3(\text{OH}_2)_3]$ (pzca^{2-} = Pyrazolat-4-carboxylat) (Abbildung 14).⁷⁰

Die Rigidität vieler MOFs ist, in Analogie zu ihren porösen anorganischen Gegenstücken wie z.B. den Zeolithen, vor allem auf die stabilen Metall–Ligand–Bindungen zurückzuführen. Folglich zeigen diese rigid MOF-Materialien als Adsorbens, das Phänomen der Physisorption mit analogen Isothermen in Sorptionsexperimenten mit Gasen als Adsorptiv an ihre inneren Oberflächen. Hierbei haben vor allem die mikroporösen Vertreter mit ihren

reversiblen Typ I Isothermen, große Aufmerksamkeit durch die mannigfaltige Funktionalisierbarkeit ihrer Porosität und Poresysteme bezüglich ihrer potentiellen Anwendung in der Speicherung von Gasen als auch der Auftrennung von Gasgemischen erhalten.⁷¹⁻⁷²

Generell versteht man unter struktureller Flexibilität den Phasenübergang eines Festkörpers unter dem Einfluss externer Stimuli, wie z.B. Temperatur, Druck, Licht, und Verbindungen. Dies kann zu einer Änderung des Zellvolumens von beträchtlichem Ausmaß führen. Kitagawa et al. waren die ersten die dieses Phänomen in MOFs beobachtet als auch kategorisiert haben.⁷³⁻⁷⁵ In Anlehnung an die allgemeine Definition sind flexible MOFs demnach zwei- und dreidimensionale Netzwerkstrukturen, welche als multistabile kristalline Materialien reversibel zwischen unterschiedlichen Phasen transformiert werden können, wovon mindestens eine porös – sprich Gastmoleküle enthält – ist.

Die Basis für die Flexibilität dieser sogenannten „soft porous crystals“ sind häufig (konformel) flexible Linker, variable Koordinationsgeometrien der verwendeten Metalle in Kombination mit nicht-kovalenten Wechselwirkungen (z.B. π - π -stacking, Wasserstoffbrückenbindungen), welche eine Adaption an die externen Stimuli begünstigen, sodass eine Gast-induzierte Expansion bzw. Kontraktion des Netzwerks ausgelöst wird (siehe Abbildung 15).⁷⁵⁻⁷⁶

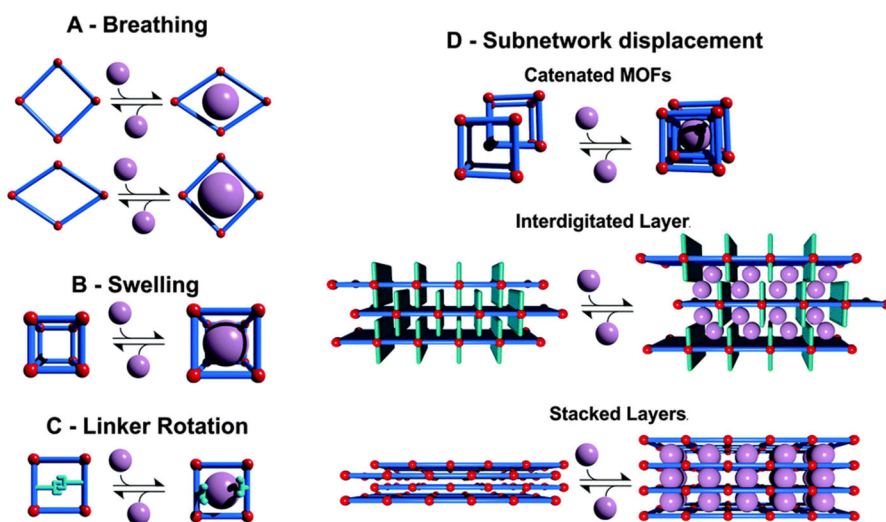


Abbildung 15. Klassifikation unterschiedlicher Flexibilitätsarten Metall-organischer Gerüstverbindungen (© 2014 mit Erlaubnis von The Royal Society of Chemistry in Anlehnung Kaskel et al.⁷⁷).

Sorptionsisothermen von flexiblen MOFs weisen daher häufig einen untypischen Verlauf in Form von Stufen, aufgrund der dynamischen Aufnahme der Gastmoleküle, auf. Folglich können ihre Sorptionsisothermen nicht nach dem von der IUPAC aufgestellten Klassifizierungsschema eingeteilt werden.⁷⁸⁻⁷⁹ Zaworotko et al. haben diesbezüglich ein ergänzendes Schema für die Isothermen von flexiblen Materialen vorgeschlagen.⁸⁰ Eine Diskontinuität in der Adsorptionsisotherme, welche den Übergang einer nicht-porösen in eine poröse Phase beschreibt, wird als sogenanntes „gate-opening“ bezeichnet. Und der dazugehörige Druckbereich in welchem der Phasenwechsel geschieht als sogenannter „gate-opening“-Druck. Wohingegen die Expansion einer bereits porösen Phase mit „breathing“ (engl. „Atmung“) bezeichnet wird. Beiden ist gemein, dass sich das Volumen der Elementarzelle während des Adsorptionsprozesses ändert.

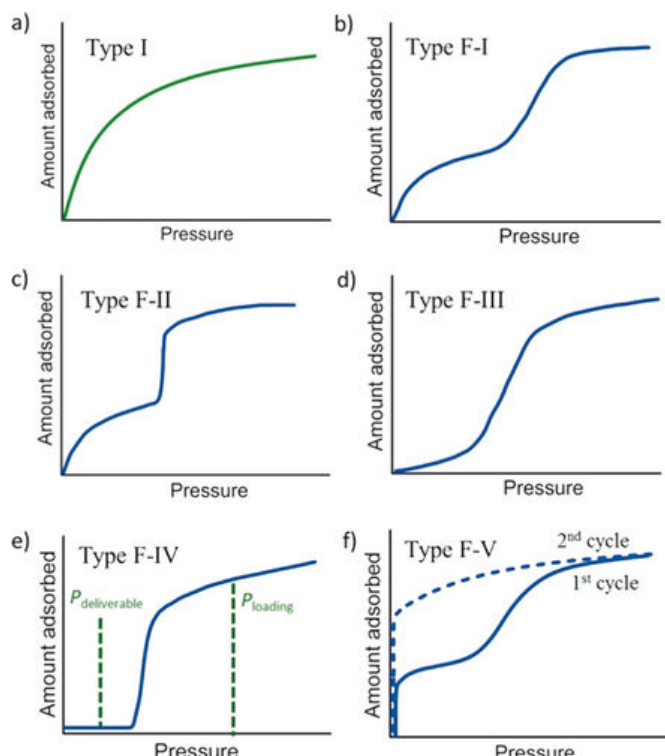


Abbildung 16. Vorgeschlagenes Klassifizierungsschema für flexible mikroporöse Materialien nach Zaworotko et al.⁸⁰: (a) Langmuir-Typ I = rigides mikroporöses Material, Type-F-I = flexibles mikroporöses Material mit gradualem Öffnen von einer kleinporigen in eine großporige Form, Typ-F-II flexibles mikroporöses Material mit abruptem Übergang von kleinporigen in eine großporige Form, Typ-F-III = flexibles mikroporöses Material mit einem graduellen Übergang von einer nicht-porösen in poröse Form, Typ-F-IV = flexibles mikroporöses Material mit einem abrupten Übergang von einer nicht-porösen in eine poröse Form. (© 2018 mit Erlaubnis von Wiley-VCH Verlag GmbH & Co. KGaA, Weinheim).

Die von Kitagawa intensiv untersuchten CIDs [M(Isa-X)(Bpy-Y)] (Isa-X = Isophthalat und seine Derivate, Bpy-Y = 4,4'-Bipyridin und seine Derivate) (engl. coordination-polymers with interdigitated structures; siehe Abbildung 15 für eine schematische Darstellung ihrer ineinandergreifenden Strukturen) zeigten hierbei häufig die mit einem „gate-opening“ verknüpften S-förmigen Typ-F-IV Isothermen.⁸¹⁻⁸⁴ Diese Adsorbat-abhängige Flexibilität wurde z.B. bei CID-5 [Zn(5-NO₂-Ip)(Bpy)] (5-NO₂-Ip = 5-Nitroisophthalat, Bpy = 4,4'-Bipyridin) zur Trennung von Gasgemischen genutzt.⁸² Ein weiterer wichtiger und früher Vertreter für ein flexibles Koordinationspolymer im Allgemeinen und mit S-förmigen Sorptionsisothermen im Speziellen stellt das zweidimensionale ELM-11 [Cu(Bpy)₂(BF₄)₂] (engl. elastic layered materials; siehe Abbildung 15 für eine schematische Darstellung als „stacked layers“) dar.⁸⁵⁻⁸⁶

Für klassische mikroporöse Adsorbentia verringert sich mit steigender Temperatur normalerweise die Steilheit der Adsorptionsisotherme. Wohingegen für sogenannte Phasenwechselmaterialien (engl. „phase change materials“, PCM) mit steigender Temperatur der Übergang von der nicht-porösen in eine poröse Phase zu höheren Drücken verschoben ist. Das ermöglicht Adsorbentia, welche S-förmige Isothermen zeigen, nur eine deutlich geringere Temperaturerhöhung benötigen um eine hohe Arbeitskapazität (engl. „working capacity“) zu erreichen. Ein ideales Adsorbens zeigt demnach einen Phasenwechsel mit einer möglichst großen vertikalen Stufe unterhalb des relativen Drucks des zu speichernden Gases. S-Förmige Isothermen werden häufiger aufgrund des Auftretens von Kapillarkondensation, ergo einem Phasenübergang des Adsorbats, bei der Porenfüllung von mikroporösen Materialien beobachtet. Ein Beispiel ist die Adsorption von Wasser an hydrophobe mikroporöse Materialien, wie z.B. MOFs, mit nach dem klassischen IUPAC-Schema Typ V Isothermen.⁷⁸

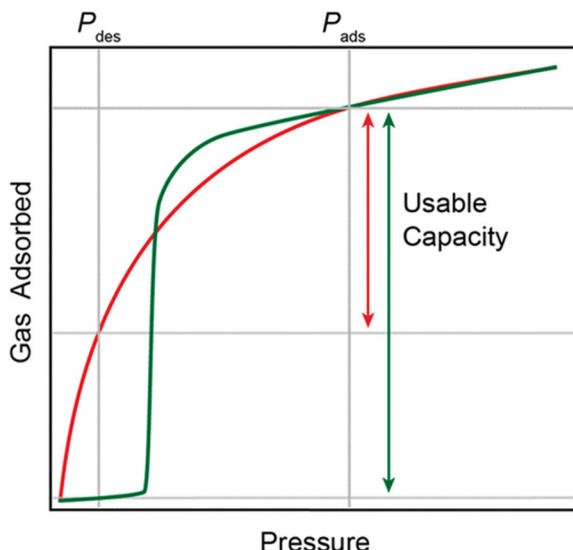


Abbildung 17. Idealisierte Darstellung der typischen Langmuir-Adsorptionsisotherme (Typ I) eines mikroporösen Adsorbens (rot) und idealisierte stufenförmige Adsorptionsisotherme (Typ V oder Typ FIV, grün). Der maximale Adsorptionsdruck (P_{ads}) und der minimale Desorptionsdruck (P_{des}) sind als vertikale graue Linien angezeigt. Die relativen nutzbaren Kapazitäten sind als Doppelpfeile in den jeweiligen Farben angedeutet. Materialen, welche stufenförmige Adsorptionsprofile aufweisen, können größere nutzbare Kapazitäten als Materialen mit Typ I-Profilen unter vergleichbaren Druckwechselbedingungen aufweisen. (© 2018 mit Erlaubnis von American Chemical Society aus Long et al.⁸⁷)

Diese Materialien werden analog aufgrund ihrer hohen Arbeitskapazität als Vorteilhaft im Einsatz von Adsorptionskühlern und Adsorptionswärmepumpen mit z.B. Wasser als Adsorbat diskutiert.^{88,89} Die Adsorption an mesoporösen Materialien, auch wenn meist in Form von Typ IV Isothermen, zeigt S-förmigen Charakter aufgrund von Multilagenadsorption gefolgt von Kapillarkondensation und bietet Zugang zu potentiell hohen Arbeitskapazitäten. Neben klassischen Adsorbaten wie N₂ und Ar, gilt dies auch für Wasser und weitere insbesondere organische Adsorbate.⁹⁰ Zuletzt können auch kooperative Effekte, z.B. in Form einer Chemisorption, stufenförmige Adsorptionsisothermen zeigen. Dies wurde von Long et al. an Diamin-funktionalisierten IRMOF-74-II anhand der Insertion von CO₂ in die Metall-Amin-Bindung unter Bildung von Ammoniumcarbamaten herausragend gezeigt.⁹¹

Die bereits vorgestellten CID-5 und ELM-11 und eine Vielzahl an flexiblen MOFs zeigen zwar diesen vorteilhaften stufenförmigen Isothermenverlauf, aufgrund ihrer jedoch meist geringen Porosität, bilden sie keine Alternative zu mesoporösen Materialien bezüglich der Speicherung von Adsorbaten. Wobei einige flexible MOF-Materialien bekannt sind, welche einen S-förmigen Typ-F-IV Verlauf gepaart mit einer hohen Sättigungsaufnahme (>250 cm³ g⁻¹) zeigen.^{80, 92-94}

Zaworotko et al. berichteten das zweifach interpenetrierte MOF X-**pcu**-5-Zn [$\text{Zn}_2(\text{Dmtdc})_2(\text{Dpe})$] (Dmtdc^{2-} = 3,4-Dimethylthieno[2,3-b]thiophene-2,5-dicarboxylat, Dpe = 1,2-Di(4-pyridyl)ethylen), welches reversibel zwischen der offenen X-**pcu**-5-Zn α -Form und zwei nicht-porösen Formen X-**pcu**-5-Zn- β und X-**pcu**-5-Zn- γ wechselt (siehe Abbildung 18). Das CO_2 Sorption bei 195 K zeigt ein S-förmiges Typ-F-IV-Profil gepaart mit einer hohen Sättigungsaufnahme von $255 \text{ cm}^3 \text{ g}^{-1}$.

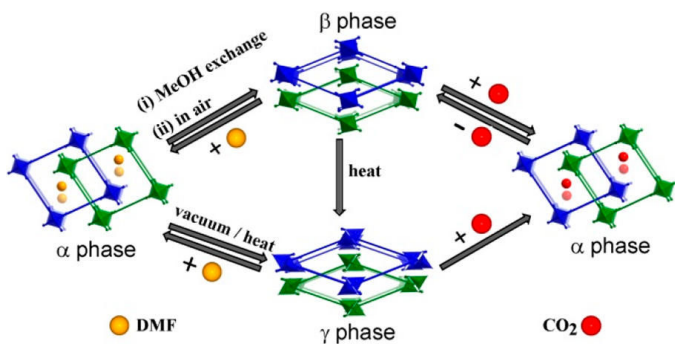


Abbildung 18. Darstellung der reversiblen strukturellen Transformation von X-**pcu**-5-Zn zwischen poröser und den nicht-porösen Phasen (© 2018 mit Erlaubnis von American Chemical Society aus Zaworotko et al.⁹⁴).

Die daraus resultierenden hohen Kapazitäten machen diese flexiblen MOFs insbesondere in Gasspeicher/Liefersysteme (insbesondere für Methan) äußerst interessant. Co(bdp) (bdp $^{2-}$ = 1,4-Phenyldipyrazolat) zeigte hierbei nicht nur einen S-förmigen Isothermenverlauf gepaart mit einer hohen CH₄-Kapazität in Hochdrucksorptionsexperimenten, sondern die für den Phasenübergang notwendigen Energien wurden auch als intrinsisches Wärmemanagement identifiziert (Abbildung 19).^{93, 95}

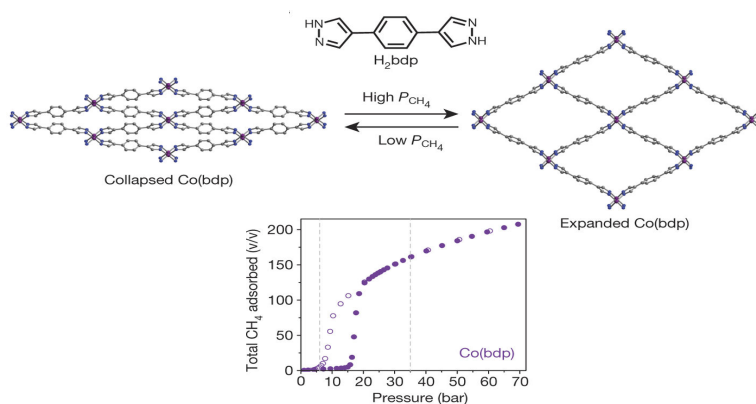


Abbildung 19. Darstellung der kollabierten und der expandierten Phase von Co(bdp) und die S-förmige CH₄-Hochdruckisotherme bei 298 K (© 2015 mit Erlaubnis der Macmillan Publishers Limited aus Long et al.⁹³).

1.2 Überblick zum Crystal Engineering anhand von strukturellen Analogismen und Synergismen von Carbonsäuren und Pyrazolen

Das Verständnis und die Beschreibung chemischer Bindungen ist ein zentraler Bestandteil der Chemie. Daran anlehnd wird das Crystal Engineering als Teildisziplin der Supramolekularen Chemie angesehen, welche sich mit dem Verständnis intermolekularer, sprich nicht-kovalenter, Wechselwirkungen in Festkörpern auseinandersetzt und diese gezielt versucht einzusetzen.⁹⁶⁻⁹⁹ Hierbei wird ein Kristall, in Anlehnung an Jean-Marie Lehns Paradigma der Übermoleküle (engl. supermolecules),¹⁰⁰ als eine große periodisch angeordnete supramolekulare Einheit gesehen, mit der Kristallisation als dem zugrundeliegendem Selbst-Organisationsprozess.¹⁰¹ In diesem Sinne stellt der Kristallisierungsprozesses einen emergenten Vorgang dar, mit der Festkörperkristallstruktur als übergeordneter Komplexitätsebene, was zur Folge hat, dass der Ausgang dieses Prozesses als auch die daraus folgenden Eigenschaften nur schwer aus den molekularen Einheiten vorhergesagt werden können. Die experimentell erhaltenen Kristallstrukturen sind folglich das Produkt eines schwer zu fassenden Gleichgewichts schwacher intermolekularer Wechselwirkungen. Das Crystal Engineering versucht – vornehmlich ex post – dies zu verstehen und supramolekulare Synthesestrategien zu entwickeln die versuchen den Kristallisierungsprozess zu entschlüsseln.

Im Folgenden werden grundlegende Aspekte des Crystal Engineerings am Beispiel von rein organischen als auch Koordinationsverbindungen von Carbonsäuren und Pyrazolen eingeführt. Insbesondere wird hierbei auf immer wiederkehrende strukturelle Analogismen und Synergismen dieser beiden funktionellen Gruppen eingegangen. Dies geschieht hauptsächlich, da dies für Carbonsäuren in der Literatur etabliert ist und so die Beschreibung der Strukturen von Pyrazolen erleichtert wird.

Die Kristallstruktur als Produkt des Kristallisierungsprozesses stellt aufgrund der vielen potentiellen Wechselwirkungen schon einer funktionellen Gruppe als auch aus dem variablen Zusammenspiel von kinetischen und thermodynamischen Einflüssen bei der Nukleation eine große Herausforderung in der Vorhersage dar. Daher hat sich mit dem simplifizierenden Konzept der supramolekularen Synthone ein wichtiges Analyse-Werkzeug im Bereich organischer Kristalle etabliert. Supramolekulare Synthone stellen hierbei die kleinsten strukturellen Einheiten innerhalb einer Kristallstruktur in Form von möglichen Motiven intermolekularer Wechselwirkungen zwischen funktionellen Gruppen dar.¹⁰² Dabei sollen Synthone die essentiellen Merkmale in Form von gerichteten intermolekularen Wechselwirkungen abbilden, um so einen nachvollziehbaren Beitrag zum Verständnis einer Kristallstruktur zu liefern. Sie sind damit analog zu dem im Kapitel zu Metall-organischen

Gerüstverbindungen vorgestellten Konzepts der sekundären Baueinheiten zu Analyse deren Strukturen.

Die generelle Direktionalität und Stärke gibt der Wasserstoffbrückenbindung ihre exponierte Rolle bei der Untersuchung supramolekularer Aggregate und sie ist dementsprechend auch eine der am häufigsten untersuchten Wechselwirkungen im Bereich des Crystal Engineerings.¹⁰³⁻¹⁰⁵ Wasserstoffbrückenbindungen sind allgemein definiert als anziehende Wechselwirkungen zwischen einem Wasserstoffatom eines Moleküls/Molekülfragments X–H, in welchem X elektronegativer als H ist, und einem Atom/einer Atomgruppe des selben oder eines anderen Moleküls.¹⁰⁶⁻¹⁰⁷

Carbonsäuren mit einem Wasserstoffbrücken-Donor als auch einem Wasserstoffbrücken-Akzeptor sind prädestiniert zur Selbstassoziation mittels Wasserstoffbrückenbindungen. Somit beruht die Analogie im Bereich des (organischen) Crystal Engineerings darauf, dass auch Pyrazole, durch ihre benachbarten pyrrolischen NH- und pyridinischen N-Donoratome, eine analoge Komplementarität hinsichtlich ihres Selbstassoziationspotentials durch Wasserstoffbrückenbindungen aufweisen. Diese Synthone als supramolekulare Motive können mithilfe der Etter-Notifikation einem Graphsymbol der Form A_y^x zugeordnet werden (mit A = D (Dimer), C (Catemer), R (Ring), S (intramolekular); x = Anzahl der Wasserstoffbrückendonoren; y = Anzahl der Wasserstoffbrückenakzeptoren).¹⁰⁸⁻¹¹⁰ Die durch Selbstassoziation gebildeten Homosynthone von Carbonsäuren und Pyrazolen dienen hierbei auf schöne Art und Weise als Beispiel für den strukturellen Analogismus beider funktioneller Gruppen (Abbildung 20).

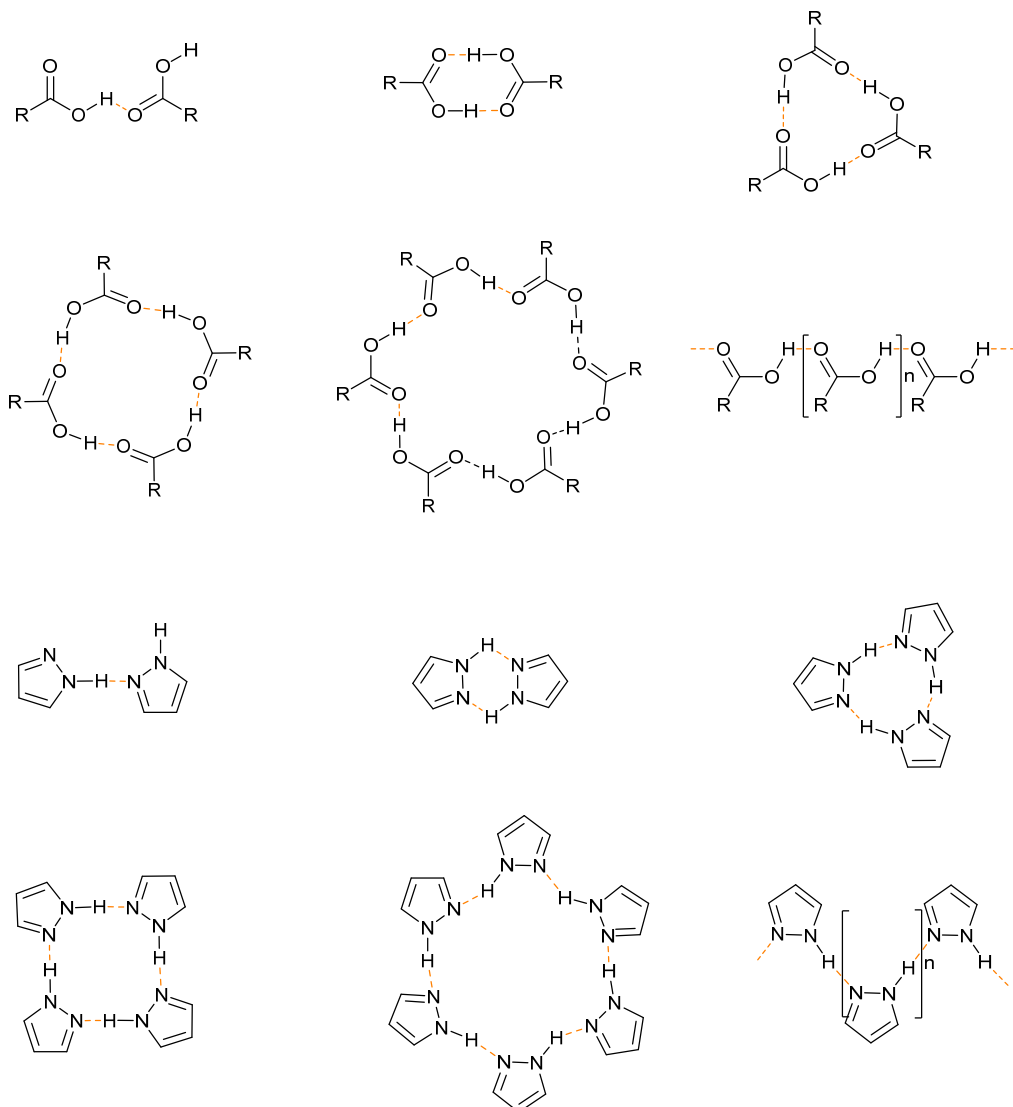


Abbildung 20. Oben: Homosynthone der Selbstassoziation von Carbonsäuren: Dimer (D), dimerisiertes, zyklisches R₂²(8)-Synthon, trimerisches R₃³(12)-Synthon, tetramerisches R₄⁴(16)-Synthon, hexamerisches R₆⁶(24)-Synthon und C(4)-catemer (Wasserstoffbrückenbindungen als orange-gestrichelte Linien, Übersicht zu supramolekularen Strukturen von Carbonsäuren auf Basis ihrer Homosynthone bei Perepichka et al.¹¹¹). Unten: Homosynthone der Selbstassoziation von 1H-Pyrazolen: Dimer (EBIMEI)¹¹², dimerisiertes, zyklisches R₂²(6)-Synthon (LADBEX)¹¹³, trimerisches R₃³(9)-Synthon (UDAYUT02)¹¹⁴, tetramerisches R₄⁴(12)-Synthon (LADIB)¹¹³, hexamerisches R₆⁶(18)-Synthon (HUMLUW)¹¹⁵ und C(3)-Catemer (NUBZUH/VONVEA)¹¹⁶⁻¹¹⁷ (Wasserstoffbrückenbindungen als orange-gestrichelte Linien, CCDC-Refcodes von Beispielstrukturen in Klammern).

Heterosynthone sind supramolekulare Motive, welche durch mehr als eine funktionelle Einheit gebildet werden. Anhand der Heterosynthone von Carbonsäuren und Pyrazolen kann ihr supramolekularer Synergismus auf Basis des Vorhandenseins eines benachbarten Wasserstoffbrücken-Donors und –Akzeptors in beiden funktionellen Gruppen verdeutlicht werden. Die gebildeten Heterosynthone spiegeln die in den Homosynthonen beider

funktionellen Gruppen gefunden Synthongeometrien des Dimers, Trimers, Tetramers und des Catemers wieder (siehe Abbildung 21).

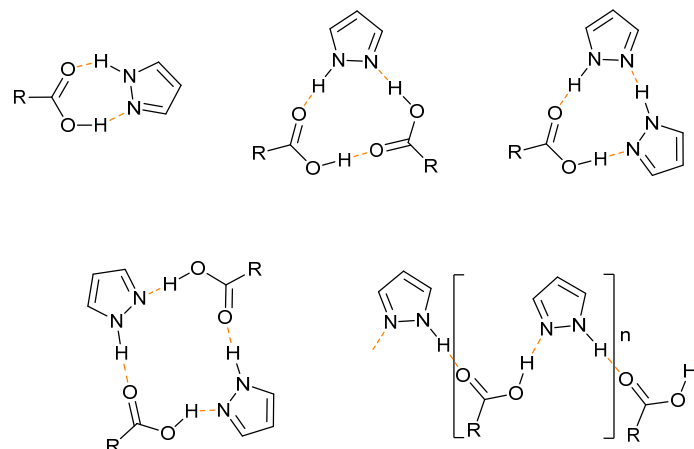


Abbildung 21. Beispiele für gefundene Heterosynthonen zwischen Carbonsäuren und 1H-Pyrazolen: dimerisiertes, zyklisches $R_2^2(7)$ -Synthon (TIDLIB)¹¹⁸, trimerisches $R_3^3(11)$ -Synthon (CUMQE^H)¹¹⁹, trimerisches $R_3^3(10)$ -Synthon (CUMQAD)¹¹⁹, tetramerisches $R_4^4(14)$ -Synthon (LABNIL)¹²⁰, und $C_2^2(7)$ -Catemer (NUBZUH)¹²¹ (Wasserstoffbrückenbindungen als orangegestrichelte Linien, CCDC-Refcodes von Beispielstrukturen in Klammern).

Die Pyrazol-4-carbonsäure als ein lineares Molekül, welches beide Funktionalitäten trägt und potentiell als ditopes Molekül Netzwerkstrukturen bilden könnte, kristallisiert mit dem dimerisierten, zyklischen $R_2^2(7)$ -Synthon in eindimensionalen Strängen in Analogie zu den Kristallstrukturen von linearen Dicarbonsäuren wie der Fumarsäure oder der Terephthalsäure.^{118, 122-124} Festkörper-NMR Untersuchungen an der Pyrazol-4-carbonsäure haben gezeigt, dass bei Raumtemperatur die O-H···N und O···H-N Wasserstoffbrückenbindungen schnell interkonvertieren. Wohingegen bei tiefen Temperaturen ein Übergang zu einer Protonen-geordneten Phase stattfindet.¹¹⁸ Die 4-(3,5-Dimethyl-1H-pyrazolyl)benzoësäure bildet ein wellenförmiges, zweidimensionales Wasserstoffbrückenbindungsnetzwerk mit **hcb**-Topologie auf Basis eines abwechselndes Catemer-Synthons, in welchem sowohl das Kohlenstoffatom der Carbonsäure als auch das Pyrazol einen 3-c Knoten darstellen.¹²¹ Diese Struktur steht folglich in Analogie zu den Kristallstrukturen der planaren Bispyrazole 4,4'-Bis-1H-pyrazol¹¹⁶ und 1,4-Bis(1-H-pyrazol-4-yl)benzol¹¹⁷ mit dem C3-Motif (siehe Abbildung 22).

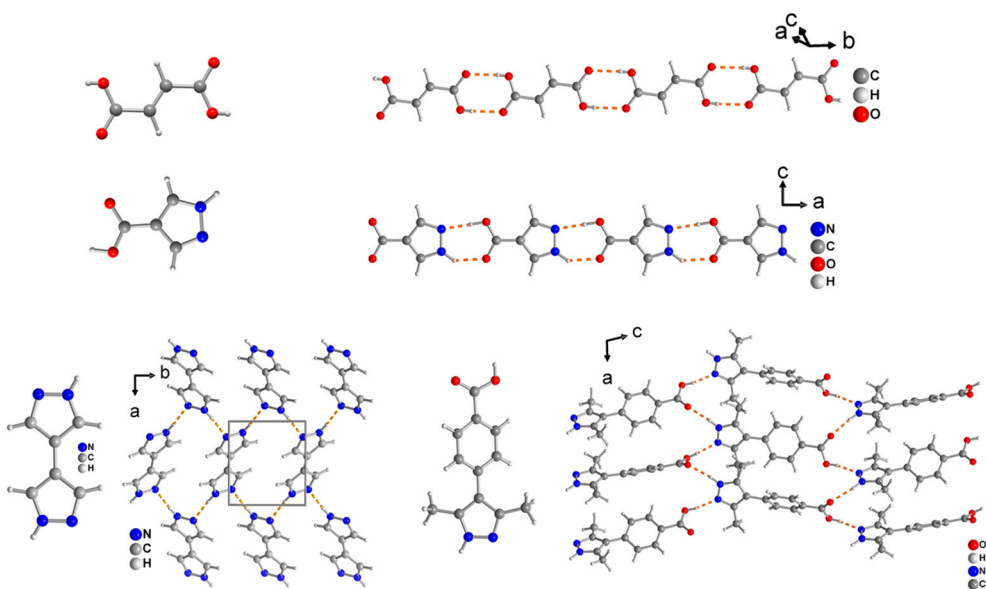


Abbildung 22. Gegenüberstellung der eindimensionalen Kettenstrukturen der Fumarsäure (FUMAAC01)¹²⁴ auf Basis des $R_2^2(8)$ -Homosynthons und der 1H-Pyrazol-4-carbonsäure (TIDLIB)¹¹⁸ auf Basis des $R_2^2(7)$ -Synthon und der zweidimensionalen Wasserstoffbrückennetzwerke in 4,4'-Bis-1H-pyrazol (UDAYIH)¹¹⁶ auf Basis des C3-Homosynthons und der 4-(3,5-Dimethyl-1H-pyrazolyl)benzoësäure (NUBZUH)¹²¹ auf Basis des catemerischen Heterosynthons.

Viele der unüblichen Eigenschaften des Wassers werden der Fähigkeit des Wassermoleküls zum Ausbilden von Wasserstoffbrückenbindungen zugeschrieben. Hierbei kann man grundsätzlich konstatieren, dass Wasser in Bezug auf die Fähigkeit Wasserstoffbrückenbindungen auszubilden selbstkomplementär mit einer tetraedrischen Direktionalität ist. Das stabilste Eispolymer unter Standardbedingungen ist I_h mit einer hexagonalen Trydimit- bzw. Lonsdaleit-Struktur in dem jedes Sauerstoff-Atom als ein tetraedrischer Knoten fungiert in dem es an den maximal möglichen vier Wasserstoffbrückenbindungen beteiligt ist. Gleiches gilt für das von König vorgestellte metastabile kubische Polymorph I_c mit einer Diamant-Topologie (siehe Abbildung 5).⁴¹

Gillon et al. identifizierten acht unterschiedliche Koordinationsumgebungen für Wasser in Kristallstrukturen mit Stickstoff und Sauerstoff als Wasserstoffbrückenakzeptoren und NH und OH als Wasserstoffbrückendonoren. Üblicherweise liegen Wassermoleküle hierbei als zweifacher Wasserstoffbrückendonator und ein- bis zweifacher Wasserstoffbrückenakzeptor vor.¹²⁵ Varughese und Desijaru unterteilten Hydrate nach der Rolle, welche das Wassermolekül in der Struktur spielt.¹²⁶ Der am häufigsten auftretende Fall ist der Einschluss von Wasser als Gast in kristalline Festkörper als Wirt. Dies kann in Form einzelner Wassermoleküle bis zu Wasserclustern erfolgen. Abhängig ihrer Dimensionalität befinden sie sich folglich in Kavitäten, Kanälen oder zwischen Schichten des Wirkristalls. Strukturelle

Untersuchungen dieser in kristallinen supramolekularen Wirten eingeschlossenen Anordnungen von Wassermolekülen hat viel zum grundlegenden Verständnis von Wasser und dessen Anomalie beigetragen. Umgekehrt kann aber auch Wasser der Wirt sein. Exemplarisch seien hier insbesondere die Gashydrate genannt, in welchen Käfige von Wassermolekülen das Wirtgitter darstellen.¹²⁷ Aber auch das von Gosh et. al. isolierte $(\text{H}_2\text{O})_{45}$ -Cluster – als das bisher größte seiner Art – mit einem Kryptanden als templierendem Gastmolekül ist beispielgebend für diesen Fall.¹²⁸ Da diese Einteilung häufig nicht trennscharf erfolgen kann, gibt es auch Fälle in denen man die Rolle des Wassers sowohl als Gast als auch als Wirt beschreiben kann.

Neben der Möglichkeit des Einschlusses von Wassermolekülen bzw. von Wasserclustern als Wirte, kann Wasser genauso gut ein integraler Bestandteil einer Festkörperstruktur sein. Das eröffnet natürlich die Möglichkeit, dass Wasser im holistischen Ansatz des Crystal Engineerings auch eine aktive Rolle als Strukturelement zugeschrieben werden kann. Die Schwierigkeit allein der Prognose, ob ein organisches Molekül ein Hydrat ausbildet, lässt aber die gezielte Nutzung des Wassermoleküls zur Synthese von Netzwerkstrukturen eher bezweifeln.¹²⁶ Aus diesen Gründen wird Wasser auch häufig als die Nemesis des Crystal Engineerings bezeichnet.¹²⁹⁻¹³⁰

Die Rolle von Wasser als Strukturelement kann exemplarisch an den Heterosynthonen von Carbonsäuren bzw. Pyrazolen mit Wasser erläutert werden. Hierfür wurde in Anlehnung an die von Zaworotko et al. getätigte Klassifizierung der Hydrate von Carbonsäuren aufgrund der bereits geschilderten supramolekularen Ähnlichkeit zu den Pyrazolen in den Homosynthonen nach ähnlichen Hydraten von 1H-Pyrazolverbindungen gesucht. Nicht überraschend konnten analoge Pyrazol-Wasser-Heterosynthone identifiziert werden.

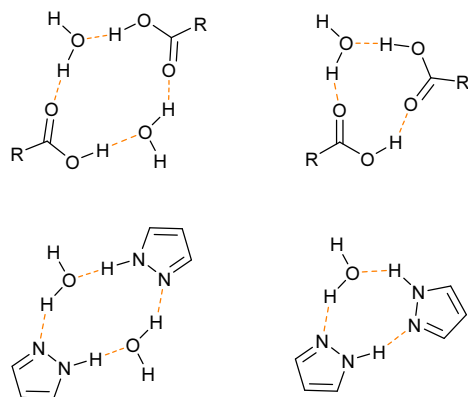


Abbildung 23. Verdeutlichung der strukturellen und supramolekularen Ähnlichkeit der Wasser-Carbonsäure Heterosynthone zu den Wasser-Pyrazol-Heterosynthonen an den Beispielen der jeweiligen $\text{R}_4^4(12)-\{(\text{H}_2\text{O})(\text{COOH})_4\}$ / $\text{R}_4^4(10)-\{(\text{H}_2\text{O})(\text{pz})_4\}$ und $\text{R}_3^3(10)-\{(\text{H}_2\text{O})_{0.5}(\text{COOH})_2\}$ / $\text{R}_3^3(8)-\{(\text{H}_2\text{O})_{0.5}(\text{pz})_2\}$ Ring-Motivpaare.

Klassischerweise setzt sich wie bisher beschrieben das Crystal Engineering mit Molekülstrukturen und deren Kristallpackung durch schwache supramolekulare Wechselwirkungen auseinander. Ein hierbei häufig anzutreffendes Phänomen ist das der Polymorphie. McCrone beschrieb 1965 Polymorphismus als das Auftreten unterschiedlicher Festkörperstrukturen durch die unterschiedliche räumliche Anordnung der molekularen Einheiten bei gleicher Zusammensetzung.¹³¹ Der Begriff Polymorph stammt vom griechischen πολύμορφος was mit so viel wie vielgestaltig übersetzt werden kann. Somit bedeutet dies anders ausgedrückt, dass das weiter oben beschriebene Zusammenspiel der vielen potentiellen Wechselwirkungen der funktionellen Gruppen zusammen mit den kinetischen und thermodynamischen Einflüssen der Nukleation, klassischerweise hervorgerufen durch unterschiedliche Kristallisationsbedingungen, zum Erhalt unterschiedlicher Formen in der Gestalt von Kristallstrukturen ein und derselben Verbindung führen. Mitscherlich war 1822 der erste, dem diesen Phänomen beim Studium von Arsenaten und Phosphonaten auffiel.¹³²⁻¹³³ Den Polymorphismus einer organischen Verbindung untersuchten erstmals Liebig und Wöhler am Beispiel von Benzamid¹³⁴, wobei es bis ins Jahr 2005 dauerte bis die Struktur der metastabilen Phase des Benzamids aufgeklärt wurde.¹³⁵

Wie jeder chemische Prozess ist auch die Kristallisation, als der dem Polymorphie-Phänomen zugrundeliegende Prozess, sowohl von thermodynamischen als auch kinetischen Faktoren abhängig. Die Eigenschaften einer Verbindung hängen von ihrer kristallinen Form ab, was für Polymorphe zu unterschiedlichen physikochemischen Eigenschaften wie z.B. Schmelzpunkt, Löslichkeit oder mechanischen Eigenschaften führen kann. Daneben können unterschiedliche Polymorphe von Explosivstoffen unterschiedliche Empfindlichkeit bezüglich ihrer Detonation, von Pigmenten eine unterschiedliche Farbigkeit, von Photosensibilitoren ein unterschiedliches Absorptionsverhalten und von organischen Halbleitern eine unterschiedliche Leitfähigkeit aufweisen. Große Aufmerksamkeit hat vor allem der Polymorphismus von pharmakologisch-aktiven Substanzen neben regulatorisch und patentrechtlichen Gründen insbesondere aufgrund der unterschiedlichen Bioverfügbarkeit unterschiedlicher Polymorphe erhalten.¹³⁶⁻¹³⁷

Eine wichtige Unterkategorie sind die sogenannten Konformationspolymorphe in welchen unterschiedliche molekulare Koformationen vorhanden sind.¹³⁸ Das Ergebnis der Rotation mit unterschiedlichen Torsionswinkeln um eine Einfachbindung eines Moleküls sind unterschiedliche Konformationen desselben. Wenn zusätzlich zur Variation des Torsionswinkels auch noch ein Wechsel in einen Potentialtopf eines (lokalen)

Energieminimas stattfindet, spricht man von Konformeren.¹³⁹ Daran Anlehnnend kann man die zwei unterschiedliche Konzepte einführen, welche mit Konformationen in Kristallstrukturen assoziiert werden können. Die konformelle Anpassung (engl. „conformational adjustment“) beschreibt das Phänomen, dass flexible Moleküle ihre Konformation im bezug zum Minimum in der Gasphase leicht ändern um die Gitterenergie des Kristalls als Summe der intra- und intermolekularen Energie zu minimieren. Daneben beschreibt die Konformationsänderung den Übergang über eine Rotationsbarriere in einen anderen Potentialtopf in ein anderes Konformer. Man spricht von Konformationspolymorphie, wenn zwei unterschiedliche Konformere desselben Moleküls in verschiedenen Kristallformen kristallisieren. Wohingegen polymorphe Formen, welche durch unterschiedliche konformelle Anpassung eines Moleküls im gleichen Potentialtopf beschrieben werden können, schlichtweg als Polymorphe bezeichnet werden (siehe Abbildung 23).¹³⁸

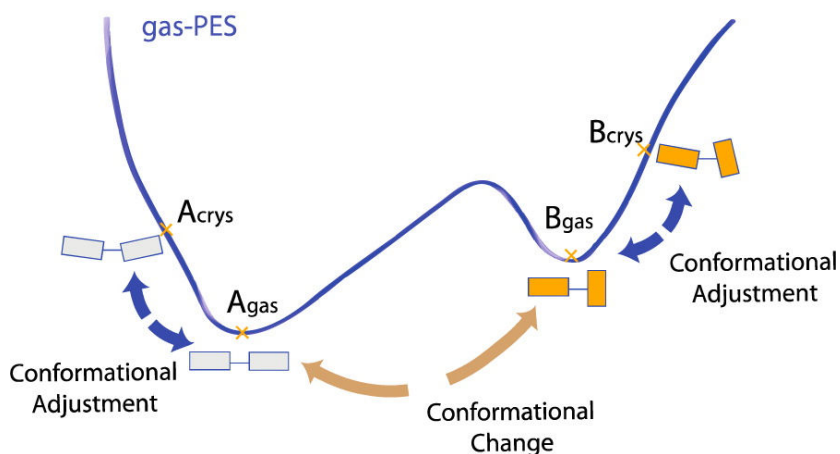


Abbildung 24. Schematische Darstellung der Konzepte der konformellen Anpassung und der Konformationsänderung (© 2018 mit Erlaubnis der American Chemical Society entnommen aus Cruz-Cabeza et al.¹³⁸)

Dies kann exemplarisch an der mannigfaltigen Polymorphie des 5-methyl-2-[(2-nitrophenyl)amino]-3-thiophenecarbonitrils, gennant ROY (für Red/OrangeYellow), erläutert werden. Hierbei entsprechen die Polymorphen jeweils unterschiedlich konformell angepassten Versionen des gleichen Konformers (Abbildung 25).¹⁴⁰

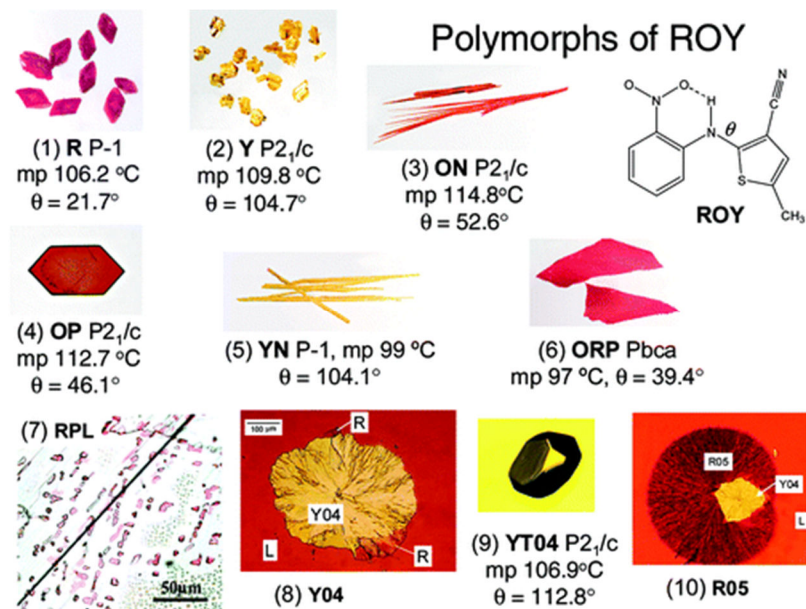


Abbildung 25. Darstellung der Polymorphe von ROY. Die Nummerierung von 1-10 stellt die Reihenfolge der Entdeckung der Polymorphe dar. Die Polymorphe haben unterschiedliche Konformationen definiert durch den Torsionswinkel θ . Die Polymorphe R (QAXMEH02), ON (QAXMEH), OP (QAXMEH03), ORP (QAXMEH05) stehen zu den Polymorphen Y (QAXMEH01), YN (QAXMEH04), YT04 (QAXMEH12) in Beziehung von Konformationspolymorphen. R05 (QAXMEH31) enthält zwei unabhängige Moleküle mit unterschiedlichen Konformationen in der asymmetrischen Einheit, welche beide der Gruppe der orange/roten ROY Polymorphe R, ON, OP, ORP zugeordnet werden können. (© 2010 mit Erlaubnis der American Chemical Society entnommen aus Yu et al.¹⁴⁰)

Wohingegen Polymorphe als „packing polymorphs“ bezeichnet werden, wenn sie sich deutlich in ihrer drei-dimensionalen Kristallpackung unterscheiden, aber das molekulare Tecton nur leichte Unterschiede in seiner Konformation zeigt und das gleiche supramolekulare Synthon ausgebildet wird.¹⁴¹⁻¹⁴² Um Strukturen höherer Dimensionalität zu bilden, sollten oligotope Moleküle der selbstkomplementären Carbonsäure- oder Pyrazolfunktionalitäten verwendet werden. Die einfachsten Verbindungen sind dementsprechend linearen Dicarbonsäuren wie die Fumarsäure oder die Terephthalsäure. Beide Dicarbonsäuren assoziieren wie oben bereits für die Fumarsäure gezeigt mittels des dimeren $R_2^2(8)$ -Synthons¹⁴³ in eindimensionale Ketten. Für beide wurden unterschiedliche Polymorphe isoliert, wobei sich die Kristallstrukturen der Fumarsäure^{122, 124} und den drei Polymorphen der Terephthalsäure^{123, 144} lediglich durch die Packung dieser Ketten auf Basis des $R_2^2(8)$ -Synthons unterscheiden (siehe Abbildung 22).

Analog sind natürlich auch symmetrische lineare ditope Bispyrazole dafür geeignet. Der einfachste Vertreter ist das oben bereits vorgestellte planare 4,4'-Bis-1*H*-pyrazol,¹¹⁶ welches auf Basis des catemeren C3-Homosynthons ein zweidimensionales 3-c **hcb** (honeycomb) Netz, mit jeder Pyrazolfunktionalität als 3-c Knoten, bildet (siehe Abbildung 22).

Für das methylsubstituierte Analogon 4,4'-Methylenebis(3,5-dimethyl-1*H*-pyrazols) ($\text{H}_2\text{Me}_4\text{mbpz}$) sind zwei Polymorphe beschrieben. In beiden Polymorphen bildet das gewinkelte $\text{H}_2\text{Me}_4\text{mbpz}$ ebenfalls über $\text{NH}\cdots\text{N}$ -Bindungen verknüpfte **hcb** Netze, wobei die **hcb** Netze α -Polymorph als wellenförmig und im β -Polymorph als treppenförmig beschrieben wurden.¹⁴⁵ Trotz der erwarteten Flexibilität des Liganden, liegt $\text{H}_2\text{Me}_4\text{mbpz}$ in beiden Polymorphen mit einem äußerst ähnlichen Drehwinkel vor. Aber die Packung der **hcb**-Schichten der beiden Polymorphen kann für das β -Polymorph mit einer AA- und für das α -Polymorph mit einer AB-Packung beschrieben werden.

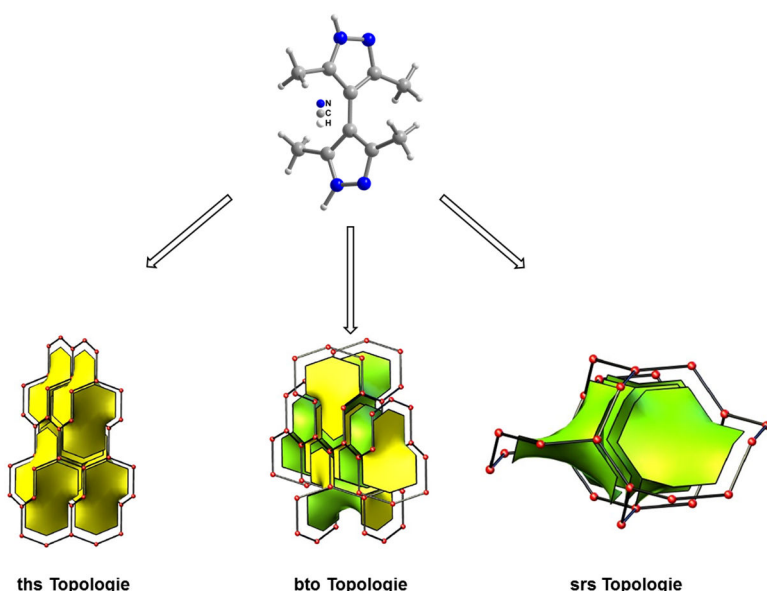


Abbildung 26. Schematische Darstellung der von den Polymorphen des Bispyrazols Me_4npz gebildeten Topologien (Bilder der Topologien entnommen aus der RCSR-Datenbank²³ unter <http://rcsr.anu.edu.au/>).

Für das Bispyrazol $\text{H}_2\text{Me}_4\text{bpz}$ (4,4'-bis(3,5-dimethyl-1*H*-pyrazols) wurde ein facettenreicher Polymorphismus, mit der Isolierung dreier Polymorphe, beschrieben.^{115, 117} Die erhaltenen Polymorphe können durch unterschiedliche 3-c (10,3) Netzwerken beschrieben werden und stellen folglich sogenannte supramolekulare Isomere dar.⁵⁸ Die α - und β - Polymorphe basieren auf dem catemerlen Synthon und haben die **ths** (Thoriumsilicid) bzw. die **bto** (Borrioxid) als ihre zugrundeliegende Topologie. Das γ -Polymorph zeigt die chirale **srs** (Strontiumsilicid) Topologie auf Basis des trimeren Homosynthons des Pyrazols (siehe Abbildung 26 und für die schematische Darstellung der Homosynthone des Pyrazols Abbildung 20).^{114, 116}

2. Motivation

Das Primärziel dieser Arbeit stellt die Synthese und Charakterisierung insbesondere der supramolekularen Wechselwirkungen von pyrazolhaltigen Netzwerkstrukturen da. 1*H*-Pyrazole integriert in oligotopen Liganden sind prädestiniert – erstens aufgrund ihrer vielfältigen Komplexchemie und zweitens durch das Vorhandensein pyrrolischer NH-Funktionalitäten und pyridinischen Stickstoffdonoratom – Koordinationsnetzwerke als auch supramolekulare Netzwerke auszubilden.

In der Literatur sind Metall-organische Gerüstverbindungen (MOFs) auf der Basis von T-förmigen Liganden in welchen eine V-förmige Dicarboxylateinheit (insbesondere Isophthalat) mit einer N-Heterozykleneinheit mit einer pyridinischen Stickstoffdonoratom (z.B. Pyridin, Imidazol, Triazol und Tetrazol), welche unter dem sogenannten „supramolecular-building-layer“-Ansatz rationalisiert werden können, bekannt. Viele dieser MOFs zeigen in einer vielversprechende Anwendungspotentiale in der Gassorption und –separation.

Es wird antizipiert, das unter der Prämisse, dass die pyrrolische NH-Funktionalität des Pyrazols nicht deprotoniert wird, T-förmige Dicarboxylat-Pyrazol-Liganden ebenfalls MOFs hinsichtlich des „supramolecular-building-layer“-Ansatzes ausbilden und die NH-Funktionalität als weitere Interaktionseinheit zur Verfügung steht. Für diese MOFs soll ein geeignetes Aktivierungsprotokoll gefunden werden und sie sollen insbesondere hinsichtlich ihrer Sorptionseigenschaften untersucht und mit exponierten Vertretern dieser Materialklasse verglichen werden.

Da insbesondere auch die Nutzung von Bispyrazolen zum Aufbau von Netzwerkstrukturen bekannt ist, soll dies an dem aus an dem durch Hüttel et al. 1955 erstmals synthetisierten Vertreter Azobis(3,5-dimethyl-1*H*-pyrazol), aber bisher zur Synthese von Festkörperstrukturen nicht genutzten, geschehen. Hierbei soll ein besonderes Augenmerk auf den Einfluss von molekularen Baueinheiten (z.B. Konformere, Metallkomplexe oder –cluster) auf die von ihnen gebildeten supramolekularen Netzwerke gelegt werden.

Alle erhaltenen Netzwerke sollen mit ihren zugrunde liegenden Topologien beschrieben und mit den gängigen Charakterisierungsmethoden analysiert werden.

3. Kumulativer Teil

In den folgenden Kapiteln werden die Ergebnisse der Dissertation, welche in Form von Erstautorschaften in internationalen Journals veröffentlicht wurden, dargestellt. Jede Publikation steht mit eigener Aufzählung für sich. Abbildungen, Tabellen und Schemata folgen der Nummerierung der Publikation. Ebenso hat jede Publikation ein eigenständiges Literaturverzeichnis am Ende des jeweiligen Kapitels und die Referenznummern gehören nicht zum Literaturverzeichnis am Ende der Arbeit.

Jede Publikation wird durch den Titel, die Liste der Autoren, dem Namen des Journals und einer Kurzzusammenfassung eingeleitet. Im Folgenden werden die Eigenanteile an Publikationen aufgezeigt.

Kapitel 2.1

S. Millan, B. Gil-Hernández, E. Milles, S. Gökpınar, G. Makhlofi, A. Schmitz, C. Schlüsener, C. Janiak*: “rtl-M-MOFs ($M = Cu, Zn$) with a T-shaped bifunctional pyrazole-isophthalate ligand showing flexibility and S-shaped Type F-IV sorption isotherms with high saturation uptakes for $M = Cu$ ” *Dalton Trans.*, **2019**, *48*, 8057-8067.

Eigenanteile an der Publikation:

- Idee und Konzeption des Projekts auf Basis einer ausgiebigen Literaturrecherche
- Synthese des Liganden und der MOFs inklusive Durchführung der gängigen Charakterisierungsmethoden und der Sorptionsmessungen.
- Eigenständige Auswertung und Darstellung aller Ergebnisse in Form einer wissenschaftlichen Publikation.
- Frau Dr. Gil-Hernández führte die finale Strukturverfeinerung $rtl\text{-}[Cu(Hlsa-az-dmpz)]$ durch.
- Herr Erik Milles war während seiner Bachelorarbeit an Vorarbeiten und der Implementierung von geeigneten Synthese und Aktivierungsprotokollen beteiligt.
- Die weiteren Koautoren waren an der Durchführung genutzter Analysen beteiligt.
- Überarbeitung, finale Abstimmung und Revision des Manuskripts in Zusammenarbeit mit Herrn Prof. Dr. Christoph Janiak.

Kapitel 2.2

Simon Millan, Jamal Nasir, Beatriz Gil-Hernández, Tim-Oliver Knedel, Bastian Moll, Ishtvan Boldog, Oliver Weingart, Jörn Schmedt auf der Günne, and Christoph Janiak*: “The Solid-State Landscape of 4,4'-Azobis(3,5-dimethyl-1H-pyrazole) With the Isolation of Conformer-dependent Polymorphs” submitted

Eigenanteile an der Publikation:

- Konzeption des Projekts auf Basis erster Ergebnisse und einer ausgiebigen Literaturrecherche
- Frau Dr. Gil-Hernández führte die finale Strukturverfeinerung der Strukturen des Hemihydrats durch
- Durchführung, Analyse und Verschriftlichung der Ergebnisse der Festkörper-NMR-Untersuchungen durch Herrn Jamal Nasir und Herrn Prof. Dr. Jörn Schmedt auf der Günne
- Theoretische Kalkulationen der Stabilitäten der einzelnen Konformere durch PD Dr. Oliver Weingart.
- Eigenständige Auswertung, Interpretation und Darstellung aller Ergebnisse in Form einer wissenschaftlichen Publikation.
- Herr Dr. Ishtvan Boldog lieferte Anmerkungen und half bei der Interpretation der Ergebnisse
- Die weiteren Koautoren waren an der Durchführung genutzter Analysen beteiligt.
- Überarbeitung, finale Abstimmung des Manuskripts in Zusammenarbeit mit Herrn Prof. Dr. Christoph Janiak.

Kapitel 2.3

S. Millan, G. Makhloufi, C. Janiak*: “Metal-4,4'-azobis(3,5-dimethyl-1H-pyrazole) complexes with 7- and 9-membered hydrogen-bonded rings originating from the pyrrolic N-H function”
Z. Anorg. Allg. Chem. **2019**, 645, 893-899.

Eigenanteile an der Publikation:

- Synthese und Charakterisierung des Liganden und der Komplexverbindungen
- Eigenständige Auswertung, Interpretation und Darstellung aller Ergebnisse in Form einer wissenschaftlichen Publikation.
- Aufnahme und erste Strukturverfeinerung durch Herrn Dr. Gamall Makhloufi
- Überarbeitung, finale Abstimmung und Revision des Manuskripts in Zusammenarbeit mit Herrn Prof. Dr. Christoph Janiak.

Kapitel 2.4

S. Millan, B. Gil-Hernández, E. Hastürk, A. Schmitz, C. Janiak*: "A 2D Zinc Coordination Polymer Built from the Mono-deprotonated 4,4'-Azobis(3,5-dimethyl-1H-pyrazole) Ligand"
Z. Anorg. Allg. Chem. **2018**, 644, 1311-1316.

Eigenanteile an der Publikation:

- Synthese und Charakterisierung des Liganden und des Koordinationspolymers
- Unterstützung bei der finalen Strukturverfeinerung durch Frau Dr. Gil-Hernández
- Eigenständige Auswertung, Interpretation und Darstellung aller Ergebnisse in Form einer wissenschaftlichen Publikation.
- Die weiteren Koautoren waren an der Durchführung genutzter Analysen beteiligt.
- Überarbeitung, finale Abstimmung und Revision des Manuskripts in Zusammenarbeit mit Herrn Prof. Dr. Christoph Janiak.

Kapitel 2.5

S. Millan, G. Makhlofi, C. Janiak*: "Incorporating the Thiazolo[5,4-d]thiazole Unit into a Coordination Polymer with Interdigitated Structure"
Crystals, **2018** 8, 30.

Eigenanteile an der Publikation:

- Synthese und Charakterisierung des Liganden und der Metall-organischen Gerüstverbindung
- finale Strukturverfeinerung durch Herrn Prof. Dr. Christoph Janiak.
- Überarbeitung, finale Abstimmung und Revision des Manuskripts in Zusammenarbeit mit Herrn Prof. Dr. Christoph Janiak.

3.1 rtl-M-MOFs (M = Cu, Zn) with a T-shaped bifunctional pyrazole-isophthalate ligand showing flexibility and S-shaped Type F-IV sorption isotherms with high saturation uptakes for M = Cu

The work presented in this chapter has been published in:

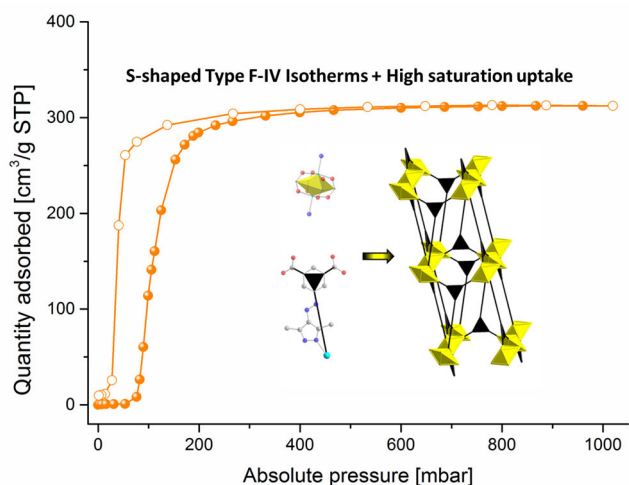
S. Millan, B. Gil-Hernández, E. Milles, S. Gökpınar, G. Makhloufi, A. Schmitz, C. Schlüsener and C. Janiak *Dalton Trans.*, **2019**, *48*, 8057-8067. DOI: 10.1039/C9DT01499C

As part of the Web Collection “Nitrogen Ligands”.

The article is reprinted with permission of the Royal Society of Chemistry.

Abstract

Two new rtl-MOFs **rtl-[Cu(H₃lsa-az-dmpz)]** and **rtl-[Zn(H₃lsa-az-dmpz)]** have been synthesized by using the new bifunctional ligand 5-(4-(3,5-dimethyl-1*H*-pyrazolyl)azo)isophthalic acid (H₃lsa-az-dmpz). Both frameworks are potentially porous structures with DMF molecules included in the channels of the as synthesized materials. The flexible MOF **rtl-[Cu(H₃lsa-az-dmpz)]** undergoes a reversible phase change into a closed form upon activation. Consequently, **rtl-[Cu(H₃lsa-az-dmpz)]** shows S-shaped Type F-IV adsorption profiles or a gate-opening effect at cryogenic temperatures with high saturation uptakes of 360 cm³ g⁻¹ for N₂ at 77 K and 310 cm³ g⁻¹ for CO₂ at 195 K. These profiles together with the reversibility could be reproduced upon repeated measurements on the same materials. The gravimetric high-pressure CO₂ adsorption shows a gate-opening at ~10 bar with an uptake of 332 mg g⁻¹. **rtl-[Zn(H₃lsa-az-dmpz)]** undergoes an irreversible transformation into a non-porous phase upon activation.



The publication is featured on the front cover in Issue 23, 2019 of Dalton Transactions:

Dalton Transactions 2019, 48, 7957. DOI: 10.1039/C9DT90133G

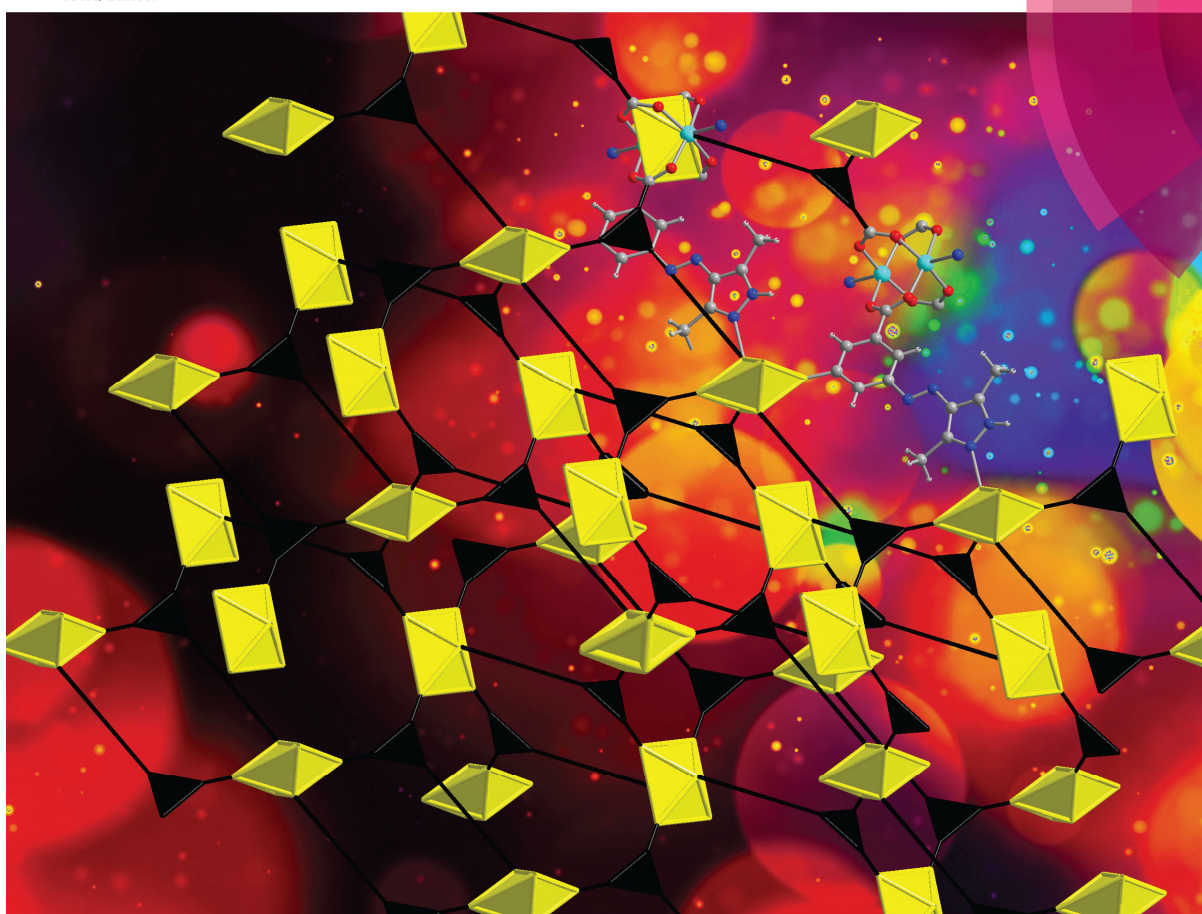
The Front Cover is reprinted with permission of the Royal Society of Chemistry.

Volume 48 Number 23 21 June 2019 Pages 7957–8504

Dalton Transactions

An international journal of inorganic chemistry

rsc.li/dalton



ISSN 1477-9226



ROYAL SOCIETY
OF CHEMISTRY

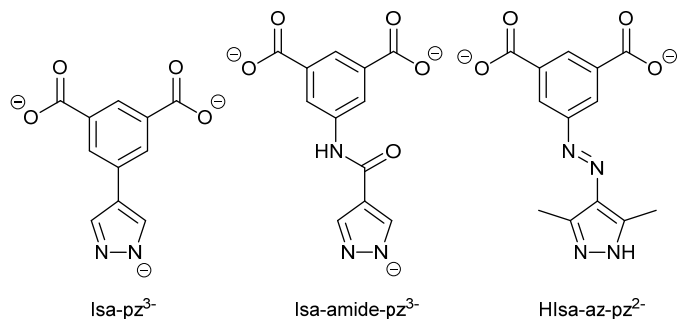
Celebrating
IYPT 2019

PAPER

Christoph Janiak *et al.*
rtl-M-MOFs ($M = Cu, Zn$) with a T-shaped bifunctional
pyrazole-isophthalate ligand showing flexibility and S-shaped
Type F-IV sorption isotherms with high saturation uptakes for
 $M = Cu$

Introduction

A plethora of MOFs have been constructed by the use of two ligands containing different functional groups. One famous strategy is the combination of linear dicarboxylates with 4,4'-bipyridine derivatives as pillars to form the so-called pillar-layer MOFs based on carboxylate-based SBUs, most classically the paddle wheel cluster of the formula $[M_2(OOC)_4N_2]$ as octahedrally shaped 6-c nodes.^{1–5} Eddaoudi *et al.* rationalized this strategy as axial-to-axial pillaring in their “supramolecular building layer approach”.⁶ These mixed-ligand MOFs yield the same intriguing properties as mono-ligand MOFs.⁷ The success of mixed-ligand MOFs directly led to the usage of bifunctional ligands in which the dicarboxylate group, which acts as the functionality to construct the layers, and an N-heterocycle, which acts as the pillar, are directly combined. Eddaoudi *et al.* named this strategy ligand-to-axial pillaring based on T-shaped ligands as trigonal 3-c nodes.^{6,8} Besides pyridines^{8–13} other N-heterocycles like triazoles,^{14,15} imidazoles¹⁶ and tetrazoles^{17,18} have been used in such T-shaped ligands to construct 3,6-connected MOFs with topologies like **rtl** (rutile),^{8,9,14–17} **apo** (α -PO₂),¹⁸ **pyr** (pyrite)¹¹ and **eea** (based on a Kagomé-lattice) (see Schemes S1 and S2 for the representation of bifunctional T-shaped ligands).^{8,10,13} Especially, the 3,6-c MOFs based on functionalized T-shaped ligands show extremely intriguing sorption properties.^{13,18–20} Heteroditopic pyrazolate-carboxylate ligands have specifically been employed to synthesize more stable versions of their carboxylate analogs due to the synergism in their coordination behavior.^{21–23} As pyrazole-carboxylates they mimic pyridine-carboxylates with the adjacent pyrrolic NH-function as an additional interaction site.^{24,25} Furthermore, Ma *et al.* reported a stable **rht**-MOF-pyr based on the T-shaped ligand 5-(pyrazolate-4-yl)isophthalic acid (Isapz^{3–}) with copper-paddle wheel- and trinuclear copper-pyrazolate-clusters (Scheme 1).^{26,27}



Scheme 1 T-shaped bifunctional pyrazolate-dicarboxylate ligands 5-(pyrazolate-4-yl)isophthalate (Isa-pz³⁻)^{26,27} and 5-(pyrazolate-4-carboxamido)isophthalate (Isa-amide-pz³⁻)^{28,29} reported in the literature and the pyrazole-dicarboxylate ligand 5-(4-(3,5-dimethyl-1H-pyrazolyl)azo)isophthalate (HIsa-az-dmpz²⁻) presented in this work.

An analogous amide-functionalized T-shaped pyrazolate-dicarboxylate ligand Isa-amide-pz³⁻ has been used by Bu *et al.* in a Co-MOF and a Zn-MOF, which show good CO₂-sorption properties (Scheme 1).^{28,29} We envisioned, that when the pyrrolic NH-function of the pyrazole moiety does not get deprotonated, which is usually the case under milder reaction conditions, these T-shaped pyrazole-dicarboxylate ligands should also be prone to yield MOFs based on the “supramolecular building-layer approach”. This was the case for their 5-membered N-heterocyclic counterparts triazole,^{14,15} imidazole,¹⁶ or tetrazole^{17,18} in analogy to mixed-ligand paddle-wheel MOFs synthesized by the combination of dicarboxylates with bipyrrazoles as pillars.^{30–32}

Mixed-ligand MOFs based on the paddle-wheel SBU often show flexible properties, when their activated forms are exposed to external stimuli such as, for example, guest adsorption, temperature changes or light, such systems are often referred to as soft porous crystals.^{7,33–39} Regarding the flexibility upon adsorption, Zaworotko *et al.* recently proposed a classification scheme for the adsorption isotherms observed for flexible microporous materials.⁴⁰ Their work highlighted, that especially flexible MOFs showing S-shaped F-IV isotherms, due to a transition from a non-porous into a porous phase, have a high potential in gas storage applications because they exceed their rigid microporous counterparts with the same uptake but Type I profiles regarding the gas uptake capacity.^{41–43} Surprisingly in respect to the huge amount of high-surface area MOFs, there exist only a handful of MOFs in the literature with such Type F-IV isotherms together with a high gas uptake of over 250 cm³g⁻¹ for the respective gas which was used for the measurement. These few MOFs are [M(bdp)] (M = Co²⁺, Fe²⁺, CH₄ at 298 K),^{44,45} DUT-8 (Ni) (N₂ at 77 K, CO₂ at 195 K, butane at 293 K),⁴⁶ JLU-Liu33L (N₂ at 77 K),⁴⁷ X-**dia**-1-Ni41 (CH₄ at 298 K)⁴⁰ and X-**pcu**-5-Zn (CO₂ at 195 K and 268 K).⁴⁸ Interestingly, X-**pcu**-5-Zn shows a reversible S-Shaped CO₂ adsorption profile over at least 30 cycles. Those S-shaped isotherms are more frequently observed for capillary

condensation phenomena, that is phase transition during adsorption and desorption.⁴⁹ MOFs showing such stepped isotherms with high working capacities were already identified as promising materials for adsorption heat transformation applications.⁵⁰

Herein, we report two isostructural MOFs **rtl**-[Cu(H₃lsa-az-dmpz)] and **rtl**-[Zn(H₃lsa-az-dmpz)] (H₃lsa-az-dmpz = 5-(4-(3,5-dimethyl-1*H*-pyrazolyl)azo)isophthalic acid) with rutile (**rtl**) topology following the ligand-to-axial pillaring approach constructed from a new T-shaped pyrazole-dicarboxylate ligand. After supercritical activation **rtl**-[Cu(H₃lsa-az-dmpz)] shows a stepped Type F-IV isotherm with high saturation uptakes for N₂ and CO₂.

Experimental

Materials and Methods

Reagents were obtained from commercial sources and used without further purification. Elemental analyses were conducted with a PerkinElmer CHN 2400 Analyzer. IR-spectra were recorded on a Bruker Tensor 37 IR spectrometer equipped with an ATR unit (Platinum ATR-QL, Diamond). ¹H and ¹³C spectra were measured with a Bruker Avance III-300. ESI-MS spectra were recorded with a Thermo Quest Ion Trap API mass spectrometer Finnigan LCQ Deca. Thermogravimetric analysis (TGA) was done with a Netzsch TG 209 F3 Tarsus (Netzsch, Selb, Germany) in the range from 20 to 600 °C with a heating range of 5 K min⁻¹ under a nitrogen atmosphere. The powder X-ray diffraction patterns (PXRD) were obtained on a Bruker D2 Phaser powder diffractometer with a flat silicon, low background sample holder, at 30 kV, 10 mA for Cu-K α radiation ($\lambda = 1.5418 \text{ \AA}$). In all diffractograms, the most intense reflection was normalized to 1. Supercritical activation was carried out on a Leica EMCPD 300 over 99 exchange cycles.

SEM images were collected on a JEOL JSM-6510 advanced electron microscope equipped with a LaB₆ cathode at 5–20 keV. The microscope was equipped with a Bruker Xflash 410 silicon drift detector. Adsorption Data for N₂ at 77 K (liquid nitrogen bath) and CO₂ at 195 K (acetone/dry ice bath) were collected on outgassed samples (120 °C for a minimum of 2 h, sample weight 35–85 mg) on a Micromeritics ASAP 2020 automatic gas adsorption analyzer. High-pressure gravimetric adsorption for CO₂ was conducted on a RUBOTHERM IsoSORB STATIC and the mass change was measured with a magnetic suspension balance (resolution 0.01 mg ± 0.03 mg) between 0–20 bar.

Single X-ray crystallography

Suitable crystals were carefully selected under a polarizing microscope, covered in protective oil and mounted on a 0.05 mm cryo-loop. Data collection: Bruker Kappa APEX2 CCD X-ray

diffractometer with microfocus tube, Mo-K α radiation ($\lambda = 0.71073 \text{ \AA}$), multi-layer mirror system, ω -scans; data collection with APEX2,⁵¹ cell refinement with SMART and data reduction with SAINT,⁵¹ experimental absorption correction with SADABS.⁵² Structure analysis and refinement: the structure was solved by direct methods using SHELXL2016,^{53,54} refinement was done by full-matrix least-squares on F^2 using the SHELXL-2016 program suite. Crystal data and details on the structure refinement are given in Table 1. Graphics were drawn with Diamond.⁵⁵ The simulated PXRD patterns were obtained by using Mercury.⁵⁶ Crystallographic data (excluding structure factors) for the structures in this paper have been deposited. CCDC 1908793 and 1908794.

Table 1 Crystal data and refinement details for **rtl**-[Cu(HIsa-az-dmpz)] and **rtl**-[Zn(HIsa-az-dmpz)].

	rtl-Cu	rtl-Zn
Chemical formula	C ₁₃ H ₁₀ CuN ₄ O ₄ ·2(C ₃ H ₇ NO)	C ₁₃ H ₁₀ N ₄ O ₄ Zn·2(C ₃ H ₇ NO)
M _r (g/mol)	495.98	497.81
Crystal system, space group	Monoclinic, <i>P</i> 2 ₁ / <i>c</i>	Monoclinic, <i>P</i> 2 ₁ / <i>c</i>
Temperature (K)	100	150
a (Å)	12.7515(16)	12.9493(11)
b (Å)	12.8834(16)	13.0923 (12) Å
c (Å)	13.5198(16)	14.0511 (13) Å
β (°)	107.355 (7)	109.842 (5)
V (Å ³)	2120.0(5)	2240.7(4)
Z	4	4
μ (mm ⁻¹)	1.080	1.14
d_{calc} (g/cm ³)	1.554	1.476
F(000)	1028	1032
Crystal size (mm)	0.04 × 0.004 × 0.004	0.05 × 0.01 × 0.01
T _{min} , T _{max}	0.627, 0.745	0.672, 0.745
No. of measured, independent and observed reflections	7626, 2129, 1172	26956, 3490, 2761
R _{int}	0.118	0.070
(sin θ/λ)max (Å ⁻¹)	0.493	0.575
R, wR(F^2), S [$F^2 > 2\sigma(F^2)$] ^[a] R, wR(F^2), S [all data] ^[a]	0.0672, 0.1474, 0.999 0.1311, 0.1756, 0.998	0.0445, 0.1105, 1.025 0.0606, 0.1196, 1.025
No. of reflections	2129	3490
No. of parameters	248	306
No. of restraints	10	1
$\Delta\rho_{\text{max}}, \Delta\rho_{\text{min}}$ ^[b] (e·Å ⁻³)	0.44, -0.36	0.85, -0.53

^[a] $R_1 = [\sum(|F_o| - |F_c|)/\sum|F_o|]$; $wR_2 = [\sum[w(F_o^2 - F_c^2)^2]/[\sum[w(F_o^2)^2]]]^{1/2}$. Goodness-of-fit $S = [\sum[w(F_o^2 - F_c^2)^2]/(n-p)]^{1/2}$. ^[b] Largest difference peak and hole.

Synthetic procedures

rtl-[Cu(HIsa-az-dmpz)]·(DMF)₂: 100 mg (0.336 mmol) of HIsa-az-dmpz 0.5H₂O were dissolved in 10 mL of DMF. The solution was added to a solution of 95 mg of Cu(BF₄)₂·xH₂O (0.6 mmol) in 10 mL of DMF. After a few minutes a greenish precipitate formed. This was dissolved again by adding 50 μ L 40% HBF₄. Afterwards the yellow solution was slowly heated over 48 h to 75 °C, held for another 48 h and finally cooled to RT over 6 h. The solution was washed four times with 3 mL DMF. Small pillared green crystals were formed (yield 78.2 mg, 47%). Before supercritical

activation with CO₂ the solvent was exchanged against acetone over one week three times per day at room temperature.

EA [%] calc. for [CuH₃Isa-az-dmpz]·(DMF)₂ CuC₁₉C₂₄C₆O₆ C 46.1, H 4.88, N 16.28; found: C 45.17, H 4.92, N 16.28.

EA [%] calc. for [Cu(H₃Isa-az-dmpz)]-act. CuC₁₃H₁₀N₄O₄ C 44.64, H 2.88, N 16.02; found C 43.85, H 2.61, N 15.93.

rtl-[Zn(H₃Isa-az-dmpz)]·(DMF)₂: 10.1 mg (0.034 mol) of H₃Isa-az-dmpz·0.5H₂O and 18.1 mg of Zn(NO₃)₂·4H₂O (0.069 mmol) were dissolved in 2 mL of DMF in a Pyrex tube. The yellow solution was heated over 24 h in an oven to 80 °C, the temperature was held for 48 h and finally cooled over 6 h to RT. The obtained small yellow block-shaped crystals were stored in the mother liquor until single crystal analysis (yield 7.8 mg, 46%). For upscaling, a solution of 200.3 mg (0.673 mmol) of H₃Isa-az-dmpz·0.5H₂O dissolved in 20 mL of DMF was added to solution of 363.7 mg (1.39 mmol) of Zn(NO₃)₂·4H₂O dissolved in 20 mL of DMF in a 100 mL vial. The same temperature program as for the single crystal synthesis was used. 264.9 mg (79%) of a polycrystalline yellow material was collected by suction filtration and shortly dried in air. The solvent was exchanged against acetone over one week three times per day. Afterwards the sample was activated *via* supercritical drying.

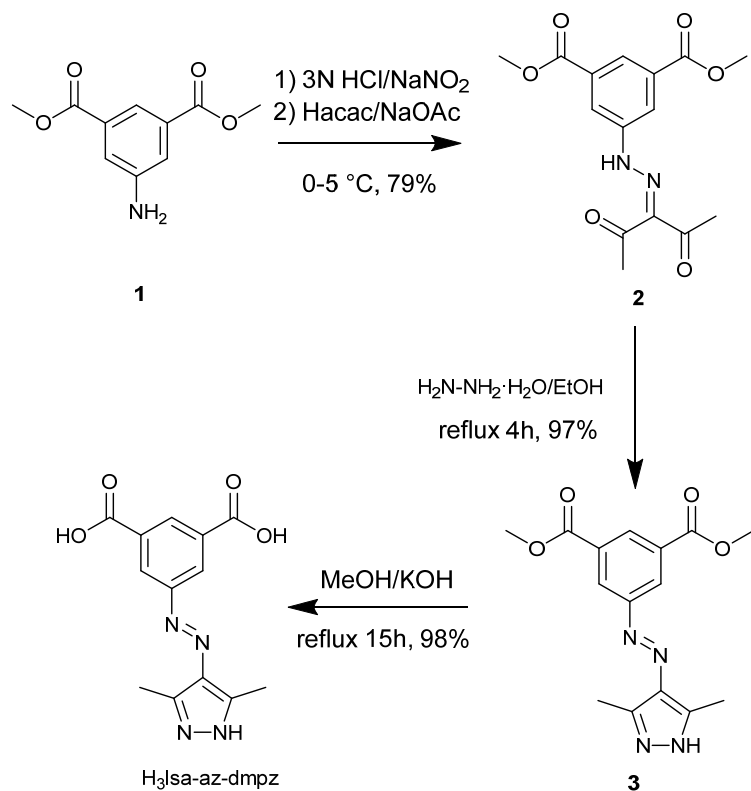
EA [%] calc. for [Zn(H₃Isa-az-dmpz)]·(DMF)₂ ZnC₁₉C₂₄C₆O₆ C 45.84, H 4.86, N 16.88; found C 45.19, H 4.62, N 16.28.

EA [%] calc. for [Zn(H₃Isa-az-dmpz)]-act. ZnC₁₃H₁₀N₄O₄ C 44.41, H 2.87, N 15.93; found C 42.97, H 3.27, N 15.16.

Results and Discussion

Synthesis of H₃Ilsa-az-dmpz

The ligand was synthesized starting via a Japp-Klingemann reaction of dimethyl 5-aminoisophthalate (**1**) with acetylectone to yield dimethyl 5-(2-(3-pentan-2,4-dionyl)hydrazone)isophthalate (**2**). Compound **2** was converted with hydrazine hydrate into dimethyl 5-(4-(3,5-dimethyl-1*H*-pyrazolyl)azo)isophthalate (**3**), which was deprotected under basic conditions to yield 5-(4-(3,5-dimethyl-1*H*-pyrazolyl)azo)isophthalic acid (H₃Ilsa-az-dmpz) as a new bifunctional T-shaped pyrazole-dicarboxylate in 75% yield over three steps (Scheme 2).



Scheme 2 Reaction scheme for the synthesis of H₃Ilsa-az-dmpz.

Syntheses and Crystal structures of rtl-Cu and rtl-Zn

The compound rtl-[Cu(H₃Ilsa-az-dmpz)] was obtained by the combination of Cu(BF₄)₂ *x*H₂O and 5-(4-(3,5-dimethyl-1*H*-pyrazolyl)azo)isophthalic acid (H₃Ilsa-az-dmpz) from DMF at 75 °C with tetrafluoroboric acid as a modulator for slowing down the crystal growth. Small grass-green crystals could be obtained. rtl-[Cu(H₃Ilsa-az-dmpz)] crystallizes in the monoclinic space group *P*2₁/c with one Cu(II) ion, one doubly deprotonated H₃Ilsa-az-dmpz²⁻ ligand and one DMF molecule which

is hydrogen-bonded *via* its carbonyl function to the pyrrolic nitrogen of the pyrazole in the asymmetric unit (Fig. 1). Each Cu(II) ion has a square-pyramidal coordination environment with Cu–O bond lengths between 1.929 (8)–1.949 (6) Å in the equatorial positions. The Cu–N1 bond is elongated with 2.151 Å due to Jahn–Teller distortion of the coordination environment. A second highly disordered DMF molecule was removed with the Squeeze routine implemented in PLATON.^{57,58} The pyrazole- and the isophthalate-moiety are tilted to each other by about 22°.

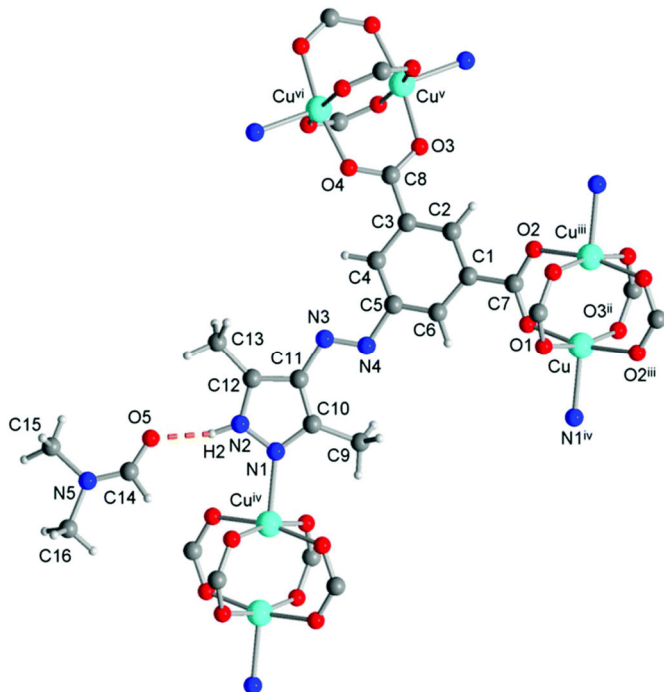


Fig. 1 Extended asymmetric unit of rtl-[Cu(Hlsa-az-dmpz)]. Symmetry transformations: i $x, -y + 1/2, z + 1/2$; ii $-x, y + 1/2, -z + 1/2$; iii $-x, -y + 1, -z + 1$; iv $-x + 1, -y + 1, -z + 1$; v $-x, y - 1/2, -z + 1/2$; vi $x, -y + 1/2, z - 1/2$. Details of hydrogen bond N2–H2···O5 (orange-dashed line): N2–H2 0.88 Å, H2···O5 1.86 Å N2···O5 2.691(14) Å N2–H2···O5 157°.

The isophthalate units of Hlsa-az-dmpz²⁻ link the paddle-wheel clusters into a **sqI**-sheet in the *bc*-plane (Fig. 2). The coordination of the pyridinic N1 of the pyrazole group in the apical position of the paddle wheel clusters extend the clusters to overall octahedral 6-c nodes and the Hlsa-az-dmpz²⁻ ligands to trigonal 3-c nodes. Consequently, the topological analysis with ToposPro yielded the binodal 3,6-c rtl-topology as the underlying net (Fig. 3).^{59,60} As mentioned in the introduction related rtl-MOFs have been constructed from T-shaped bifunctional ligands bearing pyridines, triazoles or imidazoles and tetrazoles. Yet, to the best of our knowledge this is the first report that such 3,6-connected MOFs can also be targeted by utilization of T-shaped pyrazole-dicarboxylate ligands.

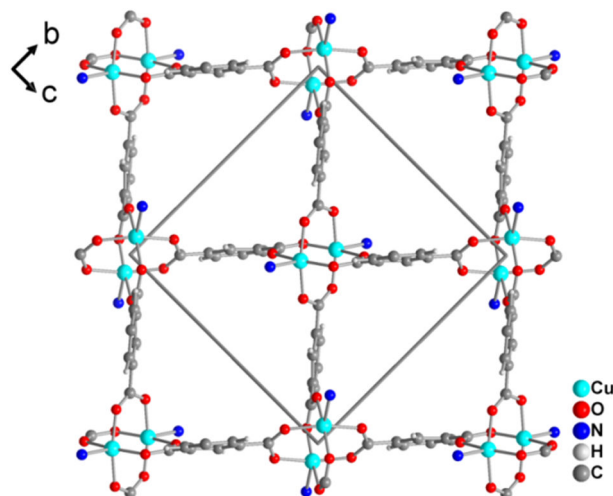


Fig. 2 Two-dimensional sql-net along the *bc*-plane in **rtI**-[Cu(Hlsa-az-dmpz)].

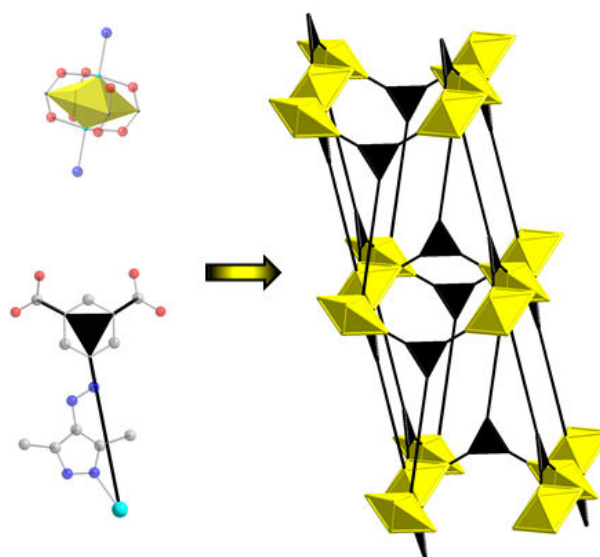


Fig. 3 Paddle wheel cluster as octahedral 6-c-node (yellow) and Hlsa-az-dmpz²⁻ as trigonal 3-c node (black) forming the 3,6-c **rtI**-topology.

Compound **rtI**-[Cu(Hlsa-az-dmpz)] is a potentially porous structure with one dimensional channels running along the *a*-axis (highlighted as yellow pillars in Fig. 4). Analysis with PLATON yields a solvent-accessible void volume of 968.8 Å³ or 46 vol% out of the unit-cell volume of 2120.0 Å³ for solvent-free **rtI**-[Cu(Hlsa-az-dmpz)].^{57,58}

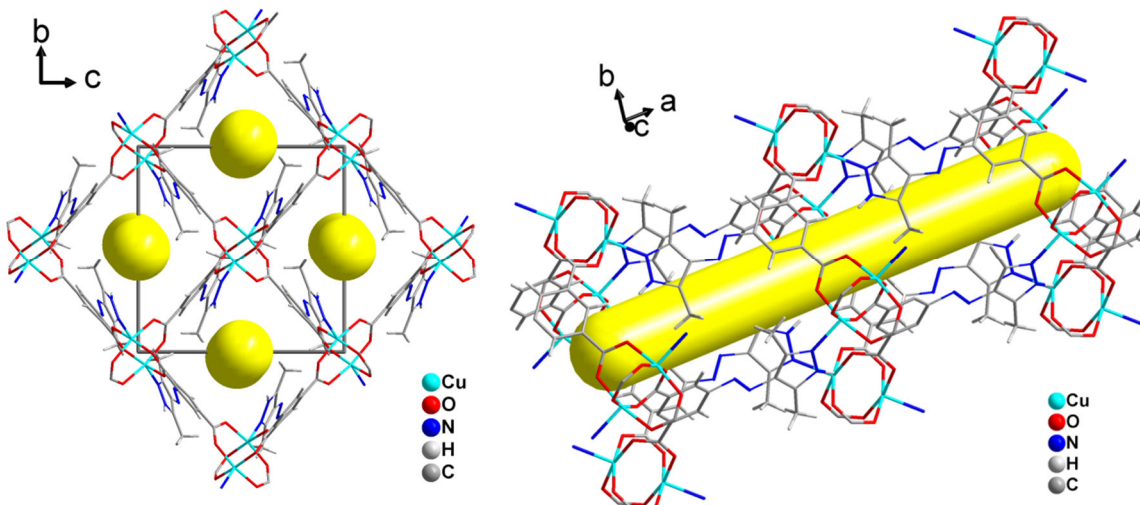


Fig. 4 Visualization of the one-dimensional channels along the *a*-axis as yellow columns in **rtl**-[Cu(Hlsa-az-dmpz)] (DMF molecules are omitted for clarity).

The combination of $\text{Zn}(\text{NO}_3)_2 \cdot 4\text{H}_2\text{O}$ with $\text{H}_3\text{Ils}\text{a-az-dmpz}$ in DMF at 80°C yielded yellow block-shaped crystals of composition $[\text{Zn}(\text{Hlsa-az-dmpz})] \cdot (\text{DMF})_2$. This compound is isostructural to **rtl**-[Cu(Hlsa-az-dmpz)] and also crystallizes in the space group $P2_1/c$ with one zinc ion, one Hlsa-az-dmpz²⁻ ligand and two DMF molecules in the asymmetric unit (Fig. S7). The Zn(II) ion has also a square pyramidal {ZnO₄N} coordination environment, but as expected for an d¹⁰-metal ion the Zn–O bond lengths with 2.028 (3) Å–2.041 (3) Å are comparable to the Zn–N1 bond length with 2.028 (3) Å. The pyrazole- and the isophthalate-moiety in **rtl**-[Zn(Hlsa-az-dmpz)] are more tilted with 33° than in **rtl**-[Cu(Hlsa-az-dmpz)]. Again in **rtl**-[Zn(Hlsa-az-dmpz)] the octahedral 6-c paddle-wheel clusters and the Hlsa-az-dmpz²⁻ ligand as trigonal 3-c nodes have the same connectivity forming a three-dimensional framework with **rtl**-topology as in **rtl**-[Cu(Hlsa-az-dmpz)]. The solvent accessible surface void volume was analysed with PLATON to be 1097.9 Å³ or 49 vol% out of the unit-cell volume of 2240.8 Å³ for solvent-free **rtl**-[Zn(Hlsa-az-dmpz)].

PXRD and thermal analysis

The phase purities of **rtl**-[Cu(Hlsa-az-dmpz)] and **rtl**-[Zn(Hlsa-az-dmpz)] were confirmed by positive matching of the PXRD patterns of the synthesized samples with the simulated ones obtained from the single crystal data (Fig. 6). The thermal analyses by TGA of both as-synthesized materials show a two-step weight loss corresponding to two DMF molecules (calc. 29.4 wt%, obs. 26.8 wt% for **rtl**-[Cu(Hlsa-az-dmpz)]; calc. 29.3 wt%, obs. 26.5 wt% for **rtl**-[Zn(Hlsa-az-dmpz)]). The first step corresponds to the weakly-bound DMF molecule in the channels and the second step to the hydrogen-bonded one (*cf.* Fig. S11-12). TGA thus

supports the sum formula of both as-synthesized frameworks as $\text{rtl-[M(HIsa-az-dmpz)]}\cdot(\text{DMF})_2$ (with M = Cu, Zn).

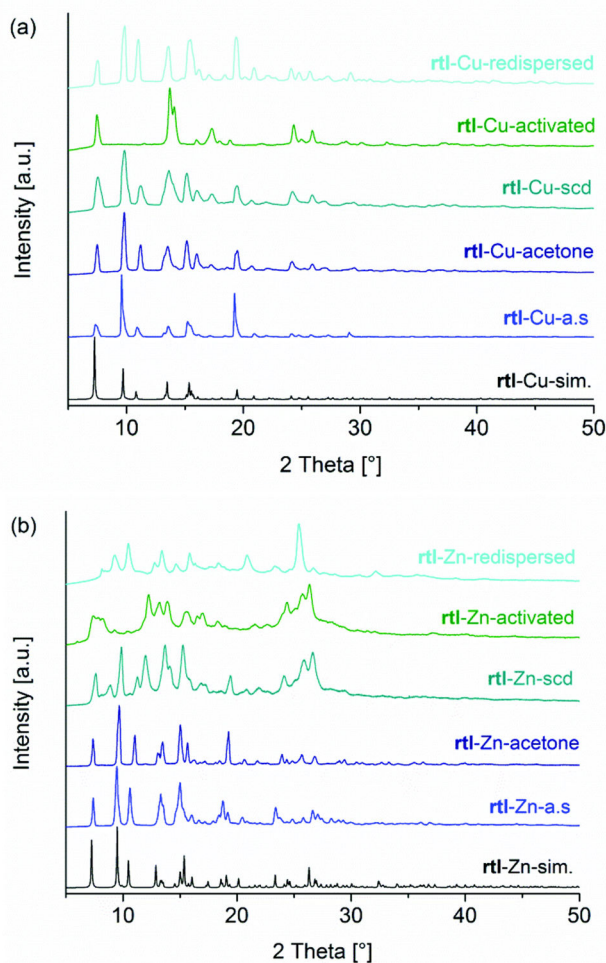


Fig. 5 Comparison of the simulated pattern PXRD pattern (black) of $\text{rtl-[M(HIsa-az-dmpz)]}$ (M = Cu (a), Zn (b)) with the as-synthesized (royal blue), acetone-exchanged (dark blue), supercritically-dried (darkcyan), activated (green) and the sample redispersed in DMF (cyan).

Prior to the gas sorption studies, the solvent was exchanged against acetone for both compounds, since acetone can act similarly like DMF as a hydrogen-bond acceptor *via* its carbonyl-function to the NH moiety of the pyrazole-ring. Both acetone-exchanged Cu- and Zn-frameworks show only slight changes when compared to the as-synthesized materials (Fig. 6) and the crystallinity was retained. For $\text{rtl-[Cu(HIsa-az-dmpz)]}$ the framework stays intact, although subtle peak broadening occurs (see PXRD pattern denoted as rtl-Cu-scd in Fig. 6a). Complete exchange of DMF against acetone in rtl-Cu-acetone can be assumed from the absence of the aldehyde signal (7.94 ppm) and the methyl groups (2.70 ppm, 2.86 ppm) of DMF in comparison to the as-synthesized sample (Fig. S8 and S9). The NMR spectrum of the digested sample after supercritical drying, rtl-Cu-scd indicates that there is

still one acetone molecule per formula unit retained in the framework. This can be rationalized as the one solvent molecule which is hydrogen-bonded to the NH-function of the pyrazole, therefore retaining the framework in its open form. The TGA of the supercritically dried sample further supports the assumption of the inclusion of one acetone molecule by a weight loss of 14.6% up to 105 °C (theoretically 14.2%). Thus, completing the activation procedure prior to the sorption experiments the sample was activated at 120 °C under high vacuum to remove the acetone molecule retained in the framework.

The obtained PXRD pattern for **rtl**-[Cu(Hlsa-az-dmpz)]-act. changes dramatically, which means that the material underwent a phase change. The shift of the reflections at lower angles to higher values are indicative for a contraction of the framework. The unit cell dimensions of **rtl**-[Cu(Hlsa-az-dmpz)]-act. were estimated with the program DICVOL04.^{61–63} The determined lattice parameters in the monoclinic crystal system are $a = 12.23(6)$ Å, $b = 15.36(9)$ Å, $c = 7.33(3)$ Å, $\gamma = 103.7(3)$ ° and a unit cell volume of 1328.35 Å³ with figures of merit of $M_{20} = 14.5$ and $F_{20} = 18.3(0.0101, 108)$. This implies a contraction of 37% of the unit cell volume. The channels in **rtl**-[Cu(Hlsa-az-dmpz)] run along the a -axis, which does not change in length (Fig. 4). Together with the S-shaped, Type F-IV sorption isotherms (see below), we assign the change in unit-cell parameters, that is the slight elongation of the b -axis and the strong decrease of the c -axis to about half the value, to the transformation of the framework into a closed non-porous structure upon activation. A detailed comparison of the PXRD patterns between the DMF-filled, the acetone-exchanged, the supercritically-dried and activated sample reveals that the reflections for the (100) plane can be identified at 7.5° 2 theta and the most prominent reflection of the (011) plane shifts from 9.8° to 13.7° 2 theta.

Dispersing a sample of **rtl**-[Cu(Hlsa-az-dmpz)]-act. in liquid DMF led to regeneration of the original phase **rtl**-[Cu(Hlsa-az-dmpz)]·(DMF)₂ (PXRD pattern denoted as **rtl**-Cu-redispersed in Fig. 6a). The phase change from the open to the closed phase upon activation can also be followed with naked eye due to a color change from grass green to yellow-green (Fig. S13). In contrast, the PXRD pattern of **rtl**-[Zn(Hlsa-az-dmpz)] shows dramatic changes after supercritical-drying accompanied with partial loss of crystallinity. Subsequent activation as well as redispersion did not return the original phase. Therefore, this phase change seems to be irreversible (Fig. 6b). It has been noted before that the relative stability of paddle-wheel clusters within MOFs follows the Irving–Williams series.⁶⁴ Therefore, it can be concluded that the more labile nature of Zn(ii) in **rtl**-[Zn(Hlsa-az-dmpz)] in contrast to the more stable Cu(ii) coordination in the paddle-wheel cluster in **rtl**-[Cu(Hlsa-az-dmpz)] is responsible for the successful activation of the latter.

Gas sorption studies

The flexible properties of MOFs showing a phase change upon ad/desorption can be usually seen as one or multiple steps in the adsorption and desorption isotherms.^{33,40,44,45,65–67} Since **rtl**-[Cu(Hlsa-az-dmpz)] showed a phase change upon activation, CO₂ and N₂ sorption on its activated form were collected at 195 K and 77 K, respectively (see Table 2). Additionally, the sorption isotherm measurement was repeated on the same probe, because the sorption properties of flexible MOFs can often change under sorption stress^{68,69} or sometimes even a shape-memory effect from for example Type F-II to Type I can be observed.⁷⁰ The N₂ sorption isotherms at 77 K isotherm as well as the CO₂ isotherm at 195 K both show a large S-shaped step in their adsorption branch. This profile can be attributed to the Type F-IV isotherm recently introduced by Zaworotko *et al.*⁴⁰ The stepped N₂ isotherm shows a gate opening effect at around 0.03 P/P_0 . The adsorption step gradually flattens towards the saturation uptake of 360 cm³ g⁻¹ which is probably a kinetic phenomenon of N₂ adsorption at 77 K (see below). From such isotherms BET-surface area and porosity calculations are not applicable. The derived Langmuir surface area for the **rtl**-[Cu(Hlsa-az-dmpz)]-framework is 1610 m² g⁻¹ in the first adsorption cycle. The desorption shows a large hysteresis starting to close only at 0.01 P/P_0 . Such hysteresis loops are characteristically for MOFs showing reversible phase transitions between a porous and a non-porous phase upon guest inclusion. The shape and the saturation uptake of the isotherm of the second cycle remains the same, but the gate opening pressure shifts to a slightly lower value of 0.02 P/P_0 (Fig. 7).

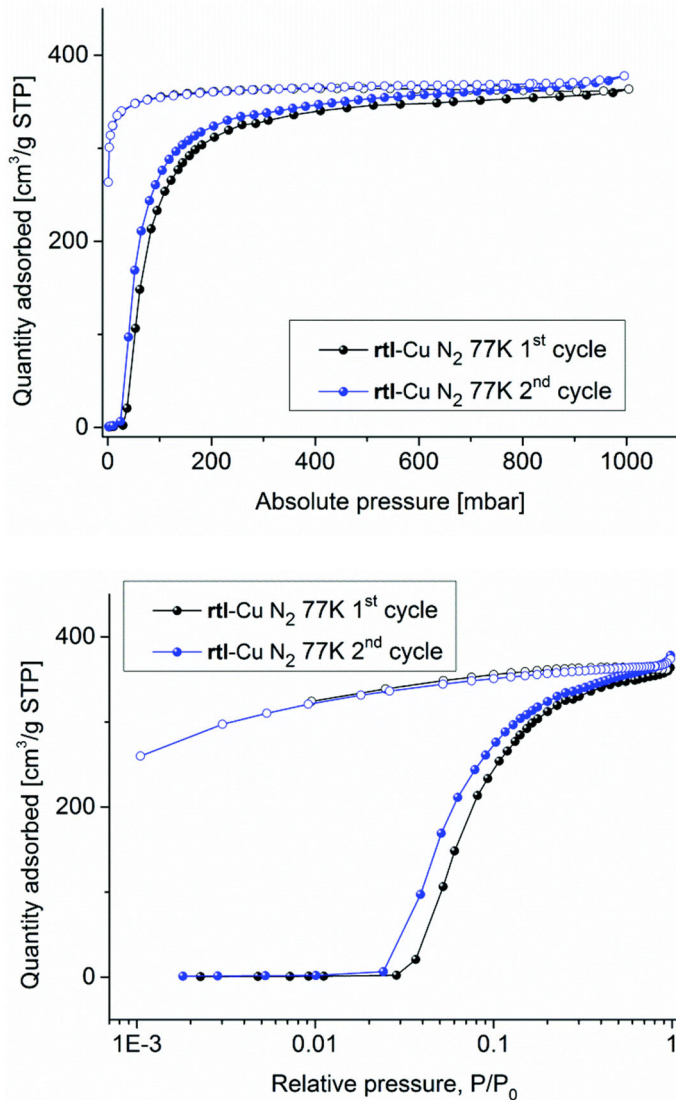


Fig. 6 N₂ sorption of rtl-[Cu(Hlsa-az-dmpz)]-act. at 77 K with filled symbols for adsorption and empty symbols for desorption (cycle 1 in black, and cycle 2 in blue; top: in absolute pressure and bottom in logarithmic relative pressure scale).

The CO₂ isotherm at 195 K also exhibits a large step in its adsorption profile with a gate opening effect at 0.07–0.08 P/P_0 (Fig. 8). In comparison to the nitrogen isotherms the transition from the step to the saturation uptake at around 350 mbar with 310 cm³ g⁻¹ in the CO₂ isotherm is more abrupt. The saturation pressure of CO₂ at 195 K is higher than for N₂ at 77 K and the kinetic diameter of CO₂ (3.3 Å) is also slightly smaller than for N₂ (3.64 Å). So, advantages of CO₂ porosity analysis at 195 K or higher temperatures *versus* N₂ analysis at 77 K are faster analysis and greater confidence that measured adsorption points are equilibrated (both due to higher diffusion rates). The saturation uptake (310 cm³ g⁻¹, 13.8 mmol g⁻¹) corresponds to 4.8 CO₂ molecules per formula unit of rtl-[Cu(Hlsa-az-dmpz)]. The desorption curve also shows a large hysteresis starting at 270 mbar and the step is closed at only 10 mbar. A Langmuir fit in the

pressure range between 399–1012 mbar yielded a surface area of $1440 \text{ cm}^3 \text{ g}^{-1}$. The profile of the 2nd cycle follows that of the 1st cycle, showing comparable gate opening pressure and saturation uptake and giving an unchanged Langmuir surface area with $1450 \text{ cm}^3 \text{ g}^{-1}$.

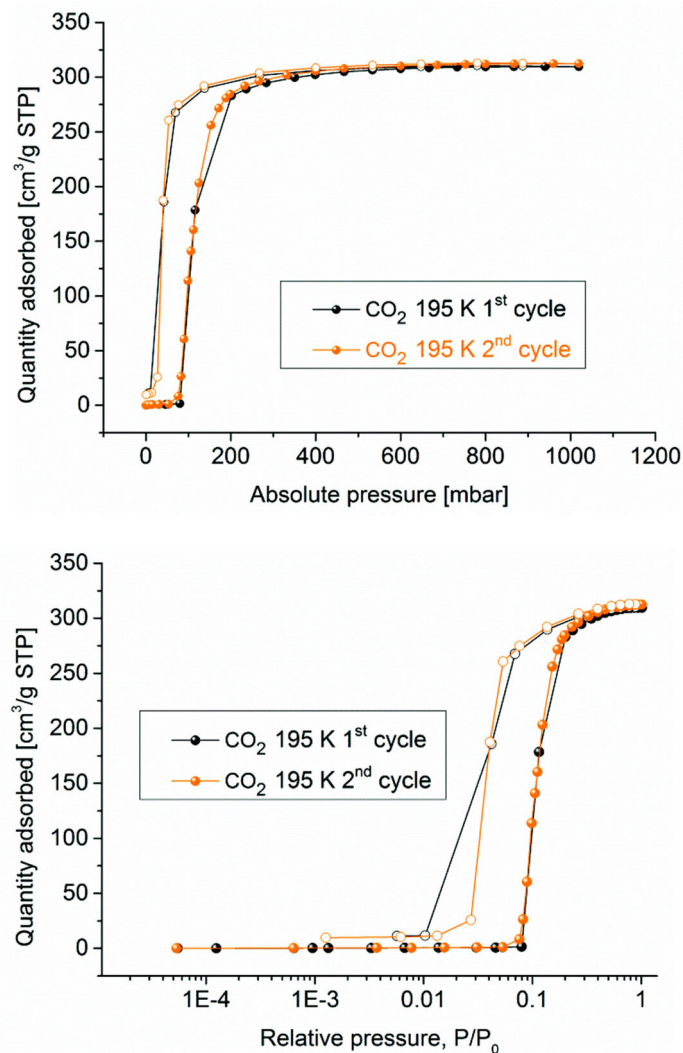


Fig. 7 Sorption isotherms of rti-[Cu(Hlsa-az-dmpz)]-act. for CO₂ at 195 K with the adsorption points in filled symbols and the desorption points in open symbols (1st cycle in black and the 2nd cycle CO₂ in orange; top: in absolute pressures and down in logarithmic scale).

Table 2 Gas sorption data for **rtl**-[Cu(HIsa-az-dmpz)].

	Saturation uptake [cm³/g, mmol/g]	Pore volume [cm³/g]	Langmuir surface area [m²/g]	Gate opening pressure (mbar, P/P₀)
N ₂ @77 K 1 st Cycle	360, 16.0	0.553 ^a	1610 ^b	29, 0.03
N ₂ @77 K 2 nd Cycle	370, 16.5	0.571 ^a	1658 ^c	25, 0.02
CO ₂ @195 K 1 st Cycle	310, 13.8	0.567 ^a	1437 ^d	80 , 0.08
CO ₂ @195 K 2 nd Cycle	312, 13.9	0.572 ^a	1447 ^e	76, 0.08
CO ₂ @298 K	0.332g/g, 7.75 mmol	0.47 ^f	-	10 bar, 0.02

^a at $P/P_0 = 0.90$. ^b calc. between 206–821 mbar. ^c calc. between 204–839 mbar. ^d calc. between 399–1020 mbar. ^e calc. between 400–1020 mbar. ^f at $P/P_0 = 0.03$ according to the Gurvich-rule.⁷⁸

In view of the large hysteresis loops, we measured the CO₂ and N₂ gas adsorption at 195 K or 77 K, respectively, for **rtl**-[Cu(HIsa-az-dmpz)], refilled the sample chamber with CO₂ and N₂ (instead of He) and tried to directly measure a PXRD pattern at atmospheric pressure and 20 °C. But the diffractogram always showed the pattern of the activated closed-pore form, indicating the gas loss at ambient pressure and temperature. From our high-pressure experiment CO₂ (see below), we see that the structure of **rtl**-[Cu(HIsa-az-dmpz)] opens at 10 bar and 298 K. Therefore, we conclude that at 1 atm at which we conducted our PXRD experiment the structure directly transforms into the closed pore form.

Usually steps in sorption isotherms are associated with structural transformations of the frameworks during the adsorption process. In this regard, such stepped S-shaped Type F-IV isotherms can be associated with an abrupt phase change of a non-porous phase into a porous phase and have been reported for various MOF and can be induced by several gases like N₂, CH₄, CO₂, Ar, O₂, ethylene.^{71–76} Sakaki *et al.* recently demonstrated by theoretical calculations that sigmoidal isotherms can be observed when the crystal deformation energy due to the transformation of a closed into an open form is compensated by the simultaneous adsorption of several molecules of the adsorbate.⁷⁷ As mentioned in the introduction: there is only a limited amount of reports in the literature showing F-IV-isotherms with saturation uptakes higher than 250 cm³ g⁻¹.^{40,44–48} This puts **rtl**-[Cu(HIsa-az-dmpz)] with around 360 cm³ g⁻¹ for nitrogen at 77 K and 310 cm³ g⁻¹ for CO₂ at 195 K in the top rank of such adsorption-induced single step phase-change materials. The gravimetric high-pressure CO₂ adsorption at 298 K also shows a single step Type F-IV profile starting at 10 bar giving a maximum uptake of 332 mg g⁻¹ (7.75 mmol) (Fig. 8). A pore volume of 0.47 cm³ g⁻¹ at 20 bar, can be derived under the assumption of the validity of the Gurvich-rule.⁷⁸ This value is in good agreement with the total pore volume of 0.57 cm³ g⁻¹ obtained from the cryogenic sorption measurements of N₂ and CO₂, when taking into account that the saturation plateau

is not finally reached. The uptake of 332 mg g^{-1} corresponds to 3.2 CO_2 molecules per formula unit.

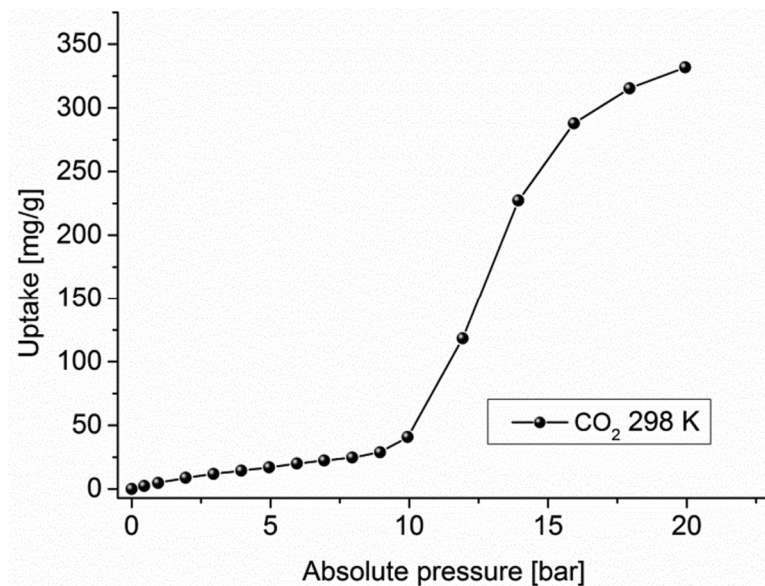


Fig. 8 High-pressure CO_2 adsorption isotherm of **rtl**-[Cu(HIsa-az-dmpz)]-act. between 0–20 bar at 298 K.

The CO_2 saturation pressure at 298 K is 64.3 bar, at 293 K it is 57.3 bar and at 195 K it is 1.00 bar. At 195 K the gate opening occurs at a relative pressure of $P/P_0 = 0.03\text{--}0.04$ (Fig. 8). The gate opening at 298 K does not only take place at a higher absolute pressure of about 10 bar, it also occurs at a slightly higher relative pressure of $P/P_0 = 0.2$ because when taking the higher saturation pressure into account. Consequently, a volumetric CO_2 measurement at 293 K up to 1 bar (with $P/P_0 = 0.017$) does not induce the gate opening (see Fig. S14).

The adsorption isotherms for N_2 and CO_2 for **rtl**-[Cu(HIsa-az-dmpz)] have a similar S-shape albeit at different, adsorbents-dependent pore-opening pressure (the more so when adjusting for the different temperatures). Besides the high potential as fluid storage material due to the high saturation uptake accompanied with the Type F-IV isotherm, the pressure-dependent structural transformation could also be utilized in gas separation applications.^{79,80} Long *et al.* recently reported on the CO_2/CH_4 selectivities of [Co(bdp)] (showing S-shaped isotherms for methane and multi-step adsorption isotherms for CO_2) with respect to different partial-pressure-based multicomponent adsorption experiments. They report size exclusion as well as cooperative effects to explain the observed selectivities.^{44,45,81}

In contrast, the activated-phase of **rtl**-[Zn(HIsa-az-dmpz)] neither adsorbs N_2 nor CO_2 at 77 K and 195 K, respectively. Since its original structure after dispersion in DMF is also not

restored (Fig. 6), this leads to the conclusion that the DMF-filled structure obtained from synthesis irreversibly transforms into a non-porous structure under the chosen activation protocol.

In this regard, it is interesting to note that related **rtl**-Cu-MOFs constructed from T-shaped ligands are rigid frameworks showing Type I isotherms and consequently do not show a phase change upon activation.^{9,10,13,14,16–20} The **rtl**-series synthesized by Krautscheid *et al.* based on functionalized triazole-dicarboxylate ligands exhibit all sorts of stepped isotherms associated with flexible MOFs.¹⁵ Also, the mixed ligand Cu-MOFs $[\text{Cu}_2(\text{bdc})_2(\text{dabco})]$ ^{1,38} and $[\text{Cu}_2(\text{ndc})_2(\text{dabco})]$ (known as DUT-8) are rigid structures.⁸² $[\text{Zn}_2(\text{bdc})_2(\text{dabco})]$ shows a reversible phase change from an open to a non-porous phase, whereas $[\text{Zn}_2(\text{ndc})_2(\text{dabco})]$ transforms like **rtl**- $[\text{Zn}(\text{Hlisa-az-dmpz})]$ into a nonporous structure. DUT-8(Ni) was reported with a Type F-IV adsorption profile and an extremely high adsorption uptake, which diminishes under sorption stress.^{46,68} Recently, the same authors also reported a rigid analog showing classical Type I isotherms and mixtures of rigid and flexible DUT-8(Ni) depending on the used synthesis parameters.⁸³ On the one hand, the influence of the metal atom on the flexible properties of paddle wheel-based MOFs is quite obvious, but from these few examples it can already be seen that in different but related MOFs with the same metal paddle-wheel clusters show different phase changes upon activation and consequently different sorption properties regarding their flexibility. This has also been underlined by mixed-metal paddle wheel MOFs showing flexible sorption properties dependent on the relative metal content.⁸⁴

Conclusions

In this contribution we presented two isostructural MOFs with **rtl**- $[\text{Cu}(\text{Hlisa-az-dmpz})]$ and **rtl**- $[\text{Zn}(\text{Hlisa-az-dmpz})]$ based on the new T-shaped ligand 5-(4-(3,5-dimethyl-1*H*-pyrazolyl)azo)isophthalic acid ($\text{H}_3\text{lisa-az-dmpz}$) verifying the hypothesis that 3,6-c connected MOFs can be targeted with T-shaped pyrazole-dicarboxylate ligands akin to T-shaped ligands with pyridine, imidazole, triazole or tetrazole heterocycles. Compound **rtl**- $[\text{Cu}(\text{Hlisa-az-dmpz})]$ undergoes a phase change upon activation. It shows S-shaped Type F-IV isotherms for N_2 at 77 K and CO_2 at 195 K with high saturation uptakes of $360 \text{ cm}^3 \text{ g}^{-1}$ and $310 \text{ cm}^3 \text{ g}^{-1}$, respectively. The derived Langmuir surface area from the nitrogen isotherm is $1610 \text{ cm}^2 \text{ g}^{-1}$. The materials robustness towards repeated sorption stress was verified by an unchanged sorption performance towards CO_2 and N_2 for at least two cycles. The gravimetric high-pressure adsorption at 298 K also shows an S-shaped Type F-IV isotherm with gate-opening at 10 bar and an uptake of 332 mg g^{-1} at 20 bar.

Acknowledgements

The authors thank Mrs Birgit Tommes for carrying out the FT-IR experiments and the crystallographic referee for his insightful comments on the DMF disorder.

Notes and references

1. K. Seki and W. Mori, *J. Phys. Chem. B*, 2002, **106**, 1380-1385.
2. D. N. Dybtsev, H. Chun and K. Kim, *Angew. Chem., Int. Ed.*, 2004, **43**, 5033-5036.
3. B.-Q. Ma , K. L. Mulfort and J. T. Hupp, *Inorg. Chem.*, 2005, **44**, 4912-4914.
4. H. Chun, D. N. Dybtsev, H. Kim and K. Kim , *Chem. Eur. J.*, 2005, **11**, 3521-3529.
5. B. Chen, S. Ma, F. Zapata, F. R. Fronczek, E. B. Lobkovsky and H.-C. Zhou, *Inorg. Chem.*, 2007, **46**, 1233-1236.
6. V. Guillerm , D. Kim , J. F. Eubank , R. Luebke , X. Liu , K. Adil , M. S. Lah and M. Eddaoudi , *Chem. Soc. Rev.*, 2014, **43** , 6141-6172.
7. F. Zare Karizi, M. Joharian and A. Morsali , *J. Mater. Chem. A*, 2018, **6** , 19288 -19329.
8. J. F. Eubank, L. Wojtas, M. R. Hight, T. Bousquet, V. C. Kravtsov and M. Eddaoudi , *J. Am. Chem. Soc.*, 2011, **133**, 17532-17535.
9. S. L. Xiang, J. Huang, L. Li, J. Y. Zhang, L. Jiang, X. J. Kuang and C. Y. Su, *Inorg. Chem.*, 2011, **50**, 1743-1748.
10. X. Liu ,M. Oh and M. S. Lah, *Cryst. Growth Des.*, 2011, **11**, 5064-5071.
11. A. Karmakar, L. M. D. R. S. Martins, S. Hazra, M. F. C. Guedes da Silva and A. J. L. Pombeiro, *Cryst. Growth Des.*, 2016, **16**, 1837-1849.
12. Q. Wang, J. Jiang, M. Zhang and J. Bai, *Cryst. Growth Des.*, 2016, **17**, 16-18.
13. Z. J. Chen, K. Adil, L. J. Weselinski, Y. Belmabkhout and M. Eddaoudi, *J. Mater. Chem. A*, 2015, **3**, 6276-6281.
14. L. Wen, W. Shi, X. Chen, H. Li and P. Cheng, *Eur. J. Inorg. Chem.*, 2012, **2012**, 3562-3568.
15. K. Kobalz, M. Kobalz, J. Möllmer, U. Junghans, M. Lange, J. Bergmann, S. Dietrich, M. Wecks, R. Glaserand H. Krautscheid, *Inorg. Chem.*, 2016, **55**, 6938-6948.
16. S. Wang, Z.-W. Wei, J. Zhang, L. Jiang, D. Liu, J.-J. Jiang, R. Si and C.-Y. Su, *IUCrJ*, 2019, **6**, 85-95.
17. S.-M. Zhang, Z. Chang, T.-L. Hu and X.-H. Bu, *Inorg. Chem.*, 2010, **49**, 11581-11586.
18. T. L. Hu, H. Wang, B. Li, R. Krishna, H. Wu, W. Zhou, Y. Zhao, Y. Han, X. Wang, W. Zhu, Z. Yao, S. Xiang and B. Chen, *Nat. Commun.*, 2015, **6**, 7328.
19. Y. Xiong , Y. Z. Fan, R. Yang , S. Chen, M. Pan, J. J. Jiang and C. Y. Su, *Chem. Commun.*, 2014, **50** , 14631-14634.
20. Y. Xiong , Y. Z. Fan, D. Damasceno Borges, C. X. Chen, Z. W. Wei, H. P. Wang, M. Pan, J. J. Jiang, G. Maurin and C. Y. Su, *Chem. Eur. J.*, 2016, **22**, 16147-16156.

21. C. Montoro, F. Linares, E. Quartapelle Procopio, I. Senkovska, S. Kaskel, S. Galli, N. Masciocchi, E. Barea and J. A. R. Navarro, *J. Am. Chem. Soc.*, 2011, **133**, 11888-11891.
22. C. Heering, I. Boldog, V. Vasylyeva, J. Sanchiz and C. Janiak, *CrystEngComm*, 2013, **15**, 9757-9768.
23. B. Tu, Q. Pang, D. Wu, Y. Song, L. Weng and Q. Li, *J. Am. Chem. Soc.*, 2014, **136**, 14465-14471.
24. C.-T. He, P.-Q. Liao, D.-D. Zhou, B.-Y. Wang, W.-X. Zhang, J.-P. Zhang and X.-M. Chen, *Chem. Sci.*, 2014, **5**, 4755-4762.
25. M. R. Bryant, A. D. Burrows, C. M. Fitchett, C. S. Hawes, S. O. Hunter, L. L. Keenan, D. J. Kelly, P. E. Kruger, M. F. Mahon and C. Richardson, *Dalton Trans.*, 2015, **44**, 9269-9280.
26. W.-Y. Gao, R. Cai, T. Pham, K. A. Forrest, A. Hogan, P. Nugent, K. Williams, L. Wojtas, R. Luebke, Ł. J. Weseliński, M. J. Zaworotko, B. Space, Y.-S. Chen, M. Eddaoudi, X. Shi and S. Ma, *Chem. Mater.*, 2015, **27**, 2144-2151.
27. W.-Y. Gao, T. Pham, K. A. Forrest, B. Space, L. Wojtas, Y.-S. Chen and S. Ma, *Chem. Commun.*, 2015, **51**, 9636-9639.
28. X. T. Liu, Y. Y. Jia, Y. H. Zhang, G. J. Ren, R. Feng, S. Y. Zhang, M. J. Zaworotko and X. H. Bu, *Inorg. Chem. Front.*, 2016, **3**, 1510-1515.
29. Y.-Y. Jia, X.-T. Liu, R. Feng, S.-Y. Zhang, P. Zhang, Y.-B. He, Y.-H. Zhang and X.-H. Bu, *Cryst. Growth Des.*, 2017, **17**, 2584-2588.
30. J. Hunger, H. Krautscheid and J. Sieler, *Cryst. Growth Des.*, 2009, **9**, 4613-4625.
31. L.-N. Jia, Y. Zhao, L. Hou, L. Cui, H.-H. Wang and Y.-Y. Wang, *J. Solid State Chem.*, 2014, **210**, 251-255.
32. K. Tomar, R. Rajak, S. Sanda and S. Konar, *Cryst. Growth Des.*, 2015, **15**, 2732-2741.
33. A. Schneemann, V. Bon, I. Schwedler, I. Senkovska, S. Kaskel and R. A. Fischer, *Chem. Soc. Rev.*, 2014, **43**, 6062-6096.
34. F.-X. Coudert *Chem. Mater.*, 2015, **27**, 1905-1916.
35. S. Henke, A. Schneemann, A. Wütscher and R. A. Fischer, *J. Am. Chem. Soc.*, 2012, **134**, 9464-9474.
36. S. Horike, S. Shimomura and S. Kitagawa, *Nat. Chem.*, 2009, **1**, 695-704.
37. G. Férey *Dalton Trans.*, 2016, **45**, 4073-4089.
38. H.-C. Kim, S. Huh, D. N. Lee and Y. Kim, *Dalton Trans.*, 2018, **47**, 4820-4826.
39. Y. Kim, R. Haldar, H. Kim, J. Koo and K. Kim, *Dalton Trans.*, 2016, **45**, 4187-4192.
40. Q.-Y. Yang, P. Lama, S. Sen, M. Lusi, K.-J. Chen, W.-Y. Gao, M. Shivanna, T. Pham, N. Hosono, S. Kusaka, J. J. Perry IV, S. Ma, B. Space, L. J. Barbour, S. Kitagawa and M. J. Zaworotko, *Angew. Chem., Int. Ed.*, 2018, **57**, 5684-5689.
41. M. Hefti, L. Joss, Z. Bjelobrk and M. Mazzotti, *Faraday Discuss.*, 2016, **192**, 153-179.
42. J. Leclaire and D. J. Hedebrant, *Green Chem.*, 2018, **20**, 5058-5081.

43. L. A. Darunte, T. Sen, C. Bhawanani, K. S. Walton, D. S. Sholl, M. J. Realff and C. W. Jones, *Ind. Eng. Chem. Res.*, 2019, **58**, 366-377.
44. J. A. Mason, J. Oktawiec, M. K. Taylor, M. R. Hudson, J. Rodriguez, J. E. Bachman, M. I. Gonzalez, A. Cervellino, A. Guagliardi, C. M. Brown, P. L. Llewellyn, N. Masciocchi and J. R. Long, *Nature*, 2015, **527**, 357.
45. M. K. Taylor, T. Runcevski, J. Oktawiec, M. I. Gonzalez, R. L. Siegelman, J. A. Mason, J. Ye, C. M. Brown and J. R. Long, *J. Am. Chem. Soc.*, 2016, **138**, 15019-15026.
46. V. Bon, N. Klein, I. Senkovska, A. Heerwig, J. Getzschmann, D. Wallacher, I. Zizak, M. Brzhezinskaya, U. Müller and S. Kaskel, *Phys. Chem. Chem. Phys.*, 2015, **17**, 17471-17479.
47. X. Sun, S. Yao, G. Li, L. Zhang, Q. Huo and Y. Liu, *Inorg. Chem.*, 2017, **56**, 6645-6651.
48. A. X. Zhu, Q. Y. Yang, A. Kumar, C. Crowley, S. Mukherjee, K. J. Chen, S. Q. Wang, D. O’Nolan, M. Shivanna and M. J. Zaworotko, *J. Am. Chem. Soc.*, 2018, **140**, 15572-15576.
49. F. Jeremias, D. Fröhlich, C. Janiak and S. K. Henninger, *New J. Chem.*, 2014, **38**, 1846-1852.
50. E. Hastürk, S.-J. Ernst and C. Janiak, *Curr. Opin. Chem. Eng.*, 2019, **24**, 26-36.
51. APEX2, SAINT, Data Reduction and Frame Integration Program for the CCD Area-Detector System, Bruker Analytical X-ray Systems, Data Collection Program for the CCD Area-Detector System, Madison, WI, USA, 1997–2006.
52. G. M. Sheldrick, SADABS: Area-Detector Absorption Correction, University of Göttingen, Göttingen, Germany, 1996.
53. G. M. Sheldrick, *Acta Crystallogr., Sect. C: Struct. Chem.*, 2015, **71**, 3-8.
54. G. Sheldrick, *Acta Crystallogr., Sect. A: Found. Crystallogr.*, 2008, **64**, 112-122.
55. K. Brandenburg, DIAMOND, Version 4.5; Crystal and Molecular Structure Visualization; Crystal Impact-K, Brandenburg & H. Putz Gbr, Bonn, Germany, 2009–2018.
56. C. F. Macrae, I. J. Bruno, J. A. Chisholm, P. R. Edgington, P. McCabe, E. Pidcock, L. Rodriguez-Monge, R. Taylor, J. van de Streek and P. A. Wood, *J. Appl. Crystallogr.*, 2008, **41**, 466-470.
57. A. Spek, *Acta Crystallogr., Sect. D: Biol. Crystallogr.*, 2009, **65**, 148-155.
58. A. L. Spek, PLATON – A Multipurpose Crystallographic Tool, Utrecht University, Utrecht, The Netherlands, 2008 L. J. Farrugia, Windows implementation, Version 40608, University of Glasgow, Scotland, 2008.
59. V. A. Blatov, A. P. Shevchenko and D. M. Proserpio, *Cryst. Growth Des.*, 2014, **14**, 3576-3586.
60. E. V. Alexandrov, V. A. Blatov, A. V. Kochetkov and D. M. Proserpio, *CrystEngComm*, 2011, **13**, 3947-3958.
61. A. Boultif and D. Louer, *J. Appl. Crystallogr.*, 2004, **37**, 724-731.
62. D. Louer and M. Louer, *J. Appl. Crystallogr.*, 1972, **5**, 271-275.
63. A. Boultif and D. Louer, *J. Appl. Crystallogr.*, 1991, **24**, 987-993.

64. Q. Yao, J. Sun, K. Li, J. Su, M. V. Peskov and X. Zou, *Dalton Trans.*, 2012, **41**, 3953-3955.
65. F. Salles, G. Maurin, C. Serre, P. L. Llewellyn, C. Knöfel, H. J. Choi, Y. Filinchuk, L. Oliviero, A. Vimont, J. R. Long and G. Férey, *J. Am. Chem. Soc.*, 2010, **132**, 13782-13788.
66. H. Wang, B. Li, H. Wu, T.-L. Hu, Z. Yao, W. Zhou, S. Xiang and B. Chen, *J. Am. Chem. Soc.*, 2015, **137**, 9963-9970.
67. Y.-L. Wang, L. Chen, C.-M. Liu, Y.-Q. Zhang, S.-G. Yin and Q.-Y. Liu, *Inorg. Chem.*, 2015, **54**, 11362-11368.
68. V. Bon, N. Kavoosi, I. Senkovska and S. Kaskel, *ACS Appl. Mater. Interfaces*, 2015, **7**, 22292-22300.
69. C. Reichenbach, G. Kalies, J. Lincke, D. Lässig, H. Krautscheid, J. Möllmer and M. Thommes, *Microporous Mesoporous Mater.*, 2011, **142**, 592-600.
70. M. Shivanna, Q.-Y. Yang, A. Bajpai, S. Sen, N. Hosono, S. Kusaka, T. Pham, K. A. Forrest, B. Space, S. Kitagawa and M. J. Zaworotko, *Sci. Adv.*, 2018, **4**, eaaoq1636.
71. R. Kitaura, K. Seki, G. Akiyama and S. Kitagawa, *Angew. Chem., Int. Ed.*, 2003, **42**, 428-431.
72. D. Tanaka, K. Nakagawa, M. Higuchi, S. Horike, Y. Kubota, T. C. Kobayashi, M. Takata and S. Kitagawa, *Angew. Chem., Int. Ed.*, 2008, **47**, 3914-3918.
73. J. Yang, Q. Yu, Q. Zhao, J. Liang, J. Dong and J. Li, *Microporous Mesoporous Mater.*, 2012, **161**, 154-159.
74. S. Sen, N. Hosono, J.-J. Zheng, S. Kusaka, R. Matsuda, S. Sakaki and S. Kitagawa, *J. Am. Chem. Soc.*, 2017, **139**, 18313-18321.
75. S.-Q. Wang, Q.-Y. Yang, S. Mukherjee, D. O'Nolan, E. Patyk-Każmierczak, K.-J. Chen, M. Shivanna, C. Murray, C. C. Tang and M. J. Zaworotko, *Chem. Commun.*, 2018, **54**, 7042-7045.
76. J. P. Zhang, H. L. Zhou, D. D. Zhou, P. Q. Liao and S. Kitagawa, *Comprehensive Supramolecular Chemistry II*, J. L. Atwood, Elsevier, Oxford, 2017, 425-474.
77. J.-J. Zheng, S. Kusaka, R. Matsuda, S. Kitagawa and S. Sakaki, *J. Am. Chem. Soc.*, 2018, **140**, 13958-13969.
78. L. Gurvich, *J. Russ. Phys.-Chem. Soc.*, 1915, **47**, 805-827.
79. L. Hamon, P. L. Llewellyn, T. Devic, A. Ghoufi, G. Clet, V. Guillerm, G. D. Pirngruber, G. Maurin, C. Serre, G. Driver, W. van Beek, E. Jolimaître, A. Vimont, M. Daturi and G. Férey, *J. Am. Chem. Soc.*, 2009, **131**, 17490-17499.
80. F.-X. Coudert, C. Mellot-Draznieks, A. H. Fuchs and A. Boutin, *J. Am. Chem. Soc.*, 2009, **131**, 11329-11331.
81. M. K. Taylor, T. Runčevski, J. Oktawiec, J. E. Bachman, R. L. Siegelman, H. Jiang, J. A. Mason, J. D. Tarver and J. R. Long, *J. Am. Chem. Soc.*, 2018, **140**, 10324-10331.

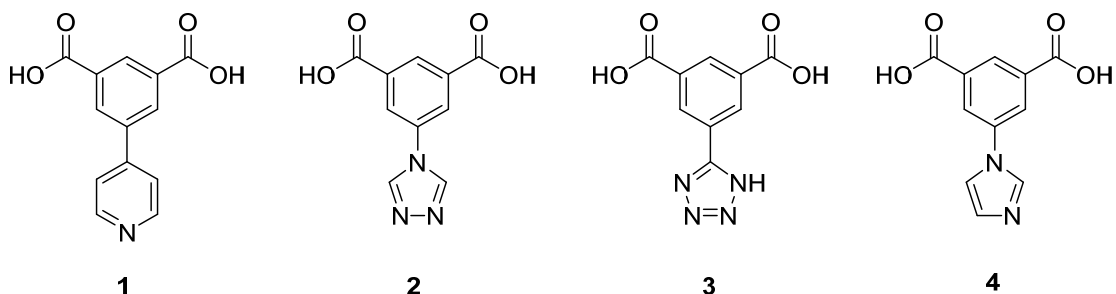
82. N. Klein, H. C. Hoffmann, A. Cadiau, J. Getzschmann, M. R. Lohe, S. Paasch, T. Heydenreich, K. Adil, I. Senkovska, E. Brunner and S. Kaskel, *J. Mater. Chem.*, 2012, **22**, 10303-10312.
83. N. Kavoosi, V. Bon, I. Senkovska, S. Krause, C. Atzori, F. Bonino, J. Pallmann, S. Paasch, E. Brunner and S. Kaskel, *Dalton Trans.*, 2017, **46**, 4685-4695.
84. J. Zhu, J. Chen, T. Qiu, M. Deng, Q. Zheng, Z. Chen, Y. Ling and Y. Zhou, *Dalton Trans.*, 2019, **48**, 7100-7104.

Supplementary Material

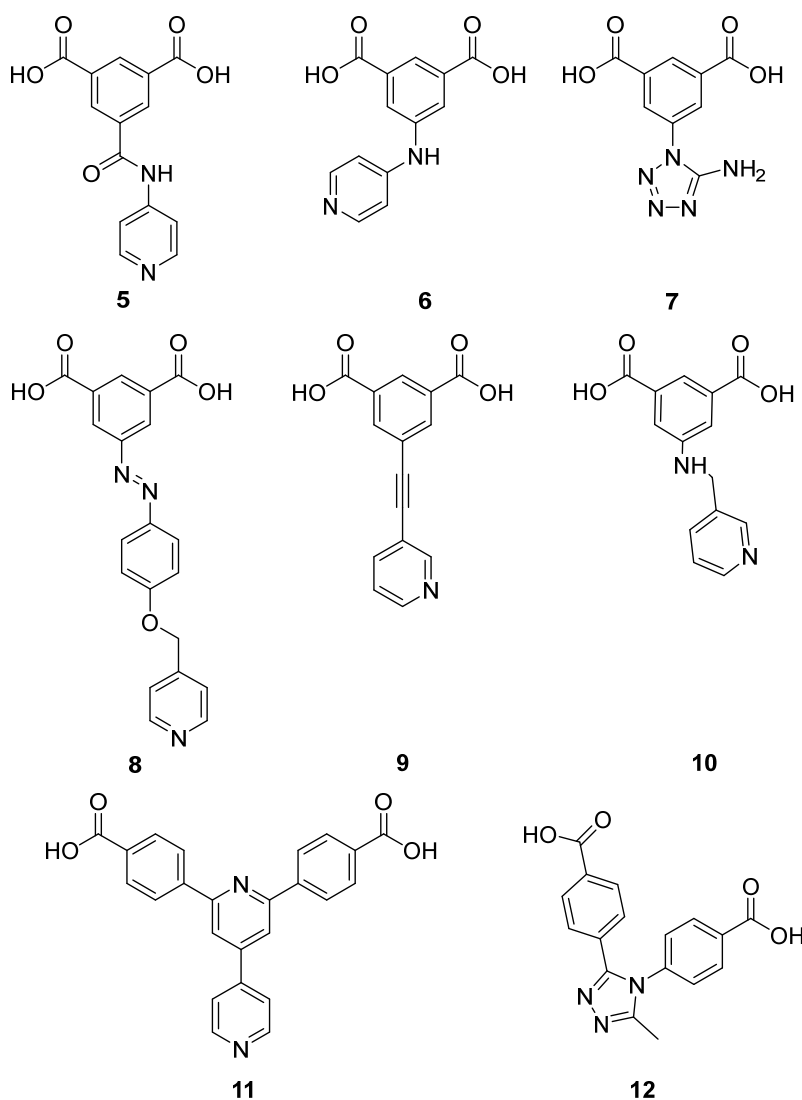
rtl-M-MOFs (M = Cu, Zn) with a T-shaped bifunctional pyrazole-isophthalate ligand showing flexibility and S-shaped Type F-IV sorption isotherms with high saturation uptakes for M = Cu

Table of contents

- S2 Examples for bifunctional T-shaped ligands
 - S3 Synthetic procedures of H₃lsa-az-dmpz
 - S4–S6 NMR spectroscopy
 - S7 Asymmetric Unit of rtl-[ZnHlsa-az-dmpz]·(DMF)₂
 - S8–S9 Digestion NMR experiments
 - S10 Thermogravimetric analysis
 - S11 Optical images
 - S12 FT-IR spectroscopy
 - S13 SEM images
 - S14 CO₂ sorption isotherm at 293 K
 - S15–16 Theoretical surface area and pore volume of rtl-[Cu(Hlsa-az-dmpz)]
 - S17–S19 Langmuir reports
 - S20–S21 Topological analysis
 - S22–S24 Selected bond lengths and angles
 - S25 References
-



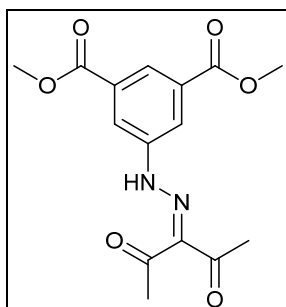
Scheme S1 Exemplary examples of T-shaped ligands reported in the literature for the construction of rtl-MOFs with the heterocycles pyridine (**1**),¹ triazole (**2**),^{2,3} tetrazole (**3**)⁴ and imidazole (**4**)⁵ as the pillaring functionality.



Scheme S2 Exemplary functionalized T-shaped ligands **5** (eea),⁵⁻⁸ (rtl),⁷ **7** (apo),⁹ **8** (eea),² **9** (eea),¹⁰ **10** (eea),¹⁰ **11** (pyr)¹¹ and **12** (rtl)¹² (topology abbreviation in parentheses).

Synthetic procedures for the ligand H₃Isa-az-dmpz

Dimethyl 5-(2-(3-pentan-2,4-dionyl)hydrazono)isophthalate:



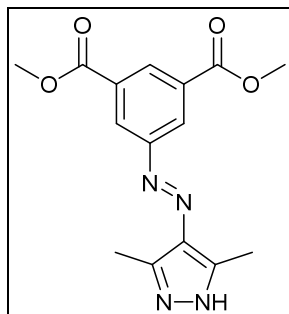
In the first step the diazonium salt was synthesized conforming to the classical procedures followed by a Japp-Klingemann reaction with acetylacetone.^{13,14} Therefore 4.18 g (20.0 mmol) of dimethyl 5-aminoisophthalate were suspended in 40 mL of 3 mol/L HCl at 0 °C. NaNO₂ (1.38 g, 20.0 mmol, 1 eq) dissolved in 10 mL of de-ionized water (DI-H₂O) was slowly added via a dropping funnel. The solution of the diazonium salt was added to an ice bath cooled solution of acetylacetone (2.1 mL, 20.0 mmol), NaOH (1.07 g, 26.8 mmol) and NaOAc (8.18, 99.7 mmol) in 160 mL of MeOH and 160 mL of DI-H₂O. The solution was stirred for 0.5 h at 0 °C and afterwards for 1 h at room temperature. The yellow powder was collected by suction and dried in air. The product was recrystallized from ethanol (420 mL) and was kept for crystallization overnight in the refrigerator. The fibrous yellow product was collected by suction (5.04 g, 15.7 mmol, 79 %).

¹H-NMR (300 MHz, CDCl₃, δ [ppm]): 14.68 (s, 1H, NH), 8.44 (t, J = 1.51 Hz, 1H, Ar H), 8.19 (d, J = 1.51 Hz, 2H, Ar H), 3.96 (s, 6H, -CH₃), 2.60 (s, 6 H, -CH₃), 2.51(s, 6 H, -CH₃).

¹³C-NMR (75 MHz, CDCl₃, δ [ppm]): 198.58, 197.08, 165.60, 142.40. 134.20, 132.29, 127.17, 120.91, 52.81, 31.85, 26.80.

ESI-MS: [M+H]⁺ 321.1, [2M+H+K]²⁺ 340.1

EA [%] calc. for C₁₅H₁₆N₂O₆ C 56.25, H 5.04, N 8.75; found C 56.31, H 4.93, N 8.64.

Dimethyl 5-(4-(3,5-dimethyl-1H-pyrazolyl)azo)isophthalate:

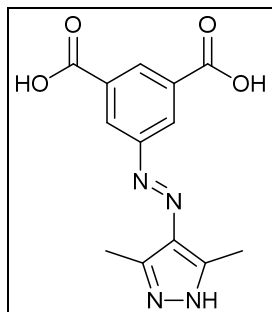
To a solution of dimethyl 5-(2-(3-pentan-2,4-dionyl)hydrazono)isophthalate (2.00 g, 6.25 mmol) in EtOH (100 mL) hydrazine hydrate (304 µl, 6.25 mL, 1 eq) was added and the mixture was refluxed for 4h. The solution was concentrated under reduced pressure and quenched with DI-H₂O. The yellow powder was collected by suction and dried overnight at 65 °C in a vacuum oven to yield 1.92 g (6.07 mmol, 97 %). The product was used without further purification.

¹H-NMR (300 MHz, DMSO-d₆, δ [ppm]): 12.95 (s, 1H, NH), 8.35 (d, J = 1.37 Hz, 2H, Ar H), 8.26 (t, J = 1.37 Hz, 1 H, Ar H), 3.89 (s, 6H, -CH₃), 2.48 (s, 3H, -CH₃), 2.37 (s, 3H, -CH₃).

¹³C-NMR (75 MHz, DMSO-d₆, δ [ppm]): 164.94, 153.01, 142.97, 139.67, 134.27, 131.09, 129.35, 125.54.

ESI-MS: [M+H]⁺ 317.3

EA [%] calc. for C₁₅H₁₆N₄O₄ C 56.96, H 5.10, N 17.71; found C 57.12, H 5.03, N 17.73.

5-(4-(3,5-Dimethyl-1H-pyrazolyl)azo)isophthalic acid (H₃Isa-az-dmpz):

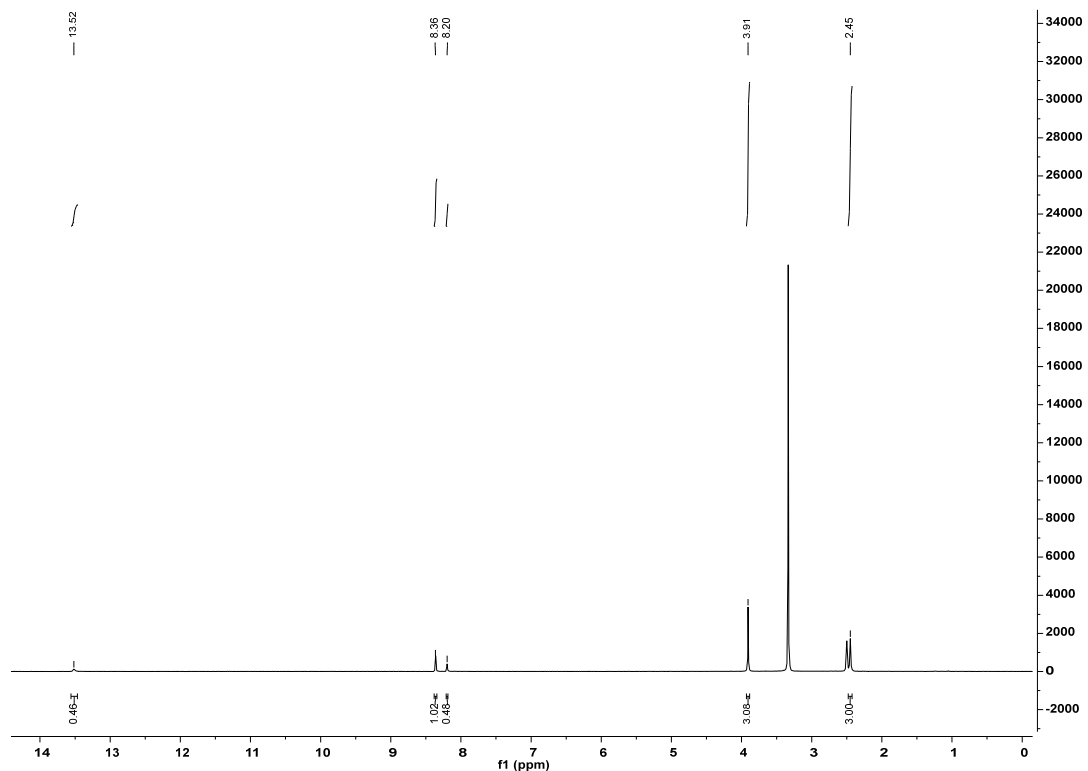
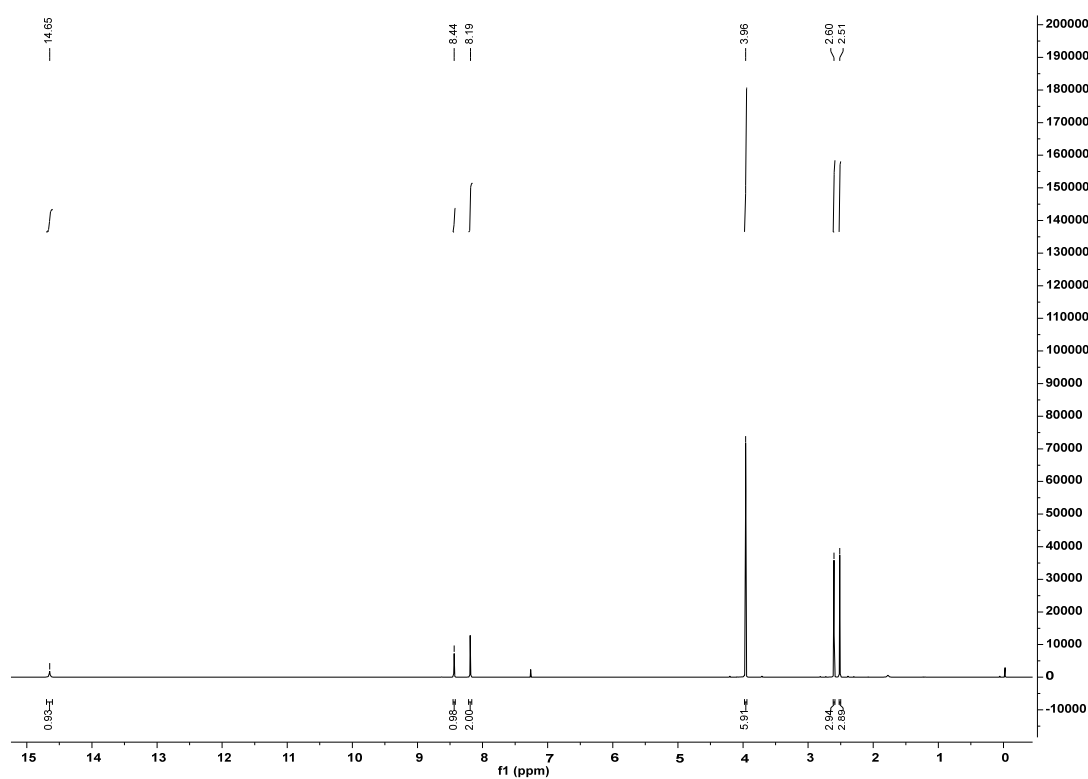
Dimethyl 5-(4-(3,5-dimethyl-1H-pyrazolyl)azo)isophthalate (1.84 g, 5.8 mmol) was dissolved in 105 mL of MeOH, 27 mL of DI-H₂O and 6.4 g (114mmol) of KOH and refluxed for 24 h. The MeOH was removed under reduced pressure. The remaining yellow solution was adjusted to pH 3 with 1N HCl. The yellow precipitate was collected with suction, washed with DI-H₂O and dried at 80 °C in a vacuum oven (1.64 g, 5.97 mmol, 98%).

¹H-NMR (600 MHz, DMSO-d₆, δ [ppm]): 13.27 (s, 3H, NH/COOH), 8.46 (t, J = 1.60 Hz, 1H, Ar H), 8.38 (d, J = 1.60 Hz, 2H, Ar H), 2.47 (s, 6H, -CH₃).

¹³C-NMR (150 MHz, DMSO-d₆, δ [ppm]): 166.27, 153.18, 141.29, 134.39, 132.40, 130.05, 125.62, 12.01.

ESI-MS: [M+H]⁺ 289,3

EA [%] calc. for H₃Isa-az-dmpz·0.5H₂O C₁₅H₁₆N₄O₄ C 52.53, H 4.41, N 18.85; found C 52.22, H 4.22, N 18.72.

NMR-Spectroscopy**Figure S1** ¹H-NMR spectrum Me₂Hlsa-az-acac in DMSO-d₆**Figure S2** ¹H-NMR spectrum Me₂Hlsa-az-acac in CDCl₃

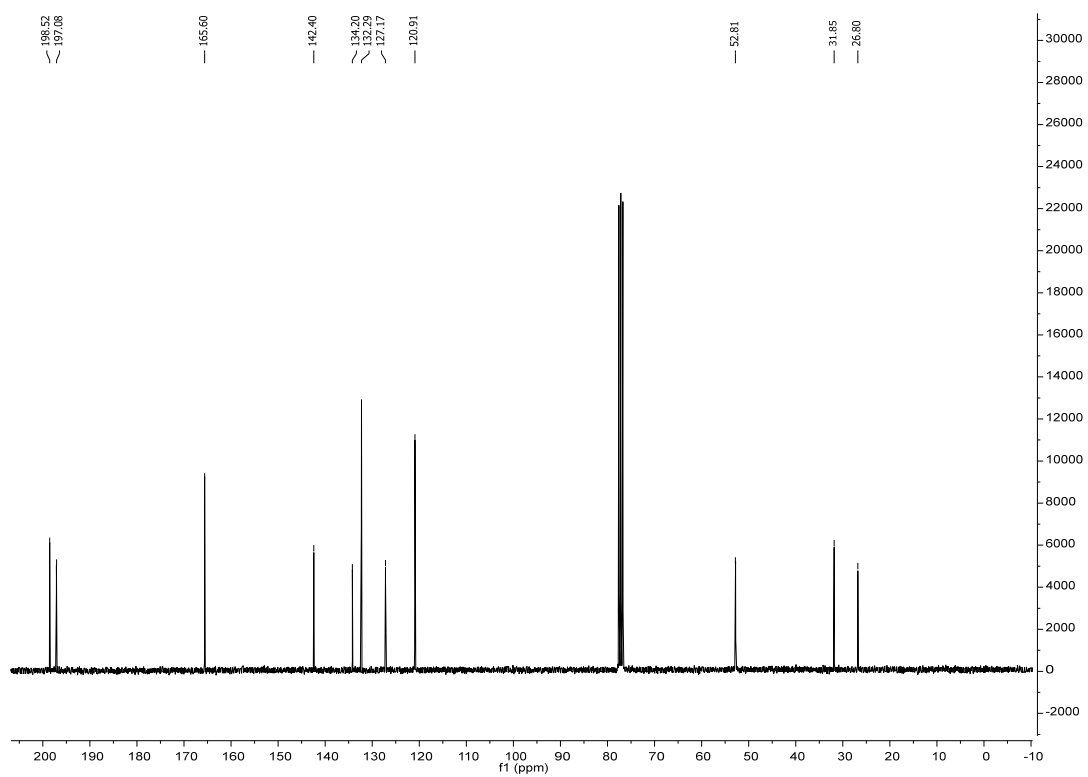


Figure S3 ¹³C-NMR spectrum of Me₂HIsa-az-acac in CDCl₃.

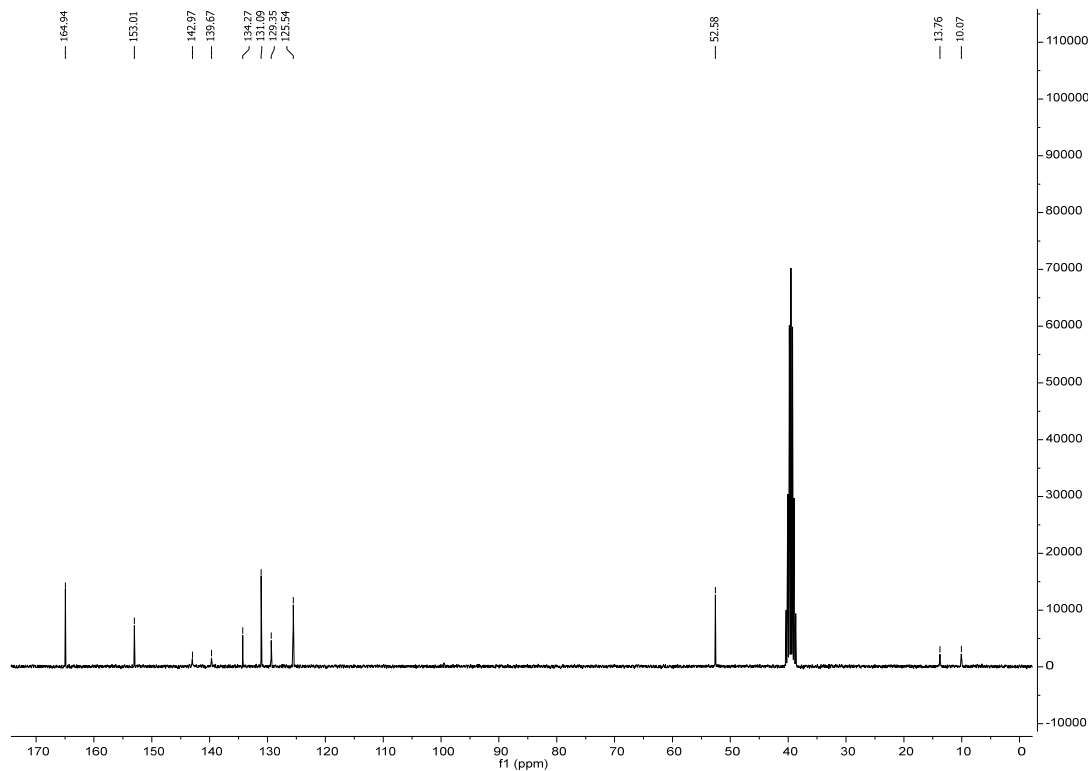


Figure S4 ¹³C-NMR spectrum of Me₂HIsa-az-dmpz in DMSO-d₆.

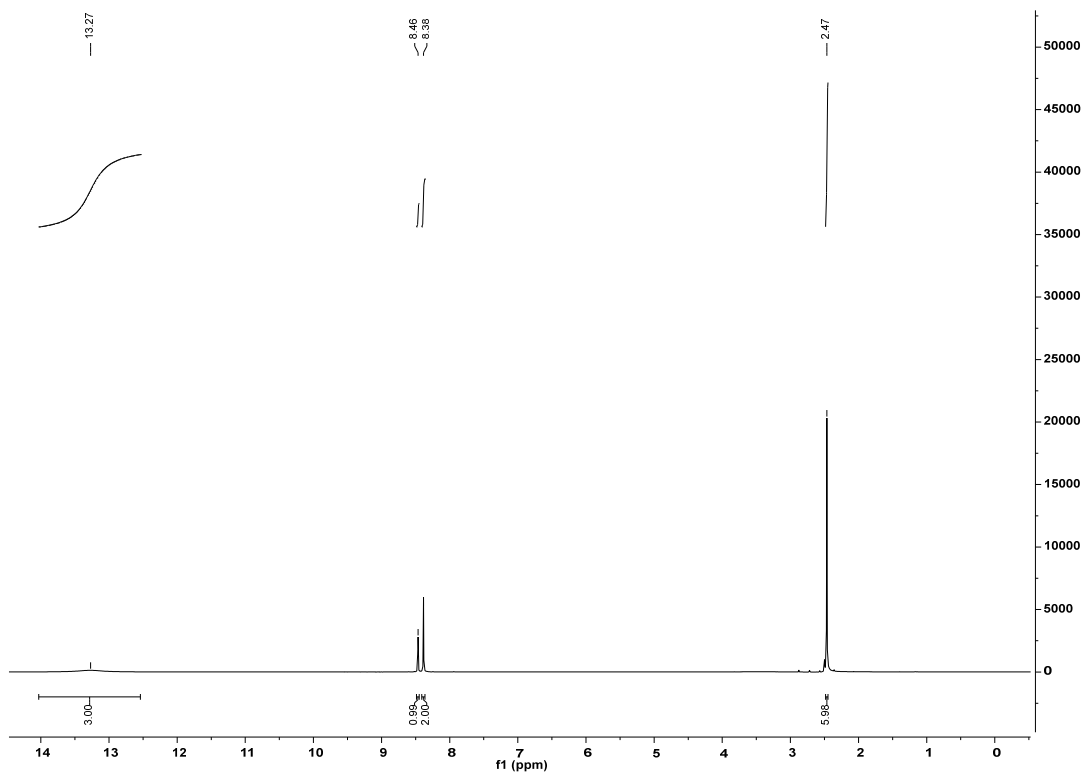


Figure S5 ¹H-NMR spectrum H₃Isa-az-dmpz in DMSO-d₆.

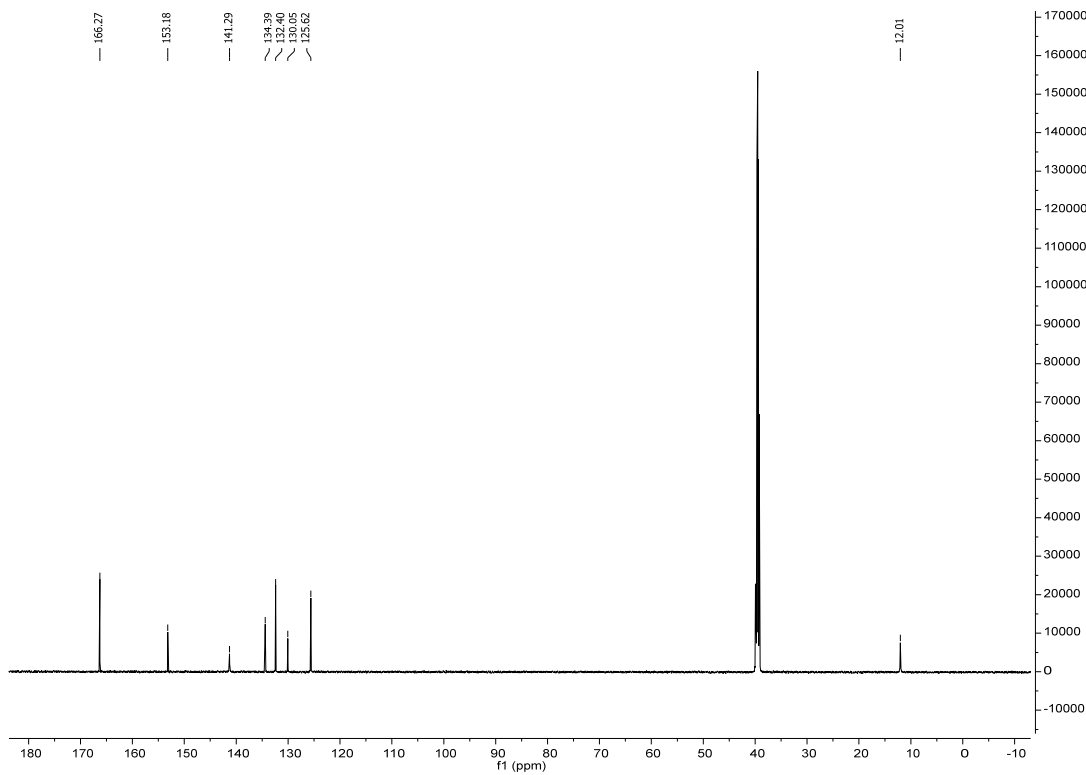


Figure S6 ¹³C-NMR spectrum of H₃Isa-az-dmpz in DMSO-d₆.

Asymmetric unit of rtl-[ZnHIsa-az-dmpz]·(DMF)₂

In rtl-Zn, one of the DMF molecules can be described as disordered, as shown in Fig. S7b.

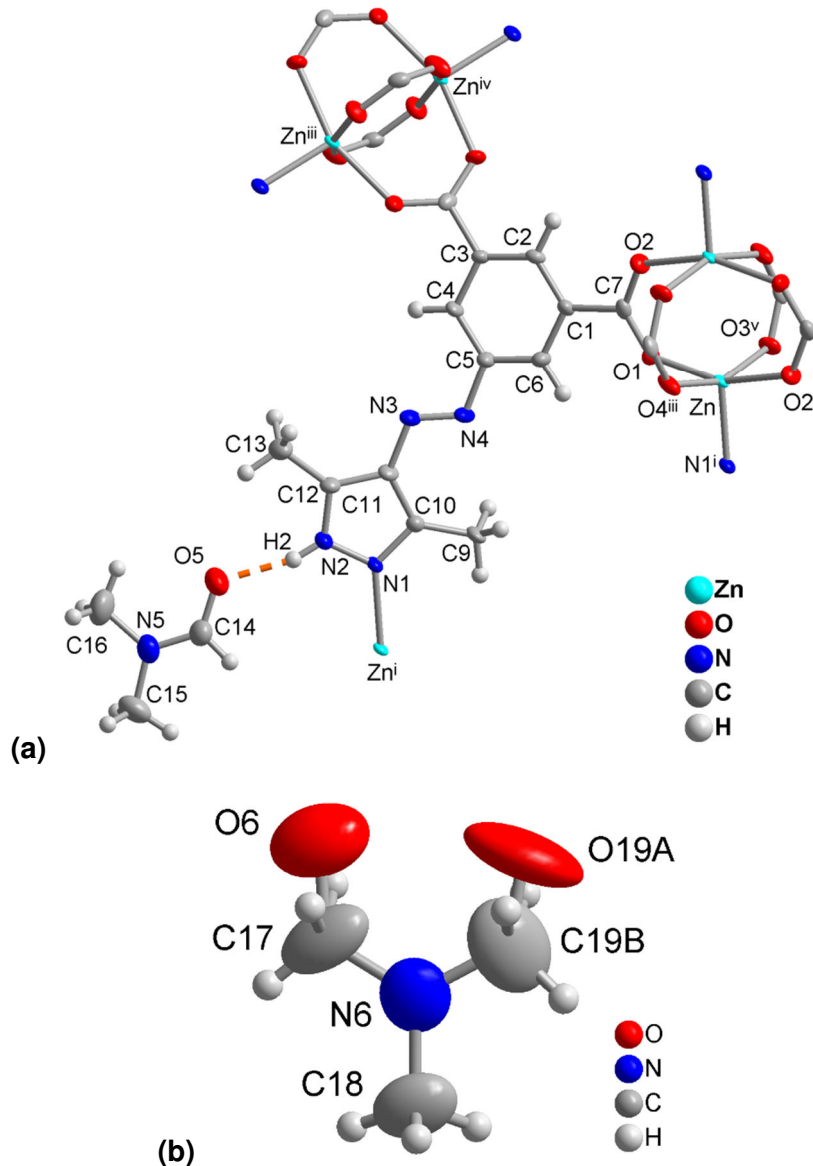


Figure S7 (a) Extended asymmetric unit of rtl-[ZnHIsa-az-dmpz]·(DMF)₂ (50% thermal ellipsoids; the disordered DMF-molecule is omitted for clarity). Symmetry transformations: i -x+2, -y, -z+1; ii -x+1, -y, -z+1;; iii x, -y-1/2, z+1/2; iv -x+1, y+1/2, -z+1/2; v -x+1, y-1/2, -z+1/2. Details of hydrogen bond N2-H2···O5 (orange-dashed line): N2-H2 0.831(1) Å, H2···O5 1.85(2) Å, N2···O5 2.656(5) Å, N2-H2···O5 164(4)°. (b) Disorder of the “free”, non-hydrogen-bonded DMF solvent molecule.

Characterization of the phases during the activation process of **rtl-[CuHIsa-az-dmpz]**.

¹H-NMR auf digested MOF samples

For the ¹H-NMR experiments 10 mg of the MOF sample were suspended in 0.7 mL DMSO-d₆ and digested by the addition of 20 µL of DCI (37% in D₂O).

Complete exchange of DMF against acetone in **rtl**-Cu-acetone can be assumed from the absence of the aldehyde signal (7.94 ppm) and the methyl groups (2.70 ppm, 2.86 ppm) (Figure S8 and S9). The NMR spectrum of the digested sample after supercritical drying **rtl**-Cu-scd indicates that there is still one acetone molecule per formula unit retained in the framework.

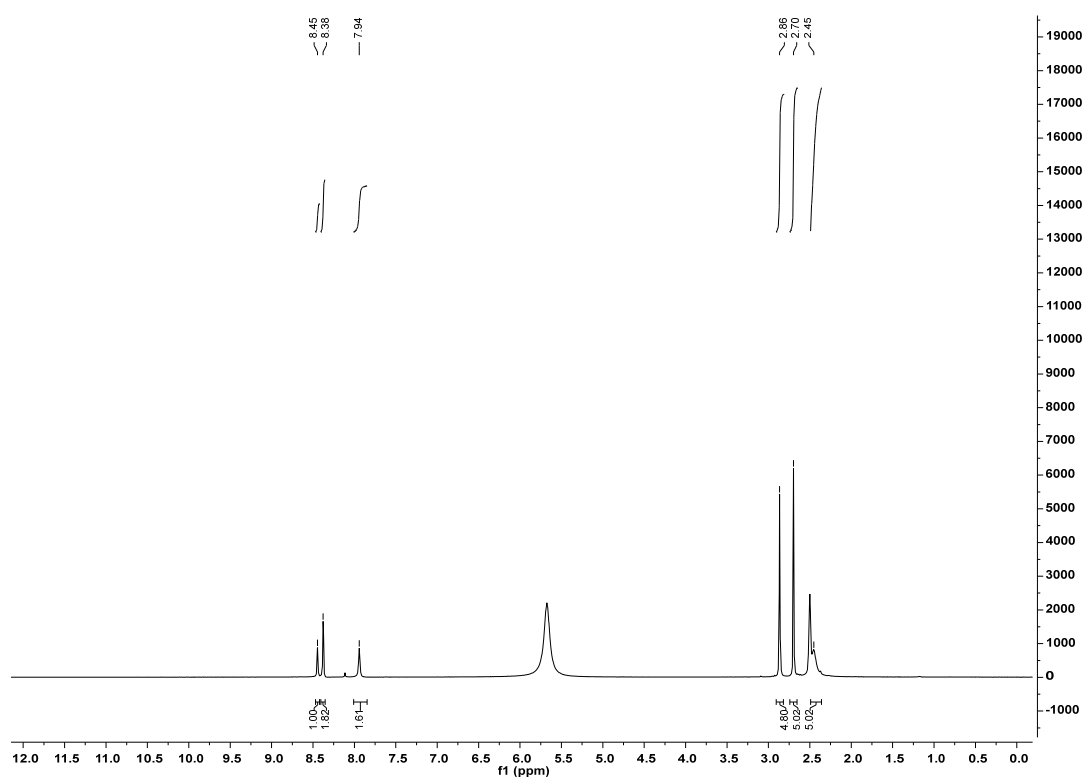


Figure S8 ¹H-NMR spectrum of digested **rtl**-Cu-as in DMSO-d₆/DCI.

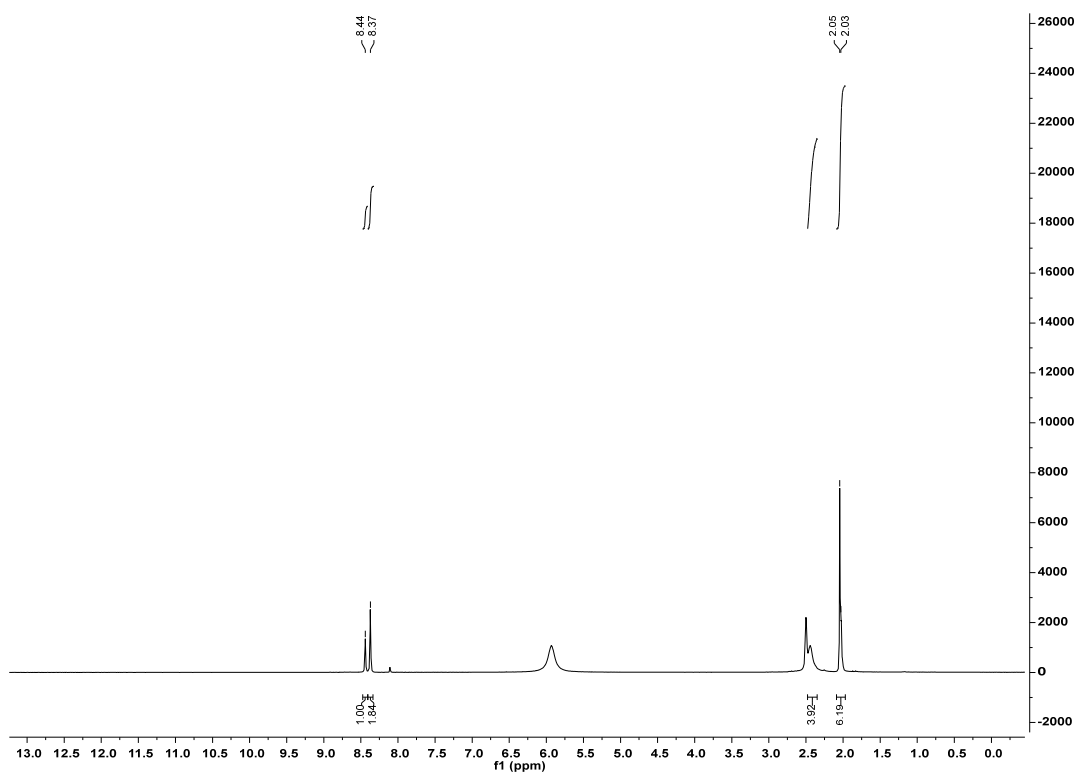


Figure S9 ¹H-NMR spectrum of digested rtl-Cu-acetone in DMSO-d₆/DCl.

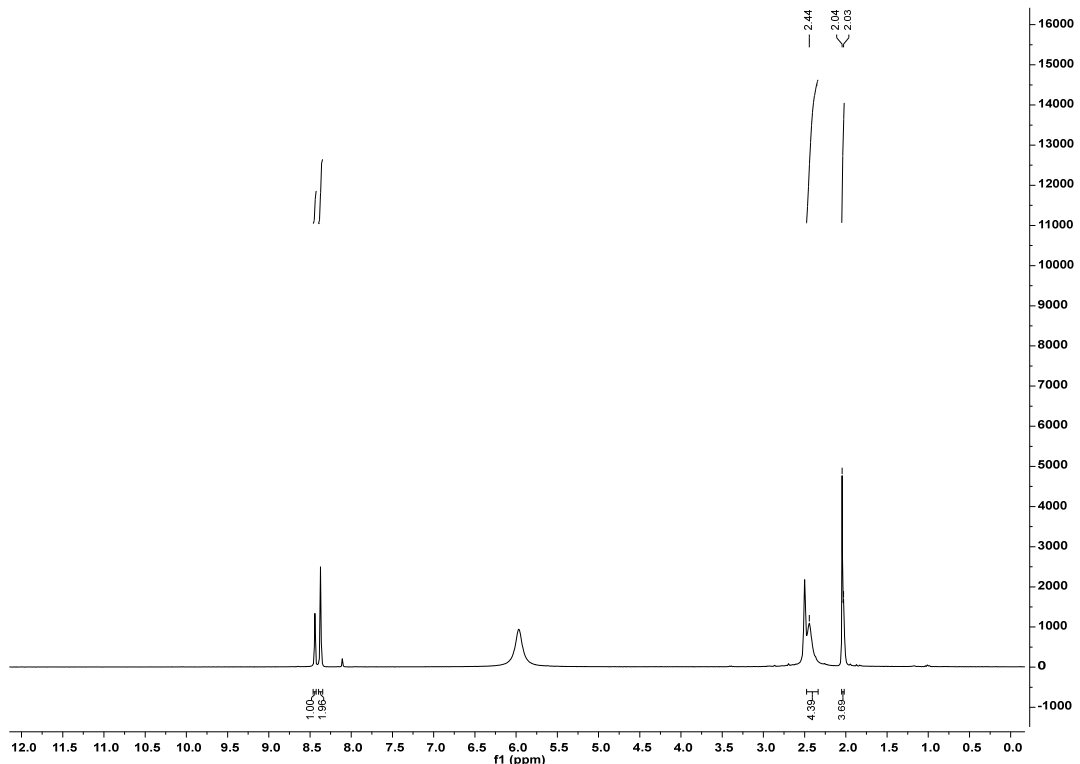


Figure S10 ¹H-NMR spectrum of digested rtl-Cu-scd in DMSO-d₆/DCl.

Thermogravimetric Analysis (TGA)

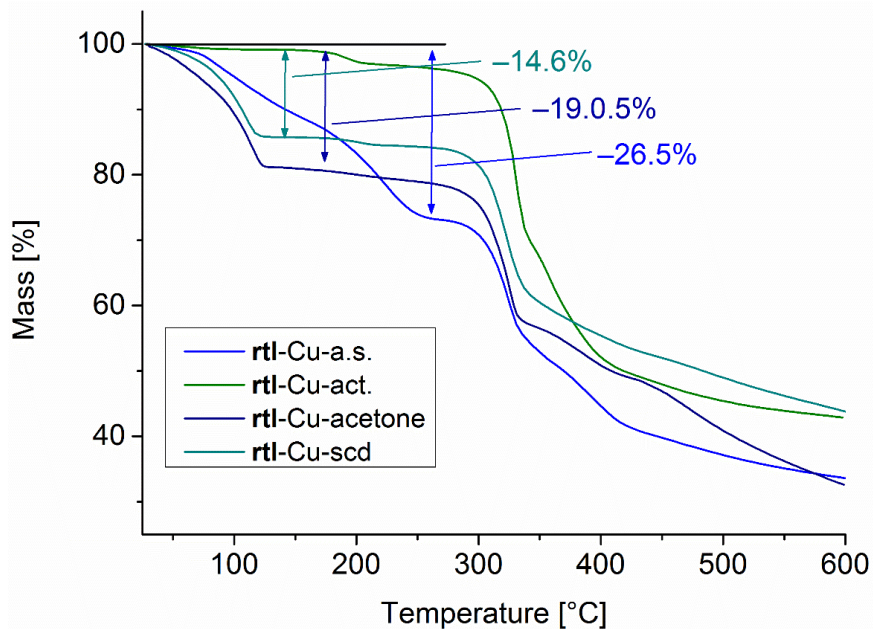


Figure S11 TGA curves of the as-synthesized (a.s.), activated (act.), acetone-exchanged (acetone) and the supercritically-dried (scd) materials of **rtl-[CuHIsa-az-dmpz]** (a.s.: blue, act.: green, acetone: marine blue, scd: dark cyan).

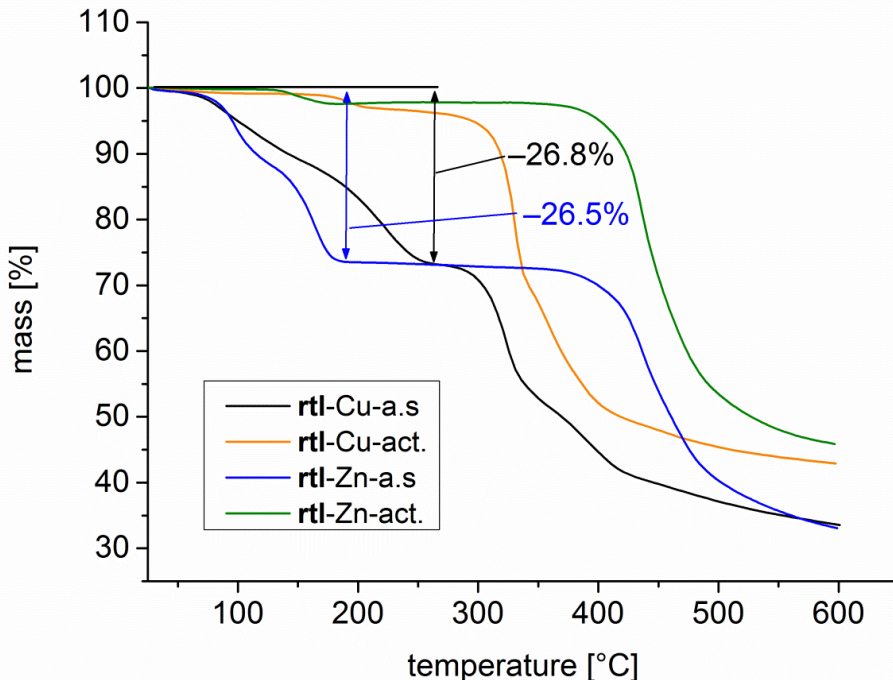


Figure S12 TGA curves of the as-synthesized (a.s.) and activated (act.) materials for **rtl-[CuHIsa-az-dmpz]** (a.s.: black, act.: orange) and **rtl-[Zn(HIsa-az-dmpz)]** (a.s.: blue, act.: green) in the temperature range 25 – 600 °C with heating rate of 5 Kmin⁻¹ under nitrogen atmosphere.

Optical images

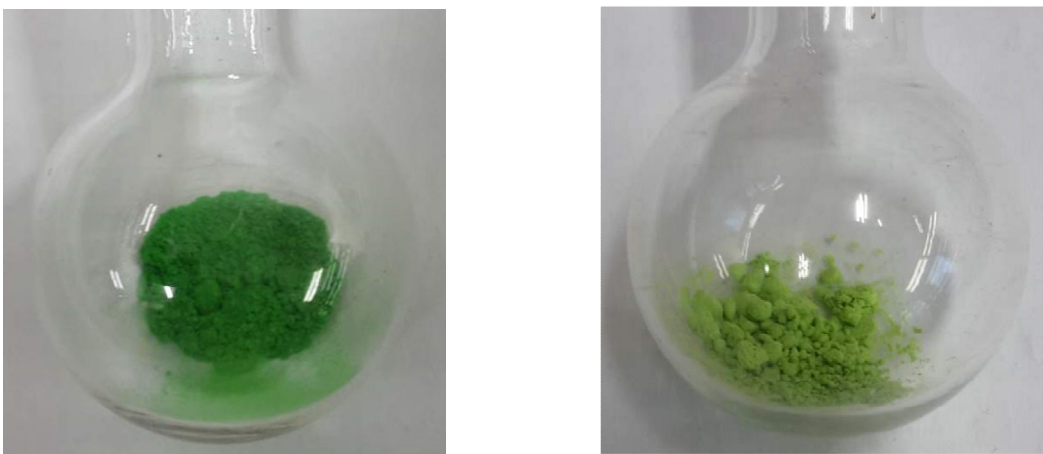


Figure S13 Optical photographs of the grass green open form of **rtl-[Cu(Hlsa-az-dmpz)]** after supercritical drying (right) and the yellow-green closed form **[Cu(Hlsa-az-dmpz]-act** (left) after activation at 120 C.

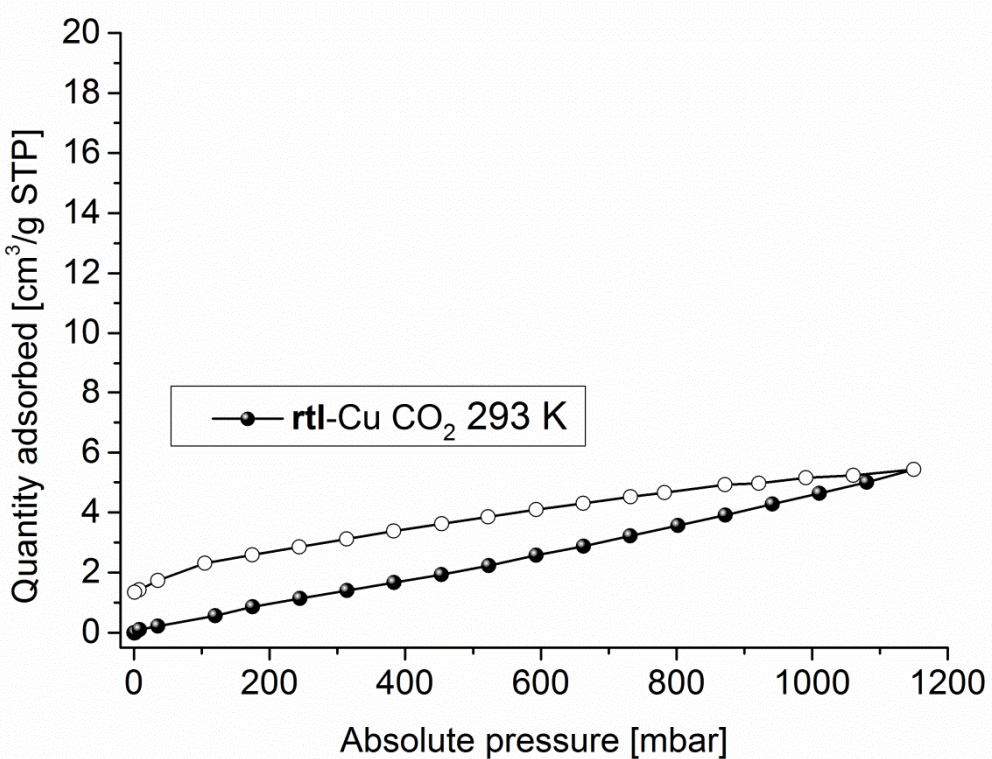


Figure S14 Sorption isotherm of **rtl-[Cu(Hlsa-az-dmpz)]-act.** for CO₂ at 293 K in the low pressure range between 0–1 bar.

FT-IR spectroscopy

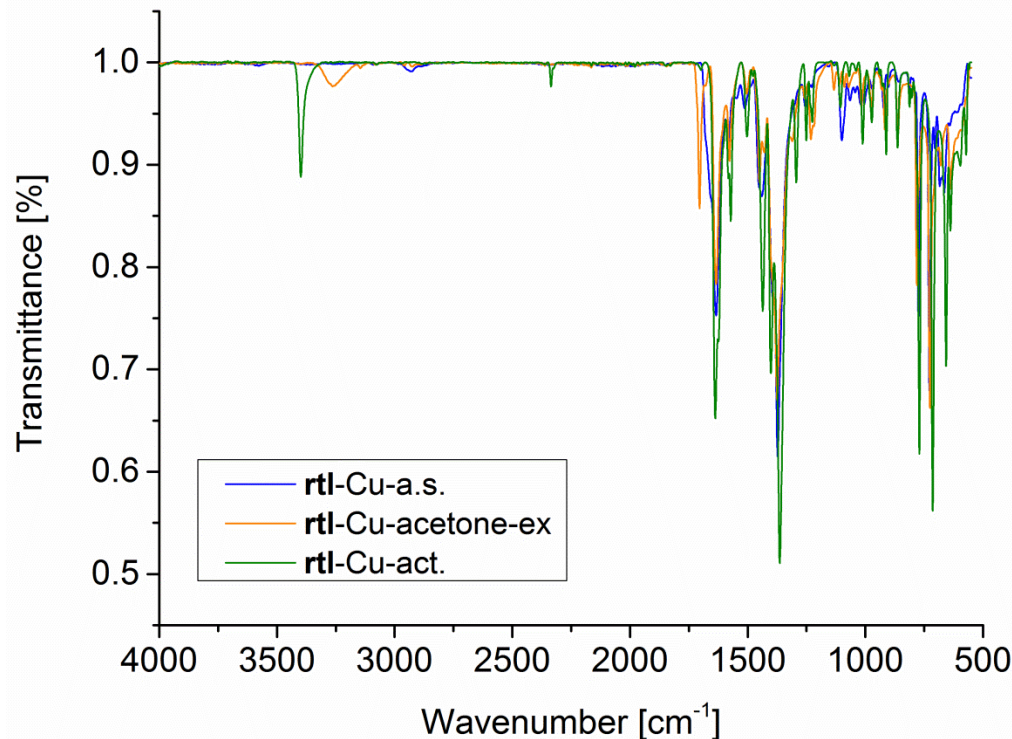


Figure S15 FT-IR spectra of **rtl-[Cu(Hlsa-az-dmpz)]-a.s.** (blue), **rtl-[Cu(Hlsa-az-dmpz)]-acetone-exchanged** (orange) and **rtl-[Cu(Hlsa-az-dmpz)]-act.** (green).

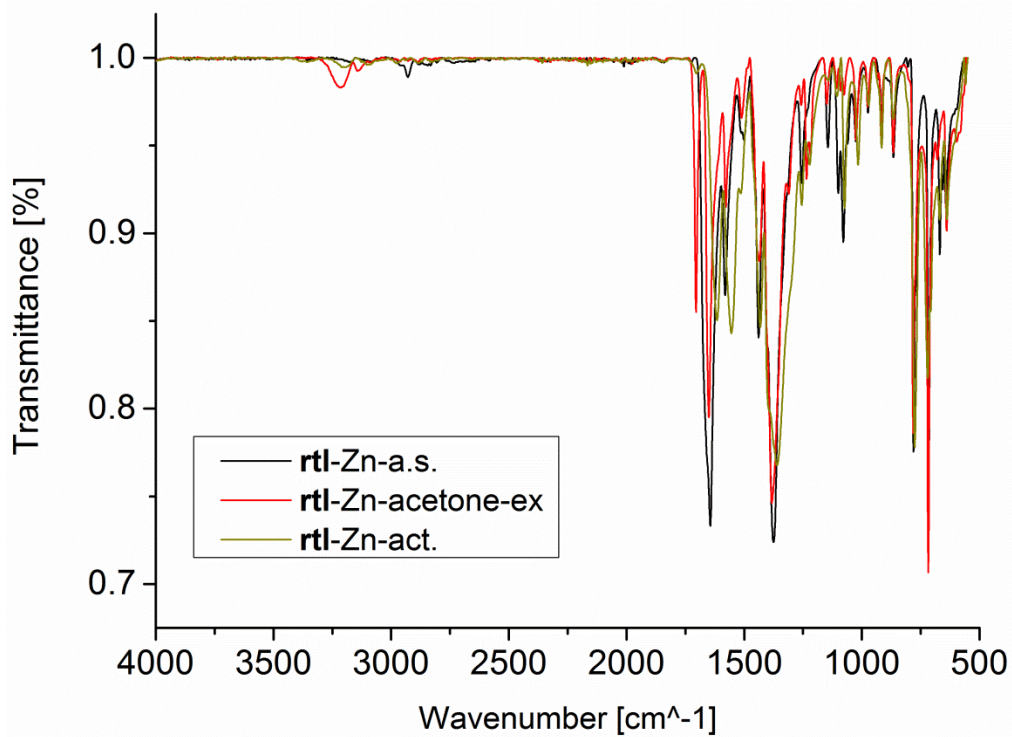


Figure S16 FT-IR spectra of **rtl-[Zn(Hlsa-az-dmpz)]-a.s.** (black), **rtl-[Zn(Hlsa-az-dmpz)]-acetone-exchanged** (red) and **rtl-[Zn(Hlsa-az-dmpz)]-act.** (olive-green).

Scanning electron microscopy (SEM)

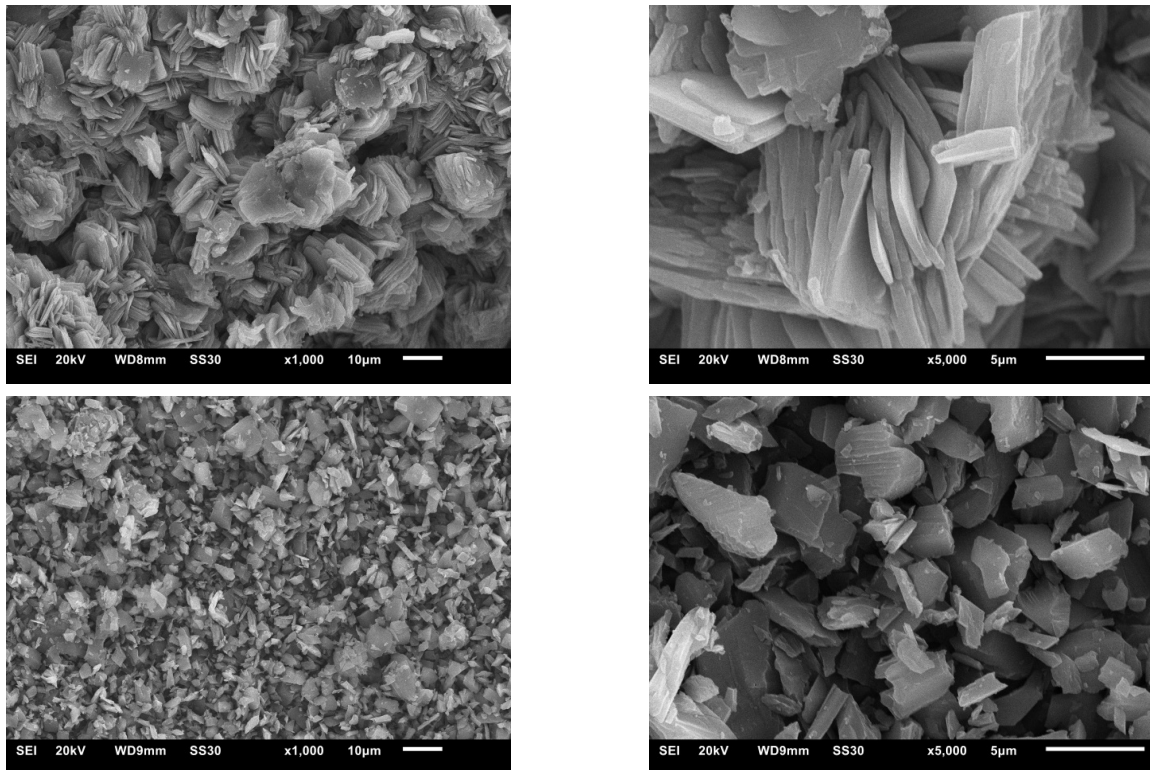


Figure S17 SEM images for rtl-Cu-a.s (top) and rtl-Cu-act. (bottom).

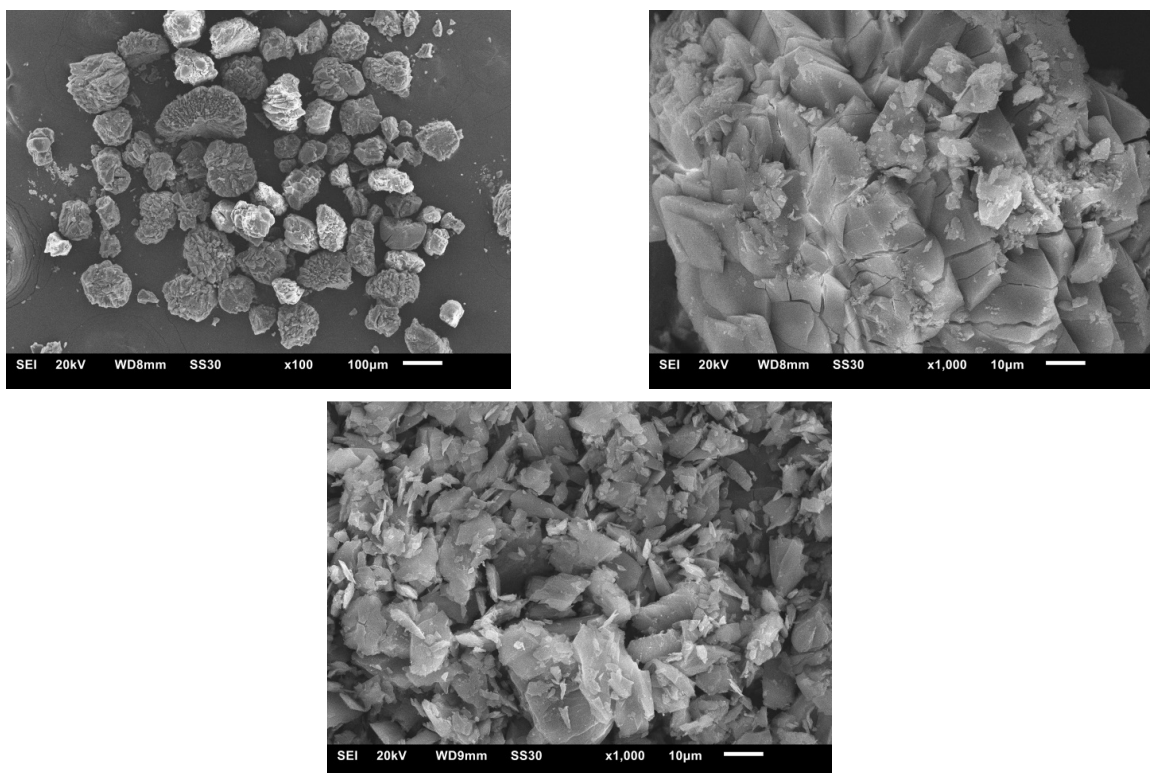


Figure S18 SEM images for rtl-Zn-a.s (top) and rtl-Zn-act. (bottom).

Theoretical surface area and pore volume of rtl-[Cu(Hlsa-az-dmpz)]

The theoretical pore volumes and surface areas were calculated with the programs Mercury^{15,16}, Platon^{17,18} and CrystalExplorer^{19,20}, respectively.

Mercury 'Void' calculation	
Probe radius 1.2 Å, grid spacing 0.7 Å	
Void volume [Å ³] (% of unit cell) specific [cm ³ /g]	859.73 (40.6) 0.37
Probe radius 0.7 Å, grid spacing 0.2 Å	
Void volume [Å ³] (% of unit cell) specific [cm ³ /g]	1081.79 (51.0) 0.47
Platon 'Calc Void'	
Total Potential Solvent Area [Å ³] (% of unit cell) specific [cm ³ /g]	969.8 (45.7) 0.42
CrystalExplorer calculation	
Surface area S _{Unit Cell} (isovalue 0.002) [Å ²] specific [m ² /g]	782 3367
Surface area S _{Unit Cell} (isovalue 0.003) [Å ²] specific [m ² /g]	595 2561
Pore Volume (isovalue 0.002) [Å ³] Specific [cm ³ /g]	981 0.42
Pore Volume (isovalue 0.0003) [Å ³] Specific [cm ³ /g]	579 0.35
Experimental gas uptake	
Langmuir surface area [m ² /g]	1610
Pore Volume N ₂ @77 K [cm ³ /g]	0.55
Langmuir surface area [m ² /g]	1440
Pore Volume CO ₂ @195 K [cm ³ /g]	0.57
Pore Volume CO ₂ @298 K [cm ³ /g]	0.47

Theoretical specific pore volumes are calculated according to (Void Volume x N_A)/(Z x M_{AU}) or (SAV x N_A)/(Z x M_{AU})

Theoretical specific surface areas are calculated according to (S_{Unit Cell} x N_A)/(Z x M_{AU})

Experimental pore volumes are calculated under the assumption of the validity of the Gurvich rule²¹ according to (specific amount adsorbed)/(density of liquid adsorbate) with ρ_{N₂} = 0.808 g/cm³, ρ_{CO₂} = 1.08 g/cm³ and ρ_{CO₂, 298K} = 0.712 g/cm³.

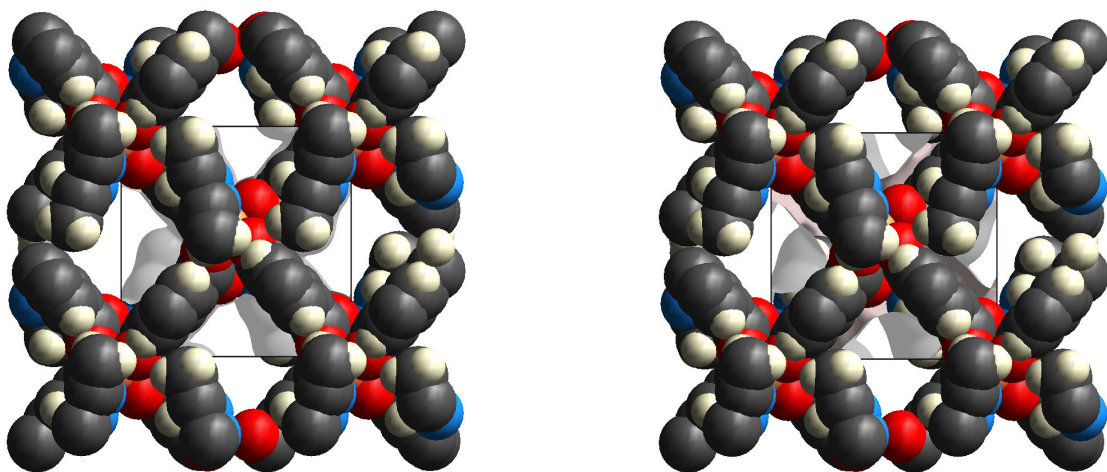


Figure S19 Illustration of the iso-surface area for **rtl**-[Cu(Hlsa-az-dmpz)] at 0.002 e/Å³ (left) and 0.0003 e/Å³ right calculated with CrystalExplorer.

The measured pore volumes are slightly higher than the ones calculated from the DMF-filled single crystal structure data. But this comparison assumes that the (flexible) structure does not change during the sorption measurement. This retention of the solid-state X-ray structure framework is obviously not the case for **rtl**-[Cu(Hlsa-az-dmpz)]. We expect that distortions of the framework have also a large impact on the theoretically calculated specific pore volumes. Concerning activation, we can state that the comparison between theoretical and experimental pore volumes indicates that the sample of **rtl**-[Cu(Hlsa-az-dmpz)] became fully activated under the chosen activation protocol.

Langmuir Report rti-[CuHlsa-az-dmpz] N₂@77 K 1st CycleLangmuir surface area: $1.610,1536 \pm 2,3402 \text{ m}^2/\text{g}$ Slope: $0,002703 \pm 0,000004 \text{ g/cm}^3 \text{ STP}$ Y-intercept: $0,099 \pm 0,002 \text{ mbarKg/cm}^3 \text{ STP}$ b: $0,027245 \text{ 1/mbar}$ Qm: $369,9310 \text{ cm}^3/\text{g} \text{ STP}$

Correlation coefficient: 0.999986

Molecular cross-sectional area: 0.1620 nm^2

Pressure [mbar]	Quantity Adsorbed [cm ³ /g STP]	P/Q [mbarJg/cm ³ STP]
205.725744	312.0763	0.659
232.934491	319.3683	0.729
258.96383	325.3148	0.796
285.81555	326.6452	0.875
309.935032	330.1213	0.939
359.061293	336.0183	1.069
410.654068	340.5038	1.206
461.6057	343.6405	1.343
512.671174	346.2907	1.48
564.532562	347.4821	1.625
634.373514	348.7545	1.819
666.378214	350.3159	1.902
718.425215	351.6511	2.043
768.891129	352.9789	2.178
820.622157	354.3191	2.316
205.725744	312.0763	0.659
232.934491	319.3683	0.729
258.96383	325.3148	0.796
285.81555	326.6452	0.875
309.935032	330.1213	0.939
359.061293	336.0183	1.069
410.654068	340.5038	1.206
461.6057	343.6405	1.343
512.671174	346.2907	1.48
564.532562	347.4821	1.625
634.373514	348.7545	1.819
666.378214	350.3159	1.902
718.425215	351.6511	2.043
768.891129	352.9789	2.178
820.622157	354.3191	2.316

Langmuir Report rtl-[CuHIsa-az-dmpz] N₂@77 K 2nd CycleLangmuir surface area: $1.658,2486 \pm 2,7142 \text{ m}^2/\text{g}$ Slope: $0,002625 \pm 0,000004 \text{ g/cm}^3 \text{ STP}$ Y-intercept: $0,101 \pm 0,002 \text{ mbarNg/cm}^3 \text{ STP}$ b: $0,025926 \text{ 1/mbar}$ Qm: $380,9808 \text{ cm}^3/\text{g} \text{ STP}$

Correlation coefficient: 0.999968

Molecular cross-sectional area: 0.1620 nm^2

Pressure [mbar]	Quantity Adsorbed [cm ³ /g STP]	P/Q [mbarJg/cm ³ STP]
204.200987	324.0059	0.63
230.721192	329.98	0.699
256.854119	334.1922	0.769
282.313722	336.0458	0.84
306.558478	338.1414	0.907
330.977862	340.535	0.972
356.518411	343.0431	1.039
381.47303	345.158	1.105
406.908688	347.0217	1.173
432.268832	348.7245	1.24
457.70152	350.4215	1.306
483.19239	352.0176	1.373
508.582072	353.4794	1.439
534.047798	354.555	1.506
559.259679	355.579	1.573
584.845838	356.632	1.64
610.273277	357.6296	1.706
635.663285	358.5215	1.773
661.021882	359.572	1.838
686.663253	360.4542	1.905
711.878063	361.3366	1.97
737.341958	362.1774	2.036
762.725863	363.0448	2.101
788.142968	363.8641	2.166
813.59189	364.6641	2.231
838.994511	365.5557	2.295

Langmuir Report rti-[CuHIsa-az-dmpz] CO₂@195 K 1st CycleLangmuir surface area: $1.436,6883 \pm 2,9633 \text{ m}^2/\text{g}$ Slope: $0,003179 \pm 0,000007 \text{ g/cm}^3 \text{ STP}$ Y-intercept: $0,046 \pm 0,005 \text{ mbarJg/cm}^3 \text{ STP}$ b: $0,069834 \text{ 1/mbar}$ Qm: $314,5445 \text{ cm}^3/\text{g STP}$

Correlation coefficient: 0.999983

Molecular cross-sectional area: 0.1700 nm^2

Pressure [mbar]	Quantity Adsorbed [cm ³ /g STP]	P/Q [mbarJg/cm ³ STP]
399.120997	302.2214	1.321
466.781301	304.8239	1.531
533.931719	306.4843	1.742
599.864788	307.6665	1.950
666.998036	308.4912	2.162
733.270840	309.0442	2.373
800.040511	309.3462	2.586
866.724333	309.5878	2.800
940.091282	309.6250	3.036
1019.693559	309.6287	3.293

Langmuir Report rti-[CuHIsa-az-dmpz] CO₂@195 K 2nd CycleLangmuir surface area: $1.447,3146 \pm 2,5086 \text{ m}^2/\text{g}$ Slope: $0,003156 \pm 0,000005 \text{ g/cm}^3 \text{ STP}$ Y-intercept: $0,043 \pm 0,004 \text{ mbarJg/cm}^3 \text{ STP}$ b: $0,073759 \text{ 1/mbar}$ Qm: $316,8710 \text{ cm}^3/\text{g STP}$

Correlation coefficient: 0.999989

Molecular cross-sectional area: 0.1700 nm^2

Pressure [mbar]	Quantity Adsorbed [cm ³ /g STP]	P/Q [mbarJg/cm ³ STP]
399.666362	305.4194	1.309
466.5052	307.7736	1.516
600.055406	310.1891	1.934
686.115609	311.1138	2.205
752.955993	311.5865	2.417
799.852213	311.9694	2.564
866.901402	312.1711	2.777
959.996144	312.2208	3.075
1019.742628	312.2971	3.265

Topology Analysis for [CuHIsa-az-dmpz] with ToposPro²²

2:C13 H10 Cu N4 O4/intercluster bonds and atoms at rings>8

Topology for Ti1

Atom Ti1 links by bridge ligands and has

Common vertex with						R(A-A)
V 1	0.0000	0.5000	0.5000	(0 0 0)	5.320A	1
V 1	0.0000	0.0000	0.0000	(0-1 0)	5.360A	1
V 1	1.0000	0.5000	0.5000	(1 0 0)	10.043A	1

Topology for V1

Atom V1 links by bridge ligands and has

Common vertex with						R(A-A)
Ti 1	-0.2055	0.7105	0.7257	(0 1 1)	5.320A	1
Ti 1	0.2055	0.2895	0.2743	(0 0 0)	5.320A	1
Ti 1	-0.2055	0.7895	0.2257	(0 0 0)	5.360A	1
Ti 1	0.2055	0.2105	0.7743	(0 0 0)	5.360A	1
Ti 1	0.7945	0.7105	0.7257	(1 1 1)	10.043A	1
Ti 1	-0.7945	0.2895	0.2743	(-1 0 0)	10.043A	1

Structural group analysis

Structural group No 1

Structure consists of 3D framework with VTi2

Coordination sequences

Ti1: 1 2 3 4 5 6 7 8 9 10

Num 3 14 19 62 51 144 99 254 163 400

Cum 4 18 37 99 150 294 393 647 810 1210

V1: 1 2 3 4 5 6 7 8 9 10

Num 6 10 38 34 102 74 198 130 326 202

Cum 7 17 55 89 191 265 463 593 919 1121

TD10=1180

Vertex symbols for selected sub-lattice

Ti1 Point symbol:{4.6^2}

Extended point symbol:[4.6(2).6(2)]

V1 Point symbol:{4^2.6^10.8^3}

Extended point symbol:[4.4.6.6.6.6.6.6.6(2).6(2).8(2).8(4).8(4)]

Point symbol for net: {4.6^2}2{4^2.6^10.8^3}

3,6-c net with stoichiometry (3-c)2(6-c); 2-nodal net

Topological type: **rtl** rutile 3,6-conn (topos&RCSR.ttd) {4.6^2}2{4^2.6^10.8^3} – vs.
[4.4.6.6.6.6.6.6.6(2).6(2).*.*.] [4.6(2).6(2)]

Table S1. Selected Bond lengths [Å] and angles [°] for [Cu(HIsa-az-dmpz)]·(DMF)₂.

Cu—O1	1.929 (8)	C3—C4	1.433 (13)
Cu—O4 ⁱ	1.929 (8)	C3—C8	1.466 (14)
Cu—O3 ⁱⁱ	1.948 (6)	C4—C5	1.384 (13)
Cu—O2 ⁱⁱⁱ	1.966 (7)	C5—C6	1.366 (13)
Cu—N1 ^{iv}	2.154 (8)	C9—C10	1.526 (13)
O1—C7	1.250 (11)	C10—C11	1.381 (14)
O2—C7	1.267 (12)	C11—C12	1.376 (15)
O3—C8	1.275 (13)	C12—C13	1.487 (17)
O4—C8	1.262 (12)	N4—C5	1.449 (12)
O5—C14	1.15 (2)	N5—C14	1.248 (18)
N1—N2	1.319 (11)	N5—C15	1.457 (19)
N1—C10	1.329 (12)	N5—C16	1.50 (2)
N2—C12	1.386 (14)	C1—C6	1.406 (14)
N2—H2N	0.8800	C1—C2	1.410 (13)
N3—N4	1.242 (11)	C1—C7	1.433 (14)
N3—C11	1.419 (13)	C2—C3	1.381 (13)
O1—Cu—O4 ⁱ	87.7 (3)	C5—C6—C1	122.2 (11)
O1—Cu—O3 ⁱⁱ	88.8 (3)	C5—C6—H6	118.9
O4 ⁱ —Cu—O3 ⁱⁱ	167.3 (3)	C1—C6—H6	118.9
O1—Cu—O2 ⁱⁱⁱ	167.4 (3)	O1—C7—O2	127.8 (10)
O4 ⁱ —Cu—O2 ⁱⁱⁱ	91.3 (3)	O1—C7—C1	115.7 (11)
O3 ⁱⁱ —Cu—O2 ⁱⁱⁱ	89.4 (3)	O2—C7—C1	116.1 (10)
O1—Cu—N1 ^{iv}	99.3 (3)	O4—C8—O3	126.5 (11)
O4 ⁱ —Cu—N1 ^{iv}	94.1 (3)	O4—C8—C3	117.4 (11)
O3 ⁱⁱ —Cu—N1 ^{iv}	98.5 (3)	O3—C8—C3	115.6 (11)
O2 ⁱⁱⁱ —Cu—N1 ^{iv}	93.4 (3)	N1—C10—C11	110.4 (10)
C7—O1—Cu	123.6 (7)	N1—C10—C9	120.9 (10)
C7—O2—Cu ⁱⁱⁱ	120.9 (7)	C11—C10—C9	128.4 (10)
C8—O3—Cu ^v	120.8 (7)	C12—C11—C10	107.5 (10)
C8—O4—Cu ^{vi}	125.0 (7)	C12—C11—N3	120.9 (11)
N2—N1—C10	105.6 (9)	C10—C11—N3	131.6 (11)
N2—N1—Cu ^{iv}	122.0 (7)	C11—C12—N2	103.2 (11)
C10—N1—Cu ^{iv}	132.3 (7)	C11—C12—C13	133.5 (12)
N1—N2—C12	113.3 (10)	N2—C12—C13	123.3 (12)
N1—N2—H2N	123.4	O5—C14—N5	136 (3)
C12—N2—H2N	123.4	O5—C14—H14	112.2
N4—N3—C11	112.8 (10)	N5—C14—H14	112.2
N3—N4—C5	113.9 (10)	C2—C3—C4	118.6 (11)
C14—N5—C15	124 (2)	C2—C3—C8	120.6 (11)
C14—N5—C16	125 (2)	C4—C3—C8	120.8 (11)
C15—N5—C16	111.0 (16)	C5—C4—C3	118.9 (11)

C6—C1—C2	116.4 (12)	C6—C5—C4	121.0 (10)
C6—C1—C7	122.9 (11)	C6—C5—N4	114.6 (10)
C2—C1—C7	120.8 (11)	C4—C5—N4	124.3 (11)
C3—C2—C1	122.6 (11)		

Symmetry codes: (i) $x, -y+1/2, z+1/2$; (ii) $-x, y+1/2, -z+1/2$; (iii) $-x, -y+1, -z+1$; (iv) $-x+1, -y+1, -z+1$; (v) $-x, y-1/2, -z+1/2$; (vi) $x, -y+1/2, z-1/2$.

Table S2. Selected Bond lengths [Å] and angles [°] for $[\text{Zn}(\text{HIsa-az-dmpz})]\cdot(\text{DMF})_2$.

Zn—O1	2.028 (3)	C5—C6	1.377 (5)
Zn—N1 ⁱ	2.028 (3)	O6—C17	1.273 (10)
Zn—O4 ⁱⁱ	2.033 (3)	N6—C17	1.368 (9)
Zn—O2 ⁱⁱⁱ	2.033 (3)	N6—C18	1.433 (9)
Zn—O3 ^{iv}	2.041 (3)	N6—C19	1.399 (10)
O1—C7	1.255 (5)	C9—C10	1.472 (6)
N1—C10	1.337 (5)	C10—C11	1.413 (5)
N1—N2	1.362 (4)	C11—C12	1.388 (6)
C1—C2	1.385 (5)	C12—C13	1.490 (6)
C1—C6	1.396 (5)	O5—C14	1.256 (6)
C1—C7	1.503 (5)	N5—C14	1.294 (6)
O2—C7	1.262 (5)	N5—C16	1.445 (7)
N2—C12	1.336 (6)	N5—C15	1.465 (6)
N2—H2N	0.830 (10)	C3—C4	1.409 (5)
C2—C3	1.376 (5)	C3—C8	1.499 (5)
O3—C8	1.255 (5)	O4—C8	1.251 (5)
N3—N4	1.255 (4)	N4—C5	1.444 (5)
N3—C11	1.405 (5)	C4—C5	1.382 (5)
O1—Zn—N1 ⁱ	102.10 (12)	O4—C8—O3	126.0 (4)
O1—Zn—O4 ⁱⁱⁱ	86.95 (12)	O4—C8—C3	116.7 (3)
N1 ⁱ —Zn—O4 ⁱⁱⁱ	102.01 (12)	O3—C8—C3	117.3 (3)
O1—Zn—O2 ⁱⁱ	158.03 (11)	N1—C10—C11	108.3 (3)
N1 ⁱ —Zn—O2 ⁱⁱ	99.85 (11)	N1—C10—C9	121.5 (3)
O4 ⁱⁱⁱ —Zn—O2 ⁱⁱ	89.36 (12)	C11—C10—C9	130.2 (4)
O1—Zn—O3 ^{iv}	87.16 (11)	C12—C11—N3	120.8 (4)
N1 ⁱ —Zn—O3 ^{iv}	100.01 (11)	C12—C11—C10	106.8 (3)
O4 ⁱⁱⁱ —Zn—O3 ^{iv}	157.94 (11)	N3—C11—C10	132.4 (4)
O2 ⁱⁱ —Zn—O3 ^{iv}	88.20 (11)	N2—C12—C11	106.1 (3)
O1—Zn—Zn ⁱⁱ	77.39 (8)	N2—C12—C13	122.3 (4)
N1 ⁱ —Zn—Zn ⁱⁱ	178.69 (9)	C11—C12—C13	131.6 (4)
O4 ⁱⁱ —Zn—Zn ⁱⁱ	76.77 (8)	O5—C14—N5	125.2 (5)
O2 ⁱⁱ —Zn—Zn ⁱⁱ	80.68 (8)	O6—C17—N6	124.8 (10)
O3 ^{iv} —Zn—Zn ⁱⁱ	81.20 (8)	O6—C17—H17	124.7
C7—O1—Zn	130.2 (3)	N6—C17—H17	109.5

C10—N1—N2	107.0 (3)	C14—N5—C16	120.9 (5)
C10—N1—Zn ⁱ	131.2 (3)	C14—N5—C15	121.0 (4)
N2—N1—Zn ⁱ	121.6 (2)	C16—N5—C15	118.0 (4)
C2—C1—C6	119.0 (3)	C6—C5—C4	120.7 (4)
C2—C1—C7	121.5 (3)	C6—C5—N4	115.0 (3)
C6—C1—C7	119.4 (3)	C4—C5—N4	124.3 (4)
C7—O2—Zn ⁱⁱ	125.6 (2)	C17—N6—C18	121.1 (7)
C12—N2—N1	111.7 (3)	C17—N6—C19B	120.2 (8)
C12—N2—H2N	126 (3)	C18—N6—C19B	118.7 (8)
N1—N2—H2N	122 (3)	C5—C6—C1	120.2 (4)
C3—C2—C1	120.8 (3)	O1—C7—O2	125.6 (4)
C8—O3—Zn ^v	124.8 (2)	O1—C7—C1	116.7 (3)
N4—N3—C11	113.1 (3)	O2—C7—C1	117.7 (3)
C2—C3—C4	119.9 (3)	C8—O4—Zn ^{vi}	131.2 (3)
C2—C3—C8	120.5 (3)	N3—N4—C5	112.2 (3)
C4—C3—C8	119.6 (3)	C5—C4—C3	119.2 (4)

Symmetry codes: (i) $-x+2, -y, -z+1$; (ii) $-x+1, -y, -z+1$; (iii) $x, -y-1/2, z+1/2$; (iv) $-x+1, y+1/2, -z+1/2$; (v) $-x+1, y-1/2, -z+1/2$; (vi) $x, -y-1/2, z-1/2$.

References

- 1 S. L. Xiang, J. Huang, L. Li, J. Y. Zhang, L. Jiang, X. J. Kuang and C. Y. Su, *Inorg. Chem.*, 2011, **50**, 1743-1748.
- 2 J. F. Eubank, L. Wojtas, M. R. Hight, T. Bousquet, V. C. Kravtsov and M. Eddaoudi, *J. Am. Chem. Soc.* 2011, **133**, 17532-17535.
- 3 L. Wen, W. Shi, X. Chen, H. Li and P. Cheng, *Eur. J. Inorg. Chem.*, 2012, **2012**, 3562-3568.
- 4 S.-M. Zhang, Z. Chang, T.-L. Hu and X.-H. Bu, *Inorg. Chem.*, 2010, **49**, 11581-11586.
- 5 S. Wang, Z.-W. Wei, J. Zhang, L. Jiang, D. Liu, J.-J. Jiang, R. Si and C.-Y. Su, *IUCrJ*, 2019, **6**, 85-95.
- 6 Y. Xiong, Y. Z. Fan, R. Yang, S. Chen, M. Pan, J. J. Jiang and C. Y. Su, *Chem. Commun.*, 2014, **50**, 14631-14634.
- 7 Y. Xiong, Y. Z. Fan, R. Yang, S. Chen, M. Pan, J. J. Jiang and C. Y. Su, *Chem. Commun.*, 2014, **50**, 14631-14634.
- 8 Z. J. Chen, K. Adil, L. J. Weselinski, Y. Belmabkhout and M. Eddaoudi, *J. Mater. Chem. A*, 2015, **3**, 6276-6281.
- 9 T. L. Hu, H. Wang, B. Li, R. Krishna, H. Wu, W. Zhou, Y. Zhao, Y. Han, X. Wang, W. Zhu, Z. Yao, S. Xiang and B. Chen, *Nat. Commun.*, 2015, **6**, 7328.
- 10 X. Liu, M. Oh and M. S. Lah, *Cryst. Growth Des.*, 2011, **11**, 5064-5071.
- 11 Q. Wang, J. Jiang, M. Zhang and J. Bai, *Cryst. Growth Des.*, 2016, **17**, 16-18.
- 12 K. Kobalz, M. Kobalz, J. Möllmer, U. Junghans, M. Lange, J. Bergmann, S. Dietrich, M. Wecks, R. Glaser and H. Krautscheid, *Inorg. Chem.*, 2016, **55**, 6938-6948.
- 13 F. R. Japp and F. Klingemann, *F. Liebigs Ann. Chem.* 1888, **247**, 190-225.
- 14 M. N. Kopylovich, M. J. Gajewska, K. T. Mahmudov, M. V. Kirillova, P. J. Figiel, M. F. C. Guedes da Silva, B. Gil-Hernandez, J. Sanchiz and A. J. L. Pombeiro, *New J. Chem.*, 2012, **36**, 1646-1654.
- 15 Mercury CSD 4.1, Program for Crystal Structure Visualisation, Exploration and Analysis from the Cambridge Crystallographic Data Center, Copyright CCDC 2001-2016, <http://www.ccdc.cam.ac.uk/mercury/>
- 16 C. F. Macrae, I. J. Bruno, J. A. Chisholm, P. R. Edgington, P. McCabe, E. Pidcock, L. Rodriguez-Monge, R. Taylor, J. van de Streek and P. A. Wood, *Journal of Applied Crystallography*, 2008, **41**, 466-470.
- 17 A. Spek, *Acta Crystallographica Section D*, 2009, **65**, 148-155.
- 18 PLATON – A Multipurpose Crystallographic Tool, Utrecht University, Utrecht, The Netherlands, A. L. Spek (2008); Windows implementation: L.J. Farrugia, University of Glasgow, Scotland, Version 40608, (2008).

- 19 CrystalExplorer17, Version 3.1; Turner, M. J.; McKinnon, J. J.; Wolff, S. K.; Grimwood, D. J.; Spackman, P. R.; Jayatilaka, D.; Spackman, M. A.: University of Western Australia, 2017. <http://hirshfeldsurface.net>
- 20 M. J. Turner, J. J. McKinnon, D. Jayatilaka and M. A. Spackman, *CrystEngComm*, 2011, **13**, 1804-1813.
- 22 L. Gurvich, *J. Phys. Chem. Soc. Russ.*, 1915, **47**, 805-827.
- 23 V. A. Blatov, A. P. Shevchenko and D. M. Proserpio, *Cryst. Growth. Des.*, 2014, **14**, 3576-3586.

Appendix

rtl-M-MOFs (M = Cu, Zn) with a T-shaped bifunctional pyrazole-isophthalate ligand showing flexibility and S-shaped Type F-IV sorption isotherms with high saturation uptakes for M = Cu

Further sorption experiments at cryogenic temperatures have been carried out for Argon at 87 K and CH₄ at 112 K. Both show Type FIV isotherms accompanied by high saturation uptakes.

Especially because MOFs with Type F-IV isotherms are discussed in gas storage and delivery devices, these results for methane at its boiling point look extremely promising for rtl-Cu as a potential storage material for CH₄. High-pressure sorption experiments should be used to further underpin these results (see Abbildung 19 in the introduction).

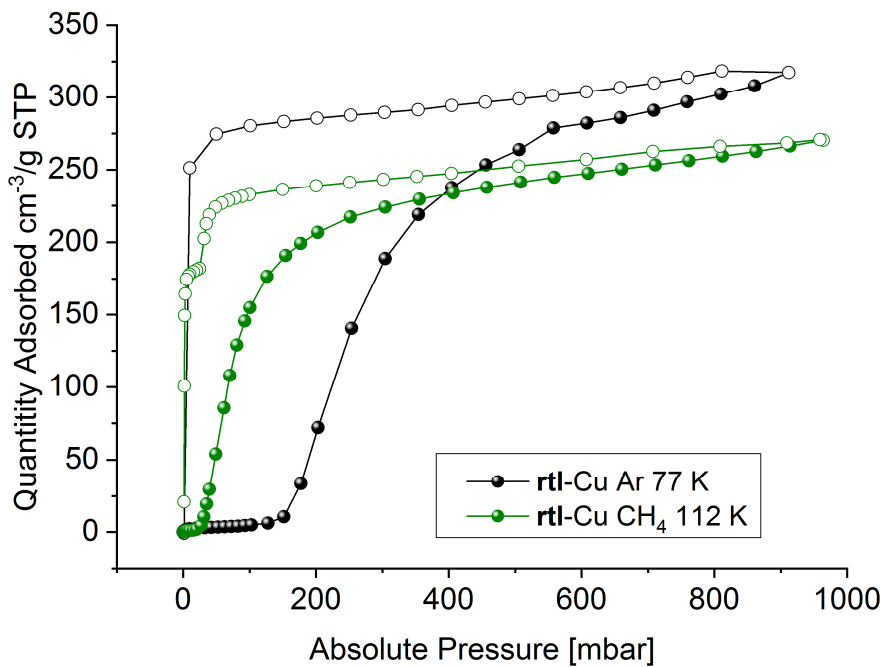


Figure S20

Table S3 Gas sorption data for rtl-[Cu(Hlsa-az-dmpz)].

	Saturation uptake [cm ³ /g, mmol/g]	Gate opening pressure (mbar, P/P ₀)
Ar@87 K	317, 14.0	150, 0.15
CH ₄ @77 K	270, 11.9	35, 0.04

3.2 Solid-state landscape of 4,4'-azobis(3,5-dimethyl-1H-pyrazole) with the isolation of conformer-dependent polymorphs

The work presented in this chapter has been submitted to:

Simon Millan, Jamal Nasir, Beatriz Gil-Hernández, Tim-Oliver Knedel, Bastian Moll, István Boldog, Oliver Weingart, Jörn Schmedt auf der Günne and Christoph Janiak* *Cryst. Growth Des.*, **2020**, submitted.

Abstract

The molecule 4,4'-azobis(3,5-dimethyl-1H-pyrazole) (H_2azbpz) can exist in different planar conformers which differ in the relative orientation of the NH atoms with respect to the central azo bond and are related by azo-pedaling, rotation of the pyrazolyl group around the C4-N(azo) bond or N1-H to N2-H proton transfer. The two symmetrical polymorphs each assemble in their own solid-state packing as a case of conformational polymorphism. Lattice energy and gas-phase conformer calculations point to the harder-to-obtain polymorph $\text{H}_2\text{azbpz-II}$, as the thermodynamic more stable form at lower temperatures but having the higher energy conformer form **II**. Both polymorphs $\text{H}_2\text{azbpz-I}$ and $\text{H}_2\text{azbpz-II}$ were reproducibly obtained by their own crystallization experiments which initially included ball milling to transform $\text{H}_2\text{azbpz-I}$ into -II. The polymorph structures were established by single-crystal and powder X-ray diffraction in combination with Raman spectroscopy and solid-state $^{13}\text{C}\{^1\text{H}\}$ cross-polarization magic angle spinning NMR. The supramolecular assembly of H_2azbpz in its two polymorphs features supramolecular honeycomb sheets (**hcb** topology) in a staggered AA'-packing (in $\text{H}_2\text{azbpz-I}$) or in an eclipsed AB-fashion (in $\text{H}_2\text{azbpz-II}$). In addition, the hemihydrate $\text{H}_2\text{azbpz}\cdot 0.5\text{H}_2\text{O}$ crystallized reproducibly from water-containing solutions, having a tetrahedral (T_d) $\{\text{H}_2\text{O}(\text{pz})_4\}$ -subunit with a pseudo T_d -water molecules, thereby giving a network structure with **dia**-topology which can be regarded as a supramolecular analog of the cubic ice polymorph I_c .

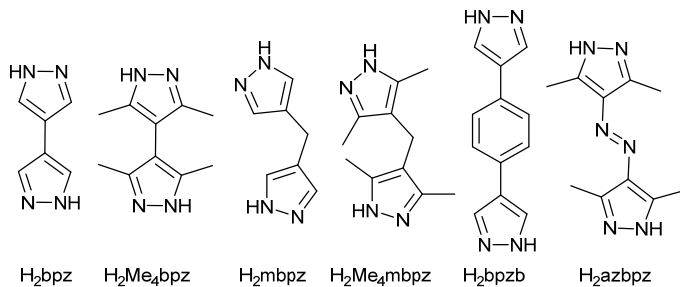


Introduction

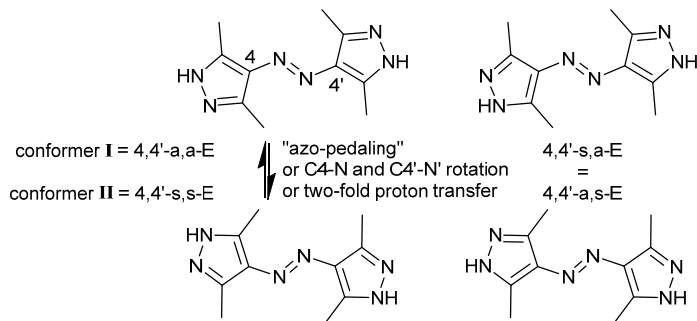
Studying the solid-state structures of organic molecules and metal-complexes has always been at the forefront of crystal engineering in order to get insights into the weak interactions which determine their solid-state structures.¹⁻⁶ In this respect, research on polymorphism, that is, the existence of different solid-state structures of a compound, has received a lot of attention. As a subsection, different three-dimensional arrangements of very similar molecular conformations into distinct crystal phases is referred to as packing polymorphism. Packing polymorphism is usually observed for molecules with relative high rotational barriers and only slight changes in weak interactions guide the differences in their crystal structures.^{7,8} The subsection of conformational polymorphism is ascribed to the isolation of different crystal structures each containing different molecular conformers.^{9,10}

1H-pyrazoles are a particularly interesting class of compounds in the context of supramolecular chemistry due to their complementary pyridinic (hydrogen-bond acceptor) and pyrrolic (hydrogen-bond donor) nitrogen atom positioned next to each other.¹¹⁻¹⁵ Polymorphism in NH-azoles is a relatively rare phenomenon,¹⁶ and only few studies on the polymorphism of *1H*-pyrazoles can be found in the literature.¹⁷⁻²⁰ A special case deals with the isolation of the tautomeric forms of unsymmetrically substituted pyrazoles in different crystal structures under the terms tautomeric polymorphism and desmotropy.²¹⁻²⁴

While the synthesis of 4,4'-azobis(3,5-dimethyl-*1H*-pyrazole) (H₂azbpz, Chart 1) is long known, its solid-state structure is not. Our interest to azo-bipyrazoles was fueled by the possibility of the curious effect of azo-pedaling, sometimes observed in the solid state for azo-compounds (Scheme 1). The effect is equivalent to rotation of each substituent around the C-N bond or a double proton transfer from the N1 to the N2 position. Such a pedal-like movement is possible in the solid-state, while the molecular volume swing during the movement is quite small. Hence the activation energies for azo-pedaling are estimated to be in the range of ~10-60 kJ mol⁻¹.^{25,26} The possible azo-pedaling is interesting in the context with solid-state proton transfer (SSPT) as *1H*-pyrazoles are among the rare compounds, which are expressing SSPT near room temperature, especially in their cyclamers (Scheme S3, SI).^{27,28}

Chart 1. Linear bispyrazoles relevant to this work.^a

^a CCDC-Refcodes and assigned supramolecular topologies in parentheses: H₂bpz = 4,4'-bis-1*H*-pyrazole (UDAYIH, **hcb**),²⁹ H₂Me₄bpz = 4,4'-bis(3,5-dimethyl-1*H*-pyrazole) (UDAYUT, **ths**; UDAYUT01, **bto**; UDAYUT02, **srs**),^{29,30} H₂mbpz = 4,4'-methylenebis(1*H*-pyrazole) (HEPHUF, **hcb**),³¹ H₂Me₄mbpz = 4,4'-methylenebis(3,5-dimethyl-1*H*-pyrazole) (HEPJAN01, **hcb**; HEPJAN02, **hcb**),^{31,32} H₂bpzb = 1,4-bis(1*H*-pyrazol-4-yl)benzene (VONVEA, **hcb**)³³ and H₂azbpz = 4,4'-azobis(3,5-dimethyl-1*H*-pyrazole) (presented in this work). Presentation of the crystal packings of these bispyrazoles can be found in the Supp. Info. in Figures S28-S29.

Scheme 1. Schematic presentation of the conformers and their possible transformations in H₂azbpz.^a

^a The three possible E-conformers of H₂azbpz in the solid state. The conformer designation is 4,4'-{a/s},{a/s}-E, where a/s is a shortening of ap/sp, which refers to the antiperiplanar and synperiplanar configuration at the C(4)-N and C(4')-N' bonds respectively,³⁴ and E is the configuration at the azo double bond. Note that the 4,4'-s,a-E and 4,4'-a,s-E forms cannot be distinguished in the solid state unless there is an additional element of orientation, e.g. a coordinating metal atom.³⁵

Herein, we present the synthesis and analysis of two polymorphs of H₂azbpz as an example of a symmetrically substituted azo-compound exhibiting polymorphism based on different conformers (Scheme 1). Additionally, the hemihydrate H₂azbpz·0.5H₂O is described, whose **dia-topology** is introduced by a pseudo-tetrahedral (T_d) water molecule.

Results and Discussion

4,4'-Azobis(3,5-dimethyl-1H-pyrazole) (H_2azbpz) (Chart 1) was first synthesized by Hüttel et al. in 1955 via a Mills condensation reaction and its crystal habit was described as flat golden prisms.³⁶ We synthesized H_2azbpz via a Japp-Klingemann reaction from 4-amino(3,5-dimethyl-1H-pyrazole) (Scheme S1, SI) following a procedure published by us recently, where we utilized H_2azbpz as a pyrazole-pyrazolate ligand (Hazbpz^-) in a two-dimensional zinc(II) coordination polymer and in its neutral form in supramolecular architectures of monomeric metal-complexes.^{35,37}

Regarding the solid-state structures of azobenzene-compounds, sometimes a conformational disorder associated with a pedal motion of the azo-group has been observed.^{25,38} and the solid-state structures of ortho- and meta-substituted azobenzene-compounds have been studied accordingly, with examples being available where conformational disorder was observed showing both conformers in one crystal structure (cf. Scheme S2, SI).³⁹⁻⁴¹

Here we discern the distinguishable molecular forms of H_2azbpz due to the isomerism of the NH function relative to the azo-function by the anti-periplanar (a) or syn-periplanar (s) position of the C(4)-N and C(4')-N' bonds relative to the azo-bond.³⁴ The conformer designations then take the form 4,4'-a,a-E (conformer I) with both C(4)-N and C(4')-N' bonds in anti-periplanar conformation and 4,4'-s,s-E (conformer II) with both in syn-periplanar position (Scheme 1). Isomerism of the proton location in the conformers of H_2azbpz is the principal difference compared to the other, well-studied symmetrically substituted N-heterocyclic azo-compounds like 4,4'-azopyridine^{42,43} or 4,4'-azo-1,2,4-triazole.⁴⁴

Density functional theory (DFT) analysis on the (B3LYP/TZVP) level reveals a gas-phase energy difference of $\Delta E_{\text{conf}}(\text{II}-\text{I}) = 2.0 \text{ kJ/mol}$ between both conformers with I being of lower energy (see Figure S15, SI). This value lies in the lower range of the energy differences calculated for symmetrically ortho- and meta-substituted azo-compounds.^{39,40} This value is also in the lower limit for calculated differences between observed conformations in conformational polymorphs.¹⁰ For the azo-pedaling motion of I to II in H_2azbpz (in vacuum) a barrier of 77 kJ/mol has been calculated (Fig. S15, SI).

Phase-pure crystallization of H₂azbpz-I and H₂azbpz-II

The first single crystal of H₂azbpz, picked serendipitously from a recrystallization experiment turned out to contain H₂azbpz in conformer II, the polymorph is thus denoted as H₂azbpz-II. The observed mismatch of the simulated powder pattern of H₂azbpz-II with the measured powder patterns of polycrystalline powders which were directly obtained from the synthesis (corresponding to H₂azbpz-I-a.s. in Figure 1), led to a detailed study of the solid-state landscape of H₂azbpz (see Supp. Info. for details). Subsequently, single crystals of the polymorph H₂azbpz-I (with conformer I) could be reproducibly and easily obtained phase pure by slow evaporation of diluted ethanolic solutions of H₂azbpz (see Figure S20, SI). Samples of H₂azbpz-II could initially not be reproduced from classical crystallization experiments, that are from solvent evaporation from diluted isopropanol, acetonitrile or acetone solutions at room temperature, from slow cooling of DMF, DMSO or N-methylformamide solutions or from vapor diffusion crystallization experiments of diethylether into solutions of DMF and DMSO. Even when H₂azbpz-II is presumed as a minority phase in the crystal batch, its amount is apparently so small that it is not distinguishable by PXRD and all the single crystals tested later on matched the unit cells of H₂azbpz-I. Therefore, the difficulty to reproduce the polymorph H₂azbpz-II seemed reminiscent of cases of disappearing polymorphs.⁴⁵

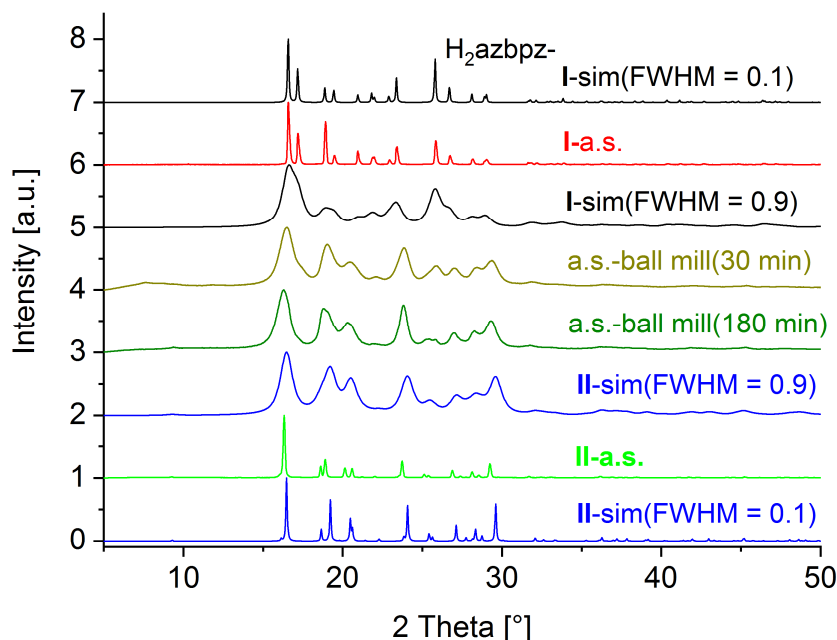


Figure 1. Comparison of the PXRD patterns of experimental H₂azbpz-I-as synthesized (a.s.) with the simulations for smaller crystallite sizes H₂azbpz-I-sim (FWHM = 0.1) and H₂azbpz-I-sim (FWHM = 0.9), denoted by their increasing frequency width at half-height maximum (FWHM), the experimental pattern after different times (30 and 180 min) of ball milling of as-synthesized H₂azbpz-I, the

experimental H₂azbpz-II-a.s. and the simulations for different crystallite sizes H₂azbpz-II-sim (FWHM = 0.1) and H₂azbpz-II-sim (FWHM = 0.9). For the indexed reflections of H₂azbpz-I and H₂azbpz-II see Figure S19 in SI.

Therefore, at first a route via a mechanochemical transformation was used (20 Hz milling for up to 180 min). While the product was reasonably pure according to PXRD, the mechanochemical conversion is typically non-quantitative. Eventually, recrystallization from supersaturated solutions in DMF at 0-2 °C was established to reproducibly obtain phase pure and highly crystalline H₂azbpz-II (see Supp. Info. for details).

The phase purity of the bulk H₂azbpz-II from ball-milling could not be established very reliably from the PXRD patterns (even if the peak at $2\theta = \sim 17^\circ$ is characteristic for H₂azbpz-I) because of the line broadening caused by the milling. Raman spectroscopy has proven to be an excellent tool for phase identification and checking of purity due to the sensitivity of the fingerprint region to slight conformational and packing differences.⁴⁶ The Raman spectra of the single crystals show a minute but unequivocal difference with the N=N stretching vibration as strongest band shifted by 7 cm⁻¹ (1430 cm⁻¹ for H₂azbpz-I and 1423 cm⁻¹ for H₂azbpz-II) (Figure 2). As already indicative from the PXRD pattern, signals in the Raman spectra obtained after ball milling for 30 min can be attributed to the presence of H₂azbpz-I and H₂azbpz-II (see inset Figure 2 and Figures S23 and S24, SI). Nonetheless, the sample obtained after 180 min clearly matches H₂azbpz-II, confirming the full mechanochemical conversion and establishing Raman spectroscopy as an additional tool to study the polymorphism of H₂azbpz.

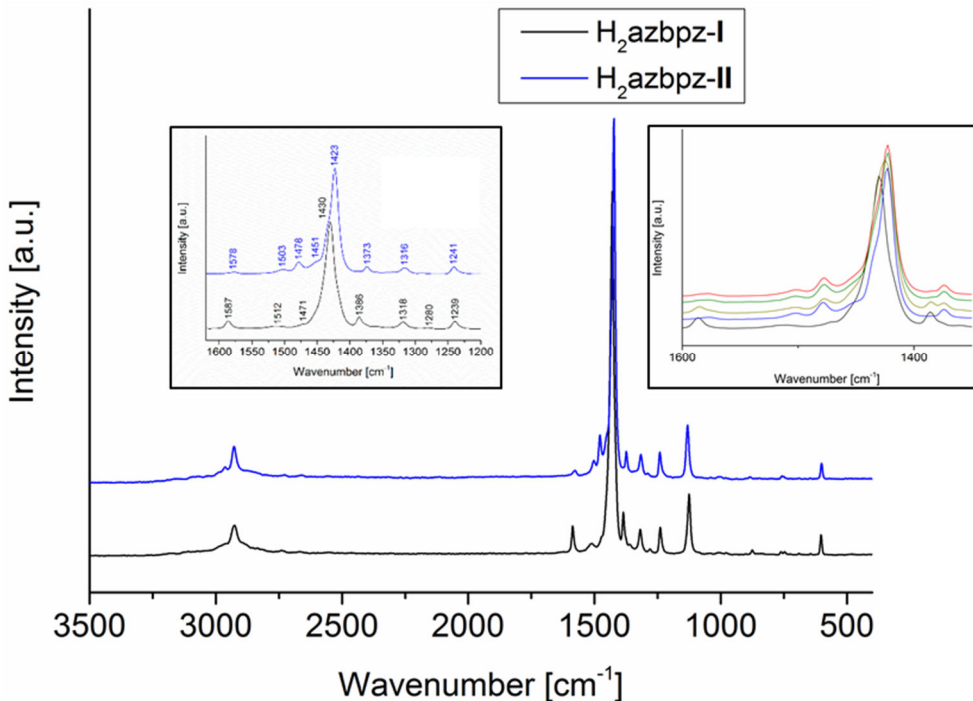


Figure 2. Raman spectra of H₂azbpz-I (black) and H₂azbpz-II (blue) with insets for the expanded region between 1600 cm⁻¹ to 1200 cm⁻¹ (see Figure S24 in SI for a larger image of the spectra of comparison of the ball-milled samples).

Crystal structures of H₂azbpz-I and H₂azbpz-II

Both polymorphs, H₂azbpz-I and H₂azbpz-II, crystallize in the monoclinic centrosymmetric space group P2₁/c with half of the molecule in the asymmetric unit and the midpoint of the azo-function as the center of inversion (see Figure 3a and 3d). The difference between the two polymorphic forms is manifested in different cell parameters (Table S1, SI). The planar H₂azbpz molecules assemble via N–H···N hydrogen bonds into two-dimensional hydrogen-bonded sheets in the bc-plane for H₂azbpz-I and the ab-plane for H₂azbpz-II (Figure 3b and 3e). Details on the hydrogen-bond geometries in H₂azbpz-I and H₂azbpz-II can be found in Table S2, SI.

The high-quality single-crystal XRD experiments allowed to the positions of the (N)-H atoms univocally (for crystallographic and refinement data see Table S1, SI). No signs of disorder were observed in both H₂azbpz-I and H₂azbpz-II. Besides the difference in the molecular conformers, and additional difference in the polymorph structures lies in their 3D packing.

Topologically all pyrazole moieties are equivalent, and when they are taken as three-connected nodes, the topology of the H-bonded sheets corresponds to the **hcb** or honeycomb net (Figure 4). The H-bonding assembly follows the expected pathway, similar

hcb networks are observed in the bispyrazoles H_2bpz , H_2mbpz , $\text{H}_2\text{Me}_4\text{mbpz}$ and H_2bpzb (cf. Chart1 and S27-28, SI).²⁹⁻³³

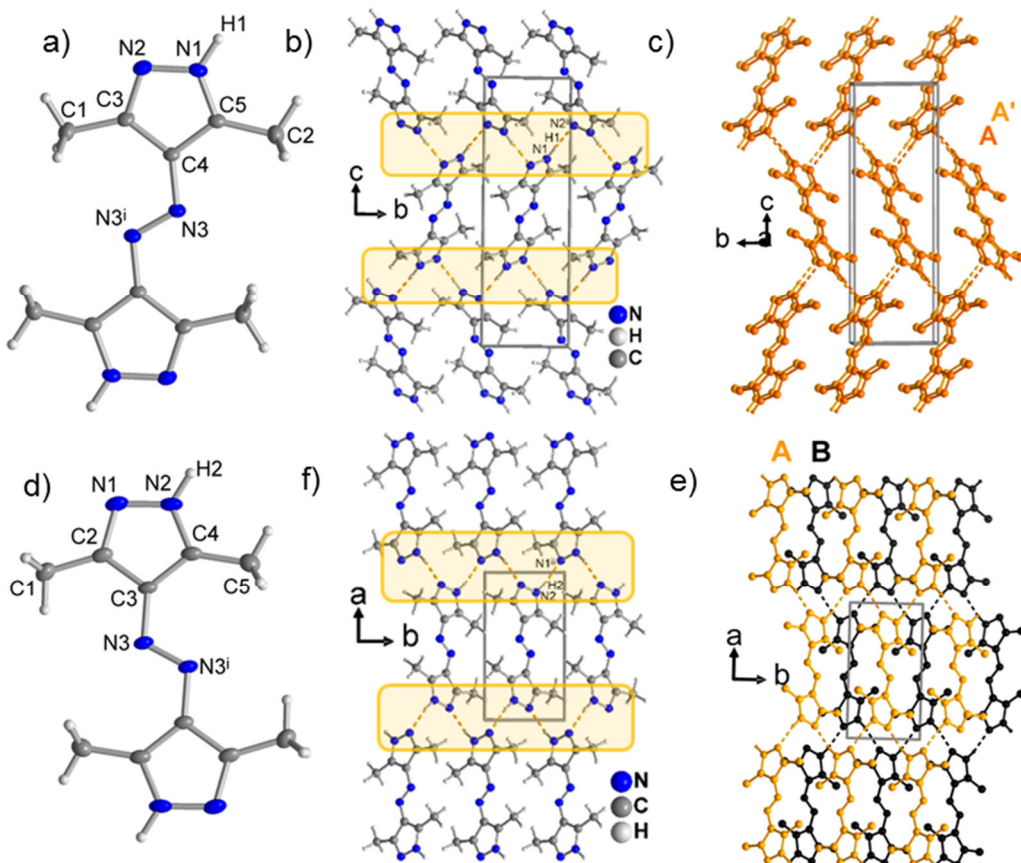


Figure 3. a) Molecular structure of conformer I found in the polymorph $\text{H}_2\text{azbpz-}\text{I}$ (50% thermal ellipsoids, H atoms with arbitrary radii, symmetry transformation: $i = 1-x, 1-y, 1-z$); b) two-dimensional hydrogen-bonded network of $\text{H}_2\text{Azbpz-}\text{I}$ along the bc-plane (catemeric C3 hydrogen-bonds along the b-axis between $\text{N}1\text{-H}1\cdots\text{N}2$ as dashed orange lines); c) AA-packing of the layers along the a-axis with a symmetry relation between the layers A (orange), A' (black) of $[x+1, y, z]$ or $[x-1, y, z]$ (CH_3 H atoms omitted for clarity); d) molecular structure of conformer II found in the polymorph $\text{H}_2\text{azbpz-}\text{II}$ (50% thermal ellipsoids, H atoms with arbitrary radii, symmetry transformation: $i = 1-x, 1-y, 1-z$); e)) two-dimensional hydrogen-bonded network of $\text{H}_2\text{Azbpz-}\text{II}$ along the ab-plane (catemeric C3 hydrogen-bonds along the b-axis between $\text{N}2\text{-H}2\cdots\text{N}1$ as dashed orange lines); f) AB-packing of the layers along the a-axis with a symmetry relation between the layers A (orange), B (black) of $[x, -y+1, 5, z + 0.5]$ or $[x, -y+1, 5, z - 0.5]$.

The **hcb**-sheets in $\text{H}_2\text{azbpz-}\text{I}$ are disposed in a staggered fashion, yielding an AA-type packing, where consequently adjacent layers have translational symmetry relations of $[x+1, y, z]$ or $[x-1, y, z]$ (Figure 3c and Figure 4). In $\text{H}_2\text{azbpz-}\text{II}$ the **hcb** sheets stack in an eclipsed fashion, yielding an AB-type packing with symmetry relations of $[x, -y+1, 5, z + 0.5]$ or $[x, -$

$y+1.5, z - 0.5]$, respectively (Figure 3f and Figure 4). A conformational polymorphism exists (see Figure 4), with the different conformers being related by the pedal-motion of the azo-bond, two-fold C4-N rotation or two-fold N1-N2 proton shift ($4,4'$ -a,a-E I vs $4,4'$ -s,s-E II), as described above (Scheme 1). AB-stacking of the **hcb** sheets, similar to the case of H₂azbpz-II, takes place also in H₂bpz and H₂bpzb (Chart 1, Figure S26 and S27, SI).^{29,33} The polymorphs of hinged H₂Me₄mpz features corrugated **hcb** sheets arranged in an AB-stacking for the α -form and in an AA-stacking for the β -form.³²

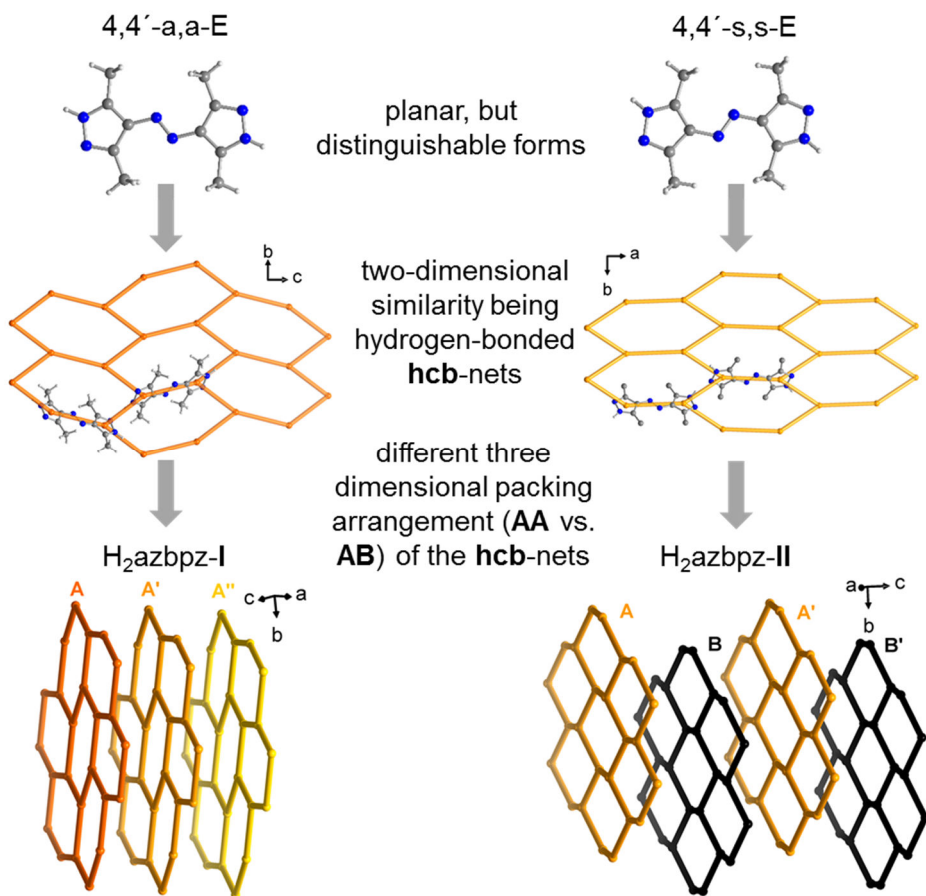


Figure 4. Topological representation of H₂azbpz-I and H₂azbpz-II as two dimensional **hcb** nets with the pyrazole fragments as 3-c nodes. Different packings through eclipsed AA-stacking in H₂azbpz-I and staggered AB-stacking in H₂azbpz-II.

Estimation of the lattice energies with CrystalExplorer

The lattice energies of the polymorphic forms were calculated as with the TONTO quantum chemical module on the B3LYP/6-311G(d,p) level as implemented in CrystalExplorer program.⁴⁷⁻⁵⁰ The different energy contributions, including the full lattice energy, are summarized in Table 1. On the molecular level, the $4,4'$ -a,a-E form I in H₂azbpz-I is energetically more favorable than $4,4'$ -s,s-E form II in H₂azbpz-II by $\Delta E_{\text{conf}}(\text{II}-\text{I}) = 2.0 \text{ kJ mol}^{-1}$

(see Scheme 1 and Figure S15, SI). Despite that, the lattice energy of the H₂azbpz-II polymorph is lower by $\Delta E_{\text{lat}} = -5.4 \text{ kJ mol}^{-1}$ than that of H₂azbpz-I (Table 1 and Figures S18 and S19, SI). While the energy differences are low, they could be interpreted that for the formation of the energetically more favorable H₂azbpz-II the energetically slightly less favorable molecular form II of H₂azbpz should form, which could be the reason, why conventional recrystallizations lead exclusively to H₂azbpz-I.^{9,50}

Table 1. CrystalExplorer lattice energies and its components for H₂azbpz-I and H₂azbpz-II and the estimated relative stability under consideration of the energy difference between forms I and II

	E _{ele}	E _{pol}	E _{dis}	E _{rep}	E _{lat} ¹
	[kJ/mol]				
	-122.9	-28.9	-146.3	176.7	-170.1
	-119.7	-29.1	-151.4	168.3	-176.5
ΔE_{lat}					-5.4
$\Delta E_{\text{conf}} (\text{II} - \text{I})$					2.0
ΔE_{rel}^2					-3.4

¹The total lattice energies E_{lat} were calculated as the sum of scaled electrostatic E_{ele}, polarization E_{pol}, dispersion E_{dis}, and exchange-repulsion E_{rep} terms according to: E_{lat} = 1.057E_{ele} + 0.740E_{pol} + 0.871E_{dis} + 0.618E_{rep}, as outlined in reference⁴⁸.² Estimation of the relative energies via correction of the lattice energies for the conformational energy difference between I and II.

Hirshfeld surface areas of H₂azbpz-I and H₂azbpz-II

The intermolecular NH···N hydrogen bonds, which ensure the connectivity within the **hcb** sheets are the strongest interactions with calculated energies of 35 kJ mol⁻¹ for H₂azbpz-I and H₂azbpz-II (Table S5 and S6, SI). The analysis of Hirshfeld surfaces⁵¹⁻⁵⁵ was carried to shed more light on the packing polymorphism in H₂azbpz-I and H₂azbpz-II; the analysis allows to assess the weaker interactions, controlling also the inter-sheet interactions.

The NH···N hydrogen bonds as the strongest interactions are visible as red spots on the Hirshfeld surfaces (corresponding to the two sharp protrusions marked with orange stars on the fingerprint plots; Figure 5a). The relative contributions of H···H, C···H and N···H contacts to the Hirshfeld surfaces in H₂azbpz-I and H₂azbpz-II differ only slightly (Figure 6). Nevertheless, the difference in crystal packing is clearly visible from the image of the non H-bonded nearest neighbors. In H₂azbpz-I all such molecules are evidently related by a translational symmetry operation, consistent with the AA-packing (Figure 3c and Figure 5d). In H₂azbpz-II two non H-bonded neighbors are translationally (i.e. are disposed parallel), while four others are disposed orthogonal (E_{int} = -20.6 kJ mol⁻¹; see Figure 5d and Figure S18 and Table S6 in SI for interaction energies). This distinction is also manifested by the

contribution and length of different close contacts between neighboring molecules in both forms. The parallel packing in H₂azbpz-I results in complementary close CH···N and CH···C contacts of the CH₃-groups with N_{azo}, N_{pz} or C_{pz} atoms (Figure 5, Figure S6 and Table S3, SI). Contrary, the packing in H₂azbpz-II is mainly governed by CH···N_{pz} contacts, more favorable for mutually perpendicular disposition (Figure 5, Figure S6 and Table S3, SI). The CH···C contacts in this form tend to be longer and mainly present between the less frequent parallel-stacked pairs of molecules (see also Figure S14, SI). The differences in the intermolecular contacts that stabilize the packing in the two structures are evidently reflected by the Hirshfeld surface area/fingerprint plots and the associated interaction energies.

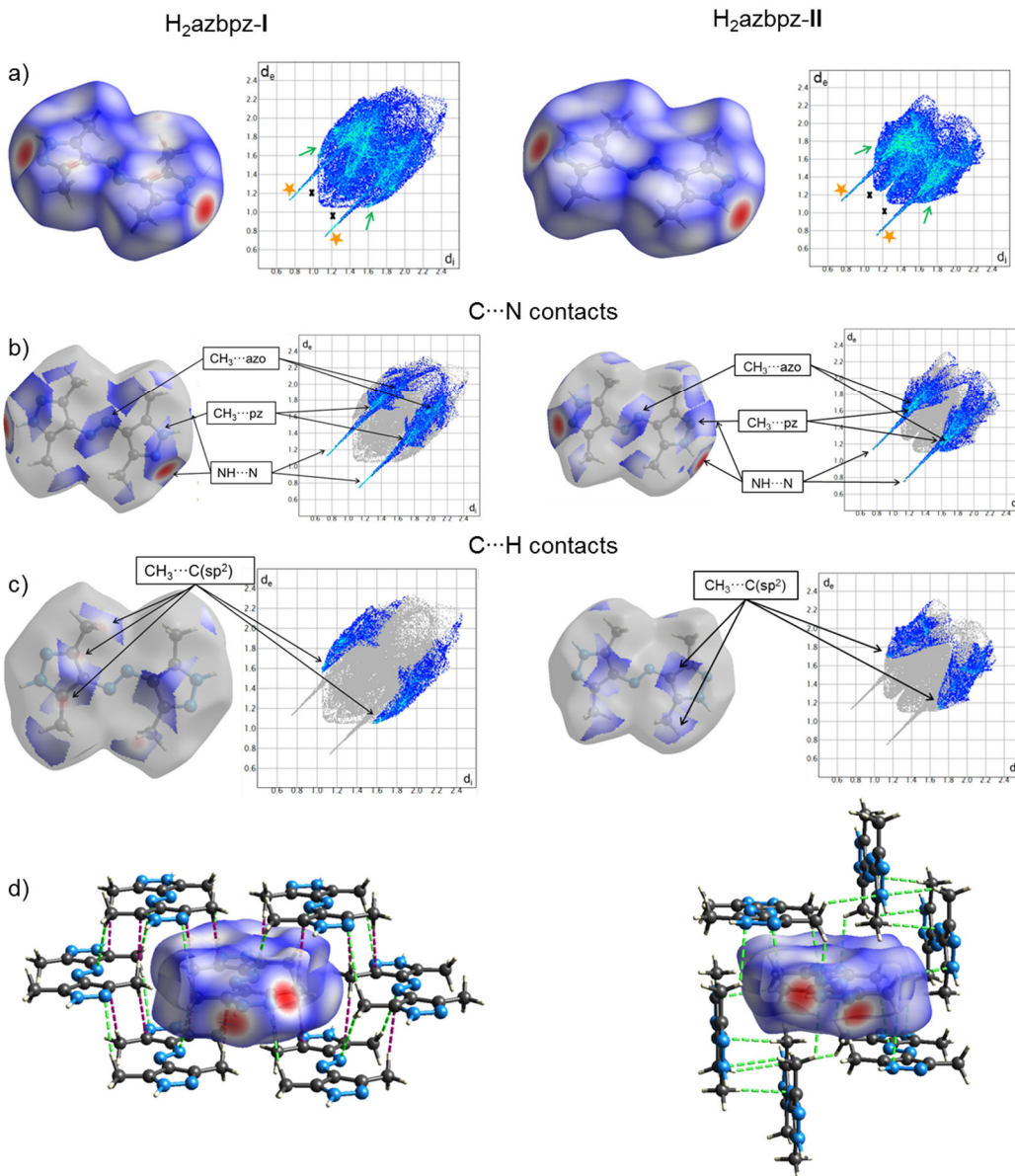


Figure 5. a) Hirshfeld surfaces mapped with the d_{norm} property (red represents the closest contacts, while blue the most distant contacts) and fingerprint plots of H₂azbpz-I (left) and H₂azbpz-II (right) with

the closest N···H-contacts (orange stars), C···H-contacts (green arrows); H···H-contacts (black crosses); b) comparison of the different contributions of C···N contacts in H₂azbpz-I (left) and H₂azbpz-II (right) c) comparison of the different contributions of C···H contacts in H₂azbpz-I (left) and H₂azbpz-II (right); d) visualization of the contribution of close contacts (CH···N-contacts as dashed-green lines with a cut-off length of 3.0 Å; CH···C-contacts as dashed violet lines with cut-off 2.8 Å) of neighboring non-hydrogen-bonded molecules in H₂azbpz-I (left) and H₂azbpz-II (right). See Figures S7-S14 in SI for visualization of the relative contribution of the different contacts to the Hirshfeld surface area.

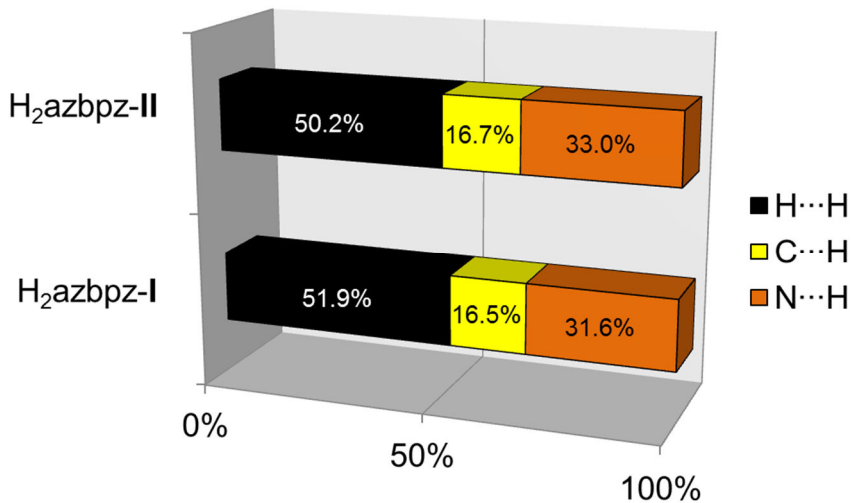


Figure 6. Relative contributions of H···H (black), C···H (yellow) and N···H (orange) contacts to the crystal packing in H₂azbpz-I and H₂azbpz-II derived from the Hirshfeld surface area fingerprint plots.

The DSC experiments in the range of 25 °C–240 °C do not show any phase transition for H₂azbpz-I upon heating and cooling. H₂azbpz-II shows an endothermic process starting at 165 °C ($\Delta H = -3.4$ kJ/mol) but no phase transition upon subsequent cooling (see Figure S22, SI). The endothermic process can be attributed to the irreversible transition of H₂azbpz-II into H₂azbpz-I and was confirmed by PXRD (Figure S20, SI). The endothermic solid-state transformation of Polymorph H₂azbpz-II into H₂azbpz-I and the blue shift of the vibrations in the Raman spectra are suggestive of an enantiotropic relation considering the Burger and Ramberger rules with H₂azbpz-II being the more stable polymorph at lower temperatures.⁵⁶⁻⁵⁸ The kinetic irreversibility of the enantiotropic transition reveals that H₂azbpz-I as the more stable polymorph at higher temperatures is obtainable below the transition temperature.⁵⁹ PXRD and Raman analysis of a sample of H₂azbpz-II heated at 180 °C showed complete conversion whereas a sample heated at 100 °C overnight did not change (see Figures S20, S23 and S24, SI). This further explains the observation that both polymorphs can be stored at room temperature without a noticeable transformation. The only evident explanation, why the metastable H₂azbpz-I forms during standard crystallization from solutions, is that it

contains the lower energy 4,4'-a,a-E conformer of the H₂azbpz molecule compared to 4,4'-s,s-E conformer H₂azbpz-II, as was discussed above.

Crystal structure of the hemihydrate H₂azbpz·0.5H₂O

Recrystallization of H₂azbpz after the synthesis from an ethanol/water solution yielded a microcrystalline powder indicating a composition of H₂azbpz·0.5H₂O by elemental analysis. Large column shaped crystals could be obtained from solution of aqueous ammonia in diluted ethanol. The hemihydrate H₂azbpz·0.5H₂O crystallizes in the monoclinic space group C2/c. The asymmetric unit contains two halves of H₂azbpz molecules denoted with A and B, both sitting on different inversion centers, and one semi-occupied water molecule residing on the general position (Figure 7). The hydrogen positions of the water molecule and the pyrazole groups are found disordered over two positions with each hydrogen atom being refined with equal half occupancy. Thus, the water oxygen atom has two covalently bonded hydrogen atoms acting as hydrogen bond donors to the pyridinic nitrogen atoms of pyrazole and accepts two hydrogen bonds from two pyrrolic N-H functions. Because of half-occupancy there is one hydrogen atom in each N--H···H-O-contact.^{60,61} The same holds for the N-H···H-N-contacts in the structure of the hemihydrate. Details on the hydrogen-bonds in H₂azbpz·0.5H₂O can be found in Table S3, SI. Phase purity of the hemihydrate H₂azbpz·0.5H₂O was established via matching the simulated powder pattern from the single crystal data (Figure S24, SI).

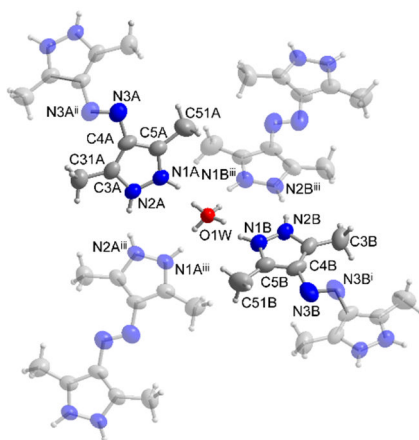


Figure 7. Expanded asymmetric unit of H₂azbpz·0.5H₂O at 298 K (50% thermal ellipsoids, hydrogen atoms with arbitrary radii) Symmetry transformation: i = 1.5-x, 1.5-y, 2-z ii = -x, 1-y, -z; iii = 1-x, y, 0.5-z.

Two pyrazole groups and the water molecule form a hydrogen-bonded R₃³(8) ring motif according to the Etter notation (Fig. 8a).⁶² Two R₃³(8) { (H₂O)_{0.5}(pz)₂ }-ring motifs are joined to

form a $\{\text{H}_2\text{O}(\text{pz})_4\}$ tetrahedral subunit as the building block of a uninodal **dia**-net in which the tetrahedral $\{\text{H}_2\text{O}(\text{pz})_4\}$ subunits (Fig. 8b) or the tetrahedral water molecules (Fig. 8c) are linked by the azo-functions. Due to the large open windows in a single **dia**- $\text{H}_2\text{azbpz}\cdot 0.5\text{H}_2\text{O}$ - net, fivefold interpenetration of Class Ia, where the nets are only related by translation, affords efficient crystal packing (Figure 8d).⁶³⁻⁶⁶

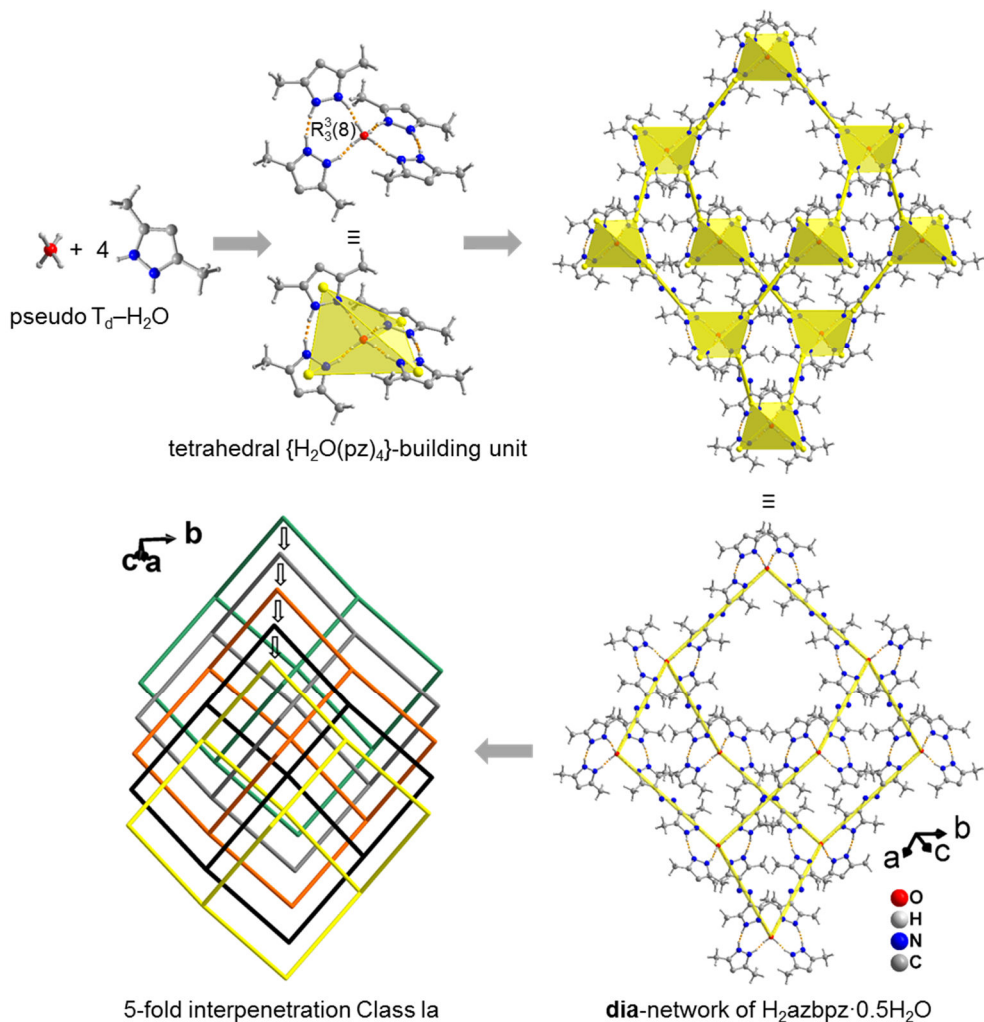


Figure 8. Topological analysis of $\text{H}_2\text{azbpz}\cdot 0.5\text{H}_2\text{O}$ with ToposPro.⁶⁶ (a) Two $\text{R}_3^3(8)$ -hydrogen bonded motifs form the tetrahedral $\{\text{H}_2\text{O}(\text{pz})_4\}$ -subunit of the underlying **dia**-net (b). (c) Topological representation of $\text{H}_2\text{azbpz}\cdot 0.5\text{H}_2\text{O}$ as a **dia**-network with the tetrahedrally-shaped $\{\text{H}_2\text{O}(\text{pz})_4\}$ -subunit or the $\text{T}_d\text{-H}_2\text{O}$ molecules as its nodes. (d) Efficient crystal packing via five-fold interpenetration of Class Ia.

Solid state NMR analysis of H2azbpz-I, H2azbpz-II and H2azbpz·0.5H2O

The two polymorphs H2azbpz-I and -II show almost the same ^1H response with two broad signals at 1.4 and 13.2 ppm with relative peak area ratio of 6:1 which correspond to the two methyl and -NH groups, respectively. Therefore it is not possible to distinguish the two

different polymorphs H₂azbpz-I, H₂azbpz-II from one another by ¹H solid-state NMR. The ¹H spin-echo solid-state NMR spectra of H₂azbpz·0.5H₂O obtained under magic-angle spinning (MAS) conditions give evidence of five resonances (Figure 14). For the hemihydrate form, H₂azbpz·0.5H₂O, more peaks can be resolved including a peak assigned to H₂O, with peak area ratios of 1.05:0.99:0.99:11.96 for NH:NH':OH:CH₃, respectively. The peak area ratios agree with compositions estimated from the crystal structure within error limits.

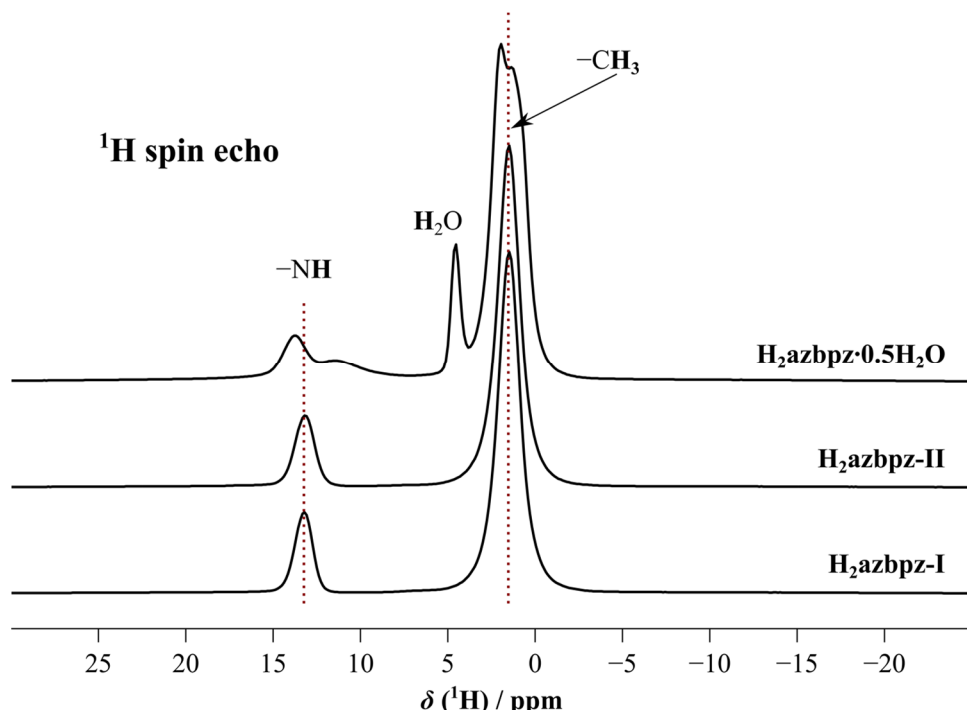


Figure 14. ¹H rotor-synchronized spin echo solid-state NMR spectra for H₂azbpz-I, H₂azbpz-II and H₂azbpz·0.5H₂O at 50 kHz MAS frequency.

However, ¹³C{¹H} cross-polarization (CP) MAS NMR provides unique spectra for H₂azbpz-I, H₂azbpz-II and H₂azbpz·0.5H₂O (Figure 15). The ¹³C resonances in H₂azbpz-I and H₂azbpz-II can be assigned to CH₃ and the C sites of the aromatic ring atoms on the basis of the chemical shift unambiguously. For the crystal structures of the fully ordered structures H₂azbpz-I and H₂azbpz-II every carbon site leads to one resolvable ¹³C NMR resonance. The hemihydrate H₂azbpz·0.5H₂O cannot be understood as a superposition of the other two polymorphs but shows a unique ¹³C NMR spectrum. Moreover the peaks of H₂azbpz·0.5H₂O are broader than the peaks of H₂azbpz-I, H₂azbpz-II which reflects the disorder in the crystal structure of the hemihydrate.

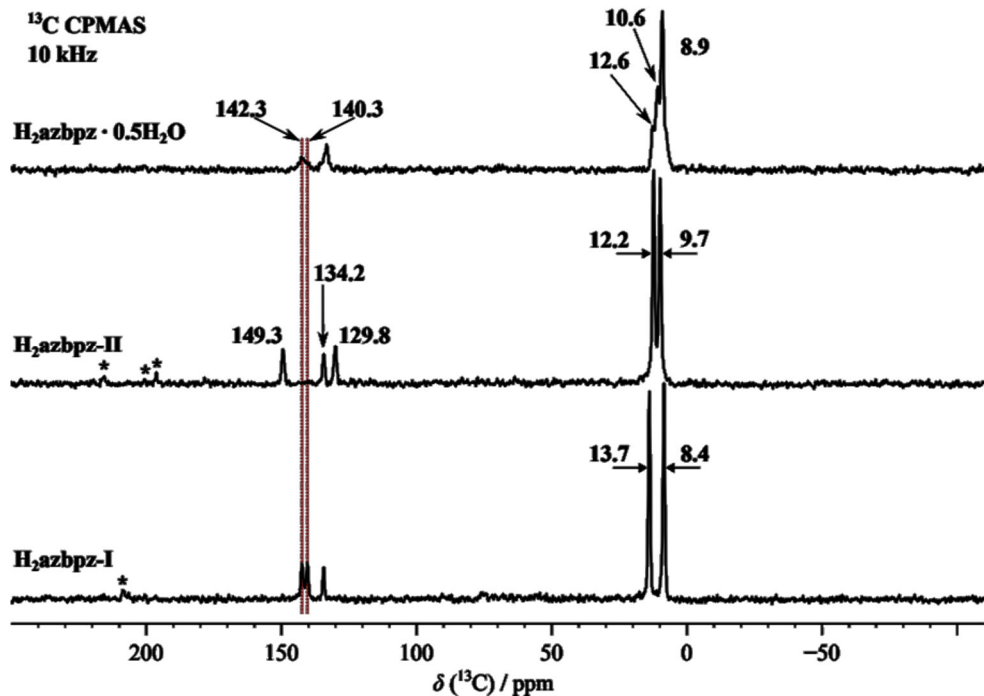


Figure 11. $^{13}\text{C}\{^1\text{H}\}$ CP MAS NMR spectra for $\text{H}_2\text{azbpz-}\text{I}$, $\text{H}_2\text{azbpz-}\text{II}$ and $\text{H}_2\text{azbpz}\cdot 0.5\text{H}_2\text{O}$ at 10 kHz MAS frequency with a contact time of 1 ms. The spectrum of the hemihydrate shows peak area ratios of 5:2:1 for the CH_3 methyl groups.

Furthermore an exchange process was observed for the H atoms bridging the two N atoms of the two pyrazole rings in the $\text{R}_3^3(8)$ -hydrogen motifs in sites A and B of the hemihydrate $\text{H}_2\text{azbpz}\cdot 0.5\text{H}_2\text{O}$ (see for example Figure 7) via ^1H exchange spectroscopy (EXSY NMR) which reached an equilibrium after multiple milliseconds of mixing time. The kinetic rate constant k for the process $\text{N}-\text{H}\cdots\text{N}' \rightarrow \text{N}\cdots\text{H}-\text{N}$ was estimated to be $342 \pm 34 \text{ s}^{-1}$ (Figures S25-26, SI).

Conclusion

Two polymorphs of 4,4'-azobis(3,5-dimethyl-1H-pyrazole) (H_2azbpz) were serendipitously isolated as a case of conformational polymorphism based on two H_2azbpz conformers. The conformers differ in the relative orientation of the NH atoms with respect to the central azo bond. The identity and phase purity of the standard polymorph $\text{H}_2\text{azbpz-}\text{I}$ and the hard-to-obtain polymorph $\text{H}_2\text{azbpz-}\text{II}$ were unequivocally established by X-ray diffraction, Raman spectroscopy and $^{13}\text{C}\{^1\text{H}\}$ CP MAS NMR. Polymorph $\text{H}_2\text{azbpz-}\text{II}$ could initially be reliably synthesized only by mechanochemically transformation, before also a crystallization route from supersaturated DMF at 2 °C was found. Noteworthy, from lattice energy and gas-phase conformer calculations, polymorph $\text{H}_2\text{azbpz-}\text{II}$, is likely the thermodynamic more stable form at lower temperatures but contains the higher energy conformer form **II**.

Both polymorphs of H₂azbpz feature supramolecular honeycomb sheets (**hcb** topology). In H₂azbpz-**I** the sheets show a staggered AA'-packing whereas in H₂azbpz-**II** the sheets stack in an eclipsed AB-fashion.

From an ethanol/water solution the hemihydrate H₂azbpz·0.5H₂O crystallizes, based on tetrahedral {H₂O(pz)₄}⁻-subunits with a pseudo T_d-water molecules. Its network structure with the **dia**-topology can be regarded as a supramolecular analog of the cubic ice polymorph I_c, introduced by T_d-water molecules.

We envision that the polymorph structures stimulate the research on solid-state structures with polypyrazoles as tectons especially for the possible synergy of an azo-pedaling with solid-state proton transfer. Studies are underway to obtain such H-bonded solid networks, preferably crystallizing in non-centrosymmetric space groups, by co-crystallizing H₂azbpz with acids.

Experimental Section

All chemicals were obtained from commercial sources and used without further purification. CHN analysis was performed with a Perkin–Elmer CHN 2400 (Perkin–Elmer, Waltham, MA, USA). IR spectra were recorded with a Bruker Tensor 37 IR spectrometer (Bruker Optics, Ettlingen, Germany) with ATR unit (Platinum ATR-QL, diamond crystal) in the range of 4000–550 cm⁻¹. Raman spectra were obtained on a Bruker MultiRAM-FT Raman spectrometer equipped with a Nd:YAG-laser (wavelength 1064 nm). All Raman spectra were measured in solid state for 2500 scans with a laser power between 10-20 mW. Solution ¹H and ¹³C spectra were measured with a Bruker Avance DRX-300. ESI-MS spectra were recorded with a Thermo Quest Ion Trap API mass spectrometer Finnigan LCQ Deca. Thermogravimetric analysis (TGA) was done with a Netzsch TG 209 F3 Tarsus (Netzsch, Selb, Germany) in the range from 25 to 1000 °C, equipped with an Al₂O₃-crucible and applying a heating rate of 5 K·min⁻¹ under a nitrogen atmosphere. The powder X-ray diffraction pattern (PXRD) was obtained with a Bruker D2 Phaser powder diffractometer with a flat silicon, low background sample holder, at 30 kV, 10 mA for Cu-K_α radiation ($\lambda = 1.5418 \text{ \AA}$). Differential scanning calorimetry (DSC) was measured using a Mettler Toledo DSC 3 with a temperature gradient of 5 K/min in the temperature range of 25 °C to 250 °C. Ball milling experiments were performed at room temperature in a Mixer Mill MM301 (Retsch GmbH & Co., Haan, Germany) using 25 ml stainless steel milling jars equipped with a 20 mm diameter stainless steel grinding ball.

Single crystal X-ray diffraction structure determination. Suitable crystals were carefully selected under a polarizing microscope, covered in protective oil and mounted on a 0.05 mm

cryo loop. Data collection: Bruker Kappa APEX2 CCD X-ray diffractometer (Bruker AXS, Ettlingen, Germany) with microfocus tube, Mo- K_{α} radiation ($\lambda = 0.71073 \text{ \AA}$), multi-layer mirror system, ω -scans; data collection with APEX2,⁶⁷ cell refinement with SMART and data reduction with SAINT,⁶⁷ experimental absorption correction with SADABS.⁶⁸ Structure analysis and refinement: The structure was solved by direct methods using SHELXL2018,⁶⁹ refinement was done by full-matrix least-squares on F^2 using the SHELX-2014 program suite. Crystal data and details on the structure refinement are given in Table S1. Graphics were drawn with Diamond.⁷⁰ For the two polymorphs H₂azbpz-I and H₂azbpz-II the protic H atoms for the NH were found and refined free with $U_{\text{iso}}(\text{H}) = 1.2U_{\text{eq}}$ and H atoms of the methyl groups were positioned geometrically (C–H = 0.98 Å) and refined using the riding model AFIX 137 with $U_{\text{iso}}(\text{H}) = 1.5U_{\text{eq}}$. For the hemihydrate H₂azbpz·0.5H₂O the protic hydrogen atoms for H₂O were found and refined freely with $U_{\text{iso}}(\text{H}) = 1.5U_{\text{eq}}$. The protic hydrogen atoms for NH were positioned geometrically (N–H = 0.086 Å) and refined using a riding model AFIX 43 with $U_{\text{iso}}(\text{H}) = 1.2U_{\text{eq}}$, H atoms for the methyl groups were positioned geometrically (C–H = 0.98 Å) and refined using a riding model (AFIX 137) with $U_{\text{iso}}(\text{H}) = 1.5U_{\text{eq}}$. For the low temperature measurement at 100 K the same crystal as for the room temperature measurement was slowly cooled with 1 K/min.

Crystallographic data (including structure factors) for the structure in this paper have been deposited with the Cambridge Crystallographic Data Centre, CCDC, 12 Union Road, Cambridge CB21EZ, UK. Copies of the data can be obtained free of charge on quoting the depository numbers CCDC-1980181-1980184 (Fax: +44-1223-336-033; E-Mail: deposit@ccdc.cam.ac.uk, <http://www.ccdc.cam.ac.uk>).

Solid-State NMR. Quantitative ¹H MAS spectra were recorded at 600.2 MHz (14.1 T) on a Bruker Avance Neo NMR spectrometer equipped with a commercial 1.3 mm MAS probe head. A series of rotor synchronized Hahn echo spectra were recorded for quantification⁷¹ at 50 kHz in zirconia rotors with varying τ delays (20, 40, 60, 80 and 100 μ s) between a 90° pulse of 2.5 μ s and 180° pulse of 5 μ s. The ¹H resonance of 1% TMS in CDCl₃ at 0 ppm served as an external reference.^{72,73} For each spectrum, 128 scans were acquired at 0.027 s acquisition time and a repetition delay of 64 s. Spectra deconvolution was done on deconv2Dxy⁷⁴ for NMR relative quantification of ¹H signals by back-extrapolation of a spin-echo experiment.⁷¹ 2D deconvoluted T_1 data were fitted using the Gnuplot package to determine ¹H T_1 relaxation times of the different ¹H signals. The ¹H EXSY experiment was measured on the 1.3 mm MAS probe head at 50 kHz and the Gnuplot package was used to fit the experimental data points from EXSY experiments to determine the exchange rate constant. ¹³C{¹H} CP MAS spectra were obtained at 10 kHz MAS rate using a ramped cross

polarization at a Larmor frequency of 150.9 MHz, a sample spinning frequency of 10 kHz and a contact time of 1 ms.⁷⁵

Crystallization of H₂azbpz-I. Single crystals were obtained from a solution of 33 mg (0.15 mmol) of microcrystalline H₂azbpz-I dissolved in 20 mL of absolute ethanol (~8 mmol/L), filtered through a Pasteur pipette with glass-wool plug to a small tube. The tube was placed in a ventilated thermostated chamber (25 °C), and rectangular platelet crystals (see Figure S34, SI) were harvested after 5-7 days of slow evaporation. Larger crystal amounts of H₂azbpz-I were obtained by upscaling the crystallization experiment by a factor of 15.

EA [%] calc. for: H₂Azbpz C₁₀H₁₅N₆ C 55.03, H 6.47, N 38.50 found: C 54.94, H 6.51 N 38.48. IR [ATR, cm⁻¹]: 3445m, 3179s, 3111s, 3044s, 2974s, 2927s, 2882s, 2832s, 2585w, 1652w, 1584m, 1498s, 1441s, 1414s, 1378m, 1321m, 1255m, 1121w, 1055w, 1010w, 972w, 838w, 781w, 761w, 722w, 567w, 448w. Raman [cm⁻¹]: 2927m, 1587m, 1512w, 1471m, 1430vs, 1386m, 1318m, 1239m, 1126m, 603w

Crystallization of H₂azbpz-II. Single crystals of H₂azbpz-II were grown from ~20 mg (0.09 mmol) of the H₂azbpz-ballmill(180min) sample (i.e. after 180 min of ball-milling), carefully dissolved in 1 mL of DMF using a sonication bath. The yellow solution was filtered through a Pasteur pipette with a glass wool plug. The solution was directly placed into a refrigerator at 2 °C. First small yellow needles of H₂azbpz-II appeared overnight (checked via PXRD) and small crystals suitable for SCXRD can be harvested after 2 days (see Figure S34, SI).

The procedure was successfully scaled up for the preparation of polycrystalline H₂azbpz-II. 506 mg (2.3 mmol) of H₂azbpz-ballmill(180min) was suspended in 5 mL of DMF under cooling with an ice bath at 0-2 °C and stirred slowly for 18 h. Afterwards, the pure H₂azbpz-II was collected as a yellow microcrystalline powder by suction filtration, washed with a minimal amount of chloroform and dried in air (376 mg, 1.7 mmol, 74%).

EA [%] calc. for: H₂Azbpz C₁₀H₁₅N₆ C 55.03, H 6.47, N 38.50 found: C 54.97, H 6.36 N 38.62. IR [ATR, cm⁻¹]: 3155m, 3077s, 3025s, 2921s, 2830s, 2790s, 1571w, 1497m, 1477m, 1435s, 1418s, 1317 w, 1258w, 1125w, 1056m, 1038w, 1009w, 973w, 841m, 779m, 769m, 722m, 680w, 568m. Raman [cm⁻¹]: 2927m, 1578w, 1503m, 1478m, 1451m, 1423vs, 1373m, 1316m, 1241m, 1131m, 601w.

Ball mill experiments for H₂azbpz-II. Between 100-150 mg of microcrystalline H₂azbpz-I as starting material was milled at 20 Hz for the specified time (up to 180 min). The milling was stopped for 20 min after every 30 min of milling to prevent overheating of the samples. The

data below are given for a sample after 180 min of milling, which corresponds to a conversion of H₂azbpz-**I** to H₂azbpz-**II**.

EA [%] calc. for: H₂Azbpz C₁₀H₁₅N₆ C 55.03, H 6.47, N 38.50 found: C 54.89, H 6.24 N 38.20. IR [ATR, cm⁻¹]: 3442m, 3172s, 3086s, 3029s, 2966s, 2925s, 2870s, 2832s, 2572w, 1648w, 1581m, 1499s, 1479s, 1416s, 1318m 1255m, 1122w, 1055m, 1009w, 1056m, 1009w, 973w, 840m, 780m, 721w, 557m, 448w. Raman [cm⁻¹]: 2927m, 1576w, 1502m, 1477m, 1423vs, 1374m, 1317m, 1239m, 1131m, 601w.

Crystallization of H₂azbpz·0.5H₂O. For the synthesis of large single crystals 56 mg of H₂azbpz-**I** were dissolved in 40 mL of EtOH under stirring in a crystallizing dish. Afterwards 8 ml 25% NH₃(aq) were added. The solution stood undisturbed for 4 days and large column like crystals appeared (see Figure S34, SI). Bulk material of H₂azbpz·0.5H₂O was obtained by dissolving 495 mg in 40 mL of EtOH and 10 mL of de-ionized water and concentration of the solution under reduced pressure. Afterwards the crystals were collected by suction filtration and shortly dried in air.

EA [%] calc. for: H₂azbpz·0.5H₂O C₁₀H₁₆N₆O C 52.87, H 6.66, 37.00 found: C 52.99, H 6.78, N 37.09. IR [ATR, cm⁻¹]: 3208s, 3125s, 3047s, 2977s, 2920s, 2897s, 2361w, 2151w, 1648m, 1594m, 1505s, 1419s, 1369m, 1318m, 1259m, 1131m, 1082w, 1052m, 1005m, 974m, 879m, 824m, 780m, 757m, 722m, 661w, 629w, 555m, 478w. Raman [cm⁻¹]: 2923m, 1592m, 1515m, 1774m, 1434vs, 1378m, 1324m, 1241m, 1141m, 603w.

References

- (1) Bernstein, J., Polymorphism – A Perspective. *Cryst. Growth Des.* **2011**, *11*, 632-650.
- (2) Brog, J.-P.; Chanez, C.-L.; Crochet, A.; Fromm, K. M., Polymorphism, what it is and how to Identify it: a Systematic Review. *RSC Adv.* **2013**, *3*, 16905-16931.
- (3) Aakeroy, C. B.; Champness, N. R.; Janiak, C., Recent Advances in Crystal Engineering. *CrystEngComm* **2010**, *12*, 22-43.
- (4) Braga, D.; Grepioni, F.; Maini, L., The Growing World of Crystal Forms. *Chem. Commun.* **2010**, *46*, 6232-6242.
- (5) Nangia, A. K.; Desiraju, G. R., Crystal Engineering: An Outlook for the Future. *Angew. Chem. Int. Ed.* **2019**, *58*, 4100-4107.
- (6) Cruz-Cabeza, A. J.; Reutzel-Edens, S. M.; Bernstein, J., Facts and Fictions about Polymorphism. *Chem. Soc. Rev.* **2015**, *44*, 8619-8635.
- (7) Munshi, P.; Guru Row, T. N., Topological Analysis of Charge Density Distribution in Concomitant Polymorphs of 3-Acetylcoumarin, A Case of Packing Polymorphism. *Cryst. Growth Des.* **2006**, *6*, 708-718.
- (8) Surov, A. O.; Manin, A. N.; Voronin, A. P.; Churakov, A. V.; Perlovich, G. L.; Vener, M. V., Weak Interactions Cause Packing Polymorphism in Pharmaceutical Two-Component Crystals. The Case Study of the Salicylamide Cocrystal. *Cryst. Growth Des.* **2017**, *17*, 1425-1437.
- (9) Nangia, A., Conformational Polymorphism in Organic Crystals. *Acc. Chem. Res.* **2008**, *41*, 595-604.
- (10) Cruz-Cabeza, A. J.; Bernstein, J., Conformational Polymorphism. *Chem. Rev.* **2014**, *114*, 2170-2191.
- (11) Foces-Foces, C.; Alkorta, I.; Elguero, J., Supramolecular Structure of 1H-Pyrazoles in the Solid State: a Crystallographic and Ab Initio Study. *Acta Crystallogr., Sect. B* **2000**, *56*, 1018-1028.
- (12) Ivasenko, O.; Perepichka, D. F., Mastering Fundamentals of Supramolecular Design with Carboxylic Acids. Common Lessons from X-ray Crystallography and Scanning Tunneling Microscopy. *Chem. Soc. Rev.* **2011**, *40*, 191-206.
- (13) Basu, T.; Sparkes, H. A.; Mondal, R., Construction of Extended Molecular Networks with Heterosynthons in Cocrystals of Pyrazole and Acids. *Cryst. Growth Des.* **2009**, *9*, 5164-5175.

- (14) Aakeröy, C. B.; Hurley, E. P.; Desper, J., Modulating Supramolecular Reactivity Using Covalent “Switches” on a Pyrazole Platform. *Cryst. Growth Des.* **2012**, *12*, 5806-5814.
- (15) Hashim, M. I.; Le, H. T. M.; Chen, T. H.; Chen, Y. S.; Daugulis, O.; Hsu, C. W.; Jacobson, A. J.; Kaveevivitchai, W.; Liang, X.; Makarenko, T.; Miljanic, O. S.; Popovs, I.; Tran, H. V.; Wang, X.; Wu, C. H.; Wu, J. I., Dissecting Porosity in Molecular Crystals: Influence of Geometry, Hydrogen Bonding, and [pi...pi] Stacking on the Solid-State Packing of Fluorinated Aromatics. *J. Am. Chem. Soc.* **2018**, *140*, 6014-6026.
- (16) Marín-Luna, M.; Claramunt, R. M.; Nieto, C. I.; Alkorta, I.; Elguero, J.; Reviriego, F., A Theoretical NMR Study of Polymorphism in Crystal Structures of Azoles and benzazoles. *Magn. Reson. Chem.* **2019**, *57*, 275-284.
- (17) Sikora, M.; Katrusiak, A., Pressure-Controlled Neutral–Ionic Transition and Disordering of NH···N Hydrogen Bonds in Pyrazole. *J. Phys. Chem. C* **2013**, *117*, 10661-10668.
- (18) Kaftory, M.; Botoshansky, M.; Sheinin, Y., Dimormorphism and Cocrystal Formation of 3-(Chloroacetamido)pyrazole. *Cryst. Growth Des.* **2005**, *5*, 2242-2247.
- (19) Catala, L.; Wurst, K.; Amabilino, D. B.; Veciana, J., Polymorphs of a Pyrazole Nitronyl Nitroxide and its complexes with Metal(ii) Hexafluoroacetylacetones. *J. Mater. Chem.* **2006**, *16*, 2736-2745.
- (20) García, M. Á.; Cabildo, P.; Claramunt, R. M.; Pinilla, E.; Rosario Torres, M.; Alkorta, I.; Elguero, J., The Interplay of Hydrogen Bonds and Halogen Bonds in the Structure of NH-Pyrazoles bearing C-aryl and C-halogen Substituents. *Inorg. Chim. Acta* **2010**, *363*, 1332-1342.
- (21) Foces-Foces, C.; Llamas-Saiz, A. L.; Claramunt, R. M.; Lopez, C.; Elguero, J., Structure of 3(5)-Methyl-4-nitropyrazole in the Solid State: Tautomerism, Crystallography and the Problem of Desmotropy. *Journal of the Chemical Society, Chem. Commun.* **1994**, 1143-1145.
- (22) Angeles García, M.; López, C.; Claramunt, R. M.; Kenz, A.; Pierrot, M.; Elguero, J., Polymorphism vs. Desmotropy: The Cases of 3-Phenyl- and 5-Phenyl-1H-pyrazoles and 3-Phenyl-1H-indazole. *Helv. Chim. Acta* **2002**, *85*, 2763-2776.
- (23) Elguero, J., Polymorphism and Desmotropy in Heterocyclic Crystal Structures. *Cryst. Growth Des.* **2011**, *11*, 4731-4738.

- (24) Desiraju, G. R., Polymorphism: The Same and Not Quite the Same. *Cryst. Growth Des.* **2008**, *8*, 3-5.
- (25) Harada, J.; Ogawa, K., Pedal Motion in Crystals. *Chem. Soc Rev.* **2009**, *38*, 2244-2252.
- (26) McGeorge, G.; Harris, R. K.; Batsanov, A. S.; Churakov, A. V.; Chippendale, A. M.; Bullock, J. F.; Gan, Z., Analysis of a Solid-State Conformational Rearrangement Using ^{15}N NMR and X-ray Crystallography. *J. Phys. Chem. A* **1998**, *102*, 3505-3513.
- (27) Klein, O.; Aguilar-Parrilla, F.; Lopez, J. M.; Jagerovic, N.; Elguero, J.; Limbach, H.-H., Dynamic NMR Study of the Mechanisms of Double, Triple, and Quadruple Proton and Deuteron Transfer in Cyclic Hydrogen Bonded Solids of Pyrazole Derivatives. *J. Am. Chem. Soc.* **2004**, *126*, 11718-11732.
- (28) Claramunt, R. M.; Santa María, M. D.; Forfar, I.; Aguilar-Parrilla, F.; Minguet-Bonvehí, M.; Klein, O.; Limbach, H.-H.; Foces-Foces, C.; Llamas-Saiz, A. L.; Elguero, J., Molecular Structure and Dynamics of C-1-Adamantyl substituted N-unsubstituted Pyrazoles studied by Solid State NMR Spectroscopy and X-Ray Crystallography. *Journal of the Chemical Society, Perkin Trans. 2* **1997**, 1867-1876.
- (29) Boldog, I.; Rusanov, E. B.; Chernega, A. N.; Sieler, J.; Domasevitch, K. V., Acentric Extended Solids by Self Assembly of 4,4'-Bipyrazolyls. *Angew. Chem. Int. Ed.* **2001**, *40*, 3435-3438.
- (30) Boldog, I.; Rusanov, E. B.; Sieler, J.; Blaurock, S.; Domasevitch, K. V., Construction of Extended Networks with a Trimeric Pyrazole Synthon. *Chem. Commun.* **2003**, 740-741.
- (31) Monge, M. A.; Puebla, E. G.; Elguero, J.; Toiron, C.; Meutermans, W.; Sobrados, I., An X-ray and ^{13}C CP/MAS NMR Study of C,C-linked Bipyrazoles and Bispyrazolylmethanes. *Spectrochim. Acta A* **1994**, *50*, 727-734.
- (32) Basu, T.; Mondal, R., Construction of first Anion-assisted Helix inside a Helix Network. *CrystEngComm* **2010**, *12*, 366-369.
- (33) Maspero, A.; Galli, S.; Masciocchi, N.; Palmisano, G., Facile Preparation of Polytopic Azoles: Synthesis, Characterization, and X-ray Powder Diffraction Studies of 1,4-Bis(pyrazol-4-yl)- and 1,4-Bis(tetrazol-5-yl)benzene. *Chem. Lett.* **2008**, *37*, 956-957.
- (34) Klyne, W.; Prelog, V., Description of Steric Relationships across Single Bonds. *Experientia* **1960**, *16*, 521-523.

- (35) Millan, S.; Makhlofi, G.; Janiak, C., Metal-4,4'-azobis(3,5-dimethyl-1H-pyrazole) Complexes with Seven- and Nine-membered Hydrogen-bonded Rings Originating from the Pyrrolic NH Function. *Z. Anorg. Allg. Chem.* **2019**, *645*, 893-899.
- (36) Hüttel, R.; Büchele, F.; Jochum, P., Über Nitro-, Nitroso- und Azopyrazole. *Chem. Ber.* **1955**, *88*, 1577-1585.
- (37) Millan, S.; Gil-Hernández, B.; Hastürk, E.; Schmitz, A.; Janiak, C., A 2D Zinc Coordination Polymer Built from the Mono-deprotonated 4,4'-Azobis(3,5-dimethyl-1H-pyrazole) Ligand. *Z. Anorg. Allg. Chem.* **2018**, *644*, 1311-1316.
- (38) Harada, J.; Ogawa, K., What Molecules Are Likely or Unlikely To Undergo Pedal Motions in Crystals? *Cryst. Growth Des.* **2014**, *14*, 5182-5188.
- (39) Harada, J.; Ogawa, K.; Tomoda, S., Molecular Motion and Conformational Interconversion of Azobenzenes in Crystals as Studied by X-ray Diffraction. *Acta Crystallogr., Sect. B* **1997**, *53*, 662-672.
- (40) Karanam, M.; Choudhury, A. R., Study of Halogen-Mediated Weak Interactions in a Series of Halogen-Substituted Azobenzenes. *Cryst. Growth Des.* **2013**, *13*, 4803-4814.
- (41) Vande Velde, C. M. L.; Zeller, M.; Azov, V. A., Thermodynamic parameters of the Pedal Motion in the Crystal Structures of two Bromomethylated Azobenzenes. *CrystEngComm* **2015**, *17*, 5751-5756.
- (42) Hutchins, K. M.; Kummer, K. A.; Groeneman, R. H.; Reinheimer, E. W.; Sinnwell, M. A.; Swenson, D. C.; MacGillivray, L. R., Thermal Expansion Properties of three Isostructural Co-crystals composed of Isosteric Components: Interplay between Halogen and Hydrogen bonds. *CrystEngComm* **2016**, *18*, 8354-8357.
- (43) Mazzeo, P. P.; Carraro, C.; Arns, A.; Pelagatti, P.; Bacchi, A., Diversity through Similarity: A World of Polymorphs, Solid Solutions, and Cocrystals in a Vial of 4,4'-Diazopyridine. *Cryst. Growth Des.* **2019**, ASAP, doi: 10.1021/acs.cgd.9b01052.
- (44) Wu, L. C.; Chung, W. C.; Wang, C. C.; Lee, G. H.; Lu, S. I.; Wang, Y., A Charge Density Study of π -Delocalization and Intermolecular Interactions. *Phys. Chem. Chem. Phys.* **2015**, *17*, 14177-14184.
- (45) Bučar, D.-K.; Lancaster, R. W.; Bernstein, J., Disappearing Polymorphs Revisited. *Angew. Chem. Int. Ed.* **2015**, *54*, 6972-6993.

- (46) Laplant, F.; De Paepe, A., Raman Spectroscopy for Identifying Polymorphs. In *Pharmaceutical Applications of Raman Spectroscopy*, Šašić, S.(Ed.), John Wiley & Sons, **2007**, 85-115.
- (47) Turner, M. J.; Grabowsky, S.; Jayatilaka, D.; Spackman, M. A., Accurate and Efficient Model Energies for Exploring Intermolecular Interactions in Molecular Crystals. *J. Phys. Chem. Lett.* **2014**, 5, 4249-55.
- (48) Mackenzie, C. F.; Spackman, P. R.; Jayatilaka, D.; Spackman, M. A., CrystalExplorer model Energies and Energy Frameworks: Extension to Metal Coordination Compounds, Organic Salts, Solvates and Open-Shell Systems. *IUCrJ* **2017**, 4, 575-587.
- (49) Thomas, S. P.; Spackman, P. R.; Jayatilaka, D.; Spackman, M. A., Accurate Lattice Energies for Molecular Crystals from Experimental Crystal Structures. *J. Chem. Theory Comput.* **2018**, 14, 1614-1623.
- (50) Thomas, S. P.; Spackman, M. A., The Polymorphs of ROY: A Computational Study of Lattice Energies and Conformational Energy Differences. *Austr. J. Chem.* **2018**, 71, 279-284.
- (51) Spackman, M. A.; McKinnon, J. J., Fingerprinting intermolecular interactions in molecular crystals. *CrystEngComm* **2002**, 4, 378-392.
- (52) McKinnon, J. J.; Spackman, M. A.; Mitchell, A. S., Novel Tools for Visualizing and Exploring Intermolecular Interactions in Molecular Crystals. *Acta Crystallogr., Sect. B* **2004**, 60, 627-668.
- (53) McKinnon, J. J.; Fabbiani, F. P. A.; Spackman, M. A., Comparison of Polymorphic Molecular Crystal Structures through Hirshfeld Surface Analysis. *Cryst. Growth Des.* **2007**, 7, 755-769.
- (54) McKinnon, J. J.; Jayatilaka, D.; Spackman, M. A., Towards Quantitative Analysis of Intermolecular Interactions with Hirshfeld Surfaces. *Chem. Commun.* **2007**, 3814-3816.
- (55) Spackman, M. A.; Jayatilaka, D., Hirshfeld surface analysis. *CrystEngComm* **2009**, 11, 19-32.
- (56) Burger, A.; Ramberger, R., On the Polymorphism of Pharmaceuticals and other Molecular Crystals. I. *Microchim. Acta* **1979**, 72, 259-271.
- (57) Burger, A.; Ramberger, R., On the Polymorphism of Pharmaceuticals and other Molecular Crystals. II. *Microchim. Acta* **1979**, 72, 273-316.

- (58) Barbas, R.; Martí, F.; Prohens, R.; Puigjaner, C., Polymorphism of Norfloxacin: Evidence of the Enantiotropic Relationship between Polymorphs A and B. *Cryst. Growth Des.* **2006**, *6*, 1463-1467.
- (59) Kawakami, K., Reversibility of Enantiotropically Related Polymorphic Transformations from a Practical Viewpoint: Thermal Analysis of Kinetically Reversible/Irreversible Polymorphic Transformations. *J. Pharm. Sci.* **2007**, *96*, 982-989.
- (60) Bernal, J. D.; Fowler, R. H., A Theory of Water and Ionic Solution, with Particular Reference to Hydrogen and Hydroxyl Ions. *J. Chem. Phys.* **1933**, *1*, 515-548.
- (61) Pauling, L., The Structure and Entropy of Ice and of Other Crystals with Some Randomness of Atomic Arrangement. *J. Am. Chem. Soc.* **1935**, *57*, 2680-2684.
- (62) Etter, M. C.; MacDonald, J. C.; Bernstein, J., Graph-Set Analysis of Hydrogen-Bond Patterns in Organic Crystals. *Acta Crystallogr. B* **1990**, *46*, 256-62.
- (63) Baburin, I. A.; Blatov, V. A., Three-dimensional Hydrogen-bonded Frameworks in Organic Crystals: a Topological Study. *Acta Crystallogr., Sect. B* **2007**, *63*, 791-802.
- (64) Baburin, I. A.; Blatov, V. A.; Carlucci, L.; Ciani, G.; Proserpio, D. M., Interpenetrated Three-Dimensional Networks of Hydrogen-Bonded Organic Species: A Systematic Analysis of the Cambridge Structural Database. *Cryst. Growth Des.* **2008**, *8*, 519-539.
- (65) Alexandrov, E. V.; Blatov, V. A.; Proserpio, D. M., A topological Method for the Classification of Entanglements in Crystal Networks. *Acta Crystallogr., Sect. A* **2012**, *68*, 484-493.
- (66) Blatov, V. A.; Shevchenko, A. P.; Proserpio, D. M., Applied Topological Analysis of Crystal Structures with the Program Package ToposPro. *Cryst. Growth Des.* **2014**, *14*, 3576-3586.
- (67) APEX2. SAINT, Data Reduction and Frame Integration Program for the CCD Area-Detector System, Bruker Analytical X-ray Systems; Data Collection Program for the CCD Area-Detector System: Madison, WI, USA, 1997–2006.
- (68) G.M. Sheldrick, SADABS: Area-Detector Absorption Correction; University of Göttingen: Göttingen, Germany, 1996.
- (69) G.M. Sheldrick, Crystal Structure Refinement with SHEXL. *Acta Crystallogr. Sect A* **2015**, *71*, 3–8.

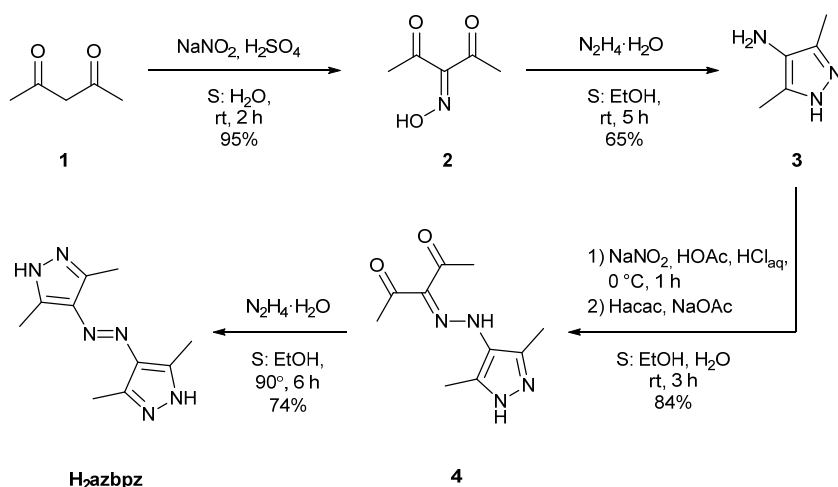
- (70) K. Brandenburg, DIAMOND, version 4.5; Crystal and Molecular Structure Visualization; Crystal Impact - K. Brandenburg & H. Putz Gbr., Bonn, Germany, **2009–2018**.
- (71) Avadhut, Y. S.; Schneider, D.; Schmedt auf der Günne, J., A Method for Improved Quantification of ^1H NMR signals under low-resolution conditions for solids. *J. Magn. Reson.* **2009**, *201*, 1-6.
- (72) Harris, R. K.; Becker, E. D., NMR Nomenclature: Nuclear Spin Properties and Conventions for Chemical Shifts—IUPAC Recommendations. *J. Magn. Reson.* **2002**, *156*, 323-326.
- (73) Harris, R. K.; Becker, E. D.; Cabral de Menezes, S. M.; Granger, P.; Hoffman, R. E.; Zilm, K. W., Further Conventions for NMR Shielding and Chemical Shifts (IUPAC Recommendations 2008). *Pure Appl. Chem.* **2008**, *80*, 59-84.
- (74) Jardón-Álvarez, D.; Schmedt auf der Günne, J., Reduction of the Temperature Gradients in Laser Assisted High Temperature MAS NMR. *Solid State Nucl. Magn. Reson.* **2018**, *94*, 26-30.
- (75) Metz, G.; Wu, X. L.; Smith, S. O., Ramped-Amplitude Cross Polarization in Magic-Angle-Spinning NMR. *J. Magn. Res., Ser. A* **1994**, *110*, 219-227.

Supporting Information

The Solid-State Landscape of 4,4'-Azobis(3,5-dimethyl-1H-pyrazole) With the Isolation of Conformer-dependent Polymorphs

Synthesis of H₂azbpz

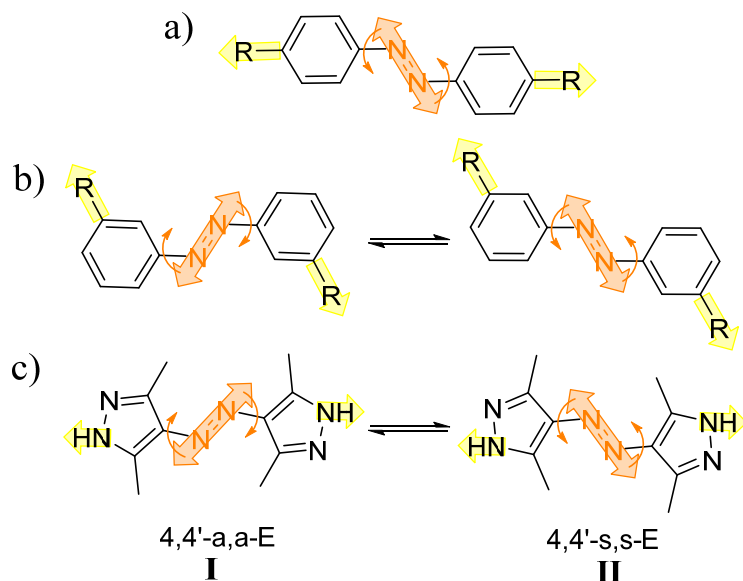
The synthesis route to H₂azbpz involves four steps and is analogous to the synthesis published by us recently.^{1,2} Acetylacetone **1** is converted first to 2,3,4-pentanetrione-3-oxime **2** by reaction with nitrous acid and then to 4-Amino-3,5-dimethyl-1H-pyrazole **3** by reaction with hydrazine. Diazotization of the 4-amino-3,5-dimethyl-1H-pyrazole (**3**) and Japp-Klingemann reaction with acetylacetone **1** yields the corresponding hydrazone **4**. Finally, H₂azbpz is obtained by the heterocyclization of the β-diketonate moiety using hydrazine hydrate.



Scheme S1. Four-step synthesis of H₂azbpz.

Nomenclature for the possible E-H₂azbpz isomers

There are three prototypal planar isomers possible for trans-H₂azbpz in the solid-state, named 4,4'-a,a-E (**I**), 4,4'-s,s-E (**II**) and 4,4'-a,s-E expressed as the isomerism of the NH function positioning relatively to the double bond (see Scheme 1 in main text for the explanation of the nomenclature). Isomerism of the proton location is the principal difference compared to the other, well-studied symmetrically substituted N-heterocyclic azo-compounds like 4,4'-azopyridine³ or 4,4'-azo-1,2,4-triazole⁴. Therefore, we can discern two different forms of H₂azbpz due to the different orientations of the pyrrolic NH function in analogy to the ortho- and meta-substituted azo-compounds (Scheme S2). On the other hand, the number of possible isomers in the less symmetric and already studied 3(3'),3(5')-azobispyrazole is 20, which makes the more symmetric 4,4'-derivative a better model target for studying the isolation of different molecular forms in the solid state.⁵



Scheme S2 Conformational landscape of azo-compounds related by the pedal motion of the azo group: a) single conformation of azobenzene and para-substituted azobenzenes b) distinguishable conformations of meta-substituted azobenzenes c) distinguishable molecular forms of H₂azbpz due to the isomerism of the NH function in respect to the azo-function with both in an anti-periplanar position in form 4,4'-a,a-E (**I**) and both in syn-periplanar position in form 4,4'-s,s-E (**II**) (see Scheme 1 in main text together with the explanation of the *ad hoc* nomenclature).

4-Amino-3,5-dimethyl-1H-pyrazole, 3

The synthetic procedure was adapted from Liu *et al.*⁶ 2,3,4-pentanetrione-3-oxime **2**, as the starting material, was prepared according to Tkach *et al.*⁷ from acetylectone **1** and used without further purification.

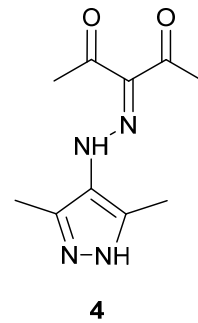
2,3,4- pentanetrione-3-oxime **2** (31.98 g, 0.228 mol) was dissolved in 160 ml of EtOH and cooled with an ice bath. Hydrazine hydrate (25.6 ml, 2.1 eq.) was added slowly over 15 min under stirring and the formed blue solution was heated at 80 °C for 90 min. Additional 9.7 ml (0.198 mmol, 0.8 eq.) of hydrazine hydrate were added and the clear solution was heated for further 3.5 h at 80 °C. It was concentrated under reduced pressure and the product was precipitated by addition of 120 ml of de-ionized water (DI-H₂O). The light yellow precipitate was filtered off, washed with a small amount of ethanol (5ml) and dried in a vacuum oven at 80 °C for 2 h. After recrystallization from 70 : 30 EtOH : H₂O mixture and drying under reduced pressure overnight (50 °C, 10⁻² bar) 18.02 g (0.162 mmol, 65 %) of (**3**) as a white solid were obtained.

¹H-NMR (300 MHz, DMSO-d₆ δ [ppm]): 1.99 (s, 6H, CH₃).

MS (EI) m/z [rel. int.]: 111.0 (100%), (70.1 (36.59%), 43.1 (43.56%), 42 (45.79%).

N-(3-pentane-2,4-dionylidene)-N'-(3,5-dimethylpyrazol-4-yl) hydrazine, 4

The hydrazone **4** was synthesized as described by Rollas *et al.*⁸ 5.00 g (0.045 mol) of **3** were suspended in 65 ml of glacial acetic acid and 11 ml of conc. HCl. The suspension was pre-cooled at 0-5 °C for 0.5 h using an ice water bath and a solution of 3.72 g (0.054 mol, 1.2 eq.) of NaNO₂ in 17 ml of cold water was added dropwise over 20 min under stirring, followed by stirring of the formed clear yellow solution for an additional hour, maintaining the given temperature during both stages. The cold solution of the diazonium salt was added dropwise to a solution of 6.0ml acetylacetone (5.91 g, 0.0590 mol, 1.2 eq.) and 11.07 g of NaOAc (0.135 mol, 3 eq.) in 46 ml EtOH and 26 ml water at 0-5 °C. The suspension was warmed to room temperature and stirred for additional 3 h. The precipitate was filtered off and washed thoroughly with water (6x 50 ml). Recrystallization from EtOH afforded 8.44 g (0.0380 mol, 84 %) an egg yolk yellow solid of **4**.



¹H-NMR (300 MHz, DMSO-d₆ δ [ppm]): 2.26 (pseudo-s, 9H, CH₃), 2.43 (s, 3H, CH₃), 12.53 (s, 1H, NH of pyrazole), 15.03 (s, 1H, RN=NHR').

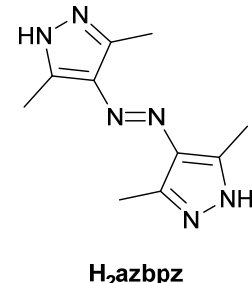
¹³C-NMR (75 MHz, DMSO-d₆ δ [ppm]): 11.15, 26.69, 30.84, 120.68, 132.30, 195.64.

ESI-MS: [MH]⁺ 223.2.

EA [%] calc. for: C₁₀H₁₄N₄O₂ C 54.04, H 6.35, N 25.21 found: C 54.16, H 6.47, N 25.27

4,4'-azobis(3,5-dimethyl-1H-pyrazole), H₂azbpz

2.177 g (9.80 mmol) of **4** was dissolved in 130 ml of EtOH. Afterwards 480 µl (9.88 mmol, 1.01 eq) of hydrazine hydrate were added. The solution was heated at 90 °C for 6 h. After cooling to room temperature the precipitate was filtered off and washed with water to yield a sufficiently pure product according to NMR and EA without recrystallization(yield: 1.12 g, 52 %). The PXRD pattern confirmed the formation of the H₂azbpz-I polymorph.



¹H-NMR (300 MHz, DMSO-d₆) δ [ppm]: 2.37 (s, 12H, CH₃), 12.36 (s, 2H, NH).

¹³C-NMR (75 MHz, DMSO-d₆) δ [ppm]: 9.97, 13.67, 134.39, 135.49, 141.50.

ESI-MS: [MH]⁺ 219.3.

EA [%] calc. for: H₂Azbpz C₁₀H₁₅N₆ C 55.03, H 6.47, N 38.50 found: C 55.14, H 6.46, N 38.55.

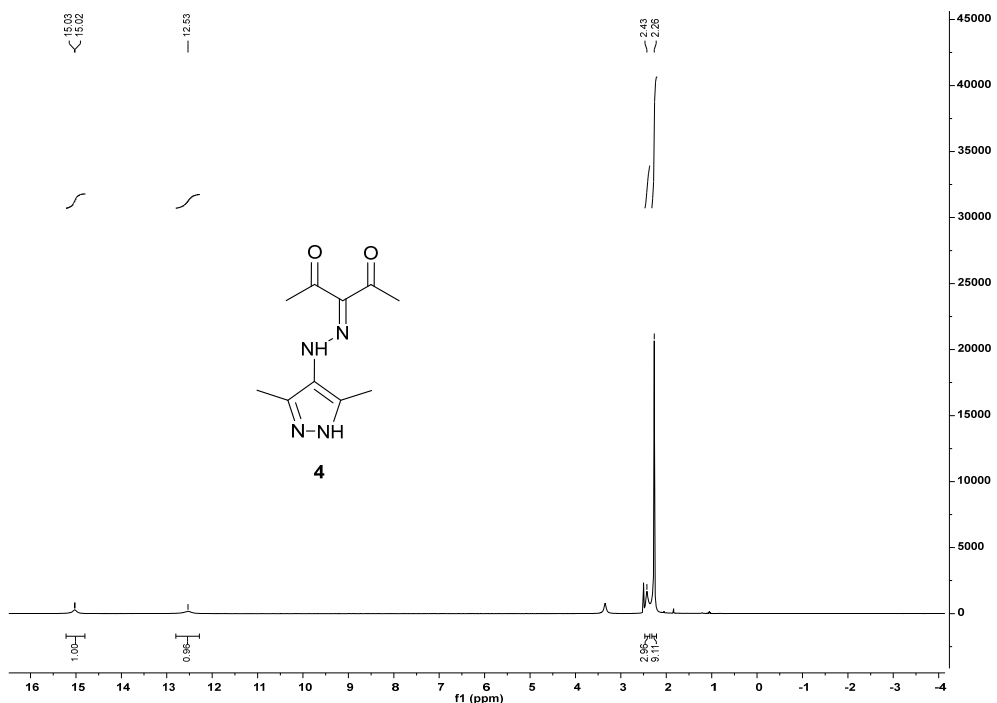
NMR spectra

Figure S1. ¹H-NMR spectrum of N-(3-pentane-2,4-dionylidene)-N'-(3,5-dimethylpyrazol-4-yl) hydrazine 4 in DMSO-d₆.

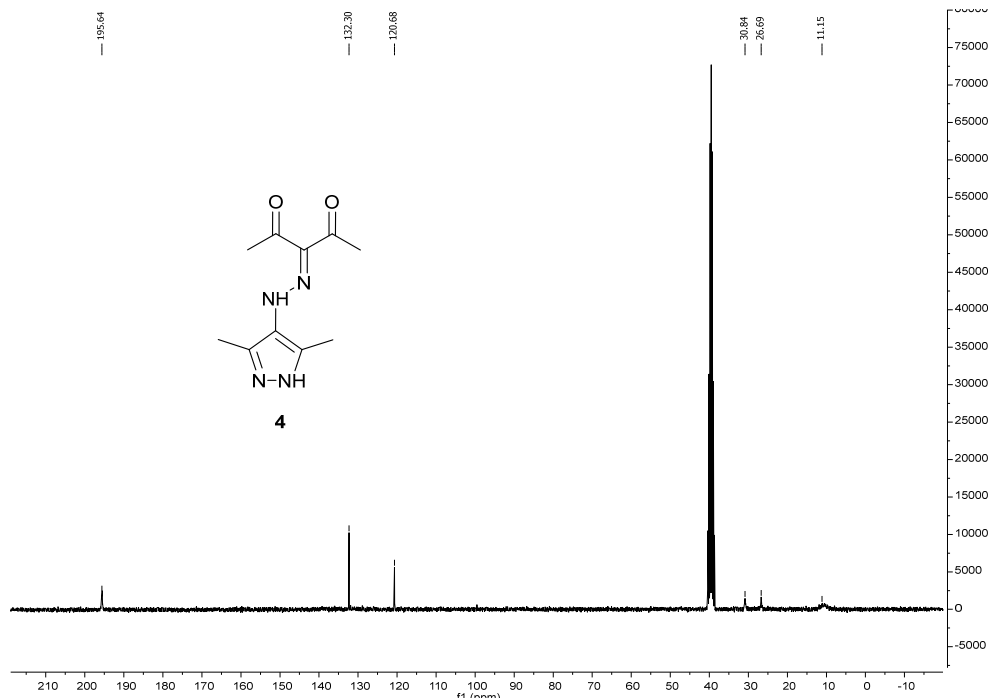
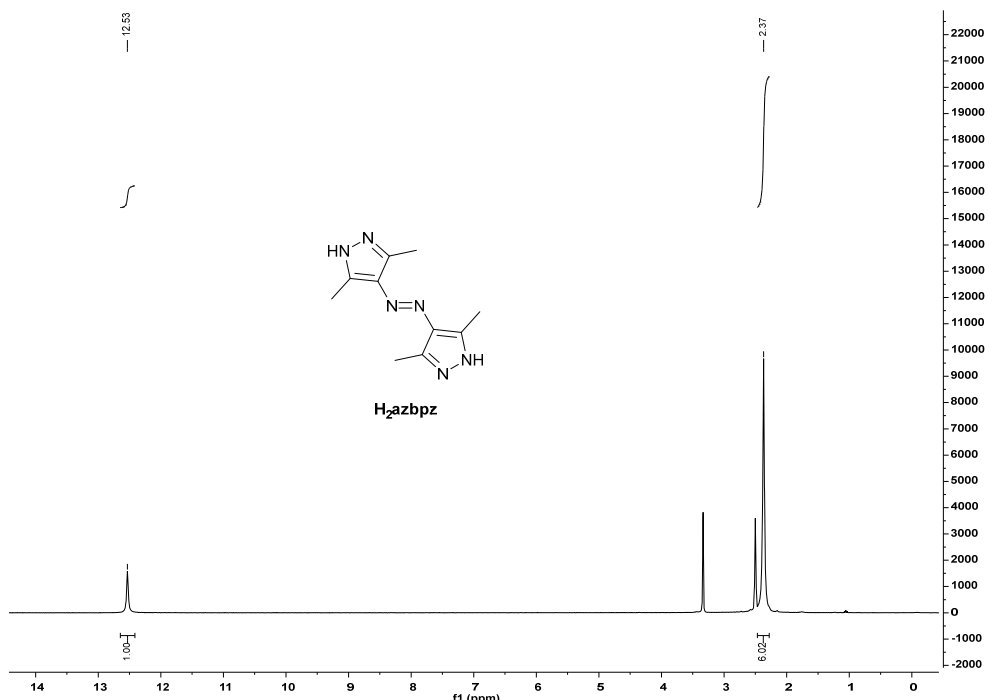
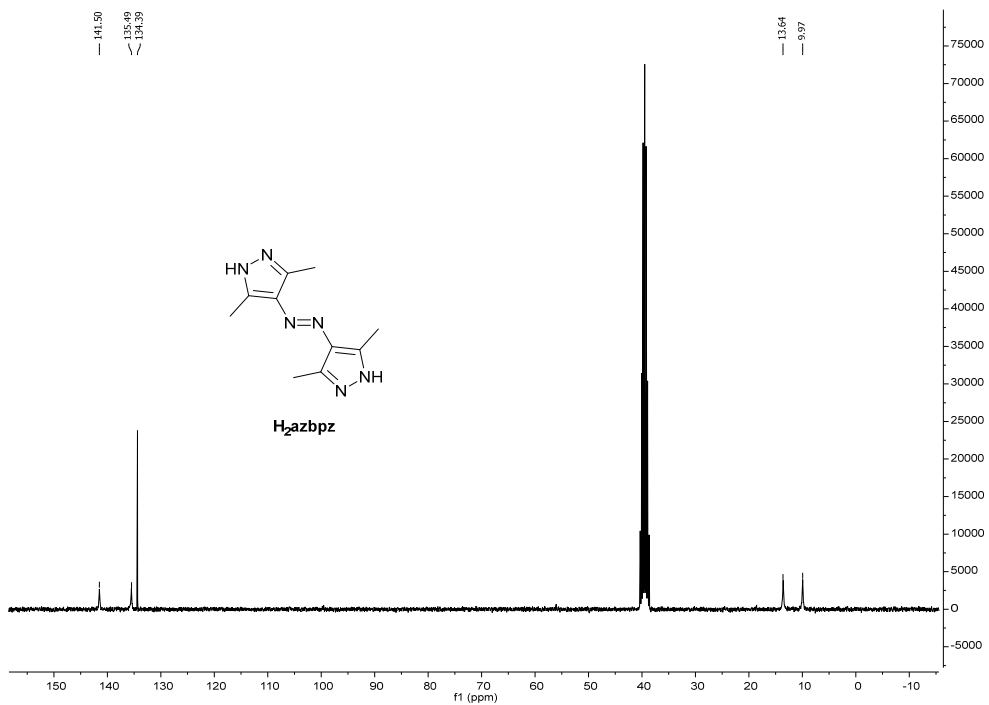


Figure S2. ¹³C-NMR spectrum of N-(3-pentane-2,4-dionylidene)-N'-(3,5-dimethylpyrazol-4-yl) hydrazine 4 in DMSO-d₆.

**Figure S3.** ¹H-NMR spectrum of H₂azbpz in DMSO-d₆.**Figure S4.** ¹³C-NMR spectrum of H₂azbpz in DMSO-d₆.

Phase transformations between the polymorphic forms or “the reappearing of the hard to-obtain polymorph H₂azbpz-II”

After obtaining the first single crystal structure of H₂azbpz-II, this polymorph could not be reproduced in crystallization experiments in solution from microcrystalline batches of H₂azbpz available after the synthesis in our laboratory. And we almost accepted on dealing with a disappearing polymorph in the case of H₂azbpz-II. A new effort was derived from the premise of H₂azbpz-II being the relative more stable polymorph also having the higher crystal density but containing the presumably higher energy molecular form. H₂azbpz-II has a higher specific density than H₂azbpz-I, which is an attribute of a more stable polymorph (i.e. sustained by stronger interactions). The higher stability of H₂azbpz-II is also supported by lattice energy calculations (see section in main text). In this respect we envisioned a potential mechanochemical conversion of H₂azbpz-I into H₂azbpz-II. Inducing formation of polymorphs mechanochemically is an established alternative strategy, yielding sometimes unique results, compared to the crystallization from solutions.^{9,10}

The ball-milling (20 Hz) of H₂azbpz-I was monitored PXRD diffraction. The initial few minutes registered primarily the broadening of the reflexes due to due to crystallite size reduction. A few simulated PXRD patterns with different FWHM (full width at half maximum) values are given in Figure 1 (main text) in order to facilitate the visual comparison of the patterns (for estimation of crystallite sizes see Table S7 and S8). The transformation then speeds up in smaller crystallites (smaller sizes are favorable due to increased contribution of the surface, where the molecular mobility is the highest).⁹ After 30 min of milling the conversion of H-azbpz-I to H-azbpz-II was mostly finished, however, the broad peak at $2\theta = \sim 16.5^\circ$ still showed a small shoulder, indicative for the incomplete conversion. The milling for 180 min yields a reasonably pure sample of H₂azbpz-II (see Figure 1).

The samples obtained from the ball milling experiments were used to obtain supersaturated solutions of the conformer II in DMF at 0–2 °C to also reproducibly obtain H₂azbpz-II as (small) single crystals. The phase purity of the crystallized bulk material of H₂azbpz-II was verified by positively matching the experimental pattern with simulated patterns obtained from the single crystal data of H₂azbpz-II (see Figure 1 and S20 in SI). The polymorph H₂azbpz-II can be identified by the absence of the reflection of the [011]-plane at $2\theta = 17.4^\circ$ (see Figure 1, for the indexed reflections of H₂azbpz-I and H₂azbpz-II see Figure S20 in SI.).

Crystallographic data

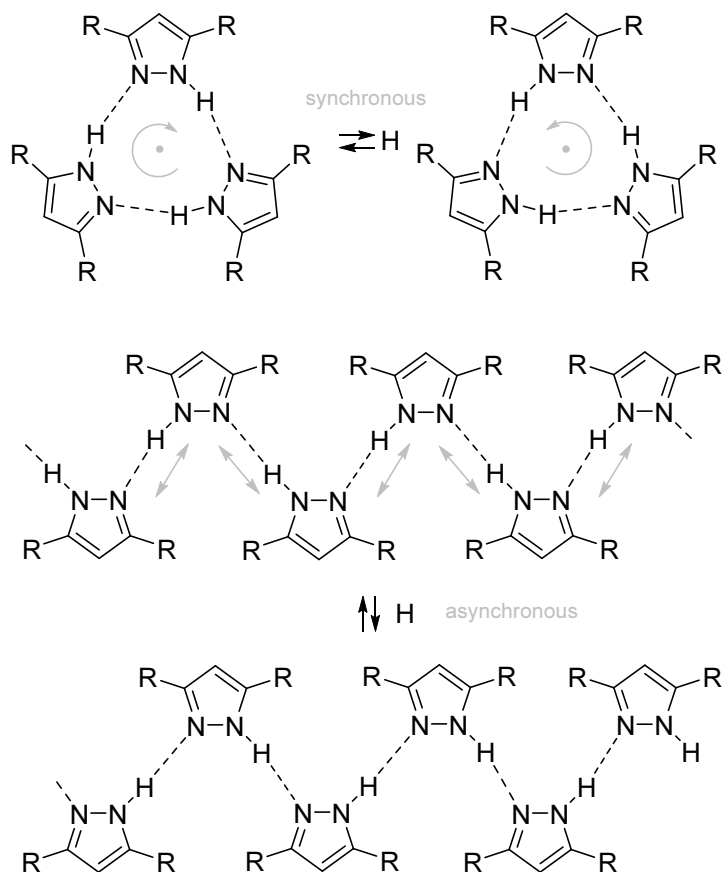
Table S3 Crystal data and refinement details of H₂azbpz-I, H₂azbpz-II and H₂azbpz·0.5H₂O.

	H ₂ azbpz-I	H ₂ azbpz-II	H ₂ azbpz·0.5H ₂ O-LT	H ₂ azbpz·0.5H ₂ O-RT
M _r (g/mol)	218.27	218.27	454.56	454.56
d _{calc} (g/cm ³)	1.287	1.332	1.247	1.219
Crystal system, space group	Monoclinic, P2 ₁ /c	Monoclinic, P2 ₁ /c	Monoclinic, C2/c	Monoclinic, C2/c
Temperature (K)	150	150	100	298
a (Å)	6.2100(16)	9.8220(12)	10.6214(10)	10.7641(6)
b (Å)	5.3950(13)	5.0834(6)	34.213(4)	34.273(3)
c (Å)	16.929(4)	11.3411(11)	6.9369(6)	7.0596(4)
β (°)	96.704(6)	104.608(7)	106.091(5)	108.030(4)
V (Å ³)	563.3(2)	547.95(12)	2422.0 (4)	2476.5(3)
Z	2	2	4	4
μ (mm ⁻¹)	0.086	0.088	0.085	0.083
F(000)	232	232	968	968
Crystal size (mm)	0.15 × 0.10 × 0.05	0.12 × 0.04 × 0.04	0.10 × 0.10 × 0.10	0.10 × 0.10 × 0.10
T _{min} , T _{max}	0.673, 0.746	0.693, 0.746	0.705, 0.745	0.689; 0.745
No. of measured, independent and observed reflections	6458, 1302, 1152 [I > 2σ(I)]	9756, 1426, 981 [I > 2σ(I)]	10125, 2595, 1866 [I > 2σ(I)]	10455, 2639 1528 [I > 2σ(I)]
R _{int}	0.030	0.043	0.039	0.034
(sin θ/λ)max (Å ⁻¹)	0.653	0.679	0.635	0.634
R, wR(F ²), S [F ² > 2σ(F ²)] ^[a]	0.0430, 0.1142, 1.082	0.0457, 0.1104, 1.039	0.0816, 0.2066, 1.017	0.0737, 0.1957, 1.042
R, wR(F ²), S [all data] ^[a]	0.0481, 0.1181, 1.082	0.0751, 0.1266, 1.039	0.1114, 0.2337, 1.017	0.1219, 0.2341, 1.042
No. of reflections	1302	1426	2595	2639
No. of parameters	78	101	160	160
No. of restraints	0	0	0	2
Δρ _{max} , Δρ _{min} ^[b] (e·Å ⁻³)	0.314, -0.259	0.313, -0.231	0.991, -0.685	0.648, -0.349

^[a] R₁ = [Σ(|F_o| - |F_c|)/Σ|F_o|]; wR₂ = [Σ [w(F_o² - F_c²)²]/Σ[w(F_o²)²]]^{1/2}. Goodness of fit S = [Σ [w(F_o² - F_c²)²] / (n-p)]^{1/2}.^[b] Largest difference peak and hole.

Hydrogen-bond analysis in H₂azbpz-I and H₂azbpz-II

To form structures of higher dimensionality than 0D and 1D the pyrazole functionalities should be combined in oligotopic molecules through hydrogen bonding. The simplest combination in a symmetric ditopic 4,4'-bipyrazole, whose derivatives demonstrated rich polymorphism (e.g. three polymorphs for the H₂Me₄bpz 'hinge-molecule' with limited 1D degree of freedom), feature both cyclic trimeric and catemeric patterns (see Scheme S3).^{11,12}



Scheme S3. Cyclic trimeric and catemeric patterns in the solid-state structure of H₂Me₄bpz.

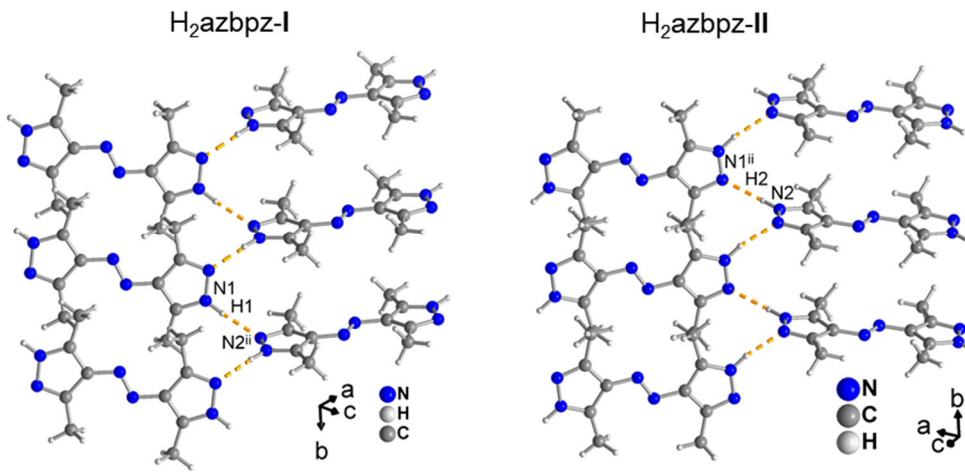


Figure S5. The catemeric hydrogen bonded patterns in H₂azbpz-**I** and H₂azbpz-**II**. Symmetry transformation codes: for H₂azbpz-**I** (ii) is -x, y-0.5, -z+0.5 for H₂azbpz-**II** (ii) is -x+2, y+0.5, -z+1.5.

Table S2. Comparison of the hydrogen-bond geometries in H₂azbpz-**I** and H₂azbpz-**II**

D–H···A	D–H [Å]	H···A [Å]	D···A [Å]	D–H···A [°]
H₂azbpz-I				
N1–H1···N2 ⁱⁱ	0.91 (2)	2.00 (2)	2.895(1)	169.9 (17)
H₂azbpz-II				
N2–H···N1 ⁱⁱ	0.92 (3)	2.00 (3)	2.891(5)	164 (2)

Symmetry transformations: for H₂azbpz-**I** (ii) -x, y-0.5, -z+0.5 for H₂azbpz-**II** (ii) -x+2, y+0.5, -z+1.5

Analysis of short contacts in H₂azbpz-I and H₂azbpz-II

It is particularly felicitous for the rationalization and prediction of the structures of 1H-pyrazoles that the substituent at the 4-th position of molecular pyrazoles has a weak influence on the type of the formed patterns, and controls rather the tertiary and quaternary structure. The second established empirical rule is that the type of the particular cyclamer or catemer formed depends on the combined volume of the substituents in the 3 and the 5-th positions.¹³ The two empirical rules give a solid background for the use of length-scaled 4,4'-bipyrazoles for the rational design of functional H-bonded solids.

Das *et al.* discussed the C–H···C_{pz} weak contacts between methyl groups and pyrazole-ring carbon atoms as C(sp³)–H···C(sp²)- and C(sp³)–H···C(sp³)-contacts in the complex [Co(4-nbz)₂(dmpz)₂]·0.5H₂O (4-nbz = 4-nitrobenzoate, dmpz = 3,5-dimethylpyrazole).¹⁴ Those interactions are usually weak due to the low acidity and basicity of the C–H and C_{pz}-moieties, respectively. However, previous works established such C–H···C_{pz} contacts theoretically,^{15,16} and crystallographic evidences were found as well.¹⁷⁻¹⁹ In conjunction of the contacts identified in the analysis of the Hirshfeld surface areas of the H₂azbpz molecules in polymorphs I and II, we analyzed both structures for interactions between the π-electronic systems of dimethylpyrazole-moieties and the azo-function of molecules to further explain the encountered packing differences.^{2,20-22}

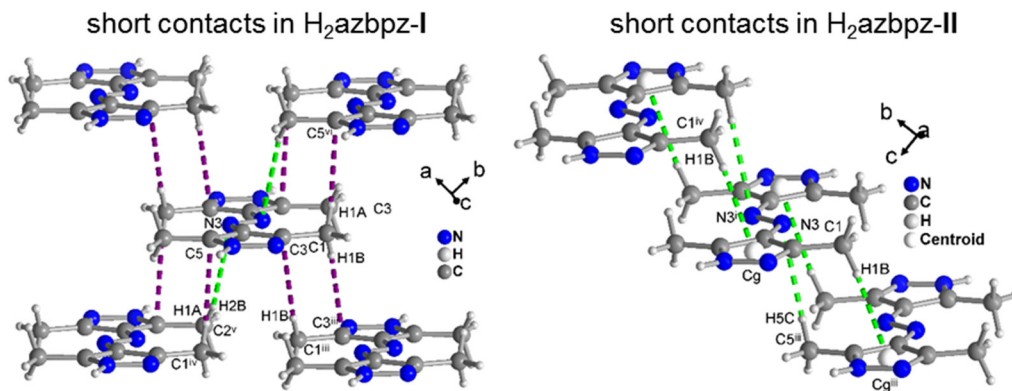


Figure S6. Representation of potential short contacts in H₂azbpz-I (left) and H₂azbpz-II (right). Symmetry transformations for H₂azbpz-II: iii = -x, 1-y, 1-z; iv = x, -1+y, z; v = 1-x, -y, 1-z; vi = x, 1+y, z; for H₂azbpz-I: iii = 1-x, 1-y, 1-z; iv = x, 1+y, z.

Table S3. Distances [Å] and angles [°] for the shortest contacts in H₂azbpz-I and H₂azbpz-II

H ₂ azbpz-I							
C—H···A	H···A	D···A	$\angle(\text{CH} \cdots \text{Cg1})$				
C(1)—H(1B) ··· C3 ⁱⁱⁱ	2.78	3.72	a) 159				
C(1)—H(1A) ··· C5 ^{iv/vi}	2.71	3.53	142				
C(1)—H(1A) ^{iv} ··· N3	3.11	4.06	163				
H ₂ azbpz-II							
CH ₃ -π	d _{ATM}	d _{PLN}	d _{CNT}	γ	$\angle(\text{CH} \cdots \text{Cg1})$	d(Cg1···C 1)	$\angle(\text{CH} \cdots \text{Cg1})$
C(1)—H(1B) ··· Cg ^{iii/iv}	2.86	4.19	2.76	15.2 3	141	3.678(2)	51
C—H···A	H···A	D···A	$\angle(\text{CH} \cdots \text{Cg1})$				
C(5)—H(5C) ^v ··· N3	2.87	3.82	158				

a) Cg1 designates the centroid of the pyrazole-moiety

Symmetry transformations: for H₂azbpz-I iii = -x, 1-y, 1-z; iv = x, -1+y, z; v = 1-x, -y, 1-z; vi = x, 1+y, z;
for H₂azbpz-II iii = x, -1+y, z; iv = x, 1+y, z

Hirshfeld surface analyses

Analyses of the supramolecular interactions of the two polymorphs H₂azbpz-I H₂azbpz-II were performed with CrystalExplorer²³ via the relative contributions of close contacts to the Hirshfeld surfaces following the procedures outlined in the references.²⁴⁻²⁸ Herein, d_i and d_e represent the distances from the surface to the nearest atoms interior and exterior to the surface. d_{norm} is a normalized contact distance taking into account the van der Waals radii of the involved internal and external atoms of the Hirshfeld surface. Shorter contacts than the sum of the van der Waals radii are displayed in red, contacts in the range of the van der Waals radii in white and longer contacts in blue. The Hirshfeld surface can be broken down into fragments of interactions of specific atom-type/atom-type pairs reflecting the nature of the atoms and the relative contribution of these interactions to the Hirshfeld surface can be quantified. These interactions can further be dissected if they stem from an atom type 1 inside the surface to an atom type 2 outside the surface or vice versa (denoted for example with atom type 1 nitrogen and atom type 2 hydrogen as N_{ins}···H_{out} and N_{ins}···H_{out}).

Hirshfeld surface analysis of H₂azbpz-I

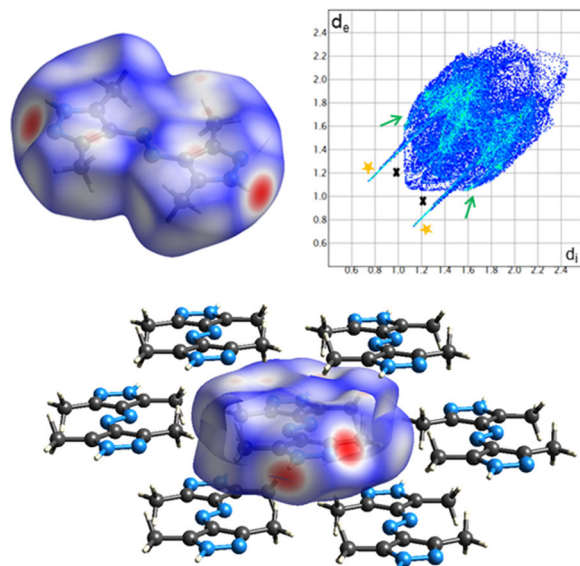


Figure S7. Top: Hirshfeld surface (right) mapped with d_{norm} and the 2D fingerprint plot (left) of H₂azbpz-I. In the fingerprint plot the closest N···H-contacts (orange stars), C···H-contacts (green arrows); H···H-contacts (black crosses) are marked. Bottom: a representative part of the immediate neighborhood of an H₂azbpz molecule with a Hirshfeld surface overlay in H₂azbpz-I.

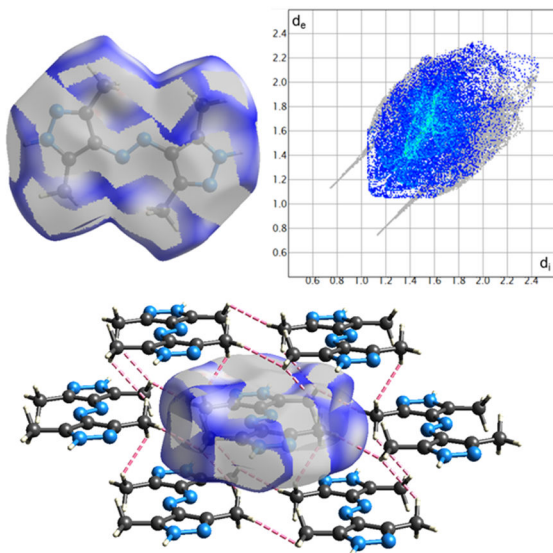
H···H contacts in H₂azbpz-I

Figure S8. The H···H contacts in H₂azbpz-I, represented only by the CH···HC type, have a relative contribution of 51.9% to the Hirshfeld surface between the CH₃-groups (shortest H···H contacts as dashed pink lines with a cut-off length of 2.55 Å).

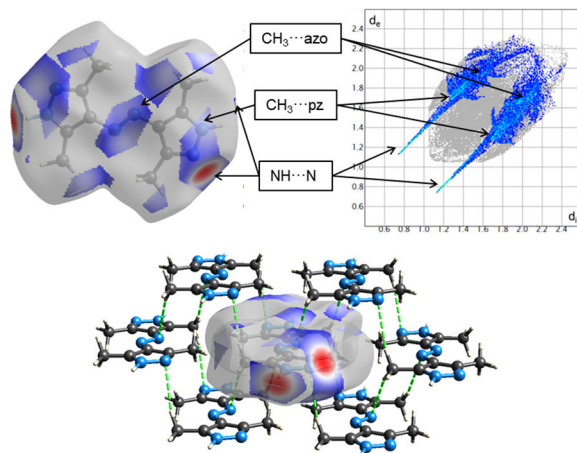
N···H contacts in H₂azbpz-I

Figure S9. The N···H contacts in H₂azbpz-I, represented by NH···H H-bonds and CH···N_{azo}, CH···N_{pz} contacts, have a relative contribution of 31.6% (reciprocal contributions are not equal: N_{ins}···H_{out} 18.2%, N_{out}···H_{ins} 13.4%). The NH···H hydrogen bonds are the strongest contacts; they are represented as red dots on the Hirshfeld surface and as sharp features in the fingerprint plot. The features responsible for the interactions of CH₃-groups and the azo-function/pyrazole-ring-nitrogens are also marked (the N···HC contacts are presented as dashed green lines with a cut-off length of 3.05 Å).

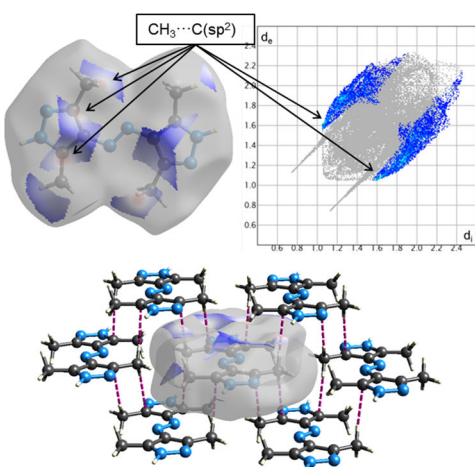
C···H contacts in H₂azbpz-I

Figure S10. The C···H contacts, represented only by the Cpz···HCH₂ type, account for 16.5% of the Hirshfeld surface in H₂azbpz-I (the reciprocal contributions are not equal: Cins···Hout 9.4% and Cout···Hins 7.1%). The location of the contacts can be seen as light red dots on the Hirshfeld surface (short C···H contacts are presented as dashed violet lines with a cut-off length of 2.8 Å).

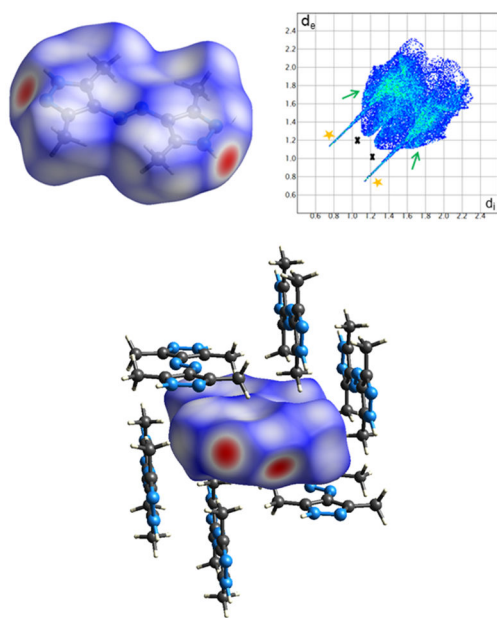
Hirshfeld surface analysis of H₂azbpz-II

Figure S11. Top: Hirshfeld surface (right) mapped with d_{norm} and the 2D fingerprint plot (left) of H₂azbpz-II. In the fingerprint plot the closest N···H-contacts (orange stars), C···H-contacts (green arrows); H···H-contacts (black crosses) are marked. Bottom: a representative part of the immediate neighborhood of an H₂azbpz molecule with a Hirshfeld surface overlay in H₂azbpz-II.

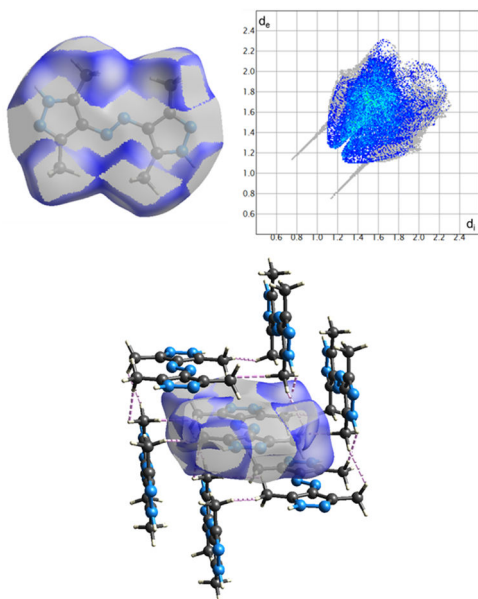
H···H contacts in H₂azbpz-II

Figure S12. The H···H contacts, represented only by the CH···HC type, have a relative contribution of 50.2% to the Hirshfeld surface of H₂azbpz-II (the shortest CH···HC contacts as dashed rosa lines with a cut-off length of 2.55 Å).

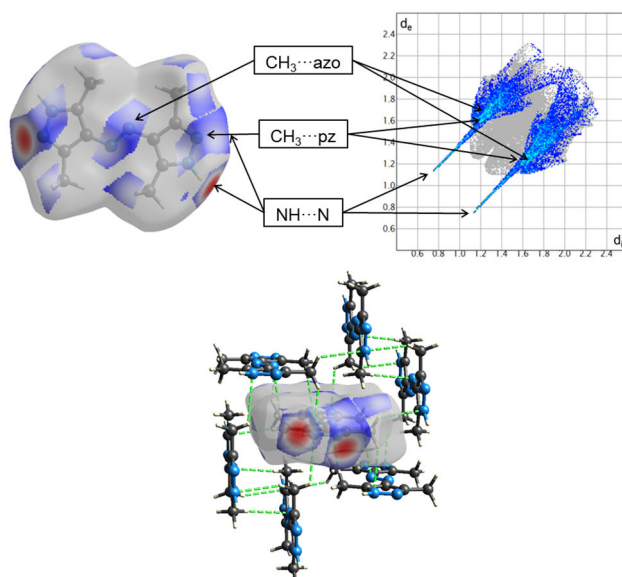
N···H contacts in H₂azbpz-II

Figure S13. The N···H contacts in H₂azbpz-II, represented by NH···H H-bonds and CH···N_{azo}, CH···N_{pz} contacts, account for 33.0% of the Hirshfeld surface (the reciprocal contributions are not equal: N_{ins}···H_{out} 18.9%, N_{out}···H_{ins} 14.1%). The NH···H hydrogen bonds as the strongest contacts are present as red dots on the Hirshfeld surface and as sharp features in the fingerprint plot. The features responsible for the interactions of CH₃-groups and the azo-function/pyrazole-ring-nitrogens are also marked. The N···H contacts are shorter in H₂azbpz-II compared to H₂azbpz-I and have slightly higher contribution (the N···HC contacts are presented as dashed green lines with a cut-off length of 3.0 Å).

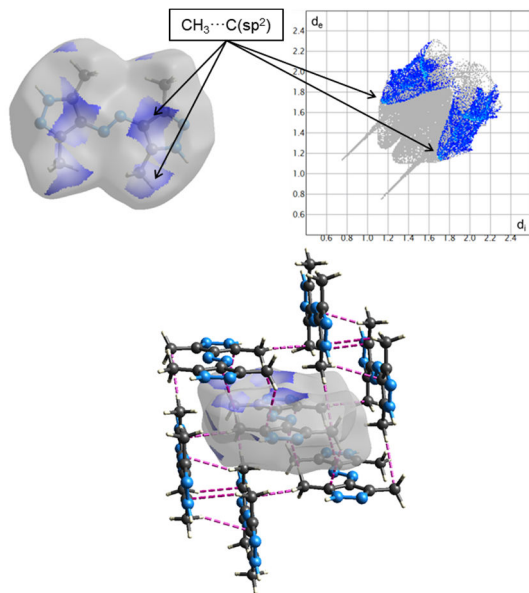
C···H contacts in H₂azbpz-II

Figure S14. The relative contribution of C···H contacts to the Hirshfeld surface of H₂azbpz-II is 16.7% (the reciprocal contributions are not equal: C_{ins}···H_{out} 9.6% and C_{out}···H_{ins} 7.1%). The features responsible for the CH₃···C(sp²)-contacts are marked on the Hirshfeld surface and in the fingerprint plot. It can be derived that those contacts only stem from molecules which are parallel displaced belonging to the same layer. Therefore they only occur on one site of the molecule. The relative contribution is comparable to that in H₂azbpz-I, but the contacts are longer. (the short C···H contacts are presented as dashed violet lines with a cut-off length of 2.9 Å).

Calculated potential energy profile of azo-pedaling motion in H₂azbpz

Relative stabilities and estimation of the rotational barrier of the bicycle-pedal rotation were calculated on the (B3LYP/TZVP) level.

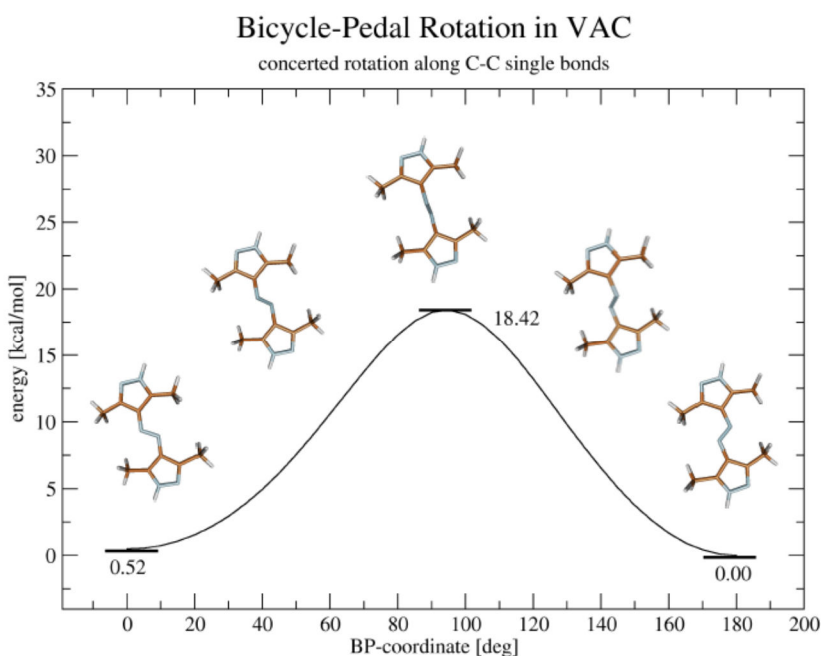


Figure S15. Calculated potential energy profile of azo-pedaling motion in H₂azbpz.

Calculation of the lattice energies and estimation of relative stabilities between the polymorphs

Lattice energies of both polymorphic forms were calculated with CrystalExplorer.²³ The wave function of the single molecules of the different forms in H₂azbpz-I and H₂azbpz-II were calculated on the B3LYP/6-311G(d,p) level with TONTO quantum chemical program implemented in CrystalExplorer. Clusters were formed with a distance of 20 Å of the central molecule and all created fragments were completed. Interaction energies were calculated as implemented in the CrystalExplorer program package to reach full convergence of the lattice energies (see Figure S17).²⁹⁻³¹

Examples of the application of CrystalExplorer for calculation of lattice energies of different bromomethylated azo-compounds³² as well as the assessment of rich conformational polymorphism of ROY (5-methyl-2-[(2-nitrophenyl)amino]-3-thiophenecarbonitrile) regarding the relative stabilities of the polymorphs³³ are given in the literature.

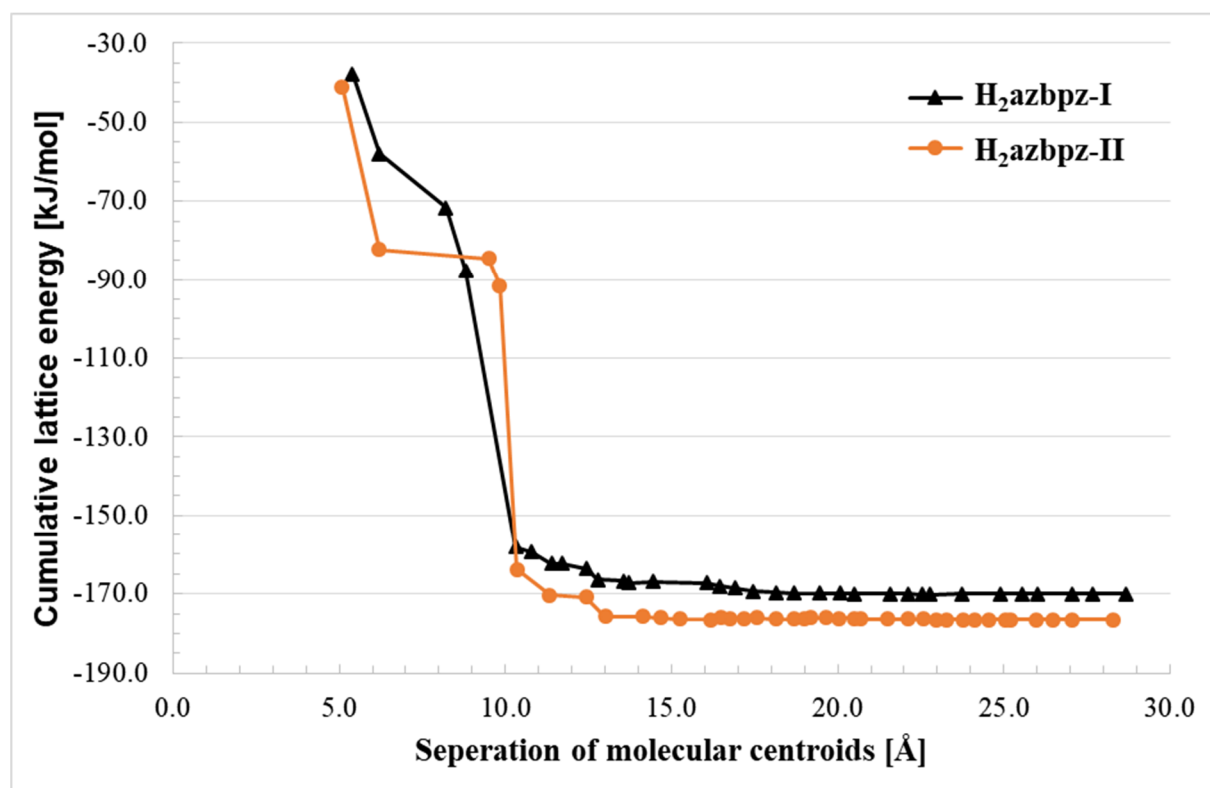


Figure S16. Convergence of the CE-B3LYP lattice energies as calculated by CrystalExplorer for the H₂azbpz-I (black) and H₂azbpz-II (orange). The cumulative lattice energies are plotted as partial sums against the separation of molecular centroids.

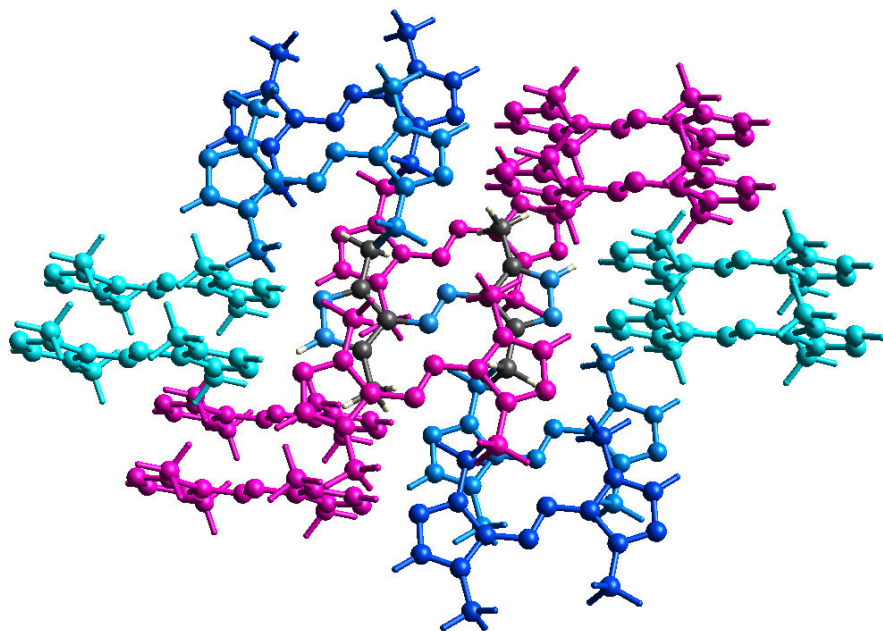


Figure S17 A representative fragment of the H₂azbpz-I structure with molecules having identical interaction energies given in the same color (See Table S5).

Table S5. Details on the main interaction energies for H₂azbpz-I as calculated by CrystalExplorer.

N	Symmetry transformation	E _{ele}	E _{pol}	E _{dis}	E _{rep}	E _{tot}	0.5·N·E _{tot}
[kJ/mol]							
4	-x, y+0.5, -z+0.5	-46.7	-11.1	-11.9	52.8	-35.3	-70.6
2	x, y, z	-13.9	-2.0	-44.0	26.9	-37.8	-37.8
2	x, y, z	-3.9	-1.9	-30.4	19.1	-20.1	-20.1
4	-x, y+0.5, -z+0.5	-0.7	-1.0	-11.7	5.8	-8.0	-16
2	x, y, z	-5.5	-0.5	-17.3	13.5	-12.9	-12.9

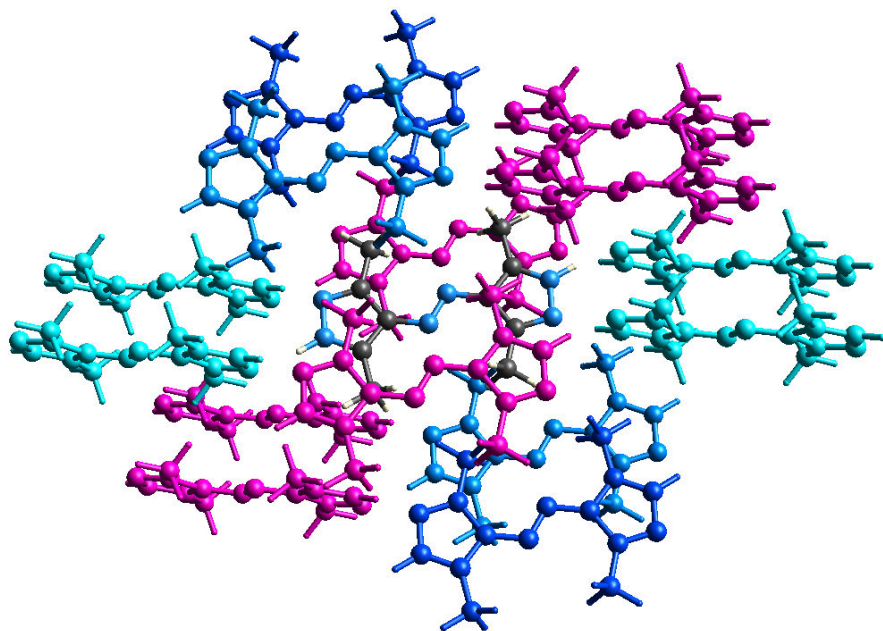


Figure S18. A representative fragment of the H₂azbpz-I structure with molecules having identical interaction energies given in the same color (See Table S5).

Table S6. Details on the main interaction energies for H₂azbpz-I as calculated by CrystalExplorer.

N	Symmetry transformation	E _{ele}	E _{pol}	E _{dis}	E _{rep}	E _{tot}	0.5·N·E _{tot}
[kJ/mol]							
4	-x, y+0.5, -z+0.5	-46.7	-11.1	-11.9	52.8	-35.3	-70.6
2	x, y, z	-13.9	-2.0	-44.0	26.9	-37.8	-37.8
2	x, y, z	-3.9	-1.9	-30.4	19.1	-20.1	-20.1
4	-x, y+0.5, -z+0.5	-0.7	-1.0	-11.7	5.8	-8.0	-16
2	x, y, z	-5.5	-0.5	-17.3	13.5	-12.9	-12.9

Crystallite size estimation

The mean size of the crystalline domains, τ , were estimated using Scherrer's equation:

$$\tau = K \lambda / (\text{FWHM} * \cos \theta)$$

with K as the "Scherrer constant", λ is the wavelength of the radiation (τ has the same dimension; Å is used further), θ is the diffraction angle and FWHM = full width at half maximum of the peaks, rad; θ = is the Bragg angle.

The contribution to the peak broadening of the instrument (Bruker D2 Phaser powder diffractometer with a flat silicon, low background sample holder, at 30 kV, 10 mA for Cu-Kα radiation ($\lambda = 1.5418 \text{ \AA}$)) was accounted *via* the creation of an instrument standard with the LaB₆ 660b NIST standard³⁴ as implemented in Match!.^{35,36} The derived crystallite size for microcrystalline H₂azbpz-I-a.s (see Figure S20) is around 34 nm with an FWHM_{total} of 0.43 and an FWHM_{instr} 0.17 and for H₂azbpz-a.s.-ball mill (180 min) is around 11 nm with an FWHM_{total} of 0.9 and an FWHM_{instr} 0.17 (see Tables S7 and S8). Subsequently, the simulated powder patterns were adjusted for the peak broadening with the derived FWHM values with Mercury.^{37,38}

Table S7. Peak data used for crystallite size estimation using the Scherrer formula for microcrystalline H₂azbpz-I-a.s.

2theta [°]	d [Å]	I/I ₀	Counts	FWHM total	FWHM instr.	Crystallite size [Å]	Use
16.764	5.2885	1000	14259	0.426	0.1906	356.6	x
16.843	5.2641	47.7	680	0.426	0.1897	355.2	x
16.885	5.2509	33.2	474	0.426	0.1891	354.4	x
17.377	5.1034	437.8	6243	0.426	0.1833	346.1	x
17.51	5.0649	27.3	389	0.426	0.1818	344	x
19.053	4.658	264.5	3772	0.426	0.1648	322.4	x
19.172	4.6296	12.7	181	0.426	0.1615	318.4	
19.636	4.5212	166	2367	0.426	0.1489	304.1	x
21.13	4.2047	142.7	2034	0.426	0.1716	332.1	x
22.053	4.0307	163.2	2327	0.426	0.1649	324	x
22.154	4.0127	9.3	133	0.426	0.1643	323.4	x
23.055	3.8578	87.4	1246	0.426	0.1593	317.8	x
23.543	3.7789	330	4706	0.426	0.1568	315.1	
23.673	3.7585	12	171	0.426	0.1561	314.4	
25.54	3.4878	10.1	143	0.426	0.1474	305.7	
25.965	3.4317	582.9	8311	0.426	0.1456	303.9	

26.087	3.4159	15.4	219	0.426	0.1451	303.5	
26.863	3.319	199.3	2842	0.426	0.142	300.6	x
28.277	3.1561	121.6	1734	0.426	0.1569	318.2	x
29.13	3.0656	150.3	2143	0.426	0.1687	333.4	x
31.885	2.8068	47	670	0.426	0.1704	337.9	x
32.15	2.7842	16.1	229	0.426	0.1704	338.1	x
32.335	2.7687	9.1	130	0.426	0.1704	338.3	x
33.125	2.7044	16.6	237	0.426	0.1704	339	x
33.516	2.6738	11.4	163	0.426	0.1704	339.3	x
33.965	2.6395	41.6	594	0.426	0.1704	339.7	x
35.467	2.5311	11.4	162	0.426	0.1704	341.1	x
36.441	2.4656	17.3	247	0.426	0.1704	342	x
38.462	2.3406	9.8	140	0.426	0.1704	344.1	x
38.97	2.3112	11.6	166	0.426	0.1704	344.6	x
40.499	2.2274	22.6	322	0.426	0.1704	346.3	x
41.292	2.1865	20.2	289	0.426	0.1704	347.2	x
41.907	2.1558	10.6	151	0.426	0.1704	347.9	x
42.817	2.1121	11.3	160	0.426	0.1704	349	x
44.818	2.0223	9.9	141	0.426	0.1704	351.4	x
46.567	1.9503	28.4	405	0.426	0.1704	353.7	x
47.274	1.9228	11.4	162	0.426	0.1704	354.6	x

Table S8. Peak data used for crystallite size estimation using the Sherrer formula for H₂azbpz-II(ball mill 180min)

2theta [°]	d [Å]	I/I ₀	Counts	FWHM total	FWHM instr.	Crystallite size [Å]	Use
6.34	13.9416	14.2	134	0.9656	0.1355	100.2	
6.964	12.6937	14.9	140	0.9656	0.4018	147.6	
8.833	10.0115	14	131	0.9656	0.378	141.7	
9.374	9.4345	29	272	0.9656	0.3551	136.5	
14.521	6.1	27.8	262	0.9656	0.2228	112.7	
16.295	5.4398	1000	9397	0.9656	0.1966	109.1	x
16.616	5.3355	17.6	165	0.9656	0.1925	108.6	x
18.794	4.7216	646.9	6079	0.9656	0.1681	105.5	x
18.93	4.6881	19.4	182	0.9656	0.1668	105.4	x
19.072	4.6535	77.1	725	0.9656	0.1643	105.1	x
19.186	4.6262	40.9	384	0.9656	0.1611	104.7	x
19.342	4.5892	32.1	301	0.9656	0.1568	104.2	x
19.512	4.5495	28.3	266	0.9656	0.1522	103.6	x
19.64	4.5202	19.6	184	0.9656	0.1487	103.2	x
20.311	4.3724	334.4	3142	0.9656	0.1315	101.1	x
20.535	4.3252	40.5	380	0.9656	0.127	100.6	x
23.815	3.7364	706.6	6640	0.9656	0.1554	104.8	x
25.284	3.5225	63.5	597	0.9656	0.1485	104.2	x
25.431	3.5025	19.7	185	0.9656	0.1479	104.1	x
25.82	3.4506	42.5	399	0.9656	0.1462	104	x
26.982	3.3046	208.6	1960	0.9656	0.1415	103.6	x
28.27	3.1569	243.3	2286	0.9656	0.1568	105.9	x
28.529	3.1288	17.4	164	0.9656	0.1605	106.4	x
29.308	3.0474	407.4	3829	0.9656	0.1704	107.9	x
31.75	2.8184	25.6	241	0.9656	0.1704	108.6	x
36.11	2.4874	30.2	284	0.9656	0.1704	109.8	x
36.825	2.4408	17	159	0.9656	0.1704	110.1	x
37.862	2.3763	16.5	155	0.9656	0.1704	110.4	x
41.818	2.1602	22.5	211	0.9656	0.1704	111.8	
44.523	2.035	13.6	128	0.9656	0.1704	112.8	
45.257	2.0037	23.2	218	0.9656	0.1704	113.1	

Powder X-ray diffractograms

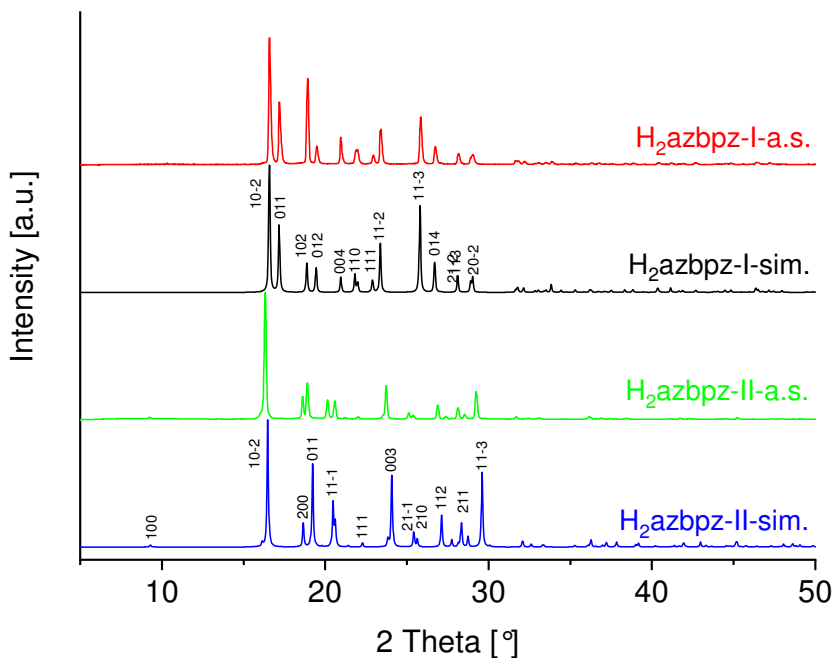


Figure S19 Comparison of the indexed PXRD spectra of H₂azbpz-I and H₂azbpz-II with the experimental as-synthesized samples after the crystallization experiments. The absence of the reflection of the [011]-plane at $2\theta = 17.4^\circ$ and the presence of the low angle reflection of the [100] plane at $2\theta = 9.3^\circ$ confirm the phase purity of H₂azbpz-II.

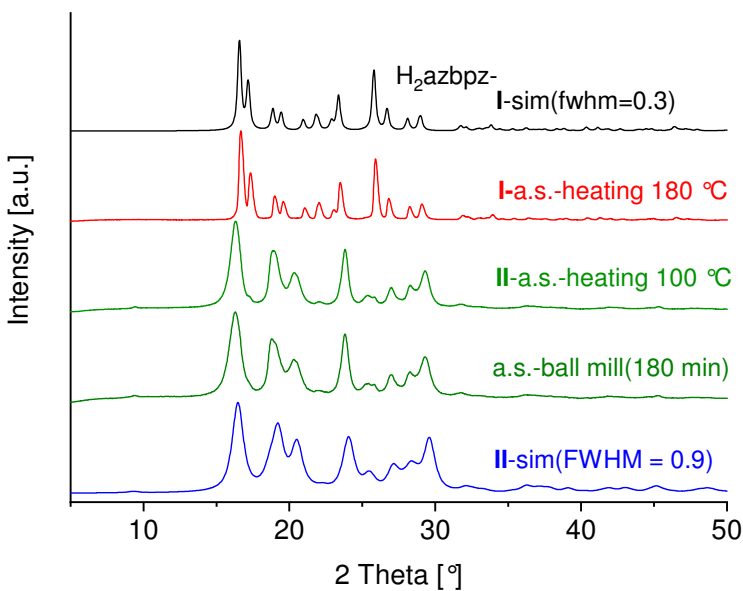


Figure S20 Comparison of the PXRD patterns of H₂azbpz-II-sim(FWHM = 0.9) (blue), H₂azbpz-II-a.s.-ball mill(180 min) (green), H₂azbpz-II-a.s.-heating 100 °C (green), H₂azbpz-I-a.s.-heating 180 °C (red), H₂azbpz-I-sim(FWHM = 0.3) (black).

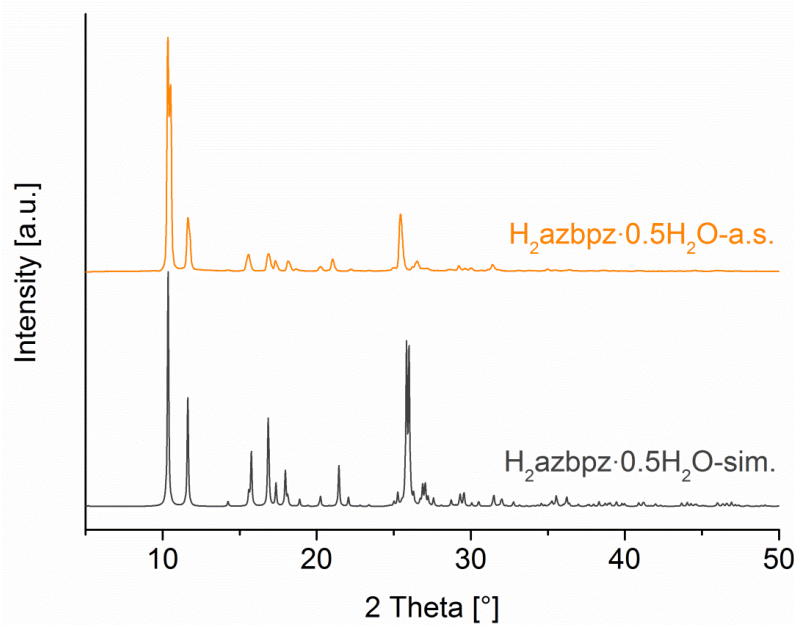


Figure S21. Comparison of the simulated (grey) and the as-synthesized (orange) of $\text{H}_2\text{azbpz}\cdot 0.5\text{H}_2\text{O}$.

DSC measurements

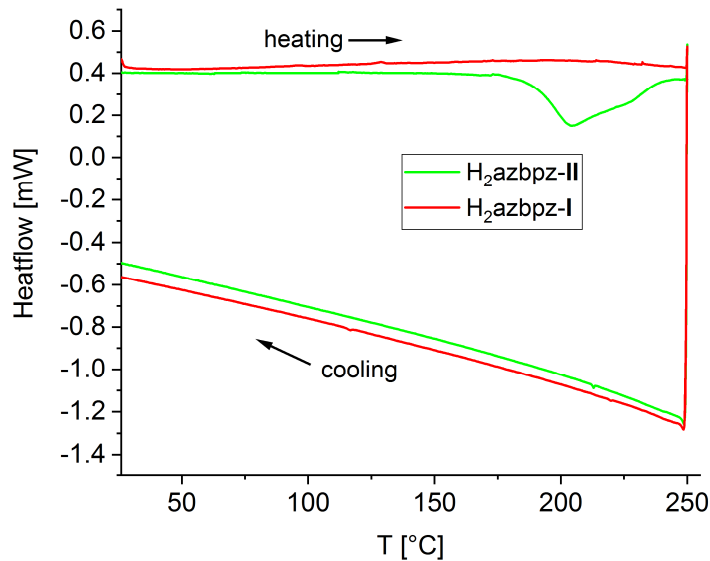


Figure S22. Comparison of DSC experiments for H₂azbpz-I (red, sample weight 5.600 mg) and H₂azbpz-II (green, sample weight 5.670 mg) in the temperature range of 25 °C–250 °C with a heating rate of ± 5 K/min. The integral of the endothermic transition for H₂azbpz-II is 87.31 mJ, $\Delta H_{\text{trans}} = 3.36 \text{ kJ/mol}$.

Raman spectra

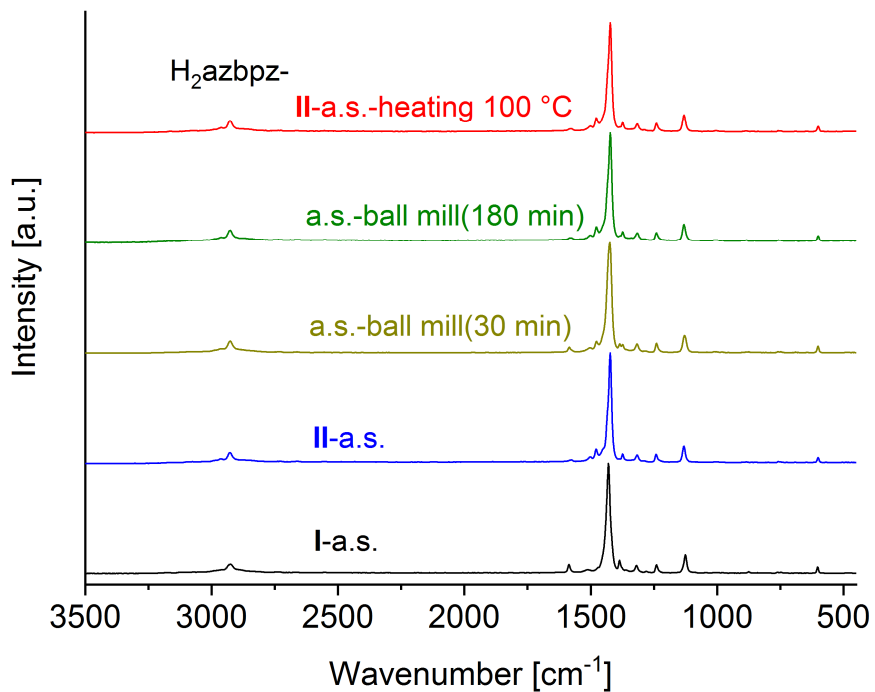


Figure S23. Raman spectra of H₂azbpz-I-a.s. (black), H₂azbpz-II-a.s. (blue), H₂azbpz-a.s. ball mill(30 min) (olive), H₂azbpz-a.s.-ball mill(180min) (green), H₂azbpz-II-a.s.-after heating 100 °C (red).

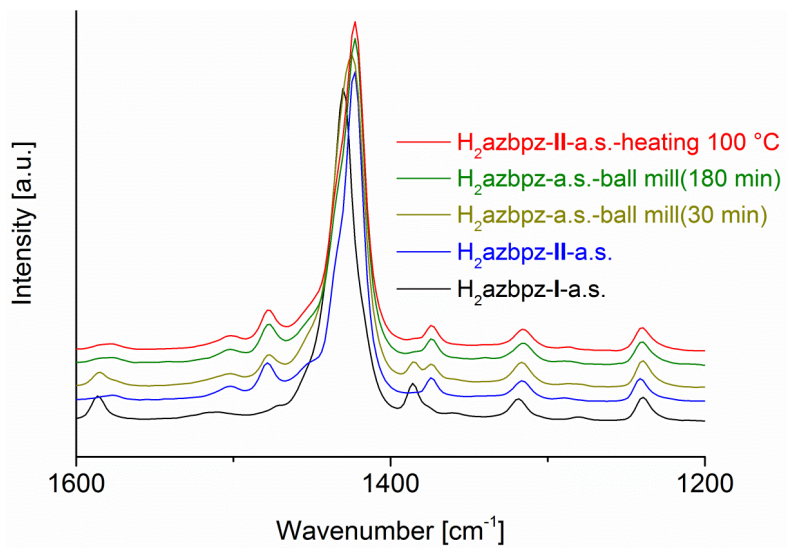


Figure S24. Excerpt of the Raman spectra between 1600-1200 cm⁻¹ of H₂azbpz-I (black), H₂azbpz-II (blue), H₂azbpz-ball mill-30 min (olive), H₂azbpz-ball mill-180 min (green), H₂azbpz-II-a.s.-heating 100 °C (red).

Solid state NMR analysis of H₂azbpz-I and H₂azbpz-II

¹H exchange spectroscopy (EXSY NMR)

In order to distinguish static from dynamic disorder in the hemihydrate form, a series of ¹H EXSY NMR spectra varying the mixing time were measured at room temperature. An exchange process was observed for the H atoms bridging the two N atoms of the two pyrazole rings in the R³(8)-hydrogen motifs in sites A and B (see for example Figure S29) which reached an equilibrium after multiple milliseconds of mixing time. (Figure 25, Figure 26a).

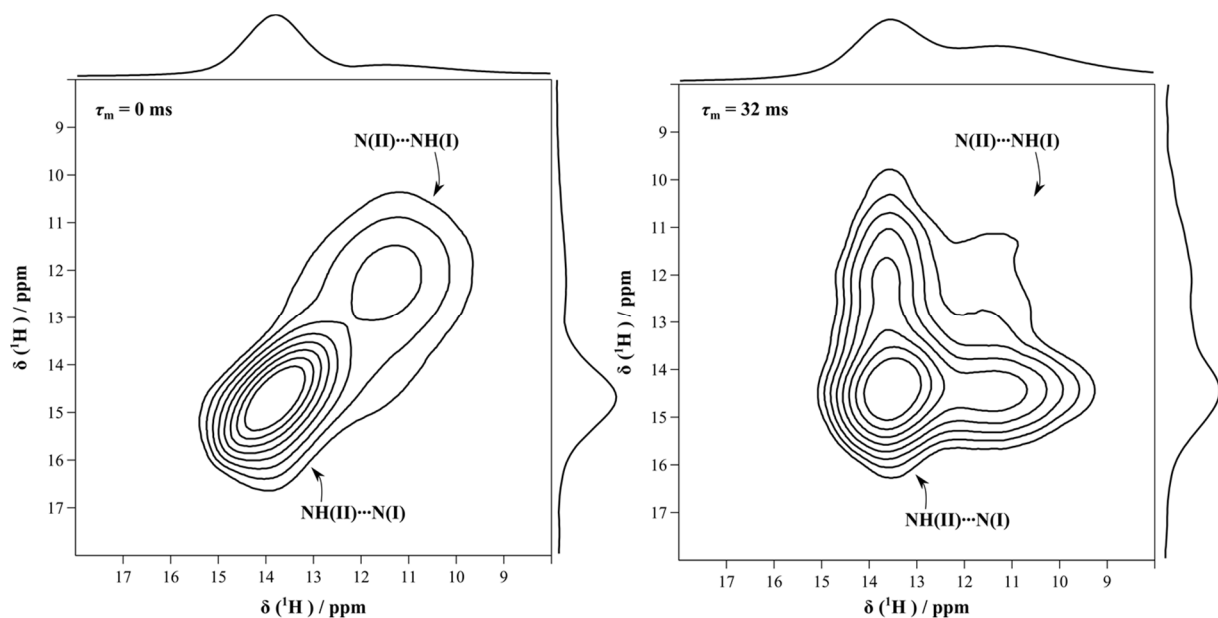


Figure S25. ¹H EXSY NMR spectra for the hemihydrate form H₂azbpz·0.5H₂O. Shown are only ¹H signals arising from the NH···N connectivities with a mixing time of 0 ms (right) and 32 ms (left) measured at 50 kHz MAS rate.

The kinetics of the exchange process was determined assuming that spin diffusion can be neglected from the behavior of the system in the initial regime (mixing times < 1 ms) where the rate of the shifting of ¹H intensity from one site (NH(II)) [$I_{H2} / (I_{H1} + I_{H2})$] to another (NH(I)) [$I_{H1} / (I_{H1} + I_{H2})$] is nearly linear (Figure 5b). The kinetic rate constant k for the process ‘NH(II)···N(I) → N(II)···NH(I)’ was estimated to be 342 ± 34 Hz.

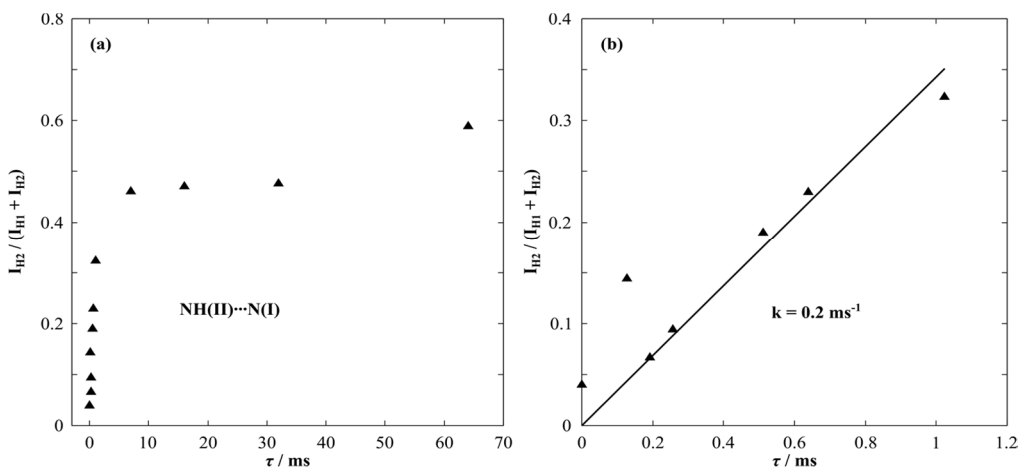


Figure S26. (a) The normalized intensities of ^1H NMR of one of the two sites undergoing exchange (the half process $\text{NH(II)}\cdots\text{N(I)} \rightarrow \text{N(II)}\cdots\text{NH(I)}$) as a function of mixing time up to 64 ms. The normalized intensities $I_{H2} / (I_{H1} + I_{H2})$ are scaled by a factor of 0.6 to set the plateau at 0.5. (b) The initial regime of the normalized intensities $I_{H2} / (I_{H1} + I_{H2})$ up to ~ 1 ms mixing time fitted using a proportionality line.

Packing analysis of related linear bispyrazoles

4,4'-bis-1H-pyrazole (H₂bpz) (UDAYIH)³⁹

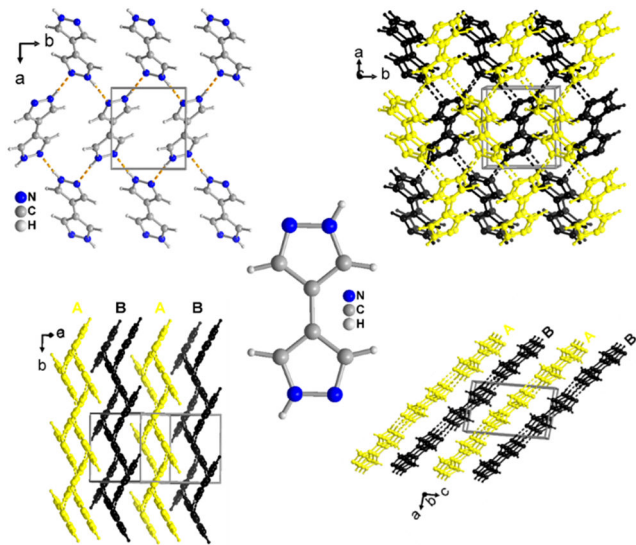


Figure S27. The analysis of the crystal packing of 4,4'-bis-1H-pyrazole (H₂bpz) (UDAYIH) highlighting the AB-packing of the hydrogen-bonded **hcb**-layers.

1,4-bis(1-H-pyrazol-4-yl)benzene (H₂bpzb) (VONVEA)⁴⁰

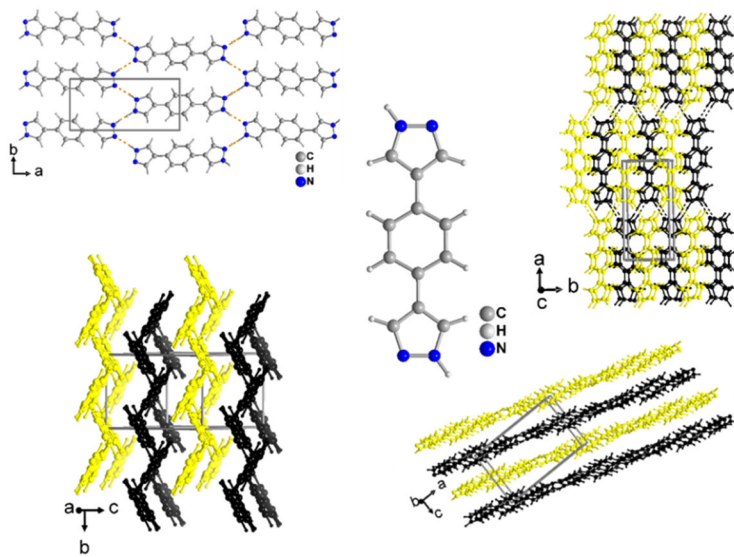


Figure S28. The analysis of the crystal packing of 1,4-bis(1-H-pyrazol-4-yl)benzene (H₂bpzb) (VONVEA) highlighting the AB-packing of the hydrogen-bonded **hcb**-layers.

The hemihydrate $\text{H}_2\text{azbpz}\cdot0.5\text{H}_2\text{O}$ with dia-topolgy introduced by a pseudo-tetrahedral water molecule

The solid-state landscape of an organic molecule can be complemented by multicomponent crystals like co-crystals, salts, solvates and hydrates.^{41,42} Although water is readily incorporated into crystal structures due its versatile hydrogen-bonding propensities, hydrates are often isolated serendipitously. Therefore they have been called the nemesis of crystal engineering.^{43,44} Gillon et al. identified eight different environments for water with O and N as hydrogen-bond acceptors and O-H and N-H as hydrogen-bond donors, respectively.⁴⁵ When water is included in such environments as an integral part of the crystal structure, water can be seen as part of the main interactions describing the crystal packing in form of water-based heterosynthons.⁴⁶⁻⁴⁹

As explained in the main text all hydrogen-bond interaction sites are used to construct the diamondoid network of **dia**- $\text{H}_2\text{azbpz}\cdot0.5\text{H}_2\text{O}$. To further shine light on the tight packing of the interpenetrating nets, we analyzed the structure of **dia**- $\text{H}_2\text{azbpz}\cdot0.5\text{H}_2\text{O}$ for interactions between dimethylpyrazole-fragments and the azo-bridges (Figure S29). The interaction of molecules of site A is governed by complementary $\text{CH}_3\text{-}\pi$ interactions of adjacent pz-fragments (similar to that identified in $\text{H}_2\text{azbpz-II}$) and a crisscross stacking of the azo-groups (Figure S29b and S29c and Table S9 for details). The interaction on site B are mainly $\pi\text{-}\pi$ interactions between pz-moieties resulting from a slippage of the H-bonded strands (Figure S29e and S29f and Table S9 for details).

Analysis of short contacts in between the interpenetrating dia-nets in H₂azbpz·0.5H₂O

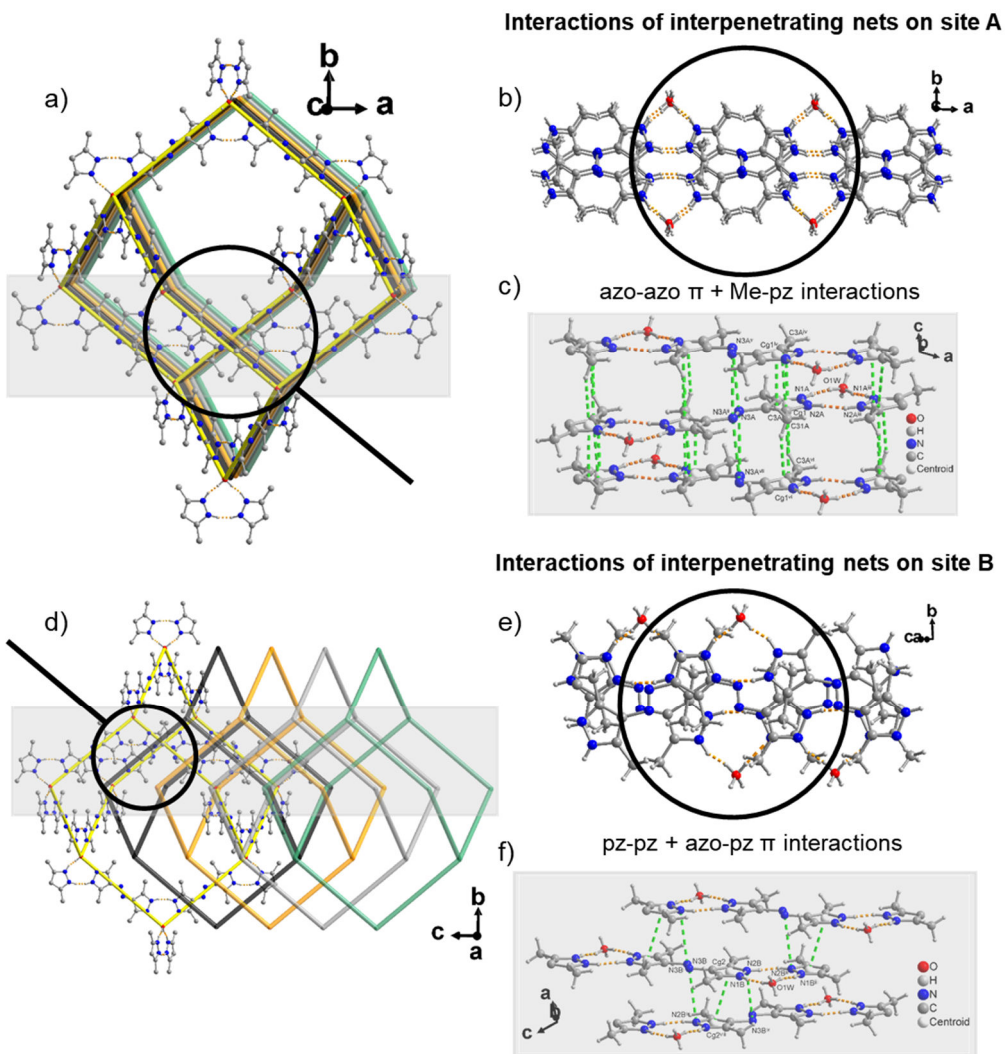


Figure S29. Analysis of the interactions between the interpenetrating nets in dia-H₂azbpz·0.5H₂O on the two molecular sites denoted with A and B. a) view on the five interpenetrating nets along the ab-plane; b) topview on site A propagating via R³(8)-hydrogen motifs showing the criss-cross azo-azo π and Me-pz interactions; c) visualization of the identified interactions between the nets highlighted in green-dashed lines; d) view on the five interpenetrating nets in the bc-plane e) topview on strains of different net types of site B propagating via R³(8)-hydrogen bonded rings along the c-axis; f) visualization of the π-π interactions in form of pz-pz and azo-pz contacts present between molecules of site B as green dashed lines. Symmetry transformations: i = 1.5-x, 1.5-y, 2-z; ii = -x, 1-y, -z; iii = 1-x, y, 0.5-z; iv = x, 1-y, 0.5+z; v = -x, y, 0.5-z; vi = x, 1-y, -0.5+z; vii = -x, y, -0.5-z; viii = -0.5+x, 1.5-y, -0.5+z; ix = 1-x, y, 1.5-z. Details on the contacts can be found in Table S9. In a) and d) C-bonded H-atoms are omitted for clarity.

Table S9. Distances [Å] and angles [°] for the shortest contacts in **dia**-H₂azbpz·0.5H₂O-RT

Site A							
CH ₃ -π	d _{ATM}	d _{PLN}	d _{CNT}	γ	∠(CH···Cg1)	d(Cg1···C1)	∠(CH···Cg1)
C(31A)-H(31E) ··· Cg1 ^{vi}	2.72	3.34	2.70	7.38	144	3.547(4)	58
C(31A)-H(31F) ··· Cg1 ^{iv}	2.82	3.65	2.79	7.95	133	3.546(4)	51
azobenzene-π							
N3A-N3A ^{v/vii}	d						
N3B-N2B (pz) ^{ix}	3.512(2)						
Site B							
π-π	d(Cg2···Cg2)	α	β	γ	d[Cg2···P ₂]	d[Cg2···P ₁]	
Cg2···Cg2 ^{viii} (pz)	3.594(2)	1.1	15.1	15.1	3.4692	3.469	
azobenzene-π							
N3B-N2B (pz) ^{ix}	d						
N3B-N2B (pz) ^{ix}	3.552 (1)						

Cg: ring centroid; α: dihedral angle between planes, β: angle Cg(I)→Cg(J) or C-H and normal to plane P; Cg···P: perpendicular distance of Cg on ring plane P; d: slippage = distance between Cg(I) and perpendicular projection of Cg(J) on ring I; d_{ATM}: distance from H to the closest sp² carbon; d_{PLN}: distance from H to the aromatic plane; d_{CNT}: distance from H to the centroid; symmetry transformations: iv = x, 1-y, 0.5+z; v = -x, y, 0.5-z; vi = x, 1-y, -0.5+z; vii = -x, y, -0.5-z; viii = -0.5+x, 1.5-y, -0.5+z; ix = 1-x, y, 1.5-z.

Although a set of intriguing supramolecular network-structures containing water as an integral part of its crystal structures were reported,⁵⁰⁻⁵² as for example the hemihydrate of 5,6-dimethylbenzimidazole containing a H-disordered water molecule in its two-dimensional H-bonded wine-rack structure,⁵³ we were rather surprised, that we could not find a report on a supramolecular **dia**-network based on a water molecule as its tetrahedral node in the literature. Due to the identified **dia**-framework based on a H₂O molecule at the center of the tetrahedral {H₂O(pz)₄}_n subunit structural similarities to the cubic ice polymorphs can be drawn. This can further be supported by reprenting **dia**-H₂azbpz·0.5H₂O in a node-and-spacer representation with the T_d-water molecules as nodes (Fig. 8c, main text). The angles between the connected tetratopic water molecules in **dia**-H₂azbpz·0.5H₂O deviate with 95.2°, 99.9°, 101.0° and 136.7° from the ideal 109.5° present in Ice I_c resulting in a distorted adamantine cage (see Figure 8b, main text, Fig. S30). It is interesting to note that the fivefold interpenetration present in **dia**-H₂azbpz·0.5H₂O is perfectly reflected by relation of the spacings between the oxygens with 2.7 Å in non-interpenetrated cubic Ice I_c and 13.34-13.35 Å in **dia**-H₂azbpz·0.5H₂O by a factor of 4.9 (Fig. S30). Therefore, **dia**-H₂azbpz·0.5H₂O can be regarded as a supramolecular interpenetrated analog of the cubic ice polymorph I_c in which the **dia**-topologies are introduced by H-disordered water molecules. Regarding the interpenetration this analogy can be expanded to the two-fold interpenetrated high pressure polymorph Ice-VII (Figure S31).⁵⁴

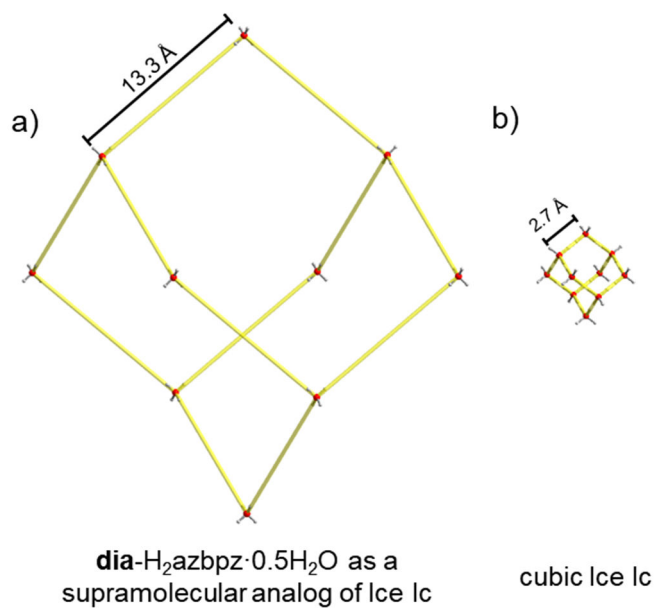


Figure 30. Adamantoid excerpt of connected T_d -H₂O molecules in a single network in **dia-H₂azbpz·0.5H₂O** (a) to highlight the supramolecular analogy to cubic Ice I_c (b). Section of the cubic Ice I_c polymorph was drawn from the cif-deposited under “ICSD 29066” were hydrogens have been added manually for drawing purposes using the program Mercury.

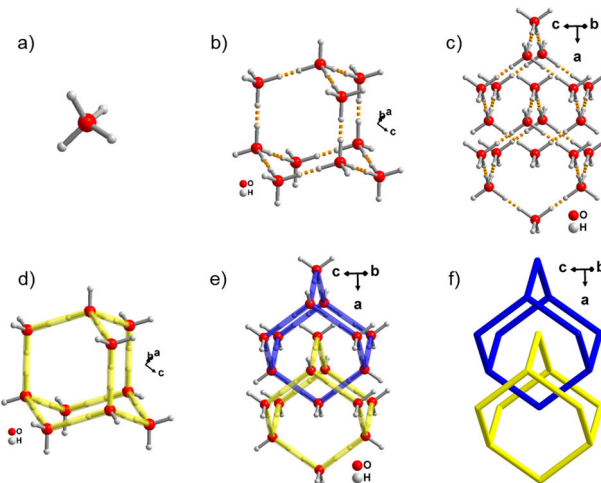


Figure S31. Visualization of the twofold interpenetrated **dia**-net in the Ice Polymorph VII. Pictures were drawn from the structure deposited under “ICSD 31868”.⁵⁴ a) Pseudo T_d -water molecule representing the hydrogen-disordered tetrahedral node present in Ice-VII b) Adamantoid excerpt of the **dia**-topology present in Ice-VII where each oxygen is involved in four hydrogen-bonds (highlighted as dashed orange lines) c) perspective view on the two independent interpenetrating hydrogen-bonded subnetworks in Ice-VII d) adamantoidal cage in the topological representation of the **dia**-topology e) perspective view on the catenated adamantan-cages in Ice-VII with the oxygen atoms as its tetrahedral nodes f) illustration of the interpenetration in Ice-VII with the two independent nets coloured in blue and yellow.

Related hydrate structures

We already stated that a structural analogy can be drawn of water-based heterosynthons of carboxylic acids and pyrazoles. Therefore also a follow-up CCDC-search was conducted for a tetrahedral $\{\text{H}_2\text{O}(\text{COOH})_4\}$ -unit based on two joined $\text{R}_3^3(10)$ carboxylic acid-water heterosynthons. This search yielded the hydrate of 2,6-dimethyl-1,3,5,7-cyclooctatetraene-1,3,5,7-tetracarboxylic acid ($\text{cotc}\cdot\text{H}_2\text{O}$) as the only result (Figure S32, SI).⁵⁷ The underlying net was later analyzed by Proserpio et al. in their systematic analysis of the interpenetration in hydrogen-bonded frameworks to be a uninodal **dia**-topology with four-fold interpenetration of class IIa. The **dia**-topology resulted from the dimeric joining of the tetrahedral tetra-acid molecules.⁵⁷

We think that in analogy to the presented topology deduction of **dia**- $\text{H}_2\text{azbpz}\cdot0.5\text{H}_2\text{O}$ the topology of $\text{cotc}\cdot\text{H}_2\text{O}$ can also be represented considering the $\{\text{H}_2\text{O}(\text{COOH})_4\}$ -units as well as the tetracarboxylic acid as tetrahedral 4-c nodes. Not surprisingly the subsequent analysis with ToposPro yields a twofold interpenetrated binodal **dia**-net of class IIa. Therefore on the one hand the hydrogen-ordered structure of $\text{cotc}\cdot\text{H}_2\text{O}$ further highlights the rarity of such tetrahedral subunits, but on the other hand only leaves **dia**- $\text{H}_2\text{azbpz}\cdot0.5\text{H}_2\text{O}$ as the first uninodal **dia**-net, where the **dia**-topology is solely introduced by a T_d -water molecule without the “assistance” of another tetrahedrally shaped entity.

Further, it is interesting to note that for the analogous but conformationally more flexible bispyrazole $\text{H}_2\text{Me}_4\text{bpz}$ (see Chart 1, main text) the existence of a hemihydrate $\text{H}_2\text{Me}_4\text{bpz}\cdot0.5\text{H}_2\text{O}$ was also reported.⁵⁸ In $\text{H}_2\text{Me}_4\text{bpz}\cdot0.5\text{H}_2\text{O}$ one part of the molecule forms H-disordered pyrazole-tetramers and the other part forms chains containing homodromic $\text{R}_4^4(10)$ $\{\text{H}_2\text{O}(\text{pz})_2\}$ -motifs including tetrahedral water molecules in an environment of $\text{OH}\cdots\text{N}$ - and $\text{NH}\cdots\text{O}$ -hydrogen bonds (Figure S33, SI). The $\{\text{H}_2\text{O}(\text{pz})_2\}$ -chain also emphasizes the complementarity of pyrazole and water in their supramolecular assembly to form heterosynthons analogous to carboxylic acids. But the structure of $\text{H}_2\text{Me}_4\text{bpz}\cdot0.5\text{H}_2\text{O}$ also highlights the importance of the planarity of H_2azbpz in combination with the complementarity to the tetrahedral water resulting in the **dia**-topology in $\text{H}_2\text{azbpz}\cdot0.5\text{H}_2\text{O}$. For the other bispyrazoles presented in Chart 1 no hydrates were reported in the literature.

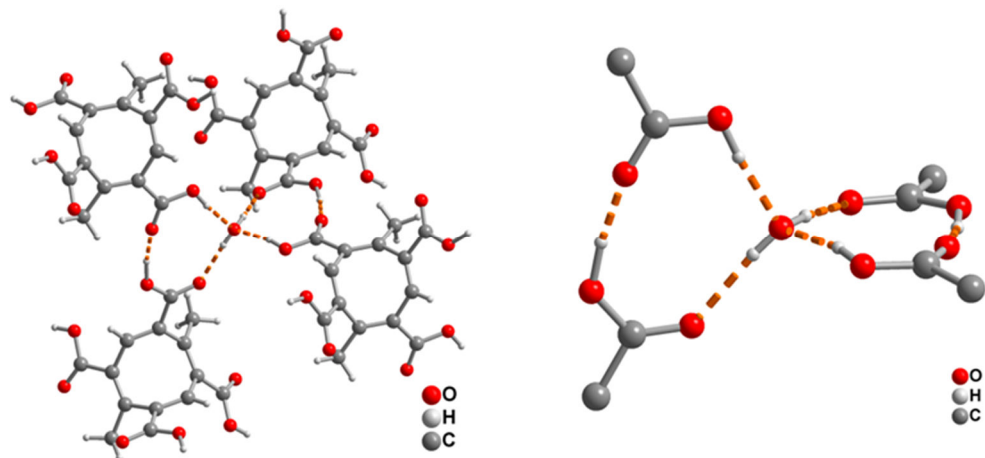


Figure S32. Representation of the tetrahedral $\{\text{H}_2\text{O}(\text{COOH})_4\}$ -subunit of two joined $\text{R}_3^3(10)$ motifs in the hydrate of 2,6-dimethyl-1,3,5,7-cyclooctatetraene-1,3,5,7-tetracarboxylic acid (Refcode QUSMEW) (hydrogen-bonds as dashed orange lines).⁵⁷

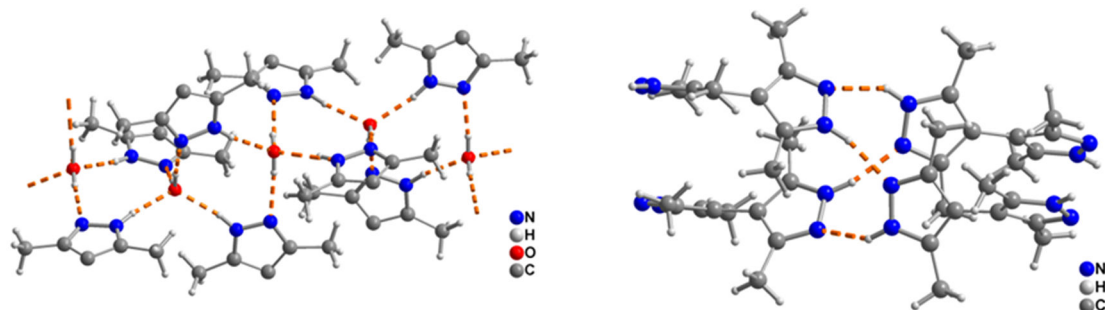


Figure S33. Two different synthons present in the hemihydrate $\text{H}_2\text{Me}_4\text{bpz} \cdot 0.5\text{H}_2\text{O}$ (Refcode EFIDUS02). Left: chain containing the water molecule; right: pyrazole tetramer, in which the NH protons are disordered over 2 positions (hydrogen-bonds as dashed orange lines).

Pictures of single crystals

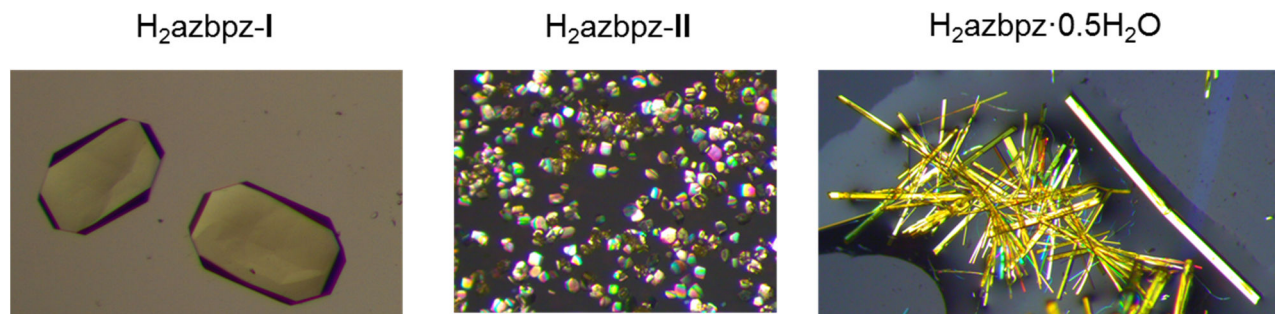


Figure S34. Images of single crystals of $\text{H}_2\text{azbpz}\text{-I}$, $\text{H}_2\text{azbpz}\text{-II}$ and $\text{H}_2\text{azbpz}\cdot 0.5\text{H}_2\text{O}$ obtained from crystallization experiments.

References

- (1) Millan, S.; Gil-Hernández, B.; Hastürk, E.; Schmitz, A.; Janiak, C., A 2D Zinc Coordination Polymer Built from the Mono-deprotonated 4,4'-Azobis(3,5-dimethyl-1H-pyrazole) Ligand. *Z. Anorg. Allg. Chem.* **2018**, *644*, 1311-1316.
- (2) Millan, S.; Makhlofi, G.; Janiak, C., Metal-4,4'-azobis(3,5-dimethyl-1H-pyrazole) Complexes with Seven- and Nine-membered Hydrogen-bonded Rings Originating from the Pyrrolic NH Function. *Z. Anorg. Allg. Chem.* **2019**, *645*, 893-899.
- (3) Hutchins, K. M.; Kummer, K. A.; Groeneman, R. H.; Reinheimer, E. W.; Sinnwell, M. A.; Swenson, D. C.; MacGillivray, L. R., Thermal Expansion Properties of Three Isostructural Co-crystals composed of Isosteric Components: Interplay between Halogen and Hydrogen Bonds. *CrystEngComm* **2016**, *18*, 8354-8357.
- (4) Wu, L. C.; Chung, W. C.; Wang, C. C.; Lee, G. H.; Lu, S. I.; Wang, Y., A Charge Density Study of π -Delocalization and Intermolecular Interactions. *Phys. Chem. Chem. Phys.* **2015**, *17*, 14177-14184.
- (5) López-Tarifa, P.; Sánchez-Sanz, G.; Alkorta, I.; Elguero, J.; Sanz, D.; Perona, A.; Claramunt, R. M., The Tautomeric Structures of 3(5),3'(5')-Azopyrazole [(E)-1,2-di(1H-pyrazol-3(5)-yl)diazene]: The Combined use of NMR and Electronic Spectroscopies with DFT calculations. *J. Mol. Struct.* **2012**, *1015*, 138-146.
- (6) Li, J.; Gao, J.; Li, H.; Yang, X.; Liu, Y., Study of the synthesis mechanism of 4-amino-3,5-dimethyl pyrazole by fibre optic in-line FT-IR spectroscopy combined with independent component analysis. *Anal. Methods* **2014**, *6*, 4305-4311.
- (7) Nikitina, P. A.; Kuz'mina, L. G.; Perevalov, V. P.; Tkach, I. I., Synthesis and study of prototropic tautomerism of 2-(3-chromenyl)-1-hydroxyimidazoles. *Tetrahedron* **2013**, *69*, 3249-3256.
- (8) Koçyiğit Kaymakçıoğlu, B.; Rollas, S., Synthesis, characterization and evaluation of antituberculosis activity of some hydrazones. *Farmaco* **2002**, *57*, 595-599.

- (9) Kamali, N.; Gniado, K.; McArdle, P.; Erxleben, A., Application of Ball Milling for Highly Selective Mechanochemical Polymorph Transformations. *Org. Process Res. Dev.* **2018**, *22*, 796-802.
- (10) Fischer, F.; Greiser, S.; Pfeifer, D.; Jäger, C.; Rademann, K.; Emmerling, F., Mechanochemically Induced Conversion of Crystalline Benzamide Polymorphs by Seeding. *Angew. Chem. Int. Ed.* **2016**, *55*, 14281-14285.
- (11) Fischer, F.; Greiser, S.; Pfeifer, D.; Jäger, C.; Rademann, K.; Emmerling, F., Mechanochemically Induced Conversion of Crystalline Benzamide Polymorphs by Seeding. *Angew. Chem. Int. Ed.* **2016**, *55*, 14281-14285.
- (12) Boldog, I.; Rusanov, E. B.; Sieler, J.; Blaurock, S.; Domasevitch, K. V., Construction of extended Networks with a Trimeric Pyrazole Synthon. *Chem. Commun.* **2003**, 740-741.
- (13) Foces-Foces, C.; Alkorta, I.; Elguero, J., Supramolecular Structure of 1H-Pyrazoles in the Solid State: a Crystallographic and Ab Initio Study. *Acta Crystallogr., Sect. B* **2000**, *56*, 1018-1028.
- (14) Chakravorty, S.; Platts, J. A.; Das, B. K., Novel C-H...C contacts involving 3,5-dimethylpyrazole ligands in a tetracoordinate Co(II) complex. *Dalton Trans.* **2011**, *40*, 11605-12.
- (15) Platts, J. A.; Howard, S. T.; Woźniak, K., Quantum chemical evidence for C–H … C hydrogen bonding. *Chem. Commun.* **1996**, 63-64.
- (16) Gronert, S.; Keefe, J. R., Identity hydride-ion transfer from C-H donors to C acceptor sites. Enthalpies of hydride addition and enthalpies of activation. Comparison with C…H…C proton transfer. An ab initio study. *J. Am. Chem. Soc.* **2005**, *127*, 2324-33.
- (17) Krishnamohan Sharma, C. V.; Broker, G. A.; Rogers, R. D., Polymorphous One-Dimensional Tetrapyridylporphyrin Coordination Polymers Which Structurally Mimic Aryl Stacking Interactions. *J. Solid State Chem.* **2000**, *152*, 253-260.
- (18) Duarte, M. T.; Piedade, M. F. M.; Robalo, M. P.; Teixeira, A. P. S.; Garcia, M. H., A supramolecular zigzag chain of organometallic dipoles mediated by PF₆⁻ anions. *Acta Crystallogr., Sec. C* **2005**, *61*, m386-m389.
- (19) Das, S.; Bharadwaj, P. K., Self-Assembly of a Luminescent Zinc(II) Complex: a Supramolecular Host–Guest Fluorescence Signaling System for Selective Nitrobenzene Inclusion. *Inorg. Chem.* **2006**, *45*, 5257-5259.
- (20) Gogoi, A.; Das, A.; Frontera, A.; Verma, A. K.; Bhattacharyya, M. K., Energetically significant unconventional π-π contacts involving fumarate in a novel coordination polymer of Zn(II): In-vitro anticancer evaluation and theoretical studies. *Inorg. Chim. Acta* **2019**, *493*, 1-13.

- (21) Janiak, C., A critical account on π - π stacking in metal complexes with aromatic nitrogen-containing ligands. *Journal of the Chemical Society, Dalton Trans.* **2000**, 3885-3896.
- (22) Roesky, H. W.; Andruh, M., The interplay of coordinative, hydrogen bonding and π - π stacking interactions in sustaining supramolecular solid-state architectures: A study case of bis(4-pyridyl)- and bis(4-pyridyl-N-oxide) tectons. *Coord. Chem. Rev.* **2003**, 236, 91-119.
- (23) M. J. Turner, J. J. McKinnon, S. K. Wolff, D. J. Grimwood, P. R. Spackman, D. Jayatilaka, M. A. Spackman, *CrystalExplorer17*, Version 17.5, © 2005–2019 University of Western Australia, 2017, <http://hirshfeldsurface.net>.
- (24) Spackman, M. A.; McKinnon, J. J., Fingerprinting intermolecular interactions in molecular crystals. *CrystEngComm* **2002**, 4, 378-392.
- (25) McKinnon, J. J.; Spackman, M. A.; Mitchell, A. S., Novel tools for visualizing and exploring intermolecular interactions in molecular crystals. *Acta Crystallogr, Sec. B* **2004**, 60, 627-668.
- (26) McKinnon, J. J.; Fabbiani, F. P. A.; Spackman, M. A., Comparison of Polymorphic Molecular Crystal Structures through Hirshfeld Surface Analysis. *Cryst. Growth Des.* **2007**, 7, 755-769.
- (27) McKinnon, J. J.; Jayatilaka, D.; Spackman, M. A., Towards quantitative analysis of intermolecular interactions with Hirshfeld surfaces. *Chem. Commun.* 2007, 3814-3816.
- (28) Spackman, M. A.; Jayatilaka, D., Hirshfeld surface analysis. *CrystEngComm* 2009, 11, 19-32.
- (29) Turner, M. J.; Grabowsky, S.; Jayatilaka, D.; Spackman, M. A., Accurate and Efficient Model Energies for Exploring Intermolecular Interactions in Molecular Crystals. *J. Phys. Chem. Lett.* **2014**, 5, 4249-55.
- (30) Mackenzie, C. F.; Spackman, P. R.; Jayatilaka, D.; Spackman, M. A., CrystalExplorer model energies and energy frameworks: extension to metal coordination compounds, organic salts, solvates and open-shell systems. *IUCrJ* **2017**, 4, 575-587.
- (31) Thomas, S. P.; Spackman, P. R.; Jayatilaka, D.; Spackman, M. A., Accurate Lattice Energies for Molecular Crystals from Experimental Crystal Structures. *J. Chem. Theory Comput.* **2018**, 14, 1614-1623.
- (32) Vande Velde, C. M. L.; Zeller, M.; Azov, V. A., Comparison of computationally cheap methods for providing insight into the crystal packing of highly bromomethylated azobenzenesThis paper is dedicated to the memory of Professor Philip Coppens, a

- true giant in crystallography, and an inspiration. *Acta Crystallogr., Sec. C* **2018**, *74*, 1692-1702.
- (33) Thomas, S. P.; Spackman, M. A., The Polymorphs of ROY: A Computational Study of Lattice Energies and Conformational Energy Differences. *Austr. J. Chem.* **2018**, *71*, 279-284.
- (34) Black, D. R.; Windover, D.; Henins, A.; Filliben, J.; Cline, J. P., Certification of Standard Reference Material 660B. *Powder Diffr.* **2012**, *26*, 155-158.
- (35) Putz, H. Match!, Version 3.8; Phase Identification from Powder Diffraction; Crystal Impact-K. Brandenburg & H. Putz Gbr: Bonn, Germany, 2003-2019.
- (36) Match!. Online Help: Crystallite Size Estimation.
https://www.crystalimpact.com/match/help/idh_crystallite_size.htm (accessed Oct 20, 2019))
- (37) Macrae, C. F.; Edgington, P. R.; McCabe, P.; Pidcock, E.; Shields, G. P.; Taylor, R.; Towler, M.; van de Streek, J., Mercury: visualization and analysis of crystal structures. *J. Appl. Crystallogr.* **2006**, *39*, 453-457.
- (38) Macrae, C. F.; Bruno, I. J.; Chisholm, J. A.; Edgington, P. R.; McCabe, P.; Pidcock, E.; Rodriguez-Monge, L.; Taylor, R.; van de Streek, J.; Wood, P. A., Mercury CSD 2.0 - new features for the visualization and investigation of crystal structures. *J. Appl. Crystallogr.* **2008**, *41*, 466-470.
- (39) Boldog, I.; Rusanov, E. B.; Chernega, A. N.; Sieler, J.; Domasevitch, K. V., Acentric Extended Solids by Self Assembly of 4,4'-Bipyrazolyls. *Angew. Chem. Int. Ed.* **2001**, *40*, 3435-3438.
- (40) Maspero, A.; Galli, S.; Masciocchi, N.; Palmisano, G., Facile Preparation of Polytopic Azoles: Synthesis, Characterization, and X-ray Powder Diffraction Studies of 1,4-Bis(pyrazol-4-yl)- and 1,4-Bis(tetrazol-5-yl)benzene. *Chem. Lett.* **2008**, *37*, 956-957.
- (41) Bond, A. D., What is a Co-crystal? *CrystEngComm* **2007**, *9*, 833-834.
- (42) Aitipamula, S.; Banerjee, R.; Bansal, A. K.; Biradha, K.; Cheney, M. L.; Choudhury, A. R.; Desiraju, G. R.; Dikundwar, A. G.; Dubey, R.; Duggirala, N.; Ghogale, P. P.; Ghosh, S.; Goswami, P. K.; Goud, N. R.; Jetti, R. R. K. R.; Karpinski, P.; Kaushik, P.; Kumar, D.; Kumar, V.; Moulton, B.; Mukherjee, A.; Mukherjee, G.; Myerson, A. S.; Puri, V.; Ramanan, A.; Rajamannar, T.; Reddy, C. M.; Rodriguez-Hornedo, N.; Rogers, R. D.; Row, T. N. G.; Sanphui, P.; Shan, N.; Shete, G.; Singh, A.; Sun, C. C.; Swift, J. A.; Thaimattam, R.; Thakur, T. S.; Kumar Thaper, R.; Thomas, S. P.; Tothadi, S.; Vangala, V. R.; Variankaval, N.; Vishweshwar, P.; Weyna, D. R.; Zaworotko, M. J., Polymorphs, Salts, and Cocrystals: What's in a Name? *Cryst. Growth Des.* **2012**, *12*, 2147-2152.

- (43) Clarke, H. D.; Arora, K. K.; Bass, H.; Kavuru, P.; Ong, T. T.; Pujari, T.; Wojtas, L.; Zaworotko, M. J., Structure–Stability Relationships in Cocrystal Hydrates: Does the Promiscuity of Water Make Crystalline Hydrates the Nemesis of Crystal Engineering? *Cryst. Growth Des.* **2010**, *10*, 2152-2167.
- (44) Bajpai, A.; Scott, H. S.; Pham, T.; Chen, K.-J.; Space, B.; Lusi, M.; Perry, M. L.; Zaworotko, M. J., Towards an Understanding of the Propensity for Crystalline Hydrate Formation by Molecular Compounds. *IUCrJ* **2016**, *3*, 430-439.
- (45) Gillon, A. L.; Feeder, N.; Davey, R. J.; Storey, R., Hydration in Molecular Crystals—A Cambridge Structural Database Analysis. *Cryst. Growth Des.* **2003**, *3*, 663-673.
- (46) Varughese, S.; Desiraju, G. R., Using Water as a Design Element in Crystal Engineering. Host–Guest Compounds of Hydrated 3,5-Dihydroxybenzoic Acid. *Cryst. Growth Des.* **2010**, *10*, 4184-4196.
- (47) Banthia, S.; Samanta, A., Long and Short Brick Network Architecture: Role of Water Molecules Acting as Three-Connecting Spacers. *Cryst. Growth Des.* **2006**, *6*, 360-362.
- (48) Babu, N. J.; Nangia, A., Water-Mediated Multicenter Synthon and Aromatic C–H → N Isostructurality. *Cryst. Growth Des.* **2006**, *6*, 1753-1756.
- (49) Mohamed, S.; Li, L., From Serendipity to Supramolecular Design: Assessing the Utility of Computed Crystal Form Landscapes in Inferring the Risks of Crystal Hydration in Carboxylic Acids. *CrystEngComm* **2018**, *20*, 6026-6039.
- (50) Li, X.; Xu, X.; Yuan, D.; Weng, X., Hexagonal Prismatic Dodecameric Water Cluster: A Building Unit of the Five-Fold Interpenetrating Six-Connected Supramolecular Network. *Chem. Commun.* **2012**, *48*, 9014-9016.
- (51) Peuronen, A.; Lehtimäki, E.; Lahtinen, M., Self-Assembly of Water-Mediated Supramolecular Cationic Archimedean Solids. *Cryst. Growth Des.* **2013**, *13*, 4615-4622.
- (52) Clarke, H. D.; Arora, K. K.; Wojtas, Ł.; Zaworotko, M. J., Polymorphism in Multiple Component Crystals: Forms III and IV of Gallic Acid Monohydrate. *Cryst. Growth Des.* **2011**, *11*, 964-966.
- (53) Zieliński, W.; Katrusiak, A., Hydrate Smaller than the Anhydrate. *CrystEngComm* **2015**, *17*, 5468-5473.
- (54) Kamb, B.; Davis, B. L., Ice VII, the Densest Form of Ice. *Proc. Natl. Acad. Sci.* **1964**, *52*, 1433-1439.
- (55) Dowell, L. G.; Rinfret, A. P., Low-Temperature Forms of Ice as Studied by X-Ray Diffraction. *Nature* **1960**, *188*, 1144-1148.
- (56) Macrae, C. F.; Bruno, I. J.; Chisholm, J. A.; Edgington, P. R.; McCabe, P.; Pidcock, E.; Rodriguez-Monge, L.; Taylor, R.; van de Streek, J.; Wood, P. A., Mercury CSD

- 2.0 - New Features for the Visualization and Investigation of Crystal Structures. *J. Appl. Crystallogr.* **2008**, *41*, 466-470.
- (57) Vij, A.; Palmer, J. L.; Chauhan, K.; Williams, R. V., The Role of Hydrogen Bonding in Pseudo-Macrocyclic Ring Formation in 2,6-Dimethyl-1,3,5,7-cyclooctatetraene 1,3,5,7-Tetracarboxylic Acid Monohydrate. *J. Chem. Crystallogr.* **2000**, *30*, 621-626.
- (58) Jin, S.; Huang, Y.; Fang, H.; Wang, T.; Ding, L., 3,5,3',5'-Tetramethyl-4,4'-bi(1H-pyrazolyl) Hemihydrate. *Acta Crystallogr., Sect. E* **2012**, *68*, o2896.

3.3 Metal-4,4'-azobis(3,5-dimethyl-1H-pyrazole) complexes with 7- and 9-membered hydrogen-bonded rings originating from the pyrrolic N-H function

The work presented in this chapter has been published in:

S. Millan, G. Makhloufi and C. Janiak *Z. Anorg. Allg. Chem.* **2019**, *645*, 893-899.

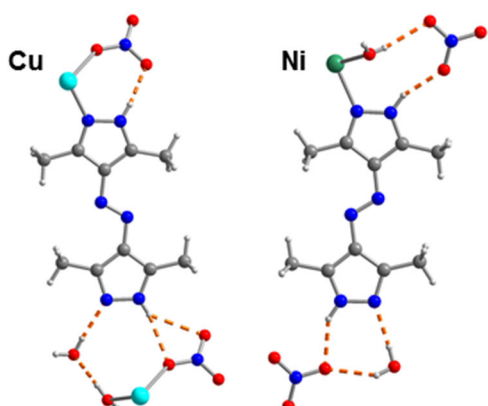
DOI: 10.1002/zaac.201900052

as part of the Special Issue dedicated to Gerd Meyer on the occasion of his 70thth birthday.

The article is reprinted with permission of John Wiley and Sons, Inc.

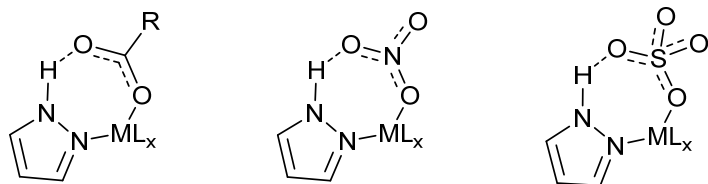
Abstract

The metal complexes $[\text{Cu}(\text{NO}_3)_2(\text{H}_2\text{O})_2(\text{H}_2\text{azbpz})_2] \cdot 2\text{H}_2\text{O}$ (**1**) and $[\text{Ni}(\text{H}_2\text{O})_4(\text{H}_2\text{azbpz})_2](\text{NO}_3)_2 \cdot 2\text{H}_2\text{O}$ (**2**) of 4,4'-azobis(3,5-dimethyl-1H-pyrazole) (H_2azbpz) incorporate the bipyrazole as a monodentate ligand and are associated into supramolecular architectures via hydrogen bonds and azo-pz π -interactions in the solid state. Whereas in **1** a cis configuration is integrated and the NH function adjacent to the metal-coordinating nitrogen atom gives rise to a seven-membered anion-assisted hydrogen-bonded ring around the metal center bringing the NH function in endo-position to the azo-bridge. The interplay of hydrogen-bonds and dimeric azo-pz π -interactions in **1** form one-dimensional supramolecular chains, which are further interconnected by a heterodromic D_{2h} -symmetric tetrameric water ring. In **2** a trans form of H_2azbpz is mono-coordinated and the synergy of hydrogen-bonded rings around the metal center and continuous azo-pz π -interactions form a two-dimensional supramolecular network structure. The supramolecular packings of **1** and **2** is further underpinned by the analysis of their Hirshfeld surface areas.



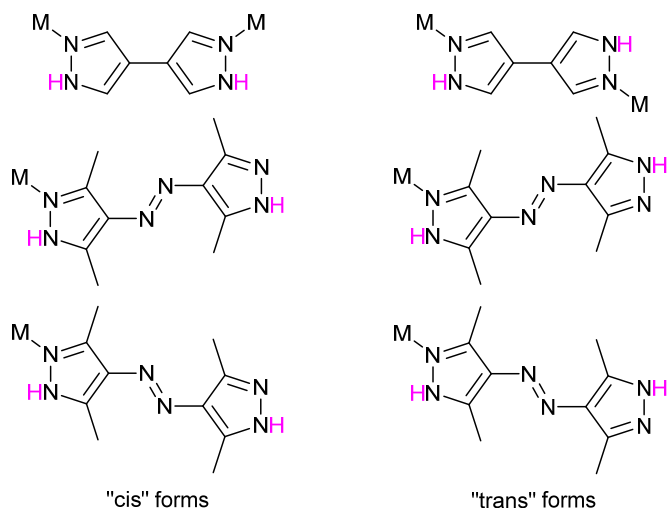
Introduction

Bipyrazoles are versatile tectons in the field of crystal engineering. Their crystal structures alone, as salts or co-crystals yield a multitude of fascinating supramolecular network structures.^[1-6] Just as versatile are the metal-ligand coordination compounds from bipyrazoles which vary in their dimensionality from 0D, 1D over 2D to 3D.^[7-9] Bipyrazoles can be used as ligands in their neutral form,^[10-14] in their mono-anionic form as pyrazole-pyrazolates^[15-17] and in their di-anionic forms as bipyrazolates.^[18-20] Neutral bipyrazoles yield coordination compounds comparable to those obtained with 4,4'-bipyridines but with the adjacent pyrrolic NH function as an additional interaction site. In such metal-coordinated pyrazoles the acidity of the pyrrolic NH-function often increases, making it a better hydrogen bond donor.^[21] In this regard, especially seven-membered hydrogen-bonded rings around the metal center in pyrazole coordination compounds with coordinating counter-balancing oxo-anions like carboxylates, nitrate or sulfate as structural motifs in the so-called second-sphere coordination are frequently observed (Scheme 1).^[10,22-30]



Scheme 1. Representation of seven-membered hydrogen-bonded rings around the metal-center with anions like carboxylates, nitrate and sulfate as a structural motif of second-sphere coordination in pyrazole coordination compounds.

The two pyrazolyl rings in bipyrazoles can rotate freely around the central C–C bond such that a metal-bridging neutral bipyrazole can adopt a cis or trans coordination configuration, in the co-planar ring limit, both with respect to the two metal or the two N-H hydrogen atoms (Scheme 2). Even with an azo spacer between the two pyrazolyl rings and with only one coordinating metal atom in the monodentate ligand 4,4'-azobis(3,5-dimethyl-1H-pyrazole) (H_2azbpz) we can still discern the cis and trans form for the planar ligand based on the relative position of the N-H atoms.^[26,28,30] In the H_2azbpz ligand there are then two cis and trans forms, each, due to an additional different orientation of the bent azo spacer (Scheme 2).



Scheme 2. Possible cis-trans conformations of bridging bipyrazole and of (monodentate metal-coordinated) H₂azbpz in the limit of a planar ligand arrangement. The endo-exo conformation of the NH-function with respect to the azo spacer is illustrated in Scheme S1 in SI.

When such cis and trans forms are seen in bipyrazole coordination compounds hydrogen-bonds have been identified to play an important role via the so-called second sphere coordination to lock the conformers into place and to localize the NH group through these supramolecular assemblies.^[31] Referring to this concept, the anionic ring around the metal center seen in metal-pyrazole-coordination compounds was regarded as a possible strategy to observe the neutral, NH-group versions of H₂azbpz in a supramolecular matrix.^[25,26,28,30] In addition the synergy of the H-bond interactions affects the cis-trans orientation of bipyrazoles in such complexes or coordination polymers. Alongside hydrogen-bonds other weak interactions usually play also a crucial role to explain the packing of metal-containing compounds. In this regard, especially non-directional π–π interactions gained a lot of attention.^[32–34] Besides the aforementioned potential interaction sites for hydrogen bonds, the dimethylpyrazole-moiety and the azo-function could also be prone to show such interactions via their π-electronic systems to adjacent entities.

Supplementing our studies on coordination compounds of H₂azbpz,^[17] we herein present the incorporation of its neutral, non-deprotonated form into the monomeric metal-complexes [Cu(NO₃)₂(H₂O)₂(H₂azbpz)₂]·(H₂O)₂ (**1**) and [Ni(H₂O)₄(H₂azbpz)₂](NO₃)₂·2H₂O (**2**). Their assembly into supramolecular architectures is analyzed with an emphasis on hydrogen-bonding ring motifs and azo-π interactions. The supramolecular crystal packing of **1** and **2** is further manifested by the analysis of their Hirshfeld surface areas.

Results and Discussion

The slow evaporation of an ethanolic solution of $\text{Cu}(\text{NO}_3)_2 \cdot 2.5\text{H}_2\text{O}$ and H_2azbpz yielded block-shaped yellow-greenish crystals of composition $[\text{Cu}(\text{NO}_3)_2(\text{H}_2\text{O})_2(\text{H}_2\text{azbpz})_2] \cdot (\text{H}_2\text{O})_2$ (**1**). The representative nature of the investigated single crystal for X-ray crystal structure elucidation was confirmed by positively matching the experimental and simulated powder X-ray diffractograms and, thereby, confirmed the overall phase-purity (Fig. S1, SI). The asymmetric unit contains one nitrato, one aqua (O_1) and one monodentate H_2azbpz ligand: all bound to the Cu(II) ion, which sits on the inversion center (Figure 1). Additionally one water of crystallization (O_2) is included. The d^9 -Cu(II) ion is coordinated in a Jahn-Teller-distorted tetragonal bipyramidal with the aqua ligands and pyrazole-group of the H_2azbpz ligands in the equatorial positions (bond lengths: Cu– O_1 1.9617(14) Å, Cu–N1 1.9902(15)). The nitrato ligands sit on the apical positions of the bipyramid with elongated bond lengths of Cu– O_5 2.5359(14) Å.

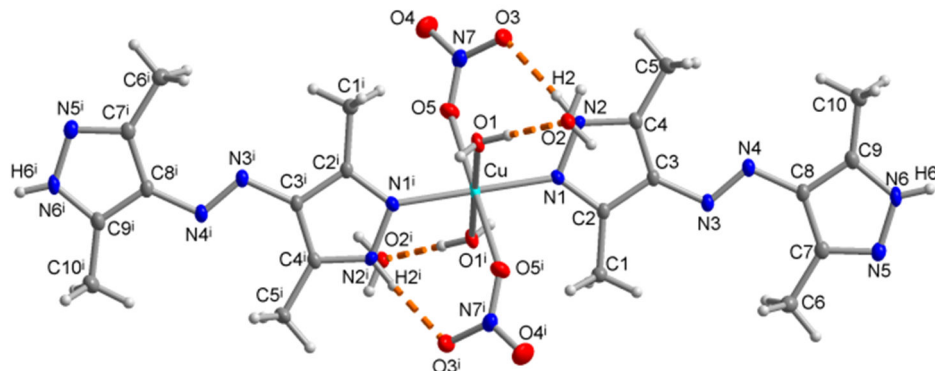


Figure 1. Extended asymmetric unit of $[\text{Cu}(\text{NO}_3)_2(\text{H}_2\text{O})_2(\text{H}_2\text{azbpz})_2] \cdot (\text{H}_2\text{O})_2$ (**1**). (50% thermal ellipsoids, hydrogen-bonds in yellow dotted lines, H atoms with arbitrary radii). Symmetry transformation: $i = 1-x, 1-y, 1-z$. Selected bond distances and angles are given in Table S1 in SI.

In **1** the copper-coordinated pyrazole group of the H_2azbpz ligand participates with the nitrate ion in a seven-membered hydrogen-bonded ring around the metal center (Cu–N1–N2–H2–O3–N7–O5) bringing the NH-function in an endo-position with regard to the azo-group. In the non-coordinating pyrazole group, the NH-function forms a bifurcated hydrogen bond to the nitrate ion and the pyridinic nitrogen atom accepts a hydrogen bond from one of the crystal water molecules. This non-coordinated pyrazole-moiety is, thus, integrated in a nine-membered hydrogen-bonded ring around the metal center of an adjacent entity (Cu–O1–H2O1–O2–H1O2–N5–N6–H6–O5) with the NH-function in the exo-position to the azo-group

(Figure 3). The nine-membered homodromic ring (Scheme S2, SI) can be denoted as $R_3^3(9)$ in the Etter-notation.^[35-39] H₂azbpz adopts a cis form with endo-exo-position of NH towards the azo-bridge (Scheme S1, SI).

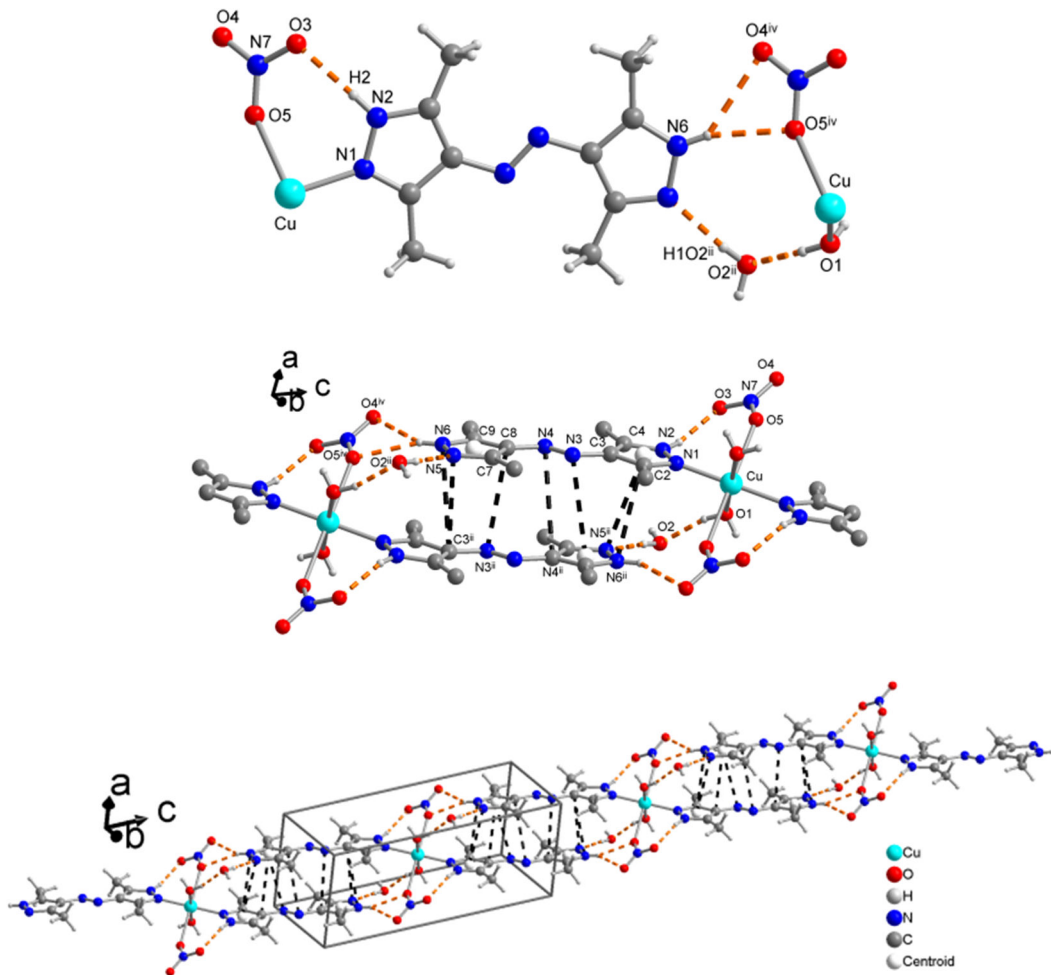


Figure 2. Top: 7-membered and 9-membered hydrogen-bonded rings with the cis form of H₂azbpz in **1** (hydrogen-bonds as orange-dashed lines). Middle: representation of the dimeric stacking of adjacent molecular fragments in **1** with azo-pi-contacts as black-dashed lines. Bottom: one-dimensional hydrogen-bonded chain along the c-axis in **1**. See Table 1 for hydrogen-bonding details. See Figure S5 for details on the azo-pi contacts. Symmetry transformations: ii = $-x+1, -y+1, -z$; iv = $x, y, z-1$.

Apart from this asymmetrical configuration of H₂azbpz (see Figure 2 Top), the seven- and nine-membered hydrogen-bonded rings around the metal center in **1** give rise to a one-dimensional hydrogen-bonded chain along the c-axis (see Figure 2 Bottom). This is accompanied by an offset dimeric stacking between the azo-function and the dimethylpyrazole-moieties (dmpz) of H₂azbpz-ligands from adjacent fragments (see Figure 2 Middle and Figure S5 for details).

These H-bonded chains are interconnected by hydrogen-bonds of the hydrogen atoms of the coordinated water molecule H1O1 and the water molecule of crystallization H2O2 not involved in forming the mentioned seven- and nine-membered hydrogen-bonded rings (see Figure 3 Top: hydrogen-bonds interconnecting the chains are represented as green-dashed lines).

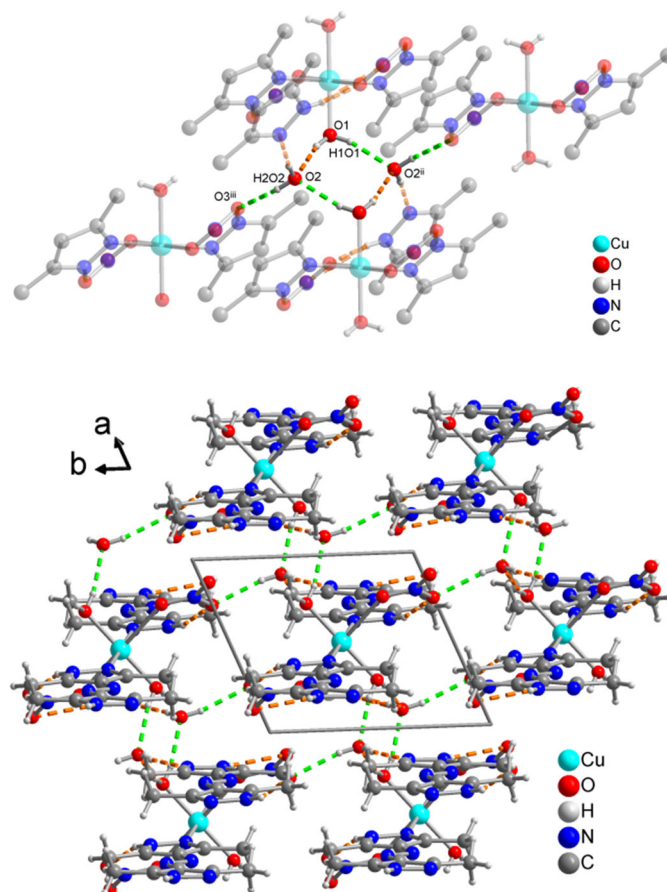


Figure 3. Top: D_{2h} -symmetric heterodromic $(\text{H}_2\text{O})_4$ -cluster found in **1** with the hydrogen bonds $\text{O}1-\text{H}1\text{O}1 \cdots \text{O}2$ and $\text{O}2-\text{H}2\text{O}2 \cdots \text{O}3$ between the one-dimensional strains in green-dashed lines. Bottom: arrangement of the one-dimensional chains. See Table 1 for details on hydrogen bonds. Symmetry transformations: $\text{ii} = -x+1, -y+1, -z$; $\text{iii} = -x+1, -y, -z+1$.

In total the water molecules build a tetrameric heterodromic water-cluster with D_{2h} -symmetry connecting four molecular entities from different chains in **1**, which results from the aqua ligands with O1 acting as double hydrogen bond donors and the crystal water molecules with O2 as double hydrogen bound acceptors (Figure 3 and S3, SI). The $\text{O} \cdots \text{O}$ distances are 2.713(2) Å and 2.664(2) Å (Table 1). It has been found, that the stability of such water clusters decreases in the order homodromic, antidromic and heterodromic (Scheme S2,

SI).^[35] This exemplifies the cooperativity of the association of the water cluster in the crystal structure of **1**. The H-bonding pattern in the cyclic water tetramer can be denoted as R₂²(8) according to the Etter-graph notation.^[36-39] The study of interactions of water aggregates in crystal matrices received attention to attain a deeper knowledge of the bulk properties of water. Such water structures include, for example, tetrameric clusters,^[40-42] a (H₂O)₁₄-cluster of S₆ symmetry,^[43] a (H₂O)₁₂-containing infinite chain,^[44] a one-dimensional water chain substructure,^[45] ribbons of cyclic water pentamers,^[46] 2D-water/ice layer with octameric subunits,^[47] three dimensional water sheaths,^[48] as well as a three dimensional chiral water aggregate.^[49] Sometimes even different structural water motifs are present as, for example, a cyclic water tetramer together with an opened octamer,^[50] a single cyclic water hexamer and tapes of edge-sharing cyclic water hexamers^[51] and a water cube and cyclic water hexamer.^[52] On this subject Ruiz-Pérez et al. identified a similar D_{2h}-(H₂O)₄-cluster besides an S₄ symmetric tetramer in the two-dimensional **sql**-coordination polymer [Co₂(bta)(H₂O)₈]_n·4nH₂O [with H₄bta = 1,2,4,5-benzenetetracarboxylic acid].^[42]

Table 1. Details of the hydrogen bonding interactions in [Cu(NO₃)₂(H₂O)₂(H₂azbpz)₂]·(H₂O)₂ (**1**)

D-H···A	D-H [Å]	H···A [Å]	D···A [Å]	D-H···A [°]
O1-H1O1···O2 ⁱⁱ	0.77(3)	1.96(3)	2.713(2)	167(3)
O1-H2O1···O2	0.81(3)	1.87(3)	2.664(2)	167(2)
O2-H2O2···O3 ⁱⁱⁱ	0.80(3)	2.07(3)	2.838(2)	161(2)
O2-H1O2···N5 ⁱⁱ	0.77(3)	1.96(3)	2.725(2)	174(3)
N2-H2···O3	0.82(2)	2.02(2)	2.803(2)	161(2)
N6-H6···O4 ^{iv}	0.81(3)	2.54(3)	3.221(2)	142(2)
N6-H6···O5 ^{iv}	0.81(2)	2.32(3)	3.100(2)	161(2)

i = -x+1, -y+1, -z+1; ii = -x+1, -y+1, -z; iii = -x+1, -y, -z+1; iv = x, y, z-1.

An analogous evaporation experiment using Ni(NO₃)₂·6H₂O instead of Cu(NO₃)₂·2.5H₂O led to greenish block shaped crystals of composition [Ni(H₂O)₄(H₂azbpz)₂](NO₃)₂·2H₂O (**2**). Again the experimental and simulated powder X-ray diffractograms were positively matched (Fig. S1, SI) and, thereby, confirmed the representative nature of the investigated single-crystal and overall phase-purity. The asymmetric unit contains one nickel atom sitting on an inversion center, one H₂azbpz, two coordinating water molecules (O1 and O3), one crystal-water molecule (O2) and one nitrate ion. The nickel atom is octahedrally coordinated by four

water molecules in the equatorial position (bond lengths: Ni–O1 2.064(2) Å, Ni–O3 2.072(2) Å) and two H₂azbpz ligands through the pyridinic nitrogen atom N1 (bond length: Ni–N1 2.108(2) Å) (Figure 4).

A nine-membered hydrogen-bonded ring around the metal center (Ni–N1–N2–H2–O4–N7–O6–H2O3–O3) is formed by the participation of the non-coordinating nitrate ion. This motif can be assigned the R₂²(9) graph set in the Etter-notation.^[35-39] As in the copper complex **1** also in **2** one pyrazole ring of the H₂azbpz ligand is not coordinating. This non-coordinated pyrazole-moiety then acts as a hydrogen bond acceptor via its pyridinic nitrogen to a water molecule and as an H-bond donor to a nitrate ion. Overall this hydrogen-bonded ring can be described as R₂²(7) in the Etter-notation (Figure 5 Top).^[35-39] Both pyrrolic NH-functions are in the exo-position to the azo-bridge in H₂azbpz, corresponding to the trans form represented on the right in middle of Scheme 2.

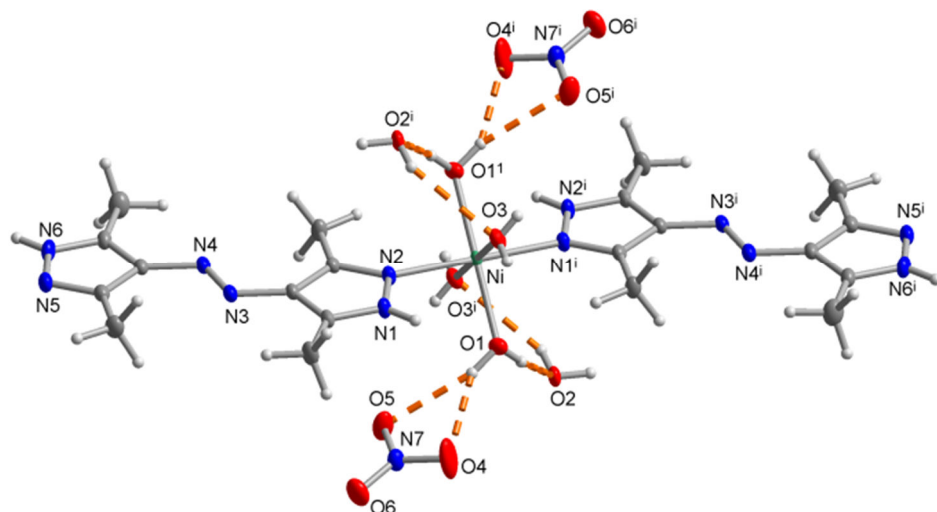


Figure 4. Extended asymmetric unit of [Ni(H₂O)₄(H₂azbpz)₂](NO₃)₂·2H₂O (**2**) (50% thermal ellipsoids H atoms with arbitrary radii). Symmetry transformation: i: -x+1, -y+1, -z+1. Selected bond distances and angles are given in Table S2 in SI.

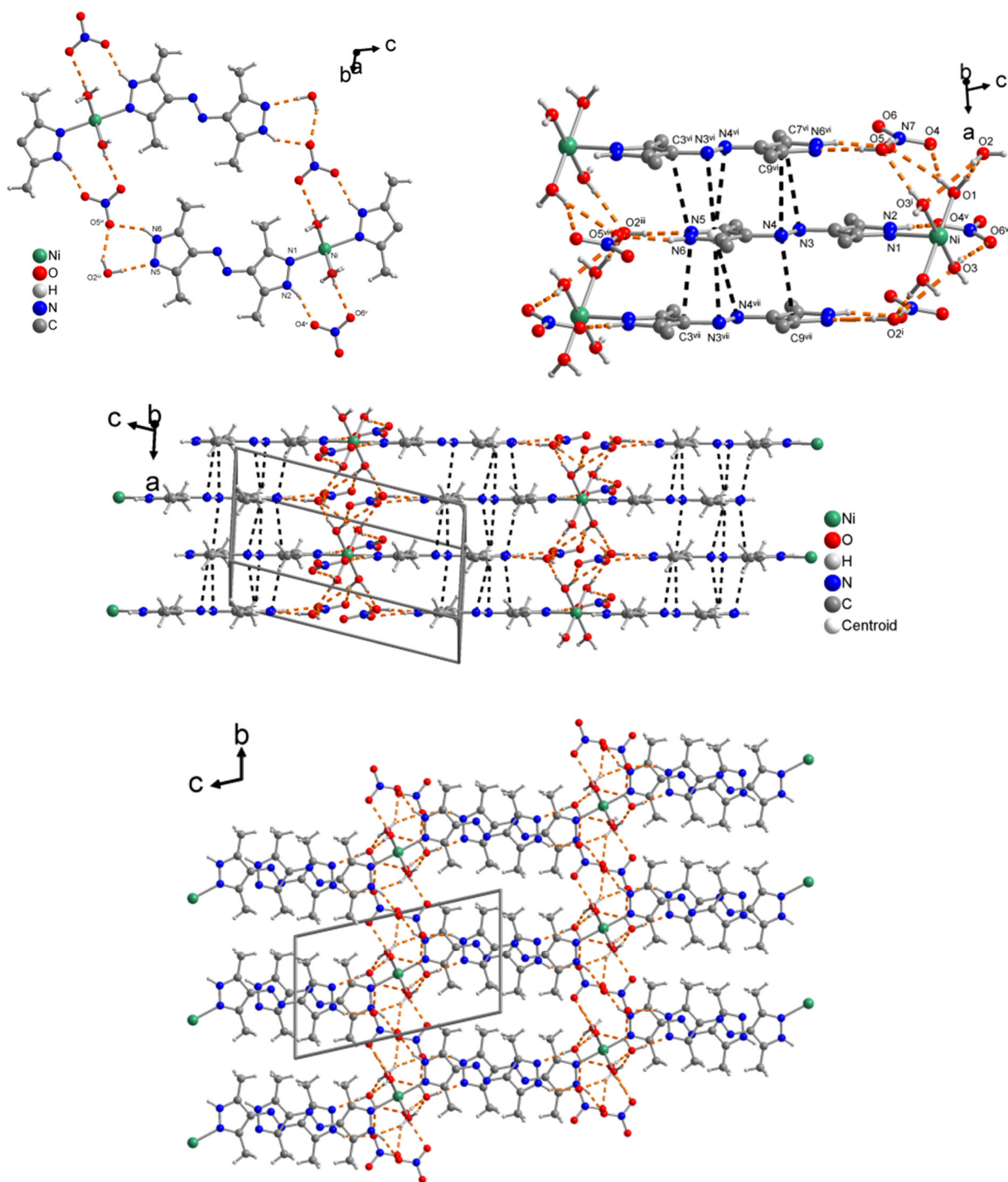


Figure 5. Top left: hydrogen-bonding interactions in **2** stabilizing the trans-configuration of H₂azbpz and nitrate anions as the connectors between the sheets. Top right: interplay of hydrogen-bonds and azo- π interactions in **2**. Middle: visualization of a two-dimensional sheet in **2**. Bottom: View along the a-axis on the AA-packing of the sheets. See Table 2 for details on hydrogen bonds. Symmetry transformations: i = -x+1, -y+1, -z+1; ii = -x, -y+1, -z+1; iii = x, y, z+1; iv = x+1, y, z; v = -x+1, -y+2, -z+1; vi = -x, -y+1, -z; vii = 1-x, 1-y, -z.

The water molecules in the Ni-complex show a trimeric motif with O···O distances of O1···O2 2.6787(13) Å, and O2···O3 2.6979(13) Å, which can be described as part of a six-membered hydrogen-bonded ring around the metal-center (Ni–O1–H1O1–O2–H1O2–O3) with the graph set R₂²(6) (see Figure S4, SI). Details on the hydrogen bonds in **2** are listed in Table 2.

The hydrogen-bond motifs in **2** lead to a two-dimensional hydrogen-bonded sheet in the ac-plane. This is accompanied by continuous π-interactions along the a-axis of azo-pz to offset arranged H₂azbpz-ligands (see Figure 5 and Figure S6, SI for details). Those sheets are stacked along the b-axis in an AA-fashion with the nitrate anions involved in the described hydrogen-bonding rings as the connectors between the two-dimensional sheets (see Figure 5).

Table 2. Details of the hydrogen bonding interactions in [Ni(H₂O)₄(H₂azbpz)₂](NO₃)₂·2H₂O (**2**).

D–H···A	D–H [Å]	H···A [Å]	D···A [Å]	D–H···A [°]
O1–H1O1···O2	0.90 (3)	1.81 (3)	2.679 (3)	163 (3)
O1–H1O2···O4	0.84 (3)	2.20 (3)	2.941 (4)	147 (3)
O1–H1O1···O5	0.85 (3)	2.35 (3)	3.146 (3)	157 (3)
O2–H1O2···O3 ⁱ	0.82 (1)	2.56 (3)	3.138 (3)	129 (3)
O2–H1O2···O5 ⁱⁱ	0.82 (1)	2.18 (2)	2.824 (3)	136 (3)
O2–H2O2···N5 ⁱⁱⁱ	0.82 (1)	1.92 (1)	2.741 (3)	176 (4)
O3–H1O3···O2 ^{iv}	0.68 (4)	2.02 (5)	2.698 (3)	175 (5)
O3–H2O3···O6 ^v	0.68 (4)	2.14 (4)	2.809 (3)	168 (5)
N2–H2···O4 ^v	0.88	1.95	2.792 (3)	158
N6–H6···O5 ^{vi}	0.88	2.05	2.839 (3)	150

(i) -x+1, -y+1, -z+1; (ii) -x, -y+1, -z+1; (iii) x, y, z+1; (iv) x+1, y, z; (v) -x+1, -y+2, -z+1; (vi) -x, -y+1, -z.

The supramolecular packing in **1** and **2** can be further underpinned by their Hirshfeld surfaces calculated with CrystalExplorer.^[53-56] The thereof derived two-dimensional fingerprint plots show the characteristic features for the already discussed hydrogen-bonds observed in **1** and **2** (see Figure 6).

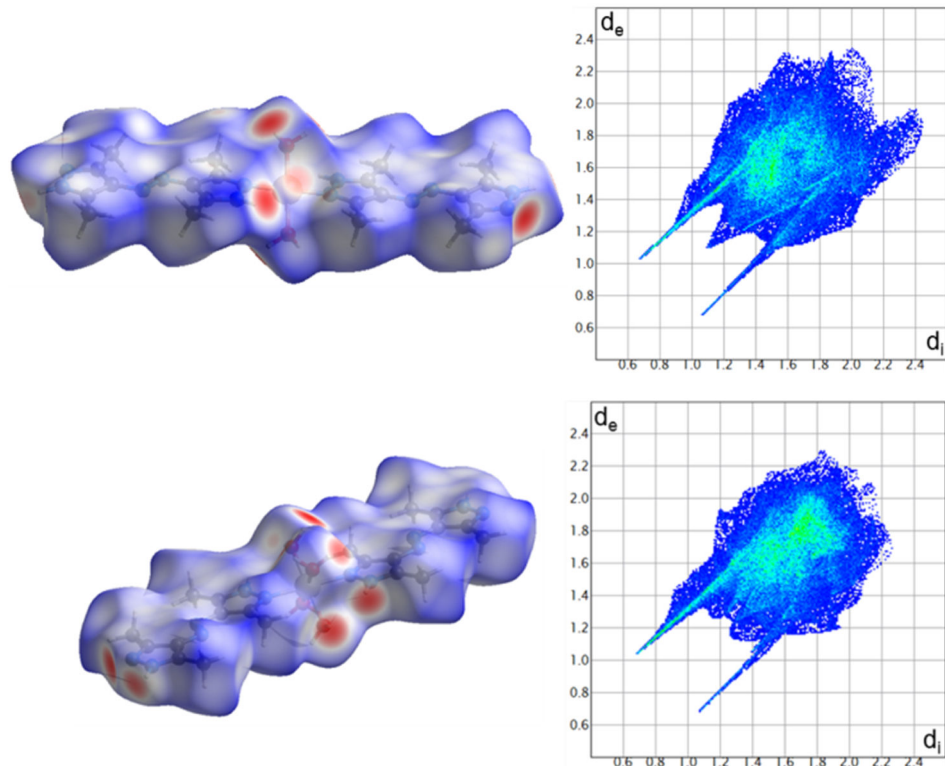


Figure 6. Representation of the Hirshfeld surface areas mapped with d_{norm} on the left and the two-dimensional fingerprint plots on the right for **1** (top) and **2** (bottom) with d_i and d_e as the distances from the surface to the nearest atoms interior and exterior to the surface. Red spots depict the closest and blue spots the most distant contacts.

Figure 7 summarizes the relative contributions to the Hirshfeld surface area close contacts for **1** and **2**. A fragmented breakdown of their contribution to the Hirshfeld surfaces can be found in Figures S7-S36 in the SI. The common feature regarding the azo- π interactions in **1** and **2** is the offset stacking of the dmpz moieties and the azo-function, which are represented as solely N···C contacts with 4.4% for **1** and N···C contacts with 7.7% and N···N-contacts with 1.7% for **2** to the Hirshfeld surface areas.^[57] Those numbers also nicely quantitatively reflect the differences between the one-dimensional chain-structure in **1**, where only one side of H₂azbpz shows azo- π contacts and the two-dimensional sheet structures in **2** where both sides of the planar ligand show such interactions (see Figure 7, Figures S20-S21 and S34-S36, SI).

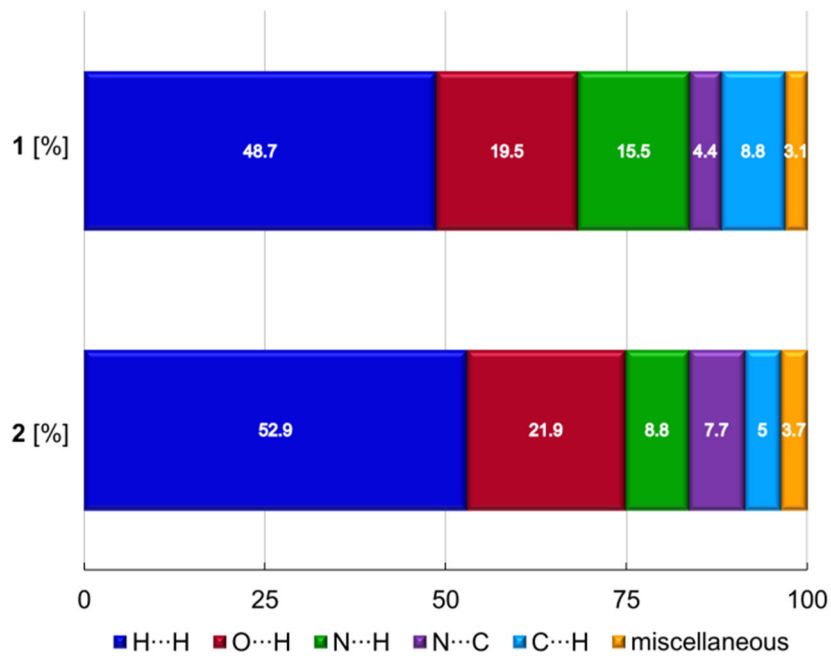


Figure 7. Relative contributions of close contacts ($\text{H}\cdots\text{H}$ (blue), $\text{O}\cdots\text{H}$ (red), $\text{N}\cdots\text{H}$ (green), $\text{N}\cdots\text{C}$ (violet), $\text{C}\cdots\text{H}$ (cyan), miscellaneous in orange the marginal contributions of $\text{C}\cdots\text{O}$, $\text{N}\cdots\text{O}$, $\text{O}\cdots\text{O}$, $\text{C}\cdots\text{C}$, $\text{N}\cdots\text{N}$ and for **1** also the $\text{Cu}\cdots\text{O}$ contacts are summarized).

It can be assumed that due to the general strength and directionality, the high relative contributions to the Hirshfeld surface areas and the identification of interactions in all directions the identified hydrogen-bonds are the main driving forces in the assembly of **1** and **2**. However, besides the hydrogen bonds the main contacts between the chains in **1** and the layers in **2** are weak van-der-Waals contacts represented as $\text{H}\cdots\text{H}$ contacts with high relative contributions to the Hirshfeld surface area between the methyl-groups of the ligands (see Figure S8 and S23, SI).

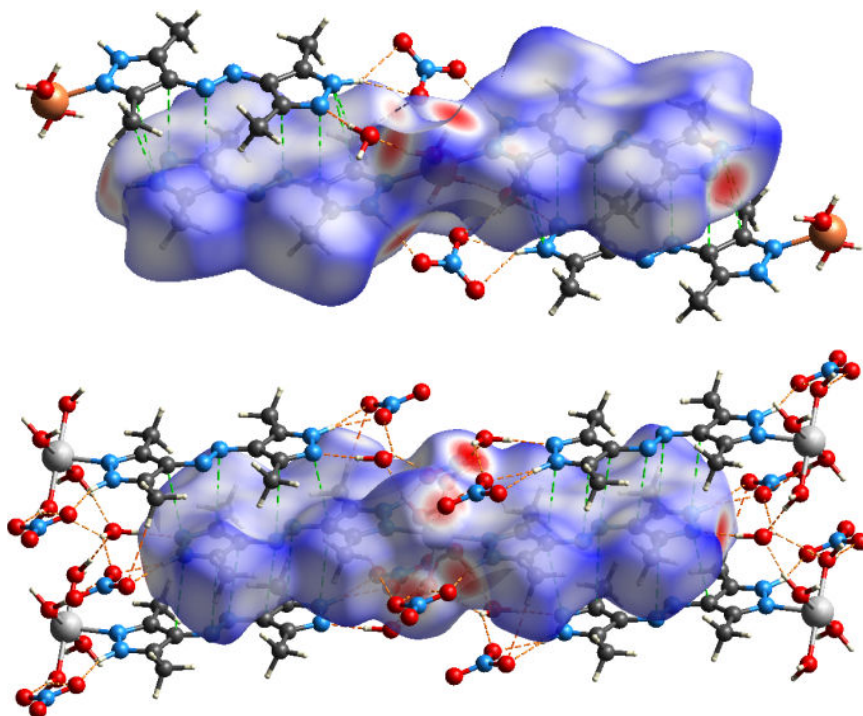


Figure 8. Visualization of the close contacts to the Hirshfeld surface mapped with d_{norm} of the $[\text{Cu}(\text{H}_2\text{O})_2(\text{H}_2\text{azbpz})_2]$ -fragment in **1** (top) and $[\text{Ni}(\text{H}_2\text{O})_4(\text{H}_2\text{azbpz})_2]$ -fragments in **2** (bottom) responsible for the one-dimensional chain or two-dimensional sheet structure, respectively (C···N contacts as green-dashed lines, hydrogen bonds as orange-dashed lines).

Conclusion

We synthesized the metal complexes $[\text{Cu}(\text{NO}_3)_2(\text{H}_2\text{O})_2(\text{H}_2\text{azbpz})_2] \cdot (\text{H}_2\text{O})_2$ (**1**) and $[\text{Ni}(\text{H}_2\text{O})_4(\text{H}_2\text{azbpz})_2](\text{NO}_3)_2 \cdot 2\text{H}_2\text{O}$ (**2**) and discussed their solid-state supramolecular interactions, resulting in the stabilization of a cis-configuration of H₂azbpz in **1** and a trans-configuration in **2** by different anion-assisted hydrogen-bonded rings around the metal centers together with the coordinating and non-coordinating pyrazole-moieties. Besides the identification of the different configuration of the ligand on a molecular level in **1** and **2** the interplay between the hydrogen-bonded ring motifs accompanied by an offset azo- π stacking of the azo-functions and the dmpz-moieties of the ligand leads to a one-dimensional chain structure in **1** and a two-dimensional sheet structure in **2**. The chains in **1** are connected by a D_{2h}-symmetric tetrameric water cluster. Whereas in **2** the hydrogen-bonded rings involving the counterbalancing nitrate anions are identified as the decisive interactions between the sheets. In addition Hirshfeld surface analysis was employed to further work out the differences in their three-dimensional crystal packing. The identified azo-dmpz interactions

were also quantitatively assessed by the relative contribution of N···C and N···N contacts to the Hirshfeld surface areas.

Experimental Section

Reagents were obtained from commercial sources and used without further purification. H₂azbpz was prepared as described by us earlier.^[17] Elemental Analysis was conducted with a Perkin Elmer CHN 2400. IR-spectra were recorded on a Bruker Tensor 37 IR spectrometer equipped with a ATR unit. The powder X-ray diffraction pattern (PXRD) was obtained on a Bruker D2 Phaser powder diffractometer with a flat silicon, low background sample holder, at 30 kV, 10 mA for Cu-K α radiation ($\lambda = 1.5418 \text{ \AA}$).

Single Crystal X-ray Structures

Suitable crystals were carefully selected under a polarizing microscope, covered in protective oil and mounted on a 0.05 mm cryo loop. *Data collection:* Bruker Kappa APEX2 CCD X-ray diffractometer (Bruker AXS Inc., Madison, WI, USA) with microfocus tube, Mo-K α radiation ($\lambda = 0.71073 \text{ \AA}$), multi-layer mirror system, ω -scans; data collection with APEX2,^[58] cell refinement with SMART and data reduction with SAINT,^[58] experimental absorption correction with SADABS.^[59] *Structure analysis and refinement:* All structures were solved by direct methods using SHELXL2016.^[59] Refinement was done by full-matrix least squares on F^2 using the SHELX-97 program suite. Crystal data and details on the structure refinement are given in Table 3.^[60,61] The datasets of **1** and **2** were solved in P1 and transformed with PLATON to P1 using the command ‘CALC ADDSYM SHELX’.^[62,63] In both compounds the hydrogen atoms for CH₃ were positioned geometrically (C—H = 0.98 Å) and refined using a riding model (AFIX 137) with $U_{\text{iso}}(\text{C}) = 1.5U_{\text{eq}}$. In **1** the protic hydrogen atoms for NH were found and refined free with $U_{\text{iso}}(\text{H}) = 1.5U_{\text{eq}}$. The hydrogen atoms of the coordinating water molecule and the water molecule of crystallization were found and refined with $U_{\text{iso}}(\text{H}) = 1.5U_{\text{eq}}(\text{O})$. In **2** The protic hydrogen atoms for NH were positioned geometrically (N—H = 0.98 Å) and refined using a riding model (AFIX 43) with $U_{\text{iso}}(\text{N}) = 1.2U_{\text{eq}}$. The hydrogen atoms of the coordinating water molecules and the water molecule of crystallization were found and refined free with $U_{\text{iso}}(\text{H}) = 1.5U_{\text{eq}}$. The found and refined H atoms were restricted with DFIX commands for their O—H, H···H and Cu···H distances. Graphics were drawn with Diamond.^[64]

Crystallographic data (excluding structure factors) for the structures in this paper have been deposited with the Cambridge Crystallographic Data Centre, CCDC, 12 Union Road, Cambridge CB21EZ, UK. Copies of the data can be obtained free of charge on quoting the

depository number CCDC-1902040-1902041 (Fax: +44-1223-336-033; E-Mail: deposit@ccdc.cam.ac.uk, <http://www.ccdc.cam.ac.uk>).

Table 3. Crystal structure and refinement details of $[\text{Cu}(\text{NO}_3)_2(\text{H}_2\text{O})_2(\text{H}_2\text{azbpz})_2]\cdot(\text{H}_2\text{O})_2$ (**1**) and $[\text{Ni}(\text{H}_2\text{O})_4(\text{H}_2\text{azbpz})_2](\text{NO}_3)_2\cdot 2\text{H}_2\text{O}$ (**2**).

Empirical formula	$\text{CuC}_{20}\text{H}_{36}\text{N}_{14}\text{O}_{18}$	$\text{NiC}_{20}\text{H}_{40}\text{N}_{14}\text{O}_{12}$
$M_{\#}$ (g/mol)	696.18	727.35
Crystal system, space group	Triclinic, P1	Triclinic, P1
Crystal size (mm)	0.09 × 0.02 × 0.02	0.08 × 0.06 × 0.02
Temperature (K)	140	140
a (Å)	7.3242(10)	6.8374 (6)
b (Å)	8.6468(11)	8.4943 (7)
c (Å)	13.6761(18)	14.6525 (12)
α (°)	73.520(8)	99.644 (4)
β (°)	75.488(8)	102.220 (4)
γ (°)	65.008(8)	101.682 (4)
V (Å ³)	744.21 (18)	794.57 (12)
Z	1	1
μ (mm ⁻¹)	0.811	0.691
$F(000)$	363	382
Max./min. transmission	0.913, 1.000	0.657, 0.746
Measured, indep., observed reflections	11992, 2644, 2451	11454, 3287, 2874
R_{int}	0.036	0.032
Data/restraints/param eters	2644 / 0 / 227	3287 / 8 / 236
Max./min. $\Delta\rho$ (e·Å ⁻³) ^a	0.28, -0.41	2.32, -0.46
R , $wR(F^2)$, $S [I > 2\sigma(I)]$ ^b	0.0268, 0.0672, 1.064	0.0553, 0.1497, 1.021
R , $wR(F^2)$, $S [\text{all data}]$ ^b	0.0318, 0.0688, 1.064	0.0635, 0.1572, 1.025

^a Largest difference peak and hole. – ^b $R_1 = [\sum(|F_o| - |F_c|)/\sum|F_o|]$; $wR_2 = [\sum [w(F_o^2 - F_c^2)^2]/\sum[w(F_o^2)^2]]^{1/2}$.

Goodness-of-fit $S = [\sum [w(F_o^2 - F_c^2)^2] / (n-p)]^{1/2}$.

[Cu(NO₃)₂(H₂O)₂(H₂azbpz)₂]·(H₂O)₂ (1):

20.1 mg (0.092 mmol) of H₂azbpz were dissolved in 14 mL of ethanol under stirring. 12.1 mg (0.052 mmol) Cu(NO₃)₂·2.5H₂O dissolved in 2mL of ethanol were added without stirring over 10 min at room temperature. The yellow-greenish solution was filtered through a Pasteur pipet filled with glass wool and allowed to stand for the solvent to evaporate undisturbed at 25 °C in an oven. After 7 days small light-green block-shaped crystals appeared. Yield: 10.3 mg (28% based on copper). The IR spectrum is given in Fig. S2 in SI.

CHN [%] calc. for Cu_{0,5}C₁₀H₁₈N₇O₅: C 34.51, H 5.21, N 28.17 found: C 33.76 H 5.15, N 27.60.

[Ni(H₂O)₄(H₂azbpz)₂](NO₃)₂·2H₂O (2):

The synthesis was carried out in analogy to 1 by using 15.1 mg of Ni(NO₃)₂·6H₂O. After one week 7.3 mg (19% based on nickel) of yellow-greenish crystals were collected. The IR spectrum is given in Fig. S2 in SI.

CHN [%] calc. for NiC₂₀H₄₀N₁₄O₁₂: C 33.03 H 5.54 N 26.96 found: C 32.47 H 5.56 N 27.72

References and Footnotes

- [1] I. Boldog, E. B. Rusanov, A. N. Chernega, J. Sieler, K. V. Domasevitch, *Angew. Chem. Int. Ed.* **2001**, *40*, 3435-3438.
- [2] I. Boldog, E. B. Rusanov, J. Sieler, S. Blaurock, K. V. Domasevitch, *Chem. Commun.* **2003**, 740-741.
- [3] T. Basu, R. Mondal, *CrystEngComm* **2010**, *12*, 366-369.
- [4] U. P. Singh, S. Narang, *CrystEngComm* **2014**, *16*, 7777-7789.
- [5] L.-L. Han, Z.-H. Li, J.-S. Chen, X.-P. Wang, D. Sun, *Cryst. Growth Des.* **2014**, *14*, 1221-1226.
- [6] T. Basu, H. A. Sparkes, R. Mondal, *Cryst. Growth Des.* **2009**, *9*, 5164-5175.
- [7] A. Cingolani, S. Galli, N. Masciocchi, L. Pandolfo, C. Pettinari, A. Sironi, *J. Am. Chem. Soc.* **2005**, *127*, 6144-6145.
- [8] J. Hunger, *Inorg. Chim. Acta* **2013**, *397*, 60-68.
- [9] L.-L. Han, T.-P. Hu, K. Mei, Z.-M. Guo, C. Yin, Y.-X. Wang, J. Zheng, X.-P. Wang, D. Sun, *Dalton Trans.* **2015**, *44*, 6052-6061.
- [10] I. Boldog, E. B. Rusanov, A. N. Chernega, J. Sieler, K. V. Domasevitch, *J. Chem. Soc., Dalton Trans.* **2001**, 893-897.
- [11] K. V. Domasevitch, I. Boldog, E. B. Rusanov, J. Hunger, S. Blaurock, M. Schröder, J. Sieler, *Z. Anorg. Allg. Chem.* **2005**, *631*, 1095-1100.
- [12] J.-H. Wang, M. Li and D. Li, *Chem Sci*, 2013, *4*, 1793-1801.
- [13] E. B. Rusanov, V. V. Ponomarova, V. V. Komarchuk, H. Stoeckli-Evans, E. Fernandez-Ibañez, F. Stoeckli, J. Sieler, K. V. Domasevitch, *Angew. Chem. Int. Ed.* **2003**, *42*, 2499-2501.
- [14] H. S. Scott, S. Mukherjee, D. R. Turner, M. I. J. Polson, M. J. Zaworotko, P. E. Kruger, *CrystEngComm* **2018**, *20*, 1193-1197.
- [15] L. Hou, L.-N. Jia, W.-J. Shi, L.-Y. Du, J. Li, Y.-Y. Wang, Q.-Z. Shi, *Dalton Trans.* **2013**, *42*, 6306-6309.
- [16] A. Zurawski, J. Sieler, K. Müller-Buschbaum, *Z. Anorg. Allg. Chem.* **2009**, *635*, 2034-2038.
- [17] S. Millan, B. Gil-Hernández, E. Hastürk, A. Schmitz, C. Janiak *Z. Anorg. Allg. Chem.* **2018**, *644*, 1311-1316.
- [18] C. Pettinari, A. Tăbăcaru, S. Galli, *Coord. Chem. Rev.* **2016**, *307*, 1-31.
- [19] F. Salles, G. Maurin, C. Serre, P. L. Llewellyn, C. Knöfel, H. J. Choi, Y. Filinchuk, L. Oliviero, A. Vimont, J. R. Long, G. Ferey, *J. Am. Chem. Soc.* **2010**, *132*, 13782-13788.

- [20] J. Fritzsche, M. Grzywa, D. Denysenko, V. Bon, I. Senkovska, S. Kaskel, D. Volkmer, *Dalton Trans.* **2017**, 46, 6745-6755.
- [21] J. Pérez, L. Riera, *Eur. J. Inorg. Chem.* **2009**, 4913-4925.
- [22] I. Boldog, J. Sieler, A. N. Chernega, K. V. Domasevitch, *Inorg. Chim. Acta* **2002**, 338, 69–77.
- [23] S. Bieller, A. Haghiri, M. Bolte, J. W. Bats, M. Wagner, H.-W. Lerner, *Inorg. Chim. Acta* **2006**, 359, 1559-1572.
- [24] L. F. Jones, C. A. Kilner, M. A. Halcrow, *New J. Chem.* **2007**, 31, 1530-1534.
- [25] A. Alsalme, K. Al-Farhan, M. Ghazzali, M. Khair, R. A. Khan, J. Reedijk, *Inorg. Chim. Acta* **2013**, 407, 7-10.
- [26] L.-Y. Du, W.-J. Shi, L. Hou, Y.-Y. Wang, Q.-Z. Shi, Z. Zhu, *Inorg. Chem.* **2013**, 52, 14018-14027.
- [27] C. S. Hawes, P. E. Kruger, *Dalton Trans.* **2014**, 43, 16450-16458.
- [28] W. Ouellette, J. Gooch, S. Luquis, J. Zubietta, *Inorg. Chim. Acta* **2015**, 427, 188-197.
- [29] K. Tomar, R. Rajak, S. Sanda, S. Konar, *Cryst. Growth Des.* **2015**, 15, 2732-2741.
- [30] E. Zhang, Q. Jia, J. Zhang, Z. Ji, *Chin. J. Chem.* **2016**, 34, 191-195.
- [31] J. Reedijk, *Chem. Soc. Rev.* **2013**, 42, 1776-1783.
- [32] C. Janiak, *J. Chem. Soc., Dalton Trans.* **2000**, 3885-3896.
- [33] D. Braga, F. Grepioni, *Acc. Chem. Res.* **2000**, 33, 601-608.
- [34] L. Brammer, *Chem. Soc. Rev.* **2004**, 33, 476-489.
- [35] G. A. Jeffrey, W. Saenger, Definition and Concepts. In: *Hydrogen Bonding in Biological Structures*, Springer Berlin Heidelberg, **1991**, 15-48.
- [36] M. C. Etter, *Acc. Chem. Res.* **1990**, 23, 120-126.
- [37] M. C. Etter, J. C. MacDonald, J. Bernstein, *Acta Crystallogr. B* **1990**, 46, 256-262.
- [38] M. C. Etter, *J. Phys. Chem.*, **1991**, 95, 4601-4610.
- [39] J. Bernstein, R. E. Davis, L. Shimoni, N.-L. Chang, *Angew. Chem. Int. Ed.* **1995**, 34, 1555-1573.
- [40] C. Janiak, T. G. Scharmann, J. C. Green, R. P. G. Parkin, M. J. Kolm, E. Riedel, W. Mickler, J. Elguero, R. M. Charlamunt, D. Sanz, *Chem. Eur. J.* **1996**, 2, 992-1000.
- [41] S. Supriya, S. K. Das, *New J. Chem.* **2003**, 27, 1568-1574.
- [42] O. Fabelo, J. Pasán, L. Cañadillas-Delgado, F. S. Delgado, A. Labrador, F. Lloret, M. Julve, C. Ruiz-Pérez, *CrystEngComm* **2008**, 10, 1743-1746.
- [43] F. Zhuge, B. Wu, L. Dong, J. Yang, C. Janiak, N. Tang, X.-J. Yang, *Aust. J. Chem.* **2010**, 63, 1358-1364.
- [44] Q. Y. Liu, L. Xu, *CrystEngComm* **2005**, 7, 87-89.
- [45] C. Janiak, T.G. Scharmann, K.-W. Brzezinka, P. Reich, *Chem. Ber.* **1995**, 128, 323-328.

- [46] J. P. Naskar, M. G. B. Drew, A. Hulme, D. A. Tocher, D. Datta, *CrystEngComm* **2005**, 7, 67-70.
- [47] C. Janiak, T. G. Scharmann, S. A. Mason, *J. Am. Chem. Soc.* **2002**, 124, 14010-14011.
- [48] R. Carballo, B. Covelo, C. Lodeiro, E. M. Vázquez-López, *CrystEngComm* **2005**, 7, 294-296.
- [49] S.-C. Chen, F. Tian, K.-L. Huang, C.-P. Li, J. Zhong, M.-Y. He, Z.-H. Zhang, H.-N. Wang, M. Du, Q. Chen, *CrystEngComm* **2014**, 16, 7673-7680.
- [50] Y.-Q. Sun, J. Zhang, Z.-F. Ju, G.-Y. Yang, *Aust. J. Chem.* **2005**, 58, 572-577.
- [51] C. Janiak, T. G. Scharmann, H. Hemling, D. Lentz, J. Pickardt, *Chem. Ber.* **1995**, 128, 235-244.
- [52] F. Zhuge, B. Wu, J. Liang, J. Yang, Y. Liu, C. Jia, C. Janiak, N. Tang, X.-J. Yang, *Inorg. Chem.* **2009**, 48, 10249-10256.
- [53] M. A. Spackman, J. J. McKinnon, *CrystEngComm* **2002**, 4, 378-392.
- [54] J. J. McKinnon, M. A. Spackman, A. S. Mitchell, *Acta Crystallogr. B* **2004**, 60, 627-668.
- [55] J. J. McKinnon, D. Jayatilaka, M. A. Spackman, *Chem. Commun.* **2007**, 3814-3816.
- [56] M. A. Spackman, D. Jayatilaka, *CrystEngComm* **2009**, 11, 19-32.
- [57] The N···N-contacts of 1.7% in **2** stem from contacts of the azo-functions with nitrogen atoms of the dmpz moieties (see Figures S33 and S34, SI).
- [58] APEX2. SAINT, *Data Reduction and Frame Integration Program for the CCD Area-Detector System*, Bruker Analytical X-ray Systems; Data Collection Program for the CCD Area-Detector System: Madison, WI, USA, 1997–2006.
- [59] G. M. Sheldrick, *SADABS: Area-Detector Absorption Correction*; University of Göttingen: Göttingen, Germany, 1996.
- [60] G. M. Sheldrick, *Acta Crystallogr. A* **2015**, 71, 3–8.
- [61] G. Sheldrick, *Acta Crystallogr A* **2008**, 64, 112-122.
- [62] A. Spek, *J. Appl. Cryst.* **2003**, 36, 7-13.
- [63] A. Spek, *Acta Crystallogr.D* **2009**, 65, 148-155.
- [64] K. Brandenburg, *DIAMOND, version 4.5; Crystal and Molecular Structure Visualization*; Crystal Impact - K. Brandenburg & H. Putz Gbr., Bonn, Germany, 2009–2018.

Supplementary Material

Metal-4,4'-azobis(3,5-dimethyl-1H-pyrazole) complexes with 7- and 9-membered hydrogen-bonded rings originating from the pyrrolic N-H function

Table of Contents

PXRD patterns

IR spectra

Representation of the possible monodentate metal-coordinating forms of H₂azbpz

Pentameric water rings with homo-, anti- and heterodromic H-atom arrangement

The tetrameric water cluster in 1 and the trimeric water motif in 2

Analysis of potential azo-π-interactions

Hirshfeld surface analysis

Selected bond lengths and angles in [Cu(NO₃)₂(H₂O)₂(H₂azbpz)₂]·2H₂O

Selected bond lengths and angles in [Ni(H₂O)₄(H₂azbpz)₂](NO₃)₂·2H₂O

References

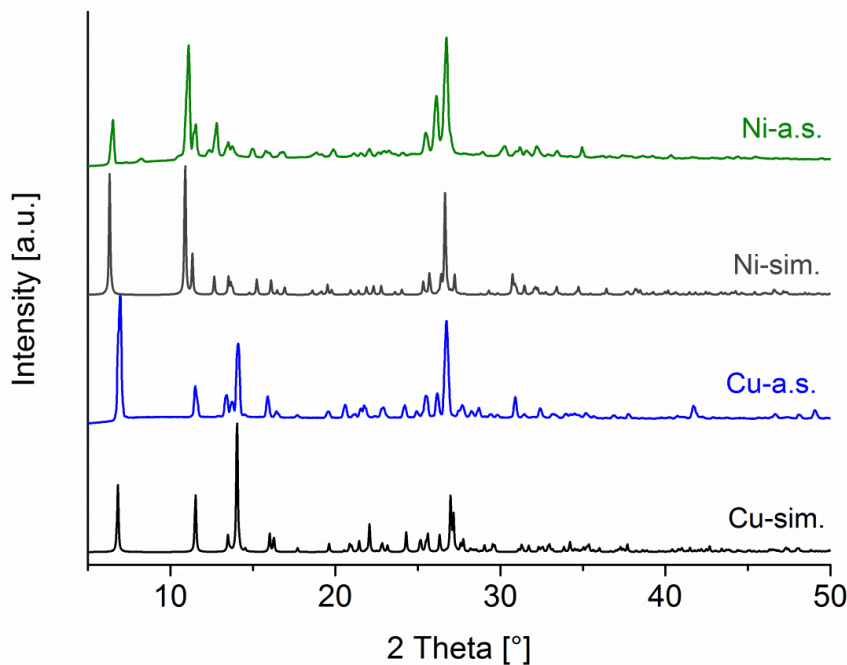


Figure S1. Comparison of the simulated and the as-synthesized PXRD patterns for $[\text{Cu}(\text{NO}_3)_2(\text{H}_2\text{O})_2(\text{H}_2\text{azbpz})_2] \cdot 2\text{H}_2\text{O}$ (black and blue) and $[\text{Ni}(\text{H}_2\text{O})_4(\text{H}_2\text{azbpz})_2](\text{NO}_3)_2 \cdot 2\text{H}_2\text{O}$ (dark grey and green).

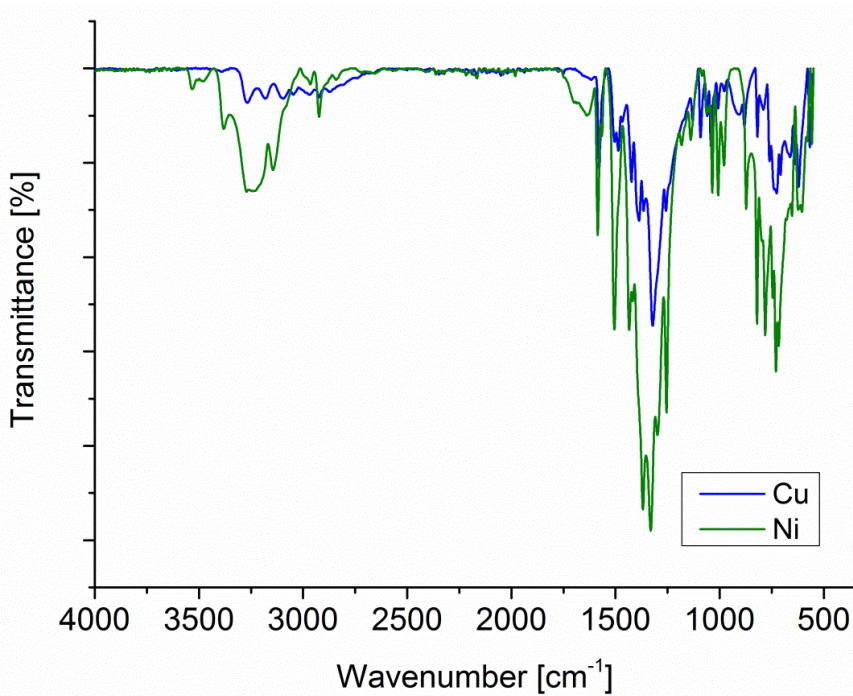
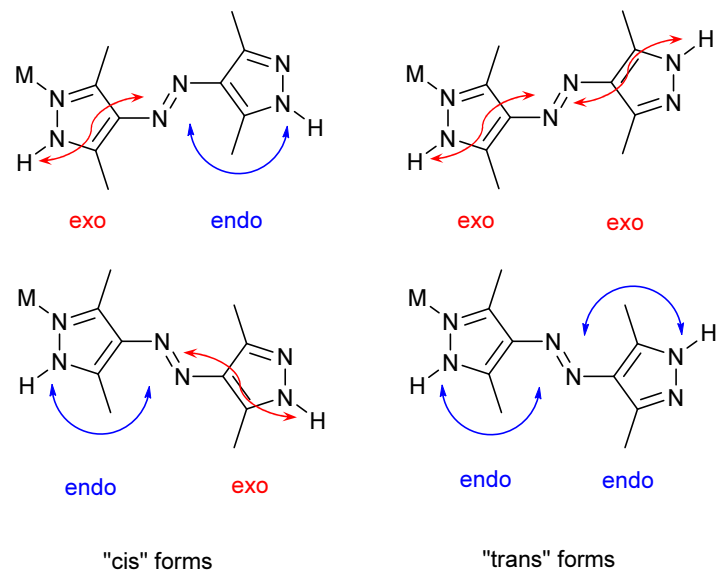
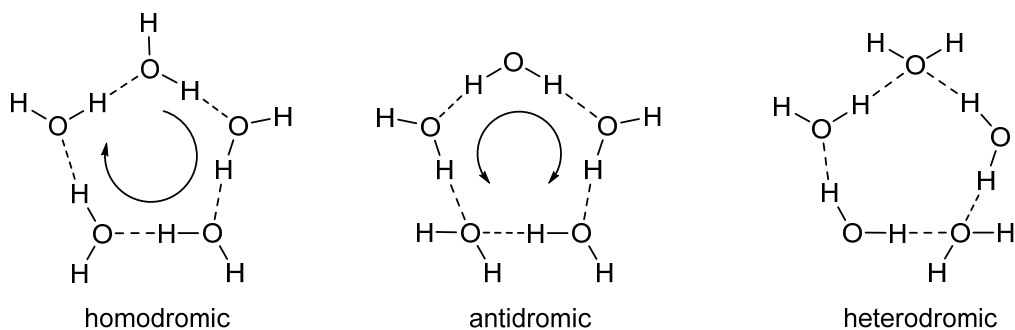


Figure S2. IR spectra of $[\text{Cu}(\text{NO}_3)_2(\text{H}_2\text{O})_2(\text{H}_2\text{azbpz})_2] \cdot 2\text{H}_2\text{O}$ (blue) and $[\text{Ni}(\text{H}_2\text{O})_4(\text{H}_2\text{azbpz})_2](\text{NO}_3)_2 \cdot 2\text{H}_2\text{O}$ (green).



Scheme S1. Representation of the possible monodentate metal-coordinating forms of H₂azbpz with two cis forms (exo-endo and endo-exo) on the left and two trans forms (exo-exo and endo-endo) on the right.



Scheme S2. Pentameric water rings with a homodromic hydrogen-bonded ring, where the hydrogen atoms all point in the same direction around the ring (clockwise or anticlockwise) and the antidromic system, where some hydrogen atoms point in the same direction. In the heterodromic system only two hydrogen atoms are aligned.

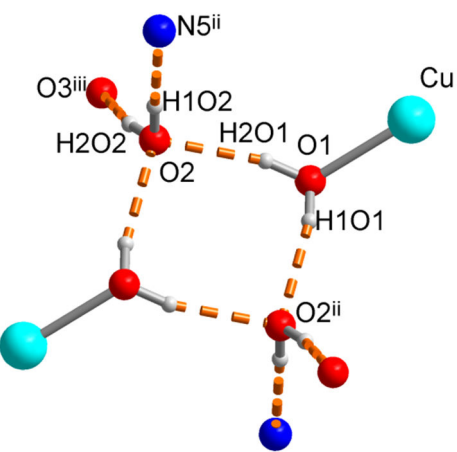


Figure S3. The heterodromic D_{2h} -symmetric tetrameric water cluster in 1 with the graph set $R^2_2(8)$ according to the Etter notation as the connecting motif between the chains.

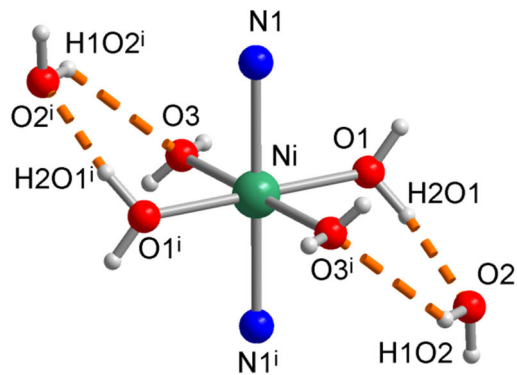


Figure S4. The trimeric water motif in 2 giving rise to the six-membered hydrogen-bonded ring around the metal-center with the graph set of $R^2_2(6)$ in the Etter notation. Symmetry transformation: (i) $-x+1, -y+1, -z+1$.

Analysis of potential azo- π -interactions in $[\text{Cu}(\text{NO}_3)_2(\text{H}_2\text{O})_2(\text{H}_2\text{azbpz})_2] \cdot 2\text{H}_2\text{O}$ and $[\text{Ni}(\text{H}_2\text{O})_4(\text{H}_2\text{azbpz})_2](\text{NO}_3)_2 \cdot 2\text{H}_2\text{O}$

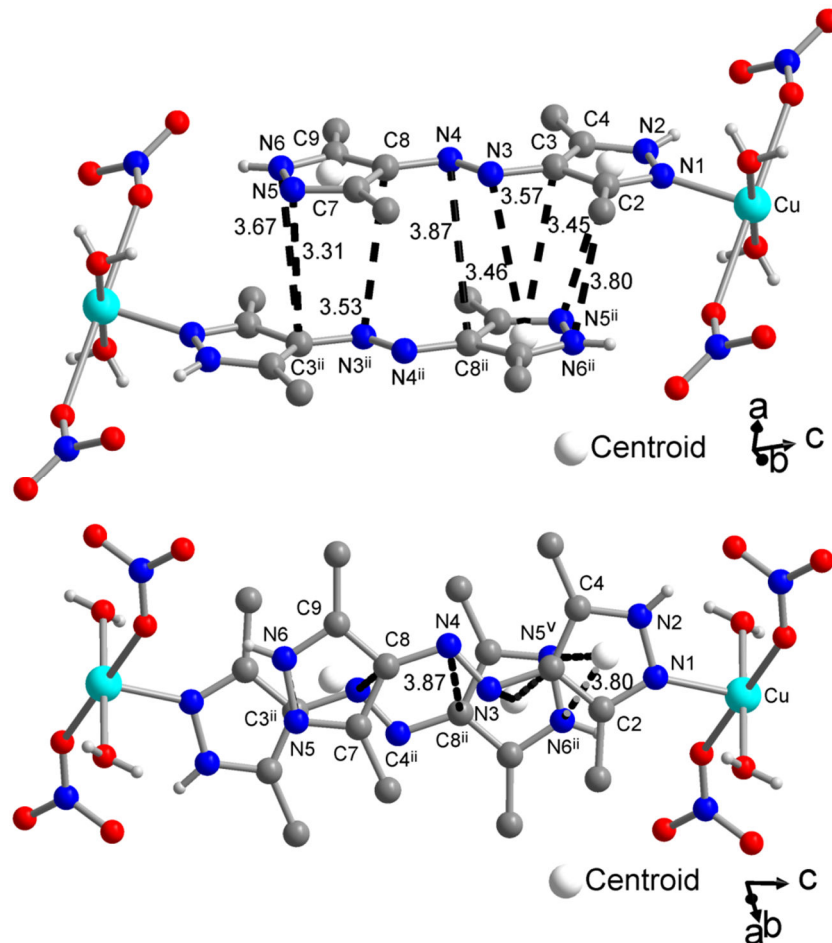


Figure S5. Representation of potential azo- π interactions (as dashed black lines) in $[\text{Cu}(\text{NO}_3)_2(\text{H}_2\text{O})_2(\text{H}_2\text{azbpz})_2] \cdot 2\text{H}_2\text{O}$ (**1**) between the azo-moiety and dmpz-moieties of adjacent Cu-complexes (protons of the methyl-groups are omitted for clarity). Symmetry transformation: $\text{ii} = -x+1, -y+1$.

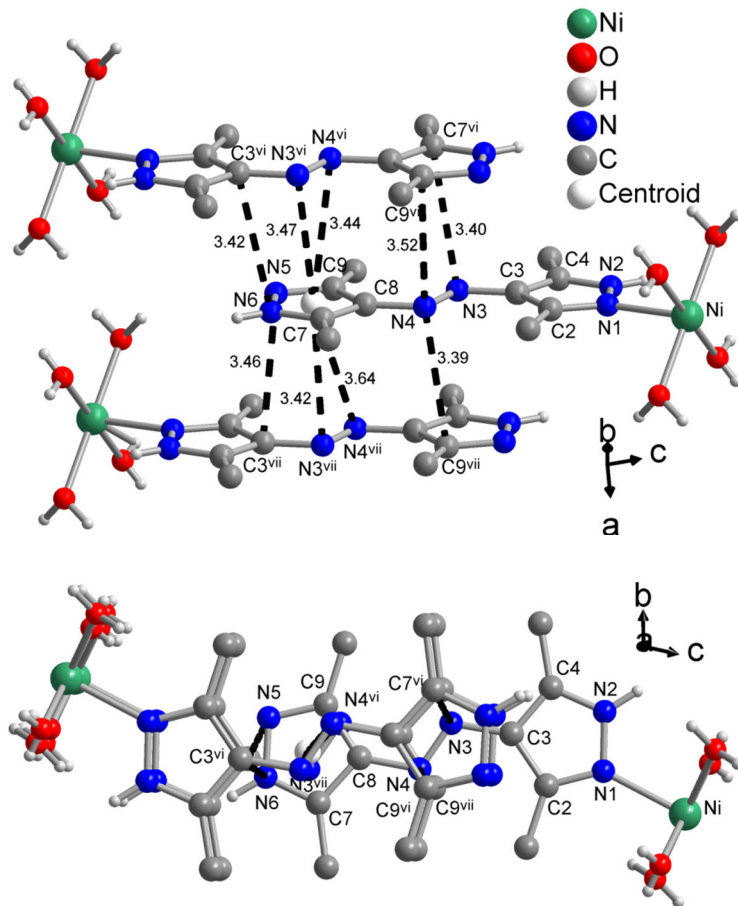


Figure S6. Representation of potential azo-pi interactions (as dashed black lines) in $[\text{Ni}(\text{H}_2\text{O})_4(\text{H}_2\text{azbpz})_2]\cdot 2\text{H}_2\text{O}$ (**2**) between the azo-moiety and dmpz-moieties of adjacent Ni-complexes (protons of the methyl-groups are omitted for clarity). Symmetry transformations: (vi) -x, 1-y, -z; (vii) 1-x, 1-y, -z.

Hirshfeld surface analysis

The supramolecular interactions in $[\text{Cu}(\text{NO}_3)_2(\text{H}_2\text{O})_2(\text{H}_2\text{azbpz})_2] \cdot 2\text{H}_2\text{O}$ (**1**) and $[\text{Ni}(\text{H}_2\text{O})_4(\text{H}_2\text{azbpz})_2](\text{NO}_3)_2 \cdot 2\text{H}_2\text{O}$ (**2**) were analyzed via the relative contributions of close contacts to the Hirshfeld surfaces calculated with CrystalExplorer.^[1-3] The axis labeling of the fingerprint plots with d_i and d_e was adjusted manually. It has to be noted that CrystalExplorer does not recognize the Jahn-Teller-distorted coordination of the nitrate anion in $[\text{Cu}(\text{NO}_3)_2(\text{H}_2\text{O})_2(\text{H}_2\text{azbpz})_2] \cdot 2\text{H}_2\text{O}$ (**1**).

Hirshfeld surface analysis of the $[\text{Cu}(\text{H}_2\text{O})_2(\text{H}_2\text{azbpz})_2]$ fragment in **1**

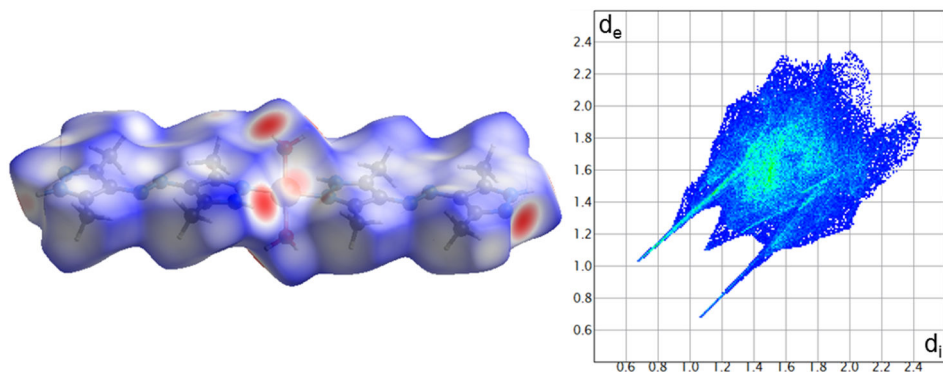


Figure S7. Representation of the Hirshfeld surface mapped with d_{norm} and the 2D fingerprint plot of $[\text{Cu}(\text{H}_2\text{O})_2(\text{H}_2\text{azbpz})_2]$ fragment in **1** with d_i and d_e as the distances from the surface to the nearest atoms interior and exterior to the surface.

H···H contacts: 48.7%

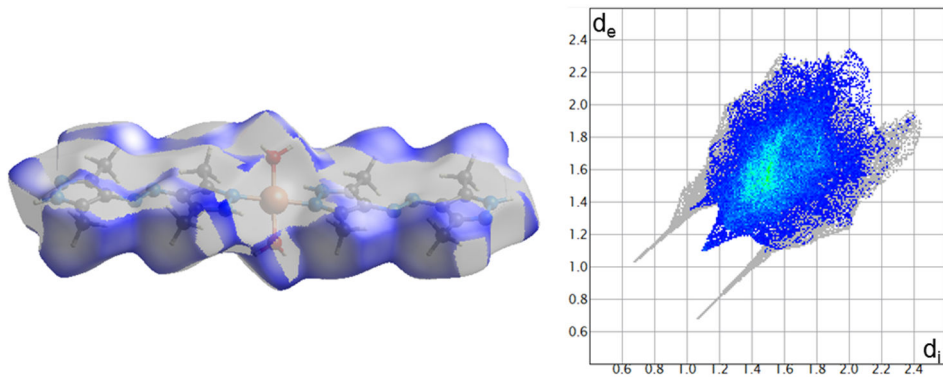


Figure S8. Representation of the relative contribution of $\text{H}\cdots\text{H}$ contacts to the Hirshfeld surface mapped with d_{norm} and the 2D fingerprint plot of the $[\text{Cu}(\text{H}_2\text{O})_2(\text{H}_2\text{azbpz})_2]$ fragment in **1** with d_i and d_e as the distances from the surface to the nearest atoms interior and exterior to the surface.

O···H contacts: 19.5% (reciprocal contributions are not equal: $O_{\text{ins}}\cdots H_{\text{out}}$ 0.7%, $H_{\text{ins}}\cdots O_{\text{out}}$ 18.8%)

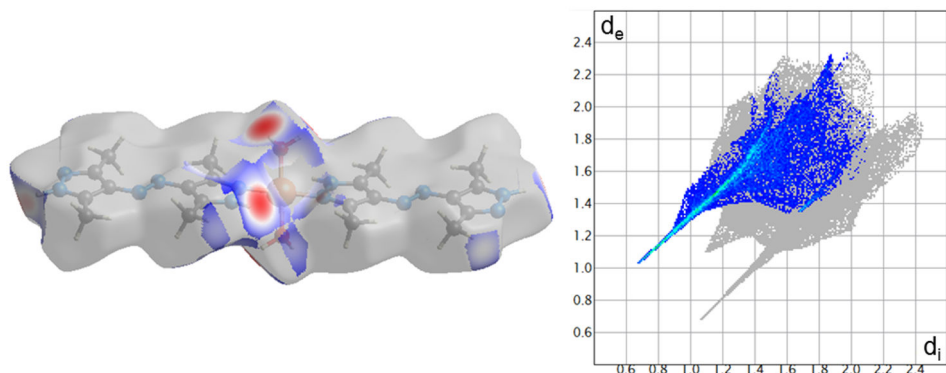


Figure S9. Representation of the relative contribution of $O\cdots H$ contacts to the Hirshfeld surface mapped with d_{norm} and the 2D fingerprint plot of the $[\text{Cu}(\text{H}_2\text{O})_2(\text{H}_2\text{azbpz})_2]$ fragment in **1** with d_i

and d_e as the distances from the surface to the nearest atoms interior and exterior to the surface.

N···H contacts: 15.5% (reciprocal contributions are not equal: $N_{\text{ins}}\cdots H_{\text{out}}$ 9.8%, $H_{\text{ins}}\cdots N_{\text{out}}$ 5.8%)

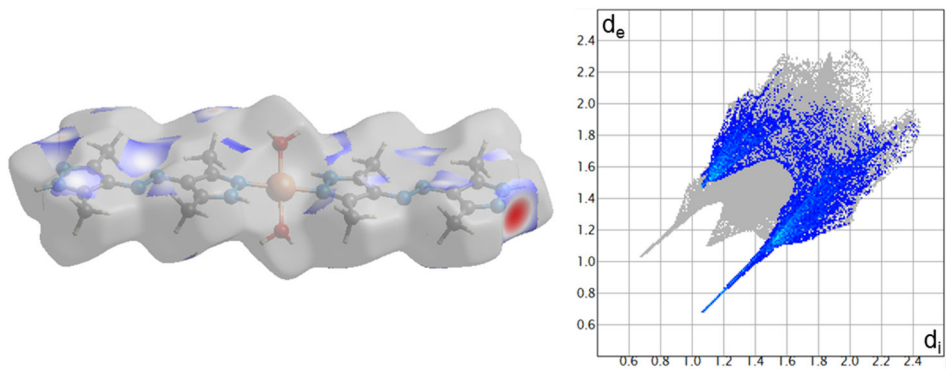


Figure S10. Representation of the relative contribution of $N\cdots H$ contacts to the Hirshfeld surface mapped with d_{norm} and the 2D fingerprint plot of the $[\text{Cu}(\text{H}_2\text{O})_2(\text{H}_2\text{azbpz})_2]$ fragment in **1** with d_i and d_e as the distances from the surface to the nearest atoms interior and exterior to the surface.

N···C contacts: 4.4% (reciprocal contributions are almost equal: $N_{\text{ins}}\cdots C_{\text{out}}$ 2.1%, $C_{\text{ins}}\cdots N_{\text{out}}$ 2.3%)

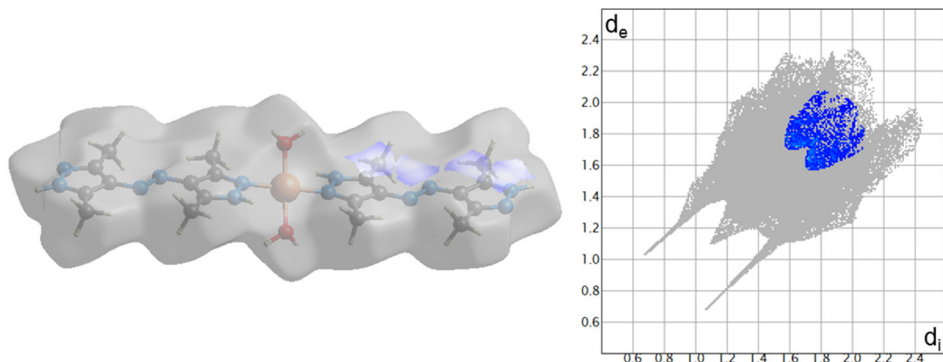


Figure S11. Representation of the relative contribution of C···N contacts to the Hirshfeld surface mapped with d_{norm} and the 2D fingerprint plot of the $[\text{Cu}(\text{H}_2\text{O})_2(\text{H}_2\text{azbpz})_2]$ fragment in **1** with d_i and d_e as the distances from the surface to the nearest atoms interior and exterior to the surface.

C···H contacts: 8.8% (reciprocal contributions are not equal: $C_{\text{ins}}\cdots H_{\text{out}}$ 5.3%, $H_{\text{ins}}\cdots C_{\text{out}}$ 3.5%)

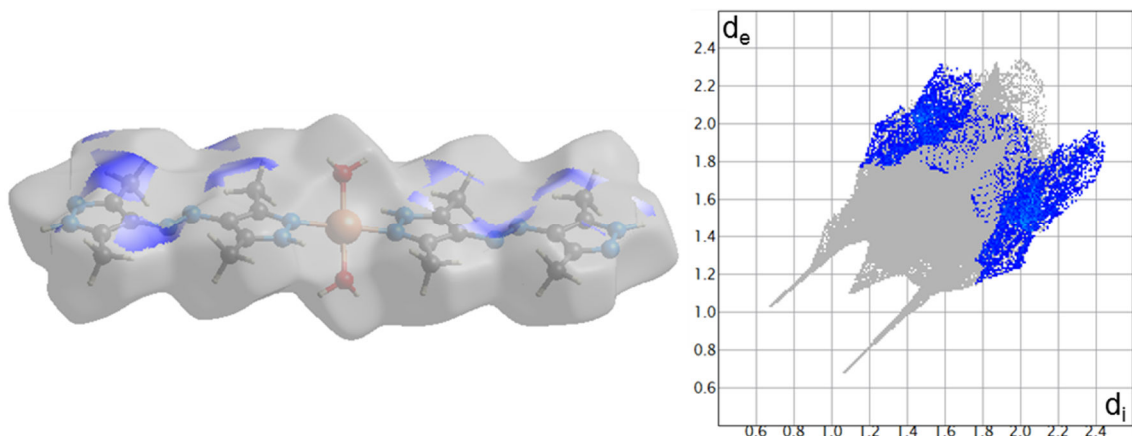


Figure S12. Representation of the relative contribution of C···H contacts to the Hirshfeld surface mapped with d_{norm} and the 2D fingerprint plot of the $[\text{Cu}(\text{H}_2\text{O})_2(\text{H}_2\text{azbpz})_2]$ fragment in **1** with d_i and d_e as the distances from the surface to the nearest atoms interior and exterior to the surface.

Cu···O contacts: 1.1% (reciprocal contributions are not equal: Cu_{ins}···O_{out} 1.1%, O_{ins}···Cu_{out} 0%)

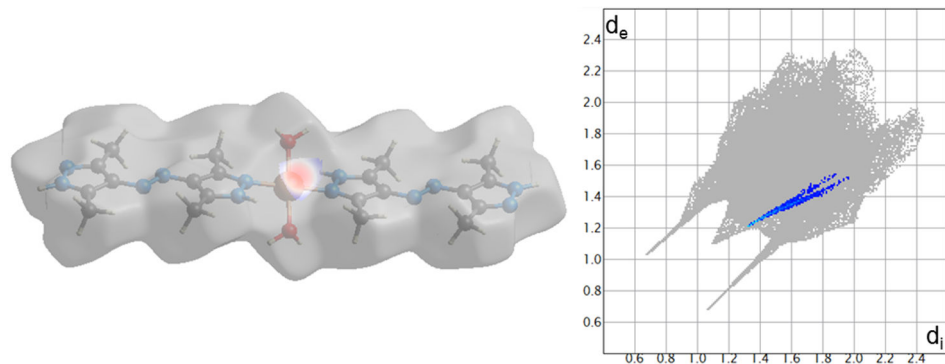


Figure S13. Representation of the relative contribution of Cu···O contacts to the Hirshfeld surface mapped with d_{norm} and the 2D fingerprint plot of the $[\text{Cu}(\text{H}_2\text{O})_2(\text{H}_2\text{azbpz})_2]$ fragment in **1** with d_i and d_e as the distances from the surface to the nearest atoms interior and exterior to the surface.

N···N contacts: 0.1%

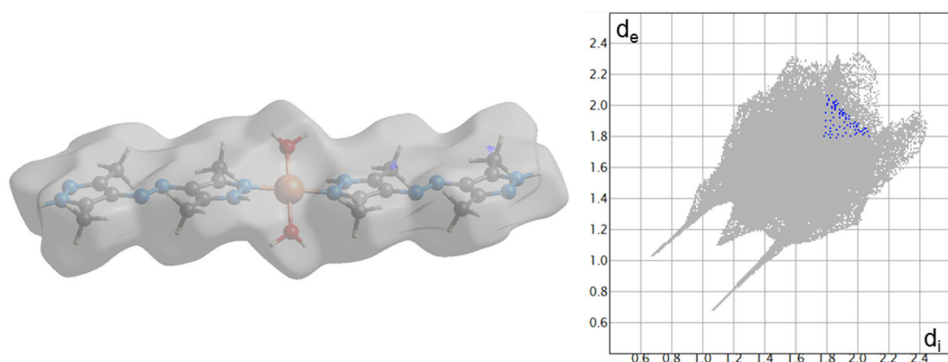


Figure S14. Representation of the relative contribution of N···N contacts to the Hirshfeld surface mapped with d_{norm} and the 2D fingerprint plot of the $[\text{Cu}(\text{H}_2\text{O})_2(\text{H}_2\text{azbpz})_2]$ fragment in **1** with d_i and d_e as the distances from the surface to the nearest atoms interior and exterior to the surface.

C···C contacts: 0.2%

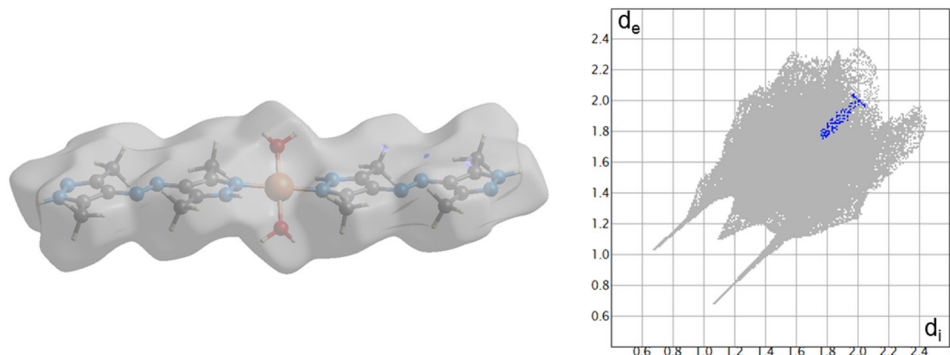


Figure S15. Representation of the relative contribution of C···C contacts to the Hirshfeld surface mapped with d_{norm} and the 2D fingerprint plot of the $[\text{Cu}(\text{H}_2\text{O})_2(\text{H}_2\text{azbpz})_2]$ fragment in **1** with d_i and d_e as the distances from the surface to the nearest atoms interior and exterior to the surface.

N···O contacts: 0.6% (reciprocal contributions are not equal: $\text{N}_{\text{ins}}\cdots\text{O}_{\text{out}}$ 0.6%, $\text{O}_{\text{ins}}\cdots\text{N}_{\text{out}}$ 0.0%)

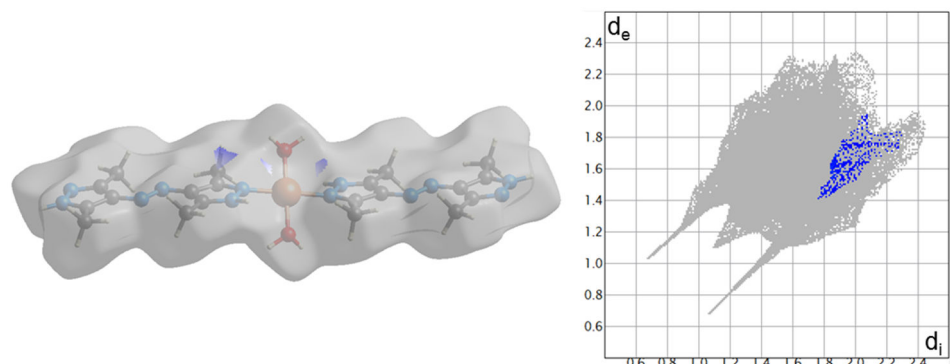


Figure S16 Representation of the relative contribution of N···O contacts to the Hirshfeld surface mapped with d_{norm} and the 2D fingerprint plot of the $[\text{Cu}(\text{H}_2\text{O})_2(\text{H}_2\text{azbpz})_2]$ fragment in **1** with d_i and d_e as the distances from the surface to the nearest atoms interior and exterior to the surface.

C···O contacts: 1.0% (reciprocal contributions are not equal: $C_{\text{ins}}\cdots O_{\text{out}}$ 1.0%, $O_{\text{ins}}\cdots C_{\text{out}}$ 0.0%)

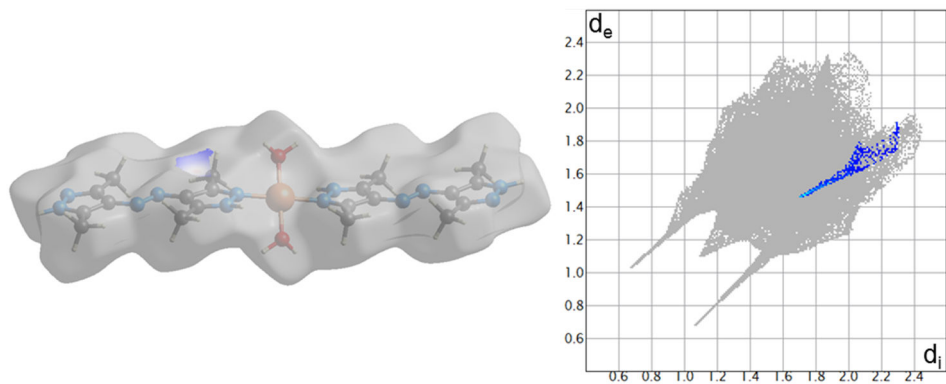


Figure S17. Representation of the relative contribution of C···O contacts to the Hirshfeld surface mapped with d_{norm} and the 2D fingerprint plot of the $[\text{Cu}(\text{H}_2\text{O})_2(\text{H}_2\text{azbpz})_2]$ fragment in **1** with d_i and d_e as the distances from the surface to the nearest atoms interior and exterior to the surface.

O···O contacts: 0.1%

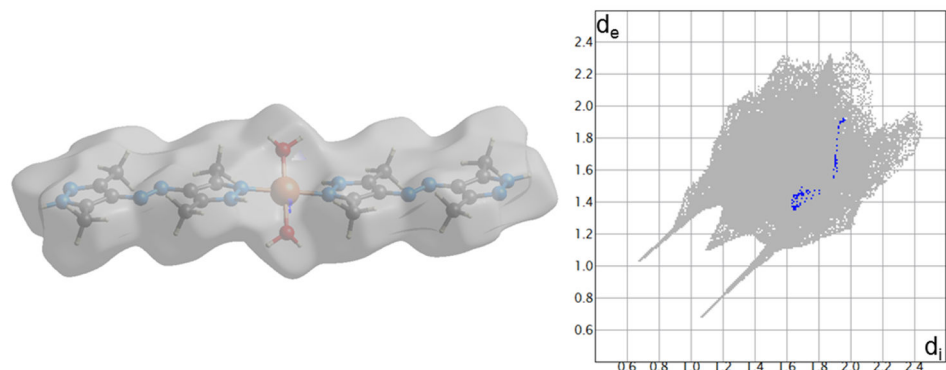


Figure S18. Representation of the relative contribution of O···O contacts to the Hirshfeld surface mapped with d_{norm} and the 2D fingerprint plot of the $[\text{Cu}(\text{H}_2\text{O})_2(\text{H}_2\text{azbpz})_2]$ fragment in **1** with d_i and d_e as the distances from the surface to the nearest atoms interior and exterior to the surface.

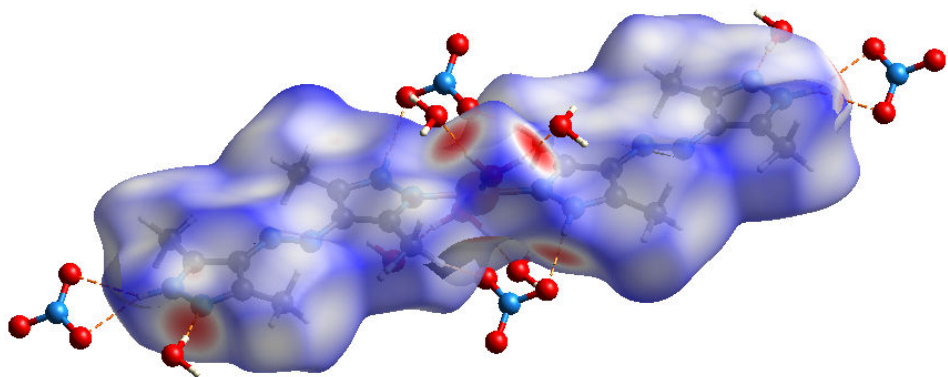


Figure S19. Visualization of the close contacts involving hydrogen bonds (orange-dashed lines) to the Hirshfeld surface mapped with d_{norm} of the $[\text{Cu}(\text{H}_2\text{O})_2(\text{H}_2\text{azbpz})_2]$ fragment in **1** (hydrogen bonds as orange-dashed lines).

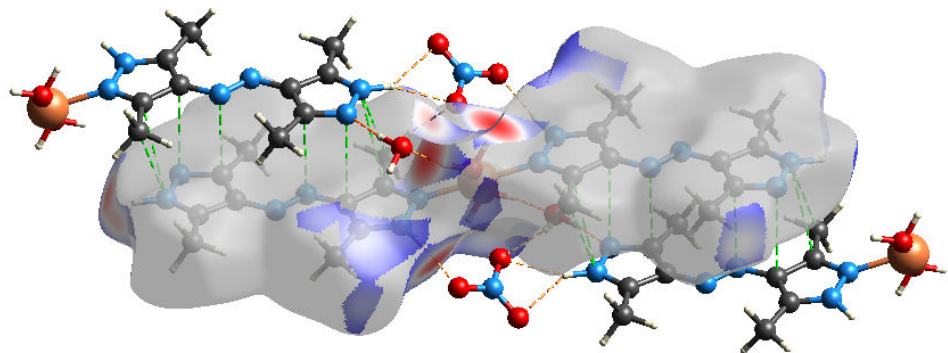


Figure S20. Visualization of the contribution of $\text{O}\cdots\text{H}$ close contacts to the Hirshfeld surface mapped with d_{norm} of the $[\text{Cu}(\text{H}_2\text{O})_2(\text{H}_2\text{azbpz})_2]$ fragment in **1** responsible for the one dimensional chain-like structure ($\text{C}\cdots\text{N}$ contacts as green-dashed lines, hydrogen bonds as orange-dashed lines).

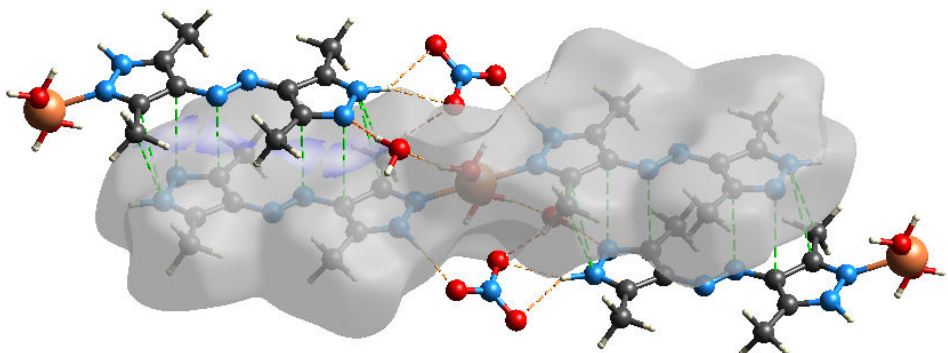


Figure S21. Visualization of the contribution of $\text{C}\cdots\text{N}$ close contacts to the Hirshfeld surface mapped with d_{norm} of the $[\text{Cu}(\text{H}_2\text{O})_2(\text{H}_2\text{azbpz})_2]$ fragment in **1** responsible for the one dimensional chain-like structure ($\text{C}\cdots\text{N}$ contacts as green-dashed lines, hydrogen bonds as orange-dashed lines).

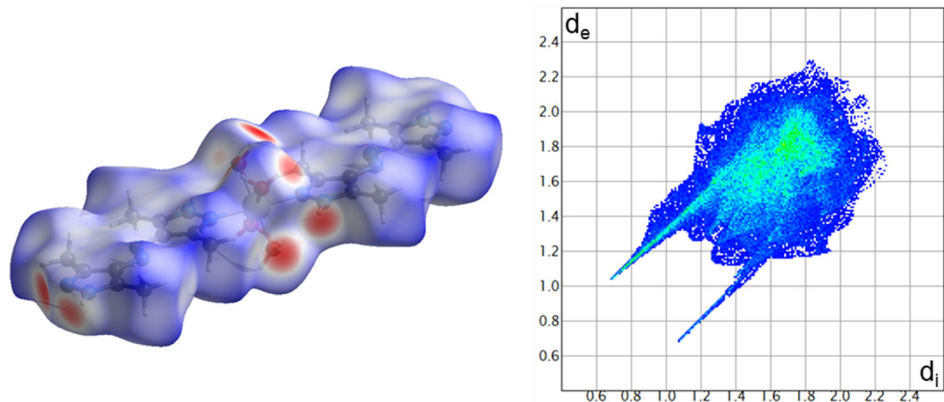
Hirshfeld surface analysis of the $[\text{Ni}(\text{H}_2\text{O})_4(\text{H}_2\text{azbpz})_2]$ -fragment in 2

Figure S22. Representation of the Hirshfeld surface mapped with d_{norm} and the 2D fingerprint plot of the $[\text{Ni}(\text{H}_2\text{O})_4(\text{H}_2\text{azbpz})_2]$ fragment in **2** with d_i and d_e as the distances from the surface to the nearest atoms interior and exterior to the surface.

H···H contacts: 52.9%

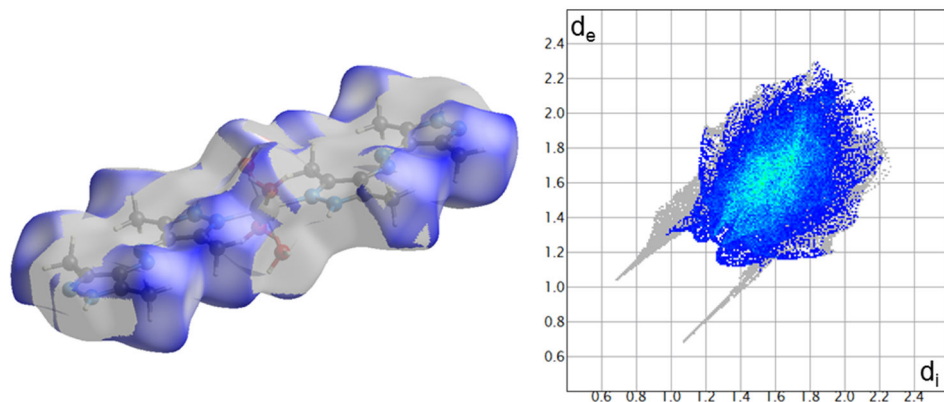


Figure S23. Representation of the relative contribution of $\text{H}\cdots\text{H}$ contacts to the Hirshfeld surface mapped with d_{norm} and the 2D fingerprint plot of the $[\text{Ni}(\text{H}_2\text{O})_4(\text{H}_2\text{azbpz})_2]$ fragment in **2** with d_i and d_e as the distances from the surface to the nearest atoms interior and exterior to the surface.

O···H contacts: 21.9% (reciprocal contributions are not equal: $O_{\text{ins}}\cdots H_{\text{out}}$ 1.4%, $H_{\text{ins}}\cdots O_{\text{out}}$ 20.5%)

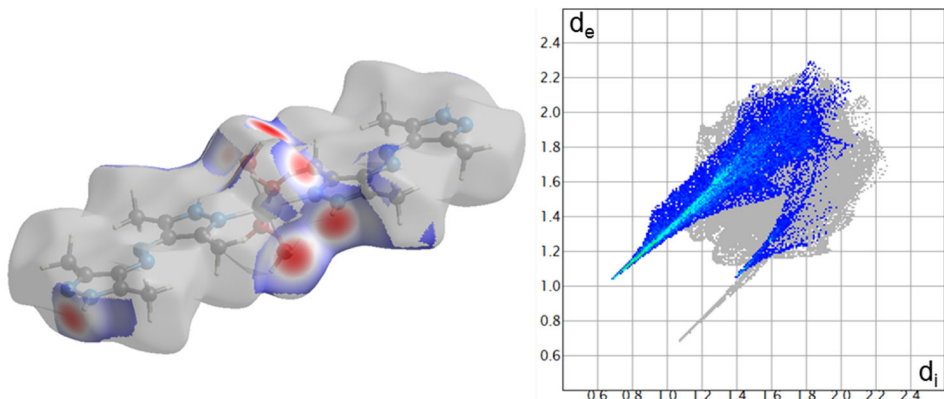


Figure S24. Representation of the relative contribution of O···H contacts to the Hirshfeld surface mapped with d_{norm} and the 2D fingerprint plot of the $[\text{Ni}(\text{H}_2\text{O})_4(\text{H}_2\text{azbpz})_2]$ fragment in **2** with d_i and d_e as the distances from the surface to the nearest atoms interior and exterior to the surface.

N···H contacts: 8.8% (reciprocal contributions are not equal: $N_{\text{ins}}\cdots H_{\text{out}}$ 5.8%, $H_{\text{ins}}\cdots N_{\text{out}}$ 3.0%)

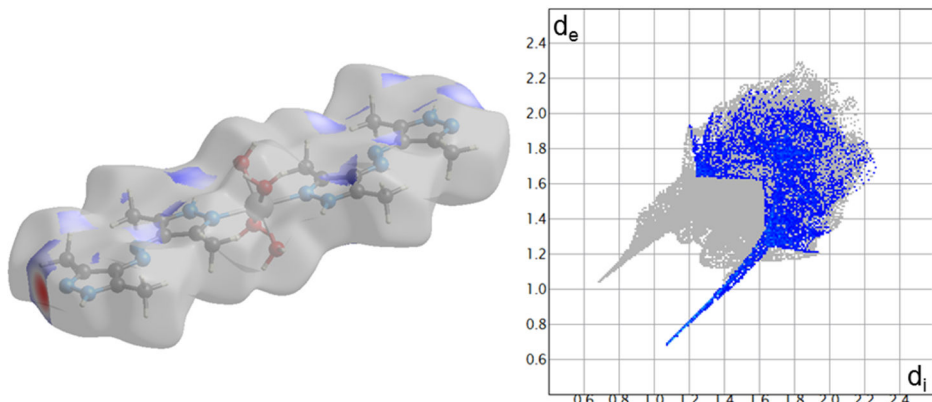


Figure S25. Representation of the relative contribution of N···H contacts to the Hirshfeld surface mapped with d_{norm} and the 2D fingerprint plot of the $[\text{Ni}(\text{H}_2\text{O})_4(\text{H}_2\text{azbpz})_2]$ fragment in **2** with d_i and d_e as the distances from the surface to the nearest atoms interior and exterior to the surface.

N···C contacts: 7.7% (reciprocal contributions are almost equal: $N_{\text{ins}}\cdots C_{\text{out}}$ 3.8%, $C_{\text{ins}}\cdots N_{\text{out}}$ 3.9%)

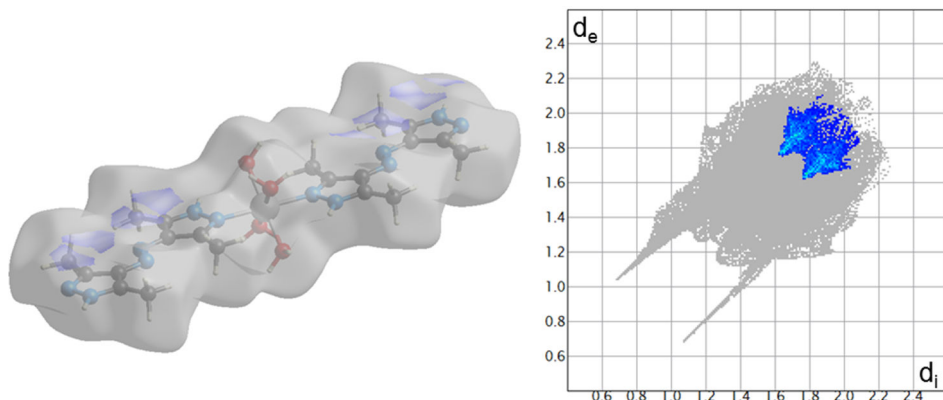


Figure S26. Representation of the relative contribution of N···C contacts to the Hirshfeld surface mapped with d_{norm} and the 2D fingerprint plot of the $[\text{Ni}(\text{H}_2\text{O})_4(\text{H}_2\text{azbpz})_2]$ fragment in **2** with d_i and d_e as the distances from the surface to the nearest atoms interior and exterior to the surface.

C···H contacts: 5.0% (reciprocal contributions are not equal: $C_{\text{ins}}\cdots H_{\text{out}}$ 3.1%, $H_{\text{ins}}\cdots C_{\text{out}}$ 1.8%)

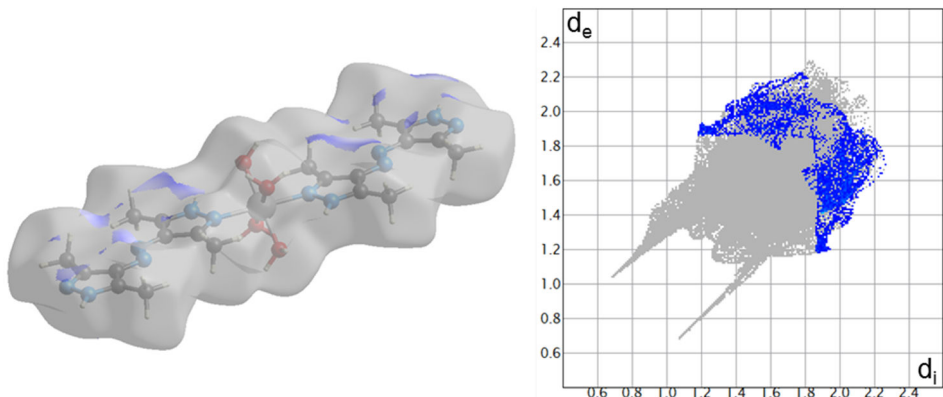


Figure S27. Representation of the relative contribution of C···H contacts to the Hirshfeld surface mapped with d_{norm} and the 2D fingerprint plot of the $[\text{Ni}(\text{H}_2\text{O})_4(\text{H}_2\text{azbpz})_2]$ fragment in **2** with d_i and d_e as the distances from the surface to the nearest atoms interior and exterior to the surface.

N···N contacts: 1.7%

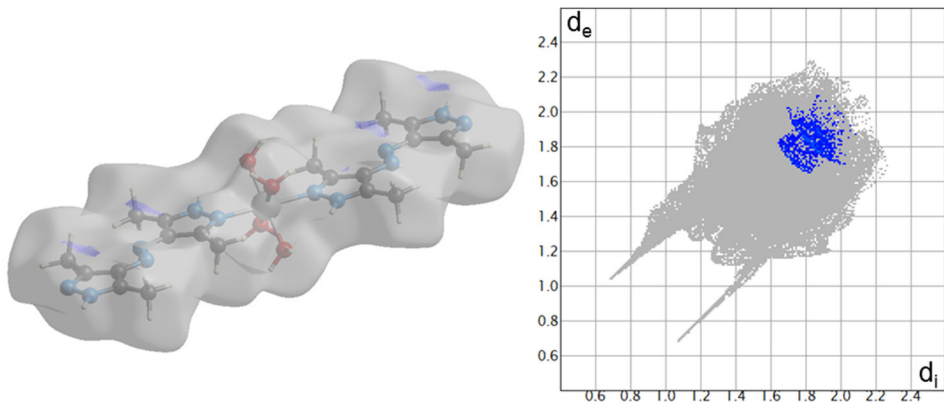


Figure S28. Representation of the relative contribution of N···N contacts to the Hirshfeld surface mapped with d_{norm} and the 2D fingerprint plot of the [Ni(H₂O)₄(H₂azbpz)₂] fragment in **2** with d_i and d_e as the distances from the surface to the nearest atoms interior and exterior to the surface.

C···C contacts: 1.7%

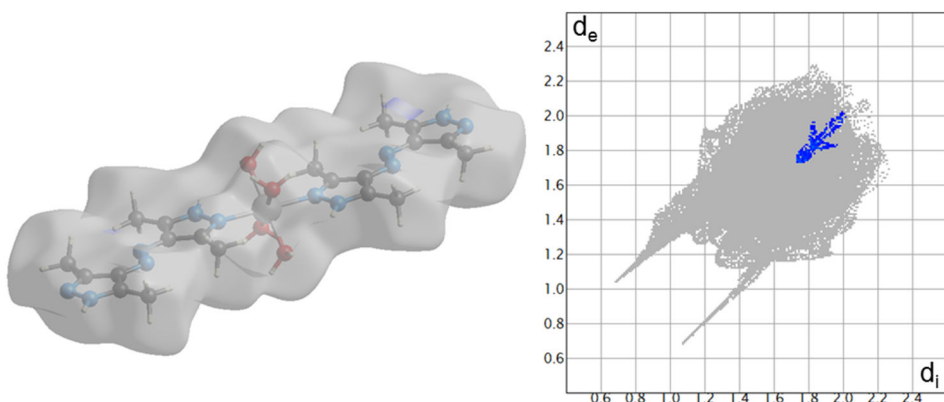


Figure S29. Representation of the relative contribution of C···C contacts to the Hirshfeld surface mapped with d_{norm} and the 2D fingerprint plot of the [Ni(H₂O)₄(H₂azbpz)₂] fragment in **2** with d_i and d_e as the distances from the surface to the nearest atoms interior and exterior to the surface.

N···O contacts: 0.9% (reciprocal contributions are not equal: $N_{\text{ins}}\cdots O_{\text{out}}$ 0.9%, $O_{\text{ins}}\cdots N_{\text{out}}$ 0%)

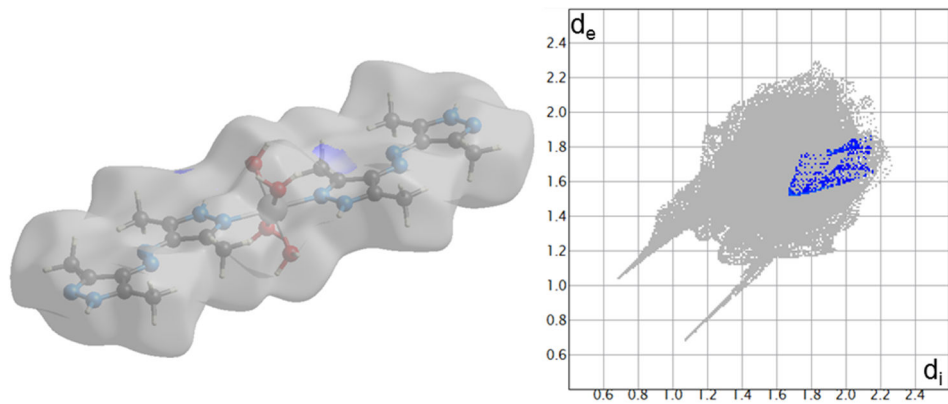


Figure S30. Representation of the relative contribution of N···O contacts to the Hirshfeld surface mapped with d_{norm} and the 2D fingerprint plot of the $[\text{Ni}(\text{H}_2\text{O})_4(\text{H}_2\text{azbpz})_2]$ fragment in **2** with d_i and d_e as the distances from the surface to the nearest atoms interior and exterior to the surface.

C···O contacts: 0.3% (reciprocal contributions are not equal: $N_{\text{ins}}\cdots O_{\text{out}}$ 0.3%, $O_{\text{ins}}\cdots N_{\text{out}}$ 0%)

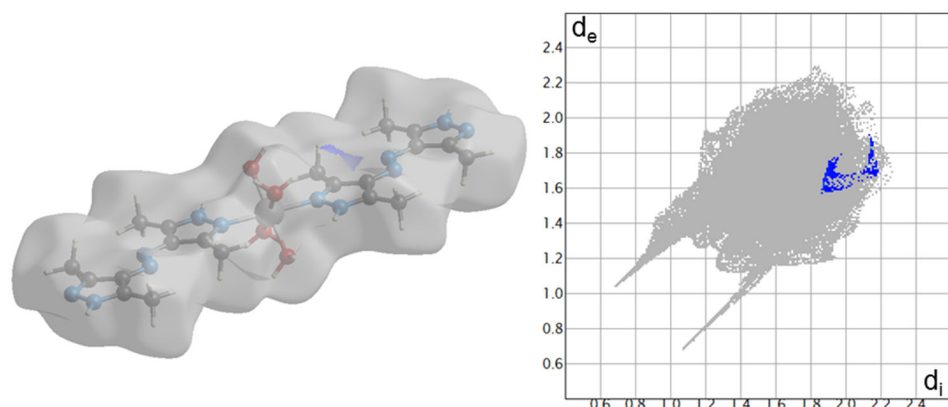


Figure S31. Representation of the relative contribution of N···O contacts to the Hirshfeld surface mapped with d_{norm} and the 2D fingerprint plot of the $[\text{Ni}(\text{H}_2\text{O})_4(\text{H}_2\text{azbpz})_2]$ fragment in **2** with d_i and d_e as the distances from the surface to the nearest atoms interior and exterior to the surface.

O···O contacts: 0.1%

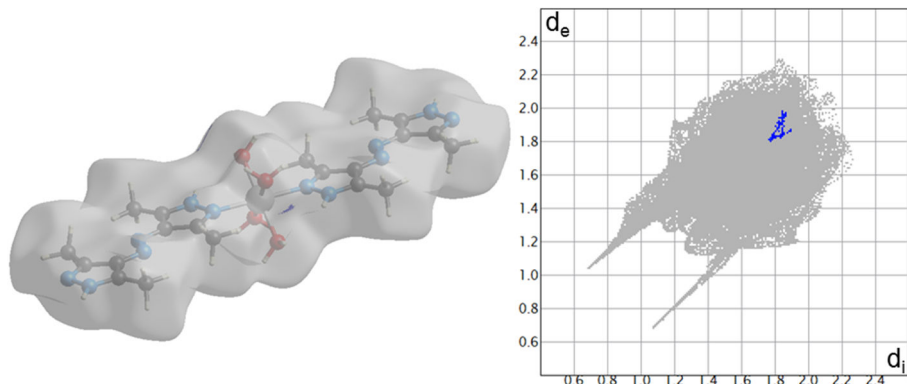


Figure S32. Representation of the relative contribution of O···O contacts to the Hirshfeld surface mapped with d_{norm} and the 2D fingerprint plot of the $[\text{Ni}(\text{H}_2\text{O})_4(\text{H}_2\text{azbpz})_2]$ fragment in **2** with d_i and d_e as the distances from the surface to the nearest atoms interior and exterior to the surface.

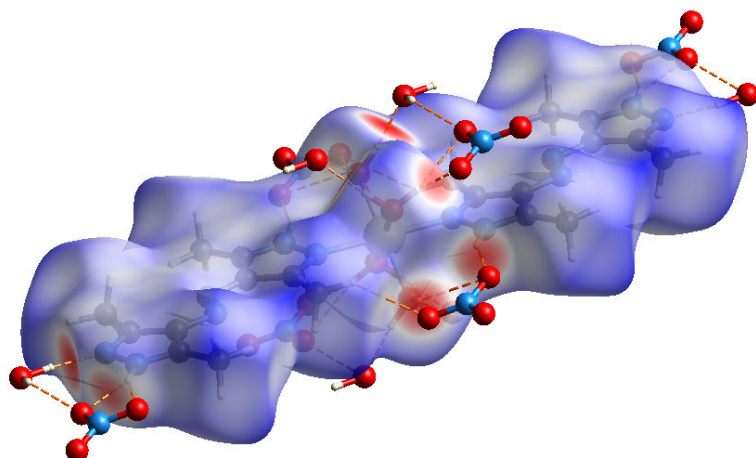


Figure S33. Visualization of the close contacts involving hydrogen bonds (orange-dashed lines) to the Hirshfeld surface mapped with d_{norm} of the $[\text{Ni}(\text{H}_2\text{O})_4(\text{H}_2\text{azbpz})_2]$ fragment in **2**.

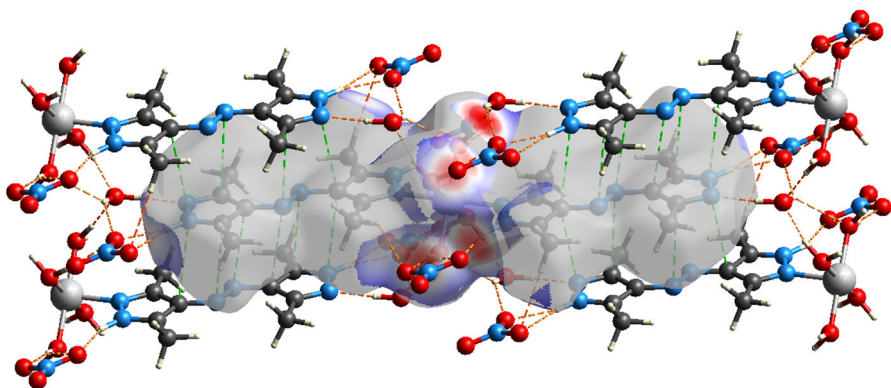


Figure S34. Visualization of the contribution of O···H to the Hirshfeld surface of the $[\text{Ni}(\text{H}_2\text{O})_4(\text{H}_2\text{azbpz})_2]$ fragments and the sheet arrangement in **2** (C···N contacts as green-dashed lines, hydrogen bonds as orange-dashed lines).

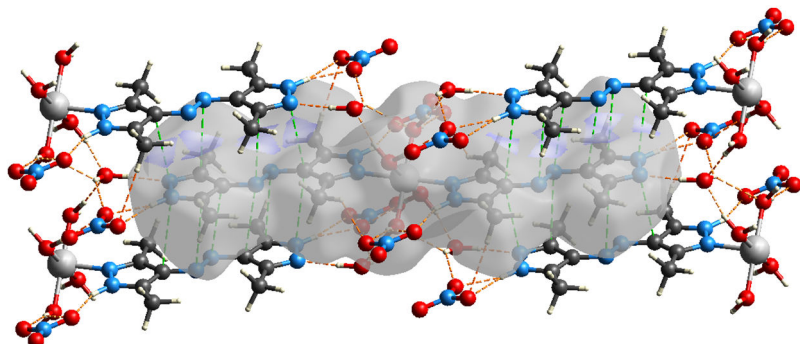


Figure S35. Visualization of the contribution of C···N contacts to the packing in the sheets of the $[\text{Ni}(\text{H}_2\text{O})_4(\text{H}_2\text{azbpz})_2]$ fragment in **2** (C···N contacts as green-dashed lines, hydrogen bonds as orange-dashed lines).

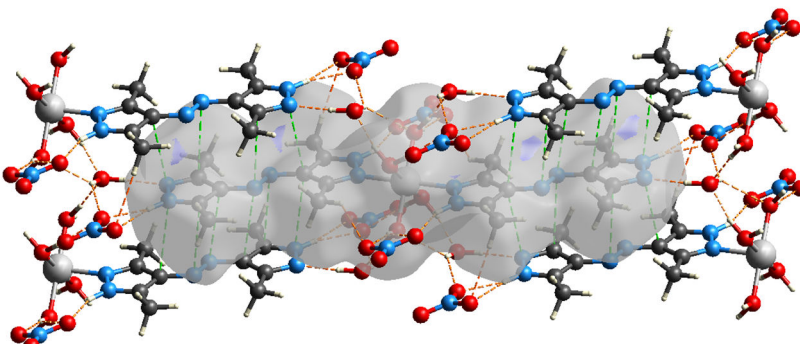


Figure S36. Visualization of the contribution of N···N contacts to the packing in the sheets of the $[\text{Ni}(\text{H}_2\text{O})_4(\text{H}_2\text{azbpz})_2]$ fragment in **2** (C···N contacts as green-dashed lines, hydrogen bonds as orange-dashed lines).

Table S1. Selected Bond lengths [Å] and angles [°] for $[\text{Cu}(\text{NO}_3)_2(\text{H}_2\text{O})_2(\text{H}_2\text{azbpz})_2] \cdot 2\text{H}_2\text{O}$.

Cu—O1 ⁱ	1.9617 (14)	N6—C9	1.337 (2)
Cu—N1 ⁱ	1.9902 (15)	N6—H6	0.81 (3)
Cu—O5 ⁱ	2.5359 (14)	C1—C2	1.493 (3)
O1—H1O1	0.77 (3)	C2—C3	1.404 (3)
O1—H2O1	0.81 (3)	C3—C4	1.397 (3)
O2—H1O2	0.77 (3)	C4—C5	1.488 (3)
O2—H2O2	0.80 (3)	C6—C7	1.493 (3)
N7—O4	1.232 (2)	C7—C8	1.423 (3)
N7—O5	1.255 (2)	C8—C9	1.387 (3)
N7—O3	1.261 (2)	C9—C10	1.491 (3)
N1—C2	1.335 (2)	N3—C3	1.398 (2)
N1—N2	1.368 (2)	N4—C8	1.397 (2)
N2—C4	1.331 (2)	N5—C7	1.325 (2)
N2—H2	0.82 (2)	N5—N6	1.364 (2)
N3—N4	1.268 (2)		
H1O1—O1—H2O1	103 (3)	H1O2—O2—H2O2	111 (3)
O1—Cu—N1 ⁱ	88.16 (6)	O4—N7—O5	120.23 (18)
O1 ⁱ —Cu—N1 ⁱ	91.83 (6)	O4—N7—O3	119.74 (17)
O1—Cu—O5 ⁱ	83.11 (6)	O5—N7—O3	120.03 (16)
O1 ⁱ —Cu—O5 ⁱ	96.89 (6)	N7—O5—Cu	135.81 (13)
N1 ⁱ —Cu—O5 ⁱ	89.29 (6)	C2—N1—N2	105.83 (15)
N5—N6—H6	120.4 (17)	C2—N1—Cu	134.42 (13)
N1—C2—C1	123.42 (17)	N2—N1—Cu	118.35 (11)
C3—C2—C1	127.33 (17)	C4—N2—N1	112.79 (15)
C4—C3—N3	131.99 (17)	C4—N2—H2	127.0 (16)
C4—C3—C2	106.78 (16)	N1—N2—H2	118.5 (16)
N3—C3—C2	121.22 (16)	N4—N3—C3	113.99 (15)
N2—C4—C3	105.38 (16)	N3—N4—C8	114.15 (16)
N2—C4—C5	121.31 (17)	C7—N5—N6	106.00 (15)
C3—C4—C5	133.31 (17)	C9—N6—N5	112.79 (16)
N5—C7—C8	109.29 (17)	C9—N6—H6	126.8 (17)
N5—C7—C6	119.95 (17)	N4—C8—C7	132.89 (18)
C8—C7—C6	130.75 (17)	N6—C9—C8	105.69 (17)
C9—C8—N4	120.88 (17)	N6—C9—C10	123.81 (18)
C9—C8—C7	106.22 (16)	C8—C9—C10	130.49 (18)

Symmetry transformation: 1-x, 1-y, 1-z.

Table S2. Selected Bond lengths [Å] and angles [°] for $[\text{Ni}(\text{H}_2\text{O})_4(\text{H}_2\text{azbpz})_2](\text{NO}_3)_2 \cdot 2\text{H}_2\text{O}$.

Ni—O1 ⁱ	2.064 (2)	N5—N6	1.361 (4)
Ni—O3	2.072 (2)	N6—C7	1.334 (4)
Ni—N1 ⁱ	2.107 (2)	N2—C4	1.336 (4)
C1—C2	1.489 (4)	N3—N4	1.270 (3)
C2—C3	1.425 (4)	N3—C3	1.394 (4)
C3—C4	1.394 (4)	N4—C8	1.396 (4)
C4—C5	1.486 (4)	N5—C9	1.334 (4)
O4—N7	1.250 (3)	C6—C7	1.485 (4)
O5—N7	1.234 (3)	C7—C8	1.397 (4)
O6—N7	1.235 (3)	C8—C9	1.430 (4)
N1—C2	1.339 (3)	C9—C10	1.483 (4)
N1—N2	1.366 (3)	O1—H1O1	0.85 (3)
O1—H2O1	0.90 (3)	O3—H1O3	0.68 (5)
O2—H1O2	0.816 (10)	O3—H2O3	0.68 (4)
O2—H2O2	0.818 (10)		
O1 ⁱ —Ni—O1	180.00 (12)	N1—C2—C3	109.2 (2)
O1 ⁱ —Ni—O3	89.93 (9)	N1—C2—C1	122.5 (3)
O1 ⁱ —Ni—N1	90.44 (9)	C3—C2—C1	128.3 (2)
O3 ⁱ —Ni—N1	93.18 (9)	N3—C3—C4	120.4 (3)
O1 ⁱ —Ni—N1 ⁱ	89.56 (9)	N3—C3—C2	133.7 (2)
Ni—O1—H1O1	122 (2)	C4—C3—C2	105.8 (2)
Ni—O1—H2O1	113 (2)	N2—C4—C3	106.3 (2)
H1O1—O1—H2O1	101 (3)	N2—C4—C5	123.3 (2)
H1O2—O2—H2O2	100 (2)	C3—C4—C5	130.4 (3)
H1O3—O3—H2O3	107 (5)	N6—C7—C8	105.9 (3)
Ni—O3—H1O3	117 (3)	N6—C7—C6	123.2 (3)
Ni—O3—H2O3	117 (3)	C8—C7—C6	130.9 (3)
C2—N1—N2	106.0 (2)	N4—C8—C7	121.5 (3)
C2—N1—Ni	137.45 (19)	N4—C8—C9	132.8 (3)
N2—N1—Ni	116.53 (16)	C7—C8—C9	105.7 (2)
C4—N2—N1	112.6 (2)	N5—C9—C8	109.3 (3)
C4—N2—H2N	123.7	N5—C9—C10	119.9 (3)
N1—N2—H2N	123.7	C8—C9—C10	130.8 (3)
N4—N3—C3	114.6 (2)	N5—N6—H6N	123.4
N3—N4—C8	113.9 (2)	O5—N7—O6	121.0 (3)
C9—N5—N6	105.9 (2)	O5—N7—O4	117.3 (3)
C7—N6—N5	113.2 (2)	O6—N7—O4	121.6 (3)

symmetry transformation: 1-x, 1-y, 1-z.

References

- [1] M. J. Turner, J. J. McKinnon, S. K. Wolff, D. J. Grimwood, P. R. Spackman, D. Jayatilaka, M. A. Spackman, *CrystalExplorer17*, Version 17.5, © 2005–2019 University of Western Australia, 2017, <http://hirshfeldsurface.net>.
- [2] J. J. McKinnon, D. Jayatilaka, M. A. Spackman, *Chem. Commun.* **2007**, 3814–3816.
- [3] M. A. Spackman, J. J. McKinnon, *CrystEngComm* **2002**, 4, 378–392.

3.4 A 2D Zinc coordination polymer built from the mono-deprotonated 4,4'-azobis(3,5-dimethyl-1H-pyrazole) ligand

The work presented in this chapter has been published in:

S. Millan, B. Gil-Hernández, E. Hastürk, A. Schmitz and C. Janiak *Z. Anorg. Allg. Chem.* **2018**, *644*, 1311-1316.

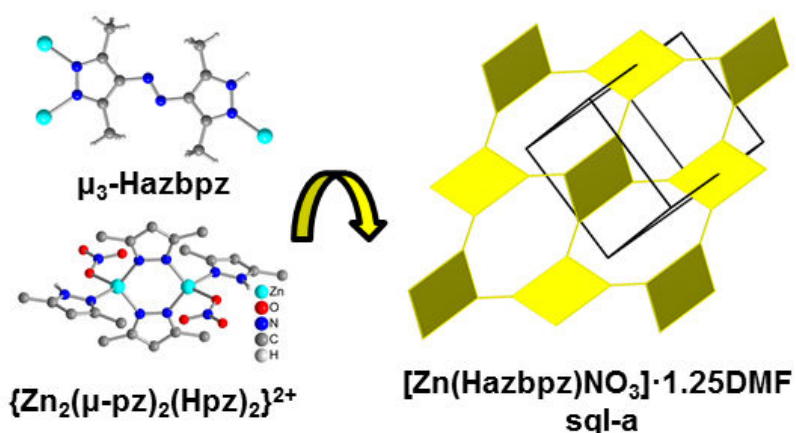
DOI: 10.1002/zaac.201800286

as part of the Special Issue dedicated to Professor Werner Uhl on the occasion of his 65th birthday.

The article is reprinted with permission of John Wiley and Sons, Inc.

Abstract

4,4'-Azobis(3,5-dimethyl-1H-pyrazole) (H_2azbpz) in its mono-deprotonated form as a pyrazole-pyrazolate ligand was assembled together with zinc(II) into the two-dimensional coordination polymer $[\text{Zn}(\text{Hazbpz})\text{NO}_3] \cdot 1.25\text{DMF}$ with **sql-a** topology, constituted by the dinuclear $\{\text{Zn}_2(\mu\text{-pz})_2(\text{Hpz})_2^{2+}\}$ secondary building unit. The μ_3 -bridging mode of the ligand is in analogy to bridging modes observed for 4-(4-pyridyl)pyrazolates ligands. After the removal of the DMF solvent molecules, ethanol can be adsorbed up to a maximum uptake of 276 mg/g at $p/p_0 = 0.9$ in an S-shaped adsorption isotherm, corresponding to two ethanol molecules per $[\text{Zn}(\text{Hazbpz})\text{NO}_3]$ formula unit. The desorption isotherm reveals that only one EtOH is desorbed until $p/p_0 = 0.4$ and the other one remains hydrogen-bonded in the framework until very low pressures.



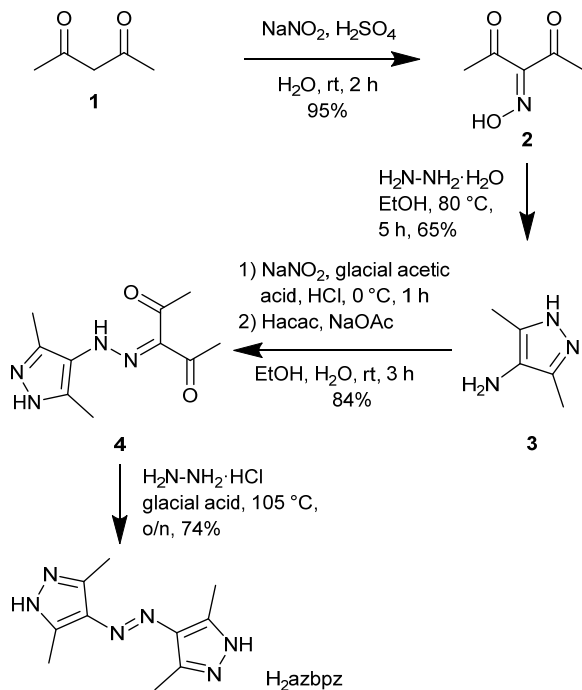
Introduction

Coordination polymers are of interest due to their intriguing topologies and their wide-spreading properties.^[1] Structures of one- and two-dimensional coordination polymers have additional weak interactions (e.g. hydrogen bonds, pi-pi stacking, halogen bonds) besides the polymer-defining coordinative metal-ligand bonds.^[2] In this context pyrazole are interesting ligands with a pyridinic and a pyrrolic nitrogen atom next to each other. Pyrazole ligands feature a multifaceted coordination and supramolecular chemistry with interesting catalytic, magnetic and optical properties.^[3] Furthermore, bipyrazole ligands are predestined to construct coordination networks with transition metals as outlined in a recent review by Pettinari et al.^[4] Bipyrazole ligands can either be used in their non-deprotonated forms as neutral bridging ligands or in their deprotonated forms as anionic bridging ligands. In their neutral forms bipyrazoles build coordination frameworks related to 4,4'-bipyridines with the adjacent NH-functions interacting with hydrogen accepting guest molecules and anions.^[5] Their doubly deprotonated forms – the bipyrazolates – build thermally and chemically stable metal-organic frameworks through strong metal-ligand bonds between the metal cation and the pyrazolate anion. Metal-bipyrazolates show interesting properties like flexibility upon gas adsorption,^[6] tunable water sorption properties^[7] or catalytic activity.^[8] The simplest bipyrazole representatives 4,4'-bipyrazolyl^[5b] and 3,3',5,5'-tetramethyl-4,4'-bipyrazolyl^[5a] are supplemented by bipyrazoles with different spacer groups between the pyrazole rings or substituents on position 3 and 5 of the pyrazole ring in order to obtain a large variety of coordination networks.^[7,9] Additionally, bipyrazoles can be used together with carboxylates in the construction of a multitude of coordination networks.^[10] On the other hand, the incorporation of mono-deprotonated bipyrazolate, that is, pyrazole-pyrazolate ligands, into coordination compounds is rather scarce. Examples are a dinuclear nickel complex^[11] and a ruthenium complex.^[12] An early example for a coordination network containing a pyrazole-pyrazolate ligand is an europium MOF, which was synthesized from the metal in the melt of the ligand, containing neutral and mono-anionic 3,3',5,5'-tetramethyl-4,4'-bipyrazolyl.^[13] Coordination networks built from a pyrazole-pyrazolate and an additional dicarboxylate ligand include a cobalt-coordination polymer containing the mono-deprotonated ligand 4,4'-methylenebis(3,5-dimethyl-1H-pyrazole) and a piperazine-based dicarboxylate^[14] and three cobalt(II) or zinc(II) MOFs synthesized from mono-deprotonated 3,3',5,5'-tetramethyl-4,4'-bipyrazole and 4,4'-biphenyldicarboxylate.^[15]

We present here $[\text{Zn}(\text{Hazbpz})\text{NO}_3] \cdot 1.25\text{DMF}$ as the first coordination polymer with the bipyrazole ligand 4,4'-azobis(3,5-dimethyl-1H-pyrazole) (= H₂Azbpz) (Scheme 1) and investigated its sorption properties towards water and ethanol.

Results and Discussion

4,4'-Azobis(3,5-dimethyl-1H-pyrazole) (H_2azbpz) was synthesized in four steps starting from acetylacetone (**1**). H_2azbpz was first described by Hüttel et al. in 1955 during their studies on nitro- and nitrosopyrazoles via a Mills coupling reaction, but to the best of our knowledge was never used for the construction of coordination compounds.^[16]



Scheme 1. Reaction scheme for the synthesis of H_2azbpz .

A solvothermal reaction between zinc nitrate and H_2azbpz in dimethylformamide (DMF) and ethanol (EtOH) at 80 °C yielded plate-shaped yellow single crystals. The representative nature of the selected crystals with respect to the bulk was verified by positive matching of the simulated and experimental powder X-ray diffractograms (Figure S1 in Supp. Info.). The single-crystal X-ray analysis revealed a coordination polymer with formula $[\text{Zn}(\text{Hazbpz})\text{NO}_3] \cdot 1.25\text{DMF}$. The product crystallizes in the monoclinic space group $P2_1/n$ with one zinc(II) ion, one mono-deprotonated ligand Hazbpz^- , one nitrate ligand and 1.25 DMF molecules in the asymmetric unit (Figure). The N-H function of the non-deprotonated pyrazole group forms a hydrogen bond to the carbonyl function of one DMF molecule. The other DMF molecule is only a quarter occupied and highly disordered as it sits on a special position (inversion center) of higher symmetry than the DMF molecule itself has (Figure S6 in Supp. Info.). The solvent content is also underpinned by the thermogravimetric analysis (TGA) and elemental analysis data (Figure 7, Experimental Section).

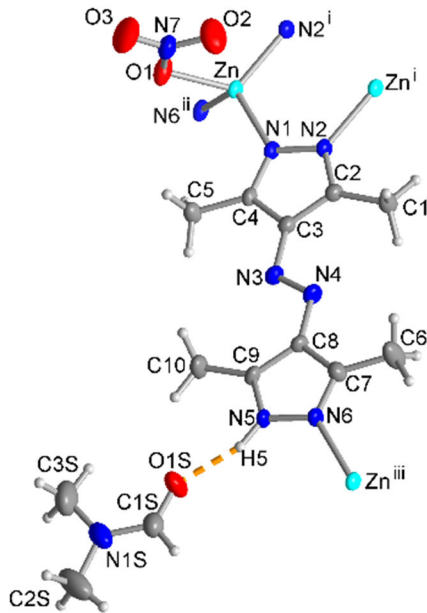


Figure 1 Extended asymmetric unit of $[Zn(\text{Hazbpz})\text{NO}_3] \cdot 1.25\text{DMF}$ (50% thermal ellipsoids, symmetry transformations: (i) $-x, -y+2, -z+1$; (ii) $x-1/2, -y+3/2, z+1/2$; (iii) $x+1/2, -y+3/2, z-1/2$). The disordered DMF molecule is omitted for clarity). Hydrogen bond (dashed orange line) distances [\AA] and angle [$^\circ$]: N–H 0.92(5), H \cdots O 1.85(5), N \cdots O 2.698(5), D–H \cdots A 153(5).

The zinc(II) ion is tetrahedrally coordinated by three nitrogen atoms and one nitrate oxygen atom. Two nitrogen atoms belong to two bridging pyrazolates (N1 and N2) and the third one belongs to nitrogen N6 from the neutral pyrazole group. Selected bond lengths and angles are given in Table 1. Each mono-deprotonated pyrazole-pyrazolate ligand bridges between three zinc atoms through its non-hydrogen-carrying nitrogen atoms in the heterocycles (Figure 1). Two $\kappa\text{N}1:\kappa\text{N}2$ -bridging pyrazolates (pz), two coordinated pyrazoles (Hpz) and two terminal nitrato ligands form the inversion-symmetric dinuclear secondary building unit (SBU) $\{\text{Zn}_2(\mu\text{-pz})_2(\text{Hpz})_2(\text{NO}_3)_2\}$ with a Zn \cdots Zn distance of 3.588(8) \AA (Figure 2).

Table 1. Selected bond lengths [\AA] and angles [$^\circ$] in $[Zn(\text{Hazbpz})\text{NO}_3] \cdot 1.25\text{DMF}$

Zn–N1	1.969(3)	N1–Zn–O1	112.44(15)
Zn–N2 ⁱ	1.977(3)	N2 ⁱ –Zn–O1	118.50(15)
Zn–O1	2.020(3)	N1–Zn–N6 ⁱⁱ	113.26(14)
Zn–N6 ⁱⁱ	2.023(4)	N2 ⁱ –Zn–N6 ⁱⁱ	106.89(15)
N1–Zn–N2 ⁱ	111.78(14)	O1–Zn–N6 ⁱⁱ	92.35(14)

symmetry transformations: (i) $-x, -y+2, -z+1$; (ii) $x-1/2, -y+3/2, z+1/2$.

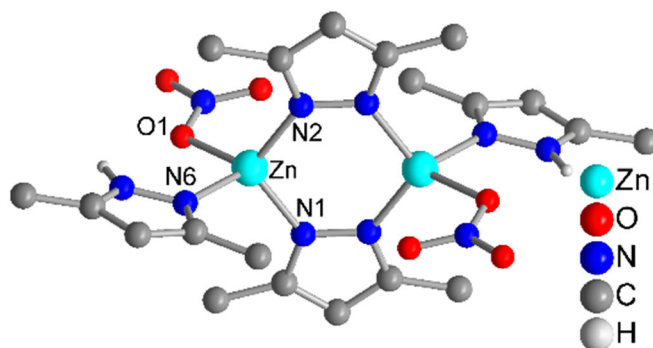


Figure 2. $\{Zn_2(\mu\text{-}pz)_2(Hpz)_2(NO_3)_2\}$ as the dinuclear building block (the hydrogen atoms at the methyl groups are omitted for clarity).

The mono-deprotonated Hazbpz⁻ ligand is perfectly planar and links the square planar 4-c secondary building units to form a two dimensional **sql-a** (= **fes**) net (Figure 3).^[17] The dimensions of the rhomboid grid are $12.0 \times 12.0 \text{ \AA}^2$ with angles of 70° and 110° measured between the centers of the dinuclear Zn₂ SBU.

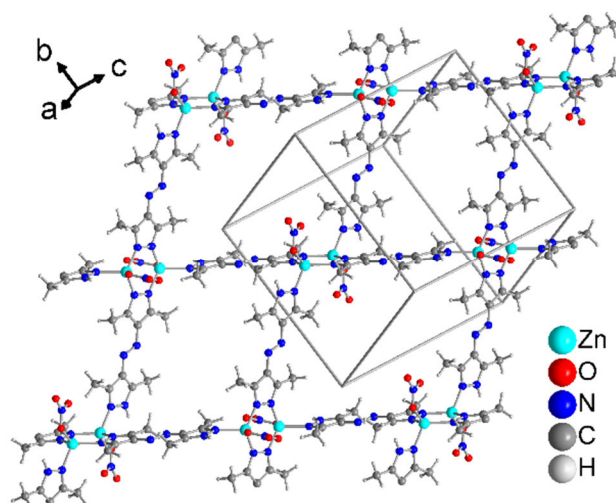


Figure 3. Section of the packing diagram of 2D-[Zn(Hazbpz)NO₃]·1.25DMF with the DMF molecules omitted for clarity.

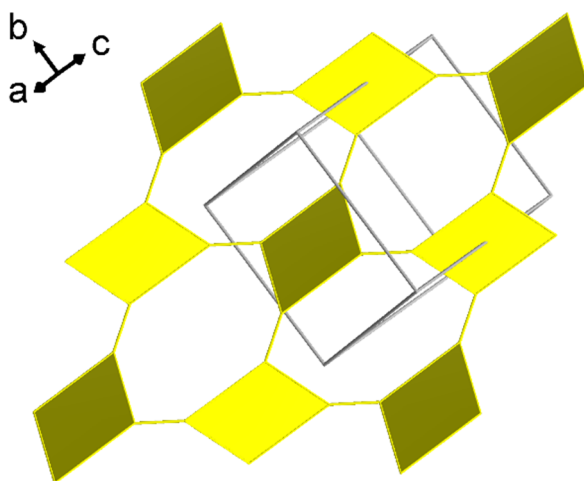


Figure 4. Topological **sql-a** representation of a single $[Zn(\text{Hazbpz})\text{NO}_3]$ -layer with the $\{\text{Zn}_2(\mu\text{-pz})_2(\text{Hpz})_2(\text{NO}_3)_2\}$ -SBU as yellow rhomboids linked by the azo-functionalities.

The square planar 4-c SBU can be topologically represented as a rhomboid building block linked by the azo-functionalities (Figure 4). The $[Zn(\text{Hazbpz})\text{NO}_3]$ -layers stack in an AB-fashion with a symmetric relation of $[x+1, y, z]$ or $[x, y, z+1]$ between the nets and the dinuclear "Zn₂"-SBUs of the adjacent grids sitting in the middle of the openings (Figure 5 and Figure 6). No significant supramolecular interactions could be identified between the layers.

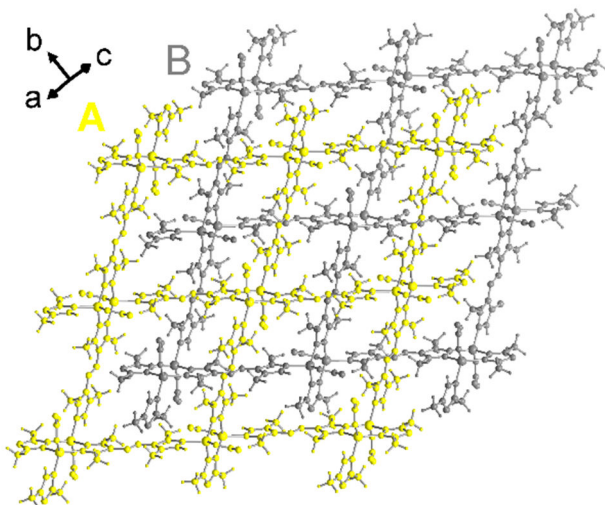


Figure 5. Section of the packing diagram of two adjacent two-dimensional nets of $[Zn(\text{Hazbpz})\text{NO}_3] \cdot 1.25\text{DMF}$ with the DMF molecules omitted for clarity; symmetry relation between layer A (yellow) and layer B (grey): $x+1, y, z$ or $x, y, z+1$.

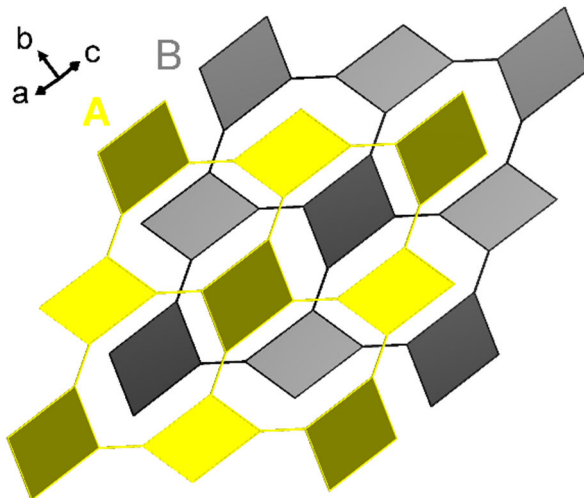


Figure 6. Topological **sql-a** representation of two adjacent AB-stacked 2D layers.

Analogous dinuclear metal units $\{M_2(\mu\text{-pz})_2(\text{Hpz})_2^{2+}\}$ can be found with $M = \text{Zn}$ and Co .^[18] Pettinari et al. noted that with an excess of 1H-pyrazole, the compound $[\text{Zn}(\mu\text{-pz})(\text{Hpz})(\text{CH}_3\text{COO})]_2$, built from the aforementioned dinuclear units, is formed. The dinuclear molecules transform with thermal treatment into the polymeric $[\text{Zn}(\mu\text{-pz})_2]$ -form. This transformation was not observed for the dimethylpyrazole analog.^[18b] Baruah et al. found that the utilization of DMF favored the formation of the dinuclear pyrazolato-bridged complexes in contrast to monomeric pyrazole complexes in reactions of zinc acetate, 1H-dimethylpyrazole and aromatic carboxylic acids.^[18c] Besides the cobalt coordination polymer by Batten et al., built from the mono-deprotonated ligand 4,4'-methylenebis(3,5-dimethyl-1H-pyrazole) and 1,4-bis((3-carboxyphenyl)methyl)piperazine (Figure S7 in Supp. Info.),^[14] our compound $[\text{Zn}(\text{Hazbpz})\text{NO}_3] \cdot 1.25\text{DMF}$ is, to the best of our knowledge, the only coordination polymer assembled from the $\{M_2(\mu\text{-pz})_2(\text{Hpz})_2^{2+}\}$ entity (Figure S8-S10 in Supp. Info.).

It is interesting to note the similarities of the coordination behavior of the mono-deprotonated ligand Hazbpz⁻ and 4-(4-pyridyl)pyrazolates (Hpypz) (Figure S5 in Supp. Info.). The latter are an extension of the intensively studied 1,2,4-triazolate system.^[19] Turner et al. have synthesized the directly related framework $[\text{Zn}_2(\text{pypz})_2\text{Cl}_2] \cdot 2\text{EtOH}$ ^[20] which is identical in its topology to $[\text{Zn}(\text{Hazbpz})\text{NO}_3] \cdot 1.25\text{DMF}$. Chen et al. used these cationic $[\text{Zn}(\text{pypz})]^+$ **sql-a** sheets with $[\text{Zn}_2(\text{btc})_4(\text{H}_2\text{O})_2]^{8-}$ -pillars to obtain a 3-dimensional porous MOF with a high methane storage capacity.^[21]

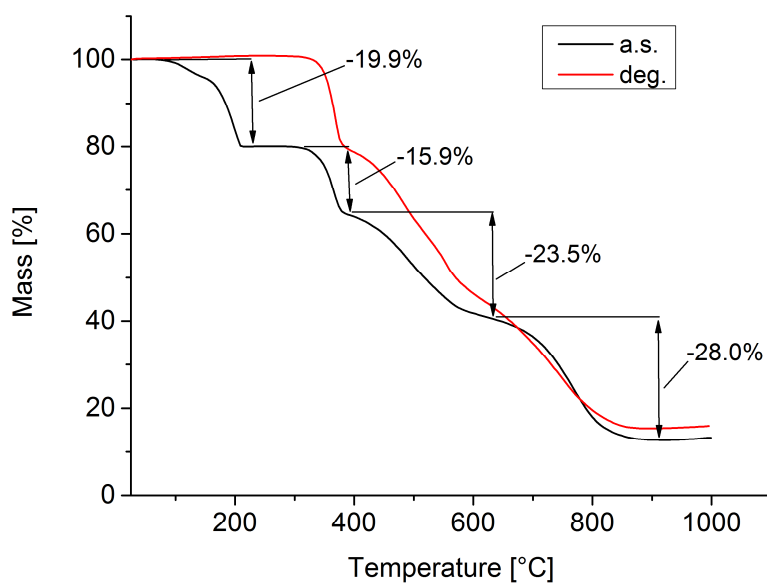


Figure 7. TGA curve of $[\text{Zn}(\text{Hazbpz})\text{NO}_3] \cdot 1.25\text{DMF}$ as-synthesized (a.s.) and degassed (deg.) with a heating rate of 5 K/min under N_2 atmosphere.

The TGA data of $[\text{Zn}(\text{Hazbpz})\text{NO}_3] \cdot 1.25\text{DMF}$ as-synthesized (a.s) show a two-step weight loss up to 200 °C, which corresponds to a total weight loss of 19.9% (Figure 7). The first step of 4.0% in the range between 100 – 150 °C is assigned to the disordered and not H-bonded quarter-occupied DMF molecule (4.2% theoretically) and the second step with 15.9% in the range between 150 – 210 °C to the H-bonded DMF molecule (16.1% theoretically). After the sample was degassed at 150 °C for 12 h under vacuum (10^{-5} mbar) the TGA curve of the activated sample shows that the solvent molecules had been fully removed (Figure 5). Solvent-depleted $[\text{Zn}(\text{Hazbpz})\text{NO}_3]$ is thermally stable up to 340 °C.

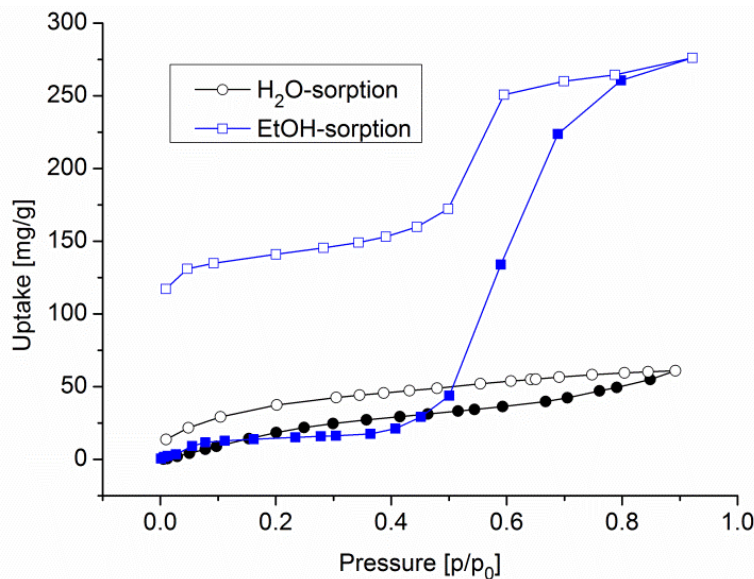


Figure 8. Water (black) and ethanol (blue) sorption isotherms at 293 K for $[Zn(Hazbpz)NO_3]$ -(deg.).

Since the included solvent molecules could be removed, the sorption properties of degassed (deg.) $[Zn(Hazbpz)NO_3]$ towards H_2O and $EtOH$ vapors were tested (Figure 8). $[Zn(Hazbpz)NO_3]$ -(deg.) adsorbs about 51 mg/g H_2O at $p/p_0 = 0.9$, which equals about one H_2O molecule per $[Zn(Hazbpz)NO_3]$ formula unit. For ethanol $[Zn(Hazbpz)NO_3]$ -(deg.) shows an S-shaped adsorption isotherm with the main step between 0.5 and 0.7 p/p_0 and a maximum uptake of 276 mg/g at $p/p_0 = 0.9$, representing about two $EtOH$ molecules per formula unit. The desorption curve shows a large hysteresis with a very slow desorption below p/p_0 0.4 or around 140 mg/g, where about one $EtOH$ molecule per $[Zn(Hazbpz)NO_3]$ formula unit would be present. This means that only one $EtOH$ is desorbed until p/p_0 0.4 and the other one remains hydrogen-bonded in the framework until very low pressures. Under the chosen measurement times, the desorption curve did not close. The last desorption data point at $p/p_0 = 0.01$ indicates the beginning desorption of the second hydrogen-bonded ethanol molecule.

Conclusions

The novel two-dimensional coordination polymer $[\text{Zn}(\text{Hazbpz})\text{NO}_3] \cdot 1.25\text{DMF}$ with **sql-a** topology was structurally characterized. The compound is based on the bipyrazole ligand H_2azbpz , which was until now not used in the construction of coordination networks. The vapor sorption characteristics for water and ethanol with the S-shaped adsorption isotherm of ethanol and a pronounced hysteresis confirm the hydrophobic nature of the material. In its mono-deprotonated version Hazbpz^- is a pyrazole-pyrazolate ligand and mimics the coordination behavior of 1,2,4-triazolates and 4-(4-pyridyl)pyrazolates. We hypothesize that by careful adjustment of the synthesis conditions this coordination behavior of bipyrazoles with a N-H hydrogen-bond donor function directly adjacent to the metal subunits can be very useful in the construction of a wide set of novel coordination polymers.

Experimental Section

The chemicals used were obtained from commercial sources. No further purification has been carried out. CHN analysis was performed with a Perkin Elmer CHN 2400 (Perkin Elmer, Waltham, MA, USA). IR-spectra were recorded on a Bruker Tensor 37 IR spectrometer (Bruker Optics, Ettlingen, Germany) with a KBr unit. ^1H and ^{13}C spectra were measured with a Bruker Advance DRX-300. ESI-MS spectra were recorded on a Thermo Quest Ion Trap API mass spectrometer Finnigan LCQ Deca. Thermogravimetric analysis (TGA) was done with a Netzsch TG 209 F3 Tarsus (Netzsch, Selb, Germany) in the range from 25 to 1000 °C, equipped with an Al-crucible and applying a heating rate of 5 K·min⁻¹ under nitrogen. The powder X-ray diffraction pattern (PXRD) was obtained on a Bruker D2 Phaser powder diffractometer with a flat silicon, low background sample holder, at 30 kV, 10 mA for Cu-Kα radiation ($\lambda = 1.5418 \text{ \AA}$). The water and ethanol sorption isotherms were measured at 293 K using a Quantachrome VSTAR vapor sorption analyzer. The sample was activated with a Quantachrome FloVac Degasser at 150 °C for 12 h under a vacuum of 10^{-5} mbar mbar.

Single Crystal X-ray Structure

Suitable crystals were carefully selected under a polarizing microscope, covered in protective oil and mounted on a 0.05 mm cryo loop. *Data collection:* Bruker Kappa APEX2 CCD X-ray diffractometer (Bruker AXS Inc., Madison, WI, USA) with microfocus tube, Mo-Kα radiation ($\lambda = 0.71073 \text{ \AA}$), multi-layer mirror system, ω -scans; data collection with APEX2,^[22] cell refinement with SMART and data reduction with SAINT,^[22] experimental absorption correction with SADABS.^[23] *Structure analysis and refinement:* The structure was solved by direct methods using SHELXL2016,^[24] refinement was done by full-matrix least squares

on F^2 using the SHELX-97 program suite. Crystal data and details on the structure refinement are given in Table 1. Graphics were drawn with Diamond.^[25]

Crystallographic data (excluding structure factors) for the structure in this paper have been deposited with the Cambridge Crystallographic Data Centre, CCDC, 12 Union Road, Cambridge CB21EZ, UK. Copies of the data can be obtained free of charge on quoting the depository number CCDC-1852726 (Fax: +44-1223-336-033; E-Mail:deposit@ccdc.cam.ac.uk, <http://www.ccdc.cam.ac.uk>).

Tabelle 2. Crystal structure and refinement details of [Zn(Hazbpz)NO₃]·1.25DMF.

[Zn(Hazbpz)NO₃]·1.25DMF	
Empirical formula	[C ₁₀ H ₁₃ N ₇ O ₃ Zn]·1.25(C ₃ H ₇ NO)
M_r /gmol ⁻¹	436.01
Crystal system, space group	Monoclinic, P2 ₁ /n
Crystal size /mm	0.05 × 0.05 × 0.01
Temperature /K	150
<i>a</i> /Å	10.7845 (12)
<i>b</i> /Å	13.7644 (14)
<i>c</i> /Å	13.8068 (14)
β /°	104.715 (6)
<i>V</i> /Å ³	1982.3 (4)
<i>Z</i>	4
μ /mm ⁻¹	1.28
<i>F</i> (000)	904
Max./min. transmission	0.750/0.680
Measured, indep., observed reflections	21901, 2993, 2337 [$I > 2\sigma(I)$]
R _{int}	0.053
Data/restraints/parameters	2993 / 1 / 256
Max./min. $\Delta\rho$ ^{a)} /e·Å ⁻³	0.834, -0.370
R, wR(F^2), <i>S</i> [$I > 2\sigma(I)$] ^{b)}	0.0433, 0.1173, 1.086
R, wR(F^2), <i>S</i> [all data] ^{b)}	0.0614, 0.1261, 1.092

a) Largest difference peak and hole. – b) $R_1 = [\sum(\|F_o\| - \|F_c\|)/\sum\|F_o\|]; wR_2 = [\sum[w(F_o^2 - F_c^2)^2]/\sum[w(F_o^2)^2]]^{1/2}$. Goodness-of-fit $S = [\sum[w(F_o^2 - F_c^2)^2]/(n-p)]^{1/2}$.

2,3,4-Pentanetrione-3-oxime (**2**) was prepared according to Tkach et al. and used without purification.^[26] Subsequently, 4-amino-3,5-dimethyl-1H-pyrazole (**3**) was synthesized through a procedure adapted from Liu et al.^[27] and coupled in a Japp-Klingemann reaction to obtain 3-(2-(3,5-dimethyl-1H-pyrazolyl)hydrazone)pentan-2,4-dione (**4**) according to Rollas et al.^[28]

4,4'-Azobis(3,5-dimethyl-1H-pyrazole) (H₂azbpz):

2.01 g (9.05 mmol) of 3-(2-(3,5-dimethyl-1H-pyrazolyl)hydrazone)pentan-2,4-dione and 0.740 g (10.8 mmol, 1.2 eq) of hydrazine monohydrochloride dissolved in 15 ml of glacial acetic acid were heated at 105 °C overnight. The yellow precipitate was filtered off and washed thoroughly with water. The crude product was recrystallized from an ethanol:water mixture to afford H₂azbpz as a yellow powder. After drying for 48 h at 60 °C in a vacuum oven (10⁻¹ mmbar) 1.47 g (6.73 mmol, 74 %) were obtained.

¹H-NMR (300 MHz, DMSO-d₆) δ [ppm]: 2.37, 12.36.

¹³C-NMR (75 MHz), DMSO-d₆): 141.45, 135.49, 134.39, 13.64, 9.97.

ESI-MS: [M+H]⁺ 219.3.

EA [%] calc. for H₂azbpz, C₁₀H₁₅N₆: C 55.03, H 6.47, N 38.50, found: C 54.89, H 6.49 N 38.24%.

[Zn(Hazbpz)NO₃]·1.25DMF:

18 mg (0.083 mmol) of H₂azbpz dissolved in 2 ml of EtOH and 0.3 ml of DMF were combined with a solution of 10 mg (0.038 mmol) of Zn(NO₃)₂·4H₂O in 1 ml of EtOH and put in a preheated oven at 80 °C for 4 days. Yield: 3.4 mg (21 %). In a scaled-up synthesis 108.1 mg (0.50 mmol) of H₂azbpz were dissolved in 15 ml of EtOH and 1.8 ml of DMF and combined with 60.2 mg (0.23 mmol) of Zn(NO₃)₂·4H₂O dissolved in 3 ml of EtOH in a 50 ml Pyrex vessel. After 4 days at 80 °C in an isothermal oven, the product was thoroughly washed with a 10 v/v% DMF/EtOH mixture. [Zn(Hazbpz)NO₃]·1.25DMF was obtained by suction filtration and short drying in air. Yield: 76.0 mg (75 %).

EA [%] calc. for: [Zn(Hazbpz)NO₃]·1.25DMF, C_{13.75}H_{21.75}N_{8.25}O_{4.25}Zn C 37.88, H 5.03, N 26.50 found: C 38.06, H 5.11, N 25.58.

EA [%] calc. for: [Zn(Hazbpz)NO₃]- (degassed), C₁₀H₁₃N₇O₃Zn C 34.85, H 3.80, N 28.45 found: C 34.97, H 3.86, N 27.78.

References

- [1] (a) S. R. Batten, R. Robson, *Angew. Chem. Int. Ed.* **1998**, *37*, 1460-1494; (b) C. Janiak, *Dalton Trans.* **2003**, *0*, 2781-2804; (c) S. Kitagawa, R. Kitaura, S.-i. Noro, *Angew. Chem. Int. Ed.* **2004**, *43*, 2334-2375; (d) L. Carlucci, G. Ciani, D. M. Proserpio *Coord. Chem. Rev.* **2003**, *246*, 247-289; (e) N. Li, R. Feng, J. Zhu, Z. Chang, X.-H. Bu, *Coord. Chem. Rev.* **2018**.
- [2] (a) C. B. Aakeröy, N. R. Champness, C. Janiak, *CrystEngComm* **2010**, *12*, 22-43; (b) K. Uemura, K. Saito, S. Kitagawa, H. Kita, *J. Am. Chem. Soc.* **2006**, *128*, 16122-16130; (c) B. Paul, B. Zimmermann, K. M. Fromm, C. Janiak, *Z. Anorg. Allg. Chem.* **2004**, *630*, 1650-1654; (d) B. Wisser, Y. Lu, C. Janiak, *Z. Anorg. Allg. Chem.* **2007**, *633*, 1189-1192; (e) S. Sengupta, S. Ganguly, A. Goswami, P. K. Sukul, R. Mondal, *CrystEngComm* **2013**, *15*, 8353-8365; (f) B. Gil-Hernandez, H. A. Höppe, J. K. Vieth, J. Sanchiz, C. Janiak, *Chem. Commun.* **2010**, *46*, 8270-8272; (g) Y. Yong, Z. Ning-Ning, L. Rong, X. Jian-Gang, L. Jian, Z. Fa-Kun, G. Guo-Cong, *Eur. J. Inorg. Chem.* **2017**, *2017*, 3811-3814; (h) S. Millan, G. Makhloufi, C. Janiak, *Crystals* **2018**, *8*, 30; (i) A. Azhdari Tehrani, S. Abedi, A. Morsali, *Cryst. Growth Des.* **2017**, *17*, 255-261. (j) B. L. Martinez, R. L. LaDuca *Z. Anorg. Allg. Chem.* **2017**, *643*, 1118-1125.
- [3] (a) S. Trofimenko, *Chem. Rev.* **1972**, *72*, 497-509; (b) A. P. Sadimenko, S. S. Basson, *Coord. Chem. Rev.* **1996**, *147*, 247-297; (c) M. A. Halcrow, *Dalton Trans.* **2009**, 2059-2073; (d) M. Viciana-Chumillas, S. Tanase, L. J. de Jongh, J. Reedijk, *Eur. J. Inorg. Chem.* **2010**, *2010*, 3403-3418; (e) C. W. Lu, Y. Wang, Y. Chi, *Chem. Eur. J.* **2016**, *22*, 17892-17908.
- [4] C. Pettinari, A. Tăbăcaru, S. Galli, *Coord. Chem. Rev.* **2016**, *307*, 1-31.
- [5] (a) I. Boldog, E. B. Rusanov, A. N. Chernega, J. Sieler, K. V. Domasevitch, *Polyhedron* **2001**, *20*, 887-897; (b) I. Boldog, J. Sieler, A. N. Chernega, K. V. Domasevitch, *Inorg. Chim. Acta* **2002**, *338*, 69–77; (c) E. B. Rusanov, V. V. Ponomarova, V. V. Komarchuk, H. Stoeckli-Evans, E. Fernandez-Ibañez, F. Stoeckli, J. Sieler, K. V. Domasevitch, *Angew. Chem. Int. Ed.* **2003**, *42*, 2499-2501; (d) K. V. Domasevitch, I. Boldog, E. B. Rusanov, J. Hunger, S. Blaurock, M. Schröder, J. Sieler, *Z. Anorg. Allg. Chem.* **2005**, *631*, 1095-1100.
- [6] (a) J. A. Mason, J. Oktawiec, M. K. Taylor, M. R. Hudson, J. Rodriguez, J. E. Bachman, M. I. Gonzalez, A. Cervellino, A. Guagliardi, C. M. Brown, P. L. Llewellyn, N. Masciocchi, J. R. Long, *Nature* **2015**, *527*, 357-361; (b) H. J. Choi, M. Dincă, J. R. Long, *J. Am. Chem. Soc.* **2008**, *130*, 7848-7850.

- [7] C. R. Wade, T. Corrales-Sanchez, T. C. Narayan, M. Dincă, *Energy Environ. Sci.* **2013**, *6*, 2172-2177.
- [8] (a) Y. Lu, M. Tonigold, B. Bredenkötter, D. Volkmer, J. Hitzbleck, G. Langstein, *Z. Anorg. Allg. Chem.* **2008**, *634*, 2411-2417; (b) M. Tonigold, Y. Lu, A. Mavrandonakis, A. Puls, R. Staudt, J. Möllmer, J. Sauer, D. Volkmer, *Chem. Eur. J.* **2011**, *17*, 8671-8695.
- [9] (a) A. Tăbăcaru, C. Pettinari, N. Masciocchi, S. Galli, F. Marchetti, M. Angjellari, *Inorg. Chem.* **2011**, *50*, 11506-11513; (b) E. Q. Procopio, N. M. Padial, N. Masciocchi, S. Galli, J. E. Oltra, E. Barea, J. A. R. Navarro, *CrystEngComm* **2013**, *15*, 9352-9355; (c) M. Grzywa, D. Denysenko, A. Schaller, A. Kalytta-Mewes, D. Volkmer, *CrystEngComm* **2016**, *18*, 7883-7893; (d) J. Fritzsche, M. Grzywa, D. Denysenko, V. Bon, I. Senkovska, S. Kaskel, D. Volkmer, *Dalton Trans.* **2017**, *46*, 6745-6755.
- [10] (a) L. Hou, Y.-Y. Lin, X.-M. Chen, *Inorg. Chem.* **2008**, *47*, 1346-1351; (b) R. Mondal, M. K. Bhunia, K. Dhara, *CrystEngComm* **2008**, *10*, 1167-1174; (c) A. Goswami, S. Sengupta, R. Mondal, *CrystEngComm* **2012**, *14*, 561-572; (d) Y.-Q. Sun, S. Deng, Q. Liu, S.-Z. Ge, Y.-P. Chen, *Dalton Trans.* **2013**, *42*, 10503-10509. (e) Y.-Q. Sun, S. Deng, S.-Z. Ge, Q. Liu, Y.-P. Chen, *J. Cluster Sci.* **2013**, *24*, 605-617. (f) K. Tomar, R. Rajak, S. Sanda, S. Konar, *Cryst. Growth Des.* **2015**, *15*, 2732-2741; (g) L.-L. Han, T.-P. Hu, K. Mei, Z.-M. Guo, C. Yin, Y.-X. Wang, J. Zheng, X.-P. Wang, D. Sun, *Dalton Trans.* **2015**, *44*, 6052-6061.
- [11] V. Lozan, P. Y. Solntsev, G. Leibeling, K. V. Domasevitch, B. Kersting, *Eur. J. Inorg. Chem.* **2007**, *2007*, 3217-3226.
- [12] T. Jozak, D. Zabel, A. Schubert, Y. Sun, W. R. Thiel, *Eur. J. Inorg. Chem.* **2010**, *2010*, 5135-5145.
- [13] A. Zurawski, J. Sieler, K. Müller-Buschbaum, *Z. Anorg. Allg. Chem.* **2009**, *635*, 2034-2038.
- [14] C. S. Hawes, B. Moubaraki, K. S. Murray, P. E. Kruger, D. R. Turner, S. R. Batten, *Cryst. Growth Des.* **2014**, *14*, 5749-5760.
- [15] (a) L. Hou, L.-N. Jia, W.-J. Shi, L.-Y. Du, J. Li, Y.-Y. Wang, Q.-Z. Shi, *Dalton Trans.* **2013**, *42*, 6306-6309; (b) T. Li, F.-L. Wang, S.-T. Wu, X.-H. Huang, S.-M. Chen, C.-C. Huang, *Cryst. Growth Des.* **2013**, *13*, 3271-3274; (c) H.-H. Wang, L.-N. Jia, L. Hou, W.-j. Shi, Z. Zhu, Y.-Y. Wang, *Inorg. Chem.* **2015**, *54*, 1841-1846.
- [16] R. Hüttel, F. Büchele, P. Jochum, *Chem. Ber.* **1955**, *88*, 1577-1585.
- [17] O. Delgado-Friedrichs, M. O'Keeffe, O. M. Yaghi, *Phys. Chem. Chem. Phys.* **2007**, *9*, 1035-1043.

- [18] (a) M. K. Ehlert, S. J. Rettig, A. Storr, R. C. Thompson, J. Trotter, *Can. J. Chem.* **1993**, *71*, 1425-1436; (b) A. Cingolani, S. Galli, N. Masciocchi, L. Pandolfo, C. Pettinari, A. Sironi, *Dalton Trans.* **2006**, 2479-2486; (c) R. Sarma, D. Kalita, J. B. Baruah, *Dalton Trans.* **2009**, 7428-7436; (d) U. P. Singh, P. Tyagi, S. Pal, *Inorg. Chim. Acta* **2009**, *362*, 4403-4408; (e) S. Jin, D. Wang, *Z. Anorg. Allg. Chem.* **2011**, *637*, 618-625; (f) J. Pan, J. Ju, Q. Wei, B. Liu, S. Jin, Z. Lin, D. Wang, *Z. Anorg. Allg. Chem.* **2014**, *640*, 1745-1753.
- [19] (a) J.-P. Zhang, X.-M. Chen, *Chem. Commun.* **2006**, 1689-1699; (b) E.-C. Yang, T.-Y. Liu, Q. Wang, X.-J. Zhao, *Inorg. Chem. Commun.* **2011**, *14*, 285-287; (c) K.-J. Chen, R.-B. Lin, P.-Q. Liao, C.-T. He, J.-B. Lin, W. Xue, Y.-B. Zhang, J.-P. Zhang, X.-M. Chen, *Cryst. Growth Des.* **2013**, *13*, 2118-2123; (d) Q.-G. Zhai, N. Bai, S. n. Li, X. Bu, P. Feng, *Inorg. Chem.* **2015**, *54*, 9862-9868.
- [20] Y. Mulyana, C. J. Kepert, L. F. Lindoy, A. Parkin, P. Turner, *Dalton Trans.* **2005**, 1598-1601.
- [21] J.-M. Lin, C.-T. He, P.-Q. Liao, D.-D. Zhou, J.-P. Zhang, X.-M. Chen, *Sci. China: Chem.* **2016**, *59*, 970-974.
- [22] APEX2. SAINT, Data Reduction and Frame Integration Program for the CCD Area-Detector System, Bruker Analytical X-ray Systems; Data Collection Program for the CCD Area-Detector System: Madison, WI, USA, 1997–2006.
- [23] G. Sheldrick, University of Göttingen, Germany Program for Empirical Absorption Correction of Area Detector Data, **1996**.
- [24] (a) G. M. Sheldrick, *Acta Crystallogr., Sect. C* **2015**, *71*, 3-8; (b) G. Sheldrick, *Acta Crystallogr. Sect A* **2008**, *64*, 112-122.
- [25] Brandenburg, K. DIAMOND, version 4.5; Crystal and Molecular Structure Visualization; Crystal Impact—K. Brandenburg & H. Putz Gbr: Bonn, Germany, 2009–2018.
- [26] P. A. Nikitina, L. G. Kuz'mina, V. P. Perevalov, I. I. Tkach, *Tetrahedron* **2013**, *69*, 3249-3256.
- [27] J. Li, J. Gao, H. Li, X. Yang, Y. Liu, *Anal. Methods* **2014**, *6*, 4305-4311.
- [28] B. Koçyiğit Kaymakçıoğlu, S. Rollas, *Farmaco* **2002**, *57*, 595-599.

Supplementary Material

A 2D Zinc Coordination Polymer Built from the Mono-deprotonated 4,4'-Azobis(3,5-dimethyl-1H-pyrazole) Ligand

Table of Contents

Comparison of PXRD patterns

NMR spectra

IR spectra

Comparison of Hazbpz⁻, 4-(4-pyridyl)pyrazolates and 1,2,4-triazolates

Special position of the disordered DMF

Secondary building units, SBUs of mono-deprotonated bipyrazoles and dicarboxylates from the literature

Symmetry transformation between adjacent nets

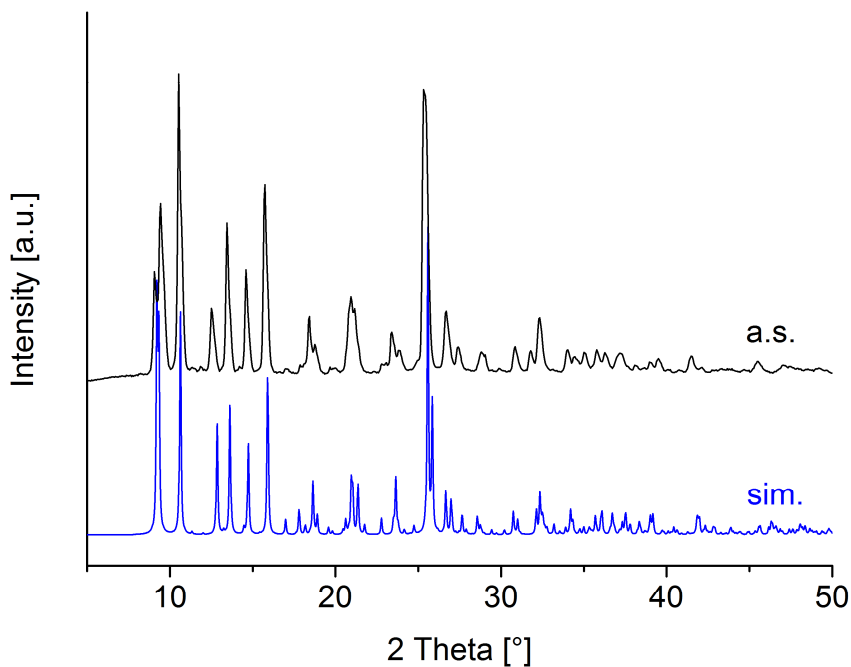


Figure S1. Comparison of PXRD patterns of the simulated diffractogram (blue) and the experimental diffractogram of the as-synthesized sample (black).

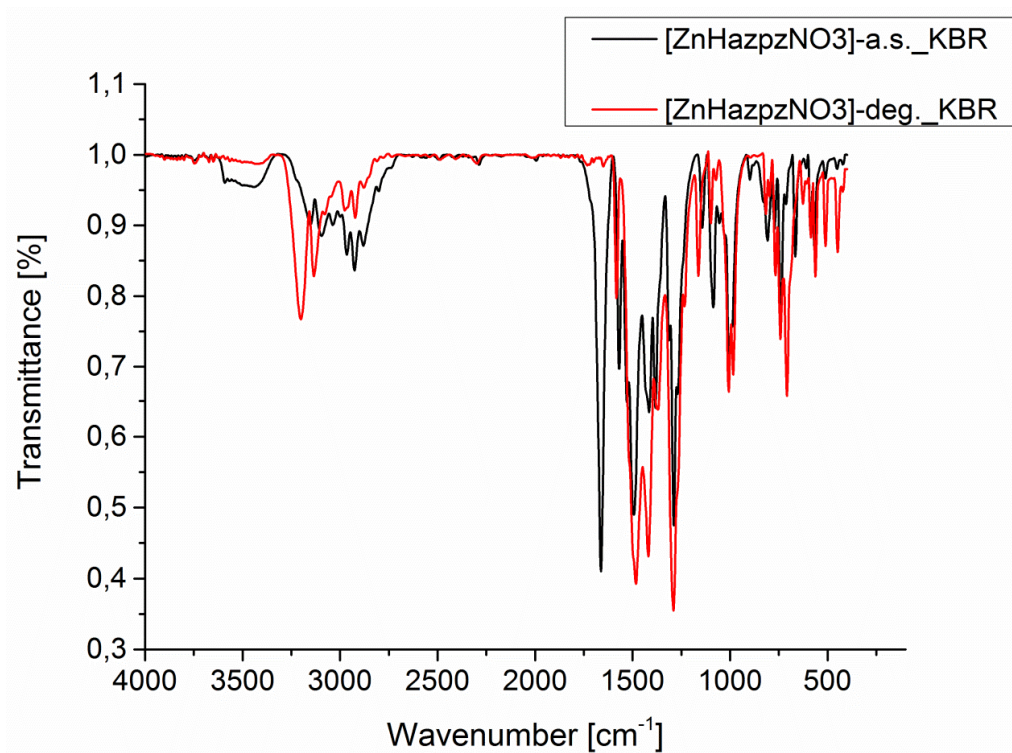


Figure S2. IR spectra of $[\text{Zn}(\text{Hazbpz})\text{NO}_3]$ -a.s. (black) and $[\text{Zn}(\text{Hazbpz})\text{NO}_3]$ -(deg.) (red), both as KBr pellets

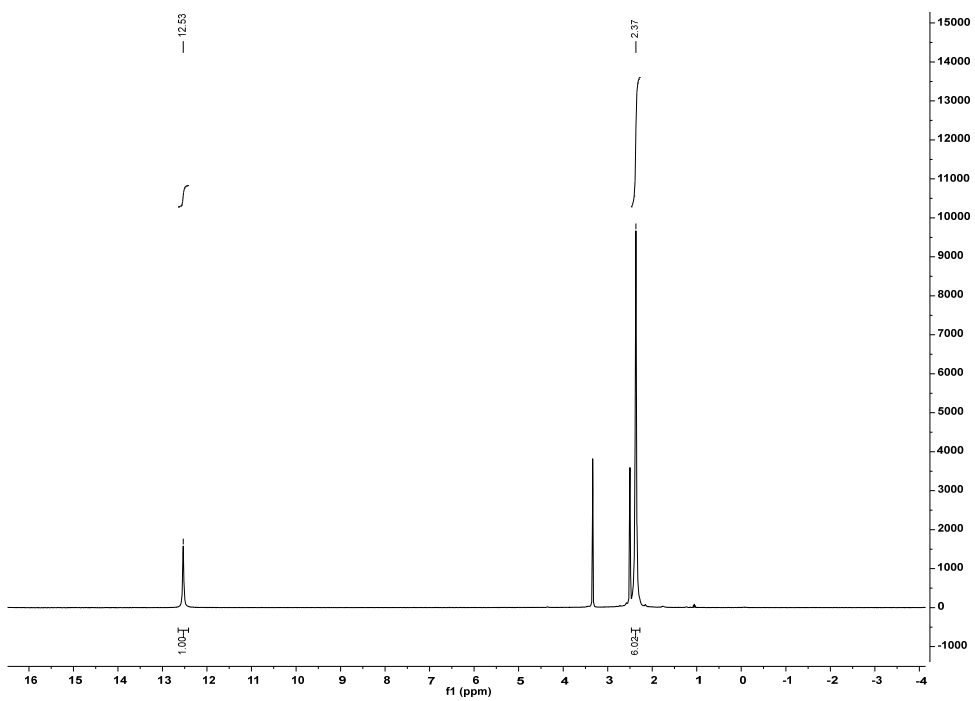


Figure S3. ¹H-NMR spectrum of H₂azbpz in DMSO-d₆.

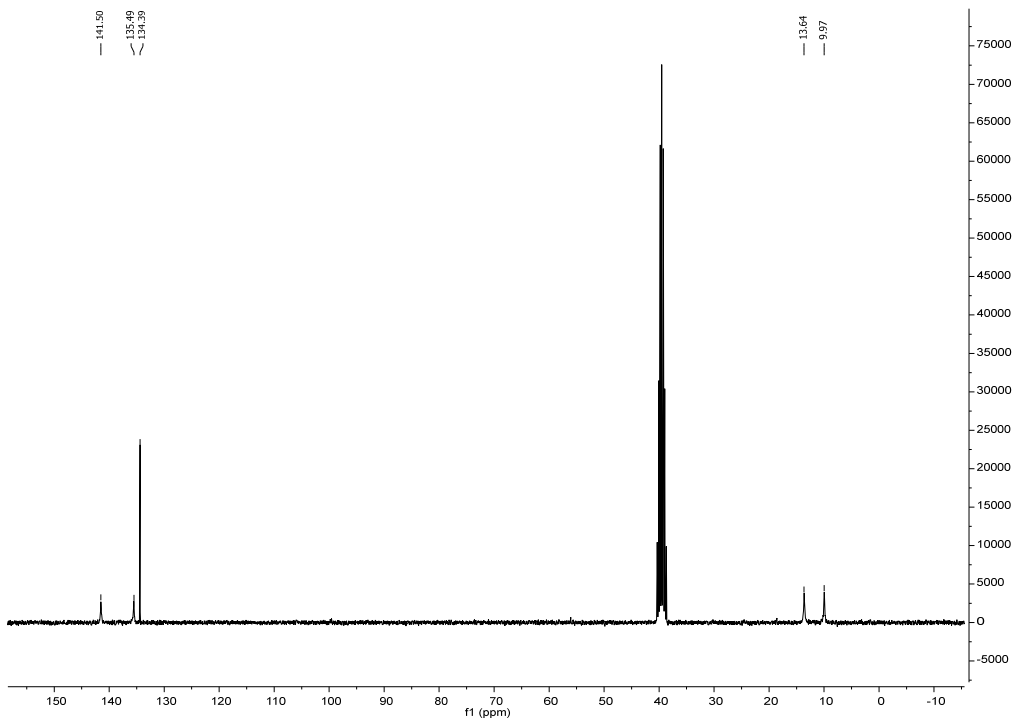


Figure S4. ¹³C-NMR spectrum of H₂azbpz in DMSO-d₆.

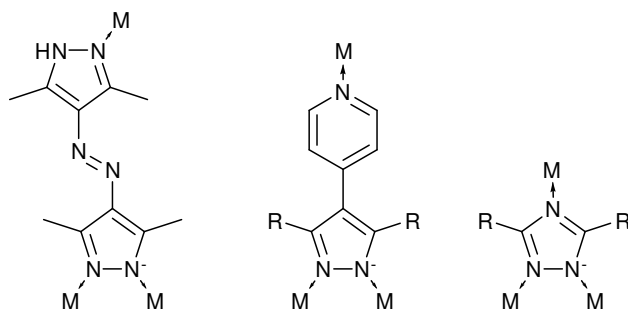


Figure S5. Similarities between the metal atom coordination mode of Hazbpz^- , 4-(4-pyridyl)pyrazolates (pypz^-) and 1,2,4-triazolates.

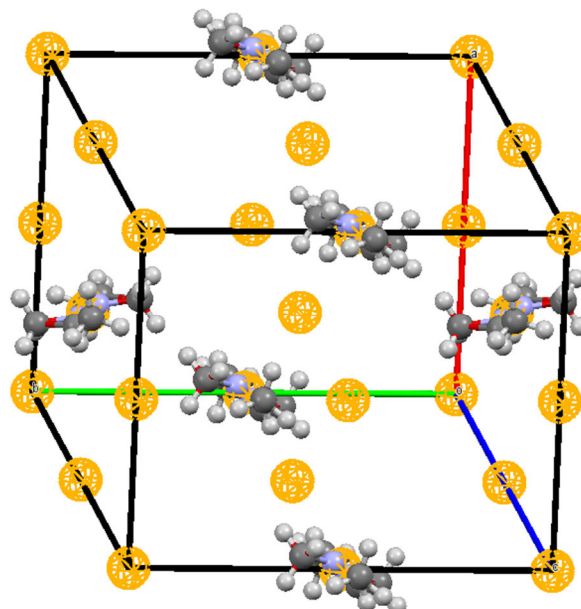


Figure S6. Unit cell showing the special position of the disordered DMF molecule sitting on an inversion center (depicted as a yellow sphere) (picture was created with the software package Mercury 3.9).^[1]

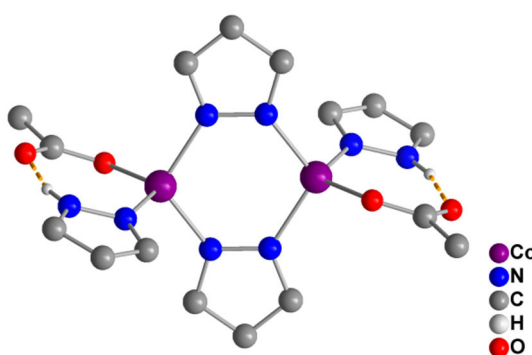


Figure S7. Dinuclear SBU $\{\text{Co}_2(\mu\text{-pz})_2(\text{Hpz})_2(\text{O}_2\text{C}-)_2\}$ in $[\text{Co}_2(\text{HL1})_2(\text{L2})]$ (pz and Hpz deprotonated and non-deprotonated pz ring of $\text{H2L1} = 4,4'\text{-methylenebis}(3,5\text{-dimethyl-1H-pyrazole}$, $\text{O}_2\text{C}-$ = carboxyl groups of $\text{L2} = 1,4\text{-bis}((3\text{-carboxyphenyl})\text{-methyl)piperazine}$). CSD-Refcode: DOWHAA.^[2]

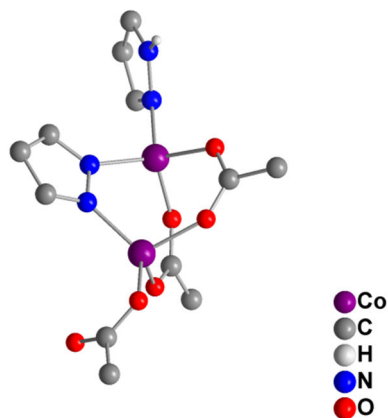


Figure S8. Dinuclear SBU $\{\text{Co}_2(\text{pz})(\text{Hpz})(\text{O}_2\text{C}-)\}$ in $[\text{Co}_2(\text{bpdc})_{1.5}(\text{Hbpz})]$ ($\text{O}_2\text{C}-$ = carboxyl groups of bpdc = 4,4'-biphenyldicarboxylate, pz and Hpz deprotonated and non-deprotonated pz ring of H₂bpz = 3,3',5,5'-tetramethyl-4-4'-pyrazole). CSD-Refcode: BEQFEK.^[3]

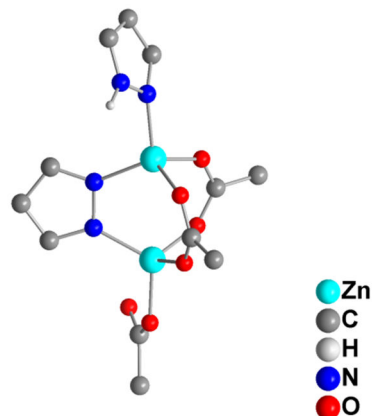


Figure S9. Dinuclear SBU $\{\text{Zn}_2(\text{pz})(\text{Hpz})(\text{O}_2\text{C}-)\}$ in $[\text{Zn}_4(\text{bpdc})_3(\text{Hbpz})_2]$ ($\text{O}_2\text{C}-$ = carboxyl groups of bpdc = 4,4'-biphenyldicarboxylate, pz and Hpz deprotonated and non-deprotonated pz ring of H₂bpz = 3,3',5,5'-tetramethyl-4-4'-pyrazole). CSD-Refcode: KIPKIF.^[4]

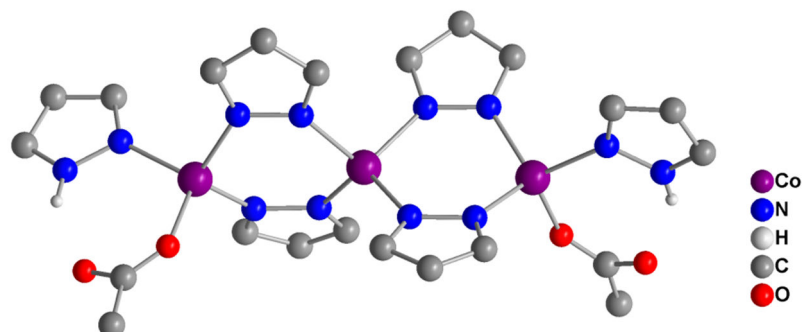


Figure S10. Trinuclear SBU $\{\text{Co}_3(\text{pz})_4(\text{Hpz})_2(\text{O}_2\text{C}-)_2\}$ in $[\text{Co}_{8.5}(\mu_4-\text{O})(\text{bpdc})_3(\text{bpz})_3(\text{Hbpz})_3]$ ($\text{O}_2\text{C}-$ = carboxyl groups of bpdc = 4,4'-biphenyldicarboxylate, pz and Hpz deprotonated and non-deprotonated pz ring of H₂bpz = 3,3',5,5'-tetramethyl-4-4'-pyrazole) CSD-Refcode: POXHER.^[5]

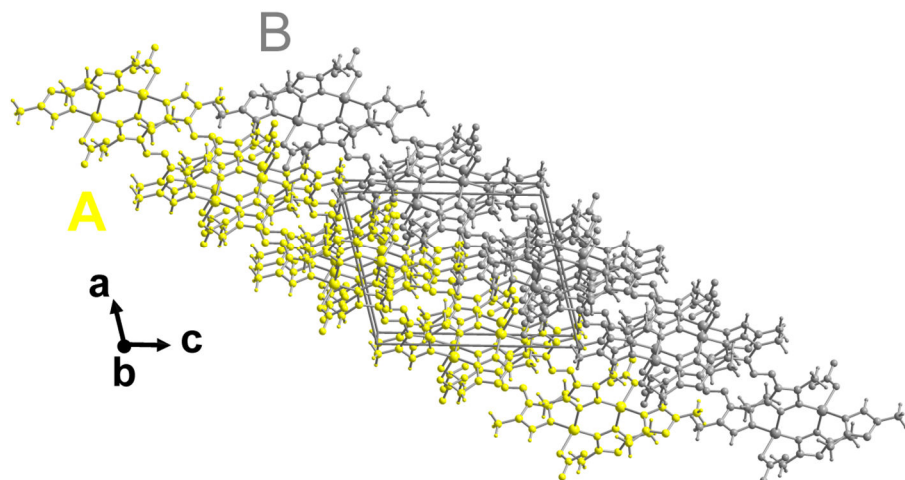


Figure S11. Two adjacent nets A and B differentiated by yellow and grey color, respectively, to show their symmetry transformation according to $x+1$, y , z or x , y , $z+1$. The nets run parallel to the 1 0 1 plane. A translation of the nets along a or c generates the symmetry-equivalent adjacent nets.

References

- [1] (a) C. F. Macrae, P. R. Edgington, P. McCabe, E. Pidcock, G. P. Shields, R. Taylor, M. Towler, J. van de Streek, *J. Appl. Crystallogr.* **2006**, *39*, 453-457. (b) C. F. Macrae, I. J. Bruno, J. A. Chisholm, P. R. Edgington, P. McCabe, E. Pidcock, L. Rodriguez-Monge, R. Taylor, J. van de Streek, P. A. Wood, *J. Appl. Crystallogr.* **2008**, *41*, 466-470.
- [2] C. S. Hawes, B. Moubaraki, K. S. Murray, P. E. Kruger, D. R. Turner, S. R. Batten, *Cryst. Growth Des.* **2014**, *14*, 5749-5760.
- [3] L. Hou, L.-N. Jia, W.-J. Shi, L.-Y. Du, J. Li, Y.-Y. Wang, Q.-Z. Shi, *Dalton Trans.* **2013**, *42*, 6306-6309.
- [4] T. Li, F.-L. Wang, S.-T. Wu, X.-H. Huang, S.-M. Chen, C.-C. Huang, *Cryst. Growth Des.* **2013**, *13*, 3271-3274.
- [5] H.-H. Wang, L.-N. Jia, L. Hou, W.-j. Shi, Z. Zhu, Y.-Y. Wang, *Inorg. Chem.* **2015**, *54*, 1841-1846.

3.5 Incorporating the thiazolo[5,4-d]thiazole unit into a coordination polymer with interdigitated structure

The work presented in this chapter has been published in:

S. Millan, G. Makhloufi and C. Janiak *Crystals*, **2018** 8, 30.

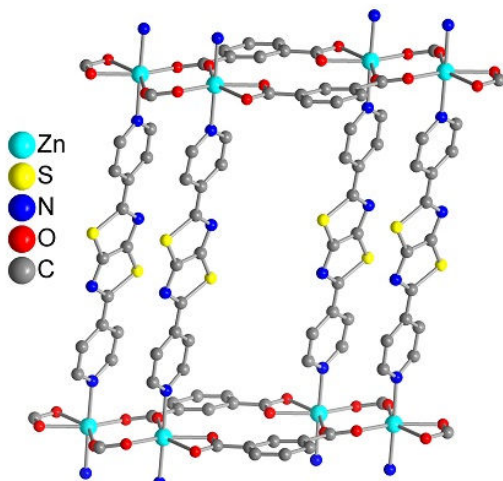
DOI:10.3390/cryst8010030

as part of the Special Issue “Structural Design and Properties of Coordination Polymers”.

The article is reprinted under the terms and conditions of the Creative Commons Attribution (CC BY) license (<http://creativecommons.org/licenses/by/4.0/>).

Abstract

The linker 2,5-di(4-pyridyl)thiazolo[5,4-d]thiazole (Dpttz), whose synthesis and structure is described here, was utilized together with benzene-1,3-dicarboxylate (isophthalate, 1,3-BDC²⁻) for the preparation of the two-dimensional coordination network [Zn(1,3-BDC)Dpttz]·DMF (DMF = dimethylformamide) via a solvothermal reaction. Compound [Zn(1,3-BDC)Dpttz]·DMF belongs to the class of coordination polymers with interdigitated structure (CIDs). The incorporated DMF solvent molecules can be removed through solvent exchange and evacuation such that the supramolecular 3D packing of the 2D networks retains porosity for CO₂ adsorption in activated [Zn(1,3-BDC)Dpttz]. The first sorption study of a tztz-functionalized porous metal-organic framework material yields a BET surface of 417 m²/g calculated from the CO₂ adsorption data. The heat of adsorption for CO₂ exhibits a relative maximum with 27.7 kJ/mol at an adsorbed CO₂ amount of about 4 cm³/g STP, which is interpreted as a gate-opening effect.



Introduction

Metal-organic frameworks are an intensively studied class of porous materials. Due to the immense quantity of possible inorganic and organic building units several applications are discussed (e.g., gas storage and separation, catalysis, sensing and heat transformation) [1-13]. Many different organic functionalities have been introduced into the frameworks either by a priori ligand functionalization or by post synthetic modification [14-16]. 4,4'-Biypidine based ligands have been used to construct a diverse set of different topologies (e.g., one-dimensional chains, ladders, two-dimensional and three-dimensional networks) [17]. 4,4'-Bipyridine ligands are also widely used in the synthesis of open network structures in combination with dicarboxylate ligands (e.g., terephthalate, isophthalate) via the so called mixed-ligand strategy [18,19]. Through functionalization of the organic ligands, the pore surface of those mixed-ligand MOFs can be tuned to enhance the selectivity in their sorption or sensing properties [20-23]. One famous family of mixed-ligands MOFs are the CIDs (coordination polymers with interdigitated structure) popularized by Kitagawa and co-workers. CIDs consist of an angular ligand (e.g., isophthalate, benzophenone-4,4'-dicarboxylate, azulene-1,6-dicarboxylate) and a 4,4'-bipyridine derivative and divalent transition metal ions. CIDs show very intriguing sorption properties due to their potential for functionalization and often inherent structural flexibility [24-29].

The heterocyclic thiazolo[5,4-d]thiazole (tztz) system (Figure 1) experienced a renaissance in the last decade after it was first prepared by Ketcham et al. in the 1960s [30]. The tztz unit was incorporated into photoactive materials due to its rigid and planar structure and electron deficiency. Both Maes et al. and Dessi et al. reviewed the synthetic procedures to obtain tztz-containing small molecules and polymers as well as their application in the field of organic electronics (e.g., OFETs, OSCs) [31,32]. In contrast, the tztz unit has been reported only in relatively few coordination compounds (15 hits in the CCDC database). The first examples were ruthenium and copper complexes with the doubly chelating 2,5-di(2-pyridyl)thiazolo[5,4-d]thiazole synthesized by Steel et al. [33]. Coordination polymers with 2,5-thiazolo[5,4-d]thiazoledicarboxylic acid (Figure 1) were obtained by Cheetham et al. with alkaline earth metals, whose connectivities vary with the cation size, and by Palmisano et al. with some transition metals, in which the ligand shows a *N,O*-chelating mode [34,35]. D'Alessandro et al. incorporated the donor-acceptor ligand *N,N*-(thiazolo[5,4-d]thiazole-2,5-diylbis(4,1-phenylene))bis(*N*-(pyridine-4-yl)pyridin-4-amine into a two-dimensional zinc MOF and studied its electrochemical properties [36]. Recently the same group published the spectroelectrochemical properties of a ruthenium coordination complex with this ligand [37]. Additionally, Dai et al. synthesized tztz-linked microporous organic polymers, which show a high CO₂:N₂ selectivity [38].

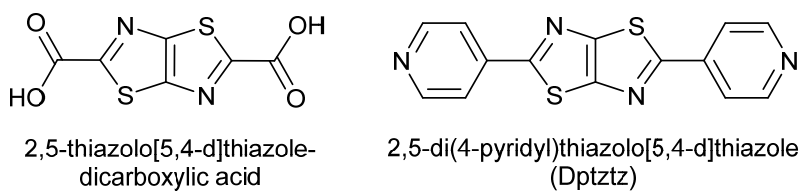
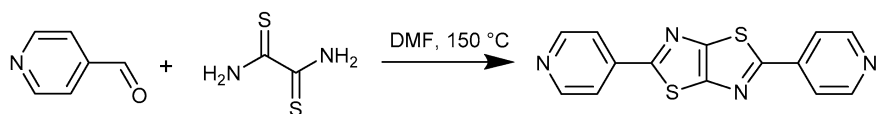


Figure 1. Examples of ttz-containing ligands.

Herein, we present the synthesis, structural analysis and the sorption properties of a new coordination polymer with interdigitated structure of the formula $[\text{Zn}(1,3\text{-BDC})\text{Dpttz}]$ consisting of Zn^{2+} ions, isophthalate and the 4,4'-bipyridine derivative 2,5-di(4-pyridyl)thiazolo[5,4-d]thiazole (Dpttz) (Figure 1, Scheme 1).



Scheme 1. Reaction scheme for the synthesis of 2,5-di(4-pyridyl)thiazolo[5,4-d]thiazole from 4-pyridinecarbaldehyde and dithiooxamide.

Materials and Methods

The chemicals used were obtained from commercial sources. No further purification has been carried out. CHN analysis was performed with a Perkin Elmer CHN 2400 (Perkin Elmer, Waltham, MA, USA). IR-spectra were recorded on a Bruker Tensor 37 IR spectrometer (Bruker Optics, Ettlingen, Germany) with ATR unit. Thermogravimetric analysis (TGA) was done with a Netzsch TG 209 F3 Tarsus (Netzsch, Selb, Germany) in the range from 20 to 700 °C, equipped with Al-crucible and applying a heating rate of $10 \text{ K}\cdot\text{min}^{-1}$ under nitrogen. The melting point was determined using a Büchi Melting Point apparatus B540. The powder X-ray diffraction pattern (PXRD) was obtained on a Bruker D2 Phaser powder diffractometer with a flat silicon, low background sample holder, at 30 kV, 10 mA for Cu-K α radiation ($\lambda = 1.5418 \text{ \AA}$). Sorption isotherms were measured using a Micromeritics ASAP 2020 automatic gas sorption analyzer equipped with oil-free vacuum pumps (ultimate vacuum $< 10^{-8} \text{ mbar}$) and valves, which guaranteed contamination free measurements. The sample was connected to the preparation port of the sorption analyzer and degassed under vacuum until the outgassing rate, i.e., the rate of pressure rise in the temporarily closed manifold with the connected sample tube, was less than $2 \mu\text{Torr}/\text{min}$ at the specified temperature of 120 °C. After weighing, the sample tube was then transferred to the analysis port of the sorption analyzer. All used gases (He, N₂, CO₂) were of ultra-high purity (UHP, grade 5.0, 99.999%).

and the STP volumes are given according to the NIST standards (293.15 K, 101.325 kPa). Helium gas was used for the determination of the cold and warm free space of the sample tubes. The heat of adsorption values were calculated using the ASAP 2020 v3.05 software. Water sorption isotherms were obtained volumetrically from a Quantachrome Autosorb iQ MP instrument equipped with an all-gas option. Prior to the sorption experiments, the compounds were degassed under dynamic vacuum.

2,5-Di(4-pyridyl)thiazolo[5,4-d]thiazole (Dpttz): 1.02 g (8.5 mmol) dithiooxamide and 2.0 mL (22 mmol, 2.6 eq) 4-pyridinecarboxaldehyde in 50 mL anhydrous DMF were refluxed for 6.5 h under nitrogen. During cooling the reaction mixture to room temperature, the product crystallized out in form of yellow prisms. The ligand was filtered and washed with a small amount of DMF and extensively with water. After drying in a vacuum oven at 60 °C overnight 1.82 g (6.1 mmol, 72%) were obtained. ¹H-NMR (300 MHz, DMSO-d₆) δ [ppm]: 8.78 (d, ⁴J_{H,H} = 6.12 Hz, 2H), 7.88 (d, ⁴J_{H,H} = 6.12 Hz, 2H); MS (EI) m/z [rel. int.]: 296 (100%); 87.9 (91%); mp 319–322 °C.

[Zn(1,3-BDC)Dpttz]: 5.0 mg (0.017 mmol) of Dpttz were dissolved in 3 mL of hot DMF in a Pyrex tube. 5.4 mg (0.020 mmol) of Zn(NO₃)₂·4H₂O and 2.8 mg (0.020 mmol) of isophthalic acid dissolved in 2 mL of DMF were added to the warm solution. The Pyrex tube was capped and placed into a preheated isothermal oven at 80 °C. After 12 h the first crystals appeared. After 3 days, the sample was removed from the oven and the solvent was directly exchanged with 3 × 3 mL of hot DMF. A light yellow crystal was selected to collect the single crystal data. Yield: 4 mg.

A larger amount of material was prepared by dissolving 100.4 mg (0.34 mmol) of Dpttz in 40 mL of hot DMF in a 100 mL Schott vial. Afterwards 88.4 mg (0.34 mmol) of Zn(NO₃)·4H₂O and 56.6 mg (0.34 mmol) of isophthalic acid dissolved in 10 mL of DMF were added and placed in an isothermal oven preheated at 120 °C. The sample was taken out after 3 days and the solvent was directly exchanged with 3 × 20 mL of hot DMF. Yield: 182.6 mg (90%). EA [%] calc. for: C₂₂H₁₂N₄O₄S₂Zn C 50.25, H 2.30 N 10.70; found: C 50.89, H 2.93, N 11.51. IR (ATR) ν_{max} [cm⁻¹]: 3433, 1608, 1564, 1443, 1391, 1213, 1014, 833, 743, 724, 662, 619, 510.

4.1 Single Crystal X-ray Structures

Suitable crystals were carefully selected under a polarizing microscope, covered in protective oil and mounted on a 0.05 mm cryo loop. *Data collection:* Bruker Kappa APEX2 CCD X-ray diffractometer (Bruker AXS Inc., Madison, WI, USA) with microfocus tube, Mo-Kα radiation (λ = 0.71073 Å), multi-layer mirror system, ω-scans; data collection with APEX2 [39], cell refinement with SMART and data reduction with SAINT [39], experimental absorption correction with SADABS [40]. *Structure analysis and refinement:* All structures were solved

by direct methods using SHELXL2014 [41,42]; refinement was done by full-matrix least squares on F^2 using the SHELX-97 program suite. The hydrogen atoms for aromatic CH and for the amide group in DMF were positioned geometrically ($C-H = 0.95 \text{ \AA}$) and refined using a riding model (AFX 43) with $U_{\text{iso}}(H) = 1.2U_{\text{eq}}(C)$. The hydrogen atoms for CH_3 of DMF were positioned geometrically ($C-H = 0.98 \text{ \AA}$) and refined using a riding model (AFX 137) with $U_{\text{iso}}(H) = 1.5U_{\text{eq}}(C)$. In $[\text{Zn}(1,3\text{-BDC})\text{Dpttz}]$ the thiazolothiazol (tztz) moiety was refined with a disorder model corresponding to a ring flip, which exchanges the S and N orientation, using PART n commands. The occupation factors of the S and N atoms were refined to about 0.904 for the A atoms and 0.096 for the B atoms. Thus, the disorder is relatively minor with only about 9.6% of the S and N atoms in the flipped position. The major atom tztz positions are designated as “A”, the minor ones as “B”. The minor positions could only be refined isotropically. The DMF crystal solvent molecule contained disorder in the two methyl groups, with two positions for each methyl group. This disorder does not give a perfect oriented Me_2N group but we decided to keep the slightly disordered DMF molecule instead of removing its contribution with SQUEEZE. Each methyl group disorder was refined independently concerning the occupation factors. Crystal data and details on the structure refinement are given in Table 1. Graphics were drawn with DIAMOND [43]. Analyses on the supramolecular interaction were done with PLATON [44]. Phase purity and the representative nature of the single crystal was verified by positively matching the simulated and experimental powder X-ray diffractogram (PXRD) of the as-synthesized sample (Figure 2). CCDC 1812892 and 1812893 contain the supplementary crystallographic data for this paper. These data can be obtained free of charge via <http://www.ccdc.cam.ac.uk/conts/retrieving.html>.

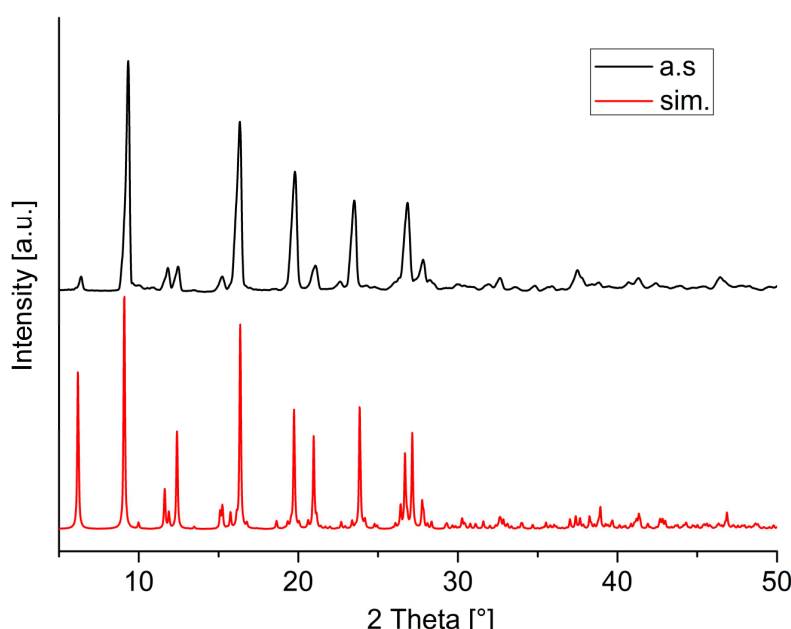


Figure 2. PXRD pattern of $[\text{Zn}(1,3\text{-BDC})\text{Dpttz}] \cdot \text{DMF}$ (simulated (red), as-synthesized (black)).

Table 1. Crystal data and refinement details.

	Dpttz	[Zn(1,3-BDC)Dpttz]·DMF
Chemical formula	C ₁₄ H ₈ N ₄ S ₂	C ₂₂ H ₁₂ N ₄ O ₄ S ₂ Zn·C ₃ H ₇ NO
Mr	296.36	598.94
Crystal system, space group	Monoclinic, P2 ₁ /c	Triclinic, P ₁
Temperature (K)	100	100
a (Å)	8.3873 (5)	9.1388 (6)
b (Å)	6.3140 (3)	10.0354 (7)
c (Å)	11.7170 (6)	14.2804 (11)
α (°)	90	88.417 (4)
β (°)	93.699 (3)	88.236 (5)
γ (°)	90	75.636 (4)
V (Å ³)	619.21 (6)	1267.86 (16)
Z	2	2
μ (mm ⁻¹)	0.423	1.181
Crystal size (mm)	0.10 × 0.05 × 0.05	0.10 × 0.05 × 0.01
Absorption correction	Multi-scan, wR2(int) was 0.1649 before and 0.0771 after correction. The Ratio of minimum to maximum transmission is 0.8473. The λ/2 correction factor is 0.0015.	Multi-scan, wR2(int) was 0.1533 before and 0.0488 after correction. The Ratio of minimum to maximum transmission is 0.9318. The λ/2 correction factor is 0.0015.
T _{min} , T _{max}	0.6330, 0.7471	0.6951, 0.7460
No. of measured, independent and observed reflections	6837, 965, 847 [I > 2σ(I)]	17151, 4743, 3696 [I > 2σ(I)]
R _{int}	0.049	0.045
(sin θ/λ)max (Å ⁻¹)	0.639	0.612
R, wR(F ²), S [F ² > 2σ(F ²)]	0.0284, 0.0675, 1.067	0.0400, 0.0849, 1.055
R, wR(F ²), S [all data]	0.359, 0.0699, 1.067	0.0609, 0.0916, 1.055
No. of reflections	965	4743
No. of parameters	91	364
Δρ _{max} , Δρ _{min} (e·Å ⁻³)	0.238, -0.182	0.645, -0.581

Results and Discussion

2,5-Di(4-pyridyl)thiazolo[5,4-d]thiazole (Dpttz) was synthesized according to the literature by the condensation of 4-pyridinecarboxaldehyde and dithiooxamide (Scheme 1) [45,46].

Single crystals of Dpttz were obtained after recrystallization from DMF in form of yellow prisms. Dpttz crystallizes in the monoclinic space group P2₁/c with half of the molecule in the asymmetric unit as the molecule sits on an inversion center (Figure 3). The molecule is almost planar with a dihedral angle between the pyridine ring and the tz tz moiety of 13.65°.

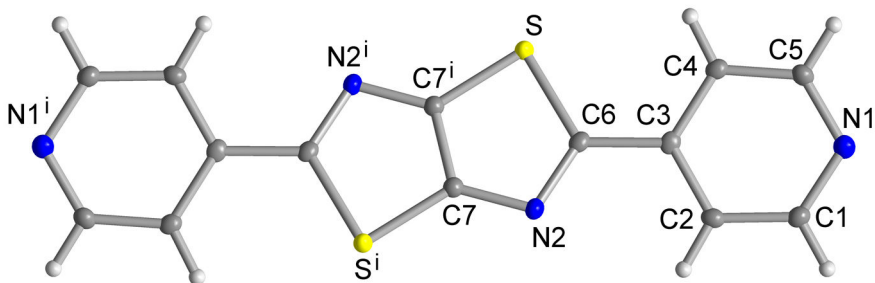


Figure 3. Molecular structure of Dpttz (50% thermal ellipsoids, symmetry transformation $1 - x, 2 - y, 2 - z$).

Complementary CH...N hydrogen bonds between N1 and C1-H1 of adjacent Dpttz molecules form 1D strands which are parallel displaced by π - π interactions (Figure S1 in Supplementary Material).

Single crystals of the coordination network [Zn(1,3-BDC)Dpttz]·DMF were obtained after three days from a solvothermal reaction of Zn(NO₃)₂·4H₂O, isophthalic acid and Dpttz in a molar ratio 1:1:1 in DMF at 80 °C. Due to the low solubility of Dpttz in common organic solvents, the reaction was carried out in a concentration of 3.4×10^{-3} mol/L and the mother liquor was directly exchanged with hot DMF after the crystallization process to remove unreacted Dpttz ligand. A larger amount of material for the sorption experiments was synthesized by scaling up the reaction by the factor of twenty in twice the concentration (6.8×10^{-3} mol/L) at 120 °C.

The crystal structure of the two-dimensional (2D) coordination network [Zn(1,3-BDC)Dpttz]·DMF was determined by single crystal diffraction analysis at 100 K. Compound [Zn(1,3-BDC)Dpttz] crystallizes in the triclinic space group *P*-1. The asymmetric unit consists of one Zn(II) ion, one molecule of the linkers 1,3-BDC²⁻ and Dpttz, each, and a dimethylformamide (DMF) solvent molecule (Figure 4, Figure S2). One carboxylate group of 1,3-BDC²⁻ connects two symmetry equivalent Zn(II) ions in a syn-syn-bis-monodentate coordination mode into a dinuclear unit with a Zn...Zn distance of 4.082 Å. The other carboxylate group chelates an adjacent Zn atom. Thereby the 1,3-BDC linkers bridge between neighboring dinuclear entities to form a one-dimensional double strand along the *b*-axis (Figure 5a). These double strands are pillared by Dpttz into a 2D coordination network structure (Figure 5b). The secondary building unit of the structure is the dinuclear unit {Zn₂(O₂C)₄N₄}. The 2D layers assemble through π - π interactions between isophthalate aryl rings and CH- π interactions between an isophthalate and a pyridyl-moiety of Dpttz of adjacent layers into a 3D supramolecular network (Figure 5c and Figure S3, Table S1). The 2D network in [Zn(1,3-BDC)Dpttz] is isotopic to the aforementioned CIDs (coordination polymers with interdigitated structure) studied by Kitagawa and co-workers [24-29].

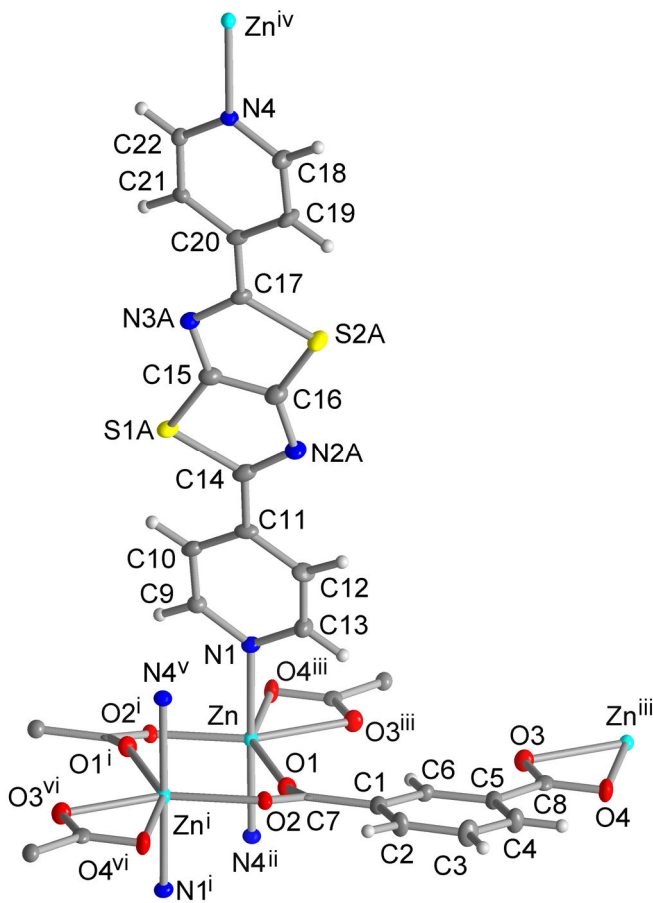


Figure 4. Extended asymmetric unit of $[Zn(1,3\text{-BDC})\text{Dpttz}]\cdot\text{DMF}$ (50% thermal ellipsoids; symmetry transformations: i = $-x + 2, -y, -z + 1$; ii = $x + 1, y, z + 1$; iii = $-x + 2, -y + 1, -z + 1$; iv = $x - 1, y, z - 1$; v = $-x + 1, -y, -z$, vi = $x, y - 1, z$). For the slight ring-flip disorder of the thiazolothiazole moiety and the DMF solvent molecule, which is omitted here for clarity, see Figure S2 in Supplementary Material. See Table 2 for selected bond length and angles.

Table 2. Selected bond lengths and angles (\AA , $^\circ$) in $[Zn(1,3\text{-BDC})\text{Dpttz}]$.

Zn–O1	2.0532 (18)	Zn–O4 ⁱⁱⁱ	2.2269 (19)
Zn–O2 ⁱ	2.0218 (18)	Zn–N1	2.166 (3)
Zn–O3 ⁱⁱⁱ	2.1569 (19)	Zn–N4 ⁱⁱ	2.151 (3)
O1–Zn–O2 ⁱ	119.30 (7)	O2 ⁱ –Zn–N4 ⁱⁱ	89.34 (9)
O1–Zn–O3 ⁱⁱⁱ	88.78 (7)	O3 ⁱⁱⁱ –Zn–O4 ⁱⁱⁱ	60.01 (7)
O1–Zn–O4 ⁱⁱⁱ	148.39 (7)	O3 ⁱⁱⁱ –Zn–N1	90.18 (9)
O1–Zn–N1	89.84 (9)	O3 ⁱⁱⁱ –Zn–N4 ⁱⁱ	90.56 (9)
O1–Zn–N4 ⁱⁱ	86.00 (9)	O4 ⁱⁱⁱ –Zn–N1	94.77 (8)
O2 ⁱ –Zn–O3 ⁱⁱⁱ	151.83 (7)	O4 ⁱⁱⁱ –Zn–N4 ⁱⁱ	89.21 (8)
O2 ⁱ –Zn–O4 ⁱⁱⁱ	91.82 (7)	N1–Zn–N4 ⁱⁱ	175.76 (8)
O2 ⁱ –Zn–N1	91.99 (9)		

symmetry transformations: i = $-x + 2, -y, -z + 1$; ii = $x + 1, y, z + 1$; iii = $-x + 2, -y + 1, -z + 1$.

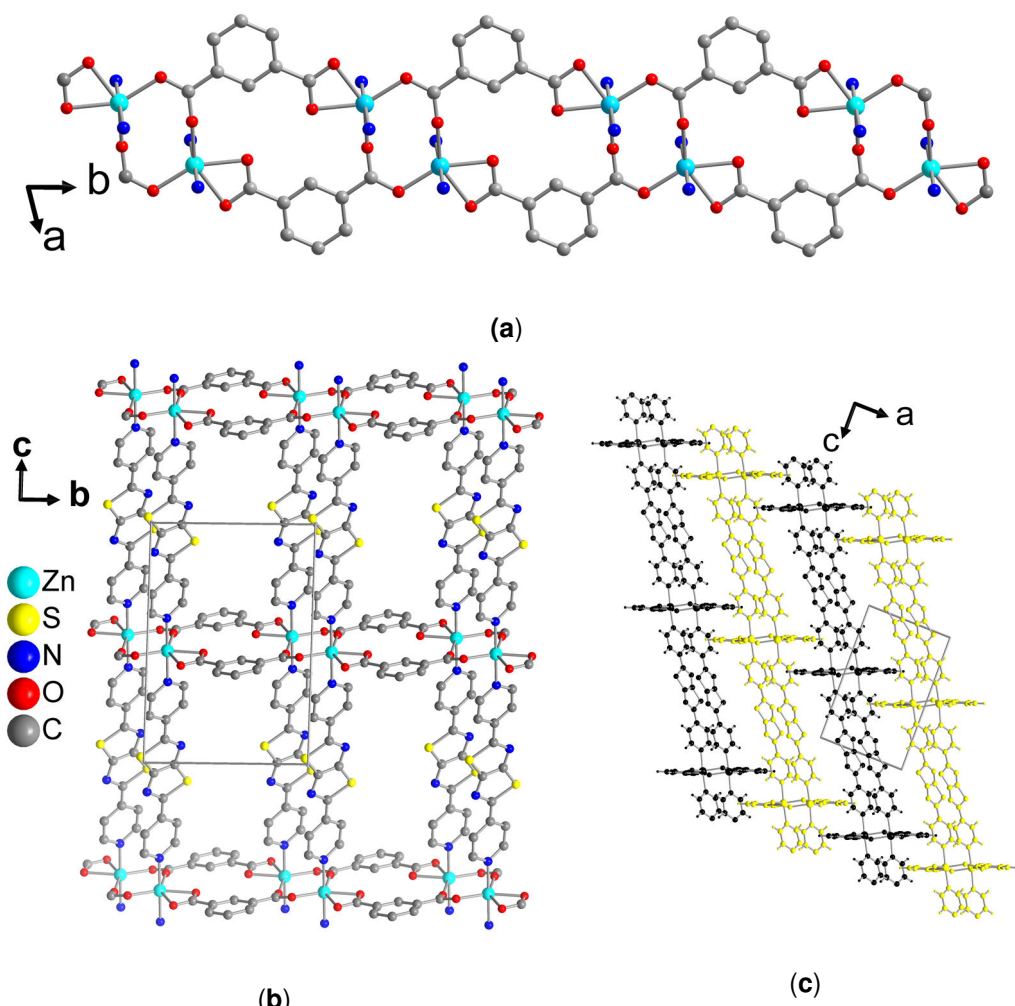


Figure 5. (a) 1D double strand of Zn^{2+} and $1,3\text{-BDC}^{2-}$ along the b -axis and (b) 2D coordination network structure in the bc plane and (c) supramolecular 3D packing of the 2D layers in $[\text{Zn}(1,3\text{-BDC})\text{Dpttz}] \cdot \text{DMF}$ (H atoms in (a),(b) and DMF solvent molecules are not shown for clarity). In (c) the 2D layers are colored alternately black and yellow for clarity.

The thermogravimetric analysis in Figure 6 shows a weight loss of 10.6% between 90 and 200 °C (calc. 12.2% for one DMF molecule per formula unit of $[\text{Zn}(1,3\text{-BDC})\text{Dpttz}] \cdot \text{DMF}$). The residual $[\text{Zn}(1,3\text{-BDC})\text{Dpttz}]$ framework shows stability up to 280 °C.

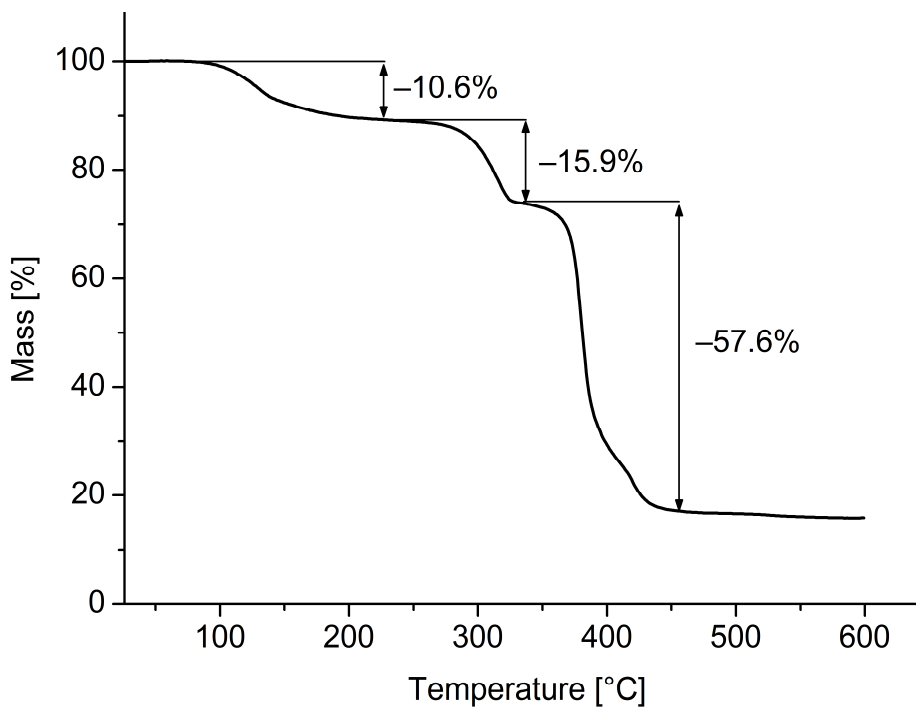


Figure 6. TGA curve of $[\text{Zn}(1,3\text{-BDC})\text{Dpttz}]\cdot\text{DMF}$ in the temperature range 26 – 600 °C with a heating rate of 10 K/min under N_2 atmosphere.

Prior to the sorption experiments the crystals of $[\text{Zn}(1,3\text{-BDC})\text{Dpttz}]\cdot\text{DMF}$ were collected by suction filtration. Afterwards they were suspended in acetonitrile for three days to induce solvent exchange as part of the sample activation procedure. Additionally, the acetonitrile solvent was exchanged three times per day. Afterwards, the sample was degassed at 120 °C for 15 h under vacuum. The activated compound $[\text{Zn}(1,3\text{-BDC})\text{Dpttz}]$ shows no uptake of N_2 at 77 K, which is in accordance with the observations by Kitagawa et al. for analogous CID structures [24-29]. For CO_2 – with its large polarizability and quadrupole moment – $[\text{Zn}(1,3\text{-BDC})\text{Dpttz}]$ shows a type I adsorption isotherm at 195 K with a maximum uptake of 138 cm³/g at 753 mmHg of CO_2 (Figure 7). At higher absolute pressures the desorption curve shows a small hysteresis, but at low pressures the hysteresis gap closes. This proves the microporous nature of $[\text{Zn}(1,3\text{-BDC})\text{Dpttz}]$. Because $[\text{Zn}(1,3\text{-BDC})\text{Dpttz}]$ is non-porous towards N_2 the CO_2 data was used to calculate the BET surface area. The BET surface area from the CO_2 adsorption isotherm is 417 m²/g (calculated from $p/p_0 = 0.00\text{--}0.04$). The pore volume is 0.246 cm³/g at $p/p_0 = 0.5$ calculated from the isotherm measured at 195 K. The calculated accessible surface area is 25.6% or 0.185 cm³/g calculated with PLATON from the DMF solvent-depleted structure. The measured pore volume is about 35% higher than the one calculated from the crystal structure data. This can be interpreted such that CO_2 can create a larger interlayer volume through strong interaction with the highly polarized surface area at 195 K.

Additionally, the CO₂ isotherms at 273 K and 293 K were measured (Figure 7). The data is presented in Table 3. From the CO₂ isotherms at 273 K and 293 K, the heat of adsorption at zero coverage was derived as 26.2 kJ/mol. The heat of adsorption of CO₂ for MOFs can vary from 20 kJ/mol to over 90 kJ/mol. A higher heat of adsorption is usually indicative for stronger framework CO₂ interactions [47]. Representative values are 20kJ/mol for [Zn(1,4-BDC)(TED)], 30 kJ/mol for HKUST-1, 47 kJ/mol for Mg-MOF-74, 63 kJ/mol for MIL-100-Cr and 96 kJ/mol for mmem-Cu-BTTri [48-52].

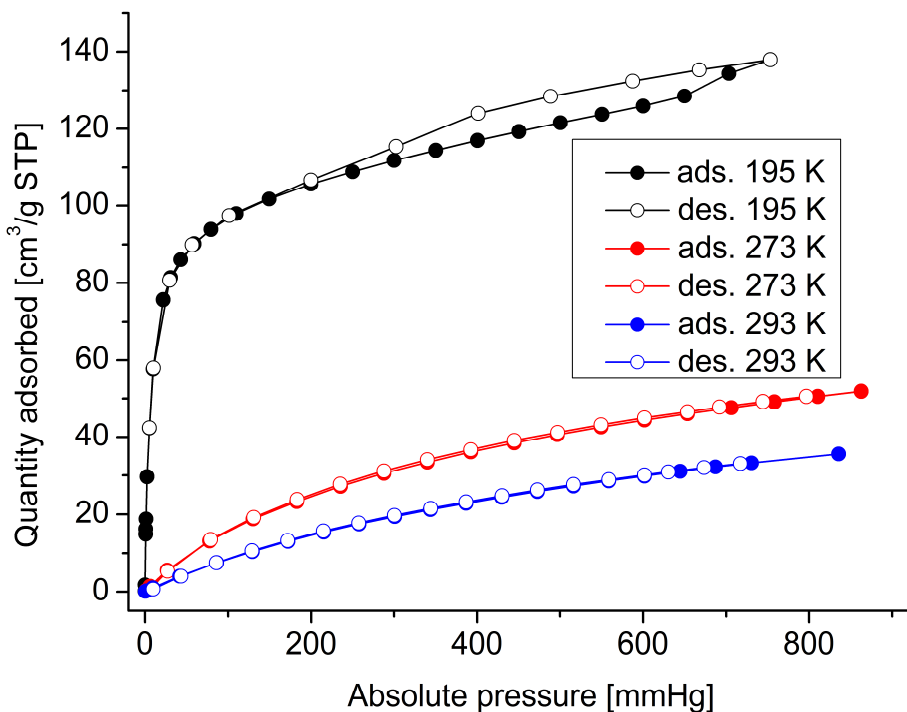


Figure 7. CO₂ adsorption (closed symbols) and desorption (open symbols) isotherms for activated [Zn(1,3-BDC)Dpttz] measured at 195 K (black), 273 K (red) and 293 K (blue).

Table 2. CO₂ sorption data for [Zn(1,3-BDC)Dpttz].

	Quantity Adsorbed (cm ³ /g, mmol/g, wt %)	Total Pore Volume (cm ³ /g)
195 K	138, 6.16, 27.1%	0.246 ¹
273 K	51.9, 2.32, 10.2%	0.092 ²
293 K	35.5, 1.59, 7.0%	0.061 ³

¹at P/P₀ = 0.50, ²at P/P₀ = 0.03, ³at P/P₀ = 0.017.

The heat of adsorption curve (Figure 8) has a relative maximum at a quantity adsorbed of about 4 cm³/g STP with 27.7 kJ/mol. Afterwards the heat of adsorption decreases to 25.7 kJ/mol. For most MOF materials, the heat of adsorption curve decreases monotonically,

since the adsorption sites with the highest affinity towards the adsorbate are occupied first and at higher loadings the adsorption sites usually have weaker affinities. Two MOF classes for which the heat of adsorption does not decrease monotonically are the MIL-53 and MIL-47 series. Férey et al. suggested that the transformation of MIL-53 from a closed or narrow-pore to the open or wide-pore phase is an endothermic process and that this process is balanced with the exothermic adsorption process. Subsequently, the MIL-53 MOFs also have a local maximum between 0 and 1 bar (see Figure S4 in Supplementary Material) [53]. Many CIDs also show gate-opening phenomena and/or an adsorbate specific expansion upon the adsorption process. Yet, to the best of our knowledge, no heat of adsorption curves for CIDs are published in the literature. But Pera–Titus and Farruseng calculated the phase transition energies for CID-21 and CID-22 (benzene and tetrazine spacer) to be 1.4 and 1.5 kJ/mol from the closed to the open phase for CO₂ adsorption at 195 K, respectively [54]. These values are in good accordance with the difference between the heat of adsorption at zero coverage and the relative maximum of the curve in Figure 8. So it can be concluded that [Zn(1,3-BDC)Dpttz] shows a gate-opening effect for CO₂, which is represented in a non-monotonic heat of adsorption curve.

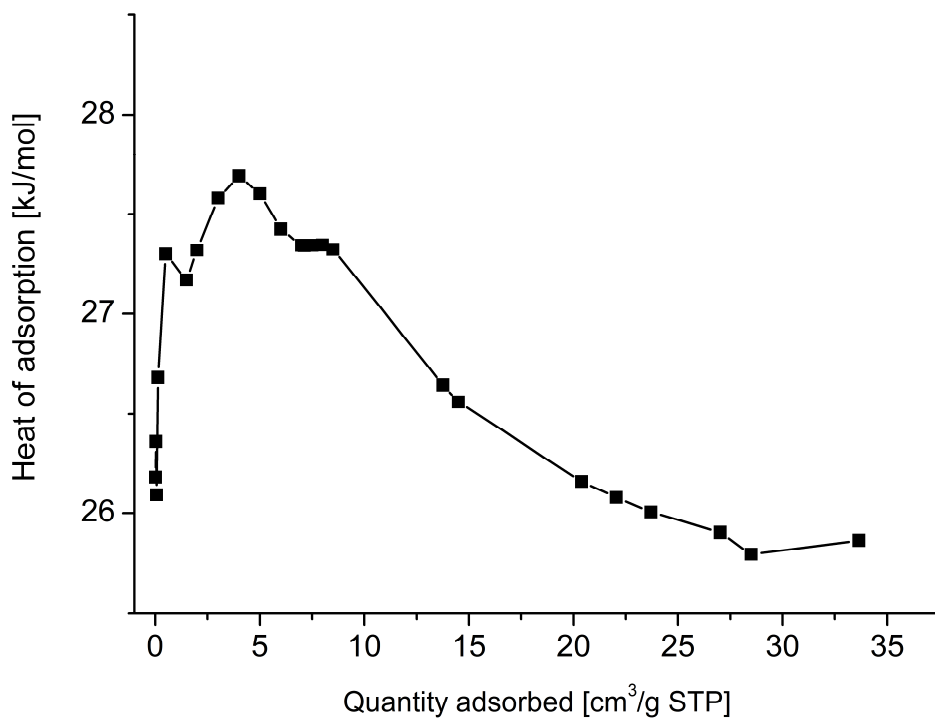


Figure 8. Heat of adsorption plot of CO₂ adsorption for [Zn(1,3-BDC)Dpttz].

Compound [Zn(1,3-BDC)Dpttz] gradually adsorbs H₂O at 293 K with a maximum uptake of 121 mg/g at 0.9 p/p₀ (Figure 9). This uptake equals 3.5 H₂O molecules per asymmetric unit. The desorption curve shows a hysteresis, indicative for a strong interaction of H₂O with the

framework. $[Zn(1,3\text{-BDC})Dpttz]$ adsorbs CO_2 at 195 K due to its large polarizability and quadrupole moment while N_2 at 77 K is not adsorbed. The adsorption characteristics of $[Zn(1,3\text{-BDC})Dpttz]$ apparently depend on the interaction between the adsorbate and the framework und not only on the pore size. The sorption characteristics of $[Zn(1,3\text{-BDC})Dpttz]$ towards H_2O with its pronounced hysteresis underpin these findings. It can be concluded that the decoration of the surface with the polarized and electron poor tztz moiety can alter sorption properties to become highly selective towards polarizable adsorbents. Further studies on different tztz-containing materials are underway in our institute.

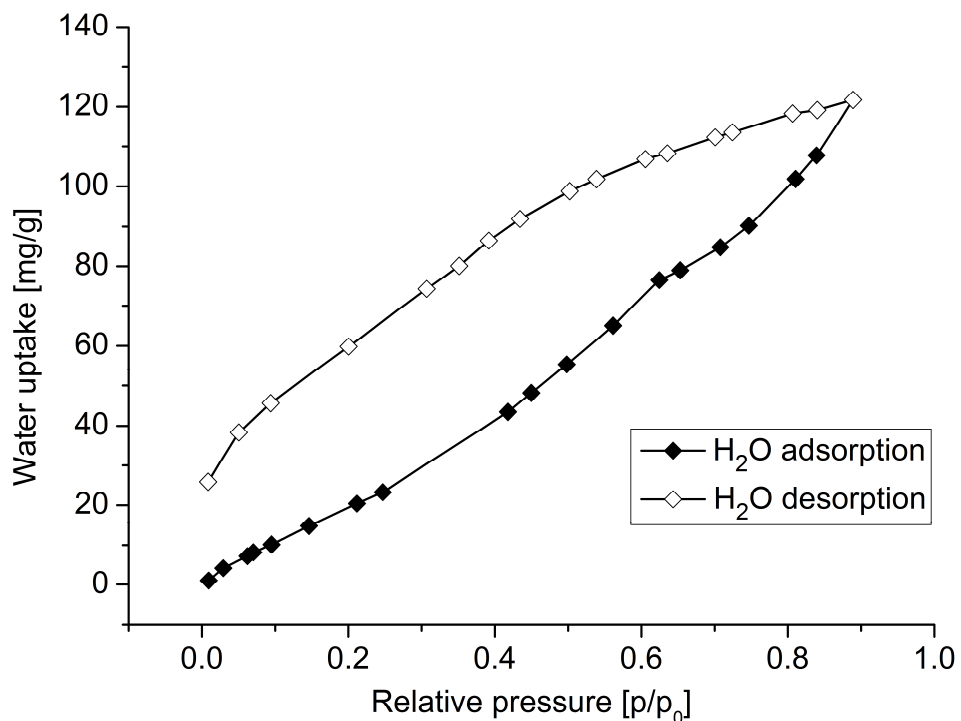


Figure 9. Water sorption isotherms at 293 K for $[Zn(1,3\text{-BDC})Dpttz]$.

Conclusions

The 4,4'-dipyridyl N,N' -donor ligand Dpttz with the central thiazolo[5,4-d]thiazole unit was successfully synthesized and its crystal structure was determined for the first time. With the linker Dpttz, the thiazolo[5,4-d]thiazole-unit was integrated into a solvent-filled coordination network of the formula $[Zn(1,3\text{-BDC})Dpttz]\cdot DMF$ belonging to the class of coordination polymers with interdigitated structure (CIDs). Synthesis of the coordination network was carried out via a mixed ligand strategy in a solvothermal reaction. Interdigitation between the 2D layers to a 3D supramolecular network appears to be controlled by $\pi\text{-}\pi$ interactions between isophthalate aryl rings and CH- π interactions between isophthalate and pyridyl moieties. Activated $[Zn(1,3\text{-BDC})Dpttz]$ shows a BET surface of 417 m²/g calculated from

CO₂ adsorption data, while N₂ which unlike CO₂ is not as polarizable and has no quadrupole moment is not adsorbed. The heat of adsorption for CO₂ exhibits a relative maximum at a quantity adsorbed of about 4 cm³/g STP with 27.7 kJ/mol, which is interpreted as a gate-opening effect. This is the first report of the sorption characteristics of a tztz-functionalized porous MOF material.

References

1. Yaghi, O.M.; O'Keeffe, M.; Ockwig, N.W.; Chae, H.K.; Eddaoudi, M.; Kim, J. Reticular synthesis and the design of new materials. *Nature* **2003**, *423*, 705–714.
2. Maurin, G.; Serre, C.; Cooper, A.; Férey, G. The new age of MOFs and of their porous-related solids. *Chem. Soc. Rev.* **2017**, *46*, 3104–3107.
3. Furukawa, H.; Ko, N.; Go, Y.B.; Aratani, N.; Choi, S.B.; Choi, E.; Yazaydin, A.Ö.; Snurr, R.Q.; O'Keeffe, M.; Kim, J.; Yaghi, O.M. Ultrahigh porosity in metal-organic frameworks. *Science* **2010**, *329*, 424–428.
4. Adil, K., Belmabkhout, Y.; Pillai, R.S.; Cadiou, A.; Bhatt, P.M.; Assen, A.H.; Maurin, G.; Eddaoudi, M. Gas/vapour separation using ultra-microporous metal–organic frameworks: insights into the structure/separation relationship. *Chem. Soc. Rev.* **2017**, *46*, 3402–3430.
5. Li, J.-R.; Kuppler, R.J.; Zhou, H.-C. Selective gas adsorption and separation in metal-organic frameworks. *Chem. Soc. Rev.* **2009**, *38*, 1477–1504.
6. Dechnik, J.; Gascon, J.; Doonan, C.J.; Janiak, C.; Sumby, C.J. Mixed-matrix membranes. *Angew. Chem. Int. Ed.* **2017**, *56*, 9292–9310.
7. Lee, J.; Farha, O.K.; Roberts, J.; Scheidt, K.A.; Nguyen, S.T.; Hupp, J.T. Metal-organic framework materials as catalysts. *Chem. Soc. Rev.* **2009**, *38*, 1450–1459.
8. Herbst, A.; Janiak, C. MOF catalysts in biomass upgrading towards value-added fine chemicals. *CrysEngComm* **2017**, *19*, 4092–4117.
9. Kitao, T.; Zhang, Y.; Kitagawa, S.; Wang, B.; Uemura, T. Hybridization of MOFs and polymers. *Chem. Soc. Rev.* **2017**, *46*, 3108–3133.
10. Lustig, W.P.; Mukherjee, S.; Rudd, N.D.; Desai, A.V.; Li, J.; Ghosh, S.K. Metal–organic frameworks: functional luminescent and photonic materials for sensing applications. *Chem. Soc. Rev.* **2017**, *46*, 3242–3285.
11. Hu, Z.; Deibert, B.J.; Li, J. Luminescent metal-organic frameworks for chemical sensing and explosive detection. *Chem. Soc. Rev.* **2014**, *43*, 5815–5840.
12. Gangu, K.K.; Maddila, S.; Mukkamala, S.B.; Jonnalagadda, S.B. A review on contemporary Metal–Organic Framework materials. *Inorg. Chim. Acta* **2016**, *446*, 61–74.
13. Jeremias, F.; Fröhlich, D.; Janiak, C.; Henninger, S.K. Water and methanol adsorption on MOFs for cycling heat transformation processes. *New J. Chem.* **2014**, *38*, 1846–1852.

14. Almeida Paz, F.A.; Klinowski, J.; Vilela, S.M.F.; Tome, J.P.C.; Cavaleiro, J.A.S.; Rocha, J. Ligand design for functional metal-organic frameworks. *Chem. Soc. Rev.* **2012**, *41*, 1088–1110.
15. Tanabe, K.K.; Cohen, S.M. Postsynthetic modification of metal-organic frameworks - a progress report. *Chem. Soc. Rev.* **2011**, *40*, 498–519.
16. Islamoglu, T.; Goswami, S.; Li, Z.; Howarth, A.J.; Farha, O.K.; Hupp, J.T. Postsynthetic tuning of metal-organic frameworks for targeted applications. *Acc. Chem. Res.* **2017**, *50*, 805–813.
17. Biradha, K.; Sarkar, M.; Rajput, L. Crystal engineering of coordination polymers using 4,4'-bipyridine as a bond between transition metal atoms. *Chem. Commun.* **2006**, *4169*–4179.
18. Bhattacharya, B.; Ghoshal, D. Selective carbon dioxide adsorption by mixed-ligand porous coordination polymers. *CrystEngComm* **2015**, *17*, 8388–8413.
19. Haldar, R.; Maji, T.K. Metal-organic frameworks (MOFs) based on mixed linker systems: Structural diversities towards functional materials. *CrystEngComm* **2013**, *15*, 9276–9295.
20. Bae, Y.-S.; Mulfort, K.L.; Frost, H.; Ryan, P.; Punnathanam, S.; Broadbelt, L.J.; Hupp, J.T.; Snurr, R.Q. Separation of CO₂ from CH₄ using mixed-ligand metal-organic frameworks. *Langmuir* **2008**, *24*, 8592–8598.
21. Henke, S.; Schneemann, A.; Wütscher, A.; Fischer, R.A. Directing the breathing behavior of pillared-layered metal-organic frameworks via a systematic library of functionalized linkers bearing flexible substituents. *J. Am. Chem. Soc.* **2012**, *134*, 9464–9474.
22. Glomb, S.; Woschko, D.; Makhloufi, G.; Janiak, C. Metal-organic frameworks with internal urea-functionalized dicarboxylate linkers for SO₂ and NH₃ adsorption. *ACS Appl. Mater. Interfaces* **2017**, *9*, 37419–37434.
23. Takashima, Y.; Martínez, V.M.; Furukawa, S.; Kondo, M.; Shimomura, S.; Uehara, H.; Nakahama, M.; Sugimoto, K.; Kitagawa, S. Molecular decoding using luminescence from an entangled porous framework. *Nat. Commun.* **2011**, *2*, 168.
24. Horike, S.; Tanaka, D.; Nakagawa, K.; Kitagawa, S. Selective guest sorption in an interdigitated porous framework with hydrophobic pore surfaces. *Chem. Commun.* **2007**, *3395*–3397.
25. Tanaka, D.; Nakagawa, K.; Higuchi, M.; Horike, S.; Kubota, Y.; Kobayashi, T.C.; Takata, M.; Kitagawa, S. Kinetic gate-opening process in a flexible porous coordination polymer. *Angew. Chem. Int. Ed.* **2008**, *47*, 3914–3918.
26. Fukushima, T.; Horike, S.; Inubushi, Y.; Nakagawa, K.; Kubota, Y.; Takata, M.; Kitagawa, S. Solid solutions of soft porous coordination polymers: Fine-tuning of gas adsorption properties. *Angew. Chem.* **2010**, *122*, 4930–4934.
27. Nakagawa, K.; Tanaka, D.; Horike, S.; Shimomura, S.; Higuchi, M.; Kitagawa, S. Enhanced selectivity of CO₂ from a ternary gas mixture in an interdigitated porous framework. *Chem. Commun.* **2010**, *46*, 4258–4260.
28. Hijikata, Y.; Horike, S.; Sugimoto, M.; Sato, H.; Matsuda, R.; Kitagawa, S. Relationship between channel and sorption properties in coordination polymers with interdigitated structures. *Chem. Eur. J.* **2011**, *17*, 5138–5144.

29. Kishida, K.; Horike, S.; Nakagawa, K.; Kitagawa, S. Synthesis and adsorption properties of azulene-containing porous interdigitated framework. *Chem. Lett.* **2012**, *41*, 425–426.
30. Johnson, J.R.; Ketcham, R. Thiazolothiazoles. I. The reaction of aromatic aldehydes with dithiooxamide. *J. Am. Chem. Soc.* **1960**, *82*, 2719–2724.
31. Bevk, D.; Marin, L.; Lutsen, L.; Vanderzande, D.; Maes, W. Thiazolo[5,4-d]thiazoles - promising building blocks in the synthesis of semiconductors for plastic electronics. *RSC Adv.* **2013**, *3*, 11418–11431.
32. Reginato, G.; Mordini, A.; Zani, L.; Calamante, M.; Dessi, A. Photoactive compounds based on the thiazolo[5,4-d]thiazole core and their application in organic and hybrid photovoltaics. *Eur. J. Org. Chem.* **2016**, 233–251.
33. Zampese, J.A.; Keene, F.R.; Steel, P.J. Diastereoisomeric dinuclear ruthenium complexes of 2,5-di(2-pyridyl)thiazolo[5,4-d]thiazole. *Dalton Trans.* **2004**, 4124–4129.
34. Falcão, E.H.L.; Naraso; Feller, R.K.; Wu, G.; Wudl, F.; Cheetham, A.K. Hybrid organic–inorganic framework structures: Influence of cation size on metal–oxygen–metal connectivity in the alkaline earth thiazolothiazoledicarboxylates. *Inorg. Chem.* **2008**, *47*, 8336–8342.
35. Aprea, A.; Colombo, V.; Galli, S.; Masciocchi, N.; Maspero, A.; Palmisano, G. Thiazolo[5,4-d]thiazole-2,5-dicarboxylic acid, C₆H₂N₂O₄S₂, and its coordination polymers. *Solid State Sci.* **2010**, *12*, 795–802.
36. Rizzuto, F.J.; Faust, T.B.; Chan, B.; Hua, C.; D'Alessandro, D.M.; Kepert, C.J. Experimental and computational studies of a multi-electron donor–acceptor ligand containing the thiazolo[5,4-d]thiazole core and its incorporation into a metal–organic framework. *Chem. Eur. J.* **2014**, *20*, 17597–17605.
37. Hua, C.; Rizzuto, F.J.; Zhang, X.; Tuna, F.; Collison, D.; D'Alessandro, D.M. Spectroelectrochemical properties of a Ru(II) complex with a thiazolo[5,4-d]thiazole triarylamine ligand. *New J. Chem.* **2017**, *41*, 108–114.
38. Zhu, X.; Tian, C.; Jin, T.; Wang, J.; Mahurin, S.M.; Mei, W.; Xiong, Y.; Hu, J.; Feng, X.; Liu, H., Thiazolothiazole-linked porous organic polymers. *Chem. Commun.* **2014**, *50*, 15055–15058.
39. APEX2; SAINT, *Data Reduction and Frame Integration Program for the CCD Area-Detector System*, Bruker Analytical X-ray Systems; Data Collection program for the CCD Area-Detector System: Madison, WI, USA, **1997–2006**.
40. Sheldrick, G.M. *SADABS: Area-Detector Absorption Correction*; University of Göttingen: Göttingen, Germany, **1996**.
41. Sheldrick, G.M. Crystal structure refinement with SHEXL. *Acta Crystallogr. Sect A* **2015**, *71*, 3–8.
42. Sheldrick, G. A short history of SHELX. *Acta Crystallogr. Sect. A* **2008**, *64*, 112–122.
43. Brandenburg, K. *DIAMOND*, version 4.4; Crystal and Molecular Structure Visualization; Crystal Impact—K. Brandenburg & H. Putz Gbr: Bonn, Germany, **2009–2017**.
44. Spek, A.L. Structure validation in chemical crystallography. *Acta Crystallogr. Sect. D—Biol. Crystallogr.* **2009**, *65*, 148–155.

45. Knighton, R.C.; Hallett, A.J.; Kariuki, B.M.; Pope, S.J.A. A one-step synthesis towards new ligands based on aryl-functionalised thiazolo[5,4-d]thiazole chromophores. *Tetrahedron Lett.* **2010**, *51*, 5419–5422.
46. Hisamatsu, S.; Masu, H.; Azumaya, I.; Takahashi, M.; Kishikawa, K.; Kohmoto, S. U-shaped aromatic ureadicarboxylic acids as versatile building blocks: Construction of ladder and zigzag networks and channels. *Cryst. Growth Des.* **2011**, *11*, 5387–5395.
47. Das, A.; D'Alessandro, D.M. Tuning the functional sites in metal-organic frameworks to modulate CO₂ heats of adsorption. *CrystEngComm* **2015**, *17*, 706–718.
48. Zhao, Y.; Wu, H.; Emge, T.J.; Gong, Q.; Nijem, N.; Chabal, Y.J.; Kong, L.; Langreth, D.C.; Liu, H.; Zeng, H.; Li, J. Enhancing gas adsorption and separation capacity through ligand functionalization of microporous metal-organic framework structures. *Chem. Eur. J.* **2011**, *17*, 5101–5109.
49. Liang, Z.; Marshall, M.; Chaffee, A.L. CO₂ adsorption-based separation by metal organic framework (Cu-BTC) versus zeolite (13X). *Energy Fuels* **2009**, *23*, 2785–2789.
50. Caskey, S.R.; Wong-Foy, A.G.; Matzger, A.J. Dramatic tuning of carbon dioxide uptake via metal substitution in a coordination polymer with cylindrical pores. *J. Am. Chem. Soc.* **2008**, *130*, 10870–10871.
51. Llewellyn, P.L.; Bourrelly, S.; Serre, C.; Vimont, A.; Daturi, M.; Hamon, L.; De Weireld, G.; Chang, J.-S.; Hong, D.-Y.; Kyu Hwang, Y.; Hwa Jhung, S.; Férey, G. High uptakes of CO₂ and CH₄ in mesoporous metal-organic frameworks MIL-100 and MIL-101. *Langmuir* **2008**, *24*, 7245–7250.
52. McDonald, T.M.; D'Alessandro, D.M.; Krishna, R.; Long, J.R. Enhanced carbon dioxide capture upon incorporation of N,N'-dimethylethylenediamine in the metal-organic framework CuBTTri. *Chem. Sci.* **2011**, *2*, 2022–2028.
53. Bourrelly, S.; Llewellyn, P.L.; Serre, C.; Millange, F.; Loiseau, T.; Férey, G. Different adsorption behaviors of methane and carbon dioxide in the isotypic nanoporous metal terephthalates MIL-53 and MIL-47. *J. Am. Chem. Soc.* **2005**, *127*, 13519–13521.
54. Pera-Titus, M.; Farrusseng, D. Guest-induced gate opening and breathing phenomena in soft porous crystals: Building thermodynamically consistent isotherms. *J. Phys. Chem. C* **2012**, *116*, 1638–1649.

4. Weitere Ergebnisse

Im folgenden Kapitel werden weitere unveröffentlichte Ergebnisse präsentiert. Die Bibliographie und die Nummerierung von Abbildungen und Tabellen ist eine Fortsetzung aus dem einleitenden Kapitel Nummer 1.

4.1 Synthese und Struktur von [Zn(Isa-az-tmpz)]

In Kapitel 3.1 wurde gezeigt, dass 3,6-c **rtl**-MOFs auf Basis von T-förmigen Pyrazol-Isophthalat-Liganden synthetisiert werden können, welche unter dem „supramolecular building layer“-Ansatz rationalisiert werden können. Die Strukturen dieser MOFs können unter dem „supramolecular-building-layer“-Ansatz rationalisiert werden.^{52,146} In diesen Strukturen spannen die Isophthalateinheiten der Liganden zweidimensionale **sql** Schichten, welche durch pyridinische N-Donor Atome von N-Heterozyklen in apikaler Position des Paddle-Wheel-Clusters miteinander verknüpft werden.⁴⁴

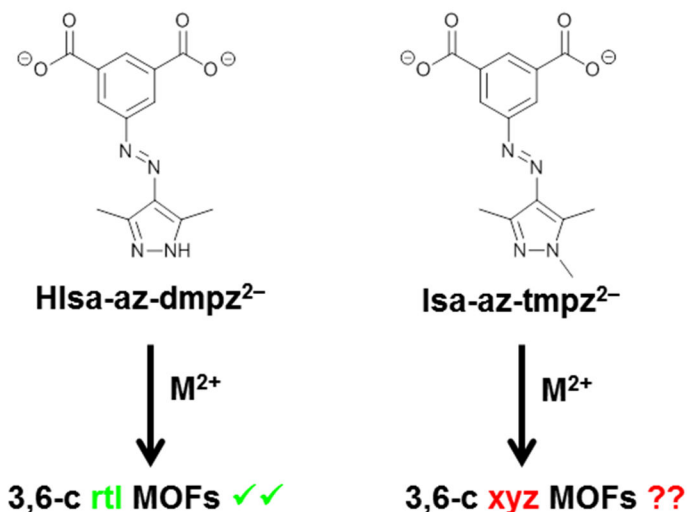


Abbildung 27. Gegenüberstellung der Liganden H₃Isa-az-dmpz mit welchem erfolgreich 3,6-c **rtl**-MOFs synthetisiert wurden und dem 1-Methyl substituierten Analogon H₂Isa-az-tmpz.

Aus Neugier um den Einfluss der NH-Funktion des Pyrazols auf die resultierende MOF-Topologie zu untersuchen, aber dennoch grundsätzlich die „Ligandendesign“-Kriterien des SBL-Ansatzes zu erfüllen, wurde entschieden das 1-Methyl substituierte Analogon 5-(4-(1,3,5-Trimethylpyrazolyl)azo)isophthalsäure (H₂Isa-az-tmpz) des ursprünglich verwendeten H₃Isa-az-dmpz Liganden zu synthetisieren (Abbildung 27). Ein weiterer Grund war die trotz unzähliger Versuche nicht erfolgreiche Aktivierung von **rtl**-[Zn(Isa-az-dmpz)] und auf diese Weise ein aktivierbares Material zu erhalten.

Zur Synthese des Liganden wurde der Hydrazon-Vorläufer Me₂Isa-az-acac mit Methylhydrazin zum 5-(4-(1,3,5-Trimethylpyrazolyl)azo)isophthalsäuredimethylester umgesetzt. Eine folgende basische Verseifung lieferte 5-(4-(1,3,5-Trimethylpyrazolyl)azo)isophthalsäure (H₂Isa-az-tmpz) als neuen bifunktionellen Liganden (Abbildung 28). Die Ausbeute über beide Stufen beträgt 67 %.

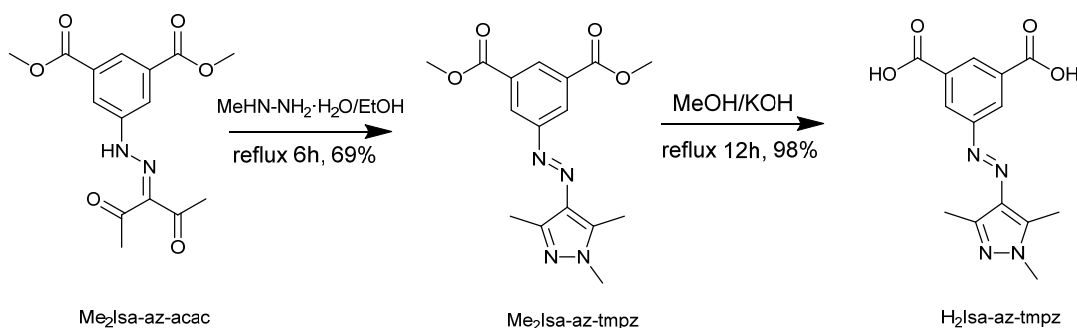


Abbildung 28. Synthese von H₂Isa-az-tmpz ausgehend vom Hydrazonvorläufer Me₂Isa-az-acac.

Die Kombination von Zn(NO₃)₂·4H₂O mit dem neuen bifunktionellen Liganden H₂Isa-az-tmpz unter ähnlichen Synthesebedingungen wie für **rtl-[Zn(Isa-az-dmpz)]** (DMF bei 80 °C) lieferte gelbe blockförmige Kristalle der Zusammensetzung [Zn(Isa-az-tmpz)]·DMF (siehe Abbildung 29). [Zn(Isa-az-tmpz)]·DMF wurde als racemischer Twin in der enantiomorphen tetragonalen Raumgruppe P4₁2₁2 mit näherungsweise den gleichen Anteilen beider enantiomorphen Formen verfeinert (siehe Tabelle 1). Die Asymmetrische Einheit enthält ein Zn(II) und den zweifach-deprotonierten Liganden Isa-az-tmpz²⁻. Ein stark fehlgeordnetes DMF-Molekül in den Poren wurde durch die in PLATON implementierte Squeeze-Funktion maskiert.¹⁴⁷ Diese Zusammensetzung wurde weitergehend durch eine Elementaranalyse verifiziert.

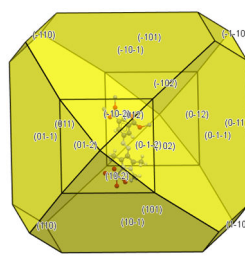
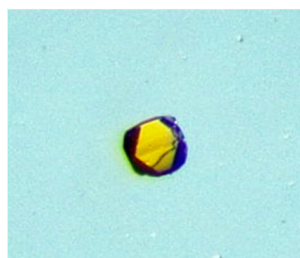
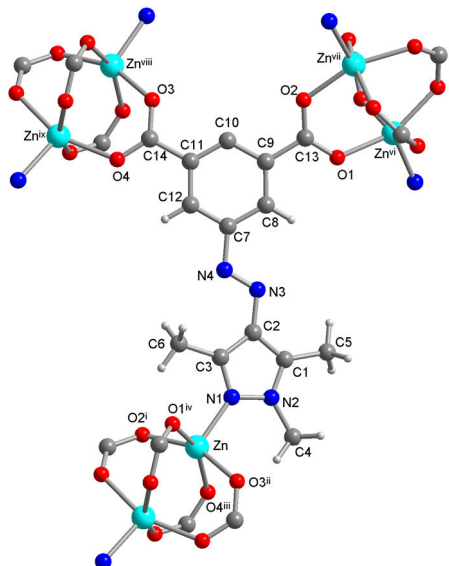


Abbildung 29. Oben: Erweiterte Asymmetrische Einheit von [Zn(lsa-az-tmpz)] (Symmetrietransformationen: (i) $-y+1/2, x+1/2, z+1/4$; (ii) $x, y+1, z$; (iii) $y, x+1, -z+1$; (iv) $x-1/2, -y+3/2, -z+3/4$; (v) $y-1, x+1, -z+1$; (vi) $x+1/2, -y+3/2, -z+3/4$; (vii) $y-1/2, -x+1/2, z-1/4$; (viii) $x, y-1, z$; (ix) $y-1, x, -z+1$); Unten: Vergleich der Kristallmorphologie von [Zn(lsa-az-tmpz)] unter dem Lichtmikroskop und der berechneten Morphologie mit Mercury¹⁴⁸.

Tabelle 1 Kristalldaten und Verfeinerungsdetails für 3,6T22-[Zn(lsa-az-tmpz)]

3,6T22-[Zn(lsa-az-dmpz)]	
Chemical formula	C ₁₄ H ₁₂ N ₄ O ₄ Zn (C ₃ H ₇ NO)
M _r (g/mol)	438.74
Crystal system, space group	tetragonal, P4 ₁ 2 ₁ 2
Temperature (K)	140
a (Å)	12.9044(7)
c (Å)	25.5728(18)
V (Å ³)	4258.5(6)
Z	8
μ (mm ⁻¹)	1.17
d _{calc} (g/cm ³)	1.141
F(000)	1488
Crystal size (mm)	0.02 × 0.02 × 0.02
No. of measured, independent and observed reflections	58045, 4925, 4559
R _{int}	0.052
R, wR(F ²), S [F ² > 2σ(F ²)] ^[a] R, wR(F ²), S [all data] ^[a]	0.0689, 0.1382, 1.26 0.0737, 0.1825, 1.26
No. of reflections	49259
No. of parameters	212
No. of restraints	0
Δρ _{max} , Δρ _{min} ^[b] (e·Å ⁻³)	0.44, -0.36
Flack parameter	0.45

[a] $R_1 = [\sum(|F_o| - |F_c|)/\Sigma|F_o|]$; $wR_2 = [\sum [w(F_o^2 - F_c^2)^2]/\Sigma[w(F_o^2)^2]]^{1/2}$. Goodness-of-fit $S = [\sum [w(F_o^2 - F_c^2)^2]/(n-p)]^{1/2}$.

Das Paddle-Wheel-Cluster nimmt normalerweise hohe Symmetrien, mit den μ_2 -Carboxylatliganden in äquatorialer Position und zwei weiteren Liganden in axialer Position, an. Die höchste annehmbare Symmetrie ist D_{4h} , wie z.B. in den archetypischen Beispielen Rhodium- und Chromiumtetraacetat.¹⁴⁹⁻¹⁵⁰

In $[Zn(\text{Isa-az-mpz})]$ hat das Paddle-Wheel-Cluster eine verringerte C_2 -Symmetrie und ist dementsprechend ohne die Anwesenheit eines Inversionszentrums oder einer Spiegelebene die Basis für die chirale Struktur (siehe Abbildung 30). Dies ist im Gegensatz zur C_i -Symmetrie des Paddle-Wheel-Clusters in $\text{rtl}-[\text{Cu}(\text{HIsa-az-dmpz})]$ und $\text{rtl}-[\text{Zn}(\text{HIsa-az-dmpz})]$.

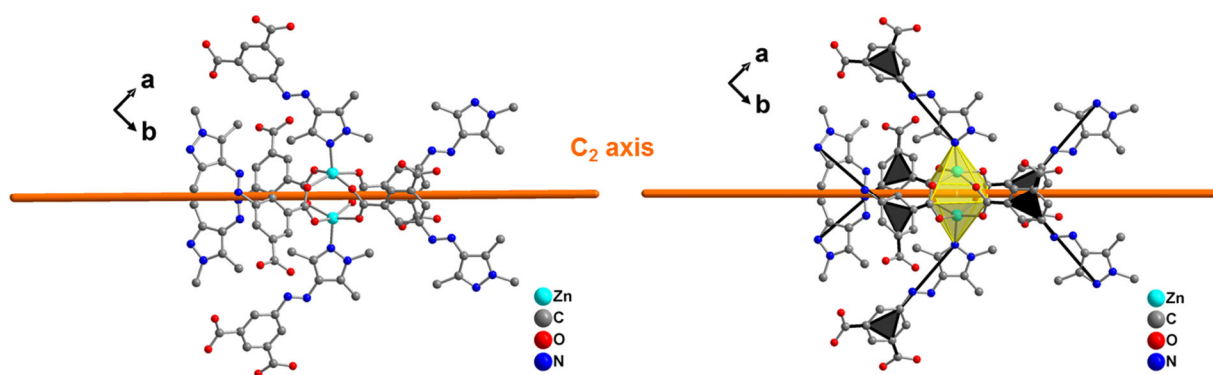


Abbildung 30. Darstellung der durch das Paddle-Wheel-Cluster laufende C_2 -Achse und der Orientierung der Isa-az-mpz²⁻ Liganden als 3-c Knoten relativ zu dieser Achse.

Die Paddle-Wheel-Cluster als C_2 -symmetrische Baueinheit bilden entlang der c-Achse eine rechtshändige 4₁-Helix. Analyse der zugrundeliegenden Topologie mit ToposPro mit dem Paddle-Wheel-Cluster als oktaedrischem 6-c Knoten und dem Isa-az-mpz²⁻ Liganden als trigonalen 3-c Knoten lieferte die selte chirale 3,6T22-Topologie für, welche noch kein RCSR-Kürzel hinterlegt ist.¹⁵¹ Diese Topologie kann in ihrer Standarddarstellung in den von Dong et al. synthetisierten Koordinationspolymeren ScCd(L)_2 ($\text{L} = 4\text{-Amino-3,5-bis(4-pyridyl-3-phenyl)1,2,4-triazol}$, S = Gastmoleküle) vorgefunden werden.¹⁵²⁻¹⁵⁵ Darüberhinaus wurde die 3,6T22-Topologie kurzlich in den MOFs $[\text{Fe}_2\text{M(BPTC)}]$ (Bptc = Biphenyl-3,4',5-tricarboxylat) und $[(\text{Me}_2\text{NH}_2)\text{Cd}_3(\text{OH})(\text{H}_2\text{O})_3(\text{TATAB})_2]$ (TATAB³⁻ = 4,4',4"-S-Triazin-1,3,5-triyltriaminobenzoat) mit jeweils trigonal-prismatischen 6-c Knoten kommuniziert.¹⁵⁶⁻¹⁵⁷

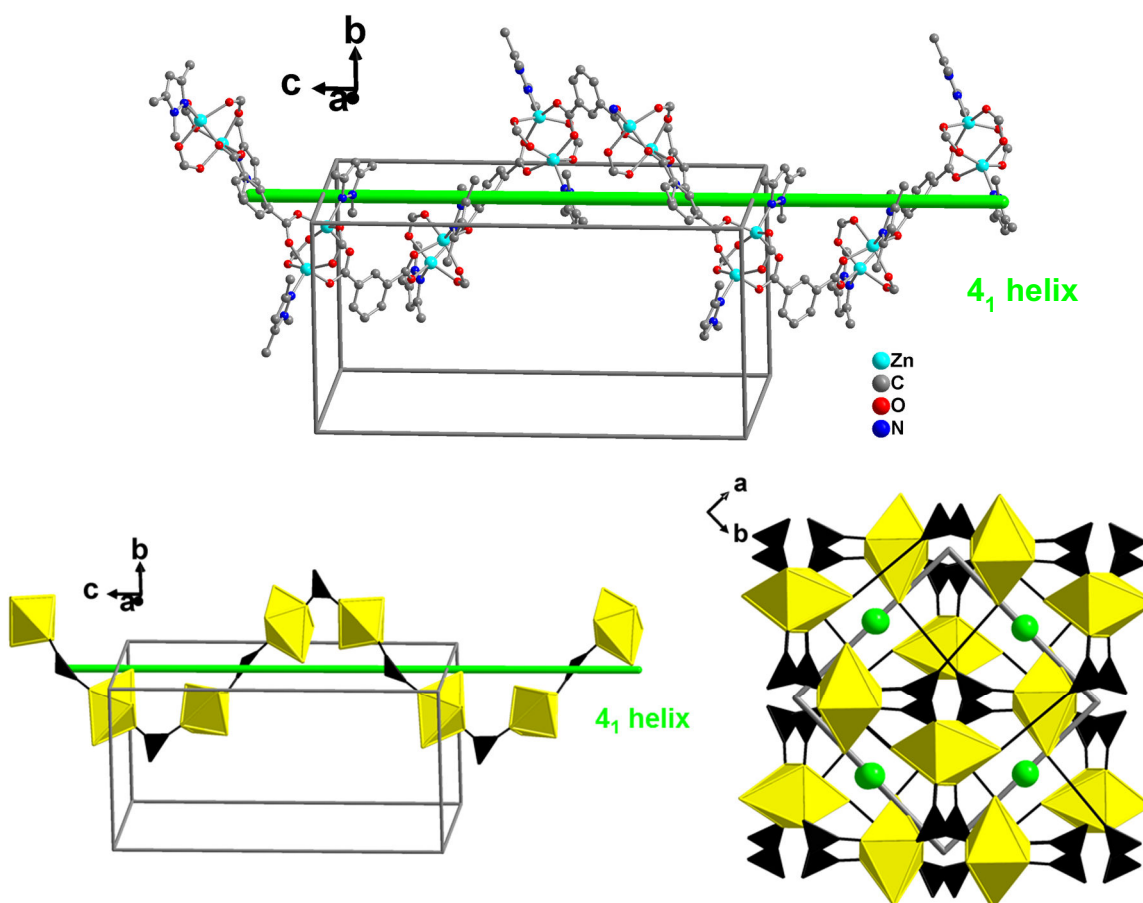
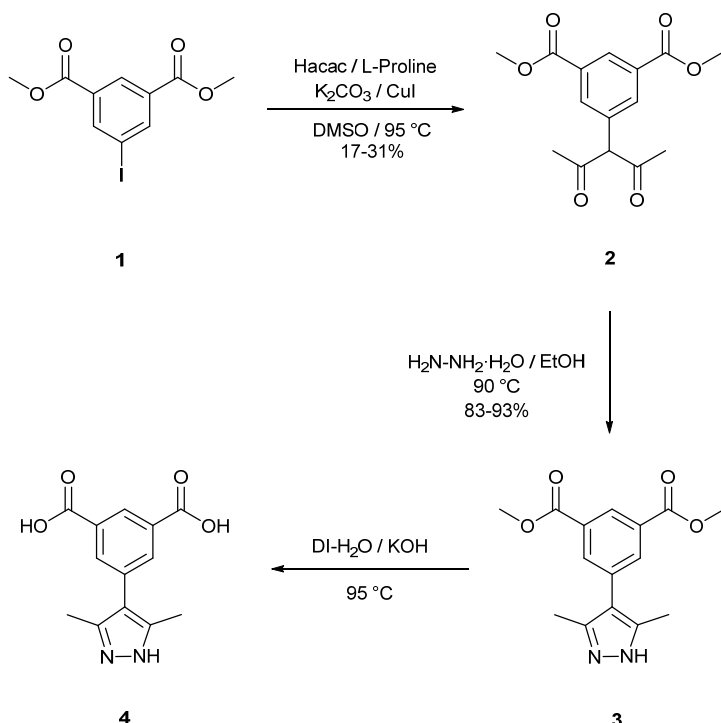


Abbildung 31. Darstellung der 4₁-Helix entlang der c-Achse mit dem Paddle-Wheel-Cluster als C₂-symmetrische Baueinheit und der Darstellung der 3,6T22-Topologie mit dem Paddle-Wheel-Cluster als oktaedrischem 6-c Knoten und dem Isa-az-tmpz²⁻ Liganden als trigonalen 3-c Knoten.

Obwohl HIsa-az-tmpz die generellen „Ligandendesign“-Prinzipien des SBL-Ansatzes erfüllt und mit Zn(Isa-az-dmpz)] sogar ein MOF mit einer 3,6-c Topologie auf Basis eines Paddle-Wheel-Clusters erhalten werden konnte, kann die **3,6T22** Topologie nicht mit dem SBL-Ansatz veranschaulicht. **3,6T22-[Zn(Isa-az-dmpz)]** stellt somit eines schönes Beispiel für die Serendipität, welche Festkörpersynthesen normalerweise beiwohnt und das obwohl sogar das angestrebte Cluster gebildet wurde. Zusätzlich kann **3,6T22-[Zn(Isa-az-tmpz)]** als Startpunkt gesehen werden um mit bifunktionellen Pyrazol-Carboxylatliganden chirale potentiell poröse Netzwerkstrukturen zu erhalten.

4.2 Synthese von 5-(3,5-dimethyl-1*H*-pyrazol-4-yl)isophthalsäure (H₃Isa-dmpz)

Die Reaktionsfolge zum bifunktionellen T-förmigen Liganden 5-(3,5-dimethyl-1*H*-pyrazol-4-yl)isophthalsäure (H₃Isa-dmpz) ist in Schema 1 angegeben. Im ersten Schritt wurde der 5-Iodoisophthalsäuredimethylester (**1**) in einer Ullmann-artigen Kupplung nach einer von Jiang et al. adaptierten Synthese zum 5-(3-(2,4-Pentandionyl) isophthalsäuredimethylester (**2**) umgesetzt.



Schema 1 Reaktionsschema für die Synthese von H₃Isa-dmpz (**4**).

Bei der säulenchromatographischen Aufreinigung wurde neben Verbindung **2** und dem Edukt 5-Iodoisophthalsäuredimethylester in den ersten Ansätzen auch eine dritte Verbindung als gelber Feststoff erhalten. Diese wurde mittels ¹H-NMR und ¹³C-NMR als 5-(2-Oxopropyl)isophthalsäuredimethylester identifiziert.

Dies kann mit den von Lei et al.¹⁵⁸ untersuchten mit C-C-Bindungsspaltungen gekoppelten Kupfer(I)-katalysierten Arylierungen von Aryliodiden mit β-Diketonen zur Synthese von α-Arylketonen nachvollzogen werden. Sie stellten fest das Cu(I)- als auch Cu(II)-Salze in DMSO mit K₃PO₄·3H₂O hohe Ausbeuten an α-Arylketonen liefern. Sie vermuteten, dass insbesondere die Gegenwart von Wasser eine entscheidene Rolle spielt. Sie überprüften es unter anderem dadurch, dass sie unter wasserfreien Bedingungen die analogen

Arylacetylacetone erhielten. Durch noch sorgfältigeres Trocknen des eingesetzten und mittel „Freeze-Pump-Thaw“-entgasten DMSOs konnte der Erhalt des 5-(2-Oxopropyl)isophthalsäuredimethylesters minimiert werden.

Die Synthese analoger einkristalliner 3,6-c MOFs zu Kapitel 2.1 mit H₃lsa-dmpz und Kupfer- und Zinksalzen blieb ohne Erfolg.¹⁵⁹

4.3 Synthese und Struktur von $[\text{Cu}(\text{Me}_2\text{Isa-acac})]\cdot\text{H}_2\text{O}$

Neben dem Zielliganden $\text{H}_3\text{Isa-dmpz}$ kann auch schon der die Vorläuferverbindung mit einer Acetylacetonatfunktion als potentieller bifunktioneller Ligand angesehen werden.¹⁶⁰ Hierzu wurde der Ligand $\text{HMe}_2\text{Isa-acac}$ (**2**) in Dichlormethan gelöst und mit einer wässrigen Lösung des Tetraamminkupfer(II)-Komplexes überschichtet. Nach einer Woche war die Dichlormethan-Phase grün gefärbt, was auf die Bildung eines Kupfer-acetylacetonates hindeutet. Daraufhin wurde die überstehende wässrige Phase des überschüssigen Tetraamminkupfer(II)-Komplexes vorsichtig abpipettiert. Die grüne Lösung wurde anschließend mit n-Hexan überschichtet und bei Raumtemperatur zur Kristallisation stehen gelassen. Nach wenigen Tagen konnten dunkelgrüne Blockkristalle erhalten werden. Diese wurden daraufhin mittels Röntgeneinkristalldiffraktometrie untersucht.

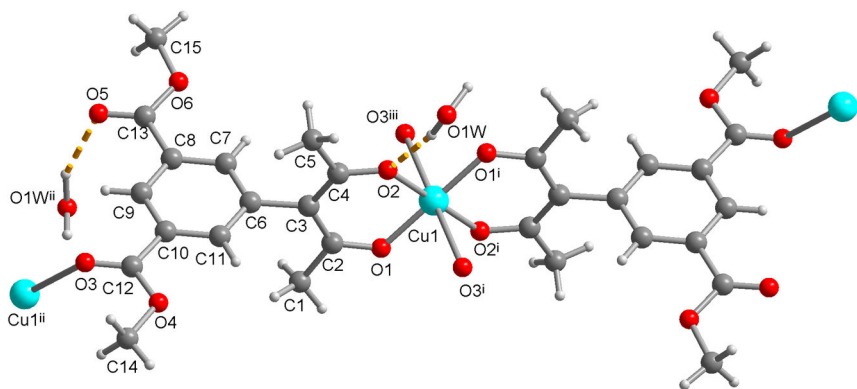


Abbildung 32 Asymmetrische Einheit von $[\text{Cu}(\text{Me}_2\text{Isa-acac})]\cdot\text{H}_2\text{O}$ (Symmetrietransformationen: $i = -x, 1-y, 1-z$; $ii = -0.5-x, 0.5+y, 1.5-z$; $iii = -0.5-x, -0.5+y, 1.5-z$).

$[\text{Cu}(\text{Me}_2\text{Isa-acac})]\cdot\text{H}_2\text{O}$ kristallisiert im monoklinen Kristallsystem mit der Raumgruppe $P2_1/n$. Die asymmetrische Einheit von $[\text{Cu}(\text{Me}_2\text{Isa-acac})]\cdot\text{H}_2\text{O}$ besteht aus einem einfach an der Acetylacetonfunktion deprotonierten Liganden $\text{Me}_2\text{Isa-acac}^-$, einem Kupferatom und einem Wassermolekül (siehe Abbildung 32). Das Kupferatom ist quadratisch planar von zwei chelatisierenden Acetylacetonatgruppen mit Bindungslängen im Bereich von 1.91 Å umgeben. Es bestehen schwache Wechselwirkungen zu Carbonyl-Sauerstoffatomen der Esterfunktionen von zwei $\text{Me}_2\text{Isa-acac}$ -Liganden in axialer Position mit einem Abstand von 2.62 Å. Daraus ergibt sich eine stark Jahn-Teller-verzerrte oktaedrische Koordinationsumgebung für das Kupferatom (Abbildung 32).

Tabelle 2. Kristalldaten und Verfeinerungsdetails für [Cu(Me₂lsa-acac)]·H₂O

	[Cu(Me ₂ lsa-acac)]·H ₂ O
Chemical formula	C ₃₀ H ₃₄ CuO ₁₄
M _r (g/mol)	682.11
Crystal system, space group	monoclinic, P2 ₁ /n
Temperature (K)	293
a (Å)	8.3633(7)
b (Å)	11.0038(9)
c (Å)	15.8641(13)
V (Å ³)	1454.1(2)
Z	2
μ (mm ⁻¹)	0.83
d _{calc} (g/cm ³)	1.558
F(000)	710
Crystal size (mm)	0.05 × 0.04 × 0.02
T _{min} , T _{max}	0.672, 0.745
No. of measured, independent and observed reflections	29789, 3444, 3143
R _{int}	0.023
R, wR(F ²), S [F ² > 2σ (F ²)] ^[a] R, wR(F ²), S [all data] ^[a]	0.032, 0.0983, 1.08 0.0383, 0.1014, 1.15
No. of reflections	3444
No. of parameters	217
No. of restraints	2
Δρ _{max} , Δρ _{min} ^[b] (e·Å ⁻³)	-0.46, -0.53

Durch die apikale Koordination einer Esterfunktion kann jedes Kupferatom als quadratisch planarer Knotenpunkt aufgefasst werden. Hieraus ergibt sich, dass [Cu(Me₂lsa-acac)]·H₂O als ein zweidimensionales Koordinationspolymer mit einer 4-c **sql**-Topologie aufgefasst werden kann (Abbildung 33). Benachbarte Schichten können durch einfache Translationssymmetrie entlang der a-Achse mit [x+1, y, z] bzw. [x-1, y, z] ineinander überführt werden, was ein AA-Packungsmuster der Schichten bedingt (Abbildung 33).

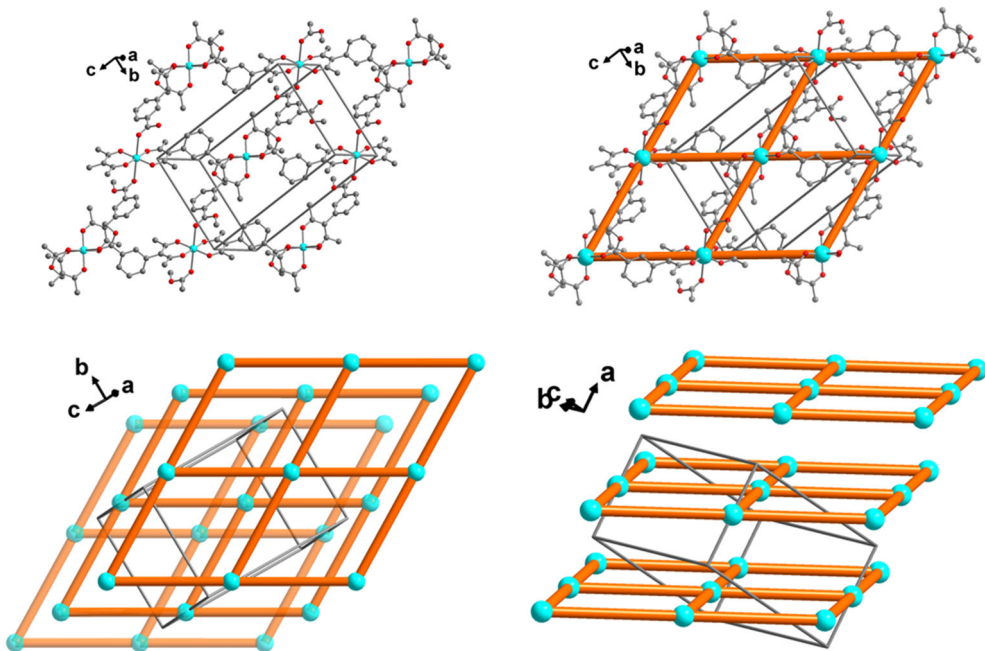


Abbildung 33. Darstellung von $[\text{Cu}(\text{Me}_2\text{Ilsa-acac})]\cdot\text{H}_2\text{O}$ als zweidimensionales **sql** Netz mit dem Kupferatom (cyan) als quadratischer 4-c Knoten und AA-Packung der **sql**-Netz entlang der a-Achse mit $[x+1, y, z]$ und $[x-1, y, z]$ als Relationen benachbarter Netze (nicht koordinierende Esterfunktion, Wassermolekül und Wasserstoffatome sind zur besseren Übersichtlichkeit nicht dargestellt).

Das sich zusätzlich in der asymmetrischen Einheit befindende Wassermolekül verbrückt zwischen dem Carbonylsauerstoffs (O_5) der nicht-koordinierenden Methylesterfunktion und einem Sauerstoffatom der Acetylacetonatfunktion (O_2) innerhalb der zweidimensionalen Schichten.

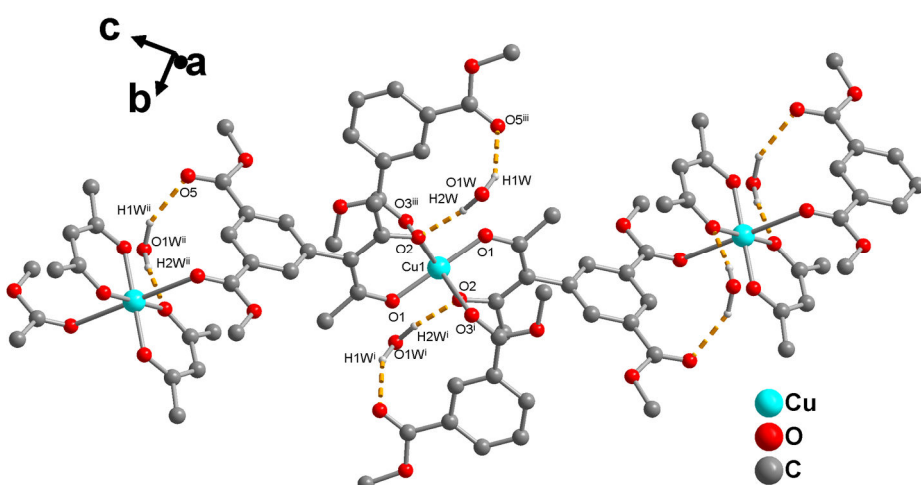


Abbildung 34. Darstellung der Wasserstoffbrückenbindungen des Wassermoleküls in $[\text{Cu}(\text{Me}_2\text{Ilsa-acac})]\cdot\text{H}_2\text{O}$ (Geometrien der Wasserstoffbrückenbindungen in \AA und $^\circ$ (gestrichelte orangefarbene Linien): $\text{O}_1\text{W}-\text{H}_1\text{W}$ 1.00, $\text{H}_1\text{W}\cdots\text{O}_5$ 2.12, $\text{O}_1\text{W}\cdots\text{O}_5$ 3.054(3), $\text{D}-\text{H}\cdots\text{A}$ 154; $\text{O}_1\text{W}-\text{H}_2\text{W}$ 0.96, $\text{H}_2\text{W}\cdots\text{O}_2$ 1.90, $\text{O}_1\text{W}\cdots\text{O}_2$ 2.843(2), $\text{D}-\text{H}\cdots\text{A}$ 167)

Die anologe Struktur des Bis(3-phenyl-2,4-pentandionato)Kupfer(II)-Komplexes wurde erstmals von Belford et al. 1965 publiziert.¹⁶¹ In neueren Arbeiten tauchte dieses Strukturmotiv unter anderem bei Maverick et al.¹⁶²⁻¹⁶⁷ und Aakeröy et al.¹⁶⁸ auf. Maverick et al. gelang u.a. der Einschluss des C₆₀-Fullerens in den „molecular square“ [Cu₄(m-Phenylenbis(β-diketonat)] auf Basis eines Bis(β-diketon)-Liganden.¹⁶⁵ Zudem gelang Maverick et al. die Synthese von Koordinationspolymeren der Zusammensetzung [Cu(Py-acac)₂]·L (Py-acac = (4-Pyridyl)-2,4-pentandion, L = Lösungsmittel). Durch Variation des Lösungsmittels erhielten sie sowohl zu [Cu(Me₂lsa-acac)]-analoge zweidimensionale 4-c **sql** Netze als auch dreidimensionale 4-c **nbo** Netzwerke.¹⁶² Aakeröy et al. untersuchten den Einfluss von unterschiedlichen Halogenidsubstituenten in para-Position auf das Packungsmuster analoger Kupferkomplexe.¹⁶⁸

5. Zusammenfassung

Im Rahmen des ersten Teils dieser Arbeit wurden Metall-organische Gerüstverbindungen auf Basis des bifunktionellen T-förmigen Liganden 5-(4-(3,5-dimethyl-1*H*-pyrazolyl)azo)isophthalat (HIsa-az-dmpz^{2-}) synthetisiert. Dies geschah unter der Prämisse, dass sich mit bifunktionellen Isophthalat-Pyrazol Liganden analog zu bifunktionellen T-förmigen Liganden in der Literatur ausgestattet mit N-Heterozyklen als N-Donorgruppen wie Pyridin, Triazol, Tetrazol und Imidazol ebenso MOFs mit 3,6-c verknüpften Topologien, welche unter dem „supramolecular building layer“-Ansatz rationalisiert werden können, synthetisieren lassen.

Konsequenterweise wurde durch die Umsetzung des Liganden mit Zink- bzw. Kupfersalzen isotrukturelle MOFs mit 3,6-c verknüpften **rtl** Topologien der Zusammensetzung **rtl**-[M(HIsa-az-dmpz)] ($\text{M}^{2+} = \text{Zn}, \text{Cu}$) erhalten. Beide Verbindungen sind potentiell porös mit einem über Wasserstoffbrücken-gebunden DMF und einem weiteren in der Kanalstruktur der Materialien.

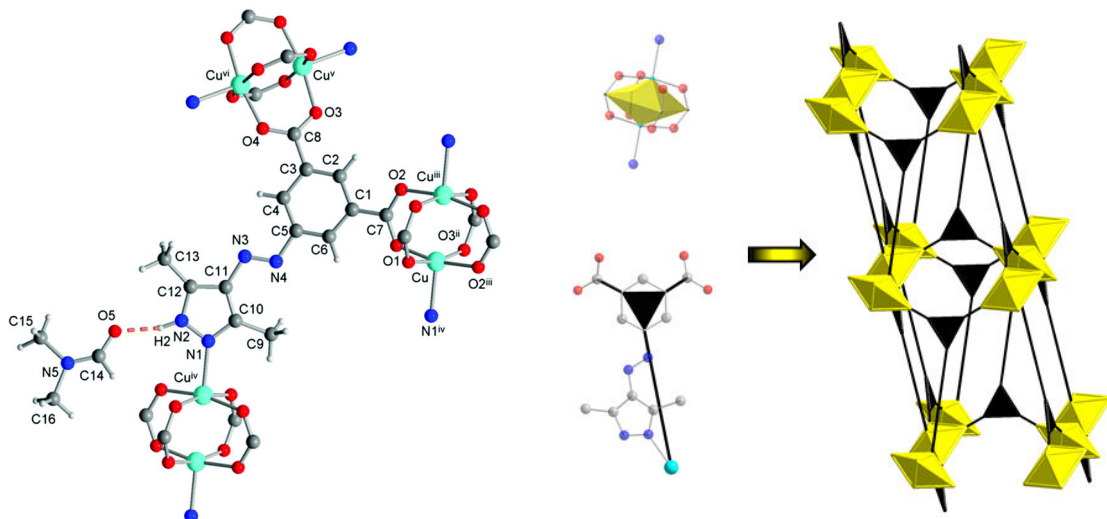


Abbildung 35. Links: Erweiterte asymmetrische Einheit von **rtl**-[Cu(HIsa-az-dmpz)]. Rechts: Dekonstruktion der **rtl**-MOFs mit dem Paddle-wheel-Cluster als oktaedrischer 6-c Knoten und dem T-förmigen Liganden HIsa-az-dmpz²⁻ als trigonalem 3-c Knoten.

rtl-[Zn(HIsa-az-dmpz)] unterging eine irreversible Phasentransformation in eine nicht-poröse Phase unter allen gewählten Aktivierungsprotokollen. Wohingegen für **rtl**-[Cu(HIsa-az-dmpz)] ein erfolgreiches Aktivierungsprotokoll, durch Lösungsmittelaustausch gegen Aceton gefolgt von einer überkritischen Trocknung und anschließendem Entgasen bei 80 °C, mit einem reversiblen Phasenwechsel in eine nicht-poröse Phase etabliert werden konnte. **rtl**-[Cu(HIsa-az-dmpz)]-act. zeigte in Gassorptionsexperimenten bei kryogenen Temperaturen S-förmige

Typ-IV Isothermen mit hohen Sättigungsaufnahmen von $360 \text{ cm}^3 \text{ g}^{-1}$ für N_2 bei 77 K, $310 \text{ cm}^3 \text{ g}^{-1}$ für CO_2 bei 195 K, $317 \text{ cm}^3 \text{ g}^{-1}$ für Ar bei 87 K und $270 \text{ cm}^3 \text{ g}^{-1}$ für CH_4 bei 112 K (siehe Abbildung 36). Für N_2 und CO_2 konnte die generelle Reversibilität diesen Phasenwechsels bestätigt werden. Die gravimetrische Hochdruck-Adsorption zeigt eine Aufnahme von 330 mg g^{-1} mit einem „gate-opening“ bei 10 bar.

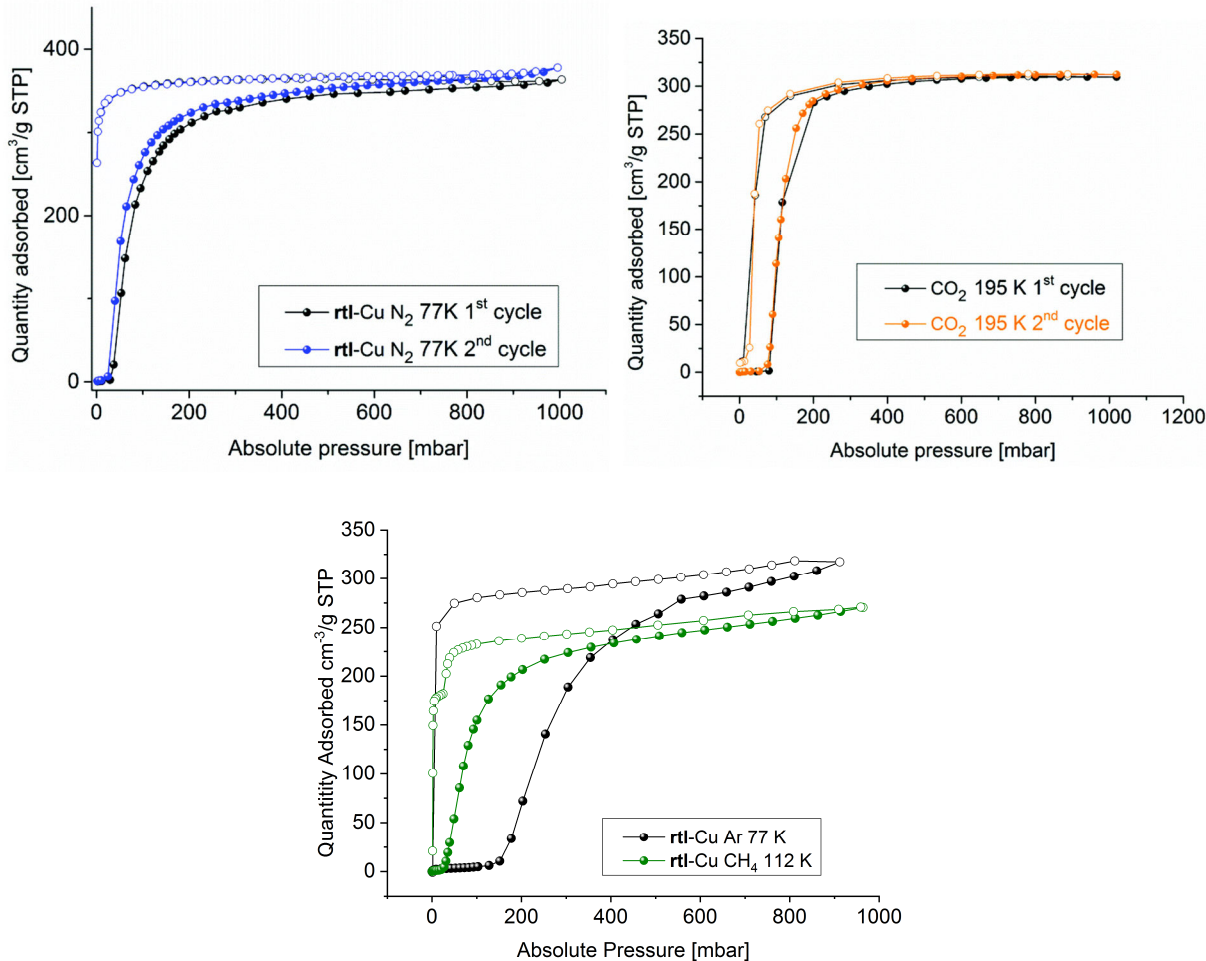


Abbildung 36. S-förmige Typ-IV Sorptionsprofile bei kryogenen Temperaturen für N_2 bei 77 K, CO_2 bei 195 K, Ar bei 77 K und CH_4 bei 112 K.

Diese Werte setzt **rtl-[Cu(Hlsa-az-dmpz)]** in einen ausgewählten Kreis flexibler MOF-Materialien, welche reversible S-förmigen Typ-IV Isothermen gepaart mit einer hohen Sättigungsaufnahme ($>250 \text{ cm}^3 \text{ g}^{-1}$) zeigen (siehe Tabelle 2). Diese flexiblen Materialien werden insbesondere aufgrund der mit ihren S-förmigen Adsorptionsprofilen assoziierten hohen Kapazitäten für Gasspeicher-/Liefersysteme diskutiert. Sodass insbesondere die Methansorption die Basis für weitere Arbeiten z.B. hinsichtlich der langfristigen Zyklustabilität von **rtl-Cu** dienen kann.

Tabelle 3. Überblick über MOFs mit einstufigen Type-F-IV Sorptionsisothermen mit hohen Sättigungsaufnahmen.

Adsorbens	Adsorbat	Sättigungs-aufnahme [cm ³ /g]	„gate-opening /- closing [P/P ₀]	reversibel
DUT-8 (Ni)⁹²	CO ₂	590 (195 K)	0.40 / 0.20	nein
	N ₂	650 (77 K)	0.10 / <0.01	nein
rtl-[CuHisa-az-dmpz]	CO ₂	310 (195 K)	0.08 / 0.02	ja
	N ₂	360 (77 K)	0.03 / <0.01	
	Ar	317 (87 K)	0.15 / <0.01	
	CH ₄	270 (112 K)	0.04 / <0.01	n.u.
JLU-Liu33¹⁶⁹	N ₂	319 (77 K)	0.06 / 0.05	n.u.
X-pcu-5-Zn-β⁹⁴	CO ₂	254 (195 K)	0.30 / 0.20	ja
X-pcu-6-Zn-β¹⁷⁰	CO ₂	245 (195 K)	0.17 / 0.16	ja
	N ₂	293 (77 K)	0.20 / 0.04	
X-pcu-7-Zn-β¹⁷⁰	CO ₂	267 (195 K)	0.33 / 0.29	ja
X-pcu-8-Zn-β¹⁷⁰	CO ₂	243 (195 K)	0.39 / 0.33	ja
CPM-325-Naph¹⁷¹	CO ₂	200 (195 K)	0.03 / < 0.03	n.u.
	N ₂	216 (77 K)	0.27 / ≈0	
[Zn(TCNQ-TCNQ)bpy]¹⁷²	O ₂	268 (77 K)	0.34 / < 0.05	n.u.
	NO	322 (121 K)	0.11 / < 0.05	
[Zn₂(bdc)₂(F₂bbpy)]¹⁷³	O ₂	250 (77 K)	0.05 / < 0.05	n.u.
Fe(bdp)⁹³	CH ₄	295 (298 K)	25 bar / 9 bar	ja
Co(bdp)⁹³	CH ₄	246 (298 K)	16 bar / 7bar	ja
X-dia-1-Ni⁸⁰	CH ₄	222 (298 K)	20 bar / < 1bar	ja

n.u. = nicht untersucht

Für das seit 1955 bekannte Bipyrazol 4,4'-Azobis(3,5-dimethyl-1H-pyrazole) (H_2azbpz) wurde erstmals eine ausführliche Untersuchung seiner Festkörperstrukturen durchgeführt.

Hierbei konnten zwei Polymorphe $\text{H}_2\text{azbpz-}\text{I}$ und $\text{H}_2\text{azbpz-}\text{II}$ isoliert werden, in welchen zwei unterschiedliche symmetrische planare Konformere von H_2azbpz (4,4'-a,a-E und 4,4'-s,s-E) eingebaut sind, welche sich lediglich durch die Position der pyrrolischen NH-Funktionalitäten voneinander unterscheiden (siehe Abbildung 37.). Für beide Polymorphe wurden reproduzierbare Syntheseprotokolle um etabliert. Für $\text{H}_2\text{azbpz-}\text{II}$ gestaltete sich dies äußerst schwierig, sodass eine mechanochemische Transformation von $\text{H}_2\text{azbpz-}\text{I}$ in $\text{H}_2\text{azbpz-}\text{II}$ gefolgt von einer Rekristallisation dieses Materials aus einer gesättigten DMF-Lösung als einzige verlässliche Methode gefunden wurde. Die Phasenzusammensetzung der erhaltenen Materialien wurde mit einer Vielzahl an spektroskopischen Methoden überprüft.

Gitterenergierechnungen unter Berücksichtigung der relativen Stabilitäten der Konformere deuten darauf hin, dass das Polymorph $\text{H}_2\text{azbpz-}\text{II}$ zwar das relativ stabile Polymorph bei niederen Temperaturen darstellt, aber das energiereichere 4,4'-s,s-E Konformer enthält.

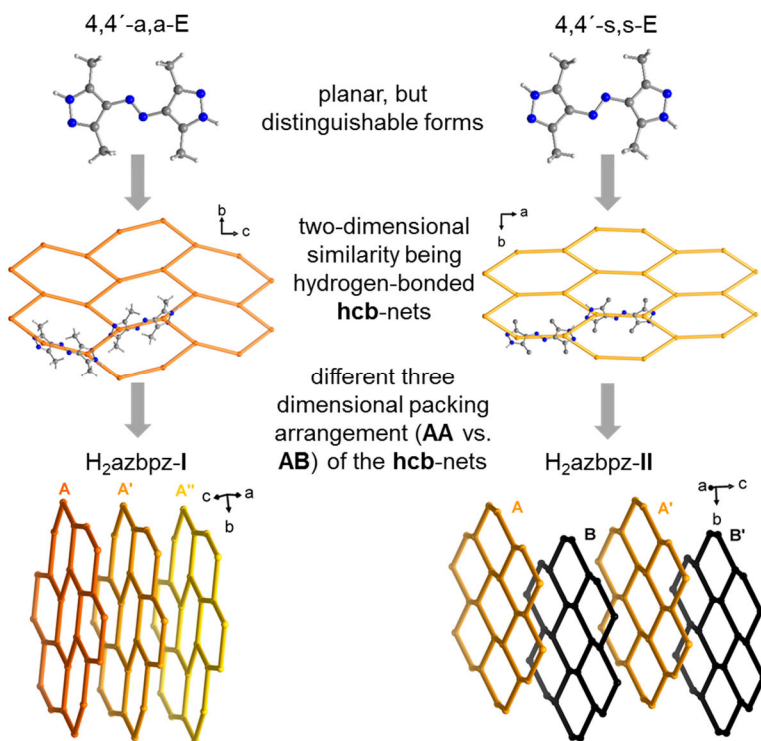


Abbildung 37. Schematische Darstellung der eingebauten unterschiedlichen Konformere 4,4'-a,a-E und 4,4'-s,s-E ($a = \text{anti-periplanar}$, $s = \text{syn-periplanar}$), der strukturell ähnlichen zweidimensionalen hcb Netze und der unterschiedlichen Stapelfolge mit AA und AB in den Polymorphen $\text{H}_2\text{azbpz-}\text{I}$ und $\text{H}_2\text{azbpz-}\text{II}$.

Die unterschiedlichen Formen des H_2azbpz -Moleküls assoziieren in den beiden Polymorphen mittels ihrer selbstkomplementären Pyrazoleinheiten als 3-c Knoten in

strukturell äußerst ähnliche zweidimensionale Wasserstoffbrückennetzwerke mit der **hcb**-Topologie. Diese **hcb**-Schichten zeigen in H₂azbpz-**I** eine gestaffelte AA-Stapelfolge und im bei tieferen Temperaturen stabileren Polymorph H₂azbpz-**II** eine versetzte AB-Packung. Die Unterschiede der Kristallpackungen in beiden Polymorphen wurden intensiver anhand der Zuhilfenahme von Hirshfeldoberflächen herausgearbeitet.

Die Untersuchung der Festkörperlandschaft von H₂azbpz wurde durch die Isolierung des Hemihydrats H₂azbpz·0.5H₂O komplementiert. Die Netzwerkstruktur von H₂azbpz·0.5H₂O kann auf der tetraedrischen {H₂O(pz)₄} Baueinheiten mit einem Wassermolekül im Zentrum rationalisiert werden. Eine effiziente Kristallpackung in H₂azbpz·0.5H₂O wird durch eine fünffache Interpenetration erhalten.

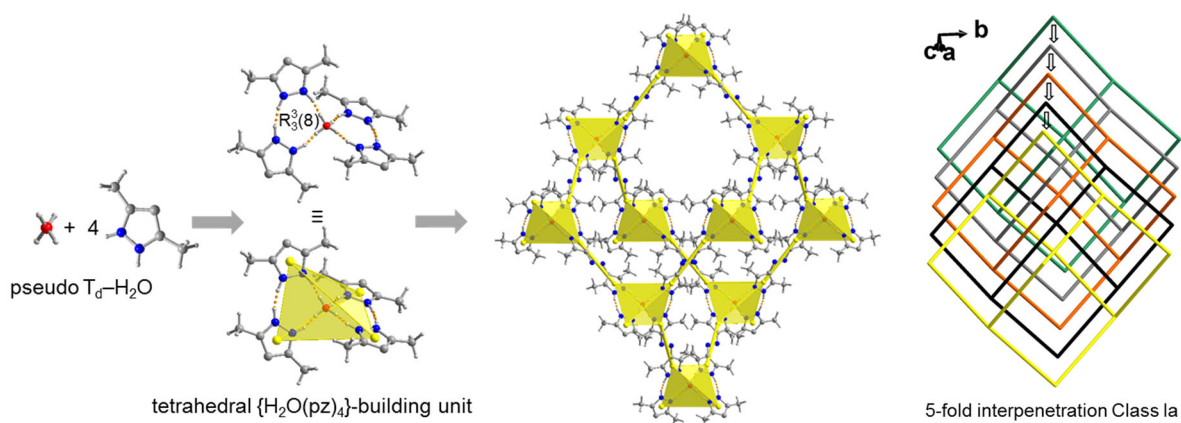


Abbildung 38. Darstellung des fünffach-interpenetrierten **dia**-Netzwerks im Hemihydrat von H₂azbpz mit einem pseudo-tetraedrischen Wassermolekül im Zentrum der {H₂O(pz)₄}-supramolekularen Baueinheit.

Obwohl die **dia**-Topologie im Forschungsgebiet der Netzwerkstrukturen als die am häufigsten anzutreffende Topologie gilt, stellt H₂azbpz·0.5H₂O einen seltenen Vertreter dar, in dem diese durch ein pseudo-tetraedrisches Wassermolekül als Geometriezentrum induziert wird. Auf diese Weise kann H₂azbpz·0.5H₂O auch als ein supramolekulares Analogon zum kubischen Eispolymer I_c angesehen werden.

Neben den rein organischen Netzwerkstrukturen von H₂azbpz konnten auch Komplexverbindungen erhalten werden, welche als solche interpretiert werden können. Die beiden Metall-Komplexe [Cu(NO₃)₂(H₂O)₂(H₂azbpz)₂]·2H₂O und [Ni(H₂O)₄(H₂azbpz)₂](NO₃)₂·2H₂O beinhalten das Bipyrazole als einen mono-dentaten Liganden. Diese Komplexe bilden supramolekulare Architekturen auf Basis von Wasserstoffbrückenbindungen und Azo-Pyrazol π-Wechselwirkungen. Interessanterweise unterscheiden sich die eingebauten molekularen Formen von H₂azbpz. Im Nickelkomplex ist

die stabilste im Kupferkomplex stabilisiert unsymmetrische

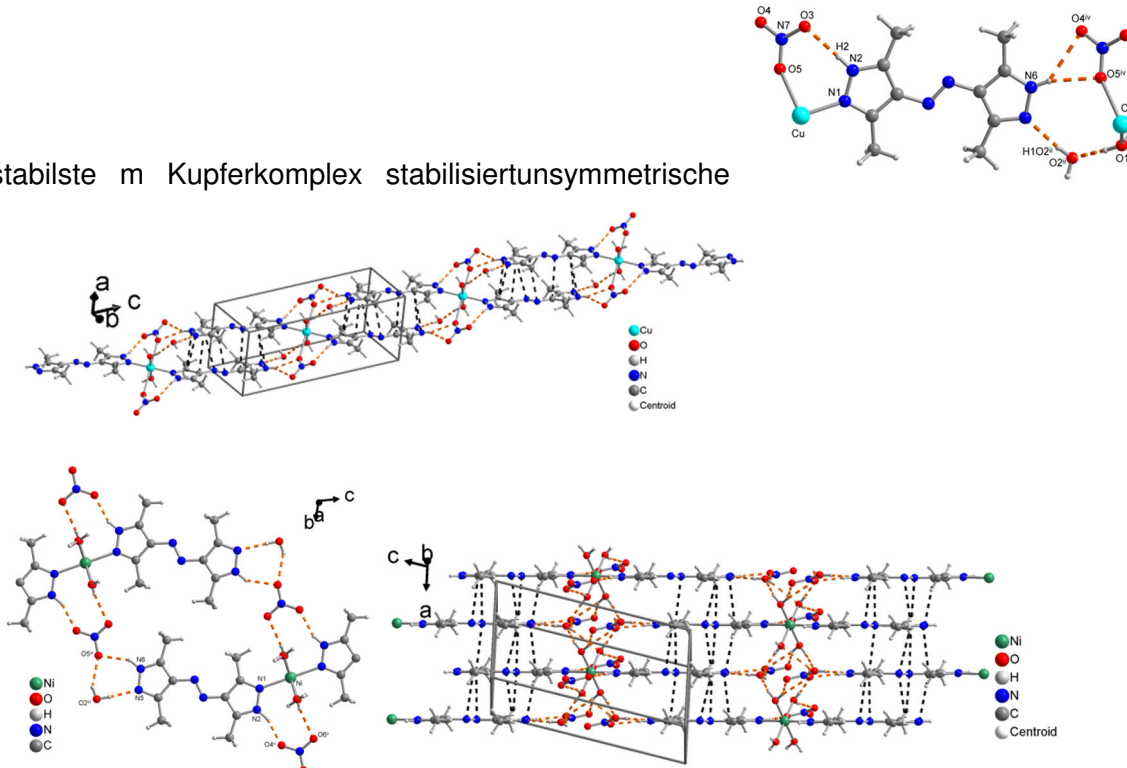


Abbildung 39. Überblick über die Stabilisierung der in $[\text{Cu}(\text{NO}_3)_2(\text{H}_2\text{O})_2(\text{H}_2\text{azbpz})_2]\cdot 2\text{H}_2\text{O}$ und der $[\text{Ni}(\text{H}_2\text{O})_4(\text{H}_2\text{azbpz})_2](\text{NO}_3)_2\cdot 2\text{H}_2\text{O}$ mittels unterschiedlicher Wasserstoffbrückenbindungsringe und die Aggregation der Metallkomplexe mittels Azo-Pyrazol π -Wechselwirkungen in eindimensionale bzw. zweidimensionale supramolekulare Netzwerke.

Das Zusammenspiel von Wasserstoffbrückenbindungen und versetzten dimeren Azo-Pyrazol π -Wechselwirkungen bildet im Kupferkomplex eindimensionale supramolekulare Ketten, welche weitergehend durch ein tetrameres D_{2h} -symmetrisches Wassercluster miteinander verknüpft sind. Die versetzten dimeren Azo-Pyrazol π -Wechselwirkungen sind in der Nickelverbindung auf beiden Seiten des mono-dentat koordinierenden H₂azbpz-Liganden vorhanden, was zu einer zweidimensionalen supramolekularen Schichtstruktur führt (siehe Abbildung 31). Die Integration des Nitrations in Wasserstoffbrückenbindungsringe spielt eine dezidierte Rolle in der Verknüpfung dieser Schichten. Die Unterschiede der Kristallpackungen beider Komplexe wurden weitergehend mit Hirshfeldoberflächen analysiert. Wobei insbesondere der Unterschied zu den relativen Beiträgen der N···C und N···N Wechselwirkungen zu den Hirshfeldoberflächen durch die identifizierten Azo-Pyrazol π -Wechselwirkungen auch quantitativ wiedergespiegelt wurde.

Darüber hinaus wurde H₂azbpz in einer mono-deprotonierten Form als sogenannter Pyrazol-Pyrazolat-Ligand in das zweidimensionale Koordinationspolymer $[\text{Zn}(\text{Hazbpz})\text{NO}_3]\cdot 1.25\text{DMF}$ integriert. Dieses Koordinationspolymer weist eine zweidimensionale **sql-a** Topologie mit dem dinuklearen $\{\text{Zn}_2(\mu-\text{pz})_2(\text{Hpz})_2^{2+}\}$ -Cluster als sekundäre Baueinheit auf (siehe Abbildung 40). Der μ_3 -Verbrückungsmodus von Pyrazolat-Pyrazol-Liganden (hier als Hazbpz⁻) ist

aufgrund den Problemen seines gezielten Einsatzes äußerst selten für Bipyrazol-Liganden anzutreffen, ähnelt jedoch dem Verbrückungsmodus der Pyridylpyrazolate mit einer weiteren NH-Funktion als Interaktionseinheit.

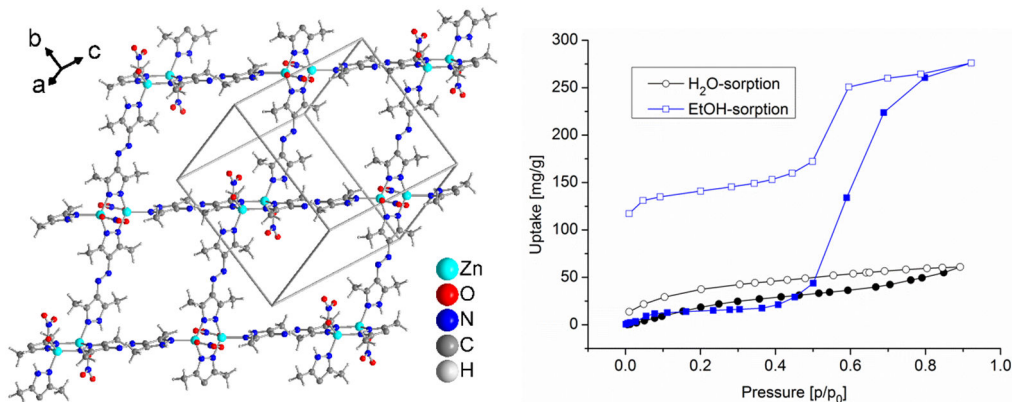


Abbildung 40. Darstellung des zweidimensionalen sql-a Netzwerks in $[Zn(Hazbpz)NO_3] \cdot 1.25DMF$ und das S-förmige Sorptionsprofil der für Ethanol des aktivierte Materials.

Das inkludierte DMF konnte entfernt werden, wobei das Material einen Phasenübergang in eine nicht-poröse Phase vollzog. Das aktivierte Material $[Zn(Hazbpz)NO_3]$ -deg. zeigte sich nicht-porös hinsichtlich der Adsorption von N_2 und CO_2 bei kryogenen Temperaturen. Die Dampfsorption von Ethanol zeigt jedoch ein interessantes S-förmiges Profil mit einer Stufe bei einem relativen Druckbereich von 0,5-0,7 und einer maximalen Aufnahme von 276 mg g^{-1} (siehe Abbildung 40). Dies entspricht der Adsorption von zwei Ethanol-Molekülen pro Formeleinheit. Die Desorptionskurve zeigt eine starke Hysterese mit einer äußerst langsamen Desorption ab einem relativen Druck von ungefähr 0,4 bzw. einer Aufnahme von 140 mg g^{-1} . Dies bedeutet, dass ein Ethanolmolekül desorbiert wird und das Andere bis zu sehr niedrigen relativen Drücken Wasserstoffbrücken-gebunden im Netzwerk verbleibt.

Wie bereits bei den rtl-MOFs beobachtet, scheint die freie NH-Funktionalität von Azopyrazol-Liganden in den aktivierte Materialien in örtlicher Nähe der sekundären Baueinheit eine Flexibilität und stufenförmige Sorptionsisothermen zu begünstigen.

In weiteren Arbeiten wurde der Ligand 2,5-Di(4-pyridyl)thiazolo[5,4-d]thiazole (Dpttz) in ein sogenanntes „coordination polymer with interdigitated structure“ der Zusammensetzung $[Zn(1,3-BDC)Dpttz]$ eingebaut, welches u.a. eine CO_2 -Aufnahme von $138\text{ cm}^3/g$ und eine BET-Oberfläche von $417\text{ m}^2/g$ aufweist (siehe Abbildung 41).

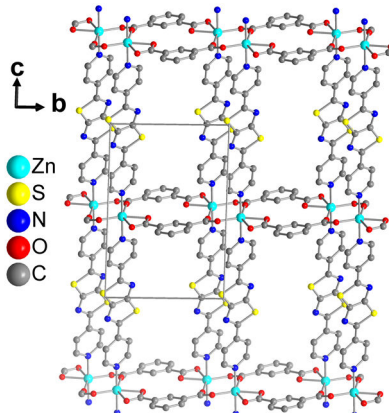


Abbildung 41. Darstellung des zweidimensionalen Koordinationspolymers $[Zn(1,3\text{-BDC})Dpttz]$.

Aufgrund der Schwierigkeit der Etablierung eines geeigneten Syntheseprotokolls für die rtl-M-MOFs und um das „Ligandendesign“-Kriterium des SBL-Ansatzes zu testen, wurde das 1-Methyl substituierte Analogon 5-(4-(1,3,5-Trimethylpyrazolyl)azo)isophthalsäure ($H_2\text{Isa-az-tmpz}$) unter zu rtl-Zn ähnlichen Synthesebedingungen zum **3,6T22-[Zn(Isa-az-tmpz)]**, welches als racemischer Zwilling kristallisiert.

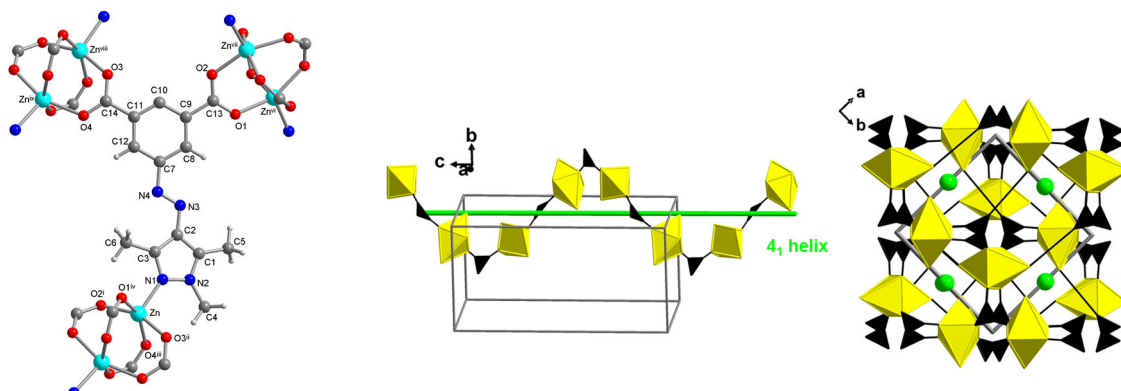


Abbildung 42. Links: Erweiterte asymmetrische Einheit von $3,6T22-[Zn(Isa-az-tmpz)]$. Rechts: Verlauf der 4_1 -Helix entlang der c -Achse mit dem C_2 -symmetrischen Paddle-wheel-Cluster als oktaedrischer 6-c Knoten und dem T-förmigen Liganden $HIsa-az-dmpz^{2-}$ als trigonalem 3-c Knoten als Basis für die $3,6T22$ -Topologie.

Das erhaltene MOF weist die chirale **3,6T22**-Topologie auf Basis eines C_2 -symmetrischen Paddle-Wheel-Clusters als SBU auf, welche weitergehend zu einer 4_1 -Helix assoziiert sind. Diese Topologie kann nicht unter dem SBL-Ansatz verstanden werden. **3,6T22-[Zn(Isa-az-tmpz)]** kann als Startpunkt gesehen werden um mit bifunktionellen Pyrazol-Carboxylatliganden chirale potentiell poröse Netzwerkstrukturen zu erhalten.

Zusammenfassend kann konstatiert werden, dass im Rahmen dieser Arbeit eine Reihe an pyrazolhaltigen Netzwerkstrukturen synthetisiert wurden. Diese Spiegeln in ihrer Vielzahl die Variabilität von Pyrazoleinheiten als versatile Strukturelementen in Liganden wieder. Insbesondere die Kombination der semi-regiden Azogruppe mit Pyrazolen erscheint als Duett für die Synthese weiterer funktionaler Netzwerke vielversprechend.

6. Experimentalteil

Im Folgenden werden die Synthesen der in Abschnitt 4 beschrieben weiteren Ergebnisse dargestellt.

6.1 Verwendete Geräte

Nachfolgend werden die in dieser Dissertation verwendeten Geräte beschrieben.

Schmelzpunktbestimmung

Schmelzpunkte wurden am *Büchi Melting Point, Modell B-540* bestimmt.

Elementaranalyse

Elementaranalysen wurden mit dem *Perkin Elmer CHN 2400 Analyzer* durchgeführt.

Massenspektrometrie

EI-Massenspektren wurden am Finnigan Trace DSQ mit Finnigan Trace GC Ultra und ESI-Massenspektren am *Bruker Daltonics UHR-QTOF maXis 4G* aufgenommen.

Magnetresonanzspektroskopie

^1H - und ^{13}C -Spektren wurden an Bruker Avance III-300 und Bruker Avance III-600 Spektrometern durchgeführt.

Thermogravimetrische Analyse

Die TGAs wurden am *TG 209 F3 Tarsus* in Aluminiumtiegeln unter Stickstoffatmosphäre mit Heizraten zwischen 5-10 K min $^{-1}$ durchgeführt.

Dynamische Differenzkalorimetrie

DSCs wurden an einem *Mettler Toledo DSC 3* mit einem Temperaturgradienten von 5 K min $^{-1}$ bestimmt.

Kugelmahlen

Mechanochemische Experimente wurden ein *Retsch Mixer Mill MM301* bei Raumtemperatur in 25 ml Mahlbehältern aus rostfreiem Stahl bestückt mit einer Metallkugel aus rostfreiem Stahl und einem Durchmesser von 20 mm.

Infrarotspektroskopie

Die infrarotspektroskopischen Messungen wurden an einem Bruker FT-IR TENSOR 37 ausgestattet mit einer ATR- und einer KBr-Einheit bei Raumtemperatur durchgeführt.

Ramanspektroskopie

Ramanspektren wurden an einem *Bruker MultiRAM* ausgestattet mit einem Nd:YAG-Laser (Wellenlänge 1064 nm) durchgeführt.

Überkritische Trocknung

Die Proben wurden über 99 Zyklen mit überkritischem CO₂ mit dem *EM CPD300* der Firma Leica überkritisch getrocknet.

Gasssorption

Gas-Sorptionsmessungen wurden entweder an einem *Micromimetics Asap 2020* oder *Quantachrome Autosorb IQ MP* durchgeführt. Die Proben wurden vor den Messungen im Hochvakuum (10^{-7} mbar) entgast. Messtemperaturen wurden entweder durch Kältebäder (Flüssigstickstoff für 77 K, Trockeneis/Aceton für 195 K, Eisbad für 273 K) oder durch *Quantachrome Cryocooler* sichergestellt.

Hochdrucksorption

Die gravimetrische Hochdruck-CO₂-Adsorptionsisotherme wurde an einem *Rubotherm IsoSORB STATIC* aufgenommen und die Massenänderung wurde mit einer Magnetschwebwaage (Auflösung 0.01 mg ± 0.03 mg) von 0–20 bar vollzogen. Zur Berechnung der Dichte der Gase wurde das Programm FLUIDCAL verwendet.

Dampfsorption

Die Wasser- und Ethanolabsorptionen wurden an einem Quantachrome VSTAR vapor sorption analyzer bei 293 K aufgenommen.

Rasterelektronenmikroskopie

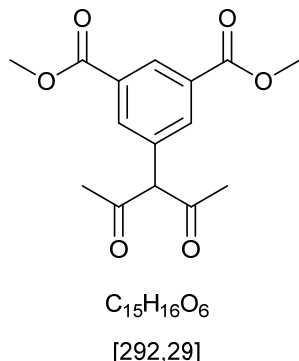
REM Bilder wurden an einem *JEOL JSM-6510* Rasterelektronenmikroskop ausgestattet mit einer LaB₆ Kathode und einem *Bruker Xflash 410 silicon drift detector* bei 5-20 keV aufgenommen.

Röntgen-Pulverdiffraktometrie

Die Röntgen-Pulverdiffraktogramme wurden bei Raumtemperatur auf low-background-Si-sampleholder mit einer Cu-K_α-Quelle am *Bruker D2 Phaser* (300 W, 30 kV, 10 mA) durchgeführt.

6.2 Weitere Synthesen

6.2.1 Synthese des 5-(3-(2,4-Pentandionyl)isophthalsäuredimethylesters



1,50 g 5-Iodoisophthalsäure ($n = 4.7 \text{ mmol}$); 0,0895 g CuI (0,47 mmol, 10 mol%), 0,108 g L-Prolin (0,94 mmol, 20 mol%) und 3,24 g K_2CO_3 (23,5 mmol, 5 Äq.) werden in einem Schlenkkolben sekukiert. Nacheinander werden 25 ml entgastes und über Molsieb gelagertes DMSO, gefolgt von 1,44 ml Acetylaceton hinzugegeben. Nach der Bestückung mit einem sekurierten Rückflusskühler wird für 22 h bei einer Badtemperatur von 90-95 °C erhitzt. Die Reaktionslösung wird mit $\approx 25 \text{ ml}$ 1N HCl auf pH 3 angesäuert und mit 50 ml H_2O versetzt. Die wässrige Phase wird dreimal mit jeweils 50 ml Ethylacetat extrahiert und die vereinigten organischen Phasen werden zweimal mit Wasser und einmal mit einer gesättigten Kochsalzlösung gewaschen (jeweils 30 ml). Nach Trocknen der organischen Phase über Natriumsulfat, wird das Ethylacetat am Rotationsverdampfer abgezogen. Es werden $\approx 1.8 \text{ g}$ eines braunen Öls erhalten. Das Rohprodukt wird säulenchromatografisch aufgereinigt. Dazu wird es mit Dichlormethan auf die Säule aufgetragen. Das Lösungsmittelgemisch wird von Hexan/Ethylacetat 20:1 graduell auf Hexan/Ethylacetat 5:1 verändert. Dabei wurden 430 mg des 5-(3-(2,4-Pentandionyl)isophthalsäuredimethylesters ($R_f = 0.33$) als weißer Feststoff, 70 mg des Eduktes als Öl und 152 mg (0.61 mmol, 13 %) (5-(2-Propanon)isophthalsäuredimethylester als gelber Feststoff erhalten.

Ausbeute: 430 mg (1,48 mmol, 31 %)

¹H-NMR (300 MHz, DMSO-d₆) δ [ppm]: (Enol-Form) 8,45 (*t*, ⁴J_{H,H} = 1,67 Hz, 1H), 8,10 (*d*, ⁴J_{H,H} = 1,63 Hz, 2H), 3,90 (s, 6H), 1,84 (s, 6H); (Keto-Form) 8,42 (*t*, ⁴J_{H,H} = 1,64 Hz, 1H), 8,08 (*d*, ⁴J_{H,H} = 1,60 Hz, 2H), 5,78 (s, 1H), 3,90 (s, 6H), 2,21 (s 6H).

¹³C NMR (75 MHz, DMSO-d₆) δ [ppm]: 165,21/165,17 (C1) 52,54 (C6) (aromatische C's) 137,82/136,16 (C5), 134,72/134,54 (C4), 130,81/130,32 (C3), 128,85/128,75 (C2) (Enol-Form) 190,70 (C11), 69,94 (C9), 30,29 (C7) (Keto-Form) 202,57 (C8), 113,28 (C10), 23,98 (C12).

ESI-MS: [M+H]⁺ 293.1

EA [%] calc. for C₁₅H₁₆O₆ C 61.64, H 5.52, found C 62.20, H 5.48.

5-(2-Propanon)isopthalsäuredimethylester:

¹H-NMR (300 MHz, DMSO-d₆) δ [ppm]: 8,35 (*t*, ⁴J_{H,H} = 1,71 Hz, 1H), 8,02 (*d*, ⁴J_{H,H} = 1,65 Hz, 2H), 4,03 (s, 2H), 3,98 (s, 6H), 2,19 (s, 3H).

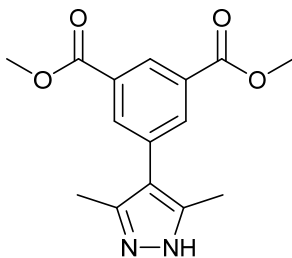
¹³C NMR (75 MHz, DMSO-d₆) δ [ppm]: 205,28 (C8), 165,40 (C1), 136,75 (C5), 135,01 (C4), 130,00 (C3), 127,79 (C2), 52,42 (C7), 48,26 (C6), 29,79 (C9).

¹H-NMR (300 MHz, CDCl₃) δ [ppm]: 8,59 (*t*, ⁴J_{H,H} = 1,56 Hz, 1H), 8,05 (*d*, ⁴J_{H,H} = 1,54 Hz, 2H), 3,94 (s, 6H), 3,83 (s, 2H), 2,22 (s, 3H).

ESI-MS: [M+H]⁺ 251.2

EA [%] calc. for C₁₃H₁₄O₅ C 62.39, H 5.64; found C 61.88, H 5.53.

6.2.2 Synthese des 5-(4-(3,5-Dimethyl-1H-pyrazolyl))isophthalsäuredimethylesters



C₁₅H₁₆N₂O₄

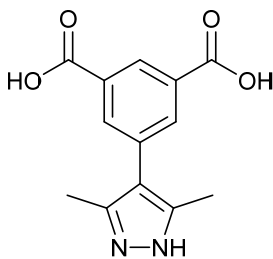
[288,30]

230 mg (0.78 mmol) des Pentandionyls aus 6.2.1 werden in 10 ml Ethanol gelöst vorgelegt. Daraufhin werden 50 µl (1,1 mmol, 1,2 Äq) Hydrazinhydrat werden hinzugefügt. Die Reaktionslösung wird anschließend über Nacht für 17 h bei 90 °C zum Rückfluss erhitzt. Danach wird die Reaktionslösung auf Raumtemperatur abgekühlt und am Rotationsverdampfer auf circa ein Drittel ihres Volumens eingeengt. Nach Zugabe von H₂O fällt das Produkt als weißer Feststoff aus. Die Suspension wird abfiltriert und das Reaktionsprodukt im Vakuumtrockenschrank (45 °C, 10⁻² bar) getrocknet.

Ausbeute: 190 mg (0.65 mmol, 83 %)

¹H-NMR (300 MHz, DMSO-d₆) δ [ppm]: 8,34 (*t*, ⁴J_{H,H} = 1,65 Hz, 1H), 8,04 (*d*, ⁴J_{H,H} = 1,61 Hz, 2H), 3,90 (*s*, 6H), 2,22 (*s*, 6H).

6.2.3 Synthese der 5-(4-(3,5-Dimethyl-1H-pyrazolyl)isophthalsäure



C₁₃H₁₂N₂O₄

[260,25]

In einen Kolben wurden 190 mg (0,65 mmol) des 5-(4-(3,5-Dimethyl-1H-pyrazolyl)-isophthalsäuredimethylesters gelöst in 5 ml Methanol vorgelegt. 1,0 g (25 Äq, 18 mmol) KOH wurden in 10 ml DI-H₂O gelöst und in den Kolben gegeben. Die Reaktionslösung wurde bei 90 °C Badtemperatur über Nacht zum Rückfluss erhitzt. Anschließend wurde das Methanol am Rotationsverdampfer abgezogen. Die Lösung wird mit 3N HCl auf pH 3 angesäuert, worauf ein weißer Feststoff ausfällt. Die Suspension wurde filtriert und der erhaltene weiße Feststoff im Vakuumtrockenschrank (10⁻² bar 50 °C) getrocknet.

Ausbeute: 162 mg (0.56 mmol, 87 %)

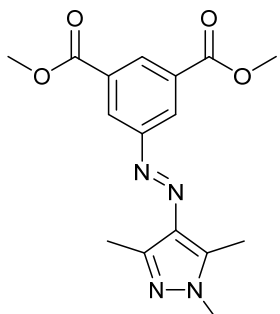
¹H-NMR (300 MHz, DMSO-d₆) δ [ppm]: 8,36 (*t*, ⁴J_{H,H} = 1,67 Hz, 1H), 8,03 (*d*, ⁴J_{H,H} = 1,63 Hz, 2H), 2,22 (*s*, 6H).

¹³C NMR (75 MHz, DMSO-d₆) δ [ppm]: 166,78 (C1), 140,94 (C7), 135,03 (C5), 133,15 (C4), 131,73 (C3), 127,39 (C2), 115,47 (C6), 11,48 (C8).

ESI-MS: [M+H]⁺ 260.25

EA [%] calc. for C₁₃H₁₂N₂O₄ C 60.00, H 4.65, N 10.76 found C 60.08, H 4.57, N 11.13

6.2.4 Synthese des 5-(4-(1,3,5-Trimethyl-1H-pyrazolyl)azo)isophthalsäuredimethylesters



C₁₆H₁₈N₂O₄

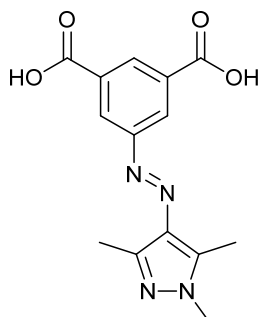
[330,34]

0.701 g (2.19 mmol) des Hydrazons Me₃Isa-az-acac werden in einem 200 ml Einhalskolben in 70 ml absolutem Ethanol gelöst. Nach Zugabe von 115 µl Methylhydrazin (1 Äq., 2,19 mmol) wird für 6 h refluxiert. Die gelbe Lösung wird auf ein Drittel ihres Volumens aufkonzentriert. Durch Zugabe von entionisiertem Wasser kann Me₃Isa-az-tmpz als gelber Feststoff ausgefällt werden. Trocknen im Vakuumtrockenofen(10⁻²bar, 70 °C) ergibt Me₃Isa-az-tmpz was unaufgereinigt weiter umgesetzt wurde.

Ausbeute: 688 mg (2.15 mmol, 98%)

¹H-NMR (300 MHz, CDCl₃) δ [ppm]: 8,66 (t, ⁴J_{H,H} = 1,66 Hz, 1H), 8,56 (d, ⁴J_{H,H} = 1,66 Hz, 2H), 3,98 (s, 6H), 3,79 (s, 3H), 2,60 (s, 3H), 2,50 (s, 3H).

6.2.5 Synthese der 5-(4-(1,3,5-Trimethyl-1H-pyrazolyl)azo)isophthalsäure



$C_{16}H_{18}N_2O_4$

[330,34]

0.572 g von Me₂Isa-az-tmpz aus 6.2.4 (1.82 mol) werden in einem Gemisch 30 ml Methanol, 10 ml H₂O und 3,1 g Kaliumhydroxyd über Nacht refluxiert. Nach Abkühlen der Reaktionslösung auf Raumtemperatur wird das Methanol am Rotationsverdampfer entfernt. Die Lösung wird mit 3N HCl auf pH 3 angesäuert, worauf ein kanariengelber Feststoff ausfällt. Dieser wird abfiltriert, ausgiebig mit H₂O gewaschen und im Vakuumtrockenschrank (10⁻² bar, 50 °C) getrocknet.

Ausbeute: 378 mg (1,25 mmol, 69 %)

¹H-NMR (300 MHz, DMSO-d₆) δ [ppm]: 8,47 (*t*, ⁴*J*_{H,H} = 1,77 Hz, 1H), 8,39 (*d*, ⁴*J*_{H,H} = 1,76 Hz, 2H), 3,75 (s, 3H), 2,57 (s, 3H), 2,38 (s, 3H).

¹³C NMR (75 MHz, DMSO-d₆) δ [ppm]: 166,20, 153,00, 140,77, 140,40, 134,46, 132,31, 129,96, 125,48, 35,92, 13,77, 9,50.

ESI-MS: [M+H]⁺ 331.4

EA [%] calc. for C₁₆H₁₈N₂O₄ C 55.63, H 4.67, N 18.53 found C 55.66, H 4.71, N 18.59

Literaturverzeichnis

1. Fischer, R. A.; Schwedler, I., Terminologie von Metall-organischen Gerüstverbindungen und Koordinationspolymeren (IUPAC-Empfehlungen 2013). *Angewandte Chemie* **2014**, 126 (27), 7209-7214.
2. Batten, S. R.; Champness, N. R.; Chen, X. M.; Garcia-Martinez, J.; Kitagawa, S.; Ohrstrom, L.; O'Keeffe, M.; Suh, M. P.; Reedijk, J., Terminology of metal-organic frameworks and coordination polymers (IUPAC Recommendations 2013). *Pure Appl Chem* **2013**, 85 (8), 1715-1724.
3. Allison, S. A.; Barrer, R. M., Sorption in the β -phases of transition metal(II) tetra-(4-methylpyridine) thiocyanates and related compounds. *J. Chem. Soc. A* **1969**, 0 (0), 1717-1723.
4. Hoskins, B. F.; Robson, R., Infinite polymeric frameworks consisting of three dimensionally linked rod-like segments. *Journal of the American Chemical Society* **1989**, 111 (15), 5962-5964.
5. Hoskins, B. F.; Robson, R., Design and construction of a new class of scaffolding-like materials comprising infinite polymeric frameworks of 3D-linked molecular rods. A reappraisal of the zinc cyanide and cadmium cyanide structures and the synthesis and structure of the diamond-related frameworks $[N(CH_3)_4][Cu_2Zn_2(CN)_4]$ and $Cu_2[4,4',4'',4''''-tetracyanotetraphenylmethane]BF_4 \cdot xC_6H_5NO_2$. *Journal of the American Chemical Society* **1990**, 112 (4), 1546-1554.
6. Powell, H. M.; Rayner, J. H., Clathrate Compound Formed by Benzene with an Ammonia–Nickel Cyanide Complex. *Nature* **1949**, 163, 566.
7. Hofmann, K. A.; Höchtlen, F., Abnorme Verbindungen des Nickels. *Berichte der deutschen chemischen Gesellschaft* **1903**, 36 (1), 1149-1151.
8. Hofmann, K. A.; Arnoldi, H., Auffällige Unterschiede homologer cyclischer Moleküle im Verhalten gegen Nickelcyanürammoniak. *Berichte der deutschen chemischen Gesellschaft* **1906**, 39 (1), 339-344.
9. Buser, H. J.; Schwarzenbach, D.; Petter, W.; Ludi, A., The crystal structure of Prussian Blue: $Fe_4[Fe(CN)_6]_3 \cdot xH_2O$. *Inorg Chem* **1977**, 16 (11), 2704-2710.
10. Woodward, J., IV. Præparatio cærulei prussiaci ex germaniâ missa ad Johannem Woodward, M. D. Prof. Med. Gresh. R. S. S. *Philosophical Transactions of the Royal Society of London* **1724**, 33 (381), 15-17.

11. Bartoll, J.; Jackisch, B.; Most, M.; Wenders de Calisse, E.; Vogtherr, C. M., Early Prussian Blue-Blue and green pigments in the paintings by Watteau, Lancret and Pater in the collection of Frederick II of Prussia. *Techne* **2007**, 25, 39-46.
12. Kinoshita, Y.; Matsubara, I.; Higuchi, T.; Saito, Y., The Crystal Structure of Bis(adiponitrilo)copper(I) Nitrate. *Bulletin of the Chemical Society of Japan* **1959**, 32 (11), 1221-1226.
13. Rayner, J. H.; Powell, H. M., 67. Structure of molecular compounds. Part X. Crystal structure of the compound of benzene with an ammonia-nickel cyanide complex. *Journal of the Chemical Society (Resumed)* **1952**, 319-328.
14. Eddaoudi, M.; Moler, D. B.; Li, H.; Chen, B.; Reineke, T. M.; O'Keeffe, M.; Yaghi, O. M., Modular Chemistry: Secondary Building Units as a Basis for the Design of Highly Porous and Robust Metal–Organic Carboxylate Frameworks. *Accounts of Chemical Research* **2001**, 34 (4), 319-330.
15. Yaghi, O. M.; Kalmutzki, M. J.; Diercks, C. S., *Introduction to Reticular Chemistry: Metal-Organic Frameworks and Covalent Organic Frameworks*. Wiley-VCH Verlag GmbH & Co. KGaA: Weinheim, 2019.
16. Rungtaweevoranit, B.; Diercks, C. S.; Kalmutzki, M. J.; Yaghi, Omar M., Spiers Memorial Lecture: Progress and prospects of reticular chemistry. *Faraday Discussions* **2017**, 201 (0), 9-45.
17. Diercks, C. S.; Yaghi, O. M., The atom, the molecule, and the covalent organic framework. *Science* **2017**, 355 (6328), eaal1585.
18. Zhang, J.-P.; Zhang, Y.-B.; Lin, J.-B.; Chen, X.-M., Metal Azolate Frameworks: From Crystal Engineering to Functional Materials. *Chemical Reviews* **2012**, 112 (2), 1001-1033.
19. Morris, R. E., Modular materials from zeolite-like building blocks. *Journal of Materials Chemistry* **2005**, 15 (9), 931-938.
20. Li, H.; Eddaoudi, M.; O'Keeffe, M.; Yaghi, O. M., Design and synthesis of an exceptionally stable and highly porous metal-organic framework. *Nature* **1999**, 402 (6759), 276-279.
21. Chui, S. S. Y.; Lo, S. M. F.; Charmant, J. P. H.; Orpen, A. G.; Williams, I. D., A Chemically Functionalizable Nanoporous Material [Cu₃(TMA)₂(H_nO)₃]_n. *Science* **1999**, 283 (5405), 1148.

22. Férey, G.; Mellot-Draznieks, C.; Serre, C.; Millange, F.; Dutour, J.; Surblé, S.; Margiolaki, I., A Chromium Terephthalate-Based Solid with Unusually Large Pore Volumes and Surface Area. *Science* **2005**, *309* (5743), 2040.
23. O'Keeffe, M.; Peskov, M. A.; Ramsden, S. J.; Yaghi, O. M., The Reticular Chemistry Structure Resource (RCSR) Database of, and Symbols for, Crystal Nets. *Accounts of Chemical Research* **2008**, *41* (12), 1782-1789.
24. Koyama, H.; Saito, Y., The Crystal Structure of Zinc Oxyacetate, Zn₄O(CH₃COO)₆. *Bulletin of the Chemical Society of Japan* **1954**, *27* (2), 112-114.
25. van Niekerk, J. N.; Schoening, F. R. L., A new type of copper complex as found in the crystal structure of cupric acetate, Cu₂(CH₃COO)₄.2H₂O. *Acta Crystallographica* **1953**, *6* (3), 227-232.
26. Chang, S. C.; Jeffrey, G. A., The crystal structure of a basic chromium acetate compound, [OCr₃(CH₃COO)₆.3H₂O]⁺Cl⁻.6H₂O, having feeble paramagnetism. *Acta Crystallographica Section B* **1970**, *26* (6), 673-683.
27. Cychosz, K. A.; Thommes, M., Progress in the Physisorption Characterization of Nanoporous Gas Storage Materials. *Engineering* **2018**, *4* (4), 559-566.
28. Riedel, E.; Janiak, C., Kapitel 2 Die chemische Bindung. In *Anorganische Chemie*, De Gruyter: 2010.
29. Yaghi, O. M., Kalmutzki, M. J., Diercks, C. S, Topology. In *Introduction to Reticular Chemistry*, O. M. Yaghi, M. J. K., C. S. Diercks, Ed. 2019; pp 429-452.
30. Delgado-Friedrichs, O.; O'Keeffe, M.; Yaghi, O. M., Three-periodic nets and tilings: edge-transitive binodal structures. *Acta Crystallogr A* **2006**, *62*, 350-355.
31. Delgado-Friedrichs, O.; O'Keeffe, M.; Yaghi, O. M., Taxonomy of periodic nets and the design of materials. *Phys Chem Chem Phys* **2007**, *9* (9), 1035-43.
32. Alexandrov, E. V.; Blatov, V. A.; Kochetkov, A. V.; Proserpio, D. M., Underlying nets in three-periodic coordination polymers: topology, taxonomy and prediction from a computer-aided analysis of the Cambridge Structural Database. *Crystengcomm* **2011**, *13* (12), 3947-3958.
33. Bonneau, C.; O'Keeffe, M.; Proserpio, D. M.; Blatov, V. A.; Batten, S. R.; Bourne, S. A.; Lah, M. S.; Eon, J.-G.; Hyde, S. T.; Wiggin, S. B.; Öhrström, L., Deconstruction of Crystalline Networks into Underlying Nets: Relevance for Terminology Guidelines and Crystallographic Databases. *Cryst Growth Des* **2018**, *18* (6), 3411-3418.
34. Ohrstrom, L., Designing, Describing and Disseminating New Materials by using the Network Topology Approach. *Chemistry* **2016**, *22* (39), 13758-13763.

35. Wells, A. F., *Structural Inorganic Chemistry*. 5th ed.; Oxford University Press: Oxford, 1984.
36. Wells, A. F., *Three-dimensional Nets and Polyhedra*. Wiley: New York, 1977.
37. Wells, A. F., *Further Studies of Three-dimensional Nets*. American Crystallographic Association: 1979.
38. Smith, J. V., Topochemistry of zeolites and related materials. 1. Topology and geometry. *Chemical Reviews* **1988**, *88* (1), 149-182.
39. O'Keeffe, M., *Z. Kristallogr.* **1991**, *196*, 21.
40. M. O'Keefe; B.G. Hyde, Plane nets in crystal chemistry. *Philos. Trans. Royal Soc. A* **1980**, *295* (1417), 553-618.
41. König, H., Eine kubische Eismodifikation. In *Zeitschrift für Kristallographie - Crystalline Materials*, 1943; Vol. 105, p 279.
42. Hoffmann, R.; Kabanov, A. A.; Golov, A. A.; Proserpio, D. M., Homo Citans and Carbon Allotropes: For an Ethics of Citation. *Angewandte Chemie International Edition* **2016**, *55* (37), 10962-10976.
43. Cairns, A. J.; Perman, J. A.; Wojtas, L.; Kravtsov, V. C.; Alkordi, M. H.; Eddaoudi, M.; Zaworotko, M. J., Supermolecular Building Blocks (SBBs) and Crystal Design: 12-Connected Open Frameworks Based on a Molecular Cubohemioctahedron. *Journal of the American Chemical Society* **2008**, *130* (5), 1560-1561.
44. Guillerm, V.; Kim, D.; Eubank, J. F.; Luebke, R.; Liu, X.; Adil, K.; Lah, M. S.; Eddaoudi, M., A supermolecular building approach for the design and construction of metal-organic frameworks. *Chemical Society Reviews* **2014**, *43* (16), 6141-6172.
45. Perry Iv, J. J.; Perman, J. A.; Zaworotko, M. J., Design and synthesis of metal-organic frameworks using metal-organic polyhedra as supermolecular building blocks. *Chemical Society Reviews* **2009**, *38* (5), 1400-1417.
46. Vardhan, H.; Yusubov, M.; Verpoort, F., Self-assembled metal-organic polyhedra: An overview of various applications. *Coordination Chemistry Reviews* **2016**, *306*, 171-194.
47. Eddaoudi, M.; Sava, D. F.; Eubank, J. F.; Adil, K.; Guillerm, V., Zeolite-like metal-organic frameworks (ZMOFs): design, synthesis, and properties. *Chemical Society Reviews* **2015**, *44* (1), 228-249.
48. Eubank, J. F.; Wojtas, L.; Hight, M. R.; Bousquet, T.; Kravtsov, V. C.; Eddaoudi, M., The Next Chapter in MOF Pillaring Strategies: Trigonal Heterofunctional Ligands To

- Access Targeted High-Connected Three Dimensional Nets, Isoreticular Platforms. *Journal of the American Chemical Society* **2011**, *133* (44), 17532-17535.
49. Xiang, S. L.; Huang, J.; Li, L.; Zhang, J. Y.; Jiang, L.; Kuang, X. J.; Su, C. Y., Nanotubular Metal-Organic Frameworks with High Porosity Based on T-Shaped Pyridyl Dicarboxylate Ligands. *Inorg Chem* **2011**, *50* (5), 1743-1748.
50. Zhang, S.-M.; Chang, Z.; Hu, T.-L.; Bu, X.-H., New Three-Dimensional Porous Metal Organic Framework with Tetrazole Functionalized Aromatic Carboxylic Acid: Synthesis, Structure, and Gas Adsorption Properties. *Inorg Chem* **2010**, *49* (24), 11581-11586.
51. Wang, S.; Wei, Z.-W.; Zhang, J.; Jiang, L.; Liu, D.; Jiang, J.-J.; Si, R.; Su, C.-Y., Framework disorder and its effect on selective hysteretic sorption of a T-shaped azole-based metal-organic framework. *IUCrJ* **2019**, *6* (1), 85-95.
52. Chen, Z. J.; Adil, K.; Weselinski, L. J.; Belmabkhout, Y.; Eddaoudi, M., A supermolecular building layer approach for gas separation and storage applications: the eea and rtl MOF platforms for CO₂ capture and hydrocarbon separation. *Journal of Materials Chemistry A* **2015**, *3* (12), 6276-6281.
53. Hu, T. L.; Wang, H.; Li, B.; Krishna, R.; Wu, H.; Zhou, W.; Zhao, Y.; Han, Y.; Wang, X.; Zhu, W.; Yao, Z.; Xiang, S.; Chen, B., Microporous metal-organic framework with dual functionalities for highly efficient removal of acetylene from ethylene/acetylene mixtures. *Nat Commun* **2015**, *6*, 7328.
54. Férey, G., Building Units Design and Scale Chemistry. *Journal of Solid State Chemistry* **2000**, *152* (1), 37-48.
55. Jansen, M.; Schön, J. C., “Design” in Chemical Synthesis—An Illusion? *Angewandte Chemie International Edition* **2006**, *45* (21), 3406-3412.
56. Férey, G., Hybrid porous solids: past, present, future. *Chemical Society Reviews* **2008**, *37* (1), 191-214.
57. Goesten, M. G.; Kapteijn, F.; Gascon, J., Fascinating chemistry or frustrating unpredictability: observations in crystal engineering of metal–organic frameworks. *Crystengcomm* **2013**, *15* (45), 9249-9257.
58. Moulton, B.; Zaworotko, M. J., From Molecules to Crystal Engineering: Supramolecular Isomerism and Polymorphism in Network Solids. *Chemical Reviews* **2001**, *101* (6), 1629-1658.

59. Kirchon, A.; Feng, L.; Drake, H. F.; Joseph, E. A.; Zhou, H.-C., From fundamentals to applications: a toolbox for robust and multifunctional MOF materials. *Chemical Society Reviews* **2018**, *47* (23), 8611-8638.
60. Liao, P.-Q.; He, C.-T.; Zhou, D.-D.; Zhang, J.-P.; Chen, X.-M., Porous Metal Azolate Frameworks. In *The Chemistry of Metal–Organic Frameworks*, Wiley-VCH Verlag GmbH & Co. KGaA: 2016; pp 309-343.
61. Pettinari, C.; Tăbăcaru, A.; Galli, S., Coordination polymers and metal–organic frameworks based on poly(pyrazole)-containing ligands. *Coordination Chemistry Reviews* **2016**, *307*, Part 1, 1-31.
62. Hou, L.; Lin, Y.-Y.; Chen, X.-M., Porous Metal–Organic Framework Based on μ 4-oxo Tetrazinc Clusters: Sorption and Guest-Dependent Luminescent Properties. *Inorg Chem* **2008**, *47* (4), 1346-1351.
63. Tonigold, M.; Lu, Y.; Bredenkötter, B.; Rieger, B.; Bahnmüller, S.; Hitzbleck, J.; Langstein, G.; Volkmer, D., Heterogeneous Catalytic Oxidation by MFU-1: A Cobalt(II)-Containing Metal–Organic Framework. *Angewandte Chemie International Edition* **2009**, *48* (41), 7546-7550.
64. He, C.-T.; Tian, J.-Y.; Liu, S.-Y.; Ouyang, G.; Zhang, J.-P.; Chen, X.-M., A porous coordination framework for highly sensitive and selective solid-phase microextraction of non-polar volatile organic compounds. *Chemical Science* **2013**, *4* (1), 351-356.
65. Tonigold, M.; Lu, Y.; Mavrandonakis, A.; Puls, A.; Staudt, R.; Möllmer, J.; Sauer, J.; Volkmer, D., Pyrazolate-Based Cobalt(II)-Containing Metal–Organic Frameworks in Heterogeneous Catalytic Oxidation Reactions: Elucidating the Role of Entatic States for Biomimetic Oxidation Processes. *Chemistry – A European Journal* **2011**, *17* (31), 8671-8695.
66. Gao, W.-Y.; Cai, R.; Pham, T.; Forrest, K. A.; Hogan, A.; Nugent, P.; Williams, K.; Wojtas, L.; Luebke, R.; Weseliński, Ł. J.; Zaworotko, M. J.; Space, B.; Chen, Y.-S.; Eddaoudi, M.; Shi, X.; Ma, S., Remote Stabilization of Copper Paddlewheel Based Molecular Building Blocks in Metal–Organic Frameworks. *Chemistry of Materials* **2015**, *27* (6), 2144-2151.
67. Gao, W.-Y.; Pham, T.; Forrest, K. A.; Space, B.; Wojtas, L.; Chen, Y.-S.; Ma, S., The local electric field favours more than exposed nitrogen atoms on CO₂ capture: a case study on the rht-type MOF platform. *Chem Commun* **2015**, *51* (47), 9636-9639.
68. Farha, O. K.; Eryazici, I.; Jeong, N. C.; Hauser, B. G.; Wilmer, C. E.; Sarjeant, A. A.; Snurr, R. Q.; Nguyen, S. T.; Yazaydin, A. Ö.; Hupp, J. T., Metal–Organic Framework

- Materials with Ultrahigh Surface Areas: Is the Sky the Limit? *Journal of the American Chemical Society* **2012**, *134* (36), 15016-15021.
69. Quartapelle Procopio, E.; Fukushima, T.; Barea, E.; Navarro, J. A. R.; Horike, S.; Kitagawa, S., A Soft Copper(II) Porous Coordination Polymer with Unprecedented Aqua Bridge and Selective Adsorption Properties. *Chemistry – A European Journal* **2012**, *18* (41), 13117-13125.
70. Wang, J.; Yao, S.; Li, G.; Huo, Q.; Zhang, L.; Liu, Y., A novel trinuclear Cd(ii) cluster-based metal-organic framework: synthesis, structure and luminescence properties. *RSC Advances* **2015**, *5* (124), 102525-102529.
71. Trickett, C. A.; Helal, A.; Al-Maythalony, B. A.; Yamani, Z. H.; Cordova, K. E.; Yaghi, O. M., The chemistry of metal–organic frameworks for CO₂ capture, regeneration and conversion. *Nature Reviews Materials* **2017**, *2*, 17045.
72. Li, J. R.; Sculley, J.; Zhou, H. C., Metal-Organic Frameworks for Separations. *Chemical Reviews* **2012**, *112* (2), 869-932.
73. Kitagawa, S.; Kondo, M., Functional Micropore Chemistry of Crystalline Metal Complex-Assembled Compounds. *Bulletin of the Chemical Society of Japan* **1998**, *71* (8), 1739-1753.
74. Kitagawa, S.; Kitaura, R.; Noro, S.-i., Functional Porous Coordination Polymers. *Angewandte Chemie International Edition* **2004**, *43* (18), 2334-2375.
75. Horike, S.; Shimomura, S.; Kitagawa, S., Soft porous crystals. *Nat Chem* **2009**, *1* (9), 695-704.
76. Zhang, J. P.; Zhou, H. L.; Zhou, D. D.; Liao, P. Q.; Kitagawa, S., 7.17 - Dynamic Behavior of Porous Coordination Polymers. In *Comprehensive Supramolecular Chemistry II*, Atwood, J. L., Ed. Elsevier: Oxford, 2017; pp 425-474.
77. Schneemann, A.; Bon, V.; Schwedler, I.; Senkovska, I.; Kaskel, S.; Fischer, R. A., Flexible Metal-Organic Frameworks. *Chem. Soc. Rev.* **2014**, *43*, 6062-6096.
78. Thommes, M.; Kaneko, K.; Neimark, A. V.; Olivier, J. P.; Rodriguez-Reinoso, F.; Rouquerol, J.; Sing, K. S. W., Physisorption of Gases, with Special Reference to the Evaluation of Surface Area and Pore Size Distribution (IUPAC Technical Report). *Pure Appl. Chem.* **2015**, *87*, 1051-1069.
79. Sing, K. S. W.; Everett, D. H.; Haul, R. A. W.; Moscou, L.; Pierotti, R. A.; Rouquerol, J.; Siemieniewska, T., Reporting Physisorption Data for Gas Solid Systems with Special Reference to the Determination of Surface-Area and Porosity (Recommendations 1984). *Pure Appl. Chem.* **1985**, *57*, 603-619.

80. Yang, Q.-Y.; Lama, P.; Sen, S.; Lusi, M.; Chen, K.-J.; Gao, W.-Y.; Shivanna, M.; Pham, T.; Hosono, N.; Kusaka, S.; Perry IV, J. J.; Ma, S.; Space, B.; Barbour, L. J.; Kitagawa, S.; Zaworotko, M. J., Reversible Switching between Highly Porous and Nonporous Phases of an Interpenetrated Diamondoid Coordination Network That Exhibits Gate-Opening at Methane Storage Pressures. *Angew. Chem. Int. Ed.* **2018**, *57*, 5684-5689.
81. Horike, S.; Tanaka, D.; Nakagawa, K.; Kitagawa, S., Selective Guest Sorption in an Interdigitated Porous Framework with Hydrophobic Pore Surfaces. *Chem. Commun.* **2007**, 3395-3397.
82. Fukushima, T.; Horike, S.; Inubushi, Y.; Nakagawa, K.; Kubota, Y.; Takata, M.; Kitagawa, S., Solid Solutions of Soft Porous Coordination Polymers: Fine-Tuning of Gas Adsorption Properties. *Angew. Chem.* **2010**, *122*, 4930-4934.
83. Hijikata, Y.; Horike, S.; Sugimoto, M.; Sato, H.; Matsuda, R.; Kitagawa, S., Relationship between Channel and Sorption Properties in Coordination Polymers with Interdigitated Structures. *Chem. Eur. J.* **2011**, *17*, 5138-5144.
84. Li, L.; Krishna, R.; Wang, Y.; Yang, J.; Wang, X.; Li, J., Exploiting the Gate Opening Effect in a Flexible MOF for Selective Adsorption of Propyne From C1/C2/C3 Hydrocarbons. *J. Mater. Chem. A* **2016**, *4*, 751-755.
85. Li, D.; Kaneko, K., Hydrogen Bond-Regulated Microporous Nature of Copper Complex-Assembled Microcrystals. *Chem. Phys. Lett.* **2001**, *335*, 50-56.
86. Kondo, A.; Noguchi, H.; Ohnishi, S.; Kajiro, H.; Tohdoh, A.; Hattori, Y.; Xu, W.-C.; Tanaka, H.; Kanoh, H.; Kaneko, K., Novel Expansion/Shrinkage Modulation of 2D Layered MOF Triggered by Clathrate Formation with CO₂ Molecules. *Nano Lett.* **2006**, *6*, 2581-2584.
87. McGuirk, C. M.; Runčevski, T.; Oktawiec, J.; Turkiewicz, A.; Taylor, M. K.; Long, J. R., Influence of Metal Substitution on the Pressure-Induced Phase Change in Flexible Zeolitic Imidazolate Frameworks. *J. Am. Chem. Soc.* **2018**, *140*, 15924-15933.
88. Hastürk, E.; Ernst, S.-J.; Janiak, C., Recent Advances in Adsorption Heat Transformation Focusing on the Development of Adsorbent Materials. *Curr. Opin. Chem. Engin.* **2019**, *24*, 26-36.
89. Canivet, J.; Fateeva, A.; Guo, Y.; Coasne, B.; Farrusseng, D., Water Adsorption in MOFs: Fundamentals and Applications. *Chem. Soc. Rev.* **2014**, *43*, 5594-5617.
90. Buttersack, C., Modeling of Type IV and V Sigmoidal Adsorption Isotherms. *Phys. Chem. Chem. Phys.* **2019**, *21*, 5614-5626.

91. McDonald, T. M.; Mason, J. A.; Kong, X.; Bloch, E. D.; Gygi, D.; Dani, A.; Crocellà, V.; Giordanino, F.; Odoh, S. O.; Drisdell, W. S.; Vlaisavljevich, B.; Dzubak, A. L.; Poloni, R.; Schnell, S. K.; Planas, N.; Lee, K.; Pascal, T.; Wan, L. F.; Prendergast, D.; Neaton, J. B.; Smit, B.; Kortright, J. B.; Gagliardi, L.; Bordiga, S.; Reimer, J. A.; Long, J. R., Cooperative Insertion of CO₂ in Diamine-Appended Metal-Organic Frameworks. *Nature* **2015**, *519*, 303-308.
92. Klein, N.; Hoffmann, H. C.; Cadiau, A.; Getzschmann, J.; Lohe, M. R.; Paasch, S.; Heydenreich, T.; Adil, K.; Senkovska, I.; Brunner, E.; Kaskel, S., Structural Flexibility and Intrinsic Dynamics in the M₂(2,6-ndc)₂(dabco) (M = Ni, Cu, Co, Zn) Metal-Organic Frameworks. *J. Mater. Chem.* **2012**, *22*, 10303-10312.
93. Mason, J. A.; Oktawiec, J.; Taylor, M. K.; Hudson, M. R.; Rodriguez, J.; Bachman, J. E.; Gonzalez, M. I.; Cervellino, A.; Guagliardi, A.; Brown, C. M.; Llewellyn, P. L.; Masciocchi, N.; Long, J. R., Methane Storage in Flexible Metal-Organic Frameworks with Intrinsic Thermal Management. *Nature* **2015**, *527*, 357-361.
94. Zhu, A.-X.; Yang, Q.-Y.; Kumar, A.; Crowley, C.; Mukherjee, S.; Chen, K.-J.; Wang, S.-Q.; O'Nolan, D.; Shivanna, M.; Zaworotko, M. J., Coordination Network That Reversibly Switches between Two Nonporous Polymorphs and a High Surface Area Porous Phase. *J. Am. Chem. Soc.* **2018**, *140*, 15572-15576.
95. Choi, H. J.; Dincă, M.; Long, J. R., Broadly Hysteretic H₂ Adsorption in the Microporous Metal-Organic Framework Co(1,4-benzenedipyrazolate). *J. Am. Chem. Soc.* **2008**, *130*, 7848-7850.
96. Desiraju, G. R., *Crystal Engineering. The Design of Organic Solids*. Elsevier: Amsterdam, 1989.
97. Desiraju, G. R., Crystal Engineering: Solid State Supramolecular Synthesis. *Curr. Opin. Solid State Mater. Sci.* **1997**, *2*, 451-454.
98. Desiraju, G. R., Crystal Engineering: A Holistic View. *Angew. Chem. Int. Ed.* **2007**, *46*, 8342-8356.
99. Desiraju, G. R., Crystal Engineering: From Molecule to Crystal. *J. Am. Chem. Soc.* **2013**, *135*, 9952-9967.
100. Lehn, J.-M., Supramolekulare Chemie – Moleküle, Übermoleküle und molekulare Funktionseinheiten (Nobel-Vortrag). *Angew. Chem.* **1988**, *100*, 91-116.
101. Dunitz, J. D., Phase Transitions in Molecular Crystals from a Chemical Viewpoint. *Pure Appl. Chem.* 1991; *63*, 177.

102. Reddy, D. S.; Craig, D. C.; Desiraju, G. R., Supramolecular Synthons in Crystal Engineering. 4. Structure Simplification and Synthon Interchangeability in Some Organic Diamondoid Solids¹. *J. Am. Chem. Soc.* **1996**, *118*, 4090-4093.
103. Aakeröy, C. B.; Seddon, K. R., The Hydrogen Bond and Crystal Engineering. *Chem. Soc. Rev.* **1993**, *22*, 397-407.
104. Desiraju, G. R., Reflections on the Hydrogen Bond in Crystal Engineering. *Cryst. Growth Des.* **2011**, *11*, 896-898.
105. Wang, L.-C.; Zheng, Q.-Y., Hydrogen Bonding in Supramolecular Crystal Engineering. In *Hydrogen Bonded Supramolecular Structures*, Li, Z.-T.; Wu, L.-Z., (Eds.) Springer, Heidelberg, 2015; 69-113.
106. Arunan, E.; Desiraju, G. R.; Klein, R. A.; Sadlej, J.; Scheiner, S.; Alkorta, I.; Clary, D. C.; Crabtree, R. H.; Dannenberg, J. J.; Hobza, P.; Kjaergaard, H. G.; Legon, A. C.; Mennucci, B.; Nesbitt, D. J., Defining the Hydrogen Bond: An Account (IUPAC Technical Report). *Pure Appl. Chem.* **2011**, *83*, 1619-1636.
107. Desiraju, G. R., Die Wasserstoffbrücke – eine aktualisierte Definition. *Angew. Chem.* **2011**, *123*, 52-60.
108. Etter, M. C.; MacDonald, J. C.; Bernstein, J., Graph-Set Analysis of Hydrogen-Bond Patterns in Organic Crystals. *Acta Cryst. B* **1990**, *46*, 256-262.
109. Etter, M. C., Encoding and Decoding Hydrogen-Bond Patterns of Organic Compounds. *Acc. Chem. Res.* **1990**, *23*, 120-126.
110. Etter, M. C., Hydrogen Bonds as Design Elements in Organic Chemistry. *J. Phys. Chem.* **1991**, *95*, 4601-4610.
111. Ivasenko, O.; Perepichka, D. F., Mastering Fundamentals of Supramolecular Design with Carboxylic Acids. Common lessons from X-Ray Crystallography and Scanning Tunneling Microscopy. *Chem. Soc. Rev.* **2011**, *40*, 191-206.
112. Boldog, I.; Rusanov, E. B.; Sieler, J.; Domasevitch, K. V., Cooperative Association of Pyrazoles and Phenols: A Versatile Binary System. *New J. Chem.* **2004**, *28*, 756-759.
113. Aguilar-Parrilla, F.; Scherer, G.; Limbach, H. H.; Foces-Foces, M. d. I. C.; Hernandez Cano, F.; Smith, J. A. S.; Toiron, C.; Elguero, J., Observation of a Series of Degenerate Cyclic Double, Triple, and Quadruple Proton Transfers in Solid Pyrazoles. *J. Am. Chem. Soc.* **1992**, *114*, 9657-9659.
114. Boldog, I.; Rusanov, E. B.; Sieler, J.; Blaurock, S.; Domasevitch, K. V., Construction of Extended Networks with a Trimeric Pyrazole Synthon. *Chem. Commun.* **2003**, 740-741.

115. Haghiri, A.; Lerner, H.-W.; Wagner, M.; Bats, J. W., 3-Phenylpyrazole, a Pseudosymmetric Structure with $Z' = 6$. *Acta Cryst. E* **2002**, *58*, o1378-o1380.
116. Boldog, I.; Rusanov, E. B.; Chernega, A. N.; Sieler, J.; Domasevitch, K. V., Acentric Extended Solids by Self Assembly of 4,4'-Bipyrazolyls. *Angewandte Chemie International Edition* **2001**, *40* (18), 3435-3438.
117. Maspero, A.; Galli, S.; Masciocchi, N.; Palmisano, G., Facile Preparation of Polytopic Azoles: Synthesis, Characterization, and X-ray Powder Diffraction Studies of 1,4-Bis(pyrazol-4-yl)- and 1,4-Bis(tetrazol-5-yl)benzene. *Chem. Lett.* **2008**, *37*, 956-957.
118. Klein, O.; Aguilar-Parrilla, F.; Lopez, J. M.; Jagerovic, N.; Elguero, J.; Limbach, H.-H., Dynamic NMR Study of the Mechanisms of Double, Triple, and Quadruple Proton and Deuteron Transfer in Cyclic Hydrogen Bonded Solids of Pyrazole Derivatives. *J. Am. Chem. Soc.* **2004**, *126*, 11718-11732.
119. Basu, T.; Sparkes, H. A.; Mondal, R., Construction of Extended Molecular Networks with Heterosynthons in Cocrystals of Pyrazole and Acids. *Cryst. Growth. Des.* **2009**, *9*, 5164-5175.
120. Benetollo, F.; Del Pra, A., Structure of 1H-Indazole-3-carboxylic acid. *Acta Cryst. C* **1993**, *49*, 779-781.
121. Bryant, M. R.; Burrows, A. D.; Fitchett, C. M.; Hawes, C. S.; Hunter, S. O.; Keenan, L. L.; Kelly, D. J.; Kruger, P. E.; Mahon, M. F.; Richardson, C., The Synthesis and Characterisation of Coordination and Hydrogen-Bonded Networks based on 4-(3,5-dimethyl-1H-pyrazol-4-yl)benzoic acid. *Dalton Trans.* **2015**, *44*, 9269-9280.
122. Brown, C., The Crystal Structure of Fumaric Acid. *Acta Cryst.* **1966**, *21*, 1-5.
123. Bailey, M.; Brown, C. J., The Crystal Structure of Terephthalic Acid. *Acta Cryst.* **1967**, *22*, 387-391.
124. Bednowitz, A. L.; Post, B., Direct Determination of the Crystal Structure of [beta]-Fumaric Acid. *Acta Cryst.* **1966**, *21*, 566-571.
125. Gillon, A. L.; Feeder, N.; Davey, R. J.; Storey, R., Hydration in Molecular Crystals – A Cambridge Structural Database Analysis. *Cryst. Growth Des.* **2003**, *3*, 663-673.
126. Varughese, S.; Desiraju, G. R., Using Water as a Design Element in Crystal Engineering. Host–Guest Compounds of Hydrated 3,5-Dihydroxybenzoic Acid. *Cryst. Growth Des.* **2010**, *10*, 4184-4196.
127. Kirchner, M. T.; Boese, R.; Billups, W. E.; Norman, L. R., Gas Hydrate Single-Crystal Structure Analyses. *J. Am. Chem. Soc.* **2004**, *126*, 9407-9412.

128. Lakshminarayanan, P. S.; Suresh, E.; Ghosh, P., Formation of an Infinite 2D-Layered Water of $(\text{H}_2\text{O})_{45}$ Cluster in a Cryptand–Water Supramolecular Complex: A Template Effect. *J. Am. Chem. Soc.* **2005**, *127*, 13132-13133.
129. Clarke, H. D.; Arora, K. K.; Wojtas, Ł.; Zaworotko, M. J., Polymorphism in Multiple Component Crystals: Forms III and IV of Gallic Acid Monohydrate. *Cryst. Growth Des.* **2011**, *11*, 964-966.
130. Clarke, H. D.; Arora, K. K.; Bass, H.; Kavuru, P.; Ong, T. T.; Pujari, T.; Wojtas, Ł.; Zaworotko, M. J., Structure–Stability Relationships in Cocrystal Hydrates: Does the Promiscuity of Water Make Crystalline Hydrates the Nemesis of Crystal Engineering? *Cryst. Growth Des.* **2010**, *10*, 2152-2167.
131. McCrone, W., In Physics and Chemistry of the Organic Solid State; Fox, D.; Labes, MM; Weissberger, A., Eds. *Wiley Interscience: New York* **1965**, *2*, 725-767.
132. Mitscherlich, E., Sur la Relation qui Existe entre la Forme Cristalline et les Proportions Chimiques. *Ann. Chim. Phys.* **1822**, *19*, 350-419.
133. Mitscherlich, E. In *Sur la rapport qui existe entre les proportions chimiques et la forme cristalline. 3. Mémoire sur les Corps qui Affectent Deux Formes Cristallines Differentes*, Annales de Chimie et de Physique, 1823; 264.
134. Wöhler; Liebig, Untersuchungen über das Radikal der Benzoesäure. *Annalen der Pharmacie* **1832**, *3*, 249-282.
135. David, W. I. F.; Shankland, K.; Pulham, C. R.; Blagden, N.; Davey, R. J.; Song, M., Polymorphism in Benzamide. *Angew. Chem. Int. Ed.* **2005**, *44*, 7032-7035.
136. Lee, E. H., A Practical Guide to Pharmaceutical Polymorph Screening & Selection. *Asian J. Pharm.* **2014**, *9*, 163-175.
137. Bauer, J.; Spanton, S.; Henry, R.; Quick, J.; Dziki, W.; Porter, W.; Morris, J., Ritonavir: An Extraordinary Example of Conformational Polymorphism. *Pharm. Res.* **2001**, *18*, 859-866.
138. Cruz-Cabeza, A. J.; Bernstein, J., Conformational Polymorphism. *Chem. Rev.* **2014**, *114*, 2170-2191.
139. Moss, G. P., Basic Terminology of Stereochemistry (IUPAC Recommendations 1996). *Pure Appl. Chem.* **1996**, *68*, 2193-2222.
140. Yu, L., Polymorphism in Molecular Solids: An Extraordinary System of Red, Orange, and Yellow Crystals. *Acc. Chem. Res.* **2010**, *43*, 1257-1266.

141. Surov, A. O.; Manin, A. N.; Voronin, A. P.; Churakov, A. V.; Perlovich, G. L.; Vener, M. V., Weak Interactions Cause Packing Polymorphism in Pharmaceutical Two-Component Crystals. The Case Study of the Salicylamide Cocrystal. *Cryst. Growth Des.* **2017**, *17*, 1425-1437.
142. Park, Y.; Boerrigter, S. X. M.; Yeon, J.; Lee, S. H.; Kang, S. K.; Lee, E. H., New Metastable Packing Polymorph of Donepezil Grown on Stable Polymorph Substrates. *Cryst. Growth Des.* **2016**, *16*, 2552-2560.
143. Leiserowitz, L., Molecular packing modes. Carboxylic acids. *Acta Crystallogr. B* **1976**, *32*, 775-802.
144. Śledź, M.; Janczak, J.; Kubiak, R., New Crystalline Modification of Terephthalic Acid. *J. Mol. Struct.* **2001**, *595*, 77-82.
145. Basu, T.; Mondal, R., Construction of First Anion-Assisted Helix Inside a Helix Network. *CrystEngComm* **2010**, *12*, 366-369.
146. Millan, S.; Gil-Hernández, B.; Milles, E.; Gökpınar, S.; Makhloufi, G.; Schmitz, A.; Schlüsener, C.; Janiak, C., rtl-M-MOFs ($M = Cu, Zn$) with a T-shaped Bifunctional Pyrazole-Isophthalate Ligand showing Flexibility and S-Shaped Type F-IV Sorption Isotherms with High Saturation Uptakes for $M = Cu$. *Dalton Trans.* **2019**, *48*, 8057-8067.
147. Spek, A., Single-crystal Structure Validation with the Program PLATON. *J. Appl. Crystallogr.* **2003**, *36*, 7-13.
148. Macrae, C. F.; Bruno, I. J.; Chisholm, J. A.; Edgington, P. R.; McCabe, P.; Pidcock, E.; Rodriguez-Monge, L.; Taylor, R.; van de Streek, J.; Wood, P. A., Mercury CSD 2.0 - New Features for the Visualization and Investigation of Crystal Structures. *J. Appl. Crystallogr.* **2008**, *41*, 466-470.
149. Cotton, F. A.; DeBoer, B. G.; LaPrade, M. D.; Pipal, J. R.; Ucko, D. A., The Crystal and Molecular Structures of Dichromium Tetraacetate Dihydrate and Dirhodium Tetraacetate Dihydrate. *Acta Cryst. B* **1971**, *27*, 1664-1671.
150. Cotton, F. A.; Rice, C. E.; Rice, G. W., Crystal and Molecular-Structure of Anhydrous Tetraacetatodichromium. *J. Am. Chem. Soc.* **1977**, *99*, 4704-4707.
151. Blatov, V. A.; Shevchenko, A. P.; Proserpio, D. M., Applied Topological Analysis of Crystal Structures with the Program Package ToposPro. *Cryst. Growth Des.* **2014**, *14*, 3576-3586.
152. Liu, Q.-K.; Ma, J.-P.; Dong, Y.-B., Reversible Adsorption and Separation of Aromatics on Cd^{II}-Triazole Single Crystals. *Chem. Eur. J.* **2009**, *15*, 10364-10368.

153. Liu, Q.-K.; Ma, J.-P.; Dong, Y.-B., Adsorption and Separation of Reactive Aromatic Isomers and Generation and Stabilization of Their Radicals within Cadmium(II)-Triazole Metal–Organic Confined Space in a Single-Crystal-to-Single-Crystal Fashion. *J. Am. Chem. Soc.* **2010**, *132*, 7005-7017.
154. Liu, Q.-K.; Ma, J.-P.; Dong, Y.-B., Reversible Adsorption and Complete Separation of Volatile Chlorocarbons Based on a Cd(II)-triazole MOF in a Single-Crystal-to-Single-Crystal Fashion. *Chem. Commun.* **2011**, *47*, 12343-12345.
155. Liu, Q.-K.; Ma, J.-P.; Dong, Y.-B., Highly Efficient Iodine Species Enriching and Guest-Driven Tunable Luminescent Properties Based on a Cadmium(II)-Triazole MOF. *Chem. Commun.* **2011**, *47*, 7185-7187.
156. Wang, X.-L.; Dong, L.-Z.; Qiao, M.; Tang, Y.-J.; Liu, J.; Li, Y.; Li, S.-L.; Su, J.-X.; Lan, Y.-Q., Exploring the Performance Improvement of the Oxygen Evolution Reaction in a Stable Bimetal–Organic Framework System. *Angew. Chem. Int. Ed.* **2018**, *57*, 9660-9664.
157. Liu, B.-H.; Liu, D.-X.; Yang, K.-Q.; Dong, S.-J.; Li, W.; Wang, Y.-J., A New Cluster-Based Metal-Organic Framework with Triazine Backbones for Selective Luminescent Detection of Mercury(II) Ion. *Inorg. Chem. Commun.* **2018**, *90*, 61-64.
158. He, C.; Guo, S.; Huang, L.; Lei, A., Copper Catalyzed Arylation/C–C Bond Activation: An Approach toward α -Aryl Ketones. *J. Am. Chem. Soc.* **2010**, *132*, 8273-8275.
159. Sado, G. Synthese neuer bifunktioneller Liganden und deren Einsatz in der Herstellung Metall-Organischer Gerüstverbindungen. Heinrich-Heine-Universität Düsseldorf, 2017.
160. Zhang, Y.; Maverick, A. W., Preparation of an Isocyano- β -diketone via its Metal Complexes, by Use of Metal Ions as Protecting Groups. *Inorg. Chem.* **2009**, *48*, 10512-10518.
161. Carmichael, J. W.; Steinrauf, L. K.; Belford, R. L., Bis (3-phenyl-2,4-pentanedionato) Copper. I. Molecular and Crystal Structure. *J. Chem. Phys.* **1965**, *43*, 3959-3966.
162. Chen, B.; Fronczek, F. R.; Maverick, A. W., Solvent-Dependent 4^4 Square Grid and $6^4\cdot8^2$ NbO Frameworks Formed by Cu(Pyac)₂ (bis[3-(4-pyridyl)pentane-2,4-dionato]copper(II)). *Chem. Commun.* **2003**, 2166-2167.
163. Chen, B.; Fronczek, F. R.; Maverick, A. W., 3-(4-Cyanophenyl)pentane-2,4-dione and its Copper(II) Complex. *Acta Cryst. C* **2004**, *60*, m147-m149.

164. Chen, B.; Fronczek, F. R.; Maverick, A. W., Porous Cu–Cd Mixed-Metal–Organic Frameworks Constructed from Cu(Pyac)₂ {Bis[3-(4-pyridyl)pentane-2,4-dionato]copper(II)}. *Inorg. Chem.* **2004**, *43*, 8209-8211.
165. Pariya, C.; Sparrow, C. R.; Back, C.-K.; Sandí, G.; Fronczek, F. R.; Maverick, A. W., Copper β -Diketonate Molecular Squares and Their Host–Guest Reactions. *Angew. Chem. Int. Ed.* **2007**, *46*, 6305-6308.
166. Pariya, C.; Fronczek, F. R.; Maverick, A. W., Bis(o-phenylenebis(acetylacetonato))dicopper(II): A Strained Copper(II) Dimer Exhibiting a Wide Range of Colors in the Solid State. *Inorg. Chem.* **2011**, *50*, 2748-2753.
167. Cherutoi, J. K.; Sandifer, J. D.; Pokharel, U. R.; Fronczek, F. R.; Pakhomova, S.; Maverick, A. W., Externally and Internally Functionalized Copper(II) β -Diketonate Molecular Squares. *Inorg. Chem.* **2015**, *54*, 7791-7802.
168. Aakeröy, C. B.; Sinha, A. S.; Chopade, P. D.; Desper, J., Halogen Bonding or Close Packing? Examining the Structural Landscape in a Series of Cu(II)-acac Complexes. *Dalton Trans.* **2011**, *40*, 12160-12168.
169. Sun, X.; Yao, S.; Li, G.; Zhang, L.; Huo, Q.; Liu, Y., A Flexible Doubly Interpenetrated Metal–Organic Framework with Breathing Behavior and Tunable Gate Opening Effect by Introducing Co²⁺ into Zn₄O Clusters. *Inorg. Chem.* **2017**, *56*, 6645-6651.
170. Zaworotko, M.; Zhu, A.-X.; Yang, Q.; Mukherjee, S.; Kumar, A.; Deng, C.; Bezrukov, A.; Shivanna, M., Tuning the Gate-Opening Pressure in a Switching pcu Coordination Network, X-pcu-5-Zn, by Pillar-Ligand Substitution. *Angew. Chem. Int. Ed.* **2019**, *58*, 18212-18217.
171. Jin, J.; Zhao, X.; Feng, P.; Bu, X., A Cooperative Pillar–Template Strategy as a Generalized Synthetic Method for Flexible Homochiral Porous Frameworks. *Angew. Chem. Int. Ed.* **2018**, *57*, 3737-3741.
172. Shimomura, S.; Higuchi, M.; Matsuda, R.; Yoneda, K.; Hijikata, Y.; Kubota, Y.; Mita, Y.; Kim, J.; Takata, M.; Kitagawa, S., Selective Sorption of Oxygen and Nitric Oxide by an Electron-Donating Flexible Porous Coordination Polymer. *Nat Chem* **2010**, *2*, 633.
173. Seo, J.; Bonneau, C.; Matsuda, R.; Takata, M.; Kitagawa, S., Soft Secondary Building Unit: Dynamic Bond Rearrangement on Multinuclear Core of Porous Coordination Polymers in Gas Media. *J. Am. Chem. Soc.* **2011**, *133*, 9005-13.

Publikationsliste

Millan, S.; Nasir, J; Gil-Hernández, B; Knedel, T.-O.; Moll, B.; Boldog, I; Weingart, O; Schmedt auf der Günne, J.; Janiak, C., Solid-State Landscape of 4,4'-Azobis(3,5-dimethyl-1H-pyrazole) with the isolation of conformer-dependent polymorphs. *Cryst. Growth Des.*, **2020**, submitted.

Liang, J., Nuhnen, A.; Millan, S.; Breitzke, H.; Gvilava, V.; Buntkowsky, G.; Janiak, C., Encapsulation of a Porous Organic Cage into the Pores of a Metal-Organic Framework for Enhanced CO₂ separation. *Angew. Chem. Int. Ed.* **2020**, accepted
doi:10.1002/anie.201916002.

Matemb Ma Ntep, T.; Breitzke, H.; Schmolke, L.; Schlüsener, C.; Moll, B.; Millan, S.; Tannert, N.; El Aita, I.; Buntkowsky, G.; Janiak, C., Facile in Situ Halogen Functionalization via Triple-Bond Hydrohalogenation: Enhancing Sorption Capacities through Halogenation to Halofumarate-Based Zr(IV)-Metal-Organic Frameworks. *Chem. Mater.* **2019**, *31*, 8629-8638.

Millan, S.; Gil-Hernández, B.; Milles, E.; Gökpınar, S.; Makhloufi, G.; Schmitz, A.; Schlüsener, C.; Janiak, C., rtl-M-MOFs (M = Cu, Zn) with a T-shaped bifunctional pyrazole-isophthalate ligand showing flexibility and S-shaped Type F-IV sorption isotherms with high saturation uptakes for M = Cu. *Dalton Trans.* **2019**, *48*, 8057-8067. (featured on the *front cover*)

Millan, S.; Makhloufi, G.; Janiak, C., Metal-4,4'-azobis(3,5-dimethyl-1H-pyrazole) Complexes with Seven- and Nine-membered Hydrogen-bonded Rings Originating from the Pyrrolic NH Function. *Z. anorg. Allg. Chem.* **2019**, *645*, 893-899.

Nuhnen, A.; Dietrich, D.; Millan, S.; Janiak, C., Role of Filler Porosity and Filler/Polymer Interface Volume in Metal–Organic Framework/Polymer Mixed-Matrix Membranes for Gas Separation. *ACS Appl. Mater. Interfaces* **2018**, *10*, 33589-33600.

Millan, S.; Gil-Hernández, B.; Hastürk, E.; Schmitz, A.; Janiak, C., A 2D Zinc Coordination Polymer Built from the Mono-deprotonated 4,4'-Azobis(3,5-dimethyl-1H-pyrazole) Ligand. *Z. anorg. Allg. Chem.* **2018**, *644*, 1311-1316.

Goldman, A.; Nardin, K.; Höfert, S.-P.; Millan, S.; Janiak, C., Two-dimensional Cobalt-Carboxylate Framework with Hourglass Trinuclear $\text{Co}_3(\text{COO})_6(\text{DMA})_3$ Secondary Building Unit. *Z. anorg. Allg. Chem.* **2018**, *644* (22), 1387-1392.

Millan, S.; Makhloifi, G.; Janiak, C., Incorporating the Thiazolo[5,4-d]thiazole Unit into a Coordination Polymer with Interdigitated Structure. *Crystals* **2018**, *8*, 30.

Fischer, J.; Millan, S.; Ritter, H., N,N'-(Hexane-1,6-diyl)bis(4-methyl-N-(oxiran-2-ylmethyl)benzenesulfonamide): Synthesis via cyclodextrin mediated N-alkylation in aqueous solution and further Prilezhaev epoxidation. *Beilstein J. Org. Chem.* **2013**, *9*, 2834-40.

Spektrenanhang

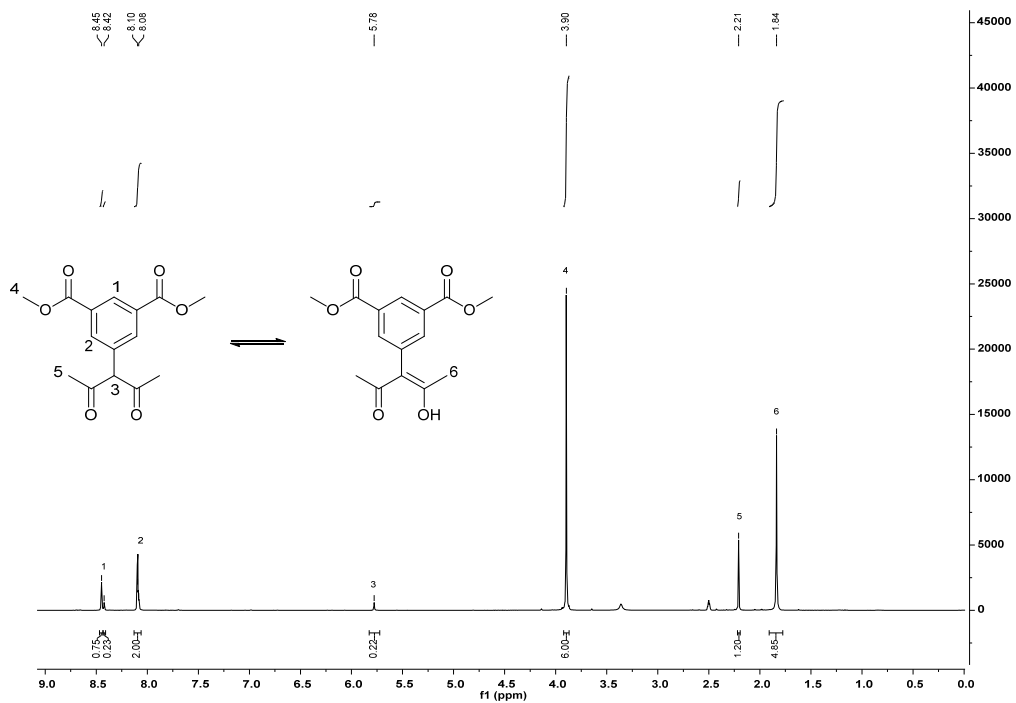


Abbildung S1. ^1H -NMR-Spektrum von 5-(1-Acetyl-2-hydroxypropenyl)-isophthalsäuredimethylester in DMSO-d_6 .

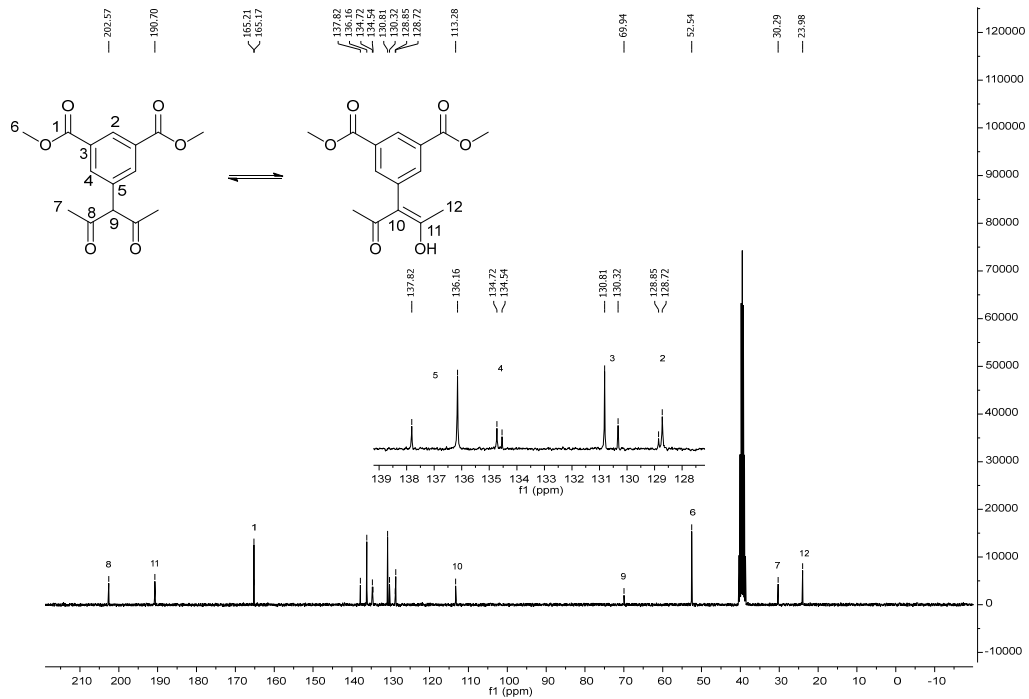


Abbildung S2. ^{13}C -Spektrum von 5-(1-Acetyl-2-hydroxypropenyl)-isophthalsäuredimethylester in DMSO-d_6 .

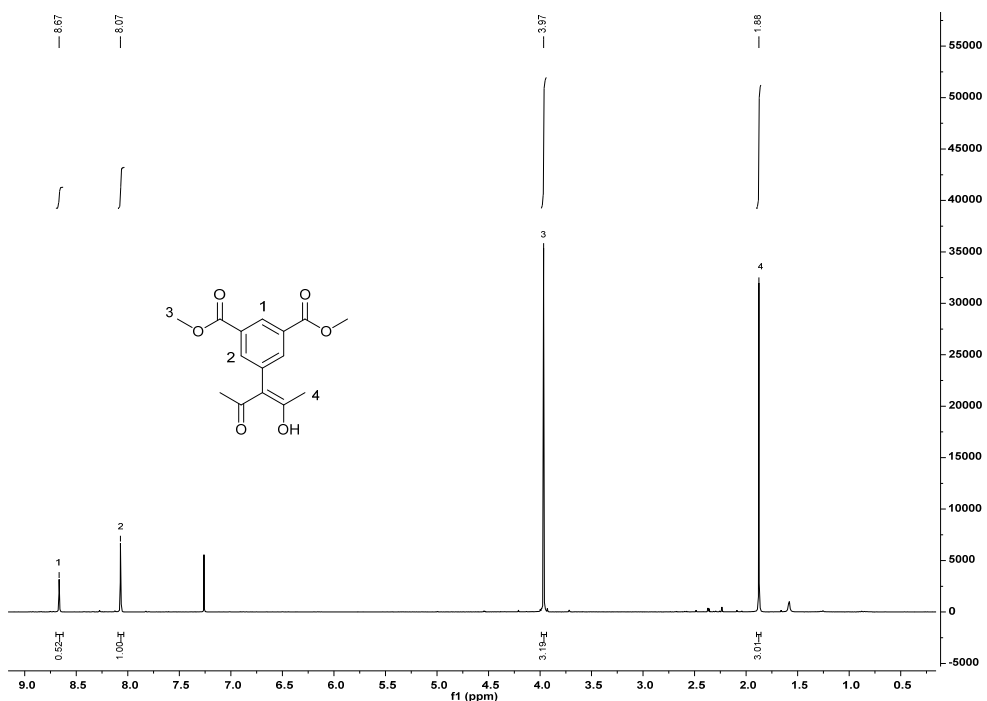


Abbildung S3. ^1H -NMR-Spektrum von 5-(1-Acetyl-2-hydroxypropenyl)isophthalsäure-dimethylester in CDCl_3 .

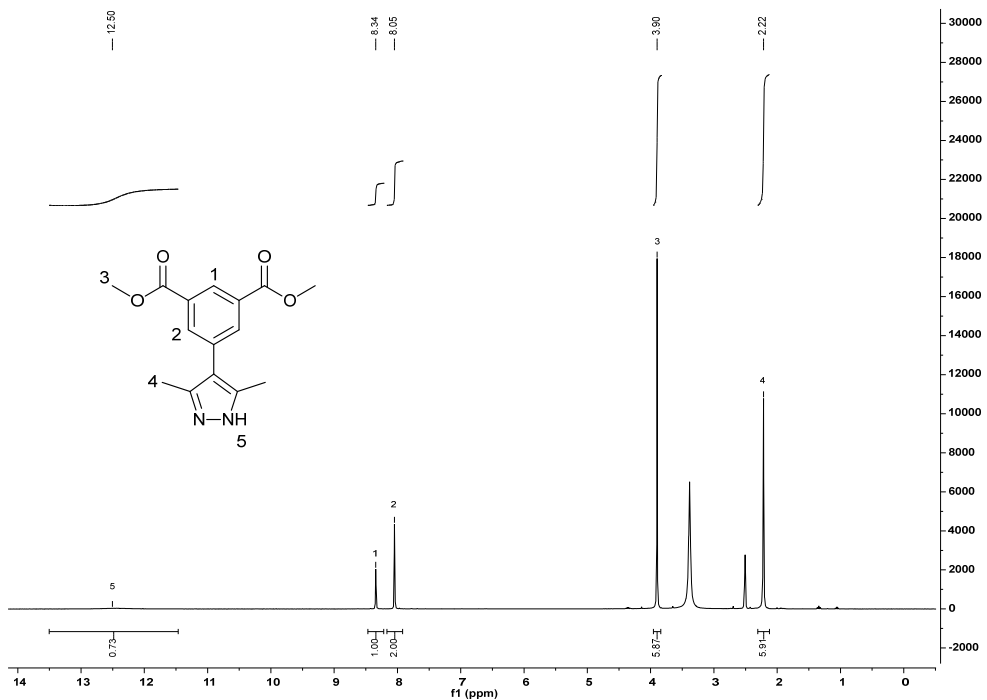


Abbildung S4. ^1H -NMR-Spektrum des 5-(3,5-Dimethyl-1*H*-pyrazol-4-yl)isophthalatsäuredimethylesters in DMSO-d_6 .

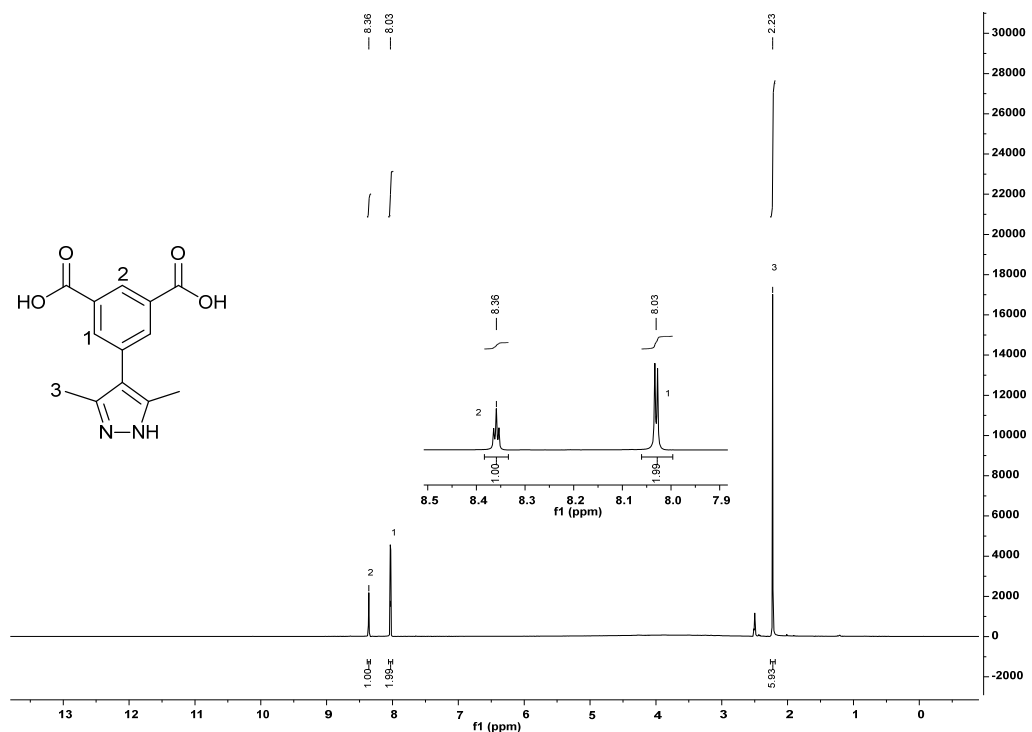


Abbildung S5. ¹H-NMR-Spektrum von 5-(3,5-Dimethyl-1*H*-pyrazol-4-yl)isophthalsäure (H₃Ilsa-dmpz) in DMSO-d₆.

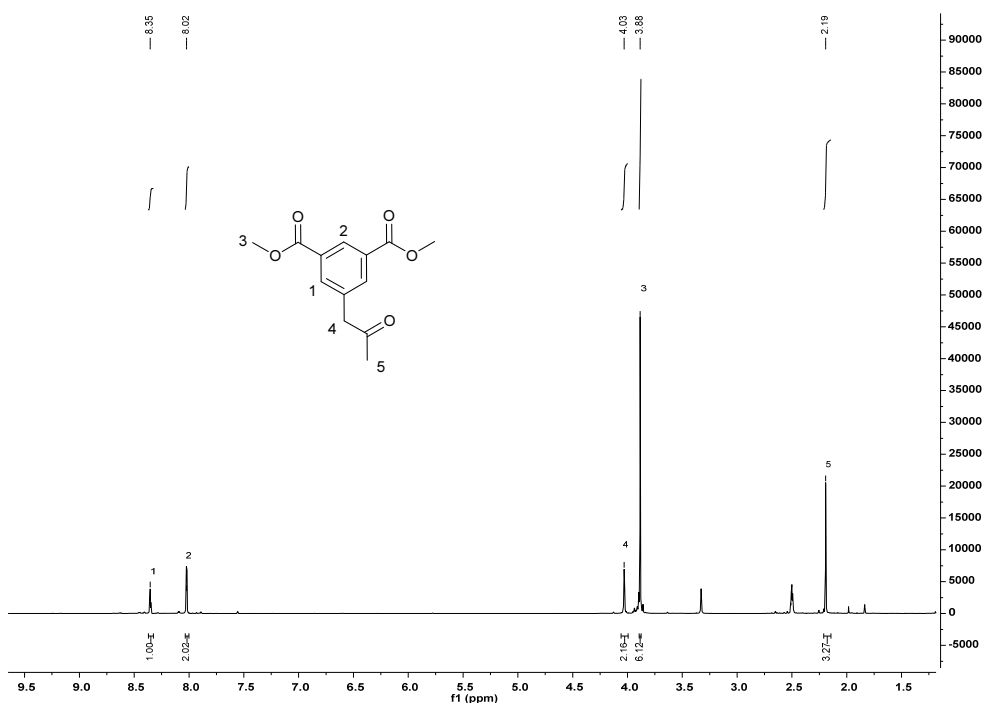


Abbildung S6. ¹H-NMR-Spektrum von 5-(2-oxopropyl)isophthalsäuredimethylester in DMSO-d₆.

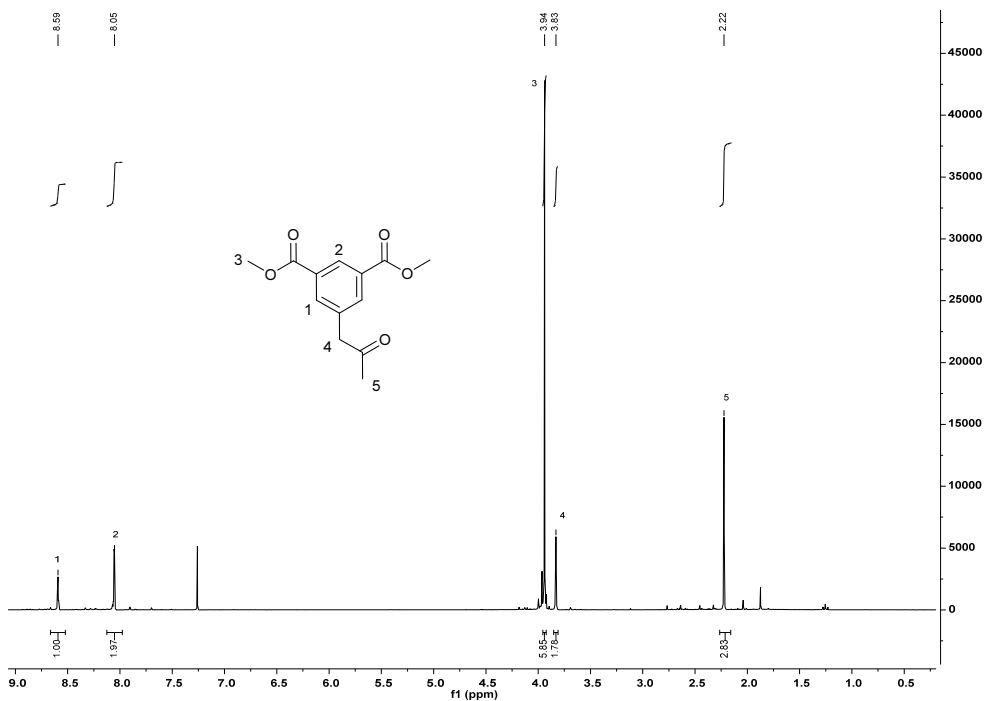


Abbildung S7. ^1H -NMR-Spektrum von 5-(2-Oxopropyl)isophthalsäuredimethylester in CDCl_3 .

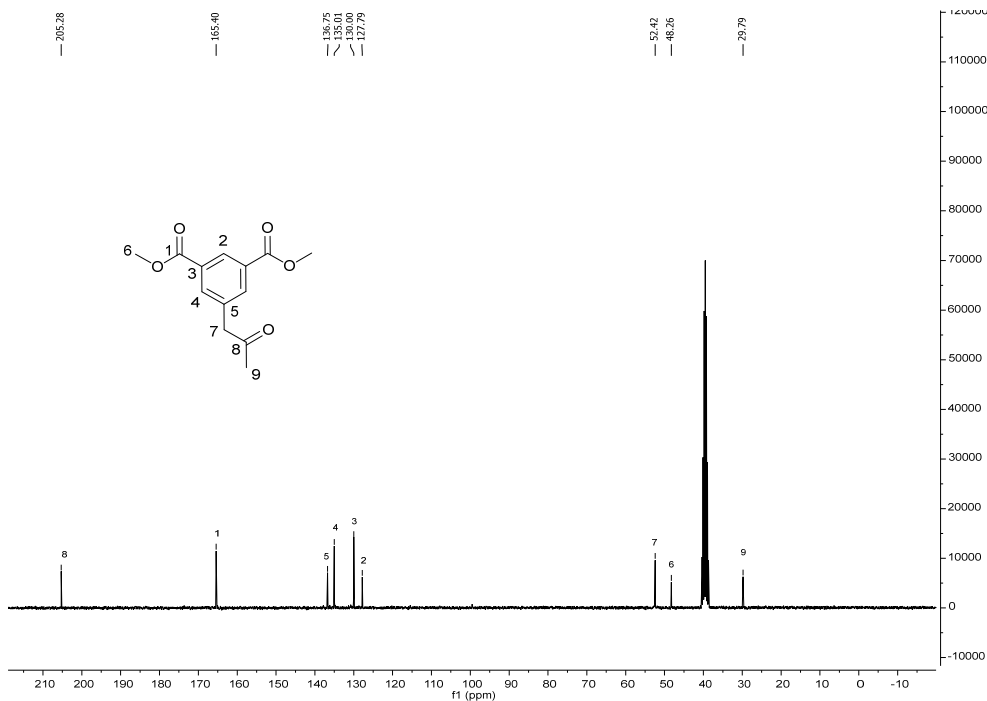


Abbildung S8. ^{13}C -NMR Spektrum von 5-(2-oxopropyl)isophthalsäuredimethylester in DMSO-d_6 .

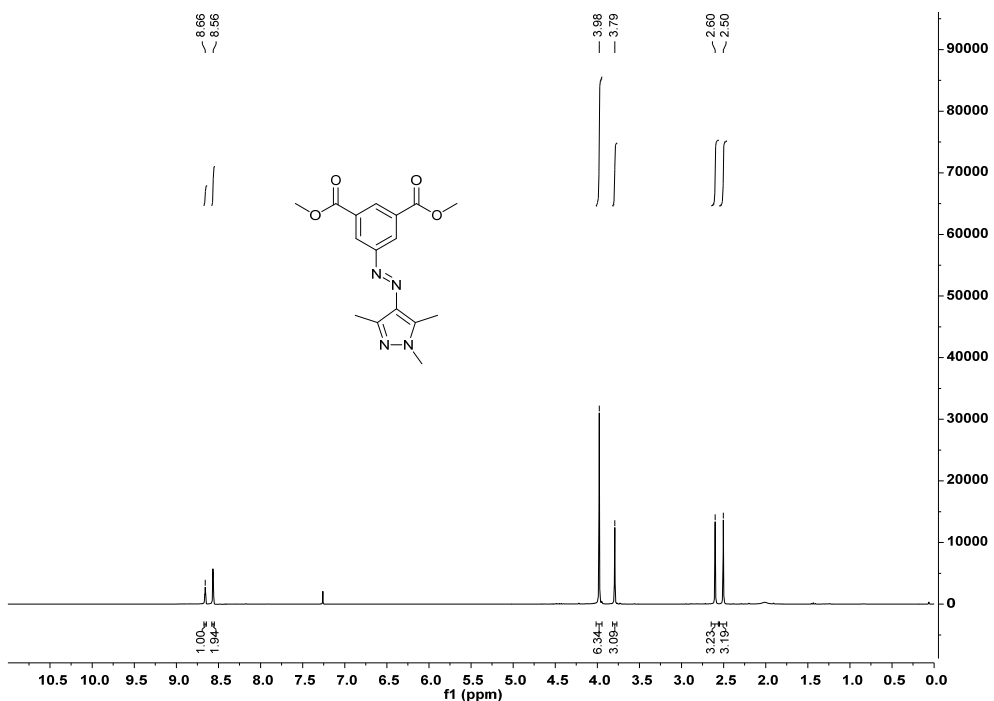


Abbildung S9. ^1H -NMR Spektrum von 5-(4-(1,3,5-Trimethyl-1H-pyrazolyl)azo)isophthalsäuredimethylesters in DMSO-d_6

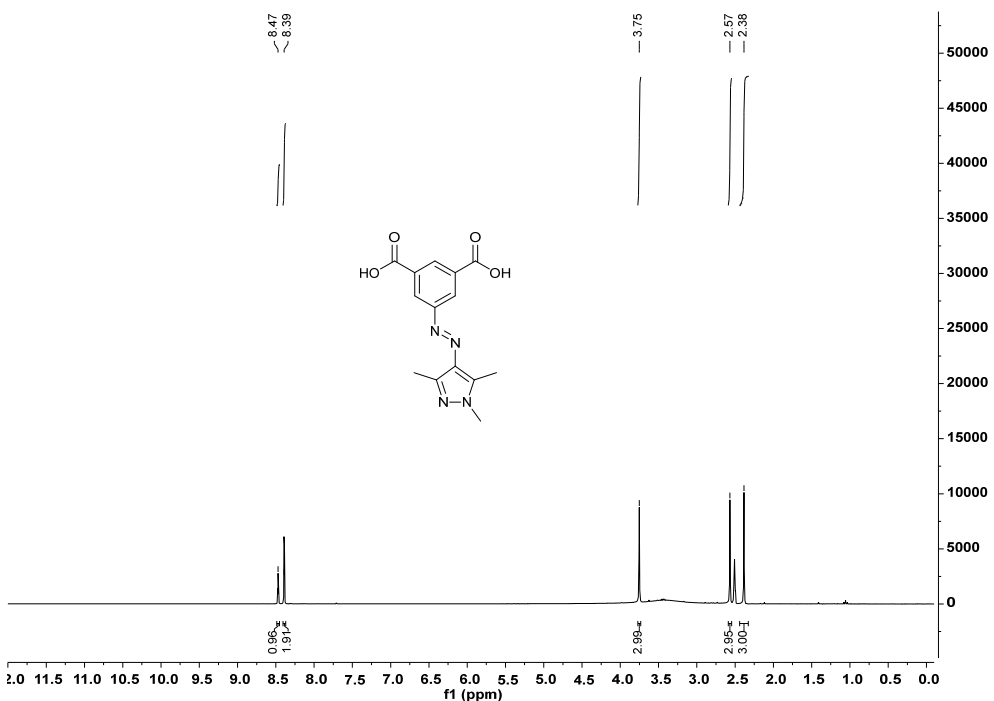


Abbildung S10 ^1H -NMR Spektrum der 5-(4-(1,3,5-Trimethyl-1H-pyrazolyl)azo)isophthalsäure in DMSO-d_6 .

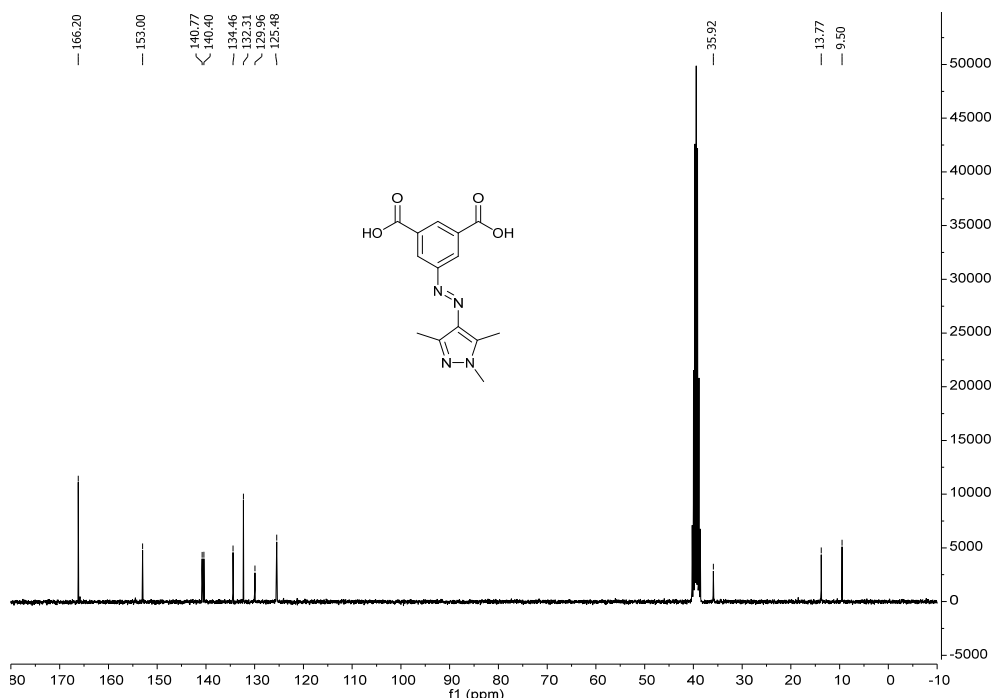


Abbildung S9. ^{13}C -NMR Spektrum der 5-(4-(1,3,5-Trimethyl-1H-pyrazolyl)azo)isophthalsäure in DMSO-d₆.